Why is the atmosphere over land becoming drier?

Exploring the roles of atmospheric and land-surface processes on relative humidity

Kirsten Maria Florentine Weber

Volume I

Submitted in partial fulfillment of the requirement for the degree of Doctor of Philosophy

The University of Sheffield
Department of Geography

March 2022

All sentences or passages quoted in this report from other people's work have been specifically acknowledged by clear cross-referencing to author, work and page(s). Any illustrations that are not the work of the author of this report have been used with the explicit permission of the originator and are specifically acknowledged. I understand that failure to do this amounts to plagiarism and will be considered grounds for failure in this project and the degree examination as a whole.

Kirsten Maria Florentine Weber

Für Papa.

Abstract

Relative humidity (RH) over land has declined steeply since 2000. This drying is broadly consistent from the edge of the deep tropics to the mid-latitudes of both hemispheres, whereas regions equatorward and poleward show increasing RH trends. The drying trend observed in the gridded global humidity dataset, HadISDH, is not captured by the CMIP5 climate models. This can be mostly explained through thermodynamic drivers, i.e. faster land-than-ocean warming under global warming. Insufficient water vapour is thus evaporated and transported from the oceans to keep RH over land constant. However, there are notable regional and seasonal differences in the trend. This thesis explores how dynamical and terrestrial drivers, which are less well represented in the models, can explain changes in RH.

RH was analysed regionally. Strong drying trends were found over eastern Brazil, Tibet, the Caspian Sea, California, Mongolia, southern Africa, southwestern Greenland, eastern USA and the Red Sea. Strong wetting trends were found over Scandinavia, northwestern India and eastern Canada. The relationship between these regional trends and a range of dynamical drivers (precipitation, sea surface temperatures [SST], wind direction and speed, as well as pressure systems and the most common modes of climate variability) were explored. The influence of terrestrial drivers was also examined through evaporation and soil moisture, terrestrial water storage, the vegetation structure, and the modelled carbon cycle response to increased CO_2 through CMIP5 experiments.

Key findings are as follows. The thermodynamic driver can be detected on small scales (e.g. the Caspian Sea). Of the dynamical drivers, a latitudinal shift of the Intertropical Convergence Zone due to tropical Atlantic SST changes reduced precipitation and thus water availability for RH over eastern Brazil. A wind direction change on different spatial scales leads to changes in RH in many regions (e.g. Greenland, southern Africa, eastern Canada). This work found a complex interplay of modes of variability behind the dynamical drivers, often influencing the RH trend through extreme years. In terms of terrestrial drivers, anthropogenic water management and land cover/land-use change affected surface and underground water availability over northern India, Mongolia and Tibet, and a modelled response of plants to increased CO_2 was found to decrease specific humidity and RH by a small amount.

Despite widespread drying trends, no evidence of large scale effects from non-thermodynamical drivers could be found. Instead, dynamical and terrestrial drivers were found to influence RH on regional to sub-regional and seasonal scales, and complex interactions between the drivers and RH were found. Drivers such as the El Niño Southern Oscillation (ENSO) were found to influence strong peaks/troughs in RH in a number of regions which influenced trends over short timescales. This small scale variability in drivers may indicate why climate models do not closely replicate the RH decline.

Acknowledgements

The thesis is the result of a journey shaped by the influence of many people around me. First and foremost, I would like to thank my supervisors for their invaluable support: Dr. Julie Jones, thank you for your treasured guidance throughout my studies, for constantly pushing my boundaries and sharpening my thinking. Thank you, Professor Colin Osborne, for warmly welcoming me into your research group of out-of-the-box thinkers with whom I frequently experienced stimulating interdisciplinary exchange. My thanks also go to you, Dr. Robert Bryant, especially for your optimism and for always encouraging me to achieve to the best of my ability. Special thanks go to you, Dr. Kate Willett, for entrusting me with your dataset and project and for insightful discussions and feedback which brought the topic to life. The four of you are the perfect supervision team!

Professor Grant Bigg and Professor Joy Singarayer examined this thesis. Many thanks for our valuable viva discussion and your suggestions, which helped to improve the presentation of this thesis!

A big thank you goes to my colleagues from the Grantham Centre for Sustainable Futures, the Department of Geography, and the School of Biosciences for always providing important and reasonable insights and knowledge into the subject matter and for your supportive chats; ever-fascinating, sometimes serious, sometimes funny and emotional. Through your internationality, I received impressions of climate conditions from all over the world! My appreciation goes out to my colleagues at the Met Office for their collaboration and unique insights into the vast world of meteorological research, as well as to other distinguished characters I met at conferences, summer schools and seminars for their inspiring thoughts, as well as my mentors who shared their advice with me.

I am hugely appreciative of you, my friends and all those I have made in Sheffield, with whom I have experienced highs and lows, who were patient and who managed to distract me from my thesis. I would like to express my deepest gratitude to my dear family for always believing in me and always being interested in the progress of the thesis. Thank you!

I feel very honoured to be a scholar of the Grantham Centre for Sustainability Futures and to have had so many great opportunities to further my research and for further education and exchange in the context of sustainability. I am endlessly grateful for the studentship that allowed me to conduct this thesis.

Contents

Volume 1

1 Introduction **1**
1.1 The hydrological cycle 2
1.2 Atmospheric humidity 3
1.2.1 Relative humidity (RH) 4
1.2.2 Changes in RH 6
1.3 Drivers of RH 9
1.3.1 The thermodynamic driver 10
1.3.2 Dynamical drivers 11
1.3.3 Terrestrial drivers 19
1.4 Research aims and structure 34

2 Data and methods **39**
2.1 Data 39
2.1.1 Observation based datasets: HadISDH and ERA-Interim 40
2.1.2 Model data: HadGEM2-ES 42
2.1.3 Precipitation from GPCC 44
2.1.4 Satellite-based datasets: GLEAM, GRACE and GIMMS 45
2.1.5 Modes of variability datasets 49
2.2 Methods 51

3 Setting the scene **55**
3.1 Overview of large-scale features of RH: global average and latitudinal bands 56
3.2 Exploring large scale relationships between RH, q and T 60
3.3 Introducing regions with a strong trend in RH 67
3.3.1 Regions with a strong drying trend 69
3.3.2 Regions with a strong wetting trend 87
3.3.3 Finding similarities between regions with a strong RH trend 92
3.4 Differences in representing RH between observations and model HadGEM2-ES 100
3.5 Chapter summary and concluding remarks 106

4 Dynamical drivers **113**
4.1 Exploring the impact of primary physical variables on regional RH 114
4.1.1 Precipitation 120
4.1.2 Eastern Brazil 123

4.1.3 Tibet . . . 132
4.1.4 The Caspian Sea region . . . 138
4.1.5 California . . . 141
4.1.6 Mongolia . . . 145
4.1.7 Southern Africa . . . 149
4.2 Which modes of variability have the strongest relationship with RH? . . . 153
4.2.1 Profiles of modes and annual correlations with RH . . . 155
4.2.2 Ranking of regional correlation strengths between detrended modes and RH . . . 157
4.3 Concluding to what extent the modes reflect RH . . . 160
4.4 Chapter summary and concluding remarks . . . 172

5 Terrestrial drivers **181**
5.1 The interannual relationship between evaporation and RH . . . 182
5.2 Exploring causes of the change in the evaporation processes through water availability . . . 189
5.2.1 The relationship between surface soil moisture and root-zone soil moisture content and RH . . . 190
5.2.2 The ability of GRACE terrestrial water storage to represent RH . . . 192
5.3 Investigating to what extent the land cover influences RH . . . 194
5.4 Model scenario: How does RH respond to the radiative versus the physiological response to CO_2? . . . 198
5.5 Chapter summary and concluding remarks . . . 202

6 Discussion and conclusion **207**
6.1 Understanding the large-scale trend through regional-scale relationships and trends . . . 207
6.1.1 How are regional trend differences manifested? . . . 208
6.1.2 Why do we see apparent latitudinal patterns in the decrease of RH? 208
6.1.3 Issues and further work: spatial heterogeneity and deviations from the four standard seasons . . . 210
6.2 Interconnectivity between the thermodynamic, dynamical and terrestrial drivers . . . 210
6.2.1 Variables are part of both the dynamical and terrestrial stories . . . 211
6.2.2 Challenges in detecting non-thermodynamic drivers . . . 213
6.3 Differences between the observations and the model HadGEM2-ES . . . 214
6.4 Concluding remarks and outlook . . . 215

Bibliography **221**

Volume 2

Figures and supplementary material **259**

List of Tables

2.1 Overview of used datasets (Becker et al., 2013; Berrisford et al., 2011; Collins et al., 2008; Dunn et al., 2016; Martens et al., 2017; Miralles et al., 2010a; Pinzon & Tucker, 2016; Pinzon & Tucker, 2014; Save, 2019; Save et al., 2016; Schneider et al., 2020; Smith et al., 2011; Willett et al., 2014). 40

2.2 Definition of used indices of modes of variability, main references and access to their data. PC stands for principal component, EOF for empirical orthogonal function, the MEI.v2 for multivariate ENSO index version 2, GPH for geopotential height and DMI for dipole mode index (Alexander et al., 2002; Barnston & Livezey, 1987; Dong & Dai, 2015; Enfield et al., 2001; Henley et al., 2015; Higgins et al., 2000; Hurrell, 2003; Hurrell et al., 2003; Mantua & Hare, 2002; Mantua et al., 1997; Marshall, 2003; Newman et al., 2016; Saji & Yamagata, 2003; Thompson & Wallace, 1998, 2000; Thompson et al., 2000; Wolter & Timlin, 2011; Zhang et al., 1997). 50

3.1 Global and latitudinal annual RH trends [%rh decade^{-1}] over land for the full (1973–2017), early (1973 for HadISDH and 1979 for ERA-Interim, until 1999) and late periods (2000–2017) for HadISDH observations and ERA-Interim reanalysis full-land coverage, i.e. not spatially matched to the HadISDH coverage. The corresponding p-value is shown in parentheses. Bold and starred entries state significant trends (very significant for $p < 0.05$ / **, significant for $p < 0.1$ / *). 57

3.2 As for Table 3.1, for global and latitudinal seasonal HadISDH RH trends in the late period (2000–2017) [%rh decade^{-1}]. 59

3.3 As for Table 3.1, for regional annual HadISDH and ERA-Interim RH trends in the early (1970s to 1999) and late periods (2000–2017) [%rh decade^{-1}]. The third number in a cell is the ratio between the number of very significant ($p < 0.05$) and all grid boxes with available data in the region. The regions are arranged in descending order according to their annual HadISDH RH trend in the late period. Framed rows indicate regions with significant opposing HadISDH and ERA-Interim trends between the early and the late period. 68

3.4 Regions with a strong trend in HadISDH RH, annually greater than 1 %rh decade^{-1}, in the late period, and their seasons (Fig. 3.3). Moderate ($r \geq 0.5$, not starred) to strong ($r \geq 0.7$ / **) and very significant ($p < 0.05$) q-RH, T-RH and T-q correlations are also shown for each region and season. The q-RH and T-q correlations are positive, the T-RH correlations negative, unless stated with a "(+)". Significant expected q, T trends based on the correlation are shown ($p < 0.1$ / *; $p < 0.05$ / **); for example, in a region with a negative RH trend and a positive q-RH correlation and a negative T-RH correlation, a negative q trend and a positive T trend would be "expected". The regions and seasons are sorted according to their priority based on their significance of the RH trend and analysed according to this in the further course of this work. . . 94
3.5 Regression coefficients RH(q), RH(T) and $q(T)$ of HadISDH anomalies based on the climatology 1981–2010 for regions and seasons, with very significant ($p < 0.05$), moderate to strong ($r \geq 0.5$) correlations in both the early and the late period in regions with a strong RH trend in the late period (Table 3.4). Double-starred trends or regressions are very significant ($p < 0.05$). NA, if a correlation is not very significant or not moderate to strong over the early and the late period. 97
3.6 Global RH trends [%rh decade^{-1}] (p-values) for annual and seasonal data in HadISDH and HadGEM2-ES *historical* + *historicalExt* in the late period based on a climatology of 1981–2010. Significant ($p < 0.1$) trends are shown with one-star; very significant ($p < 0.05$) trends are marked with a double-star. Significant trends in HadGEM2-ES with the same sign as in HadISDH are in bold. 101
3.7 As for Table 3.6, for regional RH trends. 103

4.1 Trends in SLP and winds of multiple adjacent grid boxes found at Fig. 4.1 for DJF in the late period (2000–2017) and their impact on regions over land. Regions with a strong RH trend in the late period are bold if relevant to the SLP and wind trends. Results from this Table will be discussed in the relevant region sections. 116
4.2 As for Table 4.1, for MAM. 117
4.3 As for Table 4.1, for JJA. 118
4.4 As for Table 4.1, for SON. 119
4.5 Characterisation of modes of variability that are examined for correlations with RH (Dong & Dai, 2015; Fogt et al., 2011; Fogt et al., 2012; Garcia-Soto & Pingree, 2012; Gillett et al., 2006; Gulev et al., 2021; L'Hereux, 2021; Mann et al., 2021; Mantua & Hare, 2002; Saji et al., 1999; Salinger et al., 2001; Stammerjohn et al., 2008; Thompson & Wallace, 2000; Thompson et al., 2000; Wolter & Timlin, 2011). 154
4.6 Annual trends, i.e. change in index per decade, for the AMO index, the SAM index and the IOD index for the early (1973–1999), the late (2000–2017) and the full period (1973–2017). 155

4.7 Ranked regions in descending order, with strong annual and seasonal trends in RH in the late period (Table 3.3) for which RH correlates with modes based on the calculation methods for the ranking. Table 4.9 indicates the season in which the correlations are significant. For each region, the top three modes are mentioned. Bold modes indicate that the associated regional correlation is ranked in their top 3 in Table 4.8. 158
4.8 Ranked modes of variability in descending order that most strongly correlate with regional RH in regions over the late period. The sign of the correlation (+ve, -ve) is given for significant ($p < 0.1$) correlations only. For each mode, the top three regions are mentioned. Bold regions indicate that the associated regional correlation is ranked in their top 3 in Table 4.7, i.e. a double/cross check. 159
4.9 Performance of the highest-ranked, significant ($p < 0.1$) correlations between the modes of variability and regional and seasonal RH in the late period (bold mode-regions correlations in Tables 4.7 and 4.8) on three eligibility criteria (EC) indicating an impact of the mode of variability on RH. Correlations that fulfil all EC are bold. 161
4.10 Correlation coefficients (p-values and ratios between significant and insignificant grid boxes) between regional RH, q and T over eastern Canada and southwestern Greenland and the AO in DJF for the early and late period. Bold values are significant ($p < 0.1$). 163
4.11 As for Table 4.10, for the MEI seasonal correlations in DJF over the northwest of eastern Brazil. 164
4.12 As for Table 4.9, for the MEI with monthly lags. 167
4.13 As for Table 4.10, for the MEI with a lag of -6 months, i.e. in JJA the previous year, and seasonal correlations in DJF over eastern Canada. . . . 167
4.14 As for Table 4.10, for the IPO seasonal correlations in DJF over the northwest of eastern Brazil. 168
4.15 As for Table 4.10, for the AMO seasonal (DJF) and annual correlations, respectively, over eastern Canada and California. 169
4.16 As for Table 4.10, for PNA and PDO seasonal correlations in SON over Scandinavia. 171

5.1 Overview of global correlation pattern between the detrended GLEAM E, E_t, E_i, E_b, E_w and E_s and HadISDH RH, q and T anomalies. 184
5.2 Overview of regional correlations between evaporation and HadISDH RH with significant evaporation [mm day^{-1} decade^{-1}], soil moisture [m^3 m^{-3} decade^{-1}] and precipitation trends in the late period (2000–2017). The correlation data for q and T refer to the full period (1980–2017). 187

6.1 Conclusion of important mechanisms and drivers in regions with a strong negative RH trend over the late period (eastern Brazil, Tibet and the Caspian Sea region), based on Table 3.4, and related sections. 218

6.2 As for Table 6.1, for regions with a strong negative RH trend over the late period (California, Mongolia and southern Africa). 219
6.3 As for Table 6.1, for regions with a strong negative (southwestern Greenland, eastern USA, the Red Sea and Patagonia) or a strong positive RH trend over the late period (Scandinavia, northwestern India and eastern Canada). 220

List of Figures

1.1 Global maps of average HadISDH RH for the four standard seasons and annual values for the climatology over the 1981–2010 period. 259
1.2 Location and elevation of weather stations included in the HadISDH.land-v4.0.0.2017f dataset. White dots indicate weather stations deeper than 340 m below sea level, and brown dots indicate weather stations below sea level but higher than 340 m below sea level. Sky-blue weather stations are at an elevation between 0 and 25 m above sea level, 25 m < blue < 50 m < navy < 100 m < green < 500 m < olive < 1000 m < orange < 1500 m < red < 2000 m < black < 4000 m, and fuchsia dots indicate weather stations at elevations higher than 4000 m. Regions with a strong average trend in RH in the late period (2000–2017), thus, regions of interest in this study (see Chapter 3), are framed in ochre (negative trends) and turquoise (positive trends). 260
1.3 Global annual RH anomalies for HadISDH observation data set (black), ERA-Interim re-analysis (magenta) and historical runs of the CMIP5 Met Office's model HadGEM2-ES (Collins et al., 2011; Jones et al., 2011), relative to the 1976—2005 climatology. Fig. from Dunn et al. (2017). . . . 260
1.4 Global annual land (top) and ocean (bottom) RH anomalies for in situ data set HadISDH (grey, left) and reanalyses data sets ERA5 and ERA5 mask (ERA5-masked to the HadISDH coverage) (purple solid and dotted, respectively) relative to the 1981–2010 base period. Fig. adapted from Willett et al., 2021b, S52, Fig. 2.19. 261
1.5 Annual HadISDH RH trends in anomalies over land for the full period (1973–2017) relative to a climatology over the 1981–2010 period, resolution 5° by 5°. Grid boxes of very significant trends ($p < 0.05$) are framed in grey. Regions with a strong average trend in RH in the late period are framed in ochre (negative trends) and turquoise (positive trends). White space represents either missing data or ocean. 261

1.6 Impacts of rising air temperatures (lower figure) on the hydrological cycle over ocean (left) and over land (right). Aridity increases in warmer climates, leading to expansion of dry climate zones. Evaporation and precipitation increase modestly, but on land, evaporative demand (broken wavy arrows) increases faster than precipitation, because the strong increases in air temperature and consequently saturated water vapour concentration over land (red bars at lower right) exceed growth in actual water vapour concentration (blue bars). Increases in sensible and latent heat (associated, respectively, with temperature and water vapour, and represented by the area of each bar) have the same sum over land and ocean, with sensible heat increasing more over land than oceans and latent heat increasing more over oceans. RH (ratio of blue to red bar length) decreases over land. Fig. and caption taken from Sherwood and Fu (2014), p. 738, Fig. "Warmer, drier". 262

1.7 Differences between weather, climate variability and climate change concerning temporal and spatial scales and examples for changes on different temporal scales. MJO stands for the Madden-Julian Oscillation, ENSO for the El Niño Southern Oscillation, IOD for the Indian Ocean Dipole, PDO for the Pacific Decadal Oscillation and AMO for the Atlantic Multidecadal Oscillation. Fig. by A. Turner. 263

1.8 Global distribution of air mass source regions and main air mass trajectories. Key: mE maritime equatorial (warm, very moist), mT maritime tropical (mild, moist), mTs maritropical subsiding, cT continental tropical (warm, dry), cP continental polar (cold, dry), mP maritime polar (cool, moist), A arctic, AA antarctic and cA continental air (very cold, very dry; not shown). Fig. and caption taken from O'Hare et al. (2014) (p. 101, Fig. 4.12) based on Robinson and Henderson-Sellers (1999) (p. 161). 264

1.9 Schematic representation of the neutral phase of the ENSO in the Pacific Ocean. Fig. taken from O'Hare et al., 2014, p. 132, Fig. 5.5, a. 265

1.10 Schematic representation of El Niño (left) and La Niña (right) atmospheric and oceanic conditions in the Pacific Ocean. Fig. taken from O'Hare et al., 2014, p. 132, Fig. 5.5, b and c. 265

1.11 Global impact of El Niño (above) and La Niña (below) on regional precipitation (left) and temperature (right) (ENSO impacts. Met Office. Available at: https://www.metoffice.gov.uk/research/climate/seasonal-to-decadal/gpc-outlooks/el-nino-la-nina/enso-impacts [Accessed November 25, 2021]). 266

1.12 World humidity classes (World Atlas of Desertification, United Nations Environment Programme 1997). Drylands are classified into four ranges of the Aridity Index (AI, the ratio between the mean annual precipitation and the mean annual potential evaporation): hyperarid, AI<0.05 (7.5% of global land area); arid, 0.05<AI<0.20 (12.1% land); semi-Arid, 0.20<AI<0.50 (17.7% land); dry subhumid, 0.50<AI<0.65 (9.9% land). Fig. and caption taken from Fensholt et al., 2015, p. 160, Fig. 8.1. 267
1.13 Present-day map (1980–2016) of Koeppen-Geiger classifications. Fig. and capture taken from Fig. 1 in Beck et al. (2018). 267
3.1 HadISDH global annual time series and trends over land for the early (1973–1999) and the late periods (2000–2017). Linear trends for RH are turquoise if positive or ochre if negative; for q and T trends are shown by an up arrow if positive or down arrow if negative. The RH trends are based on anomalies (black line), the q and T trends on standardised anomalies (respectively, blue and orange dots and line), relative to a climatology over the 1981–2010 period. Starred trends are significant ($p < 0.1$), double starred trends are very significant ($p < 0.05$). 268
3.2 As for Fig. 3.1, for global seasonal HadISDH data. 269
3.3 As for Fig. 1.5, for seasonal HadISDH RH trends for the early (1973–1999, left column), the late (2000–2017, centre column) and the full periods (right column). 270
3.4 Annual correlations between the detrended HadISDH T and q anomalies over land, relative to a climatology over the 1981–2010 period, in the early (left) and the late period (right). Grid boxes of very significant correlations ($p < 0.05$) are framed in grey. Regions with a strong average trend in RH in the late period are framed in ochre (negative trends) and turquoise (positive trends). White space represents either missing data or ocean. 271
3.5 As for Fig. 3.4, for seasonal correlations between the HadISDH T and q in the late period. 271
3.6 As for Fig. 3.4, for annual and seasonal HadISDH q and RH in the late period. Positive (negative) q trends relative to a climatology over the 1981–2010 period are marked with an 'x' (red 'o'), if very significant ($p < 0.05$). 272
3.7 As for Fig. 3.6, for HadISDH T and RH. 273
3.8 Annual correlations for the detrended HadISDH anomalies over land, relative to a climatology over the 1981–2010 period, between q-RH (positive: green, negative: pink) and T-RH (positive: purple, negative: orange) in the early (left) and the late periods (right). The correlation strength between q-RH and T-RH was compared, and the stronger one plotted for the grid box. Grid boxes of very significant correlations ($p < 0.05$) are crossed. White space represents either missing data or ocean. 274
3.9 As for Fig. 1.5, for annual HadISDH RH trends for the early and the late periods. 274

3.10 As for Fig. 3.2, for eastern Brazil. 275
3.11 As for Fig. 3.2, for Tibet. 275
3.12 As for Fig. 3.2, for the Caspian Sea region. 276
3.13 As for Fig. 3.2, for California. 276
3.14 As for Fig. 3.2, for Mongolia. 277
3.15 As for Fig. 3.2, for southern Africa. 277
3.16 As for Fig. 3.2, for southwestern Greenland. 278
3.17 As for Fig. 3.2, for the eastern USA. 278
3.18 As for Fig. 3.2, for the Red Sea. 279
3.19 As for Fig. 3.2, for Patagonia. 279
3.20 As for Fig. 3.2, for the western Mediterranean region. 280
3.21 As for Fig. 3.2, for Scandinavia. 280
3.22 As for Fig. 3.2, for western Alaska. 281
3.23 As for Fig. 3.2, for northwestern India. 281
3.24 As for Fig. 3.2, for eastern Canada. 282
3.25 As for Fig. 3.2, for the East China Sea. 282
3.26 HadISDH and HadGEM2-ES *historical* + *historicalExt* RH global annual anomalies over land for the early and the late periods (for HadISDH: black; for HadGEM2-ES $r2i1p1$: red, $r3i1p1$: green, $r4i1p1$: blue), relative to a climatology over the 1981–2010 period. 283
3.27 As for Fig. 3.2, for HadISDH RH anomalies (black, continuous line) and the HadGEM2-ES *historical* + *historicalExt* simulation run $r2i1p1$ RH anomalies (black, dashed line) and q and T. 284
3.28 As for Fig. 3.27, for the HadGEM2-ES *historical* + *historicalExt* simulation run $r3i1p1$. 284
3.29 As for Fig. 3.27, for HadGEM2-ES *historical* + *historicalExt* simulation run $r4i1p1$. 285
3.30 As for Fig. 3.4, for annual (bottom) and seasonal (upper four rows) HadGEM2-ES *historical* + *historicalExt* simulation runs $r2i1p1$ (left column), $r3i1p1$ (centre column) and $r4i1p1$ (right column) correlations between T and q in the full period. 286
3.31 As for Fig. 3.30, for correlations between q and RH in the full period. . . 287
3.32 As for Fig. 3.30, for correlations between T and RH in the full period. . . 288
4.1 Annual (bottom) and seasonal (upper four rows) ERA-Interim quivered u10, v10 trends (arrows) and SLP trends (colour) for the early (1979–1999, left column) and the late periods (2000–2017, right column) relative to a climatology over the 1981-2010 period. Grid boxes of very significant ($p < 0.05$) positive (negative) u10 and v10 trends separately are stated in blue (red) letters 'u' and 'v', respectively. Only grid boxes of very significant ($p < 0.05$) SLP trends are coloured. Regions with a strong average trend in RH in the late period are framed in ochre (negative trends) and turquoise (positive trends). White space represents either missing data or ocean. 289

4.2 Annual and seasonal correlations between detrended GPCC precipitation and HadISDH RH anomalies over land in the late period, relative to a climatology over the 1981-2010 period. Grid boxes of very significant trends ($p < 0.05$) are framed in grey. Grid boxes of significant ($p < 0.1$) correlations are framed in grey; significantly positive (negative) trends in precipitation relative to the climatology over the 1981–2010 period show a blue 'x' (red 'o'). 290
4.3 Correlations between anomalies of ERA-Interim SST, 10 m wind vectors in u and v direction, wind speed and SLP (top to bottom) and regional GPCC precipitation over eastern Brazil (DJF; left column) and southern Africa (SON; right column) for the late period (2000–2017). Grid boxes of very significant ($p < 0.05$) correlations are framed in grey; significantly positive (negative) trends in primary physical variables relative to the climatology over the 1981-2010 period show a blue 'x' (red 'o'). 291
4.4 Correlations between ERA-Interim anomalies of SST, 10 m wind vectors in u and v direction, wind speed and SLP (top to bottom) and regional HadISDH RH over eastern Brazil (DJF) for the early period (1979–1999, left column), the late period (2000–2017, centre column) and the full period (right column). Grid boxes of very significant ($p < 0.05$) correlations are framed in grey; significantly ($p < 0.1$) positive (negative) trends in primary physical variables relative to the climatology over the 1981–2010 period show a blue 'x' (red 'o'). 292
4.5 Correlations between ERA-Interim anomalies of SST, 10 m wind vectors in u and v direction, wind speed and SLP (top to bottom) and regional HadISDH q (left) and T (right) over eastern Brazil (DJF) for the late period (2000–2017). Grid boxes of very significant ($p < 0.05$) correlations are framed in grey, significantly positive (negative) trends in primary physical variables relative to the climatology over the 1981-2010 period show a blue 'x' (red 'o'). 293
4.6 As for Fig. 4.4, for eastern Brazil (MAM). 294
4.7 As for Fig. 4.5, for eastern Brazil (MAM). 295
4.8 As for Fig. 4.4, for eastern Brazil (JJA). 296
4.9 As for Fig. 4.5, for eastern Brazil (JJA). 297
4.10 As for Fig. 4.4, for eastern Brazil (SON). 298
4.11 As for Fig. 4.5, for eastern Brazil (SON). 299
4.12 As for Fig. 4.4, for Tibet (JJA). 300
4.13 As for Fig. 4.5, for Tibet (JJA). 301
4.14 As for Fig. 4.4, for Tibet (SON). 302
4.15 As for Fig. 4.5, for Tibet (SON). 303
4.16 As for Fig. 4.4, for the Caspian Sea region (JJA). 304
4.17 As for Fig. 4.5, for the Caspian Sea region (JJA). 305
4.18 As for Fig. 4.4, for California (annual). 306
4.19 As for Fig. 4.5, for California (annual). 307
4.20 As for Fig. 4.4, for Mongolia (DJF). 308

4.21 As for Fig. 4.5, for Mongolia (DJF). 309
4.22 As for Fig. 4.4, for Mongolia (MAM). 310
4.23 As for Fig. 4.5, for Mongolia (MAM). 311
4.24 As for Fig. 4.4, for southern Africa (JJA). 312
4.25 As for Fig. 4.5, for southern Africa (JJA). 313
4.26 As for Fig. 4.4, for southern Africa (SON). 314
4.27 As for Fig. 4.5, for southern Africa (SON). 315
4.28 Time series for the indices of modes of variability over the full period (1973–2017): from top to bottom, in the left column, the AO, the MEI, the PDO, the SAM, and in the right column, the AMO, the IPO, the PNA and the IOD. 316
4.29 Annual correlation maps between modes of variability and RH over land for the full period (1973–2017). Grid boxes of significant correlations ($p < 0.1$) are framed in grey. 317
4.30 Annual (bottom line) and seasonal (upper four rows) correlation maps between the detrended AO and HadISDH RH over the early, the late and the full periods (left to right). Grid boxes of significant correlations ($p < 0.1$) are framed in grey. 318
4.31 As for Fig. 4.30, for the AMO. 319
4.32 As for Fig. 4.30, for the ENSO (MEI). 320
4.33 As for Fig. 4.30, for the IPO. 321
4.34 As for Fig. 4.30, for the PDO. 322
4.35 As for Fig. 4.30, for the PNA. 323
4.36 As for Fig. 4.30, for the SAM. 324
4.37 As for Fig. 4.30, for the IOD. 325
4.38 Time plots and linear fits of HadISDH RH anomalies (light blue) in southwestern Greenland (top) and Eastern Canada (bottom) in DJF and by the regression through the AO (red) estimated RH (dark blue dashed), furthermore q (dark green) and T standardised anomalies (yellow) over the full period (1973–2017). Positive AO phases are indicated by filled red dots and negative phases by blue stripes. The vertical line indicates the year 2000, the end of the early period and the start of the late period. 326
4.39 As for Fig. 4.38, for HadISDH anomalies in the northwest of eastern Brazil (top) and eastern Brazil (bottom) and the MEI in DJF. 326
4.40 As for Fig. 4.38, for HadISDH anomalies in eastern Canada (DJF) and the MEI with a lag of -6 months, i.e. in JJA the previous year. 326
4.41 As for Fig. 4.38, for HadISDH anomalies in the northwest of eastern Brazil and the IPO in DJF. 327
4.42 As for Fig. 4.38, for HadISDH anomalies in California (annual; top) and eastern Canada (DJF; bottom) and the AMO. 327
4.43 As for Fig. 4.38, for HadISDH anomalies in Scandinavia and the PDO (top) and the PNA (bottom) in SON. 327

5.1 Correlations between the detrended GLEAM E and HadISDH RH, q and T anomalies over land for annual data (bottom) and the four standard seasons (upper four rows) over the full period (1980–2017). Grid boxes of significant ($p < 0.1$) correlations are framed in grey; significantly positive (negative) trends in GLEAM E relative to the climatology over the 1981–2010 period show a blue 'x' (red 'o'). Regions with a strong average trend in RH in the late period are framed in ochre (negative trends) and turquoise (positive trends). White space represents either missing data or ocean. . . . 328
5.2 As for Fig. 5.1, for E_t. . . . 329
5.3 As for Fig. 5.1, for E_i. . . . 330
5.4 As for Fig. 5.1, for E_b. . . . 331
5.5 As for Fig. 5.1, for E_w. . . . 332
5.6 As for Fig. 5.1, for E_s. . . . 333
5.7 Correlations between the detrended GLEAM E and HadISDH RH anomalies over land for annual data (bottom) and the four standard seasons (upper four rows) over the early (1980–1999), the late (2000–2017) and the full period (1980–2017). Grid boxes of significant correlations ($p < 0.1$) are framed grey; significantly positive (negative) trends in GLEAM E relative to the climatology over the 1981–2010 period show a blue 'x' (red 'o'). . . . 334
5.8 As for Fig. 5.7, for E_t. . . . 335
5.9 As for Fig. 5.7, for E_i. . . . 336
5.10 As for Fig. 5.7, for E_b. . . . 337
5.11 As for Fig. 5.7, for E_w. . . . 338
5.12 As for Fig. 5.7, for E_s. . . . 339
5.13 As for Fig. 5.7, for surface soil moisture. . . . 340
5.14 As for Fig. 5.7, for root-zone soil moisture. . . . 341
5.15 Correlations between the detrended GRACE TWS and HadISDH RH anomalies over land for annual data (bottom) and the four standard seasons (upper four rows) over the late period (2002–2017) with no temporal lag (left column), a temporal lag of -3 months (centre column) and a temporal lag of -6 months (right column) for TWS. Grid boxes of significant correlations ($p < 0.1$) are framed grey; significantly positive (negative) trends in TWS relative to the climatology over the 2005–2009 period show a blue 'x' (red 'o'). . . . 342
5.16 Correlations between the detrended GIMMS NDVI and HadISDH q and T anomalies over land for annual data (bottom) and the four standard seasons (upper four rows) over the full period (1982–2015). Grid boxes of significant ($p < 0.1$) correlations are framed in grey; significantly positive (negative) trends in the NDVI relative to the climatology over the 1982–2010 period show a blue 'x' (red 'o'). . . . 343

5.17 Correlations between the detrended GIMMS NDVI and HadISDH RH anomalies over land for annual data (bottom) and the four standard seasons (upper four rows) over the early (1982–1999), the late (2000–2015) and the full period (1982–2015). Grid boxes of significant correlations ($p < 0.1$) are framed grey; significantly positive (negative) trends in the NDVI relative to the climatology over the 1982-2010 period show a blue 'x' (red 'o'). 344
5.18 Seasonal HadGEM2-ES huss (q), tas (T) and hurs (RH) trends for the experiment $esmFdbk2$ for the full period (1860–2099) relative to a climatology over the 1981–2010 period. Grid boxes of very significant trends separately ($p < 0.05$) are framed in grey. Regions with a strong average trend in RH in the late period in the HadISDH observations are framed in ochre (negative trends) and turquoise (positive trends). 345
5.19 As for Fig. 5.18, for HadGEM2-ES $esmFixClim2$. 346
5.20 Correlations between the detrended ERA-Interim wind speed and GLEAM E over land for annual data (bottom) and the four standard seasons (upper four rows) over the early (1980–1999) and the late periods (2000–2017). Grid boxes of significant ($p < 0.1$) correlations are framed in grey; significantly positive (negative) trends in si10 relative to the climatology over the 1982–2010 period show a blue 'x' (red 'o'). 347
S1 As for Fig. 1.1, for q. 348
S2 As for Fig. 1.1, for T. 349
S3 As for Fig. 1.1, for GPCC precipitation. 350
S4 As for Fig. 1.1, for ERA-Interim SST, wind speed, SLP and 10 m wind vectors (left to right). 351
S5 As for Fig. 1.5, for seasonal HadISDH q trends for the early period (1973-1999, left column), the late period (2000-2017, centre column) and the full period (right column). 352
S6 As for Fig. 1.5, for seasonal HadISDH T trends for the early period (1973-1999, left column), the late period (2000-2017, centre column) and the full period (right column). 353
S7 Annual deviations from the Clausius-Clapeyron equation (7% q increase for 1 K increase in T) as the required increase in q to achieve agreement with the theory over the early (left) and the late periods (right), for positive T trends and q increase $< 7\%/\mathrm{K}$ only. Grid boxes with a significant ($p < 0.05$) decrease in q are marked with an 'o', with a significant increase in T are marked with an 'x'. Grey grid boxes indicate a T decrease or a q increase $> 7\%/\mathrm{K}$. 354
S8 Similar to Fig. 3.8, the coexistence of seasonal HadISDH q-RH and T-RH correlations ($r > 0.45$). 355
S9 As for Fig. 4.3, for eastern Brazil (SON) and northwestern India (annual). 356
S10 As for Fig. 4.3, for the Caspian Sea region (JJA) and Scandinavia (JJA). 357
S11 As for Fig. 4.4, for southwestern Greenland (DJF). 358
S12 As for Fig. 4.4, for the eastern USA (annual). 359

S13 As for Fig. 4.4, for the Red Sea region (MAM). 360
S14 As for Fig. 4.4, for the Red Sea region (JJA). 361
S15 As for Fig. 4.4, for the Red Sea region (SON). 362
S16 As for Fig. 4.4, for Scandinavia (JJA). 363
S17 As for Fig. 4.4, for Scandinavia (SON). 364
S18 As for Fig. 4.4, for northwestern India (annual). 365
S19 As for Fig. 4.4, for eastern Canada (DJF). 366

1 Introduction

Our blue planet stands out due to its high water content in different aggregate states. Above all, liquid and gaseous water enable life on Earth. The majority of water withdrawal is attributed to agriculture (Gruère et al., 2020; Hoekstra & Mekonnen, 2012). A lack of water results in droughts, a reduction in biodiversity and in hot areas, wildfires. If there is more water than usual, flooding can occur. Flooding events, as well as droughts and the spread of arid regions, have increased in recent decades, among other things as the consequences of climate change on the long-term scale and climate variabilities on shorter time scales (Dessler & Sherwood, 2009; McKinnon et al., 2021; Spinoni et al., 2013). Under anthropogenically increasing temperatures our climate changes, so does the distribution of water and its solid, liquid, and gaseous state (Masson-Delmotte et al., 2021). It is essential to understand the mechanisms of the climate altering the hydrological cycle in order to be able to adjust to abnormalities in the water supply, to adapt to them (adaptation) or even to prevent severe abnormalities (mitigation).

There is a multitude of variables relating to the hydrological cycle (Dai, 2011). The World Meteorological Organization recommends the Standardised Precipitation Index (SPI) for drought monitoring (Geneva, 2012; Svoboda & Fuchs, 2017). Precipitation is therefore a frequent indicator of such drought indexes, as are evaporation and temperature in application-specific cases (Berg et al., 2016; Cook et al., 2014; Scheff & Frierson, 2015). Relative humidity (RH), focussed on in this study, is a measure of how saturated the atmosphere is and also ascribed to a high potential as a drought indicator (Farahmand et al., 2015).

RH expresses the humidity saturation of the air. It determines how much moisture can still be absorbed before condensation occurs. When near-surface RH is low, it draws moisture into the air, for example, via evaporation from the ground (high vapour pressure deficit, VPD) and open water resources. Droughts are coupled with low RH (Farahmand et al., 2015). When an air parcel cools it is less able to hold moisture; the RH value increases. High RH levels lead to condensation and eventually precipitation, with flooding as a possible extreme consequence. Precipitation and evaporation as feeders of the hydrological cycle are thus directed by RH. By governing the capacity of the air to evaporate, hold and condense water vapour, RH also plays an important role in the energy budget as these processes take up heat energy from the surface, store and release it respectively. The spatially uneven distribution of RH results in a gradient that causes energy transfer through latent heat transfer, including kinetic energy, such as winds.

The occurrence of pathogens and their spread are often linked to air humidity and temperature, thus, RH (Chan et al., 2011; Lowen et al., 2007; Ma et al., 2020; Sajadi et al., 2020). Living beings such as humans, animals and plants are remarkably sensitive to RH, since, in particular, the evaporative cooling (VPD in plants) and thus the ability to deal with heat is governed by RH. Because of its central position in the hydrological cycle and its link to extreme climate events and well-being, diseases and technology, RH is a variable that is essential to understand. Understanding RH allows representing RH realistically and appropriately assessing the impact of its change, including extreme impacts on society and the economy, such as droughts and flooding, heat stress and crop health. So far, Coupled Model Intercomparison Project Phase 5 (CMIP5) models underestimate the recent decrease in RH, which, therefore, adds uncertainty to climate impact projections related to RH. More accurate modelling would lead to better predictions, higher certainty of all components of the hydrological cycle and suitable mitigation and adaptation in particular in the context of a changing climate.

This Chapter introduces the significance of RH in the water cycle (Sections 1.1 and 1.2.1). Furthermore, the change in RH within the last fifty years is emphasised (Section 1.2.2). Three potential influences on the long-term, i.e. the decadal, course of RH (Section 1.3) are presented. The research plan for the exploration of factors influencing RH is presented in Section 1.4.

1.1 The hydrological cycle

Life on Earth presupposes water. The movement and storage of this water on different spheres in our planet is described by the hydrological cycle. No water is lost in the hydrological cycle, but the water changes its physical state depending on temperature and air pressure. The main engine for the changes and the transport of water is solar energy. The energy in the water cycle transforms from (sensible) energy, i.e. temperature changes, to latent (hidden) heat, i.e. changes in the aggregate state of water, and vice versa.

The world's oceans store most of the water on our planet, namely 97%. They make up two-thirds of the earth's surface. This makes them the largest contributor to evaporation (Sherwood & Fu, 2014). Evaporation is the transition of molecules from the liquid to the gaseous phase. It happens when there is a saturation gradient between the two phases. Water molecules move with the gradient until the phases are in equilibrium. By adding energy, such as heat, the movements of the water molecules are accelerated and thus the transition from the liquid phase on the water surface to the gas phase is favoured.

The water vapour rising on the sea surface cools adiabatically with increasing altitude. When the temperature drops, the movement of the molecules slows down. The water droplets accumulate on each other (homogeneous condensation) or on tiny aerosols (heterogeneous condensation). Latent heat is released. A cloud emerges from growing liquid droplets. Since the supersaturation is seldom exceeded in a cloud and the growth of a water droplet due to the accidental collision of the molecules is excluded, the heterogeneous condensation predominates. At low temperatures in a cloud, ice crystals and snowflakes can also form.

The cloud becomes larger, and liquid droplets fall due to their weight. On its way down, it picks up more drops of water. The increasingly larger water droplets ultimately fall as precipitation. Most of the precipitation ends up in the ocean; the other part falls on the mainland. Via the continent, the water either reaches the oceans via the groundwater via rivers – the water cycle closes – or the water evaporates via an organic or inorganic layer, such as plants or soil. As soon as a layer is involved between the liquid water and the atmosphere, the evaporation process is influenced by additional variables, such as the physiological properties of the plants or the nature of the soil.

The Bowen ratio β (Equation 1.1) describes the type of heat transfer and results from the ratio of sensible heat (Q_h) to latent heat (Q_e) flux.

$$\beta = \frac{Q_h}{Q_e} \tag{1.1}$$

The closer the value approaches zero, the higher the latent heat flux. This is the case over tropical oceans and humid areas, where sufficient water is available for evaporation (Oke, 2002). Where water availability is limited, in semi-arid areas and deserts, most of the energy is converted into sensible heat flux. The Bowen ratio is then very large. High northern latitudes also have large Bowen ratios (Peterson et al., 2011).

1.2 Atmospheric humidity

An important measured variable in the water cycle is atmospheric humidity. It can not only provide information about the processes in the water cycle, precipitation and soil evaporation, but its value also has a strong influence on living beings between the soil and the sky. The human body perceives temperatures more strongly with high atmospheric moisture since water conducts better than air and due to increased re-condensation, i.e. lower net evaporation. Ambient air temperature can thus be better transported to the body. In warm, humid weather, we feel the heat more strongly, and it is more difficult for us to sweat and thus to cool ourselves. In cool, wet weather, we perceive the cold more strongly. Air humidity has an influence on our comfort and ultimately also on our health. Many animal and plant species feel the same way.
Humidity determines biodiversity. Mosquitoes, for example, multiply fastest in damp heat (Chen et al., 2010; Descloux et al., 2012). The increase in mosquito numbers can lead to an increased transmission of the disease to humans. Viruses behave according to changes in RH (Chan et al., 2011; Lowen et al., 2007; Ma et al., 2020; Sajadi et al., 2020). Linked to the degree of atmospheric saturation with moisture, floods and drought also have far-reaching consequences. People are forced to leave their homes. Social, political

and financial individual, national and international conditions are greatly changed by changes to the hydrological cycle.
Regarding humidity, i.e. energy is transported via water droplets: water vapour can absorb heat and also release it again. Sensible heat is converted into latent heat and vice versa. Atmospheric water vapour also serves as a greenhouse gas (GHG), through the water-vapour feedback (Dessler & Sherwood, 2009).

Humidity is measured with a hygrometer (Wiederhold, 2012). The earliest developed method is that of the psychrometer, which uses the dry-bulb temperature (T), in common language the air temperature, and the wet-bulb temperature (T_w). The difference between the two temperatures is measured: the dry-bulb thermometer is in the area to be measured, the wet-bulb thermometer in moisture, e.g. wrapped in a damp cloth. The water in the cloth evaporates faster in dry ambient air than in humid air and cools the thermometer down through evaporation. Sensible heat is converted into latent heat. The difference between the two measured temperatures is higher with dry air than for air with a high moisture content. The T and T_w are the same when RH = 100 %rh. A hygrometer also uses other techniques that refer to changes in various sizes. These include changing the weight of a water-absorbing object or changing its properties, such as the extension of a hair, or changing electrical parameters such as conductivity. In the global context, in-situ monitoring products like the Met Office Hadley Centre Integrated Surface Database (ISD) Humidity (HadISDH) dataset and reanalysis products like the European Reanalysis (ERA-Interim; Section 2.1.1) monitor humidity.

1.2.1 Relative humidity (RH)

The humidity content in the atmosphere is usually quantified as the absolute humidity [g m^{-3}], the specific humidity (q) [g kg^{-1}], the mixing ratio or the RH [%rh]. While absolute humidity only includes information about the mass of water vapour, q compares the latter to the total mass of air. The mixing ratio is the relation between the mass of water vapour and the mass of dry air. The RH, in addition, depends on T (Dunn et al., 2017; Lawrence, 2005). It is defined as the amount of water vapour in the air compared to the amount of water that could potentially be held as vapour at that temperature (Equation 1.2; Willett et al., 2014).

$$\mathrm{RH} = \frac{e_a}{e_s} \tag{1.2}$$

where e_a is the actual water vapour pressure and e_s is the water vapour pressure at the point of saturation. The e_a and e_s can each be substituted by the q (q_a/q_s) or by the mixing ratios (r_a/r_s; Barry and Chorley, 2009). This research looks at near-surface RH.

The vapour pressure deficit (VPD), the difference between e_s and e_a, is equivalent to the RH and, in contrast to the RH, is quasi-linearly linked to the evaporation rate. The higher the VPD, the less saturated the air is; a VPD of zero equals RH = 100 %rh. As a humidity gradient between vegetation and atmosphere, VPD is a measure that is used in particular in plant transpiration (evapotranspiration, E_t) and terrestrial water loss (e.g. El-Sharkawy et al., 1985; Grossiord et al., 2020; Kapos, 1989). Due to global warming, VPD has been increasing since the late 1990s with an increasing trend predicted, resulting in weaker gross primary productivity (GPP; Grossiord et al., 2020; Yuan et al., 2019).

The water vapour pressure at the point of saturation increases with temperature. Under typical atmospheric conditions, this is expressed by the Clausius-Clapeyron relation (Equation 1.3).

$$\frac{\mathrm{d}e_s}{\mathrm{d}T} = \frac{L_v(T)e_s}{R_v T^2} \tag{1.3}$$

where T is the air temperature, L_v specific latent heat of evaporation of water depending on T, R_v gas constant of water vapour; 461.5 J K^1 kg^1. The Clausius-Clapeyron relation assumes that the moisture supply is unlimited, for instance, evaporation over the ocean. The exponential dependence of the saturation vapour pressure on the temperature was empirically approximated by August, Roche and Magnus (Equation 1.4; Koutsoyiannis, 2012; Lawrence, 2005; Thiis et al., 2017).

$$e_s(T) = 6.1094 \cdot e^{\frac{17.625 \cdot T}{243.04+T}} \tag{1.4}$$

where e_s is in [hPa] and the air temperature T in [°C]. Warm air contains more energy than cold air. The energy keeps air and water molecules moving and not sticking to each other and condensing. Therefore, the warmer the air, the more water the air is able to hold. The holding capacity is increased by 7 %rh per 1 K increase of temperature. Following the Clausius-Clapeyron law, RH stays constant. If there is an increase of less than 7% of humidity, RH decreases. This is the case when water supply is limited.

Both the Clausius-Clapeyron equation and the Bowen ratio can describe RH and its change as a function of T and q and by means of energy balances.

Figs. 1.1, S1 and S2 show the global maps of average annual HadISDH and seasonal RH, q and T, respectively, for the climatology over the 1981–2010 period. These figures are used in the following results Chapters. They also provide information about the data coverage of the observation dataset HadISDH compared to the spatially complete reanalysis data of ERA-Interim.

RH is highest in the low-pressure troughs in the low latitudinal tropics, especially over the Amazon rainforest and the Congo Basin (up to 90 %rh; Fig. 1.1). The maximum value shifts northwards with the Intertropical Convergence Zone (ITCZ) in boreal summer. The ITCZ is the zone where the sun warms the earth most. The high latitudes show a strong summer-winter temperature contrast (Fig. S2), so that, especially in the summer months, there are strong evaporation rates and an increase in RH. In the higher low latitudes and the mid-latitudes, RH is lowest in the deserts (up to around 20 %rh).

Very little water is available there. The dry areas are more extensive in summer. There is a constant moisture supply on the coasts, so that RH values there are generally higher in contrast to inland areas. Furthermore, the RH grid box values depend on the average of the included weather stations, thus, on their location, including their altitude (Fig. 1.2; Peixoto and Oort, 1996).

The q and T follow a similar latitudinal pattern, with the highest values in the tropics declining towards the high latitudes (Figs. S1 and S2). The pattern tracks north and south with the ITCZ seasonally. With some regional and seasonal variations (e.g. Tibetan Plateau with very low q due to high elevation or very high summer temperatures in northern Africa), the q and T climatologies result in the global RH climatologies in Fig. 1.1. Regional links between q, T and RH are discussed in Chapter 3.

The sole in situ observations-only global climate-data product for humidity is HadISDH (Willett et al., 2013). The observational dataset is based on the National Oceanic and Atmospheric Administration's (NOAA) synoptic (hourly) ISD. The ISD uses the dry-bulb temperature T and the dew point temperature (T_d), calculated from T and the wet-bulb temperature (T_w), to calculate RH via the vapour pressure (e) (Equation 1.4). The results are averaged monthly and quality checked. The final HadISDH.land dataset counts more than 4000 weather stations worldwide with the highest density in NH urban areas and between 100 m and 500 m above sea level (Fig. 1.2). The weather station at the lowest altitude is in Ghor es-Safi in the Jordan valley (350 m below sea level) and the station at the highest altitude is located in Xainza, Tibet (4670 m above sea level). For the HadISDH.marine dataset, weather stations on ocean platforms, moored buoys and, in particular, ships, mostly north of 20°S, provide humidity and temperature data over the ocean (Willett et al., 2020; Zurbenko & Luo, 2015). More detailed information on the monitoring product HadISDH and the reanalysis dataset ERA-interim, which combine observations with numerical models, and, thus, offers more complete information regarding time and space, is to be found in Section 2.1.1.

1.2.2 Changes in RH

The atmospheric near-surface RH changes due to changes in q or T that do not correspond to the Clausius-Clapeyron equation. RH would increase if q rises more than 7% per degree Celsius increase in T, or vice versa.

Global observations (HadISDH) and reanalysis data (ERA-Interim) show minor deviations and even a slight positive trend in near-surface atmospheric RH over land from 1973 until the late 1990s, hereafter called the "early period" (Fig. 1.3, black and magenta curve). After two peaks in 1998 and 2000, RH decreases from 2000 to 2017, hereafter referred to as the "late period" (Chadwick et al., 2016; Dunn et al., 2017; Gulev et al., 2021; Sherwood & Fu, 2014). Decreases in land RH were first noted in Simmons et al. (2010) (datasets HadCRUHext and ERA-Interim) and recently supported by newer datasets HadISDH (Blunden & Boyer, 2021; Willett et al., 2014), ERA5 (Simmons et al.,

2021) and JRA-55 reanalysis (Dunn et al., 2021).

Over the late period, RH over the ocean deviated much less and showed weaker trends than RH over land (Fig. 1.4; Blunden and Boyer, 2021; Dunn et al., 2017; Willett et al., 2014; Willett et al., 2020). The difference between land and ocean RH changes is due, among other things, to the different degrees of warming and evaporation rates (Sherwood & Fu, 2014).

Over the northern hemisphere (NH), stronger land RH trends over the full period were found than over the southern hemisphere (SH; Fig. 1.5). Long term trends showed increasing RH values in the NH tropics and low latitudes, and high latitudes, and decreasing RH in the extratropical latitudes (Simmons et al., 2010) but, in particular, in the mid-latitudes (Dunn et al., 2017; Willett et al., 2014). This contribution resembles a zonal contribution (Dunn et al., 2017; Willett et al., 2014). These trends are evident in both the HadISDH observation dataset and the ERA-Interim reanalysis (Dunn et al., 2017).

While the air surface temperature rose sharply over land over both periods, pre- and post-2000, Dunn et al. (2017) found that q increased in the early period, but remained fairly constant in the global average in the late period.
Peterson et al. (2011) found, in line with the Clausius-Clapeyron relationship, that the q increase was greater in warm regions such as the tropics and that the T increase was lower in “wet” regions. They projected the Bowen ratio onto the latitudinal distribution: at high-latitudes, energy changes are in favour of the sensible heat. They show strong T trends. At low latitudes, latent heat fluxes are dominant and strong humidity trends are dominant.

Global circulation models are incredibly powerful tools that enable us to explore potential future climates, depending on emissions pathways. Clearly, a key question is whether these skillfully reproduce RH and its changes over present-day conditions. In short, they currently do not. Dunn et al. (2017) compared RH, q and T over land in HadISDH observation and reanalysis (ERA-Interim) with nine models of the World Climate Research (WCRP) CMIP5. Climate models are based on physical laws, e.g. the Clausius-Clapeyron relation for RH calculation in the context of thermodynamic processes. The CMIP5 models run with different forcing factors, including anthropogenic (GHG) and natural factors. These coupled models, run with all forcings over the historical period, were not able to reproduce the observed steep decadal RH decrease (example model experiments HadGEM2-ES in Fig. 1.3). They do reproduce the increasing trend in q, but it is generally too strong in the models. Atmosphere-only models show declining RH over land but not the multi-decadal pattern of a peak around 2000 then a sharp decline.
The spatial patterns between observations and models are the same for T and q trends, but differ greatly for the variable RH: outside the mid-latitudes, the models show a less strong wetting trend (Dunn et al., 2017).

Under the strongest Representative Concentration Pathways (RCP8.5), Collins et al. (2013) found that CMIP5 modules simulated a further decrease of RH over land for the time period from 2046 to 2100. Byrne and O'Gorman (2013a) confirm the findings with regard to a land-ocean warming contrast due to limited moisture availability over land. According to the results from Dunn et al. (2017) which show deviations of observation and model data, in this project, caution should be exercised when using the CMIP5 simulations to assess future RH changes, because these simulations are conducted with the same models that did not simulate past observed trends.

If the climate models do not pick up the decrease in RH, then anything that uses the climate models for looking at future impact related to hydrology must be viewed with some uncertainty, because it does not seem to pick up the current historical trend very accurately. If the recent RH trends were due to internal variability, rather than being externally forced, the timing of the trends would not be expected to be captured (Dunn et al., 2017).

Other variables also indicate decreasing global surface moisture: a decrease in RH over land would come along with an increased Bowen ratio (more sensible heat, less or constant latent heat). For 1973–2003, Peterson et al. (2011) measured a positive Bowen ratio of the trends in sensible and latent heat under an increase in global energy content, the sum of mainly enthalpy (simple: temperature increase), kinetic energy (relatively small wind speed decrease) and latent energy (q increase) and potential energy (gravitation) increases. This means that the sensible heat increases more than the latent heat. In South Africa and Australia, hot regions that are energy limited to water, Peterson et al. (2011) found a negative trend in the Bowen ratio. It can then be concluded that RH is very sensitive in these regions, which are either water or energy limited.

Although this work will focus on the surface atmosphere, clearly, the surface can both affect and be affected by changes aloft. Therefore, a key question is whether RH also changes higher up in the atmosphere and whether those changes are linked. Sherwood et al. (2010) show that RH has indeed changed throughout the troposphere. Latitudinally, these changes are broadly similar with decreases found around the mid-latitudes and increases over the tropics and poles (Fig. 2 in Sherwood et al., 2010). Typically, climate models underestimate these changes when compared with observations.

Dessler and Sherwood (2009) and Todd et al. (2018) assume that in addition to global warming, climate variabilities like the El Niño Southern Oscillation (ENSO) or strong volcanic eruptions can have an influence on the water cycle and the RH change. Dunn et al. (2017) and Byrne and O'Gorman (2018) assume three possible causes for the change in near-surface RH: the thermodynamic driver, circulation and modes of variability (later labelled as 'dynamical drivers') and stomatal efficiency changes and land use changes (later labelled as 'terrestrial drivers'). These drivers are explained in Section 1.3.

1.3 Drivers of RH

Fundamentally, RH is driven by changes in q and T, which in turn are driven by heating, cooling, moistening (evaporation) and drying out (condensation or precipitation). These changes play a role on different temporal and spatial scales; they can be local or distant and advected over the region of interest. These changes are governed by the Clausius-Clapeyron relation, or deviation from it. RH changes seasonally and over several years. Manabe and Wetherald (1967, 1975) suggest that changes in RH should be small, and even positive near the surface, allowing the atmospheric water content to rise with temperature. Sherwood et al. (2010) also state that RH should not change, but they refer to the upper atmosphere and argue that RH in the upper atmosphere is governed by temperature at last saturation rather than evaporation into the air. At the surface, Simmons et al. (2010) found that RH does change, as it is governed by evaporation (or lack of) and advection of moist/dry air.

This project considers three potential drivers: first, the thermodynamic driver, which concerns the temperature increase due to the increased amount of CO_2 in the atmosphere and, thus, increased evaporation. An increase exclusively in temperature would lower RH, while with a sufficient increase in evaporation, RH would stay stable or increase due to the Clausius-Clapeyron equation. Bringing it into the concepts of evaporation, from the moist surface, there is either advection or evaporation from the surface or both. For the thermodynamic driver, it is changes in the evaporation principally, which are related to changes in SST versus changes in land surface temperature, assuming advection stays the same. It is the evaporation over the sea which changes because of ocean warming. Once that is advected, it becomes RH change over land. This is an evaporation process. Secondly, dynamical drivers could cause a change in RH when atmospheric and oceanic circulations i.e. wind and ocean currents 'move' heat and moisture around, affecting local T and q. The dynamical drivers are an advection process but they are also modes of variability-related evaporation processes, so it is the two things combined. Thirdly, terrestrial drivers modulate evaporation and heat absorption over land and therefore could lead to a change in RH. The latter driver includes both land cover change and an increase in CO_2 which impacts plant physiology and, thus, their transpiration of water into the atmosphere and the various ways that water leaves the land surface (Betts et al., 2007). Terrestrial drivers indicate an evaporation process in a local region.

The thermodynamic driver is expected to drive the biggest portion of the RH change (Chadwick et al., 2016). However, it does not seem to be able to fully explain the observed RH changes (Dunn et al., 2017; O'Gorman & Muller, 2010; Rowell & Jones, 2006; Willett et al., 2014). This is explicitly demonstrated in Fig. 2f and section 4f of Chadwick et al. (2016), whereby there are changes in RH which cannot be explained by their simple model of the thermodynamic driver. Therefore, it is of interest to investigate potential additional drivers for RH change in order to further understand the steep negative trend.

1.3.1 The thermodynamic driver

The thermodynamic driver is essentially large scale changes in water vapour in the atmosphere (q) driven by large scale increases in energy (T), in response to global warming. It is the change in atmospheric water holding capacity and evaporation. Where water is plentiful, q is expected to increase at 7% per K (degree) of T, following the Clausius-Clapeyron relation. This would mean that RH does not change. A smaller increase or a decrease in q leads to a drop in RH, while anything higher than that leads to an increase in RH.

A key aspect of the thermodynamic driver is the land-sea warming contrast; the fact that the land is warming faster than the ocean and that the ocean is the main water vapour supplier to the land (Byrne & O'Gorman, 2013a; Byrne & O'Gorman, 2013b; Dong et al., 2009; Fasullo, 2010; Joshi et al., 2008). This is both a result of the land being drier than the oceans (Joshi et al., 2008) and a driver of the decrease in RH over some land regions (Fu & Feng, 2014). Theoretically, changes in moist static energy (q) are equal over land and ocean (Byrne & O'Gorman, 2016). Practically, in order for that to be the case, the land must warm more because there is not enough moisture to contribute to the moist static energy (Byrne & O'Gorman, 2018). This is demonstrated diagrammatically by Sherwood and Fu (2014) and reproduced here as Fig. 1.6. Over the ocean, unlimited water availability means that more energy is partitioned into latent heat, hence air humidity should in theory increase faster over the ocean than over the land (Byrne & O'Gorman, 2018). Over land, where water availability is limited, more energy is partitioned as sensible heat, hence T increases faster over land (Fig. 1.6). Other influences arise from different characteristics including reflection of shortwave radiation and ability to transport heat (Dong et al., 2009; Joshi et al., 2008), but these are small in comparison on the global scale. The slower warming over ocean actually results in a slower increase in the saturation vapour pressure, or evaporative demand over ocean compared to that over land (Joshi et al., 2008). Lots of moisture over land comes from air advected over the ocean and flowing over the land. Given the smaller rates of warming and evaporative demand increase, the actual q of air advected from oceans is not enough to keep RH stable over land (Sherwood & Fu, 2014; Simmons et al., 2010). This mechanism is relevant both for surface advection and even more so for moisture transport aloft, which is often the main source (Joshi et al., 2008, Fig. 8 therein). Moist air over the ocean rises, cooling and precipitating out moisture in the process. The amount of moisture remaining in the air parcel after it has risen, advected over land and then subsided, depends on the temperature at last saturation. Therefore, assuming an air parcel has plentiful water vapour in the first place, it is the change in temperature aloft that often governs the change in moisture, should that air parcel return to the surface (Joshi et al., 2008; Sherwood et al., 2010). This, combined with faster warming at the land surface results in decreasing RH. Considering also that water is limited over land, the Clausius-Clapeyron relation (increasing q at 7% per 1 K of T) is often not satisfied locally, so RH over land decreases both because of locally limited water availability and insufficient moisture advecting from ocean source regions (Figs.

1.5 and S7; O'Gorman and Muller, 2010).

As an additional note, Wallace and Joshi (2018) found a potential stabilisation of the warming ratio since 2000 and a steady small increase prior to that. They point to aerosols emitted by human manufacturing/society moving from land towards the ocean as a potential cause. Until then, aerosols would have shielded the land from some of the warming as they reflect/absorb incoming shortwave and longwave radiation.

Faster land than ocean warming explains the bigger picture of RH decreases but does not completely explain the regional RH trends in magnitude, nor their temporal and spatial patterns. Several papers point to the influence of both circulation and the biosphere as mechanisms of moisture transport and production (through evaporation and E_t) (Byrne & O'Gorman, 2018; Chadwick et al., 2016; Collins et al., 2013; Joshi et al., 2008; O'Gorman & Muller, 2010; Simmons et al., 2010).

Parallel to the onset of the negative RH trend in 2000, there was the so-called "global warming hiatus". This warming hiatus is attributed to the cooling of the eastern equatorial Pacific through the circulation of warm surface ocean water into deeper levels and to the cooling of Eurasia Deser et al. (2017) and Kosaka and Xie (2013). Natural climate variability (climate variation on earth without external forcing) and dynamical drivers, especially the ENSO, Pacific Decadal Oscillation [PDO] and Interdecadal Pacific Oscillation [IPO], are linked to this upheaval and extensive cooling (England et al., 2014; Roberts et al., 2015; Trenberth & Fasullo, 2013). Willett et al. (2014) found flattening in the dry and wet-bulb temperature, in q and in the vapour pressure during the hiatus. The slower warming of the surface ocean could lead to less evaporation and therefore less moisture supply from the ocean, which thus leads to a decrease in RH over land. According to Palmer and McNeall (2014), this warming hiatus could have lasted longer than a decade, and Roberts et al. (2015) do not rule out another warming hiatus due to internal climate variability. As a short term and rare event, relative to recent history at least, that has since resolved rather than continued, explicit links between the warming hiatus and decreasing RH any further are not considered in this study. However, the related modes of variability are included as dynamic drivers.

1.3.2 Dynamical drivers

Dynamical drivers change regional RH by moving air masses with specific properties (in this project, q, T) into this region or away from the region. They relate to changes in atmospheric and oceanic circulation. By moving heat around and affecting the wind direction and speed, circulation changes can affect the atmospheric water holding capacity and amount of evaporation over a region directly, or over source regions that impact other regions.

Dynamical drivers include changes in atmospheric and oceanic patterns, i.e. wind, sea level pressure (SLP) and sea surface temperature (SST), henceforth referred to as primary physical variables. This leads to more or less moisture / higher or lower temperature in a region and, thus, can change RH. Dynamical drivers include modes of variability such as the ENSO (Section 1.3.2.3) in addition to more localised horizontal movements and evaporation changes related to the primary physical variables. This thesis additionally considers precipitation as a related variable important for RH. Typically, modes of variability and periodic changes to primary physical variables are oscillating phases of climate, acting on scales of months to a few years. Many are not long-term persistent trends such as GHG induced climate change (Fig. 1.7) but some oscillations (such as the Southern Annular Mode [SAM]/Antarctic oscillation [AAO]) have had persistent trends in stratospheric ozone depletion with a contribution from GHG (Fogt & Marshall, 2020; Gulev et al., 2021). However, plausibly, climate change can affect modes of variability and variability in the primary physical variables resulting in long-term changes to the modes and primary physical variables. Correlations of both in situ/local variables and spatially distant variables correlating with local RH can indicate where and which dynamical drivers are impacting RH. Where there is a long-term trend or clustering in time of a particular phase of mode or primary physical variable, this suggests that the driver may be contributing to longer-term changes in RH and therefore is of interest to this study.

The concept of regional air masses and their trajectories can be used as an example of dynamical drivers and how they impact local RH. The climate of a region is largely determined by the formation and transport of air masses. The west coast of the USA, for example, is characterised by cool, moist, maritime polar air from the northwest, mild, dry maritropical subsiding air over the Pacific from the southwest, and inland warm, dry continental tropical air (Fig. 1.8). These trajectories can seasonally or periodically strengthen, weaken, change their direction and be blocked by other circulating systems. Each source region has different characteristics of q and T which can change with any changes to the source region heat or location. The q and T, and resulting RH, over a region thus depends on its source region(s) plus changes to q and T along the trajectories.

The following sections introduce the primary physical variables and modes of variability in more detail. The influence of climate variabilities on regional climates is explained using the example of the ENSO.

1.3.2.1 The primary physical variables of sea surface temperatures, wind direction and speed and sea level pressure

The primary physical variables, SST, wind direction and speed, and SLP, describe the movements of air parcels with the properties q and T and thus also deviations from general circulation, i.e. the sum of repetitive dynamics, which remains constant over a certain period of time, that can cause changes in regional RH (Gulev et al., 2021). SSTs are strongly linked to the air temperature over the ocean, firstly, and are thus, through advection, likely to influence the air temperature over land, particularly above coastal landmasses. Secondly, the evaporation rate over the ocean (q) depends positively on the SST. At higher SSTs, evaporation is enhanced, and moist air over the sea might be advected to the land. Thirdly, SSTs are an indicator for various modes of variability (see Section 1.3.2.3). Vector winds u10 (west to east) and v10 (south to north) at a 10 m altitude are important for advection and circulation, i.e. they carry air parcels with the properties q and T towards or away from the region. The wind speed at 10 m altitude (si10) enhances air movement and is positively linked to evaporation and E_t as the kinetic energy component. SLP is an additional explanation for winds and an indicator for atmospheric modes of variability.

This project is interested in long-term trends that deviate away from the climatology period of 1981–2010 and the clustering of 'anomalous events' in the physical primary variables. Such things could plausibly contribute to the decline in RH observed since 2000. In order to establish the climatological baseline for reference later in the thesis, the annual and seasonal climatologies for the primary physical variables are presented in Fig. S4. SSTs are highest around the equator, tracking north and south seasonally. Although the regions of interest (defined in Section 3.3) are land focused, the majority include coastlines and therefore are clearly influenced by local, and in some cases, not so local, SSTs. For wind climatologies at 10 m altitude, the strongest vector winds are the mid-latitude westerlies, especially over the SH. Their strength increases in the hemispheric winters. The extra-tropics are high-pressure regions, typically experiencing light winds, and the trade winds flow from this high-pressure region to the lower pressure of the ITCZ, where they converge. In JJA, there is a seasonal reversal of the winds over regions around the ITCZ due to the shift of the ITCZ to the north, e.g. winter northeasterly winds become summer southwesterlies over India. So-called monsoon winds occur not just in the Indian region but are strongest over the Arabian Sea and the Bay of Bengal in JJA. With high summer temperatures and high evaporation rates, these monsoonal winds result in intense precipitation months. Seasonally, the Siberian high in DJF and the low-pressure system over the Arabian peninsula and India in the monsoon season (JJA) stand out. Together, these maps show climatologically typical influences, including whether regions experience typically maritime air masses (e.g., eastern Brazil, southern Africa; Fig. 1.8) or continental air masses (e.g., Mongolia, eastern Canada, eastern USA) or a mix across the seasons (e.g., western USA), and may therefore be important for circulation related influences.

The 10 m climatologies depict the surface component of the three dimensional tricellular atmospheric circulations which comprise the Hadley Cell, Ferrel Cell and Polar Cell (O'Hare et al., 2014). Expansion of the Hadley Cell is a well-established circulation response of the atmosphere to climate heating (Grise & Davis, 2020; Gulev et al., 2021), and one that implies shifts to the dry regions typically under the subsiding part of the poleward edge of the Hadley Cell. However, Sherwood et al. (2010) found that changes in tropospheric RH (above the surface) could only partly be explained by expansion, and more recently Schmidt and Grise (2017) concluded that it did not contribute to subtropical drying over land. This project focuses on the influence of dynamical drivers at and below 10 m altitude on RH. Although changes in the primary physical variables and modes of variability imply circulation changes aloft, these are not considered explicitly here.

Since the 1980s, wind speed over land has decreased, in particular from strong winds, in the low and mid-latitudes, while it has increased over the high latitudes (McVicar et al., 2008; Vautard et al., 2010; Zheng et al., 2016). There is some evidence of increase over oceans but this remains uncertain at present (Azorin-Molina et al., 2021; Torralba et al., 2017). Previously, increasing surface roughness due to enhanced urbanisation or vegetation was thought to be the driving factor (Vautard et al., 2010). However, more recent studies point to decadal variability in large scale circulation, such as the expansion of the Hadley Cells, ENSO, the North Atlantic Oscillation (NAO) and the PDO (Azorin-Molina et al., 2018; Yang et al., 2014; You et al., 2010; Zeng et al., 2019; Zheng et al., 2016), for many different regions including Europe, Saudi Arabia and the Tibetan Plateau. Since the 2010s, the global trend seems to be recovering (Zeng et al., 2019; Zhang & Wang, 2020).

Logically, a decrease in wind speed reduces the kinetic energy available for evaporation, and therefore likely leads to reduced evaporation, on the one hand. On the other hand, reduced wind speed reduces mixing, which may mean an increase in local RH. Roderick et al. (2007) found that stilling winds were the main reason for decreases in pan evaporation over several Australian stations. They point to similar findings for the USA (Hobbins, 2004), Tibet (Shenbin et al., 2006; Zhang et al., 2007) and China (Xu et al., 2006). Wind stilling could therefore lead to a decrease in RH. Conversely, lower wind speeds result in reduced horizontal mixing which could lead to localised increases in RH, but this effect is not likely to be large or dominant (Davarzani et al., 2014). Although the stilling and recent recovery of land surface winds is relevant to changes in surface RH, the timing of wind speed decrease and recovery does not match that observed for RH. The picture is further complicated by the uncertainty in observed wind speeds trends over oceans and the importance of advected moisture laden air from over the oceans. This study considers wind speed more for its role in advection (or lack thereof) than as a local driver of evaporation.

1.3.2.2 Precipitation as a physical variable related to RH

Over the timescales relevant to this study (months to years), the influence of precipitation on RH is primarily through the additional supply or reduced supply of water to the land surface and subsurface, which is the local water source for evaporation and hence surface atmospheric moisture levels.

The highest amounts of precipitation are found in the tropics and low latitudes around the equator and the ITCZ, where northeasterly and southeasterly trades converge (Fig. S4). Due to the intense sunlight, high temperatures, and plentiful moisture availability, evaporation is high and deep convection occurs. This results in heavy precipitation over and around the low-pressure belt of the ITCZ. The extratropics are characterised by subsiding dry and are therefore typically drier and include many of the hot desert regions. Rainfall amounts are higher over the mid-latitudes, again a zone of convergence in surface winds. The poles are typically regions of low precipitation (O'Hare et al., 2014).

In southwest Canada, western Patagonia, Scotland, and New Zealand, onshore westerlies contribute to increased precipitation; in Madagascar, easterly winds contribute to increased precipitation (Figs. S3 and S4). The monsoon circulation influences precipitation on the Tibetan Plateau and Japan. The lowest amounts of precipitation are found in the Sahara desert and other cold and hot deserts, such as the Mojave-Sonoran-Chihuahuan desert, the Arctic desert, eastern Patagonia, the Namib and Kalahari desert, the Karakum desert southeast of the Caspian Sea, the Arabian peninsula, the Thar in Northwestern India and the Gobi and Ordos desserts around Mongolia.

Precipitation can vary strongly across the annual cycle, with some regions having multiple 'wet' seasons. As the ITCZ moves latitudinally due to seasonal differences in sun intensities, in December-January-February (DJF), the southern hemisphere (SH) subtropics show higher amounts of precipitation, and in June-July-August (JJA), the northern hemisphere (NH) subtropics show higher amounts of precipitation. During JJA, southeastern Asia is wet in particular due to the monsoons, which are an important source of seasonal rainfall. Seasonal air circulations with strong moist flows from the ocean to land in the tropics and subtropics are referred to as monsoons. These winds are linked to the trade winds and the pressure trough of the ITCZ. In the respective monsoon season, these winds are direction-reversed compared to the rest of the year due to the unequal ocean and land warming and cooling and the linked air pressure gradient. There are different monsoon systems worldwide, the most well known in southern and southeastern Asia.

Precipitation is also affected by the generally warming climate. Changes are, however, complex, and have proved to be difficult to observe robustly. Under global warming, convection through evaporation is increased and the air can hold more water (7% per 1 K of rise in T following the Clausius-Clapeyron relation) before it is released as precipitation. Changes in precipitation are quite complex: extreme precipitation has increased at a similar rate to q because in heavy rainfall events all/most of the water tends to rain out (Trenberth, 2011; Wentz et al., 2007). However, the mean rainfall has increased much more slowly. In terms of observations, there is not really a clear signal of increasing rainfall globally (Gulev et al., 2021). With climate change, there are regional shifts from snowfall to rainfall resulting in enhanced runoff in early spring (Callaghan et al., 2011). Due to limitations in moisture convergence, the increase over land is expected to be smaller than over the ocean (Allan et al., 2020).

1.3.2.3 Modes of variability

Seesawing changes in the atmosphere and ocean in the primary physical drivers SST, wind direction and speed and SLP, which are regularly repeated over between several weeks to several decades, come under the term climate variability. The climate variability ensemble comprises several modes of variability, the changes of which are ascribed to a specific region and frequency. The primary physical drivers can be used to derive indices for each of the modes, describing its phase (neutral, positive or negative), magnitude and evolution. An overview of the most common climate phenomena and their indices is given by Kaplan (2011), and Christensen et al. (2013) summarise their regional climate impacts. The best-studied of these modes is the ENSO. The influence of modes on the regional and global climate will be explained using the ENSO.

The ENSO summarises 3–7 year periodic variations in SST and winds/circulation over the tropical Pacific region and is, thus, a coupled atmosphere-ocean phenomenon. Its atmospheric component is described by the Walker Circulation, occurring longitudinally at approximately the position where the northern and southern latitudinally flowing Hadley Cells converge. There is a seasonality to the Walker Circulation strength. Due to the northern location of the ITCZ, the southeasterlies are particularly strong in September, while the northeasterlies are weak. Thus, the Walker Circulation is also stronger in September. In the boreal spring, the Hadley Circulation dominates. The ENSO can take on three different phases: the neutral, the positive/warm (El Niño) and the negative/cold (La Niña).

In the neutral phase, the SST in the East Pacific and Central Pacific are lower than in the West Pacific. This longitudinal temperature gradient is created by upwelling cold ocean waters (Fig. 1.9). The relatively high temperatures over the western Pacific lead to the convergence of warm and humid air and thus to low pressure. A high-pressure system prevails over the Eastern Pacific. The strong equatorial easterly winds (the surface component of the Walker Circulation) along the tropical Pacific cause a gradient in sea level with higher sea level in the western Pacific, which leads to a deep current to the east. Typically, the ENSO neutral phase results in wetter conditions over eastern Australia and South East Asia and dry conditions over western South America.

The "positive" warm phase of ENSO is called El Niño, and generally occurs when the warm pool of SSTs expands across the entire tropical Pacific, due to a weakening of the atmospheric Walker Circulation. The SSTs over the Eastern Pacific are increased, and the SLP decreased. The thermocline, the transition between water layers of different temperatures, is lowered (Fig. 1.10). With the redistribution of SST and SLP patterns, the centre of convergence is also shifted eastwards. This results in drier conditions over the eastern USA, eastern Australia, South East Asia, Central America and the north of South America, southern Africa, India, and warmer conditions over south America, south Alaska, southern Africa, India (Fig. 1.11). Whereas lower precipitation rates and higher temperatures could lead to reduced RH, wetter conditions (the south of USA, eastern Argentina, Spain and southeast China for El Niño) and lower temperatures (Scandinavia, Mexico, eastern USA, northern Australia for El Niño) could increase RH. Where both precipitation is reduced (increased) and temperature increased (reduced) due to modes of variability, their extreme phases can reduce (enhance) RH.

The "negative" cool phase of ENSO is called La Niña. This is when the neutral conditions are intensified so that the East Pacific shows a shallower thermocline, upwelling of cold water and low SST; the West Pacific shows exceptionally high temperatures, the Walker Circulation (and hence the easterly trade winds) are strengthened, and an anomalously cool pool of SSTs extends from the eastern Pacific westwards (Fig. 1.10). This results in drier conditions over Mexico and the south of South America, Spain and southeast China, and warmer conditions over Mexico, the eastern USA, the East China Sea, Southeast Asia, and northern Australia (Fig. 1.11). Whereas lower precipitation rates and higher temperatures could lead to reduced RH, wetter conditions (the north of South America, southern Africa, India, Southeast Asia, the east and southwest of Australia for La Niña) and lower temperatures (South America except eastern Brazil, the south of Alaska, southern Africa, India and eastern Australia for La Niña) could increase RH. La Niña does not necessarily always occur after an El Niño; the ENSO could go neutral and then back into El Niño, or persist as El Niño for a long protracted period.

In addition to the El Niño and La Niña phases, there are two other states of the ENSO: The upwelling in both the western and eastern Pacific, thus, cooling to both sides is called El Niño Modoki (Ashok et al., 2007) or Central Pacific (CP) El Niño (Yeh et al., 2009). SSTs and air advection over the Central Pacific ocean are then increased, creating a low-pressure system. During the La Niña Modoki, high-pressure is created in the centre of the Pacific ocean where temperatures are lower than normal. Trade winds blow from the middle of the Pacific to both sides – the west and east – and heat both shorelines, which experience abnormally high rainfall. Model experiments showed that the ENSO Modokis occur increasingly under anthropogenic warming causing a flattening of the thermocline in the equatorial Pacific (Ashok & Yamagata, 2009; Yeh et al., 2009).

Due to the shift in Walker circulation and its three-dimensional nature, and to the associated shift in the regions of warm and cool sea surface temperatures, perturbations can be conveyed across the globe through interactions with wider circulation. The ENSO affects regions that border the Pacific Ocean (Fig. 1.11), but also causes changes in regional temperatures, precipitation and winds, in areas away from this region, possibly with a time delay, so-called teleconnections. These teleconnections mostly affect the tropics, but also cause wider effects, many of which are in the NH. Typically, El Niño is associated with drier and warmer conditions over many regions, reaching northern North America and southern Africa. Notably cooler/wetter conditions can be found in Central America and over northern Europe. La Niña is associated with wetter and cooler conditions over many regions, such as northern South America (Garreaud, 2009) and southern Africa, and drier and warmer conditions over the south of the USA and Southeast Asia. Clearly, the effects of the modes can be of global importance, such as the locking up of heat in the deeper ocean during the negative Interdecadal Pacific Oscillation (IPO), an El Niño-like pattern with low frequency, on the temperatures of the Pacific Ocean, which has been linked to the warming hiatus since 2000 (England et al., 2014; Power et al., 1999).

Clearly, ENSO has strong influences on local and distant temperature and rainfall and hence would be expected to affect RH also. Several studies spot large El Niño or La Niña events (in 1998, 2010, 2015) and other modes of variability in the temperature and q records, but for RH these are not as clear (Setimela et al., 2018). They do not stand out as much against the larger background year-to-year variability. McCarthy and Toumi (2004) found large RH anomalies after an ENSO event over equatorial oceans for boreal summers due to variations in temperature. However, they conclude that linear RH trends over the period 1979–1997 are only partly due to the ENSO. Particularly where precipitation is reduced (increased) and temperature increased (reduced) due to the ENSO (Fig. 1.11), extreme El Niño or La Niña events can change RH, e.g. El Niño from December to April in southern Africa (Setimela et al., 2018).

There are several different indices used to indicate the phase of ENSO. The Southern Oscillation Index (SOI) is based on the difference of SLP at Tahiti and Darwin in Australia. There are several SST based indices of which the Niño 3.4 Index is arguably the most common. It considers Pacific SST anomalies over the central equatorial Pacific (5°S-5°N, 170°W-120°W) (Blunden & Boyer, 2021; Kaplan, 2011). The multivariate ENSO Index v2 (MEI) combines both atmospheric and oceanic variables and considers the SLP, SST, surface winds and the outgoing longwave radiation over the Pacific Ocean. High MEI values indicate El Niño conditions while negative values indicate La Niña conditions.

Strong El Niño events were recorded mainly in boreal winters in 1982/83, 1997/98 and 2015/16; the period 1990 and 1995 is also almost exclusively occupied by positive MEI values (Changnon, 2000; McPhaden, 1999; Philander, 1983; Santoso et al., 2017). Strong La Niña events were recorded in 1974–1976, 1989 and after the previously mentioned El Niño events in 1999-2001, 2008/09 and 2011.

Research is ongoing into how modes will behave under anthropogenic forcings (Christensen et al., 2013). For the ENSO, Christensen et al. (2013), Cai et al. (2015) and Cai et al. (2014) assume increased equatorial Pacific SSTs, a reduced upwelling with an increased surface-to-depth temperature gradient, a flattening in the thermocline and weakened trade winds. Tokinaga et al. (2012) summarised these findings as a slow-down in the Walker Circulation due to global warming. This would result in more frequent and stronger El Niño and La Niña events (Cai et al., 2018) with an intensification of the magnitude of rainfall variability associated with ENSO (Gulev et al., 2021). Gulev et al. (2021) indicate the uncertainty in future ENSO SST variability due to limited consensus among models (Section 4.3.3 in Gulev et al., 2021). The future of the ENSO and other modes of variability is an area of ongoing research and large uncertainty (Cai et al., 2021).

Like ENSO, other modes can change temperature, precipitation and moisture levels near and far from the region of origin over a certain period of time. Several modes can superimpose positively or negatively and reinforce or offset (Cai et al., 2021). For example, the ENSO and PDO interactions are studied in Newman et al. (2003), and vice versa in Verdon and Franks (2006). The Atlantic Multidecadal Oscillation (AMO) and ENSO interactions are studied in Levine et al. (2017). If two or more events overlap, then regional temperature and moisture content might change even more drastically. The interaction of modes is a challenging area of research, in particular, for coupled climate models (Timmermann et al., 2018).

Dynamical drivers in the form of modes of variability are often reasonably modelled in the state of the art coupled global circulation models. However, some are more challenging than others: the geographical extent, periodicity and magnitude may not be quite right, and no single historical run of a coupled climate model can be expected to reproduce the exact variety and state of each mode of variability at the exact time that has been experienced in the real world. Only for modes which are shown to be changing due to external forcings (i.e. the SAM; see Section 4.2.1) would one expect past trends to be correctly captured. Therefore, if evidence is found of the influence of dynamical drivers on long-term RH trends, this may be one reason why climate models are not representing recent RH decline particularly well.

Thermodynamic drivers, as defined in Section 1.3.1, deal directly with evaporation and moisture-holding capacity. Dynamical drivers, as defined here, are essentially changes in the advection of unusually warm/cool/moist/dry air which affects the surface atmosphere, in addition to indirect changes in evaporation and moisture-holding capacity caused by changes in the locations of warm/cool air and ocean and related vertical motions (e.g., upwelling, convection, subsidence). The winds can also inhibit or enhance ocean circulation, downwelling and upwelling and lead to further changes in sea surface temperature. The thermodynamic driver is more of a long-term trend driver whereas dynamical drivers are more likely to have periodic/interannual/interdecadal features that may explain why RH over land has declined since 2000.

1.3.3 Terrestrial drivers

In this study, the third group of reasons explored for the RH change are referred to as terrestrial drivers, which are based on the vertical energy output of the land surface, which makes up 29% of the Earth's cover. These outputs to the atmosphere are sensible and latent heat, i.e. T and q, respectively. The ratio of the energy types (Bowen ratio), as well as the absorption of radiated solar energy and precipitation, are based on the soil (whether it is clay or sandy soil etc., i.e. permeable for water) and ground and land cover and land use (LCLU) characteristics (e.g. bare surface, water surface, vegetated surface, high altitude, low altitude, which direction it faces). Processes such as absorption and reflectance (albedo dependent) and land evaporation, which in turn depend on soil moisture, land cover, but also CO_2 fertilisation on vegetation, can determine atmospheric moisture and RH change (Betts et al., 1997; Miralles et al., 2020). There are several feedbacks and interactions present making terrestrial drivers very complex to understand and assess. In many cases, RH can be a driver itself, governing evaporation rates.

The process of evaporation and its fractions are presented in Section 1.3.3.1. The global and, if applicable, regional changes in evaporation are discussed. Following this, literature on reasons for changing evaporation is considered, including changes in soil moisture, terrestrial water storage (TWS) and land-use change (Section 1.3.3.2). In the land cover change, the focus is on vegetation cover change, particularly deforestation and afforestation (Section 1.3.3.3). Since the type of vegetation has a decisive role in the energy fluxes with soil and atmosphere, possible categorisations of vegetation are briefly explained. Finally, CO_2 fertilisation is discussed – another variable that influences E_t (Section 1.3.3.4). Even if the terrestrial mechanisms are not the cause of drying, the physiological one (closing stomata in response to declining RH) or the structural one (lower leaf area index [LAI] in response to declining RH) could amplify the drying effect.

1.3.3.1 Land evaporation and its fractions

Land evaporation is the movement of energy, in terms of heat and moisture away from the land surface into the atmosphere. It is strongly affected by the availability of moisture at the surface and the type of surface. Its rate, in combination with available energy, relates to the amount of latent and sensible heating, directly influencing q and T, and therefore RH, close to the surface (Martens et al., 2018; Trenberth et al., 2009). This relationship is examined in Section 5.1 as a function of the region and is supported by the literature.

Two criteria must be met for evaporation to occur. First, there must be a moisture concentration gradient from the ground surface to the air. Secondly, there must be sufficient energy available. By adding energy, the water will change from the liquid state on the surface to the gaseous state in the air. Land evaporation provides about two-thirds of the source of water received as global precipitation (Miralles et al., 2011; Oki & Kanae, 2006; Shukla & Mintz, 1982; Xiao et al., 2020b). Evaporation is an important part of the hydrological, biogeochemical and energy cycles (Zhang et al., 2016a). The E-RH correlation could be positive or negative depending on the source type and location of E relative to RH, and is therefore complex.

The theoretical model of potential evaporation (E_p), conversion from liquid water from the soil to water vapour in the atmosphere, assumes that there is always sufficient soil moisture and that evaporation only depends on heat energy and wind. Accordingly, the potential evaporation shows a latitudinal pattern with much lower evaporation rates in low-temperature regions, like the high-latitudes and high-altitude regions, and high evaporation rates in warm regions, like the Sahara desert. Obviously, in practice, the latter registers low actual evaporation rates due to the lack of water available for evaporation. The actual evaporation (E) takes into account energy, wind and available water.

Actual land evaporation is estimated to be 67.9 $\times$ 10^3 km^3 annually (Miralles et al., 2011). It can take different forms: interception loss (E_i), bare-soil evaporation (E_b), snow sublimation (E_s), E_t, and open-water evaporation (E_w; Equation 1.5).

$$E = E_i + E_b + E_s + E_t + E_w \tag{1.5}$$

The proportion of these different forms on E depends on the regional conditions, the prevailing climate, and thus also on vegetation and soil properties. They can influence q, T and therefore RH differently; relationships between the fraction of different types of E and RH might differ in strength and sign. Due to land cover change or energy/water availability, their proportions to the total evaporation volume and the total evaporation itself can change over time.

The E is strongest in the low-latitudinal tropics around the equator (global climatologies for evaporation and its fractions not shown). In the boreal winter, a lot of water also evaporates in the SH mid-latitudes (Central Argentina, southeast southern Africa), and in the boreal summer in the NH mid-latitudes, with a focus on Eastern USA and the Southeast Asian continent (Miralles et al., 2011). The E_t follows the patterns of E, as does E_i in a weakened form. The E_b component is even weaker than E_i on the global average. The E_b occurs in hot and cold deserts, especially in the mid-latitudes (Western USA, Sahara, Southern Africa [in DJF particularly], Arabian peninsula, northwestern India, Mongolia and Tibet [in JJA], Australia). The E_w is strongest in the boreal summer in Canada and around the Caspian Sea, and in the boreal winter in the SH, as in Southern Africa. The E_s is found almost exclusively in MAM in the high latitudes and northern mid-latitudes in the NH.

E_w is considered the most straightforward evaporation type. 71% of the Earth is covered by water, such as oceans, seas, rivers and endorheic (hydrologically landlocked) basins. These endorheic basin water storages have been decreasing for two decades, which has decimated the area available for evaporation (Wang et al., 2018). Particularly affected are arid and semi-arid climates with high potential evaporation but low precipitation rates, such as Tibet, southern Africa and the Caspian Sea. According to (Wang et al., 2018) and their analysis of the Gravity Recovery and Climate Experiment (GRACE) data, the reasons for this lie in long-term climate conditions and human water management rather than the climate variability like ENSO and the PDO (Guo et al., 2021; Ni et al., 2018; Wang et al., 2018). E_w increases with increasing air T and wind. Through land cover change and fewer open-water bodies, global E_w decreases.

The E_s represents only 2% of total land evaporation (Miralles et al., 2011). In this case, the ice or snow goes directly from the frozen into the gaseous phase and skips the liquid phase (sublimation). This process requires more energy than E_w and thus occurs only in regions with low temperature, such as at high latitudes or in high-altitude areas, with high net radiation, such as the Himalayas (Miralles et al., 2011; Oke, 2002). Globally, both snow cover and snow cover duration have significantly decreased due to increasing temperature since 2000 (Li et al., 2018; Notarnicola, 2020) and since 1972 (Bormann et al., 2018), e.g. in the Tibetan Plateau (Zhang et al., 2021). A decrease in albedo due to enhanced greening or browning enhances warming and snow melting (Li et al., 2018).

Unlike E_w and E_s, the other evaporation fractions E_b, E_t and E_i have an organic layer between the terrestrial moisture and the atmosphere, such as bare land or plants. The land cover type determines the layer. 7% of land evaporation corresponds to E_b (Miralles et al., 2011). The nature of the soil at different depths, such as the porosity, determines how much moisture the soil can absorb, hold and release again.

There are two additional types of evaporation with vegetation: E_t and E_i (Miralles et al., 2020). The latter accounts for 11% of total annual land evaporation and describes the evaporation of water collected on the plant leaves through precipitation that did not reach the ground (Miralles et al., 2020; Miralles et al., 2011). The absolute E_i is highest in the tropics because of the dense canopy level of plants of different heights and the high air humidity (Miralles et al., 2010b). Measured as a proportion of the incoming rainfall, it is strongest in regions with long periods of rainfall and dense leaf cover, such as Scandinavia, and amounts to 22% of incoming rainfall evaporation over needleleaf forest, but only 13% over broadleaf evergreen forest (Miralles et al., 2010b). E_t and E_i are high in water abundant areas if vegetation productivity and LAI are high, with increased air T and wind. The E_t is more driven by RH than by T (Xiao et al., 2020b).

E_t occurs when vegetation absorbs the water from the soil and it evaporates in exchange for CO_2 during photosynthesis (Miralles et al., 2020). Pores on both the upper and/or the lower side of the plant leaf surface, called stomata, control this transpiration process. They are formed of a pair of guard cells that are under physiological control to regulate leaf water loss. The stomata opening (short-term) and stomata density (long-term) regulate the canopy conductance or resistance, i.e. the E_t rate, depending on the CO_2 concentration in the atmosphere, and the moisture availability in the soil and atmosphere. This is discussed in detail in Section 1.3.3.4. E_t depends further on the vegetation type, the design and density of stomata on a plant leaf, the plant height associated with the roughness, which regulates the wind speed due to the aerodynamic resistance, the photosynthetically active radiation, and the albedo (Betts et al., 2007; Betts et al., 1997). On a global level, E_t and precipitation strongly positively correlate (Pascolini-Campbell et al., 2021; Zhang et al., 2016b). The E_t and E_i depend on the vegetation (see normalised difference vegetation index [NDVI]), which depends on the soil moisture (Shukla & Mintz, 1982). While the correlation between transpiration and soil moisture is strongly positive, especially in the NH mid and high latitudes, for example, the correlation between interception loss and soil evaporation is very weak except for in the deep tropical rainforests (Miralles et al., 2020).

The standard equation for estimating E_t is the Penman-Monteith equation (Equation 1.6).

$$\lambda E_t = \frac{\Delta(R_n - G) + \rho_a c_p \frac{e_s - e_a}{r_a}}{\Delta + \gamma(1 + \frac{r_s}{r_a})} \tag{1.6}$$

where λE_t is the evaporative latent heat flux, [MJ m^{-2} day^{-1}], λ is the latent heat of vaporisation, 2.45 [MJ kg^{-1}], Δ is the saturation vapour pressure-T relationship [kPa °C^{-1}], R_n is the net radiation [MJ m^{-2} day^{-1}], G is the soil heat flux [MJ m^{-2} day^{-1}], $(e_s - e_a)$ represents the vapour pressure deficit of the air [kPa], ρ_a is the mean air density at constant pressure [kg m-3], c_p is the specific heat of dry air at a constant pressure of 1.013 10^{-3}, [MJ kg^{-1} °C^{-1}], γ is the psychrometric constant [kPa °C^{-1}], and r_s and r_a are the (bulk) surface aerodynamic resistance for water vapour [s m^{-1}], and the canopy surface resistance [s m^{-1}], which is equal zero for a wet, saturated surface.

E_t accounts for the largest part of land evaporation at 80% (Miralles et al., 2011). Interest in finding out what influence this evaporation has on RH is therefore particularly great. Evapotranspiration is most pronounced in the tropical rainforests (Amazon Basin, Congo Basin, E_t Indonesia) and shows a sloping gradient towards high latitudes. Inter-longitudinal differences stand out in the example of the USA, where the west indicates low evaporation rates compared to the east; this is also the case in southern Africa, where the Kalahari desert remains drier (compare Fig. 9, page 17 in Zhang et al., 2010). Regarding seasonality of E_t, in DJF, the NH is characterised by low evaporation rates; in JJA, these are strongest, the opposite for the SH mid-latitudes (compare Fig. 10, page 17 from Zhang et al., 2010). The total actual evaporation (E) is also based on this global pattern of the E_t.

Global land E_t increased until the turn of the millennium and has significantly decreased since then, mainly due to rising land temperature, which leads to stomatal closure and reduced conductance, especially over northwestern India (Jung et al., 2010; Pascolini-Campbell et al., 2021; Xiao et al., 2020b). McCurley and Jawitz (2019) state that the main driver for land E_t was precipitation. Pascolini-Campbell et al. (2021) add that as a result of land precipitation the proportion of E_t increased in 2003-2019 compared to runoff. Pascolini-Campbell et al. (2021) also found a positive correlation between the ENSO and E_t. Jung et al. (2010) saw a slowdown in the increase in E_t since the strong El Niño in 1998 due to moisture limitation. The E_t and canopy conductance are thus in line with RH decrease in southern Africa, northeastern Brazil, California, Caspian Sea, Mongolia, Tibet (Xiao et al., 2020b). Boucher et al. (2009) advocate an E_t decrease due to increasing atmospheric CO_2 concentrations. These theses are examined in more detail in Section 1.3.3.4.

The change in the individual evaporation fractions can also change total land evaporation. For the period 1981–2021, Zhang et al. (2016b), who used models and satellite

data (Global Land Evaporation Amsterdam Model [GLEAM]), reported an increase in total land evaporation, mainly supported by positive trends in E_t and E_i through an increase in temperature. For 2003–2019, (Pascolini-Campbell et al., 2021) confirm these global trends with GRACE data. There has been an opposite, and weaker, negative trend in E_b (Zhang et al., 2016b). Most of the CMIP5 models were not able to represent the observed positive E_t trend (Zhang et al., 2016b). Roderick et al. (2007) explored pan evaporation via model calculations in Australia between 1975–2005 and found an increased evaporative demand, i.e. decreased evaporation, due to wind stilling and a reduction in radiation, agreeing with studies over the Tibetan Plateau in 1961–2000 and 1966–2003, respectively, (Shenbin et al., 2006; Zhang et al., 2007) and other regions. The main reason for this is the decreasing wind speed (McVicar et al., 2012; explained in Section 1.3.2.2), mostly in the US, China and the Tibetan Plateau, and secondly, regionally increasing solar irradiance through reduced cloud cover. Padrón et al. (2020) add through reconstruction analysis for 1984–2014 that the positive E_t and negative precipitation trend is associated with three seasons in the extratropical latitudes. This can be explained almost exclusively by anthropogenic warming. Contrasting findings regarding the change in evaporation may be due to the lack of observational data at a global scale or the definition of the term 'evaporation' (Jung et al., 2010; Miralles et al., 2020).
Links between terrestrial evaporation rates and modes of variability exist (Martens et al., 2018; Pascolini-Campbell et al., 2021). Using the example of this study of selected regions (see Section 3.3), there is a negative correlation between evaporation over Scandinavia in DJF and the NAO, and a negative correlation between evaporation over northeastern Brazil in SON and the AMO.

The aridity index (AI) can be used to measure and classify land dryness, and is, therefore, linked to droughts and RH decreases. It is defined as the ratio between precipitation as atmospheric supply and potential evaporation as atmospheric demand. With increasing CO_2 and global warming, the potential evaporation increases more strongly than the moisture supply via precipitation. Worldwide aridity and drylands, therefore, increase, except in the high northern latitudes (Berg et al., 2016; Greve et al., 2019; Rodell et al., 2018; Wang et al., 2021). Aridity is strongly influenced by a soil moisture decrease (Berg et al., 2016). A surface wind change has less influence on this (Fu & Feng, 2014). Feng and Fu (2013) point out that the increase in aridity and drylands worldwide can be accentuated under dynamical and terrestrial drivers. The strongest decreases are in boreal winter (DJF), the smallest in JJA (Wang et al., 2021). The land RH decrease can be related to the Aridity Index (Fu & Feng, 2014). Greve et al. (2019) see AI as a poor proxy for aridity due to the parameterisation of potential evaporation. Regions with a strong RH trend since 2000 will be characterised by their humidity classes (Fig. 1.12) in Section 3.3.

Clearly, local evaporation can be very important for local RH. There are various components of evaporation that make up total evaporation can contribute quite differently depending on latitude, season and underlying land use.

1.3.3.2 Soil moisture as a driver for land evaporation

Reasons for the temporal change in evaporation on regional and global levels can be found in the change in moisture availability, i.e. soil moisture. This study does not discuss incoming radiation change and cloud cover change, as this would be beyond the scope of the thesis; wind change was discussed in Section 1.3.2. Land cover change is strongly linked to soil moisture and even groundwater storage and thus also affects the evaporation rate, albeit less strongly than limitation of soil moisture (Andrew et al., 2016; Dai, 2011; Jung et al., 2010). The duration of soil drought ranges from a few months to years, compared to atmospheric drought which ranges from weeks to months (Zhou et al., 2019).

Soil is an absorber, retainer and releaser of CO_2 and water. Soil moisture is one of the limiting factors for evaporation (Zhou et al., 2019). A rough distinction can be made between the first few centimetres in the soil, the surface soil moisture, and the underlying material, the root zone soil moisture. In the latter case, E_t reaches through plants of different heights, whereas in the former, primarily low plants with shorter roots that transport soil moisture leads to transpiration, or E_b acts. Groundwater reserves are only depleted naturally in arid conditions. For irrigation, water can be brought to the surface by human hands, where it contributes to evaporation via agriculture and reduces runoff (Boucher et al., 2009; Gedney et al., 2006). The closer the water is to the surface, the more its amount depends on the seasons. Water stored in higher layers is usually easier to evaporate, depending on the vegetation type, and is more closely linked to interannual RH than deeper water (Andrew et al., 2016). Xie et al. (2019) suggest that NDVI change followed TWS anomalies by a lag of up to one month in more than 40% of the global vegetated areas (Long et al., 2014; Taylor et al., 2012b; Zhou et al., 2019). Ultimately, in regions where soil moisture is limited, E_t decreases (Jung et al., 2010). Both the physiological response to elevated CO_2 concentrations and a shift or change in the length of the growing season can also affect soil moisture. The sub-topic of the runoff is further discussed in Section 1.3.3.4.

Surface and root-zone soil moisture show similar patterns to land E and globally there is no strong seasonality (global climatologies for surface and root-zone soil moisture and its fractions are not shown). Soil moisture is lowest over deserts and bare soil regions.

Global soil moisture has declined sharply in the last four decades, particularly so in subtropics and mid-latitudes, highlighting Mongolia, whereas wetting trends were found in southern Africa and the sub-arctic region (Berg et al., 2016; Dorigo et al., 2012; Zhou et al., 2019). Dorigo et al. (2012) and Zhou et al. (2019) find that precipitation mainly drives variations in soil moisture. Xiao et al. (2020b) demonstrate that soil moisture decrease happens parallel to RH decrease in arid regions due to suppressed evaporation. Thus, long-term soil moisture changes dominate before the physiological response of vegetation to elevated CO_2 concentrations (see Section 1.3.3.4) leading to increasing aridity (Berg et al., 2016). Rowell and Jones (2006) explain that summer drought over

Europe can be traced back to soil dryness in spring, leading to less summer precipitation. ENSO has a strong influence on interannual TWS, particularly in tropical and subtropical regions, such as the Amazon and the La Plata basin (Ni et al., 2018). In the case of a globally positive correlation between soil moisture and RH, RH would have to be explained, among other things, by low evaporation rates. This also includes decreased E_t from vegetation and, thus, warming (Douville et al., 2020). Limited soil moisture, in turn, can lead to tree mortality and increased evaporative demand (McKinnon et al., 2021; Zhou et al., 2019). In dry areas, high VPD and low soil moisture lead to the containment of stomatal conductance, transpiration and carbon uptake (Hong et al., 2019; Zhou et al., 2019; Section 1.3.3.4). CMIP5 models underestimate the soil moisture-RH correlations and therefore also terrestrial and atmospheric aridity (Zhou et al., 2019).

1.3.3.3 Land cover change as a driver for changes in evaporation

The different evaporation types can be traced back to the LCLU. If the LCLU changes, for example, due to anthropogenic activities, the term "land use" can also be used. Land use, the "people's responses to economic opportunities" (quote by Lambin et al., 2001), primarily includes developments in agriculture and urbanisation. Land cover can also change for natural reasons, such as warming, precipitation change and flooding, insect damage, and so on. McDowell et al. (2008), for example, predict a landscape shifting towards anisohydric species, due to the preferential mortality of isohydric species with more rapid stomata closure under increasing temperatures (see Section 1.3.3.3 for plant type explanation; Grossiord et al., 2020). This may result in a heterogeneous patchwork of vegetation (Woodward & Lomas, 2001). A change in land cover can lead to changes in soil moisture, runoff, roughness length and albedo (reflectances and transmittances) and vice versa (Gulev et al., 2021; Piao et al., 2007); this changes the evaporation by changing heat distributions and energy balances, which RH can change (Chen et al., 2020; Song et al., 2018b; Winkler, 2020). Jung et al. (2010) consider land cover change to be responsible only for regional E_t changes, not global ones.

The division into different land cover types can be made at different levels. The International Geosphere-Biosphere Program (IGBP) divides land cover into 17 zones: water, forest (evergreen needle leaf/broadleaf, deciduous needleleaf/broadleaf, mixed forest), croplands, cropland/natural vegetation mosaic, urban and built-up, snow and ice, barren or sparsely vegetated, shrubland (closed/open), savannas, woody savannas, grassland and permanent wetlands (Friedl et al., 2002; Pan et al., 2013). The global pattern of land cover types roughly follows a latitudinal pattern, which strongly mirrors that of E_t (Section 1.3.3.1) and soil moisture (Section 1.3.3.2) (Friedl et al., 2002). Exploring the integration of fluxes from heterogeneous vegetation on the planetary boundary layer, Woodward and Lomas (2001) found smaller evaporation rates from homogeneous vegetation than from heterogeneous canopy based on the flux of humidity and gradient and wind speed. The heterogeneity was significant for scales of 1 km compared to at a scale of 5 km. Therefore, the increasing heterogeneity of vegetal areas due to agriculture activities plays a role in the hydrological cycle on certain area sizes.

Vegetation Indices (VIs), such as the NDVI (the normalised difference in reflectance of overlapping red [0.58–0.67 µm] and infrared [0.725–1.10 µm] spectral bands; see Section 2.1.4) are used to measure vegetal greenness. These indices also include the albedo, the proportion of radiation reflected, which is low for water surfaces and higher for soil and vegetal surfaces, and highest for snow/ice surfaces and thus season-dependent (Hartmann Dennis, 1994). The measurements take place globally via remote sensing and reflected wavelengths. In this study, NDVI is used to measure greenness and thus vegetation health and density (see Section 2.1.4). Piao et al. (2007) find a connection between land use and increased global river runoff trends. VIs, such as the NDVI, strongly correlate with E_t (Glenn et al., 2008).

Since the early 1980s, NDVI has followed a globally positive trend due to climate change, i.e. temperature increase and precipitation change, and CO_2 fertilisation, which is discussed in Section 1.3.3.4 (Hong et al., 2019; Shukla et al., 2019; Winkler, 2020; Yuan et al., 2019). Since the late 1990s, the greening trend has flattened due to increased VPD (Yuan et al., 2019). An increase in temperatures and precipitation prolongs and intensifies the growth season where rainfall is sufficient (Hou et al., 2013). The positive NDVI trend is particularly pronounced in northwestern India and semiarid woody vegetation (Chen et al., 2020; Fensholt et al., 2012). Negative NDVI trends are found in Patagonia and California (Chen et al., 2020; Fensholt & Proud, 2012). Due to agricultural expansion, bare ground has globally decreased, especially in Asia, raising the NDVI (Song et al., 2018b).

High greenery coverage is generally characterised by lower temperatures and higher RH than regions with low vegetation cover, due to the atmospheric moisture built-up (Fensholt & Proud, 2012; Wong & Peck, 2005). Globally, this suggests that correlations between NDVI-RH should be positive. It is not so straightforward for T, because although higher NDVI is associated with lower T, since the largest areas of bare ground are hot deserts, small increases in T as part of global warming, in addition to increasing CO_2, can lead to increased vegetation growth. Globally, a negative NDVI-T correlation has been found mainly in southern Africa and northeastern Brazil (Fensholt & Proud, 2012). Positive precipitation-NDVI correlations were found in northeastern Brazil, southern Africa, northwestern India and the Caspian Sea (Fensholt and Proud, 2012; Fig. 9.1, p. 185 in Fensholt et al., 2015). The findings could indicate a positive relationship between NDVI and RH in the regions mentioned (Mortensen, 1986). NDVI and VPD are negatively correlated since stomatal closure occurs with increased VPD, and the plant aims to counteract water loss (Yuan et al., 2019). This stomatal closure would also reduce vegetation growth (Yuan et al., 2019). Helbig et al. (2020) state that VPD would have increased in the growing season, and thus E_t over peatland is more pronounced than over forest. Thus, increased greening causes a cooling effect via decreased aerodynamic resistance and increased turbulent (latent) heat fluxes (Chen et al., 2020). Since 2000, Winkler et al. (2021) found a slowing down of positive NDVI trends and, furthermore, vegetation browning in especially the tropical forests. Jia et al.

(2019) summarise the seasonal changes of land cover as follows: from the point of view of phenology, the growing season extends into the boreal winter due to winter warming and results in a decrease in snow cover, and thus enhanced E_t. In tropical areas, greater LAI and E_t were found due to global warming and enhanced precipitation. In theory, a longer growing season could mean there is a deciduous leaf canopy which remains in place for a more extended period. This could draw down water to a greater extent, and within this scenario, warming and greening would draw down soil moisture, and result in an inverse relationship between TWS, i.e. water availability for evaporation, and greenness.
An increase in the NDVI, i.e. greening, can also mean that vegetation recovers from a drought (de Jong et al., 2011). In particular, large plants and trees help control the water cycle and protect the region from drought and flooding. Root-zone soil moisture can serve as a proxy for NDVI (Dorigo et al., 2012), and NDVI can represent E_t over long-term time periods (Zhang et al., 2010).

The IGBP land cover class "forests" is a particularly strong water and CO_2 store, due to its high biomass, and is especially active in E_t and E_i (McCurley & Jawitz, 2019). Since E_t has the largest share of E worldwide, afforestation/deforestation could be expected to impact RH strongly. The forest classification is a tree-covered land area larger than 0.5 ha (FAO, 2022). The trees must be taller than 5 m and have a canopy cover of at least 10% (see Fig. 2 in Pan et al., 2013, and Fig. 1 in Lefsky, 2010). This applies to 4.03 billion hectares and 30% of land cover (Pan et al., 2013). Structure, distribution and biomass are determined, in addition to the location and interaction with the environment and soil topography (Pan et al., 2013). Compared to other plant types, trees are highly responsive to elevated atmospheric CO_2 concentrations (Ainsworth and Long, 2005; Section 1.3.3.4).

Although the tree cover and biomass density of forests have increased since the 1990s, in particular in the extratropics through temperate reforestation and afforestation, total forest area has declined by 3%, in particular through tropical deforestation (Keenan et al., 2015; Pan et al., 2013; Song et al., 2018b). Natural forest areas are decreasing, while planted forest areas are increasing (Keenan et al., 2015). These changes apply to all climatic zones, with arid and semi-arid ecosystems poorer in vegetation and topographically higher regions richer in trees. Van Der Sleen et al. (2015) note accelerated tree growth, thus increasing undisturbed tropical forest over the past few decades. From 2000–2012, satellite data detected a global forest loss of 2.3 million square metres worldwide, including a large amount in tropical Brazil (Hansen et al., 2013b). The reasons for boreal forest loss (Hansen et al., 2013b) were fire and forestry. In contrast, 0.8 million square kilometres were gained in, for example, Indonesia, Malaysia, Paraguay, Bolivia, Zambia and Angola among other places.

As part of the land cover changes, deforestation has a direct impact on the roughness, thus, aerodynamic resistance, E_t, the albedo (higher for croplands and pastures than for forests) and atmospheric CO_2. Via radiative, physiological and structural effects, deforestation influences q and T, and thus RH. Compared to lower vegetation, large trees and forests contribute strongly to evaporation, as their deeper roots have more access to groundwater (Duveiller et al., 2021). The loss of forests has affected evaporation particularly strongly, with related effects on cloud formation, precipitation, and incoming radiation to the surface. The removal of forest cover has therefore been associated with severe droughts, increasingly damaging for the remaining vegetation under global warming (McDowell et al., 2008). However, where deforestation leads to decreased E_t, a move to agricultural land that is subsequently irrigated can offset this with an increase in evaporation (Gordon et al., 2005). Large-scale deforestation is considered as a progressive effect of deforestation of smaller areas. Lawrence and Vandecar (2014) estimate that complete deforestation would increase the global temperature up to 0.7 K due to decreased E_t. The consequences of this would be reduced rainfall, CO_2 unlock and enhanced warming, resulting in dryness. Any deforestation leading to an increase in VPD can lead to further tree mortality (Grossiord et al., 2020; Yuan et al., 2019; Zhou et al., 2019).

Deforestation can affect local temperatures through changes to moisture levels, albedo, cloud formation and roughness length (Duveiller et al., 2021) but this differs depending on latitude and spatio-temporal scales. Generally, temperate deforestation, especially in winter, is associated with cooling (Bonan, 1999; Lejeune et al., 2018). Over the tropics, deforestation is associated with warming (Alkama & Cescatti, 2016; Bonan, 1999; Lawrence & Vandecar, 2014; Querin et al., 2016).

A small-size tropical deforestation was found to lead to a local increase of rainfall but globally reduced rainfall in a GCM based study (Lawrence & Vandecar, 2014). The research was carried out on teleconnections of deforestation in the tropics, e.g. complete deforestation of the Amazon leading to a decrease in precipitation over California (see Fig. 1 in Lawrence and Vandecar, 2014). This suggests that deforestation can affect the RH of other regions.

The classification into isohydric and anisohydric species refers to the reaction of plants to drought: while isohydric plants react to atmospheric and soil water-limitation by closing their stomata, anisohydric plants have a poor stomatal adjustment capacity and keep transpiring (Hugalde & Vila, 2014). Anisohydric plants are therefore more affected by drought stress. The Koeppen-Geiger climate classification is also based on the habitats of the vegetation (updated version: Beck et al., 2018; Fig. 1.13). The botanist Koeppen and the climatologist Geiger divide into the main groups of tropical/megathermal (A), dry (desert and semi-arid; B), temperate/mesothermal (C), cold, continental/microthermal (D) and polar climates (E) (Peel et al., 2007). This classification scheme together with the world humidity classification (Fig. 1.12), which McCurley Pisarello and Jawitz (2021) found coherent, will be used in Section 3.3 to characterise regions with a strong RH trend.

In summary, the type of LCLU can clearly affect both local and distant (in some cases) temperature, moisture, and thus RH. This can be quite dependent on latitude and season, with LCLU changes being compounded by other things such as irrigation.

1.3.3.4 Physiological and structural response to elevated CO_2

Mainly due to anthropogenic activities, such as fossil fuel combustion and land-use change, post-industrial, global CO_2 concentrations have increased steeply (Hou et al., 2013). These elevated CO_2 concentrations have various effects on the hydrological cycle: directly through the radiative effect, as the trapped longwave radiation leads to a global temperature and saturation vapour pressure increase (see Section 1.3.1), and indirectly through its physiological and structural effects on the vegetation (Betts et al., 1997; Cao et al., 2010). The indirect influence on clouds is out of the scope of this thesis. The physiological effect is a key driver for temperature. When CO_2 doubles, the temperatures increase almost sevenfold by the radiative effect compared to the physiological effect, while the runoff increase is rather caused by the physiological effect and reduced E_t (Cao et al., 2010). Cao et al. (2010) therefore conclude an RH decrease over land due to decreased E_t. Although increasing temperature can lead to increased greening through the mechanisms described above, plant physiology itself can have an important effect. The amplification of aridity and RH decrease can appear via different physiological mechanisms (Berg et al., 2016):

(a) Plants reduce their transpiration of water into the atmosphere at high temperatures to reduce water loss and drought stress. With lower stomatal conductance (or its reciprocal, stomatal resistance), they save water, which corresponds to a high water use efficiency (WUE, i.e. ratio of water loss to carbon gain) by partially closing stomata (e.g., Donohue et al., 2017b; Ruggiero et al., 2017; Sellers et al., 1996. RH would decrease in this case (Cao et al., 2010).

(b) Partial stomatal closure and later a reduction in stomatal density also occur when there is an oversupply of CO_2, to keep the CO_2 concentration inside the leaf as constant as possible (Keenan et al., 2013). The required amount of CO_2 can be absorbed through fewer openings (experimentally, Gedney et al., 2006; Medlyn et al., 2001; via model simulations, Boucher et al., 2009). The stomatal closure leads to less cooling through transpiration and an increase in surface T (Betts et al., 1997; Boucher et al., 2009; Bunce, 2004; Sellers et al., 1996). Also, VPD would increase in this case, and RH would decrease (Byrne & O'Gorman, 2016; Douville et al., 2020). Soil moisture would increase because of less uptake by the plants, so a negative correlation between soil moisture/runoff and RH would be expected. After ocean moisture transport, which accounts for the thermodynamic driver component and to a large extent the dynamical driver component, the physiological effect is crucial to land humidity (Byrne & O'Gorman, 2016).

(c) Elevated air CO_2 concentrations stimulates photosynthesis (Lapola et al., 2009). Under CO_2 fertilisation, the plant grows faster and stronger, corresponding to a structural change in leaf canopy, i.e. higher LAI and productivity (Norby & Zak, 2011; Winkler et al., 2019). The increased evaporative area leads to increased light interception and an increase in E_t (Hong et al., 2019; Kauwe et al., 2013). CO_2 fertilisation would increase RH.

With decreased stomatal conductance, high WUE and thus decreased E_t (case a and b), RH would decrease; with increased stomatal conductance, low WUE and, therefore, increased E_t, RH would increase (case c). Both effects can occur with a time lag, and partially or entirely cancel each other out (Betts et al., 1997; Gray et al., 2016; Norby & Zak, 2011; Osborne, 2016). The LAI increases in the mid and high latitudes without any physiological effects and just the CO_2 radiative effect of global warming (Betts et al., 1997). Physiologically, however, an elevated CO_2 concentration affects the tropics most strongly, as, for example, model simulations of the coupled biosphere-atmosphere model SiB2-GCM demonstrate (Sellers et al., 1996).

Various experiments have been conducted to explore plant physiological responses to elevated CO_2. The free-air CO_2 enrichment (FACE) experiment exposed vegetation to elevated CO_2 levels (Ainsworth & Long, 2005; Leakey et al., 2012; Norby & Zak, 2011). They found that responses depended on plant functional type (PFT) and environmental conditions. These experiments could shed light on the link between physiological effects and RH.

In addition to measurements, global land-atmosphere coupled models were used to explore raised CO_2 concentrations and to measure its radiative and physiological influence on vegetation (Byrne & O'Gorman, 2016). Examples include the CMIP5 simulations and HadGEM2-ES with the CMIP5 model experiments $esmFdbk2$ and $esmFix2$ (explained in Section 2.1.2 and evaluated in Section 5.5). Capturing physiological feedback on CO_2 and appropriately representing transpiration and assimilation fluxes still presents significant challenges for models, in particular for disturbed vegetation (Donohue et al., 2017b; Douville et al., 2020; Grossiord et al., 2020; Hong et al., 2019; Keenan et al., 2015; Keenan & Riley, 2018; Keenan et al., 2013; Winkler et al., 2019). This is due to various factors, such as climate zones, plant species and soil conditions, and the fact that experiments cannot report data on the entire lifespan of trees (Medlyn et al., 1999).

1.3.3.4.1 Stomatal closure

At leaf-level, the elevated CO_2 concentration gain to water loss ratio comes along with an enhanced WUE almost universally (Donohue et al., 2017b) and was found for canopy-level transpiration, in particular, in NH temperate and boreal forests over the past two decades (Keenan et al., 2013; van der Sleen et al., 2014). This holdback of water and the resulting high WUE can benefit the plant, particularly under dry conditions, and reduce drought stress (Leakey, 2009; Leakey et al., 2012; Osborne, 2016). The condition of suppressed transpiration leads to less moisture in the air and more energy going into sensible heating, thus, contributing to the radiative forcing and amplifying a local rise in temperatures (Betts et al., 2007; Cao et al., 2010; Sellers et al., 1996). Based on FACE, Medlyn et al. (2001) give a statistically significant more than 20% decrease in stomatal conductance in response to an elevated CO_2 concentration, with the strongest reduction in young, deciduous and water-stressed trees being more affected than nutrient-stressed trees. This suggests that age, species, and water and nutrient supply play a role. Gimeno et al. (2018) found in their FACE experiments no water savings for water-limited mature eucalypt woodlands under an elevated CO_2 concentration for the period of two years. The global physiological effects of CO_2 on vegetation are small but can play a decisive role regionally, especially under the radiative effect of CO_2 (Field et al., 1995).

Runoff is the difference between land precipitation and evaporation (Gedney et al., 2006). It is the water above ground that the soil cannot absorb due to saturation or impermeability. Both observations and model simulations showed that stomatal closure due to CO_2 physiological forcing resulted in increased vegetal WUE and suppressed E_t, and increased runoff over the twentieth century (Betts et al., 1997; Boucher et al., 2009; Gedney et al., 2006). This includes surface soil moisture, root-zone soil moisture, and drainage (Douville et al., 2020; Gimeno et al., 2018). This increase in runoff, plus soil moisture, due to an elevated CO_2 concentration, is more pronounced in wet areas than in dry areas, although according to the CMIP5 carbon feedback experiments, there can even be a decrease in soil moisture in dry regions (Hong et al., 2019). Any long-term soil moisture decrease due to stomatal closure would mean that the root-zone soil moisture is increased, while the surface soil moisture is reduced. Atmospheric evaporative demand and land aridity would increase, which would result in a non-linear relationship between increased CO_2 concentrations and RH (Berg et al., 2016; Douville et al., 2020). Another reason for the decrease in runoff is expanded irrigation (Gedney et al., 2006). Conversely, when adding CO_2 fertilisation to their vegetation model, Piao et al. (2007) found a global reduction in runoff between 1901–1999 with strongest trends in the tropics. They concluded that CO_2 net has less influence on runoff, whereas land-use change in the tropics and climate variability determine the runoff trend.

1.3.3.4.2 CO_2 fertilisation and greening

The decrease in E_t caused by the influence of an elevated CO_2 concentration on stomata conductance and CO_2 fertilisation, and therefore leaf photosynthesis (Ellsworth et al., 2017; Medlyn et al., 1999), may lead to changes in vegetation structure, in particular, an increase in LAI (Betts et al., 2007; Gimeno et al., 2018; Hong et al., 2019; Kauwe et al., 2013), accelerated tree growth (Ainsworth & Long, 2005; Norby & Zak, 2011; Van Der Sleen et al., 2015), biomass density (Pan et al., 2013) and productivity (NPP: Hou et al., 2013; GPP: Kauwe et al., 2013; Winkler et al., 2019; for above-ground production: Ainsworth and Long, 2005; Haverd et al., 2020). The global greening trend and biomass gain over the past three decades is associated with CO_2 fertilisation (Hong et al., 2019; Pan et al., 2013). However, greening seems to come more from rising temperatures and a lengthening of the growing season than from CO_2 fertilisation (Winkler, 2020). The increase in LAI is most pronounced in regions characterised by increased precipitation (Betts et al., 1997), including globally established forests (Pan et al., 2013). In dry areas, an elevated CO_2 concentration induced LAI increase leads to soil moisture decrease, and in wet areas, to soil moisture increase (Hong et al., 2019). In addition to the LAI increase due to an elevated CO_2 concentration, it has also been hypothesised that there are equivalent root depth and roughness length increases (Betts et al., 1997).

Elevated CO_2 concentrations and CO_2 fertilisation have been associated with an increased WUE in NH temperate and boreal forests over the past two decades, leading to a decrease in evaporation (Keenan et al., 2013). This WUE increase is underestimated by models (Keenan et al., 2015). Despite the increase in WUE, the width of growth rings in tropical forests, Van Der Sleen et al. (2015) do not associate with an elevated CO_2 concentration over the last 150 years, thus rejecting the hypothesis of a positive correlation between CO_2 fertilisation and tree growth over the long-term in these ecosystems. Clearly, there are latitudinal and biome related differences in plant physiological responses that could be relevant to regional differences in RH trends.

1.3.3.4.3 Comparing physiological and structural responses, and further offsetting

Several potential feedbacks could offset a physiological or structural response to an elevated CO_2 concentration on large scales (Gray et al., 2016). Betts et al. (2007) suggest that CO_2 fertilisation leads to more growth and larger leaf canopies (an increase in LAI). The greater evaporative area leads to water loss (Kauwe et al., 2013). It reduces canopy conductance, which offsets the physiological response, namely stomatal closure, because canopy transpiration and thus also soil water depletion are kept constant (Field et al., 1995; Leakey et al., 2012). Using the example of soya beans in dry years, Osborne's (2016) comment on (Gray et al., 2016) names another offset mechanism: aerodynamics, which change with the height of the plants and to the extent to which the plant is exposed to wind (Betts et al., 1997; Norby & Zak, 2011). Air circulations interact strongly with the leaf surface, while small dense crops are comparatively sheltered. The third effect is that of heating, which occurs through suppressed evaporation, and could again lead to drought. Thus, the assumption of a boost in crop yield in dry years, due to an elevated CO_2 concentration by saving water in crops, can be rejected (Ainsworth & Long, 2005; Osborne, 2016). A 2-year FACE experiment on mature water-limited Eucalyptus also showed no water savings in the ecosystem (Gimeno et al., 2018). In summary, the structural response can offset the physiological response, an increase in plant height can change the airflow, and a local increase in temperatures can occur because of reduced E_t.

Due to the offsets arising from these various mechanisms, simulations find a regional net effect of an elevated CO_2 concentration on vegetation, which is less pronounced at the global scale (Betts et al., 1997; Field et al., 1995). If the affected regions are also influenced by rising surface temperatures as a result of climate change, this can amplify the effects on the hydrological cycle. Field et al. (1995) conclude that an elevated CO_2 concentration primarily impacts the climate through its radiative impacts.

CMIP5 models generally find stronger physiological effects in doubling CO_2 than structural effects as a response to an elevated CO_2 concentration, which results in a decrease in land evaporation and an increase in soil moisture and runoff (Cao et al., 2010; Hong et al., 2019). The balance is only reversed in dry areas so that structural effects (increase LAI/productivity) are stronger so that soil moisture decreases there (Hong et al., 2019).

1.3.3.4.4 Other factors contributing to a change in stomatal conductance

The vegetal feedback on an elevated CO_2 concentration depends on further atmospheric and terrestrial parameters, such as the plant species, moisture availability, nutrients and other regional aspects (Andrew et al., 2016; Glenn et al., 2008; Grossiord et al., 2020; Sellers et al., 1996). In general, plants strive to use their resources efficiently. Therefore, when plants are limited in their needs, they reduce their leaf area (Glenn et al., 2008), which would imply reduced E_t.

On the spatial scale, one reason for the different effects of physiological and structural factors may be the dynamical drivers; continents are exposed to different circulations and thus moisture supply and stability, which affect both the physical/structural response to an elevated CO_2 concentration and are influenced by them. Zonally asymmetric rainfall anomalies, due to forest responses to an elevated CO_2 concentration, may arise from local differences in moisture recycling and land-ocean interactions (Kooperman et al., 2018). When discussing the spatial scale, the temporal scale must also be taken into account: it may be that structural responses to an elevated CO_2 concentration lag behind the physiological response by up to a number of decades, which also makes it difficult to understand and decouple the interaction between the two (Betts et al., 1997). Model simulations also do not see a consistent global correlation between an elevated CO_2 concentration fertilisation and NPP change, with the most remarkable changes in southern Africa and the tropical Amazon basin (Hong et al., 2019; Hou et al., 2013; Lapola et al., 2009), regions with increased rainfall (Betts et al., 1997).

Because of these many conditions, it is challenging to predict the response of vegetation to an elevated CO_2 concentration and impact on Et, q and T, and therefore, RH, especially on the larger scale of the diversity of climate and terrestrial conditions. The expectation is that the influence of the above-defined terrestrial drivers on RH will be localised in scale and quite possibly small compared to other drivers, or even offset by them. Nevertheless, it is clear that there are several mechanisms by which plant physiology and LCLU can affect RH.

1.4 Research aims and structure

The main purpose of this study is to explore the potential for contributions of non-thermodynamic drivers to the decline in RH over land. Furthermore, this study intends to evaluate the ability of common climate models, such as HadGEM2-ES, to reproduce this decline. The recently observed decline in RH is not reproduced in historical simulations from climate models. This has important implications for projected climate impacts that are related to land surface RH, suggesting that there are considerable uncertainties. By improving the understanding of the potential drivers of land surface

RH that are more difficult for climate models to accurately represent, such as modes of variability, plant physiology and LCLU, this research may help to improve climate modelling. In addition to climate monitoring, climate modelling and climate impacts modelling, the results are relevant to a large number of scientific areas including the terrestrial water cycle, soil and plant sciences and atmospheric dynamics.

The thermodynamic driver as a reason for the decrease in RH has been investigated extensively (Byrne & O'Gorman, 2013a; Byrne & O'Gorman, 2013b, 2016, 2018; Dunn et al., 2017; Joshi et al., 2008; Vicente-Serrano et al., 2018; Wallace & Joshi, 2018). Since they cannot fully describe the decreasing RH trend, this study explores whether any other drivers, that act on different temporal and spatial scales, might help explain some of the regional differences. The variable of RH is looked at surprisingly rarely in climate research. It is not a priority variability of impact, unlike air temperature and precipitation, which have a direct impact on people and society. The q is more often used as a physical quantity which relates more to the amount of water vapour and precipitation. RH is a more complicated variable due to its dependence on T and q, and is difficult to observe accurately.

Global monitoring products (q, T, RH), e.g. the global gridded land surface humidity dataset HadISDH and ERA-Interim reanalysis, serve as the data basis for this research. They are used to explore relationships with dynamical drivers composed of sea level pressure, 10m winds, sea surface temperature, precipitation and large-scale modes of variability. Remote sensing datasets are used in addition to exploring relationships with terrestrial drivers comprising land evaporation, TWS and vegetation cover. The analyses are carried out on a global as well as on a regional scale, for typical 3-month seasons (December-January-February [DJF], March-April-May [MAM], June-July-August [JJA] and September-October-November [SON]) as well as annually. Furthermore, the impact of CO_2 induced stomatal conductance changes on RH is explored using the HadGEM2-ES general circulation model experiments $esmFdbk2$ and $esmFixClim2$. Additionally, RH trends and the regional relationship between q, T, and RH in HadGEM2-ES simulations is explored.

Those working in concerned disciplines are given an insight/overview into the fields relevant to them, e.g. hydrologists, soil scientists, atmospheric physicists, plant physiologists and climate modellers. Comprehensive environmental findings are essential for planning our future, especially under the strong influence of climate change and global warming. This study's findings will guide politicians and will also be used by non-governmental organisations, industry and other stakeholders around the world to make educational and cultural decisions.

Climate impact models take the climate models a step further. They focus on the impact of climate change on socio-economic sectors, e.g. heat stress, food security, such as crop growth and their susceptibility to diseases, and extreme events like flooding and droughts. The better RH is understood and the more precise the underlying physics in the climate models, the more accurate the climate impact predictions on the socio-economic sector, e.g. vulnerability of the agricultural system to the hydrological cycle. With high certainty in these predictions, prudent decisions can be made to prevent catastrophes or adapt to them.

Chapter 1 explained the importance of atmospheric humidity for living things such as humans, plants and fauna, and its position in the global water cycle. Specifically, RH is defined. The global decline in RH over land is described using current literature. An introduction to three possible drivers for this change is given. These drivers are each then discussed in upcoming Chapters, with the help of experiments. At the end of this Chapter, the research niche, the aim of the thesis, and the project outline are presented.

Chapter 2 describes the data and methods used in this thesis and introduces the regions of interest.

Chapter 3 sets the scene by exploring regions with a strong RH trend, highlighting their characteristics, in the context of simultaneous changes in q and T. The contribution of regional RH trends to the global trend and, thus, the relevance of work on the selected regions, are elaborated on. Relationships between RH and T and q, in form of correlations and regressions, provide important insights for the later analysis of dynamical and terrestrial drivers. The differences in representing the global and seasonal RH trends and the relationship between RH, q and T between observations and HadGEM2-ES are extracted.

Chapter 4 explores whether dynamical drivers could explain any of the long-term changes in regional RH. The Chapter introduces the coupling of selected modes of variability with regional RH. The significance and strength of the relationships are ranked to determine which modes and which regions to include in the analysis. To explain the link between modes and RH in more detail, relationships with primary variables, i.e. mean SLP, SST, and wind speed and direction, are included.

Chapter 5 assesses the terrestrial drivers and their role in land surface RH change. This is divided into different types of E, i.e. E_t, E_i, E_b, E_w and E_s, which are examined with the help of several datasets. For regions in which evaporation is dominated by evapotranspiration and interception loss, land cover change and plant phenology are examined using the NDVI datasets. GLEAM soil moisture and GRACE TWS datasets are used to understand the land cover change further and to analyse regional changes in open-water evaporation and snow sublimation. Links between regional wind speed and evaporation, and thus the impact on RH, is examined. In addition, the analysis of soil moisture variability provides information on the subject of plant physiology and the effect of CO_2 on stomatal conductance. The latter is also analysed by comparing the model runs HadGEM2-ES $esmFixClim2$ and $esmFdbk2$ regarding increasing CO_2 being seen either by radiation or by the carbon cycle.

Chapter 6 provides a summary of the main findings, linking together explanations for the most holistic understanding of the global decrease in RH over land. The success of the methods used in this thesis and their results are reviewed in retrospect. Proposals are made for the continuation of the project and for improving climate models that are not yet able to represent the trend in RH.

2 Data and methods

The analysis of drying trends around the globe is carried out on various temporal and spatial scales using a wide range of datasets: climate monitoring datasets from in situ observations, reanalysis, remote sensing datasets and climate model data.

2.1 Data

The datasets used in this thesis are shown in Table 2.1. This study is based on the Met Office Hadley Centre's Integrated Surface Dataset of Humidity HadISDH. This is an annually updated in situ observation-based surface humidity (q) and temperature (T) monthly mean land surface climate monitoring product developed by Willett et al. (2014). It is supported by the European Centre for Medium-Range Weather Forecasts (ECMWF) atmospheric reanalysis ERA-Interim (Berrisford et al., 2011; Dee et al., 2011), which showed similar relative humidity (RH) trends to HadISDH in the last two decades (2000–2017) (Dunn et al., 2017; Vicente-Serrano et al., 2018). As a representative of the CMIP5 models, the UK Met Office Hadley Centre Earth System Model HadGEM2-ES (Collins et al., 2008) is used in this work. These three datasets are used for the trend analysis of RH, q and T (Chapter 3). ERA-Interim also provides data for the primary physical drivers SST, wind speed and direction and SLP (Section 4.1). In Section 4.1.1, the Global Precipitation Climatology Centre (GPCC) Full Data Monthly Product (Schneider et al., 2020) helps to establish the connection between precipitation and RH.

As part of the terrestrial drivers (Chapter 5), the remote sensing datasets Global Land Evaporation Amsterdam Model (GLEAM; Martens et al., 2017; Miralles et al., 2010a; Miralles et al., 2010b), Gravity Recovery and Climate Experiment (GRACE; Save, 2019; Save et al., 2016) and Global Inventory Modeling and Mapping Studies (GIMMS; Pinzon and Tucker, 2016; Pinzon and Tucker, 2014) are used to assess the influence of evaporation and soil moisture, terrestrial water storage (TWS) and green vegetation (normalised difference vegetation index, NDVI) on RH. The HadGEM2-ES model is also used to evaluate the radiative (the thermodynamic and dynamical drivers) versus the physiological (terrestrial driver) response to elevated air CO_2 on RH.

The spatial and temporal resolution of the datasets was tailored to the resolution of the HadISDH dataset (5° by 5°, monthly and minimum start/maximum end in 1973/2017). The period for climatology is 1981–2010 unless otherwise stated. The datasets were not spatially matched with the HadISDH dataset.

Table 2.1: Overview of used datasets (Becker et al., 2013; Berrisford et al., 2011; Collins et al., 2008; Dunn et al., 2016; Martens et al., 2017; Miralles et al., 2010a; Pinzon & Tucker, 2016; Pinzon & Tucker, 2014; Save, 2019; Save et al., 2016; Schneider et al., 2020; Smith et al., 2011; Willett et al., 2014).

Dataset	Type	Variables	Time period used	Chapter	References, comments
HadISDH.land v4.0.0.2017f	Observation	RH, q, T	1973-2017	3, 4, 5	Willett et al. (2014), Dunn et al. (2016), Smith et al. (2011)
ERA-Interim	Reanalysis	RH, SST, u10, v10, si10, SLP	1979-2017	3, 4	Berrisford et al. (2011), Dee et al. (2011)
HadGEM2-ES	Coupled AOGCM	RH, q, T from experiments *historical*, *historicalExt*	1973-2017	3	For the *historical* and *historicalExt*, runs *r2i1p1*, *r3i1p1*, *r4i1p1*; Collins et al. (2008)
		RH from experiments *esmFdbk2*, *esmFixClim2*	1860-2099	5	
GPCC v2020	Observation	Precipitation	1973-2017	4	Becker et al. (2013), Schneider et al. (2020)
GLEAM v3.3a	Satellite, model	Types of evaporation rates: E, E_w, E_t, E_i, E_s, E_b; surface and root-zone soil moisture	1980-2017	5	Martens et al. (2017), Miralles et al. (2010)
GRACE	Satellite	TWS	2002-2017	5	Save et al. (2016), Save (2019)
GIMMS3g	Satellite	NDVI	1982-2015	5	Pinzon & Tucker (2014), Pinzon & Tucker (2016)

The datasets for monthly indices of modes of variability widely embracing the time period of HadISDH (1973–2017) are outlined in Section 2.1.5, and their impact on RH is explored in Chapter 4.

2.1.1 Observation based datasets: HadISDH and ERA-Interim

HadISDH observations and ERA-Interim reanalysis were used to work out regional RH trends. The latter also provided primary physical variables for analysing the impact of dynamical drivers on RH.

HadISDH

The MetOffice Hadley Centre led project HadISDH.land utilised the National Oceanic and Atmospheric Administration's (NOAA) National Centers for Environmental Information's (NCEI) Integrated Surface Database (ISD; Smith et al., 2011) humidity data. It is a quality-controlled and homogenised, gridded in-situ dataset providing air T and multiple surface atmospheric humidity variables from 1973 to the present (Willett et al., 2014; Willett et al., 2021b; Willett et al., 2013). The ISD data are then processed as part of the HadISD sub-daily observations dataset (Dunn, 2019; Dunn et al., 2014; Dunn et al., 2012; Dunn et al., 2016) which filters for the length of record and applies quality control. The stations are then further filtered as part of the HadISDH processing for intermittency and length of the record, resulting in <4000 stations (Fig. 1.2). Near-surface (2 m) air T and dew point temperature (T_d) are reported, the latter measured as either RH directly or wet bulb temperature (T_w) but then converted to T_d prior to transmission. These are converted to q and RH (in addition to other humidity variables) via nonlinear equations (Table 1 in Willett et al., 2014), and then averaged to monthly means. Pairwise homogenisation comparing neighbour stations' measurements (described in Dunn et al., 2014; Menne and Williams, 2009) is applied to these monthly means to find and adjust for changes in the observation time series caused by changes to the instrument, instrument location, instrument housing, observing practice etc. After homogenisation, the values are gridded by simply averaging over 5° by 5° grid boxes. The dataset is updated annually (Willett et al., 2021b). This dataset is the heart of the thesis, and the negative RH trend based on this should be explained. There is also a related HadISDH.marine dataset for the ocean (Willett et al., 2021b) but this is not used in this study.

HadISDH.land.v4.0.0.2017f was used as this was available near the beginning of this thesis. A more recent version could have been used but the accompanying ERA-Interim dataset ended in August 2019 so would have involved bringing in the newer ERA5 product (Hersbach et al., 2020). Also, the GIMMS3g NDVI dataset ended in December 2015. The data were downloaded from https://www.metoffice.gov.uk/hadobs/hadisdh/.

ERA-Interim

The European Reanalysis (ERA-Interim) developed by the European Centre for Medium-Range Weather Forecasts (ECMWF) is a mathematical forecast model for 1979 until August 2019 with a spatial resolution of about 80 km (Berrisford et al., 2011; Dee et al., 2011). Based on station observations, satellites, ships, buoys, aircrafts and radiosondes of various datasets, the reanalysis forecasts globally complete fields of surface variables at each time step, blending them with actual observations. In addition to 2 m T, q and RH, SST, wind vectors and speed, and SLP are used for this study. As for HadISDH, monthly humidity data are calculated from sub-daily 2m T, dew point T and surface pressure, using the same equations as for HadISDH (converted data provided by K. Willett). There is temporal instability of SST in the dataset, as different SST observation datasets were assimilated at different times over the period of record (June/July 2001 and December 2001/January 2002), i.e. changes of datasets in July 2001 and January 2002 (Kumar et al., 2012). In ERA-Interim, lakes are translated from lake surface temperatures provided by Moderate Resolution Imaging Spectroradiometer (MODIS; Dutra et al., 2010; Minallah and Steiner, 2021). Accurate lake surface temperatures benefit the thesis' analysis on lake SST (Sections 4.1 and 4.2), such as in the Caspian Sea region. ERA-Interim data are used in Section 4.1, so the SLP, winds etc. may be less affected, and influence on regional surface temperature might be possible. Vegetation is represented by its height (low, high) and based on the Global Land Cover Characteristics (GLCC), a series of evolution of classifications of vegetation, soil and snow evolution which are derived from one year of Advanced Very High Resolution Radiometer (AVHRR) data (Dee et al., 2011; Loveland et al., 2000). The vegetation height represents the roughness length and thus the aerodynamic resistance, linked to wind and evaporation. Applied to this is the Tiled ECMWF Scheme for Surface Exchanges over Land (TESSEL) scheme, which models four-layer soil and snow, thus, thermal and water storage (Dee et al., 2011). ERA-Interim does not include any changes to land cover or land use (LCLU), which could influence albedo and evaporation. Albedo is not covered in this thesis, whereas the link between land evaporation and RH is covered by the GLEAM data set. A change in LCLU could also influence a change in roughness length, which may affect the wind speed. The data can be downloaded from https://apps.ecmwf.int/datasets/data/interim-full-daily/levtype=sfc/.

2.1.2 Model data: HadGEM2-ES

Following up on Dunn et al. (2016), who found that a collection of *historical* and *historicalExt* runs from nine models in the fifth phase of the Coupled Model Intercomparison Project (CMIP5; Taylor et al., 2012a), were not able to represent the global negative RH decrease since the early 2000s, the MetOffice Hadley Centre Global Environment Model version 2-Earth System (HadGEM2-ES) is also chosen as a representative of CMIP5 in this study. HadGEM2-ES is a coupled atmosphere-ocean general circulation model (AOGCM). It provides a wide range of long-term projections that could be useful across this study (historical experiments and the coupled model long-term idealised simulations $esmFdbk2$ and $esmFixClim2$, see below) and are accessible in the study's time frame. Representing biophysical and biogeochemical processes, the HadGEM2-ES model has a resolution of 1.875° by 1.25° for the atmospheric domain and 1° within the ocean. It reaches almost 40 km into the atmosphere with sub-hourly time steps over the atmosphere and land and 1h for the ocean domain (Collins et al., 2011). The Joint UK Land Environment Simulator (JULES, derived from the Met Office Surface Exchange Scheme [MOSES II]; Essery et al., 2003) and the Top-down Representation of Interactive Foliage and Flora Including Dynamics (TRIFFID; Best et al., 2011; Clark et al., 2011) Dynamic Global Vegetation Model (DGVM; Cox, 2001) represent the land surface scheme and vegetation dynamics (Bellouin et al., 2011; Collins et al., 2011; Jones et al., 2011). It should be noted that MOSES II does not perceive climatic changes of lakes via their area but focuses on soil moisture (Collins et al., 2011). Keeping the lake surface area constant could overestimate evaporation processes, thus, atmospheric humidity if the thermodynamic driver, i.e. stronger land-than-ocean warming, applies to open water bodies like lakes. The historical land use is based on the History Database of the Global Environment (HYDE). TRIFFID DGVM calculates with five plant functional types (PFTs; depending on the climatic conditions: broadleaf and needleleaf tree, C3 and C4 grass, shrubs) and soil. Urban areas, lakes and ice are based on the International Geosphere-Biosphere Program (IGBP) land cover map. Anthropogenic disturbance, i.e. and land-use change or agriculture, is represented by the reduction of woody PFTs (trees and shrubs) so that only grass PFTs, i.e. crop and pasture, are allowed (Jones et al., 2011). Abandoned agricultural areas are replaced with C3 and C4 grasses (Collins et al., 2011). This agriculture mask is a very simplified scheme because agriculture can be more than crop and pasture, such as livestock farming in Mongolia. Both biophysical and biogeochemical effects of LCLU change (anthropogenic and natural), such as surface albedo and roughness and evapotranspiration and runoff, can be simulated in this way. Indirectly, this affects radiative feedback such as bare soil fraction, wind speed and soil moisture (Jones et al., 2011). Irrigation is not included in the HadGEM2-ES, which could cause problems, mainly when depicting the larger hydrological cycle from groundwater storage to evaporation (Collins et al., 2011). The strongest impact of surface boundary conditions on this project's results might be humidity variables RH and q with the HadGEM2 analysis (Sections 3.4 and 5.4).

The *historical* (1850–2005) and *historicalExt* (historical extension; 2006–2017) were merged and used to look at the model representation of recent conditions, e.g. RH ($hurs$, as in HadGEM2-ES called), q ($huss$) and T (tas) trends and their relationships (Section 3.4). The experiments are forced with historically representative forcing, i.e. greenhouse gases, aerosols and natural factors (volcanos, solar forcings) to replicate the recent history of climate (Emori et al., 2016). Different realisations (runs) are initiated with the same settings, but they differ in their modes of variability because these are natural flows within the climate system to balance various things. One slight difference here can lead to a big difference there, known as the butterfly effect. So, at any one time, one realisation could have a very different state of ENSO or the SAM or the NAO or AMO etc. (internal variability; Taylor et al., 2012a). This results in a difference between the models and observations on a year-to-year scale. An attempt is usually made to calculate this variability out of an ensemble of runs. In this study, the runs ($r2i1p1$, $r3i1p1$ and $r4i1p1$ with the first number as the number of the ensemble member, the second number as the number of initialisation state, and the third number of used physical parametrisations), were examined individually to be able to make more precise statements about them if necessary. The runs were chosen due to their completeness of time for the selected experiments and variables.

The experiments ESM Feedback 2 ($esmFbk2$) and ESM Fixed Climate 2 ($esmFixClim2$) were selected to explore if there is a change in RH linked to stomatal changes responding to increases in CO_2. The carbon cycle (radiation) in $esmFixClim2$ ($esmFdbk2$) sees the same amount of CO_2 forcing as the historical period followed by the representative concentration pathway (RCP) 4.5 rise in CO_2 (Betts et al., 2015; Emori et al., 2016). RCP4.5 is a future warming "business as usual" scenario and means that by 2100 the radiative forcing is about 4.5 W m^{-2}; this corresponds to a CO_2 equivalent of 650 ppm (Thomson et al., 2011b). Conversely, the radiation (carbon cycle) in $esmFixClim2$ ($esmFdbk2$) sees no change in CO_2, which is set at piControl levels. In other words, $esmFdbk2$ prioritises the radiative response, whereas $esmFixClim2$ focuses on the carbon cycle response. Vegetation plays a major role in the carbon cycle. Increasing CO_2 leads to enhanced stomatal conductance efficiency, whereby partially closed stomata inhibit evapotranspiration, reducing a source of moisture into the atmosphere. For both experiments, T, q and RH trends were calculated over the entire model period of 1850–2099, hopefully magnifying any trend present in order to improve the signal-to-noise ratio. Given the absence of climate change-related to the radiative response to increased CO_2 in *esmFixClim*2, and therefore an absence of thermodynamically or dynamically driven related changes in RH, a change in RH in *esmFixClim*2 would indicate a CO_2 related stomatal driven component of RH, and thus the presence of a terrestrial driver. There is no land-use change in the ESM runs either. Additionally, comparing the observations with the *historical*/*historicalExt* and *esmFdbk*2/*esmFixClim*2 may elucidate interesting differences that may be useful in the field of model validation and development, and observation dataset developments. The data were downloaded from https://esgf-data.dkrz.de/search/esgf-dkrz/.

2.1.3 Precipitation from GPCC

Based on in situ rain gauge data from up to 50,000 weather stations worldwide, the Full Data (FD) Monthly Product V2020 of the Global Precipitation Climatology Centre (GPCC) by Deutscher Wetterdienst (DWD) used in this study provides quality-controlled precipitation data [mm month^{-1}] over land (Schneider et al., 2020; Schneider et al., 2008). The original gridded resolution is 2.5° by 2.5°, and the dataset covers the time period from 1891 to 2019. The gridding of gauge observations occurs via interpolation and spatial averaging of anomalies, including the land fraction with a concluding superimposing of anomalies on the background climatology (Schneider et al., 2014b).

As a freshwater source, precipitation is a central component of the hydrological cycle. In the dynamical drivers' category, it impacts RH primarily through the enrichment of runoff, soil moisture and terrestrial water storage, providing water for evaporation. Precipitation could directly influence RH if a season had an anomalously high number of rainfall events, depending on the type of precipitation event. The dataset shows regional and seasonal rain changes that can be linked to modes such as the El Niño Southern Oscillation (ENSO) and the North Atlantic Oscillation (NAO) (Figs. 15-17 in Becker et al., 2013). The GPCC dataset has been widely used: among others, Spinoni et al. (2013) estimated the high reliability of GPCC to analyse rainfall deficits and thus analyse the frequency, duration and severity of droughts worldwide. Simmons et al. (2010) compared GPCC precipitation rates and the ERA-Interim dataset and found overall positive correlations with q and RH.

The Full Data (FD) Monthly Product V2020 of the Global Precipitation Climatology Centre (GPCC) used in this study were downloaded from https://opendata.dwd.de/climate_environment/GPCC/html/fulldata-monthly_v2020_doi_download.html.

2.1.4 Satellite-based datasets: GLEAM, GRACE and GIMMS

The remote sensing datasets GLEAM, GRACE and GIMMS were used to determine the influence of terrestrial evaporation via vegetation cover and soil moisture on RH.

Evaporation from GLEAM

With the help of the Global Land Evaporation Amsterdam Model (GLEAM) version 3a, the influence of land evaporation on RH and the dependence on soil moisture can be explored. The model estimates daily land evaporation rates (potential evaporation E_p, actual evaporation E) and all its components (transpiration E_t, interception loss E_i, bare-soil evaporation E_b, snow sublimation E_s and open-water evaporation E_w) as well as surface soil moisture and root-zone soil moisture from satellite data derived from microwave sensors (Miralles et al., 2010a; Peng et al., 2017). Through mathematical models, four GLEAM modules are calculated:

I. the evaporation module, which calculates E_p via the Priestley-Taylor equation (Priestley and Taylor, 1972). This equation is an alternative to the Penman-Monteith equation, which relies exclusively on variables based on observations detected from space, namely net radiation and air temperature.

II. the stress module, where a stress factor is calculated using the vegetation optical depth (a proxy for vegetation water content) and estimates of root-zone soil moisture characteristics are made (Miralles et al., 2016). Together with the E_p, the stress factor results in E.

III. the soil module, which uses as inputs: precipitation, interception loss and snowmelt to output a moisture profile. Hence, via evaporation and drainage, E_t and E_b are estimated where the soil layer depends on the vegetation height (Martens et al., 2016).

IV. the interception module, which uses Gash's analytical model to calculate E_i derived from vegetation and precipitation characteristics, such as wetting up, saturated conditions and drying out after the end of the storm (Miralles et al., 2010a).

E_w and E_s are again based on the Priestley-Taylor equation, including open water and ice characteristics. Each land grid cell, 0.25° spatial resolution, is subdivided into four cover fractions: bare soil, short and tall vegetation (based on MODIS Global Vegetation Continuous Fields MOD44B) and open water (Martens et al., 2016). Their weighted average evaporation for these land covers determines the final evaporation rate for the grid box (Martens et al., 2016).

GLEAM has been used in many ways, including by Martens et al. (2018), Miralles et al. (2013) and Greve et al. (2014) to explore links between global evaporation and modes of climate variability, such as ENSO. Results from these studies suggest that El Niño events have led to vegetation stress and both evaporation, soil moisture and NDVI decrease, especially in water-limited regions between 30°N and 60°S, e.g. in southern Africa. In this study, the use of GLEAM data is taken a step further, and all latter components and their influence on RH are examined individually. The multi-decadal trend in global terrestrial evapotranspiration is positive, so are E and E_i due to increased leaf area index (LAI) with E_s decreasing between 1981–2010 (Zhang et al., 2016a).

The GLEAM v3.3a dataset is constantly evolving (Martens et al., 2016; Miralles et al., 2011); for example, the vegetation was increased from short to tall, and Soil Moisture and Ocean Salinity (SMOS) soil moisture data was integrated to improve terrestrial evaporation (Martens et al., 2016). The GLEAM v3.3a data used in this study were downloaded from https://www.gleam.eu/.

Terrestrial water storage from GRACE

Exclusively consisting of satellite data, and thus, being the only real independent dataset that observes the for the RH critical zone, the GRACE Center for Space Research at the University of Texas, Austin (CSR) release RL05 offers the unique possibility to investigate the continuous impact of change of the totality of the terrestrial water on HadISDH RH change. The GRACE experiment is based on a twin set of spacecraft launched by the National Aeronautics and Space Administration (NASA) and the German Aerospace Center (DLR) in March 2002. The twin satellites move around the Earth in a low-earth orbit (Rodell et al., 2004; Tapley et al., 2019; Wahr et al., 2004). The distance between the satellites is measured using a GPS and microwave ranging system, and since May 2018, the GRACE Follow-up (FO) uses also laser interferometry. The distance between the two satellites is about 220 km but changes when one of the two satellites accelerates/decelerates. The difference in speed occurs with a change in the gravitational forces experienced by the satellites (Wahr et al., 2004). The strength of gravity is determined by the local mass of the Earth, which also includes the shape of the oceans and terrestrial water resources. With geoid variability, the gravitational force changes over a location. For example, when water is redistributed, GRACE can measure this redistribution of water through the distance between the two satellites via variations in Earth's gravity field (Dickey et al., 1998). Since April 2002, GRACE has delivered a global inventory of monthly terrestrial water storage anomalies, offering some understanding of the status of data integrated vertically through the water column, i.e. groundwater, soil moisture, snow, ice, and surface water (Bettadpur, 2007). Further quantification of these fractions of terrestrial water storage is possible through the use of additional data (Feng et al., 2013; Syed et al., 2008).

For wider dissemination, GRACE data are regridded by the CSR, JPL (Jet Propulsion Laboratory) and GFZ (GeoforschungsZentrum Potsdam) to a spatial resolution: 0.25° by 0.25° (Rodell et al., 2004; Wahr et al., 2004). Atmospheric and climate effects are removed using European Centre for Medium-Range Weather Forecasts (ECMWF) model outputs (Rodell et al., 2004; Yu et al., 2019). Known uncertainty in these data includes (i) system-noise error in the satellite-to-satellite microwave ranging measurements, (ii) the accelerometer error, and (iii) error in the ultra-stable oscillator and orbit error (quoted by Wahr et al., 1998), which can be attenuated by filtering and regridding (Landerer & Swenson, 2012; Long et al., 2014). With the change in terrestrial water storage measured, the accuracies of the product are higher than 1.0 cm, tested for the first time by Wahr et al. (2004) over the large drainage basins of the Mississippi, the Amazon and the Bay of Bengal. The TWS anomalies are based on the mean gravity field 2004–2009; on this climatology were the HadISDH anomalies calculated when used in correlations with the GRACE data. As noted, individual water components cannot be separated without additional datasets, but several attempts have been made to filter out evapotranspiration (Long et al., 2014; Rodell et al., 2004).

GRACE data have been used many times to increase our understanding of global and regional surface hydrology and hydrological balance. Dai (2011) used GRACE and GPCC precipitation data to simulate the Palmer Drought Severity Index (PDSI) and pointed out that GRACE included human-induced variations, such as irrigation, which common drought indices lack. Wang et al. (2018) concluded based on GRACE data that endorheic (closed) basin water stores are declining worldwide. Ni et al. (2018) found strong correlations between the interannual TWS variability and the ENSO, particularly around the Amazon and towards Venezuela and Bolivia. Yu et al. (2019) used GRACE to assess drought in Mongolia between 2002 and 2017. Rodell et al. (2018) expanded the analysis to global freshwater availability via GRACE for more than thirty regions and categorised changes in climate change, shorter-term anthropogenic and natural variability. Terrestrial water storage was found to be linked with NDVI change with a delay of up to 1 month (Xie et al., 2019). The lag depends on the type of vegetation (Andrew et al., 2016). These former studies show that GRACE terrestrial water storage anomalies support studies to explain global and regional hydrological trends. The GRACE data used in this study were downloaded from http://www2.csr.utexas.edu/grace/RL05.html; other options for downloading these data exist: e.g. Tapley et al. (2019).

NDVI from GIMMS3g

The GIMMS3g NDVI represents a global assessment of photosynthetically active biomass, i.e. land surface phenology parameters including, to a certain extent, land cover (de Jong et al., 2011; Julien & Sobrino, 2009). Key to these data is the extended time series (pre-2000). The index is based on chlorophyll pigments and cell structures of healthy vegetation absorbing red wavelength and reflecting near infra-red energy. A change in the NDVI can indicate a change in surface vegetative cover such as deforestation, afforestation, reforestation or urbanisation, or physiological effects such as greening or die-back, which could lead to an RH change via evaporation and thermal effects (Dorigo et al., 2012).

The NDVI is defined as the normalised difference in reflectance of overlapping red (0.58–0.67 µm) and infrared (0.725–1.10 µm) spectral bands measured by Advanced Very High-Resolution Radiometer (AVHRR) instruments on the National Oceanographic satellites and Atmospheric Administration (NOAA) and the European Organisation for the Exploitation of Meteorological Satellites (EUMETSAT) satellites covering the time period July 1981 until end of 2015 (Pinzon & Tucker, 2014). The higher the reflective IR and the absorbed red energy, the higher the NDVI, the 'greener' the plant. Preprocessing of these data includes correction for (i) satellite orbital drift, (ii) cloud contamination based on reflectance and brightness temperature and (iii) radiometric and atmospheric effects caused by stratospheric volcanic aerosols for the periods of 1982–84 (volcanic eruption of El Chichon) and 1991–94 (volcanic eruption of the Mount Pinatubo) to minimise varying solar zenith angle effects (Fensholt & Proud, 2012; Pinzon & Tucker, 2014; Tucker et al., 2005).

Data used here were bi-weekly values with an 8-km resolution corresponding to the obtained 0.25° latitudinal/longitudinal grid (Pinzon & Tucker, 2014). The NDVI algorithm derives values in a range between -1 and 1, with negative values typically representing open water bodies and values around 0 representing bare soil. Positive low values (0–0.1) indicate barren areas of rocks, sand or snow, moderate values (0.2–0.3) shrub and grassland and high values (0.6–0.8) temperate and tropical forests (Gandhi et al., 2015). Given the nature of the NDVI algorithm, values can be sensitive to vegetation types and phenology (Dorigo et al., 2012). Stated errors amount to a maximum of 0.005 (Pinzon & Tucker, 2014).

These data have been used widely to investigate climate-vegetation trends and associated feedback. Annual and seasonal means for global E_t derived from the GIMMS NDVI for 1983–2006 were investigated by Zhang et al. (2010). Fensholt et al. (2004) also established an acceptable global agreement between GIMMS and Terra MODIS NDVI (MOD13C2 Collection 5; which offer higher resolution and calibration), which underpins the use and relevance of the GIMMS3g time series to detect and understand global vegetation cover dynamics. However, the authors note that trend analysis in arid areas should be interpreted with caution. They also found NDVI negative trends in southern Africa and around the Caspian Sea and positive trends in northern India between 2000–2010. The latter was also found for the 1981–2006 period from de Jong et al. (2011). In this instance, the authors applied NDVI harmonic analysis to GIMMS3g, to detect longer-lasting greening trends due to an earlier onset of greening due to warming, especially in the NH (including these chosen regions: Alaska, Scandinavia, Mongolia). Using these data, they were able to link trends to increased evapotranspiration and drought stress. Similarly, Fensholt et al. (2012) confirm the increase in greenness for a similar period (1981–2007), in particular in semi-arid zones. They concluded that areas, where vegetation depends on precipitation and temperature, were affected in particular. They noted positive trends in northwestern India and negative trends in Patagonia and California. Furthermore, they also found highly positive correlations between GIMMS NDVI and atmospherically corrected Terra MODIS NDVI in more recent parts of the time series (2000–2007). In semi-arid areas, such as northeast Brazil, water availability in wet months can determine NDVI response (e.g. Azevedo et al., 2018). Zhang et al. (2010) successfully used a modified Penman-Monteith approach to link GIMMS

NDVI with canopy transpiration and soil evaporation. The connection between GIMMS NDVI and soil moisture was also analysed by Dorigo et al. (2021), examining the result of far-reaching negative NDVI and soil moisture trends between 1988–2010, particularly in Mongolia. For Tibet, (Zhang et al., 2013) found an earlier greening start of climate-sensitive temperate vegetation in the early period (1982–1999) due to warm springs and winters and a delay in the late period (2000–2008) using GIMMS3g NDVI. However, their research also states that the data on the western Tibetan Plateau is fraught with data quality issues caused by cloud contamination. Recently, Yuan et al. (2019) have also used GIMMS3g NDVI in correlation with VPD, finding a negative relationship with the greening trend flattening due to increased VPD in the late 1990s. Finally, Julien and Sobrino (2009) looked at GIMMS NDVI in the context of dynamical drivers. They found strong influence from El Niño (via Southern Oscillation Index, SOI), Northern Atlantic Oscillation (NAO) and Pacific Decadal Oscillation (PDO) on growing-season parameters. GIMMS3g NDVI data used in this study were downloaded from https://ecocast.arc.nasa.gov/data/pub/gimms/3g.v1/.

2.1.5 Modes of variability datasets

Using the modes of variability and their indices described in Table 2.2, i.e. the Arctic Oscillation (AO), the Atlantic Multidecadal Oscillation (AMO), the Multivariate ENSO Index (MEI), the Interdecadal Pacific Oscillation (IPO), the Pacific Decadal Oscillation (PDO), the Pacific-North America (PNA) index, the Southern Annular Mode (SAM) and the Indian Ocean Dipole (IOD), an attempt is made in Chapter 4 to explain regional RH changes. The selection of modes covers a large temporal and spatial bandwidth.

The AO, also called Northern Annular Mode (NAM), is very similar to the North Atlantic Oscillation (NAO), which consists of SLP anomalies between the Reykjávik, Iceland and Lisbon, Portugal, the British Overseas Territory Gibraltar and Ponta Delgada on the Azores Islands. As the NAO is confined to the North Atlantic, the AO incorporating the whole NH was chosen (Higgins et al., 2000). Their annual SLP fields and during the boreal winter are identical (Rogers & McHugh, 2002; Zhou et al., 2001). For the southern hemisphere (SH), the Marshall SAM index was used as it is based on station data and allows for the fact that the SAM structure changes between seasons (Marshall, 2003).

There are various indices to characterise and monitor the ENSO. The classic/oldest index is the Southern Oscillation Index (SOI), based on pressure differences across the tropical Pacific, above Darwin, Australia and Tahiti, French Polynesia. Others (Niño 1.2, 3, 3.4, 4, and the Oceanic Niño Index [ONI]) are ocean-based, i.e. on sea surface temperature (SST) anomalies. The MEI was chosen to also capture atmospheric variables, such as SLP and winds.

No indices were selected that are directly linked to the monsoon as this is out of scope with the thesis.

Table 2.2: Definition of used indices of modes of variability, main references and access to their data. PC stands for principal component, EOF for empirical orthogonal function, the MEI.v2 for multivariate ENSO index version 2, GPH for geopotential height and DMI for dipole mode index (Alexander et al., 2002; Barnston & Livezey, 1987; Dong & Dai, 2015; Enfield et al., 2001; Henley et al., 2015; Higgins et al., 2000; Hurrell, 2003; Hurrell et al., 2003; Mantua & Hare, 2002; Mantua et al., 1997; Marshall, 2003; Newman et al., 2016; Saji & Yamagata, 2003; Thompson & Wallace, 1998, 2000; Thompson et al., 2000; Wolter & Timlin, 2011; Zhang et al., 1997).

Index of variability	**Variables, Definition**	**References, comments**	**Link downloaded from**
AO	Daily SLP (1000 mb height) anomalies (20°-90°N) projected on the leading mode of the EOF based on the 1979-2000 period	Thompson and Wallace (1998, 2000), Higgins et al. (2000), Hurrell et al. (2003)	https://www.cpc.ncep.noaa.gov/products/precip/CWlink/daily_ao_index/ao.shtml; accessed 15 Jan 2019
AMO	Unsmoothed, detrended North Atlantic Kaplan SST (V2) anomalies via NOAA PSL	Enfield et al. (2001)	https://psl.noaa.gov/data/timeseries/AMO/; access 29 Jan 2019
ENSO MEI.v2	Interpolated, leading PC time series of the EOF of the standardised SLP, SST, u/v winds, outgoing longwave radiation anomalies over the tropical Pacific (30°S-30°N, 100°E-70°W; JRA-55, NOAA CDR); Overlapping bi-monthly, i.e. December-January, January-February etc.	Wolter & Timlin (2011)	https://psl.noaa.gov/enso/mei/; accessed 26 Dec 2019
IPO	Difference of averaged SST anomalies based on the climatology of 1971-2000 over the central equatorial Pacific (10°S–10°N, 170°E–90°W), and the Northwest (25°N–45°N, 140°E–145°W) and Southwest Pacific (50°S–15°S, 150°E–160°W)	Henley et al. (2015), Dong and Dai (2015)	https://psl.noaa.gov/data/timeseries/IPOTPI/ (TPI [from HADISST1.1] unfiltered: Standard PSL Format); accessed 29 Jan 2019
PDO	Standardised 1st EOF of SST anomalies including subtracting the global warming signal in the North Pacific Ocean (20°-90°N)	Mantua et al., (1997), Zhang et al. (1997), Mantua and Hare (2002), Newman et al. (2016)	http://research.jisao.washington.edu/pdo/PDO.latest.txt; accessed 30 Nov 2018
PNA	GPH (typically 500 or 700 mb) anomalies over the North Pacific and North America	Barnston and Livezey (1987); “bridge” between the AO and ENSO (Alexander et al., 2002)	https://psl.noaa.gov/data/correlation/pna.data; accessed 12 Feb 2019
SAM	Zonal mean SLP of twelve meteorological stations between 40° and 65°S	Marshall et al. (2003)	http://www.nerc-bas.ac.uk/icd/gjma/sam.html; accessed 15 Jan 2019
IOD DMI	SST anomalies based on a climatology of 1981-2010 (HadISST1.1) between the western equatorial (50°E-70°E and 10°S-10°N) and southeastern equatorial Indian Ocean (90°E-110°E and 10°S-0°N)	Saji & Yamagata (2003)	https://psl.noaa.gov/gcos_wgsp/Timeseries/DMI/%20(Standard%20PSL%20Format); accessed 21 Feb 2019

2.2 Methods

After the datasets mentioned in Section 2.1 have been regridded to HadISDH data resolution (5° by 5°, monthly), absolute values are used to create climatologies, i.e. long-term average, used over the period 1981–2010 (2005–2009 for GRACE, 1982–2010 for GIMMS) and anomalies, i.e. deviation from the mean, calculated. These anomalies are used to calculate trends and regressions and, in detrended form, for correlation analysis. The datasets were not spatially matched with the HadISDH dataset.

This study defines the time period from 1973 (for some datasets the early 1980s) until 1999 as the "**early period**" and the time period from 2000–2017 (2015 for GIMMS) as the "**late period**". This definition was made as the negative HadISDH RH trend started around 2000. The HadISDH data are analysed from 1973 to 2017, so this is called the "**full period**" and is defined as "long-term" in this study. It was chosen to break the year into four standard 3-month **seasons** (DJF, MAM, JJA, SON) because most regions with a strong RH trend are located in the mid-latitudes and seasonality is crucial, e.g. in terms of T, precipitation and vegetation. Creating annual means, i.e. over all months, or seasons enhances the signal-to-noise ratio which may make the trend fitting and removal cleaner/less susceptible to outlying data points. The global RH trend is examined for various **regions** (Chapter 3). Regional means are calculated using the cosine of the grid box centre latitude to apply an area-based weighting. As calculations over the full period or the whole year or large heterogeneous regions could offset the trends/correlations over the smaller temporal and spatial scale, averages of grid box trends and the counts of significant grid boxes help keep the data variance.

Decadal trends are calculated via the linear least-squares regression (Ordinary Least Squares fit of linear trends) with the two-sided p-value/significance test. Confidence intervals covering the 5th to 95th percentiles are calculated and corrected for AR(1) autocorrelation in the time series if necessary to correct the degrees of freedom, following the methods of Santer et al. (2008). For all variables in this study except for the indices of modes of variability, trends and correlations are based on **anomalies**. Anomalies are less prone to errors when there are missing and sparse data and less noisy than actual values. This reduces the risk of biased grid box averages and diagnostics. Anomalies also make it much easier to spot changes and features in the data by enhancing the signal-to-noise ratio. For plotting q and T time series on the same axis, thus, their direct comparison, standardised anomalies, also called normalised anomalies, via the division of anomalies by the climatological standard deviation, were used.

The **correlations** describe the relationship between two variables and are used for year-to-year (interannual, short-term) comparison. The time series were detrended for correlations. The **detrending** is done via locally weighted scatterplot smoothing (**LOWESS**), i.e. weighting over certain data points and the fit to the data following the removal of the curve. The detrended time series have been **Pearson** correlated at the grid box level after applying the **Shapiro-Wilk test** at grid box level to all variables involved in the correlation analysis to confirm that data were normally distributed, i.e. the null hypothesis that the data are normally distributed is accepted ($p > 0.05$). A normal distribution is present in the data for many natural phenomena, e.g., when considering RH measurements, and other variables used in this thesis and their anomalies over a longer period of time, annual or seasonal data. The Pearson analysis assumes that both sets of data are approximately normally distributed. For non-normally distributed data, a rank correlation coefficient, such as, e.g. Spearman correlation analysis working as well with monotonic relationships, or an adjusted significance test, can be used. The Spearman correlation did show similar results to the Pearson correlation which would not change the interpretation of data. Extreme data, i.e. peaks and troughs of RH anomalies or precipitation extremes, can cause the data to deviate from a normal distribution. These extreme years were examined in the analysis in addition to the linear trend and correlation analysis. If the correlation coefficient $r < 0.5$, the correlation is interpreted as weak in this study, if $0.5 \leq r < 0.7$, then the correlation is interpreted as moderate, and if $r \geq 0.7$ then this is interpreted as a strong correlation.

To decide the priority of correlations between indices of modes of variability and regional RH to be analysed, a **ranking** of the strength of their relationship was performed (Section 4.2.2). Explicitly, this is done using the following steps:

1. For each region-season pair for which there is a significant RH trend, the regional absolute correlation coefficient between RH and a mode of variability was computed from the mean of the individual grid box absolute correlation coefficients. This was done for each mode of variability. EXAMPLE: For region X where there is a significant trend in RH in DJF and the annual time series, the regional absolute correlation coefficients for mode Y are 0.7 and 0.6 respectively.

2. The scaled regional correlation was then computed by multiplying the regional absolute correlation coefficient for each region-season-mode by the percentage of significant ($p < 0.1$) grid box correlations in relation to the available data for that region-season-mode. EXAMPLE: The proportion of grid boxes for each region-season pair giving significant region-season-mode correlations are 5 out of 8 and 6 out of 8 for DJF and annual respectively. This results in 0.7 being multiplied by 0.625 and 0.6 being multiplied by 0.75, resulting in scaled regional correlations of 0.4375 and 0.45 respectively.

3. For each region-mode, the combined region-mode relationship was quantified by computing the mean over all region-season scaled regional correlations for that mode. EXAMPLE: The combined region-mode relationship for region X and mode Y is the mean of 0.45 and 0.4375, which is 0.44375.

4. The combined region-mode relationships are then ranked and sorted in descending order regarding the regions then modes, on the one hand (Table 4.7), and the modes then regions, on the other hand (Table 4.8).

5. The top three couplings for each region and mode appearing in both lists were further analysed for the modes' impact on regional RH.

The **regression** describes the type of relationship between an independent variable (e.g., a potential driver) and a dependent variable (e.g. RH). The regression coefficient allows the interdecadal comparison between the early (1973–1999) and late period (2000–2017). Like trends, they are calculated via the linear least-squares regression. Regressions other than linear, e.g. quadratic or exponential, are not considered in this study.

Correlations and regressions are calculated for each grid box and spatially averaged afterwards (**average correlation**). This way, the regional detail is not disregarded through early averaging, and information depending on the location is maintained, in particular, in heterogeneous regions. This method described regions much more appropriately than the correlated average, also called the 'ecological fallacy' (Dunlap et al., 1983; Monin & Oppenheimer, 2005). The impact of the primary physical variables on RH (Section 4.1) was analysed using correlations between each grid box of the global fields of the former and regionally averaged HadISDH RH, q and T.

To avoid bias caused by missing data, **thresholds** are used when creating averages and correlations/regressions to ensure there is enough completeness for each year or time period. For climatologies, there must be at least 15 years of January, February, etc. data for any grid box, following Willett et al. (2014). For annual values, there must be at least 60% of the months in a year present, with at least two months per three month season (DJF, MAM, JJA and SON) over each year to avoid bias. The same criteria are used for averages, correlations and regressions. For trends, the threshold is 80%; it was chosen high as trends can be susceptible to outliers.

The **significance** of trends and regressions was calculated via the two-tailed p-value. For correlations, significance was based on the Wald-test with a t-distribution. Significance levels of 95% ($p < 0.05$) are referred to as very significant, marked with two stars (**) in the texts and '+' or 'x' on maps, and 90% as significant, marked with only one star (*). The 95% significance level gives more confidence (i.e. that the results are 5% less likely to be due to chance) than the 90%. 90% can be useful to be able to more clearly see patterns in the results, which was applied to examine the impact of GLEAM E and soil moisture, GRACE TWS and GIMMS NDVI on RH via trend and correlation analysis. The latter are variables grouped as the so-called "terrestrial driver". Due to the complexity of their interaction with RH described in Section 1.3.3, care should be taken to ensure that possible links are not overlooked. In addition, these terrestrial drivers depend heavily on the vegetation cover, for example, and can therefore be found on a sub-gridbox scale. Due to the spatial heterogeneity of vegetation cover, it is likely that correlation coefficients on the gridbox level are lower. A lower threshold of significance (90%) for terrestrial drivers was therefore chosen so that possible links are not overlooked. Regions that fulfil only the lower significance level ($p < 0.1$) might be much more challenging to explain.

For regions with strong correlations between modes of variability and observed regional RH (Section 4.3), an **estimated RH time series** was calculated based on the linear relationship with the mode. The linear relationship can be expressed as $f(x) = m \cdot x + b$ with slope m as the regression coefficient. Replacing b with the observed RH intercept and inserting the mode index values for x into that linear equation, the estimated RH values were obtained for each grid box as $f(x)$. Correlation coefficients and comparison of the trend between the observed and the estimated RH data indicate the extent to which the mode of variability represents the interannual variability and the trend in observed RH, respectively.

3 Setting the scene

The global annual relative humidity (RH) trend since 2000 is made up of a great diversity of trends taking place on smaller spatial and temporal scales. On the spatial scale, the global trend consists of regional trends, which in turn consist of grid boxes. On the time scale, the annual trend consists of seasonal trends. Owing to the short time period, these seasonal trends are often determined by extreme anomalies in a few years.

In this Chapter, large scale and regional RH trends and the relationship between RH and its fundamental drivers of specific humidity (q) and air temperature (T) are considered on different spatial and temporal scales. While the main focus of this thesis is exploring the dynamical and terrestrial drivers of RH, the thermodynamic drivers, i.e. the land-ocean warming contrast (Section 1.3.1), clearly play the largest role. It is beyond the scope of this thesis to quantify this explicitly but by exploring the degree to which large scale relationships between RH and q and T hold or deviate this work can identify regions where trends in RH might be more affected by dynamical and terrestrial drivers.

Section 3.1 gives an overview of large-scale features of the RH trends. In this context, standardised anomalies of q and T and their link to RH are explored. Their anomalies are standardised so that they can be plotted together. Section 3.2 explores latitudinal and seasonal patterns of the interannual (year-to-year) and interdecadal relationship between q, T and RH. Section 3.3 introduces the focus regions for this study. These are regions with a strong trend in RH which contribute towards the global decline in RH. Here, their time series and sub-regional spatial patterns are presented. For these regions, correlations and regressions between q, T, and RH are also explored.

Section 3.4 brings the HadGEM2-ES model into play, considering RH in simulations that contributed to the Coupled Model Intercomparison Project Phase 5 (CMIP5; Taylor et al., 2012a). The regional and seasonal RH trends from HadISDH are compared with the equivalent trends of three historical forcing model runs. This comparison can reveal information about the ability of HadGEM2-ES to simulate past variations in RH.

The four sections set the scene for an approach to explain the contribution of regional, seasonal trends to the global, annual trend. The details of the regional trends are presented to be easily accessed in later Chapters.

3.1 Overview of large-scale features of RH: global average and latitudinal bands

The HadISDH anomalies, updated to 2017, show, as in Willett et al. (2014), a negative global RH trend of -0.11 %rh decade^{-1} (p = 0.0, very significant) in the full period (1973–2017) based on the climatology of 1981–2010 (Table 3.1). The global annual RH anomaly time series (Fig. 3.1) show that this trend can be divided into two temporally limited trends: a significantly positive (until 2000; 0.17 %rh decade^{-1}, p = 0.0) and a three times stronger, significantly negative trend (since 2000; -0.42 %rh decade^{-1}, p = 0.0; Fig. 3.1 and Table 3.1). The most positive RH anomaly during the period of the dataset, 1973–2017, is in 2000 (Fig. 3.1). RH has fallen at its sharpest rate in the following two years since 1988. Due to the peak and the subsequent negative slope, followed by the most negative RH anomalies in 2009 and even more negative in 2012, also towards the end of the data period in 2017, the break in the trends was set at 2000. Dunn et al. (2017) had chosen a different break, i.e. before 2000. The extra few years of data in this project allowed for a later start to the ‘late’ period, as an RH peak in 2000 and several RH troughs towards the end of the period determine the trend. The decline seems relatively clear. Alternatively to a fit ‘by eye’ it could have been statistically tested for a breakpoint. There are a number of different breakpoint detection techniques (Peterson et al., 1998), which could have changed the breakpoint location; however, it is unlikely to have changed it by more than a year or two either side which would have probably not significantly alter the thesis conclusions: a break in trends could have been defined by determining the strongest negative significant negative slope within the 45 years by deriving the linear regression. The trend break was performed on the global annual RH data but can be adjusted on a seasonal and regional level. Instead of a linear regression fit, other types of regression fits (e.g. quadratic or exponential) could be tried. Regression fits benefit from many data points. The HadISDH data used in the thesis is only over 45 years (1973–2017) or the late period (2000–2017). Therefore, it makes sense to also examine short periods and extreme events of single years that shape the trend in detail.

Since RH is a byproduct of q and T, and a change in one or both can cause an RH change, the time series and trends of q and T are considered in the following. Throughout the entire period and in both the early and the late periods, q and T increase, but the increase in q in the late period (2000–2017) is not significant ($p > 0.1$). In the early period, q and T very significantly, moderately correlate ($r = 0.58$, $p = 0.0$). In the late period their correlation is weak, although still significant ($r = 0.48$, $p = 0.0$). Regressing $q(T)$ gives a rate of 1.03 g kg^{-1} K^{-1} ($p = 0.0$) and 1.45 g kg^{-1} K^{-1} ($p = 0.0$) for the early and the late periods, respectively. This clearly demonstrates that while the early period saw similar levels of warming and moistening, the later period warming exceeded the moistening rate (Fig. 3.1), which is consistent with a reduction in RH in the late period. This shows conclusively that something appeared to change between the early and late periods, and that RH decrease is linked to insufficiently increasing q alongside rising T, rather than decreasing q.

Table 3.1: Global and latitudinal annual RH trends [%rh decade^{-1}] over land for the full (1973–2017), early (1973 for HadISDH and 1979 for ERA-Interim, until 1999) and late periods (2000–2017) for HadISDH observations and ERA-Interim reanalysis full-land coverage, i.e. not spatially matched to the HadISDH coverage. The corresponding p-value is shown in parentheses. Bold and starred entries state significant trends (very significant for $p < 0.05$ / **, significant for $p < 0.1$ / *).

Region	Full period trend (1973-2017)	Early period trend (1973-1999 for HadISDH, 1979-1999 for ERA-Interim)		Late period trend (2000-2017)	
	HadISDH	HadISDH	ERA-Interim	HadISDH	ERA-Interim
Globe	**-0.11 (0.00)****	**0.17 (0.00)****	**-0.1 (0.04)****	**-0.42 (0.00)****	**-0.37 (0.00)****
NH - high latitudes [90° N - 60° N]	**0.4 (0.00)****	**0.28 (0.00)****	0.03 (0.7)	**0.44 (0.02)****	-0.06 (0.67)
NH - mid latitudes [60° N - 30° N]	**-0.17 (0.00)****	**0.24 (0.02)****	-0.13 (0.26)	**-0.59 (0.00)****	**-0.48 (0.01)****
Low latitudes [30° N - 30° S]	**-0.13 (0.00)****	0.09 (0.15)	-0.08 (0.31)	**-0.44 (0.00)****	**-0.41 (0.00)****
SH - mid latitudes [30° S - 60° S]	**-0.32 (0.00)****	-0.09 (0.6)	**-0.22 (0.07)***	**-0.51 (0.08)***	-0.22 (0.26)
SH - high latitudes [60° S - 90° S]	-0.16 (0.26)	-0.42 (0.27)	**-0.21 (0.01)****	-0.4 (0.23)	**-0.32 (0.00)****

Table 3.1 updates Willett et al. (2014) until the year 2017. At the global level, the observational data (HadISDH) and the reanalysis data (ERA-Interim) show significant trends. In the late period, the trends of the two datasets are of the same order of magnitude. HadISDH gets reinforcement in its credibility through ERA-Interim on a global scale in the late period (Vicente-Serrano et al., 2018; Willett et al., 2014). The early period generally has less agreement between HadISDH and ERA-Interim, indicating larger uncertainty over the early period. Note that the shorter record of ERA-Interim, which begins in 1979 rather than 1973, may be part of the reason why trends are more different in the early period. Also, the limited coverage of HadISDH in the southern hemisphere (SH) and high latitudes will likely also lead to differences. Over the late

period northern hemisphere (NH) mid-latitudes, the agreement between HadISDH and ERA-Interim trend on a global level (which is dominated by the NH land) and in the low latitudes is given.

In the late period, HadISDH trends are significant in all regions except the southern hemisphere (SH) high latitudes, but at northern hemispheric (NH) high latitudes, the trend is positive, whereas, in all other latitude bands, the trends are negative. In the early period, especially in the NH high and mid-latitudes, the HadISDH trends are positive and weakened in their strength compared to those of the late period. Latitudinal trends in the early period in ERA-Interim are only significant for the globe and SH mid and high latitudes and deviate from the observed data in the individual latitudinal areas as well as in the global as a whole. Overall, this shows that the latitudinal trends in RH were mixed in the early period both between regions and the two datasets, but over the late period the decreasing RH trend appears to be robust over the majority of regions with the exception of the high NH latitudes.

Fig 3.2 shows seasonal global trends in HadISDH. The consistently negative RH trends in the late period on a global level are very significant in all seasons except March-April-May (MAM). The trend is strongest in June-July-August (JJA) (-0.53 %rh decade^{-1}, $p < 0.05$), followed by December-January-February (DJF) (-0.43 %rh decade^{-1}, $p < 0.05$) and September-October-November) (SON) (-0.38 %rh decade^{-1}, $p < 0.05$). As in the annual RH time series, seasonal RH peaks in 2000 stand out, especially in MAM and SON. The annual RH troughs in 2007–2009 and 2012–2013 are reflected in all seasons. In addition, an RH trough in 2015 can be found in JJA. The seasons shape the course of the annual RH anomalies.

Considering seasonal trends, in MAM, JJA and SON, global mean T is significantly increasing, as is q in SON (Fig. 3.2, starred trends next to arrows), over the late period. As for the global annual mean (Fig. 3.1), while standardised anomalies of the q often exceeded T in the early period, it is the other way around in the late period: In the early period in SON, the rate of increase in q is stronger than for T; the blue time series (q) goes above the orange time series (T). In contrast, in the late period, the rate of increase in q is less than for T. This leads to an increase in the RH in the early period and a decrease in the late period.

The strong negative global RH trend in JJA in the late period is present in both hemispheres (Table 3.2), although not in the high latitudes or SH mid-latitudes. In the NH, JJA (boreal summer) shows a similar magnitude RH trend (-0.49 %rh decade^{-1}, $p < 0.05$), to the SH (-0.65 %rh decade^{-1}, $p < 0.1$; austral winter).The largest trend is found in the SH SON (austral spring; -1.03 %rh decade^{-1}, $p < 0.05$), more than twice as strong as the global trend in SON (-0.38 %rh decade^{-1}, $p < 0.05$). This consideration is important because the position of the Inter-Tropical Convergence Zone (ITCZ; more northerly in the boreal summer than in winter) influences hemispheres and latitudinal temperatures, atmospheric dynamics and vegetation.

Table 3.2: As for Table 3.1, for global and latitudinal seasonal HadISDH RH trends in the late period (2000–2017) [%rh decade^{-1}].

Region	DJF	MAM	JJA	SON
Globe	**-0.43 (0.03)****	-0.33 (0.29)	**-0.53 (0.00)****	**-0.38 (0.02)****
Northern Hemisphere	-0.38 (0.17)	-0.3 (0.25)	**-0.49 (0.01)****	-0.15 (0.34)
Southern Hemisphere	-0.55 (0.15)	-0.4 (0.47)	**-0.65 (0.1)***	**-1.03 (0.04)****
NH - high latitudes	0.71 (0.26)	0.15 (0.65)	-0.02 (0.91)	**0.63 (0.01)****
NH - mid latitudes	-0.56 (0.15)	**-0.52 (0.08)***	**-0.75 (0.01)****	**-0.47 (0.07)***
Low latitudes	**-0.56 (0.01)****	-0.28 (0.37)	**-0.46 (0.04)****	**-0.44 (0.04)****
SH - mid latitudes	-0.22 (0.57)	-0.22 (0.84)	-0.64 (0.34)	-0.99 (0.27)
SH - high latitudes	-0.24 (0.66)	-0.48 (0.3)	0.00 (p> 0.99)	-0.75 (0.38)

Considering latitudinal zones, the NH mid-latitudes and the low latitudes stand out. In the NH mid-latitudes, the negative trend is strongest (and significant at $p < 0.1$) in JJA (boreal summer), MAM (boreal spring) and SON (boreal autumn) - these are the growing seasons in which it is generally green and warm in these latitudes. The low latitudes, where the four standard seasons are less pronounced, show very significant ($p < 0.05$) negative trends of roughly the same order of magnitude in DJF, JJA and SON. The NH high latitudes show significant positive trends in SON. In DJF, positive trends are of higher magnitude but not significant, perhaps due to the stronger variability in this season.

The SH mid and high latitudes show no significant trends in any season, not even in SON (Table 3.2). This contrasts with the very significant and negative trend in the entire SH, and also the late period HadISDH SH mid-latitude annual trend shown in Table 3.1. Less land and poorer data coverage of that land contributes to greater variability, resulting in greater uncertainty in the SH.

Overall, this analysis demonstrates that the RH decrease appears to be dominated by the NH mid-latitude growing season, and low latitudes generally, but that negative trends are found in all latitudes and seasons apart from the NH high latitudes.

The geographical distribution of the regions contributing to the latitudinal trends in the late period outlined as framed in maps (e.g. Figs. 3.3 and 3.9), above can be seen, for example, the large regions of negative trends in the NH mid-latitudes in all seasons, with the largest region of strongest trends in JJA (e.g. California, eastern USA, Caspian Sea, Mongolia; see Section 3.3). The spatial pattern of seasonal RH trends is investigated to explore these geographical differences further. Seasonal HadISDH RH trends for the early, late and full periods are shown in Fig. 3.3; annual HadISDH RH trends are shown in Fig. 3.9. It can be clearly seen that there are larger regions of stronger trends in the late period in all seasons (centre column) than in the early period (left column). These trends are primarily negative (brown/ocher colour), whereas there are larger regions of relatively positive trends (green/turquoise) in the early period. When looking over the full period (right column), it is evident that trends are weaker than in either of the periods but mainly negative. This underlines the off-setting that happens when adding the two contrasting periods together. The late period must be viewed separately from the early period. The system of off-setting can also be viewed at the annual average level, at which the trends appear to be significantly weaker than in the individual seasons (compare Figs. 3.9, 1.5 and 3.3). The phenomenon of off-setting is visible on both temporal and spatial geographical scales.

The RH trends on the global, hemispheric and latitudinal levels have been explored. The strongest RH trends are in the mid and low latitudes (negative) and the high latitudes (positive) continuing the trends found by Willett et al. (2014). Only the NH high latitudes show a significant positive trend in the late period. There are regional differences within the latitudinal averages, showing the importance of exploring RH change on both regional and large-scale average scales.

3.2 Exploring large scale relationships between RH, specific humidity and air temperature

Fundamentally, RH is a by-product of q and the T: the Clausius-Clapeyron relation states that for RH to remain constant, there must be an approximately 7% increase in water vapour per 1 K increase in T. Any deviation from this results in a change in RH (Chadwick et al., 2016; see Fig. S7).

It, therefore, makes sense to explore the relationship between q and T. This is done through correlations between q and T (Fig. 3.4). These are based on detrended time series of q and T anomalies to determine how q and T are related on a year-to-year (interannual) scale. If they do not change evenly in accordance with the Clausius-Clapeyron theory, RH may change, e.g. if q cannot react to increasing T due to water scarcity.

In theory, there might be weak T-q correlations when q does not change very much, but T (and RH) does, or T does not change very much, but q (and RH) does, or q

and T changes are completely decoupled for reasons such as observational errors, or due to local external influences, e.g. irrigation, land cover/land use (LCLU) change or urbanisation. If T-q correlations are weak or even negative, then a region may be water limited. Where T-q positively correlate, there must be enough water for q to increase in response to increasing T. So, these regions are either not water-limited or not very water-limited. Where T-q negatively correlate, this implies that water is very limited. There is not enough water to evaporate in response to increasing T, and a negative correlation implies a drying response – like plants reducing their evapotranspiration or water sources drying out.

The T-q correlations are widespread significant positive (green), especially in NH high latitudes and along the coasts (Fig. 3.4), i.e. with a T increase, q also increases. Regionally, the positive T-q correlation stands out in southern Alaska, eastern Canada, Greenland, western and central Europe and Scandinavia, matching with good water availability. In regions such as deserts and arid regions, where water is limited, water is not available for evaporation with a T increase (McVicar et al., 2012). The weak or even negative T-q correlation pattern (light green or pink) corresponds strongly to regions experiencing an RH decrease (Figs. 3.4 and 3.3). Regions such as the Chihuahuan and Mojave desert, in parts of Northeastern Brazil (including Caatinga), eastern Patagonia (Pampas), Sahara and Arabian deserts, southern Africa (Kalahari desert) and Serengeti, India, Tibet (Gobi desert), Mongolian steppe and Central Australia are known desert regions and water-limited, i.e. there is not enough water available to react to T increase with q increase (McVicar et al., 2012; Miralles et al., 2016). In general, water-limited regions seem to be weakly to negatively T-q correlated.

The T-q correlations are limited in their statement on regional RH trends. Although the weak or negative T-q correlation pattern resembles regions identified as water-limited through the ratio precipitation/potential evaporation (Fig. 1 in McVicar et al., 2012), it does not clearly correspond to all regions with a drying trend identified in Fig. 3.9 (the eastern USA, southern Greenland, the Mediterranean, the Red Sea). The regions with increased RH in the late period, such as Scandinavia and northwestern India, are also not clearly identifiable and show a positive T-q correlation. Regions like some deep tropics and high latitude regions are described by McVicar et al. (2012) as energy-limited, i.e. the availability of energy rather than water influences evapotranspiration. Some areas of negative T-q correlations look a bit anomalous but quite possibly (for example, southeast of southern Africa in SON), there is a bias of observations being in more urban areas that are drier than their rural surroundings because they are more concrete rather than vegetation. These would need to be quite large urban areas to influence grid box scale RH, or the weather stations were biased towards urban areas in that particular box. In some regions with negative RH trends, the T-q correlation could be strong but not enough to keep RH constant to decrease RH. Comparing T-q correlations on grid box level between the early and the late period, an expansion of weaker and more negative T-q correlations is noticeable in the late period (e.g. north of the Caspian Sea, eastern Brazil, southern Africa, Mongolia and Tibet). This reduction in strong T-q correlations indicates an increased deviation of the Clausius-Clapeyron equation to the early period as seen in the time series in Figs. 3.1 and 3.2.

A strong T-q coupling can last for only several years or decades (as also Donat et al., 2019). It can be interrupted or become stronger or weaker over several years (desertification). The T-q correlation varies seasonally due to temperature changes and water availability (Fig. 3.5). In DJF, perhaps given the precipitation-rich boreal winter in large parts of the NH, the correlation is strongly positive in the high and upper mid-latitudes of the NH, indicating that these regions are not water limited. In particular, during the austral summer, southern Africa and North and Central Australia show strongly negative correlations, indicating water-limitation. During MAM, the pattern shifts with the ITCZ north, and the T-q correlations on the NH subtropics become weaker and negative. These are weakest or more negative, and extend furthest north, during boreal summer (JJA); this fits with the found RH decrease which is strongest in JJA. Also in JJA, negative correlations increase over the deserts in the NH mid and low latitudes, especially in the Chihuahuan Desert, the Sahara (although note limited grid boxes here), and Indian Desert. The atmosphere near the coast, such as over northeastern USA, Great Britain and northern Europe/Scandinavia, are nourished with sufficient water and storm tracks and persist in a strong T-q correlation even in summer. The T-q correlations in SON are similar to those in MAM but with less expansive negative T-q correlations over southern Asia. Due to monsoonal storm tracks and precipitation over Asia, patterns might not follow the four standard seasons.

The start for looking for robust features in interannual co-variability that might be relevant for long-term changes in RH has been undertaken by looking at T-q correlations. In the following, the q-RH and T-RH correlations across the globe are examined with the anticipation that they will help categorise or identify different types of regions.

In regions with a strong coupling between the RH with q or T, the latter two could be introduced into the analysis as a proxy. The q and T show less complex behaviour than RH. The consideration of q-RH and T-RH correlation is essential for further drivers changing q and T, as q and T determine RH simultaneously and without lag on the RH on a temporal and spatial level. Influences on q and T could also be seen as drivers of RH.

It must be remembered that this interannual co-variability (correlation) is distinct from the long-term trend, as the correlations were calculated on detrended data. For example, a region could show strong positive correlations between q and RH on the year-to-year (interannual) scale, yet the long-term trend in q is positive while the long-term trend in RH is negative. Partly, these correlations are over the annual scale so do not capture long-term trends. Partly, these correlations are not strong ($r < 0.7$), so while there may be a positive correlation driven by some strong years, other years do not behave in quite the same way.

As previously mentioned, the Clausius-Clapeyron relation states that RH would remain constant under optimal conditions while q would increase/decrease by approximately 7% per degree Kelvin (or Celsius) increase/decrease in T. So, a weak q-RH relationship would be expected either where the T-q co-variability is very strong and very close to Clausius-Clapeyron relation, and so RH would not change, i.e. neither water nor energy is a limiting factor, or where T-q co-variability is very weak (see above: q does not change very much, but T [and therefore RH] does, or q and T changes are decoupled). A negative q-RH relationship would be unusual and very unlikely to be strong. It would imply that T changes occur with much smaller q changes such that RH changes are driven mainly by T and therefore opposite to q changes. That could be the case, for example, in NH high latitudes during the boreal summer and water-limited regions. A positive q-RH relationship would be expected everywhere else, where T-q is neither very weak nor very strong).

The T-RH correlations would be weak either where changes in RH are small compared to changes in T (e.g. very strong T-q correlation, i.e. Clausius-Clapeyron relation), changes in T are small compared to changes in RH (e.g. strong q-RH) or changes are completely decoupled. Positive T-RH correlations would occur where q changes in the same direction as T (strong q-RH positive and T-q positive). The T-RH correlations would be negative where q changes very little (weak q-RH, weak T-q) or in the opposite direction to T (strong positive q-RH, strong negative T-q).

Significant negative q-RH correlations hardly occur, which is physically justifiable (Fig. 3.6). T and RH correlate positively, mainly in the high latitudes, with the largest regions of significant correlations in the boreal winter, and negatively, mainly in the mid to low latitudes, becoming near-global in the NH summer season of JJA (Fig. 3.7). The SON pattern is similar to that in MAM, with negative T-RH correlations being weakened in the mid-latitudes. There are a few, possibly related reasons for the positive T-RH correlations: the higher northern latitudes in DJF may be covered in ice/snow and generally cold and dry, so sublimation (snow/ice evaporating into water vapour) can occur when there is enough energy (T and wind), increasing the water vapour, but it will not occur under cold/dark/still conditions resulting in lower humidity. The winter storm track/circulation will also play a role. Over northern Europe when it is mild in the winter it is often wet - the westerlies bring mild, moist air from over the ocean. The positive T-RH does become less strong to the east of Eurasia. When there are easterly winds Northern Europe is cold and dry. Another reason could be that the planetary boundary layer tends to be much shallower over winter with a tendency for inversions where the air is very stable and typically cold and dry. Another element could be that as there were warmer winters, there has been less ice and snow cover in some regions so the region has tended to stay moister because there are more sources of water vapour from lakes, rivers and vegetation compared to previous years. Also, there may be some links to the winter boundary layer.

To highlight some regions, the difference between the eastern and western USA is strong. A positive q-RH correlation characterises both; the T-RH correlation is negative over the west and weaker or even positive over the east in all seasons except JJA. Eastern and western Patagonia behave inversely in MAM and JJA. Some regions appear to be very stable across the seasonal cycle in terms of correlations. For example, southern Africa has strongly negative T-RH correlations, less so in JJA. The Saudi Arabian Peninsula and the southern half of Australia consistently show positive q-RH with negative T-RH correlations. Over northwestern India, q-RH correlations are notably stable over all seasons, whereas strongly negative T-RH correlations occur only in MAM and JJA.

The arid regions, which stand out due to a weak T-q correlation and partly represent changing RH (Figs. 3.4 and 3.5), do not appear in the q-RH and T-RH pattern (Figs. 3.6 and 3.7). In the few regions with strongly negative T-q correlations, the q-RH correlations are strong and positive and the T-RH correlations are strong and negative, e.g. southern Africa in DJF (decreasing RH trend) and northwestern India in JJA (increasing RH trend).

The different signs of T-RH correlations find an explanation. Over land, at least away from large water bodies and the deep tropics, there is unlikely to be sufficient water available for evaporation to keep rises in q at pace with rising temperatures. Therefore, theoretically, T and RH should be negatively correlated with each other. At low temperatures, the kinetic energy is reduced, molecules move more slowly. Therefore, the maximum possible vapour pressure, which binds the water and air molecules, is lower, and the air density is greater. A positive T-RH correlation can occur at low temperatures, below the freezing limit, especially if the subsoil has frozen water in the form of ice or snow; therefore, humidity is very low.
This positive T-RH correlation could also have something to do with a threshold: in the high latitudes, especially in winter, the ground is covered with snow and ice. So there is a lot of frozen water available. Below freezing temperature, frozen water changes directly into the gas phase (snow sublimation) and is not available for direct evaporation. Snow sublimation skips the melting and the liquid phase and thus needs more energy than evaporation. Increased temperatures increase the chance of snow sublimation or evaporation, consequently increasing RH. The water stays locked in ice and snow at decreasing temperature, therefore, decreased RH.

If T in the high latitudes have increased and are closer to the melting point, then it takes a smaller T rise to meltwater and create available water in these regions and seasons. Under global warming, with a decrease in snow or ice cover at the end of the winter and T above freezing temperature for a longer time, the negative T-RH correlation could be restored in these regions: With the presence of more liquid water and vegetation exposure, in addition to evaporation, there is the heating of the air, thus, decreased RH. The correlation could be changed if little snow leads to little melting and a decreased runoff in spring after a time lag.

Figs. 3.8 and S8 compare the absolute strengths of the annual q-RH and the T-RH correlation for each grid box and show the stronger one. The q-RH correlations domin-

ate the largest area over land at an annual average level. They are exclusively positive (green), i.e. q-RH correlations are strongest and positive. Although negative q-RH correlations are present (pink shaded regions), they are very weak (Fig. 3.6). The strength of the q-RH correlation (dark green) increases towards the low latitudes.
In the lower mid-latitudes and in particular, in the low latitudes around the equator and subtropics, the stronger positive q-RH correlations are replaced by stronger negative T-RH correlations (orange-brown) appears sporadically, tending to a stronger correlation towards the lower latitudes. In the tropics, the air is often saturated. Hence, q cannot increase anymore, RH cannot be increased anymore, only decreased (by T). Hence in the tropics, the temperature is the leading parameter for RH. Towards the upper mid-latitudes, negative T-RH correlations are weak and only stronger than q-RH correlations in small regions. In the NH high latitudes, positive, weak to moderate T-RH correlations (purple) dominate at the annual level. Most of the correlations shown are very significant ($p < 0.05$).

The q-RH and T-RH correlations coexist, with one of the two in most regions being significantly stronger than the other (Figs. 3.8 and S8). Fig. 3.8 only provides information about the stronger correlation in the grid box and its significance. The weaker correlation, and thus any coexistence, are neglected after the comparison. In general, positive q-RH correlations predominate in combination with negative T-RH correlations. It is noticeable that in DJF in the NH high latitudes (Fig. S8), positive T-RH correlations are strong but only show a slight difference in their strength to positive q-RH correlations, i.e. both correlations are of equal strength, indicating that RH is driven by both q and T equally on the short-term scale. In the mid-latitudes, positive q-RH correlations in combination with negative T-RH correlations predominate, indicating that a short-term decrease in q reduces RH with T having a negative impact on RH. In SON, however, positive T-RH correlations predominate in the high latitudes. In MAM and JJA, locally, T negatively drives RH in the NH mid-latitudes more strongly than q. In JJA, both q-RH correlations and T-RH are weak in the high latitudes. Whether a correlation predominates and which one depends on the presence of water and energy, in which range the temperatures are, e.g. below freezing point, and what state the water is in, e.g. liquid versus frozen water.

In terms of pattern and strength, the correlations in the early and late periods differ only slightly (Fig. 3.8). The q-RH correlation in the mid and low latitudes, e.g. southern Africa and the Red Sea have become slightly stronger (dark green), and in some places, their strength exceeds the T-RH correlation, e.g. in Northeastern Brazil and the Mediterranean. The latter can also be attributed to a slight decrease in the T-RH correlation. Over eastern Canada, a positive T-RH correlation exceeds the q-RH correlation in the late period. However, on a global scale, these changes affect only some grid boxes, and, in general, it can be concluded that the global pattern has not changed. That means that these relationships might be expected to hold over even longer time periods. So whatever has been driving the long-term changes in RH, either q or T, has not changed the interannual relationship between these variables. At the global level, this correlation pattern can be built on, for example, to analyse the interdecadal relationship between q, T and RH, as is done in the next section. The higher data density in the late period, that can change regional averages, particularly smaller regions or regions heterogeneous in terms of correlations, should be noted.

Correlations with detrended time series gave information about the interannual relationship between two variables, to ensure that any further relationships explored with non-detrended data are not purely due to trends in both time series. A connection between q, RH and T could be found in many regions, i.e. a significant, strong correlation. Regression analysis applied to non-detrended data can evaluate the potential influence of the predictor on the long-term trend in the predictand. The regression coefficient quantifies the magnitude of the relationship, while correlation coefficients describe the strength of the relationship. Regression coefficients are particularly meaningful if they are based on strong correlations. Comparison of regression coefficients for the early and late periods determine whether the magnitude of the relationships, i.e. the dependence of RH(q), RH(T), or q(T), have changed. The change in magnitude, i.e, the regression coefficient indicates a strengthening or weakening of the relationship. It is possible that the strength of the correlation remain unchanged. Based on strong correlations, regressions can possibly explain RH trends. – While dimensionless correlation coefficients could be compared, regression coefficients between different variables, e.g. RH(q), RH(T) and q(T) cannot be compared because they have different units.

The regression strength in Section 3.3.3 for regions is compared for very significant ($p < 0.05$), moderate to strong ($r \geq 0.5$) correlations over the early and late periods.

In summary, assessing co-variability by looking at annual and seasonal correlations showed that a weak or negative T-q correlation can be far-reaching regionally related with an RH change in water-limited regions (California, eastern Brazil, southern Africa, around the Caspian Sea region, Mongolia, Tibet). Limitations in either water or energy can lead to changes in RH. At the seasonal level, latitudinal patterns were found in the q-RH and T-RH correlations, differing in strength, sign and coexistence. In most places, the correlation q-RH is positive and stronger than the T-RH correlation, indicating that a change of RH depends in most regions more on q than on T. In cold climates, T-RH are positively correlated. Still, this negative regression RH(T) is generally less pronounced than the positive RH(T) in warmer areas (not shown).

Given that the correlation strength between q-RH and T-RH remains similar across both periods, it is concluded that there has been no significant change in the way that q and T co-vary interannually. Regions, where differing relationships exist and coexist that might help to explain the character of changes in RH over time were identified. The longer-term relationship, i.e. the magnitude between RH and q and T, revealed that positive RH(q) and negative RH(T) predominate (for regions, see Section 3.3.3; not shown globally). The interdecadal analysis is deepened at the regional level to examine the regression at different time periods.

According to this global overview, Section 3.3.3 presents correlations and regressions between the RH, q and T for regions with a strong RH change in the late period.

3.3 Introducing regions with a strong trend in RH: their time series and sub-regional spatial patterns

Individual regions determine the global trend, while trends in particular seasons and extreme anomalies in years in these regions guide their annual trend. The global full period RH trend is negative (-0.11 %rh decade^{-1}, $p = 0.0$; Table 3.1). Hence the contributing, negative regional trends are of particular interest. Negative trends can be partly offset by positive regional trends on different temporal and spatial levels, which are interesting in themselves. Since the global annual decreasing trend appeared to start in 2000, regional trends are considered in this late period.

To identify the regions, the global map of annual RH trends for the late period (2000–2017; Fig. 3.3, middle column) was analysed for regions of relatively consistent and strong trends and then region boxes drawn around them. To ease analysis, the region shape is restricted to cuboids, which inevitably means that grid boxes of different trends may be included in some regions, but this was minimised.

Regions coloured intensely ochre/brown (strong negative trend) and green (strong positive trend) in the late period were identified in Fig. 3.3 (center). For the regions identified, the regional RH trend was calculated for HadISDH and ERA-Interim (Table 3.3). As this study focuses on large-scale features, the big question is why the atmosphere is becoming drier, and to understand why there are opposing behaviours, i.e. wetting trends, ergo both negative and positive RH trends over the late period are included.

Sixteen regions with a strong trend were identified (Table 3.3). All regional trends are significant ($p < 0.1$) in the corresponding periods in both HadISDH and ERA-Interim, except for western Alaska. The RH trend over Alaska might be tainted with uncertainty because the ERA-Interim trend is negative, however, not significantly, while the HadISDH trend is positive. Apart from this exception, ERA-Interim captures not only a similar annual global trend to HadISDH (Table 3.1) but also the regional trends in the late period are generally comparable in terms of trend direction and magnitude to those in HadISDH, differing in the direction in only five regions/periods. ERA-Interim shows stronger trends than for HadISDH in approximately one-third of the regions.

The regions are located in different latitudes. Thirteen regions are in the NH, three in the SH, and most of them are located in the mid-latitudes. Exceptions are eastern Brazil, the Red Sea, northwestern India (all at low latitudes) and southwestern Greenland, Alaska and Scandinavia (high latitudes). Most regions are adjacent to large bodies of water, i.e. oceans, seas, straits or large lakes; exceptions are Mongolia and, to a

Table 3.3: As for Table 3.1, for regional annual HadISDH and ERA-Interim RH trends in the early (1970s to 1999) and late periods (2000–2017) [%rh decade^{-1}]. The third number in a cell is the ratio between the number of very significant ($p < 0.05$) and all grid boxes with available data in the region. The regions are arranged in descending order according to their annual HadISDH RH trend in the late period. Framed rows indicate regions with significant opposing HadISDH and ERA-Interim trends between the early and the late period.

Region [start latitude, start longitude, end latitude, end longitude]	Trend in early period (until 2000) [%rh decade^{-1}]		Trend in late period (since 2000) [%rh decade^{-1}]	
	HadISDH	**ERA-Interim**	**HadISDH**	**ERA-Interim**
Regions with a negative trend since 2000				
Eastern Brazil [-25,-55,5,-30]	-0.17 (0.22) (4/13)	-0.73 (0.00)** (12/22)	-2.61 (0.00)** (10/12)	-1.24 (0.00)** (16/22)
Tibet [20,85,35,105]	0.51 (0.04)** (7/12)	1.06 (0.00)** (8/12)	-1.97 (0.00)** (11/12)	-0.62 (0.03)** (4/12)
Caspian Sea [40,45,60,60]	0.26 (0.45) (0/12)	-0.92 (0.02)** (6/12)	-1.94 (0.01)** (11/12)	-1.79 (0.00)** (10/12)
California [30,-130,50,-115]	0.47 (0.13) (3/8)	0.18 (0.63) (2/9)	-1.85 (0.00)** (8/8)	-1.14 (0.01)** (5/9)
Mongolia [40,90,55,115]	0.56 (0.01)** (8/15)	0.14 (0.67) (4/15)	-1.74 (0.00)** (11/15)	-2.62 (0.00)** (15/15)
Southern Africa [-35,15,-15,35]	-0.92 (0.03)** (1/12)	0.15 (0.8) (2/16)	-1.64 (0.08)* (7/13)	-3.45 (0.00)** (15/16)
Southwestern Greenland [60,-60,75,-40]	-0.69 (0.01)** (2/4)	0.08 (0.75) (0/10)	-1.46 (0.02)** (5/6)	-1.63 (0.00)** (9/10)
Eastern USA [35,-100,45,-70]	0.65 (0.05)* (5/12)	0.94 (0.03)** (8/12)	-1.3 (0.01)** (10/12)	-1.33 (0.01)** (9/12)
Red Sea [20,25,35,40]	0.51 (0.00)** (4/7)	0.18 (0.38) (3/9)	-1.22 (0.00)** (6/8)	-0.76 (0.01)** (5/9)
Patagonia [-60,-75,-40,-60]	0.26 (0.4) (1/7)	-0.67 (0.00)** (9/10)	-1.13 (0.03)** (3/7)	-0.82 (0.01)** (5/10)
Mediterranean [35,-10,50,5]	-0.4 (0.03)** (3/9)	-0.41 (0.08)* (2/9)	-0.88 (0.01)** (8/9)	-0.98 (0.00)** (7/9)
Regions with a positive trend since 2000				
Scandinavia [60,20,80,55]	0.17 (0.47) (0/18)	-0.22 (0.28) (7/21)	1.44 (0.00)** (16/19)	0.65 (0.01)** (17/21)
Western Alaska [60,-180,75,-155]	0.22 (0.44) (0/8)	0.37 (0.09)* (5/13)	1.41 (0.00)** (5/8)	-0.12 (0.62) (2/13)
Northwestern India [20,65,35,80]	1.2 (0.01)** (7/7)	1.05 (0.06)* (5/9)	1.35 (0.03)** (4/8)	2.11 (0.00)** (7/9)
Eastern Canada [45,-80,60,-55]	-0.04 (0.85) (4/10)	-0.26 (0.27) (3/15)	1.32 (0.00)** (8/10)	0.68 (0.02)** (8/15)
East China Sea [20,120,35,135]	-0.25 (0.22) (3/8)	-0.61 (0.01)** (5/7)	0.91 (0.05)** (5/8)	0.73 (0.03)** (4/7)

smaller extent, the region called "Tibet" (note that this region is not just Tibet but also extends south, see Section 3.3.1.2) and northwestern India. Large water bodies could strongly impact the atmospheric moisture, thus, RH in a region.

The size of the region could have an impact on the RH trend composition (Fig. 3.3). It varies from 22 grid boxes (such as Scandinavia, eastern Brazil, southern Africa) to seven grid boxes such as California, the Red Sea region and the East China Sea. The larger the region, the greater the likelihood of heterogeneity of the land characteristics (water availability, coasts, topography). Ergo in large regions, a broader range of influences might contribute to the regional RH trend. All regional and seasonal trends listed in Table 3.4 have >50% of grid boxes with a significant trend in the same direction as region average, except Patagonia in JJA (3/7 grid boxes significant).

Some regions show significant RH trends not only over the late period, but also have a trend of the same sign over the early period, e.g. southern Africa, southwestern Greenland, and the Mediterranean have significant negative trends in HadISDH over both periods (Table 3.3). Northwestern India has significant positive trends in HadISDH over both periods. The trend direction in Tibet, Mongolia, the eastern USA and the Red Sea region changed significantly between periods.

In order of their strength of annual RH trend in the late period, the regions with the drying trend are presented in Section 3.3.1, then those with a wetting trend (Section 3.3.2). RH, q and T trends, time series, correlations and, if the latter are very significant ($p < 0.05$) and strong ($r > 0.7$) appropriate, regressions are discussed, as well as geographical information on the region that could be of interest for further analysis, such as the topography and water bodies, average climate and land cover (via Koeppen-Geiger, Beck et al., 2018, Fig. 1.13), aerodynamic and oceanic circulations (Fig. 1.8) and gradients in temperature (Fig. S2), moisture (Fig. S1) and precipitation (Fig. S3), and seasonality. If applicable, modes of variability impacting the region (further explained in Chapter 4) and drying/wetting events and changes over time are mentioned.

3.3.1 Regions with a strong drying trend

The regions with a strong drying trend (regions' outlines in Fig. 3.9), Table 3.3) are described below.

3.3.1.1 Eastern Brazil

The hereafter named the region "eastern Brazil" (start latitude: 25° S, start longitude: 55° W, end latitude: 5° N, end latitude 30° W) comprises Brazil's regions Nordeste completely and Sudeste except for its southernmost tip. Only the northernmost part of Paraná is included in the Sul region; the eastern half of the Centro-Oeste and Norte regions are also part of the "eastern Brazil" region. French Guiana and the eastern band of Suriname from the northwesternmost corner of the region. Thus, the states of Amazon, Roraima Rondônia and Acre are not part of the region observed in this study. Inland there are also the Brazilian Highlands, the wet savannah. Rivers and wetlands become more familiar towards the region's west with the onset of the tropical Amazon (Various, 1996). Most of the weather stations used in HadISDH are located along the coast and inland in the southern half of the region (Fig. 1.2). There is a lack of measurements in the northern centre.

The majority and inner part of the region show humid, tropical savanna and the Amazon tropical rainforest climate (Koeppen-Geiger classes Aw, Am, Af; Figs. 1.12 and 1.13). Towards the northeast coast humidity decreases, and this is followed by semi-arid areas (BSh). In the southern part, the climate changes into temperate conditions (Koeppen-Geiger C-group). The main region is the destination of very warm and maritime equatorial air mass trajectories from the SH Atlantic. From the NH Atlantic, the north is affected by mild and moist maritime tropical northwesterly winds. The north-easterly/southeasterly ratio is driven by the seasonal movement of the ITCZ so that the proportion of northeasterly winds increases over the austral summer (DJF) (Fig. S4). Hence, in DJF, the precipitation rate is strongest, particularly inland (Fig. S3). Thus, the region's south has lower q values, especially in JJA, while the temperature and the normalised difference vegetation index (NDVI) are seasonally almost unchanged and homogeneous over the region (Figs. S1 and S2; NDVI climatologies are not shown).

Large droughts in the 21st century have been associated with natural variability (Rodell et al., 2018). El Niño events tend to bring reduced rainfall in this region, and La Niña increased rainfall, not so in 2011–2012 when La Niña was characterised by a cooling concentrated in the central Pacific beginning a five-year-long drought (Marengo et al., 2017; Rodrigues & McPhaden, 2014). At the beginning of this drought, there were also floods in Amazonia (also in 1989, 1999, 2009), which were attributed to ENSO (La Niña) (Azevedo et al., 2018; Marengo & Bernasconi, 2015). 2012 and 2014 were characterised by low rainfall (Rodell et al., 2018). The drought, finished by the 2015–2016 El Niño, reduced rainfall and increased temperatures, causing the Sobradinho Reservoir's surface in northern Bahia to shrink significantly (Azevedo et al., 2018). In connection with this, the RH has been reduced by 28%rh, while the NDVI decreased between 2012–2016.

In DJF and SON, the late period RH trend is significantly negative across the region; in MAM and JJA, it refers to the northern part (Fig. 3.3). In the late period, the q decreases in all seasons, mainly in the northeastern cap towards the south but not in northwestern grid boxes (Fig. S5). T changes on a grid-box level are insignificant and weak (Fig. S6), and for the regional mean, the T trend is not significant in the late period (Fig. 3.10).

The annual downward RH trend in the early period over eastern Brazil (-0.17 %rh decade^{-1}, $p = 0.22$, 4/13 grid boxes significant; Table 3.3) intensifies in the late period and spreads over a larger, significant area (-2.6 %rh decade^{-1}, $p = 0.0$, 10/12 grid boxes significant) (Fig. 3.9). The trend in the late period is particularly pronounced in SON

(-3.43 %rh decade^{-1}, $p = 0.0$, 8/12 grid boxes significant) and DJF (-3.02 %rh decade^{-1}, $p = 0.0$, 8/12 grid boxes significant), extending over the entire region (Figs. 3.9 and 3.10). In JJA (-2.62 %rh decade^{-1}, $p = 0.0$, 9/12 grid boxes significant) and MAM (-1.4 %rh decade^{-1}, $p = 0.01$, 5/12 grid boxes significant) the negative trend mainly extends over the north of the region. The years 2010 (JJA; low q), 2012 (SON; low q), 2013 (MAM; low q), 2014–15 (DJF; low q), 2016 (JJA; low q, high T) and 2017 (SON; high T) indicate particularly strong negative RH anomalies. In addition, there were strong turning points in 2012–13 (DJF) and 2009–2010 (JJA), i.e. from a high anomaly to a low anomaly or vice versa (Fig. 3.10).

Over the late period, RH is more strongly positively correlated to q than over the early period (for the late period, in DJF: $r = 0.61$, $p = 0.0$, JJA: $r = 0.76$, $p = 0.0$, SON: $r = 0.8$, $p = 0.0$). The q-RH correlation is not significant in MAM. The T-RH correlation is only significant for MAM (in the late period: $r = -0.6$, $p = 0.01$; in the earlier period: $r = -0.47$, $p = 0.01$). The T-q are strongly positively correlated for all seasons ($r > 0.75$, $p = 0.0$) except SON ($r = 0.52$, $p = 0.01$) in the early period and only for MAM in the late period MAM ($r = 0.65$, $p = 0.0$). There is a positive trend in both q and T in the early period, whereas in the late period T levels off, whereas q declines fitting with the stronger correlations between q and RH in this period.

Due to the lack of significant T-trends (Fig. S6) and strong T-RH correlations (except in MAM; Figs. 3.7 and 3.8), RH is expected to be driven by q and the onshore easterlies. While T-q strongly correlated during the early period, this was not the case during the late period (except in MAM; Fig. 3.4), indicating that a deviation from the Clausius-Clapeyron theory leads to the RH decrease in the late period.

Only in JJA and SON, q-RH correlations are moderate to strong ($r \geq 0.5$) in the early and the late period so that the regression coefficient can be compared. The RH(q) regression increased from 1.78 %rh g^{-1} kg to 5.23 %rh g^{-1} kg in JJA, and from 1.73 %rh g^{-1} kg to 4.77 %rh g^{-1} kg in SON (all $p < 0.05$), i.e. RH's dependence on q is increased in the late period, indicating greater water limitation. The dependence of q on T slightly decreased in MAM when T-q correlations are moderate to strong in both periods: from 0.71 g kg^{-1} K^{-1} in the early period to 0.6 g kg^{-1} K^{-1} in the late period.

For eastern Brazil, all four standard seasons are further analysed in the following chapters due to their high significance and strength.

3.3.1.2 Tibet

The region hereafter called “Tibet” (start latitude: 20° N, start longitude: 85° E, end latitude: 35° N, end latitude 105° E) covers the eastern half of the Tibetan Plateau, all of Bangladesh and Bhutan, the east half of Nepal and the northern two-thirds of Myanmar. The Chinese provinces of Qinghai, Sichuan, Yunnan and the Indian provinces between Myanmar and Bangladesh are also included. In Tibet and China, the Himalayas, the highest weather stations in the world, are located in the northeast of the region and in the west and south at a reducing height. There are hardly any measuring stations included in HadISDH in Myanmar, Nepal, Indian and Bangladesh (Fig. 1.2). Towards the coast, the climate is humid, tropical savanna-like (Koeppen-Geiger classes Af, Aw), which becomes semi-arid hot towards the north (BSh; Figs. 1.12 and 1.13). Inland China has a humid and subtropical climate with dry winters (Cwa, Cwb). The northern wind band brings cold, subarctic to polar tundra around the Tibetan Plateau (BSk, Dwb, Dwc, ET). The westerly winds are especially strong in the northwestern part of the region, and the temperatures are particularly low (Fig. S2). There is little green there due to climate-sensitive alpine meadow and steppe (Zhang et al., 2013). The monsoon brings moisture to the southwest of the region in JJA and raises the q values (Figs. S1, S3 and S4). Drought in Tibet has been found to be favoured by a high-pressure anomaly over Scandinavia and the North Atlantic storm track having a more south-west to northeast orientation, and by a positive ENSO (Bothe et al., 2009). The authors found wetness to be linked to a low-pressure anomaly over central Europe and La Niña.

With an RH minimum of 28%, the northeastern part of the Tibetan Plateau in DJF and March is one of the driest places on earth (Niu et al., 2020). The RH rose until 2003, after which it showed a 20 times steeper negative trend, among other things, due to warming (Niu et al., 2020; Wang et al., 2008a). The heating over the plateau reduces the temperature gradient between Tibet and the Indian Ocean (Zhang et al., 2021). Associated with heating is an advanced vegetation growing season (Zhang et al., 2013). Increased NDVI values are linked to higher atmospheric CO_2 levels, thus fertilisation (Zhao et al., 2018). Due to warming, snow cover has been decreasing in the recent decades, which in turn increases heating, followed by reduced soil moisture in late spring (Zhang et al., 2021). Droughts around the northeastern part of the region were detected in 2006 and 2009–2010 and 2011 (Zhao et al., 2018). Accompanied by a decline in precipitation due to a monsoon decrease and irrigation, Tibetan endorheic basin water storage has declined only slightly since 2002 (Rodell et al., 2018; Wang et al., 2018).

The slightly positive annual trend in the early period in Tibet (0.51 %rh decade^{-1}; $p = 0.04$; 7/12 significant versus total grid boxes) changes into a negative trend of four times the strength in the late period (-1.97 %rh decade^{-1}; $p = 0.0$; 11/12 grid boxes significant; Fig. 3.9). The negative trend is particularly pronounced in DJF in the north of the region (-2.47 %rh decade^{-1}; 5/12 grid boxes significant, $p > 0.1$; Fig. 3.3). Since this trend is not significant on the regional average, it will not be examined further in this study. JJA and SON also show strongly negative and significant ($p < 0.05$) trends (respectively, -1.73 %rh decade^{-1}, 6/12 grid boxes significant; -2.04 %rh decade^{-1}, 3/12 grid boxes significant). In JJA, the regions north, northwest and southeast around the Tibetan Plateau are affected (Fig. 3.3). In SON, the west of the region, i.e. Tibet and the westernmost part of China, Xinjiang, are affected. The negative trends are accompanied by RH peaks in 2009–2010 and 2013–2014, strong in DJF and MAM (Fig. 3.11). Both troughs are reflected in high T and low q anomalies. In SON, the trend is strongly influenced by three RH troughs: 2009, 2012 and 2015. Negative q anomalies accompany the first two, and the third occurs with a positive T anomaly. In JJA, the years of negative RH anomalies 2006, 2009, 2013 and 2015 stand out. Strong positive T anomalies characterise the first three troughs; the latter two, however, are mainly characterised by negative q anomalies.

The q-RH correlate significantly, moderately positively in JJA and SON over the early, late, and full period except in JJA in the late period when the q-RH correlation is insignificant (Fig. 3.6). The T-RH correlations are for both seasons and periods insignificant ($p > 0.05$). Whereas most grid boxes in the region show negative T-RH correlations, the significant positive T-RH correlation in one grid box in the west of the Tibetan Plateau in SON (Fig. 3.7) could be due to the fact that the measurement data were recorded in this cold climate. There are significant and strong T-q correlations over all periods indicating no regional water limitation. However, the insignificant q-RH correlation in JJA in the late period implies that there are only single years where RH follows q, whereas it does not in other years (Fig. 3.11).

The T-q correlations in JJA and SON are moderate and significant ($r > 0.5$) in the early and the late period so that the regression coefficient can be compared. The $q(T)$ in JJA and SON have decreased from 0.68 g kg^{-1} K^{-1} in the early period to 0.26 g kg^{-1} K^{-1} in the late period in JJA and from 0.57 g kg^{-1} K^{-1} to 0.44 g kg^{-1} K^{-1} in SON (all $p < 0.05$, except for the late period in JJA). The q's dependence on T is decreased in the late period, indicating a deviation from the Clausius-Clapeyron theory due to water-limitation.

For Tibet, the seasons JJA and SON are further analysed in the following sections due to their high significance and strength in RH trends.

3.3.1.3 The Caspian Sea region

The "Caspian Sea" (start latitude: 40° N, start longitude: 45° E, end latitude: 60° N, end latitude 60° E) region includes the states that surround the northern half of the Caspian Sea; the main part corresponds to southwestern Russia and western Kazakhstan. There are also west Uzbekistan, northwestern Turkmenistan, the northern half of Azerbaijan, the eastern third of Georgia. Considering geographical features, in the northwest of the Caspian Sea is the Caspian Depression, a wet and swampy area below sea level. In the northeast are the Ural Mountains, running north-south. Greater Caucasus Mountains north of Georgia and Azerbaijan extend west towards the Black Sea. The Aral Sea is in the southeast of the region, which has been heavily silted up since the 1960s (Micklin, 2007, 2010). The elevation and the density of weather stations used in HadISDH increase towards the north in the northern half of the region. The southern half contains weather stations that are located on the Caspian Sea. Around the lake and Kazakhstan, the climate is arid and cold in boreal winter (Koeppen-Geiger class BWk) and becomes more humid and colder towards the north (BSk, Aw; Figs. 1.12 and 1.13). Cold and dry continental polar air masses from the northeast penetrate the region forming local coastal ice in the north of the Caspian Sea during the boreal winter (Fig. 1.8). The south is poor in precipitation; precipitation reaches the north mainly in JJA when the wind comes slightly from the north due to the low-pressure system over India (Figs. S3 and S4). The vegetation shows an equal gradient with precipitation (not shown). In the Caucasus, meadows, deciduous and mixed forests shape the landscape. Wheat is mainly grown north of the Caucasus (Various, 1996). In DJF and SON, a high-pressure system over Russia attracts south and southwest winds (Fig. S4).

The world's largest inland water body, the Caspian Sea, is nourished by the Volga River in the northwest, the Ural River in the northeast, and the Kura River in the southwest (Fig. 1 in Chen et al., 2017; Arpe and Leroy, 2007). An increase in the Caspian Sea level was observed up to 1995, particularly close to the Volga river delta in the northwest (Cazenave et al., 1997); shortly after, the sea level dropped, so did the surface area (Arpe et al., 2012; Wang et al., 2018). This has been related to increased evaporation, especially during the drought over European Russia in 2010, impacting the Volga basin (Arpe et al., 2012; Chen et al., 2017). Rodell et al. (2018) compare the Caspian Sea drying with the circumstances of the Aral Sea shrinking and associate a decrease in precipitation since 2002 and groundwater depletion with the regional decrease in terrestrial water storage (TWS). Fig. 2 in Koriche et al. (2021b) summarises the decrease in the Caspian Sea level and the effects of a smaller compared to a large Caspian Sea.

A small and insignificant annual RH increase in HadISDH in the early period (0.26 %rh decade^{-1}; $p = 0.45$, 0/12 grid boxes significant) is followed in the late period by a strongly negative trend in the Caspian Sea region (-1.94 %rh decade^{-1}, $p = 0.0$; 11/12 grid boxes significant) (Table 3.3; Fig. 3.9). This is influenced, in particular, by JJA over the southern three-quarters of the region (-4.57 %rh decade^{-1}, $p = 0.0$; 9/12 grid boxes significant) and thus represents the strongest regional and seasonal RH trend worldwide within the late period (Fig. 3.12). There were two negative troughs in JJA, in 2010 and 2014. The former is accompanied by a high-T anomaly value. The latter is not accompanied by a T anomaly, but by a strongly negative q anomaly. There was a recent Russian heatwave in 2020 following the positive T trend. In MAM, there is a strong negative, albeit not significant, trend, especially in the north of the region (-1.64 %rh decade^{-1}, $p = 0.23$; 3/12 grid boxes significant). The downward trend in MAM is mainly driven by a RH trough in 2013–2014. During these years, the T anomalies were positive, while the q showed weak negative anomalies. In the early period, there are weak, insignificant positive trends in all seasons.

In JJA, q-RH are significantly positively correlated, in the late period ($r = 0.6$, $p = 0.01$) stronger than in the early period ($r = 0.4$, $p = 0.04$). The T-RH are linked strongly in both the early and the late period (respectively, $r = -0.66$, $p = 0.0$ and $r = -0.7$, $p = 0.0$), the strongest though in the region's center (Fig. 3.7). In JJA, T-q correlate weakly significant in the early period and even weaker but insignificant in the late period, indicating that the region has become more water-limited in the latest decades. The temperature and q correlate well in the winter months but less so in summer.

In JJA, RH is generally guided by the T increase and in the late period, accompanied by a strong influence of the q decrease (Figs. S6 and S5).

As in JJA, q-RH and T-RH correlations are moderate to strong ($r \geq 0.5$) in both the early and the late period their regression coefficient can be compared. The RH(q) regression increased from 2.79 %rh g^{-1} kg to 6.39 %rh g^{-1} kg, and the negative RH(T) regression increased in their absolute strength from -1.74 %rh K^{-1} to -3.16 %rh K^{-1} (all $p < 0.05$), i.e. RH's dependence on both q and T is increased in the late period.

Since the Caspian Sea, as an open water body, occupies a large part of the region, the Caspian Sea, the thermodynamic driver of faster warming over land compared to the sea, could play a major role. It is expected that prevailing winds from the Caspian Sea to land will play a role in evaporation.

For the Caspian Sea, RH trends in the JJA season will be further analysed in the following chapters due to their high significance and strength.

3.3.1.4 California

The "California" region (start latitude: 30° N, start longitude: 130° W, end latitude: 50° N, end latitude 115° W) contains the state of the same name, Washington, Oregon, Nevada and western Idaho and Nevada and the north of Mexico's Baja California. The weather stations used in HadISDH are located in northern America, closest to the coast (Fig. 1.2). The elevation of the stations increases towards the inland and mountain ranges. Near the west coast are the Cascade and the Sierra Nevada mountain ranges that could block onshore winds. Behind it, inland, follows the Great Basin and the Mojave Desert. Onshore cold, moist, maritime polar northwesterlies hit the region's north, partly penetrating the continent and flowing southwards along the coast (Fig. 1.8). The southern subregion is hit by dry maritropical subsiding. Thus the northwest of the region is humid and develops into hyper-arid to the southeast (Fig. 1.12). The coastal area in the southern part of the region is temperate Mediterranean climate (group C and is crossed inland by continental/microthermal climates (group D), towards the south of dry climates (deserts and semi-arid; group B) (Fig. 1.13). In the north, it gets icy during the boreal winter; very hot in the south in the boreal summer with low RH values (Figs. 1.1 and S2). In the rainy season in DJF, the southern part is largely spared from rain (Fig. S3).

The region has experienced devastating forest fires, like in 2020, and drought, especially in recent years, for example, in 2007–2009 and in 2012–2015 (AghaKouchak et al., 2015; Diffenbaugh et al., 2015; Griffin & Anchukaitis, 2014), and the so-called 'heat dome' affecting the north of the region in summer 2021. Due to increased T and a long-term rainfall deficit with 2015 as one of the driest years, snowpack and TWS have significantly decreased (Asner et al., 2016; Easterling et al., 2017; Rodell et al., 2018; Wang et al., 2018). As an essential element, water management, including irrigation for the strong production of vegetables and fruits, further exacerbates droughts (AghaKouchak et al., 2015; Rodell et al., 2018). Wet years are associated with El Niño in the southern part of the region (Easterling et al., 2017).

The negative RH trend is strongest in DJF in the late period, however, not significant ($p < 0.05$), as are RH trends in the other seasons (Fig. 3.13). Only the RH trend for annual data is significant with a significant positive T trend (Fig. S6).

The annual HadISDH trend in California changes from positive to negative between the early period (0.47 %rh decade^{-1}, $p = 0.13$, 3/8 grid boxes significant) and the late period (-1.85 %rh decade^{-1}, $p = 0.0$; 8/8 grid boxes significant) and increases almost fourfold in magnitude (Table 3.3). Even though the annual trend in the late period is significant, none of the seasonal trends is significant (Fig. 3.13). In the late period, the strongest trend occurs in DJF (-2.21 %rh decade^{-1}, $p = 0.14$; 1/8 grid boxes significant), concentrated on the west coast and in the centre of the region (Fig. 3.3). The years 2007, 2012 and 2014 show extreme negative RH anomalies (Fig. 3.13).

Strongly negative, but not significant trends are also found in MAM, JJA, and SON (respectively: -1.83 %rh decade^{-1}, $p = 0.23$, 1/8 grid boxes significant; -1.78 %rh decade^{-1}, $p = 0.17$, 2/8 grid boxes significant; -1.4 %rh decade^{-1}, $p = 0.15$, 2/8 grid boxes significant). The trends in MAM and SON are concentrated in the south of the region and in JJA in the northern part (Fig. 3.3). The RH troughs in 2008 in MAM and JJA are accompanied by a strongly negative q anomaly, indicating that RH is moisture driven (Fig. 3.13). The RH troughs in 2014 in MAM and JJA, on the other hand, are characterised by a relatively high-T anomaly. The striking positive T anomalies after 2014 can be observed in all four seasons, which is coupled to a positive q anomaly in DJF, MAM and SON, leading to only a moderate change in RH. In JJA alone, this positive T anomaly after 2014 is not accompanied by a positive q anomaly, so RH does show a reduction in this season.

In DJF, where RH drops the most in the late period, q and RH are strongly correlated over both periods (early period: $r = 0.75$, $p = 0.0$; late period: 0.72, $p = 0.0$), indicating that RH is driven by the soil moisture and precipitation availability on the interannual level (McKinnon et al., 2021). In contrast, T and RH correlate insignificantly. The q and T, on the other hand, correlate very strongly with each other in both periods ($r > 0.84$, $p = 0.0$). Similar relationships occur on an annual average. On an annual level, there are significant positive q-RH and T-q correlations in the early, the late and the full period, and significantly negative but weak T-RH correlations only in the early, indicating that California's RH is strongly connected to q rather than to T. However, it is T showing increasingly positive anomalies in the late period, particularly since 2014 (Fig. 3.13).

Given the coastal nature of this region, exposed to prevailing westerlies in its north, with extensive fetch over the Pacific Ocean, changes in RH might be expected to be largely driven by the thermodynamic factors of faster warming over land compared to the ocean. However, it is also plausible that other factors linked to dynamical drivers and terrestrial drivers are contributing.

The annual q-RH and T-q correlations are moderate to strong ($r \geq 0.5$) in the early and the late period so that the regression coefficient can be compared. The RH(q) regression coefficient increased slightly from 3.94 %rh g^{-1} kg to 4.23 %rh g^{-1} kg, and the $q(T)$ increased from 0.25 g kg^{-1} K^{-1} to 0.29 g kg^{-1} K^{-1} (all $p < 0.05$), i.e. RH's dependence on q is slightly increased in the late period, so is q's dependence on T.

3.3.1.5 Mongolia

The region "Mongolia" (start latitude: 40° N, start longitude: 90° E, end latitude: 55° N, end latitude 115° E) covers almost the entire country of Mongolia, including the Gobi and Ordos desert, without the western tip including the Altai Tavan Bogd National Park and the eastern outer end of the country (Fig.1.2). To the north, the region includes parts of southern Russia, including Lake Baikal and the Yablonovy Mountains, and to the south, the northern Chinese province of Inner Mongolia. In the centre of the region the weather stations included in HadISDH are located at very high altitudes (up to over 4000 m) with decreasing topography from west to east, in the north and south mostly over 1500 m (Fig. 1.2; Yu et al., 2019; Yu et al., 2016). Most of the region is classified as hyper-arid to arid and cold (BWk, BSk; Figs. 1.12 and 1.13; Fernandez-Gimenez et al., 2015). On the north side, there are subarctic or boreal with severe winters (Dwd) and on the south side semi-arid bands. The air masses from the Mongolia region are a source for continental tropical air masses flowing south (Fig. 1.8). Regarding the climatological means, the steppe landscape is shaped by high (lower) air pressure fields in DJF (JJA) and westerly winds, which in summer become weaker and point towards the south-east direction (Fig. S4). Mongolia's climate is characterised by long, cold winters, predominantly in the north with permafrost, and short summers, predominantly in the south (Fig. S2; Yu et al., 2019). In JJA, 70% of annual precipitation falls and is concentrated in the region's north (Fig. S3). Thus q is highest in JJA and lowest in DJF with RH lower than 45%. (Figs. 1.1 and S1; Niu et al., 2020). Due to the altitude, the vegetation is sparse and mostly grassland; the region is also characterised by low soil water capacity and high evaporation rate (Yu et al., 2019). Due to abnormally positive temperatures, the region was hit by a severe drought in 2007–2009, led by a soil moisture drying trend since the late 1980s (Dorigo et al., 2012; Yu et al., 2019).

The Mongolia Plateau is characterised by a lake landscape, especially in the northwest. Since the late 1990s, it has experienced strong LCLU change: lakes in the region are shrinking due to precipitation reduction (Tao et al., 2015). Due to overgrazing and coal mining in Inner Mongolia, grassland degradation has occurred with a predicted increasing trend (Gao et al., 2015; Tao et al., 2015).

The slightly positive RH trend in the early period (0.56 %rh decade^{-1}, $p = 0.01$, 8/15 grid boxes significant) is replaced by a strongly negative RH trend in the late period

(1.74 %rh decade^{-1}, $p = 0.0$, 11/15 grid boxes significant; Fig. 3.9). The trend is particularly strong in DJF and MAM (Fig. 3.3). In DJF, (-2.6 %rh decade^{-1}, $p = 0.03$, 6/15 grid boxes significant) the RH decreases particularly in the centre of the region and in the southeast (Fig. 3.3). The years 2009 (low RH, high T) and 2014–2015 (low RH, high q, high T) stand out (Fig. 3.14). In the MAM (-2.22 %rh decade^{-1}, $p = 0.03$, 5/15 grid boxes significant), the east's drying trend is significant and shows troughs in 2009 and 2015 (high T). In JJA (-1.02 %rh decade^{-1}, $p = 0.24$, 2/15 grid boxes significant), strong positive T anomalies over the late period and a negative anomaly in q in 2009 guide a negative RH trend; that seasonal trend is only strong and significant in the very north of the region. Under limited precipitation, the T trend is predicted to rise in the upcoming couple of decades (Hessl et al., 2018).

In Mongolia, the regionally averaged q-RH correlation is strong in MAM over both periods (early: $r = 0.57$, $p = 0.0$, late: $r = 0.66$, $p = 0.0$), and in DJF only over the early period ($r = 0.7$, $p = 0.0$). In none of the seasons, the T-RH correlation is either significant or strong. Strong T-q correlations are found in DJF (early: $r = 0.8$, $p = 0.0$, late: $r = 0.83$, $p = 0.0$), and in MAM only in the early period ($r = 0.78$, $p = 0.0$), not in the late period. The strong T-q correlations shown in DJF are aligned to the Clausius-Clapeyron theory and would suggest that RH hardly changes (only taking into account the detrended data), but in the 2009 and 2014–2015 when RH is anomaly low, T anomalies are stronger than q anomalies (Fig. 3.14). While in DJF, RH seems to be neither q nor T driven at this stage, RH is strongly q driven in MAM. Since neither q nor T shows significant trends in the late period (Figs. S5 and S6), the RH trend could be influenced by various drying events lasting.

The q-RH correlations in MAM and the T-q correlations in DJF are strong and moderate, respectively, and significant, in the early and the late period so that the regression coefficient can be compared. The RH(q) regression in MAM more than doubled from 4.15 %rh g^{-1} kg to 8.54 %rh g^{-1} kg, and the $q(T)$ in DJF slightly decreased from 0.07 g kg^{-1} K^{-1} to 0.05 g kg^{-1} K^{-1} (all $p < 0.05$). RH's dependence on q is increased in MAM in the late period.

For Mongolia, the seasons DJF and MAM are further analysed hereinafter due to their high significance and strength in RH trends.

3.3.1.6 Southern Africa

The region from now on referred to as "southern Africa" (15°-35° E, 15°-35° S) includes the entire countries of South Africa, Lesotho, Eswatini, Botswana and Zimbabwe, large parts of Namibia, the south of Zambia and Malawi, western Malawi and the southeast of Angola. In the southeast, between Lesotho and Eswatini, the landscape is characterised by the Drakensberg mountain range. The Namib Desert, shaped by the cold Benguela Current, extends along the west coast. In the centre is the Kalahari steppe. The Orange River crosses the region from east to west. It provides drinking water and water for agriculture in South Africa and Lesotho, especially for wine and wheat. This river feeds the Gariep reservoir at the southeastern foot of the Drakensberg mountains. A tributary of the Orange River nourishes the Katse Dam in Lesotho. The weather stations used in HadISDH are distributed quite homogeneously across the region (Fig. 1.2).

The Koeppen-Geiger division in southern Africa is complex (Fig. 1.13; Mahlalela et al., 2020), which could make the analysis challenging: The humidity gradient runs from west to east with hyper-arid, hot climate Namib desert (BWh) in the west of Namibia different arid B-categories and temperate C-categories and temperate climates in the centre, to thin strips of humid and tropical climate on the east coast (Figs. 1.12 and 1.13). The region's west is mostly influenced by southerly and southwesterly flow (from the eastern flank of flow around the subtropical anticyclone), with the SH westerlies influencing the far southwest of the region in southern winter (Fig. S4; Hannaford et al., 2015). There is robust system connectivity in the northwest of Namibia with oceanic processes: the cold Benguela ocean current can directly influence rainfall or moisture within the interior. In dryland areas, they are strongly influenced by fogs or dewfall and able to block rainfall or humidity changes into the interior.

In the austral winter (JJA), much of the region becomes driest (with the exception of the far southwest), and the temperatures and RH decrease (Figs. 1.1 and S2). The precipitation rate is highest in DJF in the northern part of the region, but for the Eastern Cape, 35% of the annual rainfall falls in SON (Fig. S3, Mahlalela et al., 2020). Low rainfall is associated with El Niño (Reason, 2017; Setimela et al., 2018). The precipitation trend due to natural variability was found negative in the late period over northeastern southern Africa (Rodell et al., 2018).

According to GRACE, in the Kalahari steppe, TWS increased from 2002 to 2016, and in the Great Rift Valley and further southern Africa since 2014 (Wang et al., 2018). The ENSO phenomenon can be used to forecast precipitation over the region. El Niño is often given as the reason for drought, especially in Botswana in the austral summer (October until March) in 2015–2016 (Archer, 2019; Blamey et al., 2018; Gore et al., 2020; Setimela et al., 2018; Siderius et al., 2018; Swemmer, 2020). Classic El Niño events affect rainfall over southern Africa stronger than El Niño Modoki events (Ratnam et al., 2014). Also, other modes of variability impact the regional precipitation: during the 2015–2016 winter, Indian Ocean SSTs were measured anomalously high, which is associated with the Indian Ocean Dipole (IOD; Archer et al., 2017). The Southern Annular Mode (SAM) affects the austral winter (JJA) rainfall in the eastern cape region but has less of an impact than ENSO (Jury & Levey, 1993; Reason, 2017). Since 2000 in net, Botswana has experienced reforestation, grass loss and wetland expansion, and Namibia deforestation and grass expansion (Al-Hamdan et al., 2017).

The negative trend in southern Africa was also present in the early period (-0.92 %rh decade^{-1}, p = 0.03, 1/12 grid boxes significant). It almost doubled in the late period (-1.64 %rh decade^{-1}, p = 0.08, 8/8 grid boxes significant) (Table 3.3). In the austral spring (SON), the trend extends over the entire region with a focus on the centre of the region, i.e. northern South Africa and eastern Namibia (-2.83 %rh decade^{-1}, $p = 0.01$, 6/13 grid boxes significant) with troughs in 2005 and 2015 accompanied with low q and high T anomalies (Fig. 3.3; Zhongming et al., 2016), a significant negative q and a positive T trend (Figs. 3.15, S5 and S6). In winter (JJA: -2.15 %rh decade^{-1}, $p = 0.02$, 2/14 grid boxes significant), the strongest RH (and q) trends are concentrated over the northeast corner between Botswana, Zimbabwe and northeastern South Africa over the late period (Fig. 3.3) with troughs in 2007 and 2012 (low q); T shows no significant trend (Fig. 3.15). In autumn (MAM; -1.47 %rh decade^{-1}, $p = 0.44$, 0/13 grid boxes significant), the trend focuses on the south of the region but is insignificant. In JJA in the south and in SON over the east, a significant drying trend was already present in the early period (Fig. 3.15).

The regional mean q-RH correlations over the late period are significantly positive in both seasons and even stronger in the late period (JJA: $r = 0.76$, $p = 0.0$; SON: $r = 0.92$, $p = 0.0$), indicating that RH may be driven by prevailing onshore winds. The T-RH correlations are very weak and moderate in SON in the late period, indicating that mainly q drives RH over southern Africa. The T-q correlations are low and insignificant except for JJA in the early period.

Only in SON are q-RH correlations significant and strong ($r \geq 0.7$) in the early and the late period so that the regression coefficient can be compared. The RH(q) regression increased from 5.6 %rh g^{-1} kg to 6.35 %rh g^{-1} kg (both $p < 0.05$), i.e. RH's dependence on q is increased in the late period.

For southern Africa, the seasons JJA and SON are further analysed in the following sections due to their high significance and strength.

3.3.1.7 Southwestern Greenland

Southwestern Greenland (start latitude: 60° N, start longitude: 60° W, end latitude: 75° N, end latitude 40° W) is described below. Weather stations used in HadISDH are located exclusively on the coast (Fig. 1.2). The climate is polar and tundra-like (ET in the Koeppen-Geiger classification; Fig 1.13). Generally, the Icelandic Low influences the climate of Southern Greenland determines its climate (Berdahl et al., 2018): in the summer months, winds over the region are weakened (Fig. S4). These phenomena are strongly linked to the Arctic Oscillation (AO), which determines the position of the jet stream (Hanna & Cappelen, 2003; Mosley-Thompson et al., 2005). Temperatures on southern Greenland's coasts are generally higher than in the interior and north (Various, 1996). RH values are highest in JJA (Fig. 1.1). The RH declines in the entire region, i.e. around the coast, in the late period in DJF, are not accompanied by any significant q or T trends (Figs. 3.3, S5 and S6).

It is noteworthy that this region spends much of its time with snow/ice cover, whereas other regions do not. In the context of global warming and climate change, Greenland's ice mass has been under a sharp decline in the last few decades in the south and on the coasts (Chu, 2014; Druckenmiller et al., 2021; Rodell et al., 2018; Ryan et al., 2019). The mass loss due to melting is accompanied by increased evaporation and runoff, leading to decreased ice sheet albedo, which again amplifies warming (Ryan et al., 2019). The melting in 2012 is associated with a heatwave due to the negative North Atlantic Oscillation (NAO) shifting warm southerly winds towards Greenland (Hanna et al., 2014). In the country's interior, especially in the higher elevations, a slight increase in mass has been observed (Cazenave, 2006; Hanna & Cappelen, 2003). Since the late 1990s, precipitation has decreased over western Greenland (Lewis et al., 2019). whereas it has increased at coastal stations in the northeast and south (1961–2012; Mernild et al., 2015).

The strength of the annual negative RH trend over southwestern Greenland has doubled in the late period compared to the early period (respectively, -1.46 %rh decade^{-1}, $p = 0.02$; 5/6 significant grid boxes; -0.69 %rh decade^{-1}, $p = 0.01$; 2/4 significant grid boxes; Table 3.3). Across the entire region, there are particularly strong trends in the late period in DJF (-3.78 %rh decade^{-1}, $p = 0.01$; 5/6 significant grid boxes) and MAM (-2.83 %rh decade^{-1}, $p = 0.05$; 0/6 significant grid boxes), but not very significant in the latter (Fig. 3.16). In MAM, the strongly negative RH anomaly, for example, MAM 2011, DJF and JJA 2015, are accompanied by both a negative q anomaly and a negative T anomaly (Fig. 3.16). Heatwaves like the one in 2012 over Greenland lead to intense melting (Bonne et al., 2015; Nghiem et al., 2012). These correlations might be expected from a cold, energy limited region. The positive RH trend, though insignificant, in JJA is worth mentioning, which is shaped by low RH anomalies (high T anomalies) around 2000, while the other seasons start the late period with high RH, and high RH anomalies between 2010–2013, while the other seasons show low RH in these years (Fig. 3.16).

In DJF, there is a strong correlation of q-RH in both periods (early: $r = 0.7$, $p = 0.0$; late: $r = 0.71$, $p = 0.0$). In MAM, this correlation is slightly stronger (early: $r = 0.83$, $p = 0.0$, late: $r = 0.84$, $p = 0.0$). The situation is similar between T-RH, with correlations being notably weaker (DJF: early: $r = 0.56$, $p = 0.0$, late: $r = 0.59$, $p = 0.0$; MAM: early: $r = 0.68$, $p = 0.0$, late: $r = 0.61$, $p = 0.0$). Correlations between q and T are very strong: In DJF ($r = 0.97$, $p = 0.0$) over both periods, and in MAM over $r = 0.92$ and $r = 0.91$ (both $p = 0.0$) in the early and late periods, respectively. So it is the winter and spring months that really drive the strong correlations rather than summer and autumn.

Despite strong T-RH correlations, there has not been a significant positive trend in T during the late period (although it should be noted that there has been a positive T trend in JJA from the mid-1990s to around 2010). By a T increase, runoff from melting ice into the sea could occur, so SST may not have warmed as much as in other areas because lots of cold water draining into them. Greenland's weather stations are located around the coast and might strongly react to q or T changes happening around the coast, such as a change in ice loss. Furthermore, ocean currents or circulation (dry and cold air from the US versus warm, moist-holding air from Europe) could drive a change in moisture and T, thus, RH.

In DJF, q-RH and T-q correlations are strong ($r \geq 0.7$) in the early and the late period so that their regression coefficients can be compared. The RH(q) regression increased from 5.69 %rh g^{-1} kg to 7.5 %rh g^{-1} kg, and the $q(T)$ increased slightly from 0.1 g kg^{-1} K^{-1} to 0.12 g kg^{-1} K^{-1} (all $p < 0.05$), i.e. RH's dependence on q, and q's dependence on T are increased in the late period. The dependence of RH on T has slightly increased from 0.49 %rh K^{-1} in the early period to 0.62 %rh K^{-1} in the late period.

Since only the RH trends in DJF are significant over a large area, the other seasons are not considered further.

3.3.1.8 The eastern USA

The region "eastern USA" (start latitude: 35° N, start longitude: 100° W, end latitude: 45° N, end latitude 70° W) covers about the eastern half of the USA and is bounded to the west by the eastern foothills of the Great Plains east of the Rocky Mountains and the states of Nebraska, South Dakota, Oklahoma and Kansas, to the south by Oklahoma, Arkansas, Tennessee and Northern Carolina and to the north by the northern US states right below the Canadian border. Just off the east coast, the Appalachian Mountains stretch from Alabama in a northeast direction to New Brunswick, Canada. Several lakes (Lake Michigan, Lake Huron, Lake Ontario, Erie and Niagara) lie on the United States and Canada border. The Mississippi, Ohio and Arkansas rivers run from north to south through the same name states in the west of the region. The density of weather stations is high and homogeneous (Fig. 1.2). The stations are inland between 500–1000 m of altitude and higher on the region's western edge. According to Koeppen and Geiger (Fig. 1.13), the region has humid-temperate climate (Cfa, east side climate with warm, temperate summers and cool winters, precipitation especially in summer; Fig. S3) in the south and humid-continental climate (Dfa, damp winter cold climate with hot summers, moist soils) in the north. The region is influenced by mild and moist maritime Atlantic tropical air masses and cold polar air masses from the north (Fig. 1.12). In winter (DJF), a climatological mean high-pressure system over the centre of the United States tends to cause northwesterly winds in the western part of the region (Fig. S4). A second, smaller climatological mean high-pressure on the east coast within the high-pressure belt results in weaker westerly winds coming from inland towards the Atlantic. Precipitation occurs throughout the year, with a maximum in spring and summer (Fig. S3). Large regions of the eastern USA are irrigated (Siebert et al., 2006). In December–March, it is not uncommon for cold and polar air to break in from northern Canada. In July, due to the Atlantic subtropical high, weak winds blow into the region from the south and only bring summer rain to the north (Various, 1996). High temperatures are to be expected, especially in the interior of the region and in the south. While the Great Plains are still steppe, the natural vegetation of the rest of the region is deciduous forest, especially over the Appalachian Mountains.

Negative RH trends are common in all seasons in the late period and are seasonally not associated with significant q or T trends (Figs. 3.17, S5 and S6).

The positive trend in the eastern USA over the early period (0.65 %rh decade^{-1}, $p = 0.05$, 5/12 significant grid boxes) switches to a strongly negative trend in the late period (-1.3 %rh decade^{-1}, $p = 0.01$, 10/12 significant grid boxes; Fig. 3.9). Over the seasons, in MAM (-1.91 %rh decade^{-1}, $p = 0.19$), JJA (-1.26 %rh decade^{-1}, $p = 0.41$) and SON (-1.09 %rh decade^{-1}, $p = 0.26$) this trend is strong, but not significant (for all $p > 0.1$, 0/12 significant grid boxes; Figs. 3.3 and 3.17). The trend is strongest in North Carolina and Tennessee in the mentioned seasons, and additionally in MAM further north across Ohio, West Virginia, Virginia, Pennsylvania and New York (Fig. 3.3). The trend in DJF is neither significant nor as strong (-0.79 %rh decade^{-1}, $p = 0.38$, 0/12). In MAM, the negative RH anomalies in 2006–2007 (q high, T high, as expected) and 2014 (q low, T low), in JJA and 2006–2007 and 2012 (both high T) and SON 2010 (high T) stand out (Fig. 3.17). The droughts in 2007 (Boyer et al., 2013; Luo & Wood, 2007) are also visible on the annual scale. The 2012 drought started in the southern United States and was caused by the La Niña conditions (Rippey, 2015). A very strong polar jet stream pulled winter winds north so that the eastern USA was affected by little snowfall and rain, resulting in reduced melting and soil moisture (Mallya et al., 2013; PaiMazumder & Done, 2016; Rippey, 2015). In addition, there was a hot summer in 2012 (Rippey, 2015).

Both q-RH and T-RH correlations on the annual level in the late period are weak ($r = 0.44$, $p = 0.0$; $r = 0.16$, $p = 0.03$, respectively). Correlations between T-q are strong over the early and the late period for all seasons and the annual average (annual in the early period: $r = 0.74$, $p = 0.0$, in the late period: $r = 0.8$, $p = 0.0$).

As none of the seasonal RH trends is significant, the analysis for eastern USA is continued at the annual level.

The annual T-q correlations are strong ($r \geq 0.7$) in the early and the late period so that the regression coefficient can be compared. The $q(T)$ regression coefficient has barely changed from 0.28 g kg^{-1} K^{-1} in the early period to 0.29 g kg^{-1} K^{-1} in the late period (all $p < 0.05$). Hence q's dependence on T remains of equal magnitude, suggesting that the region changed neither in water nor in energy limitation.

3.3.1.9 The Red Sea region

The "Red Sea" (start latitude: 20° N, start longitude: 25° E, end latitude: 35° N, end latitude 40° E) called in this study region includes Egypt, Israel and Jordan. In the north, the Greek island of Cyprus, Lebanon, the southwestern of Syria and the north-eastern of Saudi Arabia is included. The density of weather stations included in HadISDH is highest on the Mediterranean coast, low in the interior and in the southeast along the Red Sea (Fig. 1.2). Topographically, the "Red Sea" region is determined to the east by the Hejaz and Tihamah mountain ranges at the Saudi-Arabian west coast. Most of the region has a warm and hyper dry continental tropical climate, particularly in Egypt and Saudi Arabia (Koeppen-Geiger class BWh; Figs. 1.12 and 1.13). The Nile Delta and the Israeli and Lebanon Mediterranean coast, on the other hand, are more humid to dry sub-humid with a temperate, Mediterranean climate (Koeppen-Geiger Cs-class). Northwesterlies flow into the region from the southeastern Mediterranean Sea (Fig. S4). In the boreal summer, T are high and q lower (Figs. S1 and S2). This results in particularly low RH in JJA (Fig. 1.1). The precipitation rate is low (< 25 mm p.a.); in DJF, it is highest in the north of the region (Fig. S4). This results in a dry, hot desert climate. Thorn bushes in Arabia, as well as the desert, cover the land area. The northern part of the Red Sea has been exposed to increased T over the past decades (Chaidez et al., 2017).

The RH decrease is particularly strong in the east of the region in northern Saudi Arabia and Israel/Lebanon in the late period (Fig. 3.9). RH anomalies show a slight seasonal difference on spatial level (Fig. 3.3). Only in JJA and in SON, T increases, but no significant q change occurs on the grid-box level (Figs. S5 and S6).

In the Red Sea region, the increasing RH trend in the early period (0.56 %rh decade^{-1}, 4/7 significant grid boxes) changes to a strong decreasing trend in the late period (-1.22 %rh decade $^{-1}$, 6/8 significant grid boxes; Fig. 3.9). The largest area of significant trends is found in the northern part of the Red Sea in MAM and JJA (respectively, -1.32 %rh decade $^{-1}$, 3/8 significant grid boxes; -1.21 %rh decade $^{-1}$, 4/8 significant grid boxes; Fig. 3.3). In MAM, the negative RH peak in 2008 (high T) stands out (Fig. 3.18). The T-q show a strong positive correlation (Figs. 3.4 and 3.5), while T-RH and even more q-RH do not correlate significantly or weakly (Figs. 3.6 and 3.7).

The T-q correlations in JJA and SON are moderate and significant ($r \geq 0.5$) in the early and the late period so that the regression coefficient can be compared. The $q(T)$ regression coefficients in JJA and SON have decreased from 0.57 g kg^{-1} K^{-1} in the early period to 0.25 g kg^{-1} K^{-1} in the late period in JJA and from 0.43 g kg^{-1} K^{-1} to 0.38 g kg^{-1} K^{-1} in SON (all $p < 0.05$). The q's dependence on T is decreased slightly in the late period. In MAM, the T-q correlations are strong ($r > 0.7$) and regression stays the same over both periods (0.21 g kg^{-1} K^{-1}).

For the Red Sea, the seasons MAM, JJA and SON are further analysed hereinafter due to their high significance and strength in RH trends.

3.3.1.10 Patagonia

The southern part of Chile and Argentina in South America is hereafter called “Patagonia” (start latitude: 60° S, start longitude: 75° W, end latitude: 40° S, end latitude 60° W). The capitals Santiago and Buenos Aires as the northern border and the Falkland Islands in the east of the region are included in this study. The density of the weather stations used in HadISDH is low and is located on the coasts and in the northern part on the border between Chile and Argentina (Fig. 1.2). The region is strongly influenced by the SH westerlies, which are furthest north over the region in austral winter (Fig. S4). The Chilean part is temperate-humid (Koeppen-Geiger C-class) with a sloping gradient to the east (BWk) due to the rain shadow effect of the Andes mountain range (Fig. 1.13). The vegetation follows the humid and topographic gradient (Fig. 1.12): in the west, there is temperate deciduous forest, on the higher central strip, there is mixed deciduous forest, and in the east, it is semi-desert (Various, 1996). The temperatures are slightly lower in the west than in the east and the austral winter (Fig. S2).

Extreme drought occurred in western Patagonia in 2016. In connection with this, ENSO teleconnections and a positive SAM phase, the combination of which leads to a weakening of the jet stream and westerlies with the latter as storm tracks having the most direct influence on precipitation (Garreaud, 2018). Rodell et al. (2018) find that the warming trend since 2002 has resulted in ice-field melt. They also note a negative precipitation trend over this period (see Fig. 4.2).

In DJF, the southernmost tip of Patagonia shows a significant negative RH trend since 2000 (Figs. 3.3 and 3.9). This stretches a little further north in MAM and SON. In JJA, the significant dryness is primarily localised in the region's east. Strongly positive anomalies accompany the trend in JJA. Garreaud (2018) notes that precipitation reductions and T increases over western Patagonia over the past 40 years have been related to the positive SAM trend, which has been strongest in DJF; although the different timescale to this study should be noted.

The slightly positive trend in the early period in Patagonia (0.22 %rh decade^{-1}, p = 0.4; 1/12 significant grid boxes) changes into a negative trend of six times the strength in the late period (-1.21 %rh decade^{-1}, p = 0.3, 3/7 significant grid boxes; Table 3.3 and Fig. 3.9). This negative trend is particularly strong in JJA ($p < 0.1$) on the east coast (-1.94 %rh decade^{-1}, $p < 0.1$, 4/7; Fig. 3.3) and in SON in the southern part and extending to the centre and over the region (-1.98 %rh decade^{-1}, $p = 0.17$, 2/7 significant grid boxes; Fig. 3.11). In JJA, RH troughs were found in 2007 and 2012–2013 (both low q). RH in SON shows a positive peak in 2000 (low T), the strength of which surpasses the proceeding anomalies.

In JJA (the only season with a significant trend $p < 0.1$), Patagonia shows a moderate q-RH correlation in the late period ($r = 0.65$, $p = 0.0$), and T-q are also moderately correlated ($r = 0.61$, $p = 0.0$). T and RH are barely correlated. There seems to be an interannual link between q-RH (Fig. 3.6), but only the T trend is significantly positive over the late period long-term (Fig. 3.7), which could explain the negative RH trend in JJA.

3.3.1.11 The western Mediterranean region

The western "Mediterranean" region (start latitude: 35° N, start longitude: 10° W, end latitude: 50° N, end latitude 5° E) includes Portugal, Spain and France except for the far east and southeast. The western part of the north of Algeria is also part of the region. The density of the weather stations used in HadISDH is highest in France and averages between 500 and 1000 m above sea level (Fig. 1.2). Generally, there is a temperate-humid climate over France and Portuguese coast and Spanish northwestern coasts (Koeppen-Geiger C-class); over large parts of Spain, Portugal and Algeria, it is dry sub-humid to semi-arid (Koeppen-Geiger B-class; Figs. 1.12 and 1.13). Spain is traversed by the Cantabrian Mountains Chain in the north and towards France the Andorran Pyrenees. The Iberian Chain, the Sierra Morena Mountain Range and the Betic Chain on the south coast run through the country west to east. France is mainly characterised by the Massif Central and by the Alps in the southeast in the south. The mistral, a cold, dry wind from the north, created by a low-pressure belt, is noticeable in the south of France. However, this feature might be a bit too small scale regarding the entire region. In the north of central Spain, the Central Chain is continued in Portugal by the Serra da Estrela mountain range; in the north of Portugal, there is the Northern Meseta mountain range. The region is subject to different air mass influences: cold and moist maritime polar air comes from the north-west, from east dry, maritropical subsiding, from south warm and dry continental tropical air masses and also from west cool and dry continental polar (Figs. 1.8). The atmospheric circulation coming from the Atlantic is controlled by Azores High, particularly pronounced in JJA, and the Icelandic low, particularly pronounced in DJF (Fig. S4). Especially during the boreal summer months, hot southerly winds from the Sahara desert's direction (Sirocco, Leveche) can increase T, particularly in the region's south. In the south of the region, in particular, the precipitation rate depends on the season and is particularly low in summer (Fig. S3).

The frequency of dry years in terms of precipitation, soil moisture availability and positive T anomalies has increased over lands around the Mediterranean Sea (Hoerling et al., 2012; Zampieri et al., 2009). The RH shows a negative trend in the late period, particularly over Portugal, Spain, and western France (Figs. 3.3 and 3.9).

In the western Mediterranean, RH is decreasing throughout the period of record (early: -0.4 %rh decade^{-1}, p = 0.03, 3/9 significant grid boxes; late: -0.88 %rh decade^{-1}, $p = 0.01$, 8/9 significant grid boxes; Table 3.3 and Fig. 3.9). While in the earlier period RH decreased particularly in MAM and JJA over Spain and Portugal (respectively, -0.76 %rh decade^{-1}, $p = 0.05$, 4/9 significant grid boxes; -0.71 %rh decade^{-1}, $p = 0.07$, 3/9 significant grid boxes), in the late period, the decreasing trend was strongest in MAM and SON including southwestern France as well (respectively, -1.2 %rh decade $^{-1}$, $p = 0.02$, 1/9 significant grid boxes; -1.22 %rh decade $^{-1}$, $p = 0.01$, 1/9 significant grid boxes). Particularly negative RH anomalies were found in 1995 (low q), 1997 and 2017 in MAM (high T) and SON (low q; Fig. 3.20). In SON, the negative trough at the end of the late period influenced the strong negative seasonal trend.

Strong T-q correlations are found for all seasons; weak q-RH correlations in SON and moderate T-RH correlations in MAM in the late period: In MAM, the correlations between q-RH and T-RH are insignificant or very weak ($r < 0.5$), except for the T-RH correlation in the late period ($r = -0.54$, $p = 0.02$). In contrast, there are strong significant T-q correlations in this season (early: $r = 0.77$, $p = 0.0$, late: $r = 0.85$, $p = 0.0$). In SON, as well, the T-q correlation is all the stronger (early: $r = 0.9$, $p = 0.0$, late: $r = 0.95$, $p = 0.0$). The correlations between q-RH and T-RH are insignificant or very weak.

3.3.2 Regions with a strong wetting trend

Regions with a strong wetting trend in the late period (Fig. 3.9, Table 3.3) are described below.

3.3.2.1 Scandinavia

The region "Scandinavia" (start latitude: 60° N, start longitude: 20° E, end latitude: 80° N, end latitude 55° E) is located in the south of the Barents Seas, including the White Sea, Finland, northeast of Norway and Sweden and northwest Russia. The density of the weather stations decreases towards the east (Fig. 1.2). The climate is subarctic without any dry season (Koeppen-Geiger class Dfc; Fig. 1.13). Southwesterly winds from continental Europe are particularly pronounced in DJF and SON (Figs. 1.8 and S4). In JJA and SON, they are replaced by weaker northerly and northeasterly winds. Precipitation, lowest in the winter and highest in the summer, results in a cool continental climate with snowy climate and coastal ice in winter (Fig. S3). The predominant vegetation is boreal coniferous forest; NDVI values are highest in JJA (not shown).

Significant wetting trends can be found in all seasons in the late period except in MAM: in DJF, RH increases in the Russian part, in JJA, over the northern Norwegian coast, and in SON, RH increases are widespread over the entire region (Fig. 3.3). While neither q nor T significantly changed for the regional mean in these seasons (Fig. 3.21), T increased in DJF and MAM around the coast in the late period (Fig. S6). Due to anomalous southerly winds for the past couple of decades, increasing salinity, and reduced sea-ice formation, the Barents Sea is warming (Kohnemann et al., 2017; Lind et al., 2018; Skagseth et al., 2020). Glacier melt was found in the Scandinavian area (Rodell et al., 2018).

Annually, no significant RH trend across Scandinavia can be seen in the early period (0.179 %rh decade^{-1}, 0/18 significant grid boxes; Fig. 3.9; Table 3.3). It is only in the late period that the annual average is significantly increasing by 1.451 %rh decade^{-1} (16/19 significant grid boxes). The positive trend is strongly pronounced in DJF and SON over the entire region and in JJA in the west (respectively, 1.701 %rh decade^{-1}, 2/19 significant versus insignificant grid boxes; 1.633 %rh decade^{-1}, 7/19 significant versus insignificant grid boxes; 1.337 %rh decade^{-1}, 5/19 significant versus insignificant grid boxes; Figs. 3.3 and 3.21). In DJF, the RH anomalies in 2008 and 2012–2016 are both accompanied by highly positive q anomalies surpassing the T anomalies which strongly correlates with RH and q (Fig. 3.21). With similar correlations, in SON, there are in particular positive RH anomalies in 2012 and 2017. In JJA, there are no years with particularly strong RH anomalies. It should also be said that in MAM and JJA, strong q and T anomalies can be seen in 2016 and, in for T, also in 2013; however, these strong q and T anomalies did not result in any strong RH excesses.

The T-q strongly positively correlate in all seasons ($r > 0.82$, $p = 0.0$). The q-RH and T-RH also correlate moderately to strongly and significantly positively in MAM, most strongly in DJF and SON. It is noticeable that in JJA, q-RH do not significantly correlate and T-RH correlate significantly but weakly to moderately negatively. In boreal winter, interannual RH is strongly q and T driven, but hardly in JJA.

As the T-q correlations in JJA and SON are strong ($r \geq 0.7$) in the early and the late period, their regression coefficient can be compared. The $q(T)$ regression coefficient in JJA has slightly decreased from 0.4 g kg^{-1} K^{-1} in the early period to 0.34 g kg^{-1} K^{-1} in the late period and in SON they slightly increased from 0.24 g kg^{-1} K^{-1} to 0.26 g kg^{-1} K^{-1} (all $p < 0.05$). The q's dependence on T has barely changed in either of the seasons. In SON, the q-RH and T-RH correlations are moderate ($r \geq 0.5$) and RH(q) regressions have increased from 2.86 %rh g^{-1} kg in the early period and 3.48 %rh g^{-1} kg in the late period. The RH(T) regressions barely change between periods, from 0.82 %rh K^{-1} to 0.83 %rh K^{-1}.

For Scandinavia, the seasons JJA and SON are further analysed in the following due to their high significance and strength in RH trends.

3.3.2.2 Western Alaska

The land west of Anchorage without the Aleutian Islands to the eastern tip of Russia is called hereafter "western Alaska" (start latitude: 60° N, start longitude: 180° W, end latitude: 75° N, end latitude 155° W). Weather stations are sparsely distributed on the coast and in the inner band (Fig. 1.2). The climate is polar, tundra-like (Koeppen-Geiger class ET), and inland subarctic boreal (Koeppen-Geiger Ds classes) in the north (Fig. 1.13). In the southern half, there is a subarctic climate (Fig. 1.12). The region lies in the Arctic front zone. It is affected by cold and moist tropical maritime air masses in the summer, which cause the majority of the annual precipitation (Figs. 1.8 and S3). Polar northerly air flows cause lower T in the north in most of the seasons, except for the summer when winds are weaker and northwards (Fig. S4). RH values are lowest in MAM and highest in SON (Fig. 1.1). RH increased particularly on the west coast of Alaska (Fig. 3.9). Neither q nor T shows any significant trend on the annual level (Figs. S5 and S6).

The years 2002 and 2015 in the analysis period were the hottest years in Alaska for a long time (NOAA National Centers for Environmental Information, 2016), although they have since been superseded (Di Liberto, 2021). The impact of climate change could be noted by glaciers retreating since the early 21st century (Rodell et al., 2018).

In the early period, the positive RH trend over western Alaska is not significant (0.34 %rh decade^{-1}, 0/8 significant grid boxes), but is in the later period (1.51 %rh decade $^{-1}$, 5/8 significant grid boxes; Fig. 3.9). The RH increase occurred in the early period in DJF and MAM and in the late period over all seasons (MAM: 1.42 %rh decade $^{-1}$, 2/8 significant grid boxes; JJA: 0.94 %rh decade $^{-1}$, 3/8 significant grid boxes; SON: 1.64 %rh decade $^{-1}$, 2/8 significant grid boxes). While the regional average trend is significant, trends are not significant in any grid box in DJF (1.23 %rh decade $^{-1}$, 0/8 significant grid boxes; Fig. 3.9). It is striking how strongly the q and T correlate (Fig. 3.22). Usually, the RH correlates strongly with them. This is not the case in JJA over the full period and in MAM in 2008–2013.

In all seasons in both periods, except JJA, q-RH, even stronger T-RH significantly and strongly positively correlate ($r \geq 0.5$, $p = 0.0$); so do T-q without any seasonal exceptions ($r > 0.79$, $p = 0.0$).

3.3.2.3 Northwestern India

The region called "northwestern India" (start latitude: 20° N, start longitude: 65° E, end latitude: 35° N, end latitude 80° E) incorporates as well the larger centre of Pakistan and southeast of Afghanistan. There are no measurements in the latter country, and the weather station density is higher in India than in the Pakistan part, some of them on the north Arabian Sea (Fig. 1.2). In the northwest, the climate is very arid and hot (Koeppen-Geiger BWh-class; Figs. 1.12 and 1.13). With a gradient to the southwest, south of Pakistan in Rajasthan and the Thar desert, it becomes a semi-arid steppe (BSh); to the east, it becomes humid and partly tropical (Koeppen-Geiger C-class and A-class; Fig. 1.13). The Himalayan mountain range begins in the northeast (Fig. 1.2). Warm and dry continental winds reach the region from the northwest, except in JJA, when the monsoon wind from the southwest brings rain into the low-pressure system over the region (Figs. S3 and S4; Rathore and S., 2004). During JJA, it is mainly the southeast of the region affected by the monsoon; in the other seasons, it stays dry there, and little rain tends to reach the northwest. Due to a low-pressure system and depression over the region, Rajasthan encountered heavy rainfalls in August 2016 (Srivastava & Pradhan, 2018). Increased winter precipitation over northwest India is associated with El Niño (Dimri, 2013). The total annual precipitation over Rajasthan was found to increase over the last decades (Rodell et al., 2018; Vivek & Manoj Kumar, 2020). On the other hand, groundwater extraction for crop irrigation and Himalayan glacier mass loss has been found via TWS analysis since 2002 (Rodell et al., 2018). As for the precipitation rate, vegetation is also concentrated in the southeast (not shown). RH has increased in the southern half of the region, particularly in DJF and SON, in both the early and late periods (Fig. 3.3). Only in the late SON period did q show a significant increase in the southeast, while T remains almost unchanged (Figs. 3.23, S2 and S3).

Northwestern India is one of the few regions where RH has been increasing across the entire annual averages (early: 1.17 %rh decade^{-1}, 7/7 significant grid boxes; late: 1.4 %rh decade^{-1}, 4/8 significant grid boxe; Yadav et al., 2017). The late period is discussed below. The strong positive trend in the DJF and SON is mainly evident in the Rajasthan region (respectively 2.31 %rh decade^{-1}, 2/8 significant grid boxes; 2.05 %rh decade^{-1}, 2/9 significant grid boxes; Figs. 3.3 and 3.23). The positive trends in DJF and SON are characterised by relatively regular RH anomalies in ascending order (Fig. 3.23). In the DJF, the positive RH peak 2014–2015 stands out, accompanied by a positive q anomaly and a negative T anomaly. The years 2010 and 2013 show strongly positive RH anomalies in SON, also accompanied by a positive q anomaly and a less positive T anomaly. However, the seasonal RH trends are not significant. On the annual level, RH peaked most strongly in 2013 with anomalously high q and low T (not shown). The q increased significantly in the late period. The q-RH correlate significantly strongly positively ($r > 0.8$, $p = 0.0$), whereas T-RH and T-q correlate negatively weakly on the annual level ($r < |-0.41|$, $p = 0.0$). So, RH is q-driven over all seasons, while it is also T-driven in only MAM and JJA (Figs. 3.6 and 3.7).

Annual q-RH correlations are significant and strong ($r \geq 0.7$) in the early and the late periods (Fig. 3.6) so that the regression coefficient RH(q) can be compared: the RH(q) regression slightly decreased from 4.37 %rh g^{-1} kg to 4.08 %rh g^{-1} kg (both $p < 0.05$), i.e. RH's dependence on q has decreased slightly in the late period.

3.3.2.4 Eastern Canada

The states Quebec, New Brunswick, Prince Edward Islands, north of Nova Scotia and Maine, west of St Pierre and Miquelon, and Newfoundland and Labrador make up the "eastern Canada" region (start latitude: 45° N, start longitude: 80° W, end latitude: 60° N, end latitude 55° W). The Saint Lawrence River flows into the Atlantic Ocean in the lower third of the region (Various, 1996). The density of weather stations is high in the south and decreases with increasing latitude (Fig. 1.2). According to Koeppen-Geiger, the southernmost part of the region is characterised by a humid continental, damp winter-cold climate with warm and humid summers (Dfb), the centre of less humid, short, warm summer continental climate (Dfc) with long, cold winters and the north of subarctic, boreal coniferous forest climate and tundra (ET), where pack ice forms in winter (Figs. 1.12 and 1.13). The latter two sub-regions are influenced by the Arctic air masses and the north by the Arctic Ocean's currents, e.g. shaped by the Labrador Current (Fig. 1.8). In SON and DJF, flow is often from the northwest around the climatological low pressure (cyclone) over southern Greenland (Fig. S4). In JJA, north-westerly winds weaken and south-westerly winds along the south and the east coast bring summer rain (Fig. S3). The south is largely used as cultivated land; deciduous and mixed forests grow at higher latitudes and boreal coniferous forests grow in the north of the region (Various, 1996).

Eastern Canada shows a strong, positive trend only in the late period (early: -0.04 %rh decade^{-1}, $p = 0.95$; 4/10 significant grid boxes; late: 1.32 %rh decade^{-1}, $p = 0.0$, 8/10 significant grid boxes; Table 3.3; Fig. 3.9). This positive RH trend is especially strong in DJF (3.03 %rh decade^{-1}, $p = 0.03$, 7/10 significant grid boxes; Fig. 3.24). The seasonal trend is driven by the peaks in 2010–2013 and 2016, when q and T anomalies strongly correspond to RH. The increase in JJA in the late period (1.32 %rh decade^{-1}, $p = 0.1$, 3/10 significant grid boxes) comes with positive q anomalies, exceeding positive T anomalies (Fig. 3.24).

Annual and boreal winter correlations between T-q-RH are significant, positive and strong ($r > 0.68$, $p = 0.0$; Figs. 3.4 and 3.5). They are even stronger in the late period than in the early period (not shown). In DJF, the q-RH correlation is very strong, especially in the late period compared to the early period (early: $r = 0.68$, $p = 0.0$, late: $r = 0.96$, $p = 0.0$), and also for the T-RH (early: $r = 0.78$, $p = 0.0$; late: $r = 0.97$, $p = 0.0$) and the T-q correlation (early: $r = 0.77$, $p = 0.0$, late: $r = 0.97$, $p = 0.0$).

In DJF, q-RH correlations are moderate ($r \geq 0.5$), and T-RH and T-q correlations are evenly strong ($r \geq 0.7$) in the early and the late period so that their regression coefficients can be compared. The RH(q) barely increased, from 11.97 %rh g^{-1} kg to 12 %rh g^{-1} kg, neither did the $q(T)$ from 0.1 g kg^{-1} K^{-1} to 0.13 g kg^{-1} K^{-1} (all $p < 0.05$), i.e. RH's dependence on q, and q's dependence on T have not changed between the two periods. The dependence of RH on T has slightly increased from 1.42 %rh K^{-1} in the early period to 1.5 %rh K^{-1} in the late period. The correlations and regressions show similarities in terms of correlation with southwestern Greenland (Section 3.3.1.7), also located in the high latitudes. However, the RH trend in southwestern Greenland is negative while it is positive in eastern Canada. While the $q(T)$ regression coefficient is at similar magnitudes in both regions, RH(q) and RH(T) are stronger over eastern Canada, i.e. the RH short-term change depends more on the change in both q and T in eastern Canada (see Section 3.3.3).

Since only the RH trends in DJF are significant over a large area, only the winter season is considered further.

3.3.2.5 The East China Sea region

The "East China Sea" region (start latitude: 20° N, start longitude: 120° E, end latitude: 35° N, end latitude 135° E) has a small land-to-ocean ratio (Fig. 1.2). In addition to the East China Sea, the Yellow Sea and Taiwan, the southwestern part of Japan and the southern tip of South Korea are included. It also includes the Chinese provinces of Jiangsu, Zhejiang and northeast Fujian. The density of weather stations is high, both on the islands, coastal areas and inland. Temperate, humid climate covers most of the region (Koeppen-Geiger classifications Cfa, Cwa; Figs. 1.12 and 1.13). Northerly winds bring dry air masses to the region in all seasons except JJA (Figs. 1.8 and S4). In JJA, the monsoon season, winds are reversed and bring precipitation from the south (Fig. S3). Positive RH changes are significant mainly in SON in the grid boxes in southwestern Japan (Fig. 3.3). Insignificant q trends accompany the RH trend (Figs. 3.25 and S5).

There is a positive annual RH trend in the late period in the region of the East China Sea (0.91 %rh decade^{-1}, 5/8 significant grid boxes) in comparison to the earlier period (-0.53 %rh decade^{-1}, 3/8 significant grid boxes; Fig. 3.9). In SON, all over the area, and in JJA, in the northern part, this trend is particularly strong (respectively, 1.827 %rh decade^{-1}, 2/8 significant grid boxes; 1.05 %rh decade^{-1}, 2/8 significant grid boxes; Fig. 3.3). The positive trend in SON (and MAM) is determined by a highly positive RH anomaly in 2016, accompanied by a highly positive T anomaly and an even more highly positive q anomaly, i.e. strongly positive RH-q-T correlations (Fig. 3.25). In JJA, the increasing trend is based on a positive RH anomaly 2014–2015, accompanied by a negative T anomaly. In 2016 all seasons have positive RH, q and T anomalies. In SON 2015, SSTs over the South China Sea were higher than usual due to an El Niño with anomalous patterns from the normal one, known as El Niño Modoki II (Liu et al., 2017; Xiao et al., 2020a). In 1997–1998, El Niño did amplify the IOD. A positive IOD leads typically to cooling in the southeastern tropical Indian Ocean (Utari et al., 2020). The El Niño Modoki II in 2015–2016 almost offset the IOD resulting in a weakening of the Asian monsoon and higher SST in the west-central tropical Indian Ocean instead of cooling (Liu et al., 2017; Utari et al., 2020; Zhang et al., 2018). The summer of 2016 was also characterised by increased solar heating (Moon et al., 2019).
Because the RH trend is strongly dominated by the peak in 2016 and due to the strong RH-q-T correlation, it seems as if the RH increase in the late period occurred in connection with warming and even more strongly increased q. The atmospheric moisture increase could have happened due to increased evaporation and advection from land to ocean or precipitation change.

Due to the low proportion of land area, no further analysis of the region is carried out due to the low resolution of the datasets.

3.3.3 Finding similarities between regions with a strong RH trend

The global annual average long-term trend results from diverse regional, seasonal and short period trends (Sections 3.3.1 and 3.3.2). This work explores the regions, seasons and periods that contribute most to the global trend or are of most interest in terms of strong trends. To make this analysis more manageable, a filtering system has been devised in order to identify priority regions and seasons for further analysis. If the trends in Table 3.3, Sections 3.3.1 and 3.3.2 correspond to the following eligibility criteria (EC), they will be included in the further analysis:

1. The regional/annual RH trend over the late period must be significant in both datasets HadISDH and ERA-Interim ($p < 0.1$; highlighted by one star / *).

2. The absolute RH trend must be greater than 1 %rh decade^{-1}.

Regional RH trends are expected to be heterogeneous, thus, complex. The two ECs have been chosen to reduce complexity by increasing the signal-to-noise ratio and looking at strong rather than all trends. The strong trends are analysed to detect evidence of thermodynamic, dynamical and terrestrial drivers on RH, a probably complex variable.

After applying EC1, western Alaska, which does not show a significant RH trend in the late period in ERA-Interim, is no longer applicable. The Mediterranean and the East China Sea do not meet the EC2 as their annual RH trend in the late period is below 1 %rh decade^{-1}. The remaining regions are listed in Table 3.4.

For regions that show significant ($p < 0.1$ / *) seasonal RH trends, the very significant ($p < 0.05$ / **) seasonal RH trends are prioritised. Since California, the eastern USA and northwestern India only show significant trends on annual and not on seasonal levels, they will be only considered annually in the further course. The strongest seasonal RH trends are the Caspian Sea (JJA: -4.57 %rh decade^{-1}), southwestern Greenland (DJF: -3.78 %rh decade^{-1}) and eastern Brazil (SON: -3.43 %rh decade^{-1}, DJF: -3.02 %rh decade^{-1}). The weakest RH trends in Table 3.4 are around the Red Sea in JJA (-1.21 %rh decade^{-1}) and SON (-1.08 %rh decade^{-1}).

In some regions, RH trends were already evident in the early period: southern Africa (JJA, SON) shows a negative (positive) RH (T) trend in both periods (a significant negative q trend only in the late period) with interruption of high RH (high q) anomaly around 2000 (Fig. 3.15). The interruption flattens the RH trend over the full period. Since T significantly increased over both periods, the RH trend could be due to the thermodynamic driver, i.e. faster land than ocean warming. Also, northern India shows positive RH and q trends in both periods and low RH and q anomalies between the early and late periods (Figs. 3.3, 3.9, 3.23, S5). In Mongolia (DJF, MAM) and the region around the Red Sea (SON), the negative RH trend in the late period (no q or T trends) preceded a positive trend in the early period (significantly increased q and T in Mongolia, 3.14, and only a significant q trend around the Red Sea, 3.18; Figs. S5 and S6).

Although a correlation does not imply causation, mathematically, RH is the result of q and T. Hence strong q-RH or T-RH relationships imply that RH is q or T driven, respectively. A region can have strong T-RH correlations (positive or negative) and strong q-RH correlations (positive) and strongly T-q correlations (positive or negative) so be driven strongly by both. Regional negative T-RH correlations could indicate that a region is water-limited, and weak T-RH correlations could imply plenty of water or a limitation in energy. For q-RH, no negative q-RH relationship is expected. Strong positive q-RH correlations could suggest water limitation if the region is driven mostly by negative q anomalies or plentiful water if positive q anomalies drive it. Energy limitation is a lot more abstract.

Table 3.4: Regions with a strong trend in HadISDH RH, annually greater than 1 %rh decade^{-1}, in the late period, and their seasons (Fig. 3.3). Moderate ($r \geq 0.5$, not starred) to strong ($r \geq 0.7$ / **) and very significant ($p < 0.05$) q-RH, T-RH and T-q correlations are also shown for each region and season. The q-RH and T-q correlations are positive, the T-RH correlations negative, unless stated with a "(+)". Significant expected q, T trends based on the correlation are shown ($p < 0.1$ / *; $p < 0.05$ / **); for example, in a region with a negative RH trend and a positive q-RH correlation and a negative T-RH correlation, a negative q trend and a positive T trend would be "expected". The regions and seasons are sorted according to their priority based on their significance of the RH trend and analysed according to this in the further course of this work.

Region	Season	Presence of significant (p<0.1), moderate (r>0.5) to strong (r>0.7**) correlations shown by sign (+, -) and early (E), late (L) or both (EL) periods.			Expected trend in q and/or T in the late period (p<0.1 / *; p<0.05 / **)	First priority trends p < 0.05	Second priority trends p < 0.1
		q-RH (+)	T-RH (-, if not stated otherwise)	T-q (+)			
Negative RH trends over the late period							
Eastern Brazil	DJF** MAM** JJA** SON**	L - EL** EL**	E L - -	E** E**L E** E	q** - q** q**	X X X X	
Tibet	DJF* MAM* JJA** SON**	- L E L	- E**L - -	EL - EL E**L	- T* T* T*	 X X	X X
Caspian Sea	JJA**	EL	EL**	-	q**, T**	X	
California	annual**	EL	-	EL	-	X	
Mongolia	DJF** MAM**	E** EL	- -	E**L** E**	- -	X X	
Southern Africa	JJA** SON**	L** E**L**	- L	E -	- q**, T*	X X	
Southwestern Greenland	DJF** MAM*	E**L** E**L**	EL, (+) EL, (+)	E**L** E**L**	- -	X 	 X
Eastern USA	annual**	E	-	E**L**	-	X	
Patagonia	JJA*	L	-	L**	T**		X
Red Sea	MAM** JJA** SON**	- - -	L - -	EL E**L** EL**	T* T* -	X X X	
Positive RH trends over the late period							
Scandinavia	JJA** SON**	- EL	L, (-) EL, (+)	E**L** E**L**	- -	 X	
Northwestern India	annual**	E**L**	-	-	q**	X	
Eastern Canada	DJF**	EL**	E**L**, (+)	E**L**	-	X	

This section aims to find similarities between the regions in Table 3.4 in correlations, trends, and regressions.

From Section 3.1 it is known that if the regional q-RH or T-RH correlation is at least moderate and significant ($p < 0.05$), it can be said that RH is driven on an interannual basis by q or T, respectively. There are more regions with a strong q-RH correlation ($r > 0.7$) in the late period, i.e. eastern Brazil (JJA, SON), southern Africa (JJA, SON), southwestern Greenland (DJF, MAM), northwestern India (annual) and eastern Canada (DJF), than regions with a strong T-RH correlation, i.e. eastern Brazil (MAM), the Caspian Sea region (JJA), the Red Sea (MAM), Scandinavia (JJA), and eastern Canada (DJF). Some regions show both a moderate q-RH and T-RH correlation, i.e. Tibet (MAM), the Caspian Sea (JJA), southern Africa (SON), southwestern Greenland (DJF, MAM) and Scandinavia (SON). In eastern Canada (DJF), both the q-RH and T-RH correlations are even strong ($r \geq 0.7$). Not strongly driven by either q or T (for q-RH, T-RH, $r < 0.5$) are Tibet (DJF), Mongolia (DJF), eastern USA (annual), Red Sea (MAM, SON); these show strong T-q correlations, indicating an agreement with the Clausius-Clapeyron theory and in general no water limitation. Significant T-q correlations occur in most of the regions, except for eastern Brazil (MAM), Mongolia (MAM), southern Africa (SON) and northwestern India (annual). Strong T-q correlations ($r \geq 0.7$) are given in Mongolia (DJF), southwestern Greenland (DJF, MAM), the eastern USA (annual), Patagonia (JJA), the Red Sea region (JJA, SON), Scandinavia (JJA, SON) and eastern Canada (DJF).

Considering both correlations and trends, q drives RH both interannually and long term in the late period in eastern Brazil (DJF, JJA, SON), Caspian Sea (JJA), southern Africa (SON) and northwestern India. In these regions if there is a significant q trend, there is also a correlation, i.e. RH is long-term and short-term driven by q. The other way around, a short-term q-RH relationship does not implicate a q trend, and short-term and long-term T-RH relationships are less strongly coupled. Only in Tibet (MAM), Red Sea (JJA), the Caspian Sea (JJA) and southern Africa (SON), RH is both short-term and long-term driven by T. The latter two regions show among strong T-RH correlations and T trends also strong q-RH correlations and q trends in the late period.

Even if there is no significant q or T trend (see Figs. S5 and S6), RH can significantly change, which is the case for most of the regions in the late period, i.e. eastern Brazil (MAM), Tibet (DJF), California (annual), Mongolia (DJF, MAM), southern Africa (JJA), southwestern Greenland (DJF, MAM), the eastern USA (annual), the Red Sea (MAM, SON), Scandinavia (JJA, SON) and eastern Canada (DJF). However, most of them show a significant q-RH or T-RH correlation indicating which variable drives RH, except Tibet (DJF), Mongolia (DJF) and the Red Sea (SON). The latter three regions show neither significant q and/or T trends nor significant q-RH and/or T-RH correlations in the late period. It could be challenging to analyse these regions because it is unknown how the variables interact and in which direction they are moving. It could be that the spatial inhomogeneity of the RH trend of the correlations within the region leads to non-significant values in these regions on average.

It is noticeable that T-RH correlations are positive in southwestern Greenland (DJF, MAM), Scandinavia (SON) and eastern Canada (DJF; Table 3.4). The three regions are located in the high latitudes of the NH. They are often exposed to frigid temperatures in the months of boreal autumn to boreal spring, under which water changes its physical state to ice, causing a positive T-RH relationship (explained in Section 3.2). These regions also show a very significant, strongly positive T-q correlation in the late period, i.e. changing q changes T, and vice versa. The regions have in common that neither q nor T shows a significant trend in the late period. Southwestern Greenland sets itself apart from the commonality of the latitudinal pattern in its trend. While in the NH high-latitudes RH generally increased over the late period, it gets drier on Greenland's coast (Figs. 3.3 and 3.9). The particular case of southwestern Greenland could have to do with the coastal location of the weather stations, locally specific dynamics and sparse vegetation cover.

The hypothesis established in Section 3.2 that a non-significant, weak T-q correlation could indicate a change in RH can be confirmed for many regions in the late period, such as eastern Brazil (DJF, JJA, SON), Tibet and Mongolia in MAM, southern Africa (JJA, SON), northwestern India (annual). However, as already identified in Section 3.2 for the latitudinal pattern, a negative RH trend is not necessarily associated with a weak T-q correlation. Negative T-q correlations do not occur on regional averages but only sporadically in grid boxes.

It is interesting to look at the longer-term relationship at a regional scale, i.e. the magnitude between RH and q and T, and to compare their regression coefficients between the early and the late periods. Regression coefficients can be interpreted most clearly if the regressions over both time periods are based on strong correlations. Therefore, only regressions for very significant ($p < 0.05$) and moderate to strong ($r \geq 0.5$) correlations were calculated in Table 3.5. A regression coefficient that remains the same over time indicates that the independent variable determines the dependent variable to a similar extent over the two time periods.

For moderate to strong significant correlations there are more significant regional RH(q) than RH(T) regressions, but above all, $q(T)$ regressions, i.e. T-q and q-RH relationships seem to be particularly strong in regions with changing RH. In the late period, the regression coefficient RH(q) is stronger than in the early period for regions with a negative RH trend in the late period (Table 3.5). It almost tripled in eastern Brazil in JJA and SON in the late period compared to the early period. In the Caspian Sea (JJA) and Mongolia (MAM), RH(q) has doubled. A substantial increase in the negative regression coefficient RH(T) was only seen over the Caspian Sea region (JJA). The $q(T)$ regression coefficients changed barely. The regression coefficients for regions with a positive RH trend in the late period also show only small changes. RH is, therefore, more strongly dependent on q in the late period than in the early period. The influence of T on

Table 3.5: Regression coefficients RH(q), RH(T) and $q(T)$ of HadISDH anomalies based on the climatology 1981–2010 for regions and seasons, with very significant ($p < 0.05$), moderate to strong ($r \geq 0.5$) correlations in both the early and the late period in regions with a strong RH trend in the late period (Table 3.4). Double-starred trends or regressions are very significant ($p < 0.05$). NA, if a correlation is not very significant or not moderate to strong over the early and the late period.

Region (sign of RH trend)	Season	Regression coefficient for very significant (r > 0.5) correlations					
		RH(q) [%rh g^{-1} kg]		RH(T) [%rh K^{-1}]		$q(T)$ [g kg^{-1} K^{-1}]	
		Early period	Late period	Early period	Late period	Early period	Late period
NE Brazil (-)	DJF** MAM** JJA** SON**	NA NA 1.78 ** 1.73 **	NA NA 5.23 ** 4.77 **	NA NA NA NA	NA NA NA NA	NA 0.71 ** NA NA	NA 0.6 ** NA NA
Tibet (-)	JJA** SON**	NA NA	NA NA	NA NA	NA NA	0.68 ** 0.57 **	0.26 * 0.44 **
Caspian Sea (-)	JJA**	2.79 **	6.39 **	-1.74 **	-3.16 **	NA	NA
California (-)	annual**	3.94 **	4.23 **	NA	NA	0.25 **	0.29 **
Mongolia (-)	DJF** MAM**	NA 4.15 **	NA 8.54 **	NA NA	NA NA	0.07 ** NA	0.05 ** NA
Southern Africa (-)	JJA** SON**	NA 5.6 **	NA 6.35 **	NA NA	NA NA	NA NA	NA NA
Southwestern Greenland (-)	DJF**	5.69 **	7.5 **	0.49 **	0.62 *	0.1 **	0.12 **
Eastern USA (-)	annual**	NA	NA	NA	NA	0.28 **	0.29 **
Red Sea (-)	MAM** JJA** SON**	NA NA NA	NA NA NA	NA NA NA	NA NA NA	0.21 ** 0.57 ** 0.43 **	0.21 ** 0.25 ** 0.38 **
Scandinavia (+)	JJA** SON**	NA 2.86 **	NA 3.48 **	NA 0.82 **	NA 0.83 **	0.4 ** 0.24 **	0.34 ** 0.26 **
Northwestern India (+)	annual**	4.37 **	4.08 **	NA	NA	NA	NA
Eastern Canada (+)	DJF**	11.97 **	12 **	1.42 **	1.5 **	0.1 **	0.13 **

both q and RH does not change much, except for the Caspian Sea (JJA). This can indicate that in none of the other regions with a strongly negative RH trend hardly any other region was there more water available for evaporation with the same or increasing energy.

In some regions, strong q/T-RH correlations are accompanied by a q/T trend and a significant RH(q) or RH(T) regression. In southern Africa in SON and on the annual level in northwestern India: with an almost constant RH(q) regression, q, thus RH decreased significantly in the late period in southern Africa (SON). In northwestern India (annual), q and RH increased. In the Caspian Sea region (JJA), with a significant q and T trend, the RH dependence of q and T is increased in the late period. The situation is similar in eastern Brazil (JJA, SON), with a significantly negative q trend and an increased RH(q) dependency. These combinations lead to the strongest seasonal RH trends (Table 3.3).

The regions generally reflect the annual and seasonal troughs of the global RH trends (time series in Figs. 3.1, 3.2 and 3.10–3.20); for example, the annual RH trough in 2008–2009 is present in Mongolia (DJF, MAM), the Red Sea region (MAM, JJA), Tibet (JJA, SON). Abnormally low RH values in eastern Brazil (DJF, MAM, SON), Mongolia (DJF, MAM), Canada (DJF), Red Sea (MAM, SON) and in the Tibet region (DJF) contributed enormously to the global RH trough in 2012 (annual, all four standard seasons), wherein in eastern Brazil the RH trough coincides with low q anomalies, and in Mongolia, Tibet and Red Sea (MAM) with high T anomalies and in eastern Canada (DJF) and the Red Sea (SON) by both. Although high T anomalies are present in Mongolia in years with strong RH anomalies, there is no significant, moderate T-RH correlation. The same is counted for the Red Sea region (MAM), and for the anomalously low q in 2012–2013 in eastern Brazil (MAM) without any significant q-RH correlation. In contrast, in Brazil (DJF), the strong RH trough in 2012–2014 is supported by low q anomalies, whereas a significant q-RH correlation is given in the late period. These are some examples that, (i) the regions reflect well global dry years, (ii) regions of all latitudes and seasons contribute to global drying trend and drought extremes (except eastern Canada with a positive RH trend), and (iii) strong regional RH anomalies are often accompanied by q and T anomalies. The RH, q, T peaks and troughs can lead to trends but do not always do so.

Similarities between the regional and seasonal trends based on RH, q and T, and correlations could only be found to a minimal extent, which agrees with the global and latitudinal analysis in Section 3.2. In many regions, the RH(q) and RH(T) regressions have increased in strength, paired with a q or T trend; this combination matches the RH trend.

Also, no clear similarities could be found regarding the strength of the RH trend, climatic zone, biomes or geographical location (coastal or continental). Except for southwestern Greenland, the NH high latitudes show strong similarities in trends and correlations. Tibet, Mongolia, and northwestern India (annual) would be expected to have monsoon influence, at least in JJA.

It is expected that regional RH trends in regions with q or T in combination as proxies for RH are easier to explain. This includes regions that have both significant and, if possible, strong q, T short-term (correlations) and long-term (trends, significant regressions based on correlations) relationships in the late period:

1. Regions with a significant q-RH correlation and a significant q trend: eastern Brazil (DJF, JJA, SON), the Caspian Sea region (JJA), southern Africa (SON) and northwestern India (annually);
2. Regions with a significant T-RH correlation and a significant T trend: Tibet (MAM), the Caspian Sea (JJA), southern Africa (SON) and the Red Sea region (JJA);
3. Regions with both significant q-RH and significant T-RH correlations: Tibet (MAM), the Caspian Sea region (JJA), southern Africa (SON), southwestern Greenland (DJF, MAM), Scandinavia (SON), eastern Canada (DJF); regions with both a significant negative q trend and a significant positive T trend: the Caspian Sea region (JJA) and southern Africa (SON);
4. Regions with significant RH(q) or RH(T) regression and a significant q or T trend, respectively: eastern Brazil (JJA, SON), southern Africa (SON), northwestern India (annual), the Caspian Sea region (JJA);

Mongolia (DJF) shows neither q-RH nor T-RH correlations nor q or T trends in the late period (Fig. 3.14), and this would lead to the assumption that the negative RH trend in this region is more difficult to explain. However, in 2009 and 2014–2015, regional RH shows troughs accompanied by abnormally high T. In addition to regions with many clear indicators regarding changes in RH (e.g. q-RH correlation and changes in q) that do not contradict each other (see points 1 and 2 above), relevant extreme events or periods of drought or heat waves, that best possibly contribute to a significant trend in RH, q and T, might also help with the explanation. Regression and correlation analysis explores linear relationships between variables, so exploration of troughs/peaks may reflect non-linear relationships.

In summary, the RH is strongly positively linked to q in many regions, both short-term (correlations) and long-term (regressions), with q trends in the late period, only occurring in some regions (Table 3.4), indicating that RH in many regions is strongly moisture-driven. A significant link between T-RH is less frequently seen; this is mostly negative; however, it can also be positive in the high latitudes in cold seasons.

The T-q correlation seems to be an essential, over time, stable criterion. RH(q) regression could be an indicator for decreasing RH. An increase in the regression means that RH reacts more strongly to q in the late period compared to the early period. Ergo, with smaller changes in q, T has a stronger influence on RH and thus generate a trend. The reason for this could be a change in water or energy availability.

Analyses of time series and single events also seem to be informative. Peaks and troughs can be instructive, especially at the dynamical level, e.g. the strong El Niño events in 2014–2015. These extreme events are explored in terms of links to El Niño in Chapter 4.

When analysing the regional RH trends, all indications (trends, correlations, single years/peaks/troughs, comparison of early/late period etc.) must be considered individually and then brought into context.

Overall, the regions were chosen adequately (Tables 3.3 to 3.5). They represent all seasons and cover RH behaviour through q and T trends and anomalies in single years, as well as correlations and regressions between the early and the late period.

The differences in the features of the regional and seasonal RH trends suggest that the causes of each RH trend may be unique. This uniqueness asks dynamical and terrestrial drivers in particular for answers. These drivers occur on different spatial and temporal scales than the thermodynamic driver. The latter can, however, form the basis for the trend and influence the other drivers. The uniqueness of RH trends and their characterisation represent a challenge for climate models.

Uncertainties can arise due to the increased data in the late period. Adding data in the form of grid boxes without knowing their exact location and environmental conditions might influence the inhomogeneity of the region's characteristics and impact the regional average to trends, correlations, and regressions.

Twenty-one annual and seasonal, very significant ($p < 0.05$) RH trends in twelve different regions (Table 3.5) will be analysed in the following course of this project. The strongest and most significant trends are prioritised (eastern Brazil, Tibet, Caspian Sea, California, Mongolia, southern Africa). Regions with only a few significant grid boxes and weaker trends enjoy secondary priority (e.g. southwestern Greenland, eastern USA, the Red Sea region; Table 3.4).

3.4 Differences in representing RH and its trends between observations and model HadGEM2-ES

The negative RH trend since 2000, detected by the observational data HadISDH and the reanalysis product ERA-Interim, could not be captured by the CMIP5 models (Dunn et al., 2017; Vicente-Serrano et al., 2018). HadGEM2-ES is part of the CMIP5 collection and for the purpose of this work shall represent CMIP5 models. In this Chapter, "historical" simulations are used, i.e. a simulation that has been forced with historical anthropogenic and natural forcings (see Section 2.1.2). The HadGEM2-ES seasonal time series for the variables RH, q and T for the complete model runs of $r2i1p1$, $r3i1p1$ and $r4i1p1$, the same forcing, but different ensemble members, are considered in the following and compared with HadISDH in the time period from 1973–2017.

Compared with the HadISDH RH anomalies, it is noticeable that the HadGEM2-ES simulations have smaller amplitudes (Fig. 3.26). As expected from the results of Dunn et al. (2017) and Vicente-Serrano et al. (2018), the observed decline in RH since 2000 is not captured by the simulations. Prominent peaks in the late period are 2008 and 2010 ($r2i1p1$) and the trough in 2008 ($r4i1p1$). Opposite signs, i.e. peaks and troughs, in different runs indicate that model runs differ for each year, indicating that these peaks and troughs are not a result of external forcings.

Table 3.6: Global RH trends [%rh decade^{-1}] (p-values) for annual and seasonal data in HadISDH and HadGEM2-ES *historical* + *historicalExt* in the late period based on a climatology of 1981–2010. Significant ($p < 0.1$) trends are shown with one-star; very significant ($p < 0.05$) trends are marked with a double-star. Significant trends in HadGEM2-ES with the same sign as in HadISDH are in bold.

Season	HadISDH trend	HadGEM2-ES *historical* + *historicalExt* trends		
		r2i1p1	*r3i1p1*	*r4i1p1*
annual	**-0.42 (0.00)****	0.00 (0.98)	-0.01 (0.75)	**-0.06 (0.1)***
DJF	**-0.42 (0.03)****	-0.01 (0.91)	-0.10 (0.24)	-0.06 (0.41)
MAM	-0.33 (0.29)	-0.02 (0.84)	-0.00 (1.00)	-0.09 (0.19)
JJA	**-0.53 (0.00)****	0.04 (0.60)	-0.03 (0.74)	**-0.14 (0.03)****
SON	**-0.38 (0.02)****	0.01 (0.94)	0.04 (0.52)	0.07 (0.34)

The global RH trends of the three HadGEM2-ES model runs in the late period are not significant ($p > 0.1$) on a global level with two exceptions: the annual trend (-0.06 %rh decade^{-1}, $p = 0.1$) and the trend in JJA (-0.14 %rh decade^{-1}, $p = 0.03$) in model run $r4i1p1$ (Table 3.6). The latter is the strongest of all seasonal trends and consistent with JJA also being the strongest in HadISDH, but it is still less than a quarter of the respective HadISDH trends' strength.

The model runs are not expected to capture the year to year variability, given that the modes of variability in the model will not necessarily align with those observed. So interannual time series between the HadISDH and HadGEM2-ES runs will not be compared. Instead, long-term trends are considered.

In HadISDH, as discussed in Section 3.1, a significant ($p < 0.1$) increase in global T can be seen in all seasons in both periods, except for the DJF late period. In the late period, q only increases significantly in SON, in the early period in all seasons. The signs of the increases in q and T globally are the same in HadISDH and the HadGEM2-ES model runs (Figs. 3.27–3.29). However, they are not significant in run $r2i1p1$ (Fig. 3.27). In contrast, the increases in run $r3i1p1$ are significant in all seasons in the late period but not in the early periods (Fig. 3.28). Over both periods, there are significant increases in q and T in MAM and SON, and in the late JJA period in run $r4i1p1$ (Fig. 3.28). In JJA, only the q increase in the early period is significant. In the early period in DJF, the T increase is significant, and none of the increases in the late period.

All model runs show strong positive q and T anomalies from about 2010–2017 (Figs. 3.27–3.29). Standardised T anomalies are slightly more positive than q anomalies, similar to HadISDH. Runs $r3i1p1$ and $r4i1p1$ show mostly positive anomalies earlier than 2010, whereas in $r2i1p1$, these are slightly negative in 2009. The HadGEM2-ES trends of the q and T anomalies in the early period are flatter than those in HadISDH (Figs. 3.1 and 3.27–3.29). The T-q correlation seems strong in all model runs (Fig. 3.30). In the second half of the late period, the q, T anomalies development is similar to HadISDH, and the T-q co-variability over the full period seems tighter in the models than in the observational data which could be quantified by calculating the T-q correlation coefficients in future studies. In particular, the less steep rise in q compared to T in the observations is not present in the model simulations. The historical model-runs capture the HadISDH q and T quite well. As it does not represent the observational RH trends, the relationship between RH, q and T might be not adequately calculated in the HadGEM2-ES.

The HadGEM2-ES model is spatially complete, whereas HadISDH has gaps. As HadISDH is an estimate of the globe and the regions, the full coverage of the model is used in this study. Note that Dunn et al. (2017) matched the model coverage with the corresponding HadISDH coverage. The coverage of HadISDH RH, q and T data, unevenly distributed across the globe, has an impact on the average trend across the globe or a region. The reanalysis product ERA-Interim, which has spatially and temporally complete data, spatially and temporally matches the HadISDH RH trends in the late period (Dunn et al., 2017; Vicente-Serrano et al., 2018), which indicates that the difference of spatial completeness between the observations and the model is less of an issue.

It is known that regional trends can differ considerably from the global average. So, to build on the work of Dunn et al. (2017) the regions identified in Section 3.3 that show a strong RH trend in the late period are analysed.

The HadGEM2-ES Model runs are all initiated with the same settings; they follow the same forcings, but they differ in their natural variability. The runs' internal variability can have an influence, especially at the regional level. Some runs can better represent the trends in some regions than in others. One could conclude that RH trends in northeastern Brazil and southern Africa are better captured by runs $r3i1p1$ and $r4i1p1$, in Tibet by runs $r2i1p1$ and $r3i1p1$, the Mediterranean and California by run $r2i1p1$ (Table 3.7). The runs show other significant trends, especially on an annual level, which, contrary to the listed ones, differ from HadISDH trend in their sign. The deviation is particularly evident in the regions with a positive HadISDH RH trend, eastern Canada and Scand-

Table 3.7: As for Table 3.6, for regional RH trends.

Region	Season	HadISDH trend	HadGEM2-ES *historical* + *historicalExt* trends		
			r2i1p1	*r3i1p1*	*r4i1p1*
Regions with a significant annual negative HadISDH RH trend over the late period					
Eastern Brazil	annual	-2.61 (0.00)**	0.223 (0.74)	-1.04 (0.04)**	-1.11 (0.03)**
	DJF	-3.02 (0.00)**	1.04 (0.43)	-0.7 (0.19)	-0.98 (0.11)
	MAM	-1.4 (0.01)**	-0.08 (0.91)	-1.13 (0.08)*	-0.39 (0.59)
	JJA	-2.62 (0.00)**	0.31 (0.77)	-1.36 (0.13)	-1.61 (0.3)
	SON	-3.43 (0.00)**	-0.32 (0.81)	-1.02 (0.31)	-1.31 (0.13)
Caspian Sea	annual	-1.94 (0.01)**	0.59 (0.35)	-0.38 (0.45)	-0.54 (0.34)
	JJA	-4.57 (0.01)**	1.24 (0.46)	-1.07 (0.39)	-0.37 (0.74)
Tibet	annual	-1.97 (0.00)**	-0.87 (0.01)**	-1.01 (0.047)**	-0.4 (0.41)
	DJF	-2.47 (0.09)*	-1.48 (0.09)*	-0.98 (0.54)	0.10 (0.93)
	JJA	-1.73 (0.01)**	-0.47 (0.54)	0.27 (0.61)	-0.07 (0.87)
	SON	-2.04 (0.01)**	-0.25 (0.66)	-0.37 (0.46)	-0.73 (0.04)**
Patagonia	annual	-1.14 (0.03)**	0.48 (0.06)*	0.35 (0.15)	0.16 (0.57)
	JJA	-1.92 (0.095)*	0.44 (0.36)	0.37 (0.47)	-0.03 (0.95)
South-western Greenland	annual	-1.460 (0.02)**	-0.20 (0.42)	-0.47 (0.05)*	-0.21 (0.45)
	DJF	-3.78 (0.01)**	-0.57 (0.53)	-0.51 (0.71)	-0.50 (0.52)
	MAM	-2.83 (0.05)*	0.22 (0.7)	-0.98 (0.32)	-0.62 (0.15)
Mongolia	annual	-1.74 (0.00)**	-0.22 (0.77)	-0.15 (0.81)	-0.34 (0.65)
	DJF	-2.6 (0.03)**	-1.44 (0.55)	-1.57 (0.13)	-0.80 (0.64)
	MAM	-2.22 (0.03)**	-0.45 (0.8)	-0.72 (0.57)	-0.31 (0.82)
Red Sea	annual	-1.22 (0.00)**	0.33 (0.36)	0.51 (0.13)	0.14 (0.6)
	MAM	-1.32 (0.02)**	0.41 (0.72)	0.59 (0.32)	0.17 (0.69)
	JJA	-1.21 (0.00)**	0.96 (0.51)	0.83 (0.04)**	0.38 (0.16)
Southern Africa	annual	-1.641 (0.08)*	1.25 (0.19)	-2.14 (0.03)**	-1.43 (0.07)*
	JJA	-2.15 (0.02)**	-0.86 (0.57)	-1.17 (0.38)	-1.47 (0.29)
	SON	-2.83 (0.01)**	1.93 (0.22)	-0.80 (0.65)	0.15 (0.91)
California	annual	-1.85 (0.00)**	-0.56 (0.05)*	-0.17 (0.6)	0.61 (0.05)*
Eastern USA	annual	-1.3 (0.01)**	-0.33 (0.65)	-0.53 (0.43)	0.87 (0.21)
Regions with a significant annual positive HadISDH RH trend over the late period					
NW India	annual	1.35 (0.03)**	0.25 (0.78)	0.90 (0.36)	-0.09 (0.93)
Eastern Canada	annual	1.32 (0.00)**	-0.45 (0.26)	-0.93 (0.00)**	-0.46 (0.09)*
	DJF	3.03 (0.03)**	0.21 (0.58)	-0.39 (0.29)	-0.74 (0.03)**
Scandina-via	annual	1.44 (0.00)**	-1.12 (0.00)**	-0.14 (0.51)	-1.02 (0.00)**
	JJA	1.32 (0.02)**	-0.56 (0.19)	-0.36 (0.50)	-0.94 (0.097)*
	SON	1.6 (0.01)**	-0.20 (0.68)	-0.02 (0.94)	-0.20 (0.65)

inavia, as well as Patagonia. HadGEM2-ES appears to show negative trends generally for most seasons and regions in the late period, just a lot smaller than HadISDH. So decreasing RH is a feature of the model but not to the same order of magnitude and HadGEM2-ES seems to be more spatially consistent in the negative RH trends as it does not show many regions/seasons of positive trends and only two that are significant.

The strong coupling between observational RH and the thermodynamic drivers q and T was explored in the previous chapters. It shall be investigated whether this coupling is also shown in the HadGEM2-ES model runs.

The q-RH correlations of all three HadGEM2-ES model runs are the same in the global pattern at the annual and seasonal level (Fig. 3.31). In DJF, it is noticeable that q-RH correlate negatively in the high latitudes and upper mid-latitudes. For HadISDH, weakly negative q-RH correlations are limited to JJA and the high northern latitudes, whereas in the rest of the year, q-RH correlations are positive. The negative q-RH correlations in HadGEM2-ES have receded in the remaining seasons and are concentrated in the very high latitudes. In the high latitudes, the T-RH correlations in DJF are negative in all model runs. This stands in contrast to the positive T-RH correlations in cold climates in HadISDH. The model's negative T-RH correlations in DJF differ only slightly in their pattern from JJA. However, the correlation strength varies on a global level: while runs $r2i1p1$ and $r3i1p1$ show negative T-RH correlations across the board in the high and mid-latitudes of both hemispheres, run $r4i1p1$ occurs with less significant and weaker correlations; except in the extra-tropics where correlations are significant and strong (Fig. 3.32). Similarities between HadISDH and HadGEM2-ES can be found in the T-q correlations, which are weak or negative in water-limited areas (Fig. 3.30). These arid regions stand out more in the model due to their strong negative correlations. They only show a difference to HadISDH in a few regions, such as the eastern USA.

The differences in the q-RH and T-RH correlations in DJF, particularly in the high and upper mid-latitudes between HadISDH and HadGEM2-ES, exemplify the disagreement between the two datasets. Although the high latitudes in HadISDH are noticeable with increasing RH in some cases, the conflict can uncover reasons why HadGEM2-ES does not capture the observed RH decrease: the model cannot be expected to represent changes driven by dynamical drivers in the same way as the observations because such things manifest differently in each model run, as has explained earlier. Also, changes influenced by terrestrial drivers also are unlikely to be comparable because the LCLU and their change in the model are not precisely in line with the reality.

The strongest seasonal trends in HadISDH are in the Caspian Sea region (JJA), southwestern Greenland (DJF), eastern Brazil (SON, DJF) and southern Africa (SON). None of them could be represented in HadGEM2-ES (Table 3.7). They should be examined for their short-term co-variabilities (correlations) between q-RH and T-RH. For the Caspian Sea region (JJA), HadISDH showed weak q-RH correlations in the early period, moderate in the late period, moderate T-RH correlations in the early period and strong in the late period (Section 3.3.1.3). The q-RH and T-RH correlations are represented with minor deviations from HadGEM2-ES, e.g. q-RH correlations are weak in $r2i1p1$ and $r3i1p1$ and T-RH correlations moderate in the late period (not shown). Small deviations in correlations and co-variability can strongly influence RH; In addition, there are trends in q and T, or regressions, which the model may not correctly represent. In southwestern Greenland (DJF), observational q-RH and T-RH correlate strongly and moderately positively, respectively, in both periods (Section 3.3.1.7). In all HadGEM2-ES historical runs, the correlations are negative and strong. The reaction of RH to a change in q or T is inverse and enhanced. In eastern Brazil (SON), the q-RH correlations are positive and moderate and strong in the early and late periods, respectively, in both HadISDH and in the three model runs (Section 3.3.1.1). The T-RH correlation is weak in HadISDH in both periods but is indicated by the model as moderate or strong. In the model, the relationship between T and RH is much stronger than in the observations. The situation is similar for eastern Brazil (DJF), where the T-RH correlation is stronger in the model, but the q-RH correlation is weaker. In both seasons, the model does not realistically capture the relationship between q and T and RH. The negative RH trend in southern Africa (SON) is accompanied by a strongly positive q-RH correlation, both in HadISDH and HadGEM2-ES (Section 3.3.1.6). The negative weak and moderate T-RH correlations in the early and late periods, respectively, are adequately represented by $r2i1p1$ and $r4i1p1$. In $r3i1p1$, the T-RH correlations in both periods are strongly negative. This outlier in run $r3i1p1$ could bring the result of the RH trend in the ensemble far away from the observations.

There is strong disagreement between the observation data and the model simulations regarding RH's relationship with q and T. Due to the lack of significant, moderate to strong correlations in HadGEM2-ES, which correspond to the observation data, regressions based thereon and their development in the two periods are not analysed further. For the almost realistically represented q-RH and T-RH correlations, e.g. around the Caspian Sea, it could be interesting to use regressions to establish whether, even though the regional RH trends are different between HadGEM2-ES and HadISDH, are the increase in the strength of the relationship between RH, q and T, discovered in HadISDH, similar in HadGEM2-ES, but this is beyond the scope of this thesis.

At the global level, various discrepancies between observational and model data were found, such as a misrepresentation of q-RH and T-RH correlations in cold climates between HadISDH and HadGEM2-ES in sign and strength. Regional examples confirm these misrepresentations. From this, it can be deduced why the model does not adequately represent RH interannual variability and RH trends. A small change in the natural variability in the HadGEM2-ES runs, a temporal or spatial shift or a change in amplitude can have a major impact on the overall picture, i.e. a butterfly effect. This phenomenon manifests itself in the variables q and T, directly linked to RH. Therefore, the next step in understanding the model calculations would be to explore the reason why these correlations are wrong which would be down to how relevant processes are represented in the model. Applying results and interpretations from observation data

(Sections 3.2, 3.3 and following sections) to the model, RH drivers could be more appropriately introduced. An improved calculation of RH could bring the RH trends in the model closer to those of the observation data.

3.5 Chapter summary and concluding remarks

The large-scale features of RH trends and large-scale relationships between RH, q and T have been assessed at a regional level. The Chapter identifies those regions and seasons where RH trends are significant and strong, and thus contribute to the global annual trend. The q and T anomalies essentially together describe the RH anomalies. Therefore, latitudinal, regional and seasonal patterns of the inter-annual relationship between q, T and RH were determined using correlation coefficients based on detrended data and using time series. It was thus possible to determine for each region with a strong RH trend in the late period, at which time of year the RH depends on q or T and whether this changed from the early to the late period (regression coefficients). This Chapter's overview of the regions, their trends, correlations and climate events serve as a "reference work" for the coming chapters and will help better understand the influence of dynamical and terrestrial drivers. In addition, the differences in representing regional RH trends between observations (Sections 3.2 and 3.3) and model HadGEM2-ES on global and regional and on the annual and the seasonal level were determined.

The global annual RH decline in the late period trend can be broken down spatially and temporally. Sixteen regions with strong, positive or negative annual and seasonal RH trends were identified to represent global, annual RH trends. The RH trends were strongest in eastern Brazil, Tibet, the Caspian Sea, California, Mongolia and southern Africa. Here, positive and negative trends are examined to understand RH further.

The global annual RH trend over the late period is significant and negative and reflected in the four standard seasons. The global trend starts with a peak at the beginning of the late period (2000; especially in MAM and SON) with RH troughs in the second half of the period (2007–2009, 2012–2013). In the boreal summer (JJA), the declining RH is maximal and is influenced by an RH trough in 2015. These extreme years are also well represented in regional time series. The RH peak in 2000 is apparent in eastern Brazil (JJA, SON), Tibet (JJA), southern Africa (JJA) and southern Greenland (DJF). RH throughs in 2007–2009 are present in eastern Brazil (JJA), Tibet (JJA, SON), California (annual), Mongolia (DJF, MAM), eastern USA (annual) and the Red Sea (MAM). The RH trough in 2012–2013 is apparent in eastern Brazil (DJF, MAM, SON), Tibet (SON), California (annual), Mongolia (MAM), southern Africa (JJA), eastern USA (annual) and the Red Sea (MAM). There is another RH trough in JJA in 2015 in eastern Brazil (JJA) and Tibet (JJA). Strong interannual RH variability and extremes in single years may indicate the impact of dynamical drivers that bring about abnormally hot or dry years in certain regions. In other regions, RH seems to decline more continuously without strong extreme years; this is mostly associated with a significant T increase in the late period

(Tibet [JJA, SON], southern Africa [SON], Red Sea [MAM, JJA]). This continuously increasing T might be consistent with the concept of the thermodynamically driven decrease in RH whereby increasing temperatures over land out-pace those of q increase, which is largely influenced by the slower warming ocean. The thermodynamic driver is assumed to play the largest role in RH changes and is expected to be responsible for a background level of RH change upon which additional dynamical and terrestrial drivers also contribute.

The RH anomalies, particularly extremes on which most seasonal and regional negative (positive) RH trends are based, as described above, are driven by abnormally low (high) q and/or anomaly high (low) T, indicating extreme droughts and/or heat as to cause for the RH decline, e.g. Tibet in JJA with RH troughs in 2006 and 2009 (both high T), in 2013 (high T, low q) and 2015 (low q). In other years, q and T extremes are less pronounced. It is striking on the global level that T-q correlate more positively in the early period (Clausius-Clapeyron equation), indicating that there is plenty of water available for evaporation. In contrast, in the late period, they partly decoupled (strongest in JJA), with T increasing faster than q, indicating water limitation such that there is insufficient water available to keep RH constant with rising T. On the global scale, this phenomenon is summarised as a thermodynamic driver. It can be applied globally because the ocean is not warming up fast enough so that it cannot provide sufficient humidity over land. If the explanation of the thermodynamic driver was sufficient, large-scale regional consistency in trend magnitude and temporal behaviour would be expected.

Correlations in this study can only partially describe the phenomenon, as they are based on detrended data and therefore do not perceive any long-term changes in q and T. The weak to negative T-q correlations infer water-limitation and can be found in many, but not all, regions with a strong negative RH trend. These regions are southern Africa, Tibet, and Mongolia. Additionally, in California, weak to negative T-q correlations are especially pronounced in the dry summer months. However, the weak T-q correlations do not describe all regions. In the Caspian Sea, southwestern Greenland, the majority of the NH, and most regions with a strongly positive RH trend, T-q correlations are strong and positive, indicating sufficient water availability. Therefore, the T-q correlation, or a low Bowen ratio (ratio between the change in sensitive heat and latent heat), is not necessarily an indication of strong RH trends.

RH correlations with q and T also do not consistently relate to regions with strong RH trends. Globally, they follow a latitudinal and seasonal pattern. The q-RH correlations are strongly positive, although weaker in JJA in the NH, indicating the lack of water availability in regions that also exhibit a negative RH trend. The T-RH correlations are mixed with positive T-RH correlations in cold regions and seasons (NH in DJF), corresponding to a high Bowen ratio (Peterson et al., 2011) due to snow sublimation or snow melting with energy input. In other latitudes and seasons, the T-RH correlations are negative. The overall global q-RH and T-RH correlation patterns have not changed between the early and the late period. In contrast, this study found evidence on the grid box scale of the lower T-q correlation in the late period (north of the Caspian Sea, eastern Brazil, southern Africa, Mongolia and Tibet) that was seen in the global average time series. There are very small regional and subregional changes. Region to region, there are differences in significance, strength and sign of the q-RH and T-RH correlations. Overall, the q-RH correlations are stronger in eastern Brazil (JJA, SON), Tibet (SON), California (annual), Mongolia (MAM), Southern Africa (JJA, SON), southwestern Greenland (DJF, MAM), Patagonia (JJA), and northwestern India (annual). The T-RH correlations are stronger in eastern Brazil (MAM), the Caspian Sea (JJA), the Red Sea (MAM) and Scandinavia (JJA), indicating that q is driving the interannual RH variability because there are more regions with a strong q-RH correlation.

In some regions (the Caspian Sea region [JJA] and southern Africa [SON]), there are significant q and T trends alongside significant trends in RH and also significant q-RH and T-RH correlations. In others (Mongolia [DJF], eastern USA [annual] and the Red Sea [MAM, SON]), neither q, T trends nor significant q-RH, or T-RH correlations are present. In the high latitudes, there are neither significant q nor T trends. Thus, neither q-RH and T-RH correlations, nor significant trends in q and T are a reliable indication of regions with a strong RH trend. As suggested above, these region to region differences in trends and correlations suggest the influence of additional drivers (dynamical and terrestrial), which likely impact on smaller spatial scales than the thermodynamic driver.

Whereas the correlations provide information about the strength of any linear relationships between the core variables, regression permits a more quantitative assessment of how much a change in q and or T may contribute to the change in RH. The regression coefficients essentially combine correlations and trends. Most notable are the changes between the early and the late period in the RH(q) regressions that point to a stronger RH dependency on q in the late period, particularly in eastern Brazil (JJA, SON) and the Caspian Sea (JJA), but also in regions with a positive RH trend such as Scandinavia [SON]. Interestingly, the increase in RH dependence on T in the late period is evident only in the Caspian Sea (JJA), a region with a large but shrinking water body. The regional RH change can be supported with a significant q or T trend as in the latter region. However, as in the Caspian Sea region with an extraordinary profile, this combination does not apply in any other region. No strong regional changes between the early and the late period in the regression coefficients $q(T)$ were found. The comparison of regression coefficients RH(q), RH(T) and $q(T)$ between the early and the late period cannot be a reliable indicator for a strong RH trend, again showing that there is little consistency in the driving forces of RH change region to region.

The regional trends, correlation and regression coefficients were calculated on regional averages. The heterogeneity (station location and density, trends and correlations of different directions, strengths and significance) is removed from the system by calculating averages. For example, in southwestern Greenland, the weather stations are only on the coast, and in Tibet (SON), the significant and strongest RH trends are limited to the northwest. The topography, i.e. heterogeneity in the altitude, aspect and land use, in the Tibet region plays a major role. Regarding regional and seasonal heterogeneity, the following should be noted: (i) the regions' shape is restricted to cuboids, which inevitably means that grid boxes of different trends may be included in some regions, but this was to minimise as far as possible; (ii) when calculating annual calculations, the seasonal heterogeneity is lost, and (iii) the four standard seasons might not apply for all regions, e.g. wet/dry seasons and monsoon regions. Thus, trends might not be significant/strong for the restriction of four standard seasons. Consequently, it can be helpful to carry out the analyses on dynamical and terrestrial drivers on a subregional and, if possible, on a seasonal level to retain the variance in the data.

The findings from the observations help with the assumption of why HadGEM2-ES does not capture the late period's global and regional RH trends. While some runs can better represent the trends in some regions than in others, in general, it can be said that the model trends do not match the majority of either the strengths, direction, or significance of global, regional and seasonal RH trends. There are also no strong RH peaks and troughs (less intense amplitude), possibly indicating the lack of dynamical drivers (e.g. strong El Niño years) represented in the model. The RH anomalies are not increased around 2000 (beginning of the late period) and not abnormally low towards the end, as is the case with the observations. The global JJA trend in $r4i1p1$ alone is strongest, indicating increased NH land warming in boreal summer and the thermodynamic driver. As with observations, T-q correlate strongly positively, but the model shows less discrepancy (deviation from the Clausius-Clapeyron equation) in the late period, i.e. q rises almost as strong as T, or T rises almost as slowly as q.

The model's T-q correlation patterns broadly match the observations, but correlations between q-RH and T-RH do not. In contrast to the observations with generally positive q-RH correlations and weakly negative q-RH correlations limited to JJA and the high northern latitudes, HadGEM2-ES shows negative q-RH correlations in DJF in the high latitudes and upper mid-latitudes. In the model, the T-RH correlations in the DJF in the high latitudes are negative, which, in contrast, were found to be positive north of the snow line in the observations. RH-correlations in run $r4i1p1$ were generally weaker than in the other runs, which might offset correlations.

On a global scale, there are three key differences between HadISDH and HadGEM2-ES that might help to explain the differences in RH trends. These are: (i) the lack of high amplitude RH anomalies for any one year, which this thesis assumes are linked to the dynamical drivers, (ii) the lack of decoupling of T-q in the late period in HadGEM2-ES which could be linked to the thermodynamic driver, and (iii) the different q-RH and T-RH correlations in cold climates and seasons. These differences apply to all runs. This is not due to the spatial completeness of HadGEM2-ES, as ERA-Interim proves (Dunn et al., 2017). At the regional level, for example, the strong RH decline over the Caspian Sea region (JJA) is not captured, nor is the lack of strong q-RH correlation, which might be due to the region's characteristics of a large water body. This may not be well represented in the model.

If dynamical drivers cause the extreme years that influence the RH, the model will likely differ since the dynamical drivers are not represented at simultaneous time points in the models. If volcanic eruptions caused the extreme years, the model should have captured this.

The large diversity of trend magnitude, accompanying q and T trends, and correlations between q, T and RH in drying regions in the observations, and the impossibility of lumping all regions together, also suggests that it is challenging for models to replicate the observed RH trend.

In summary, the (not all, surely) regional characteristics of the RH trend (short term: extreme years and interannual variability [correlations] and long-term: trends and decadal variability [regressions]) are similar to those of the global average characteristics. The observed RH changes are due to regional and seasonal or limited time period water or energy limits. A combination of q and T anomalies characterise them. Several q-T-RH behaviour features have been identified as indicators of RH trends. Still, none of these is universally applicable to all regions. These include: (i) weak T-q correlations that indicate vulnerable regions since water-limited evaporation regions are absent, which keep RH stable; (ii) increasing regression coefficients RH(q) and RH(T), i.e. a stronger response from RH to small changes in q and T, and analysis of extreme years driving the event (dynamical drivers); and (iii) significantly increased T in the late period. Regions cannot be grouped regarding the strength of the RH trend, climatic zone, biomes or geographical location (coastal or continental). Every region is unique due to their different locations and characteristics. Year-to-year variability in RH is large, which is to be expected given that it is influenced by changes to both q and T. Annual RH anomalies must also be examined individually, with drought or heat due to regional water or energy change towards the limit being the guiding principles. Seasonal considerations of RH trends are also important. The relatively short duration of the early and late periods means that peaks and troughs in the time series can be very influential in both exacerbating or offsetting the trend. All indications must be considered individually and then brought into context in the analysis.

This complexity of RH on the spatial and temporal level must be reflected in the model to capture the RH trend. Climate models are incredibly powerful and useful tools in understanding historical and future climate change. However, the significant difference found between modelled and observed RH suggests that model projected impacts related to land RH have an additional component of uncertainty and that this is true for all regions and seasons with a strong RH trend examined in this thesis. In the model, the parameters q and T are not related to RH in the same way as in observations at a range of spatial and temporal scales, and dynamical drivers cannot contribute to extreme years in the same way. This is a shortcoming of the models. The model would be expected to reasonably reconstruct the land-sea warming contrast and hence the thermodynamic driver to a large extent, as has been demonstrated by Byrne and O'Gorman (2016) and Chadwick et al. (2016). The large differences seen between the observations and model here suggests that terrestrial and dynamical drivers could be playing a role in RH change.

In the following Chapters, dynamical (Chapter 4) and terrestrial (Chapter 5) drivers are examined for the reasons for a change in q and T, thus, RH. The regional descriptions have mentioned links between the thermodynamic driver and dynamical drivers. Analyses of the regional time series (Section 3.3) and RH's thermodynamic correlations support understanding the impact of dynamical and terrestrial drivers on RH.

4 Dynamical drivers

The previous Chapter analysed the influence on relative humidity (RH) of a number of related variables, i.e. air temperature (T) over land and, related to this, specific humidity (q). Where the land is warming faster than the ocean, q does not increase fast enough over the ocean to bring enough moisture over land to satisfy the Clausius-Clapeyron relation (increasing q at 7% per 1 K of T), and hence RH decreases. The strength of the correlations and regressions between RH, q and T varies regionally and seasonally. The thermodynamically driven changes in T and q resulting from land-sea warming differences conceptually explain the observed decrease in RH (Simmons et al., 2010). This does not fully explain the seasonal and regional changes in RH, however. Since RH cannot change without some change in q and/or T, it is necessary to identify drivers of the changes in q and T that lead to changes in RH. Such dynamical drivers will be explored next in order to help explain additional changes in T and q (and thus RH) that might help explain the regional and seasonal patterns in RH trends.

This Chapter explores the links between dynamical drivers and global and regional RH, q and T. It focuses on regions with a strong RH trend and investigates whether dynamical drivers, such as atmospheric and oceanic patterns, which possibly took place earlier and spatially distant from the region, could help to explain any of these RH trends. To assist the interpretation of potential reasons for links between drivers and RH, the physical variables of sea surface temperatures (SST), vector winds and wind speed at 10 m (u10, v10, si10) and sea level pressure (SLP) are examined.

Regional relationships between precipitation and RH are investigated first (Section 4.1.1). Regional changes in precipitation can represent the consequences of changes in dynamical drivers and can thus inform the evaluation of how those drivers affect RH. Correlations between regional RH and the global fields of SST, wind direction and speed and SLP (from the ERA-Interim reanalysis) are used to explore the large-scale climate drivers of regional RH (Sections 4.1.2 to 4.1.7).

Global correlation maps between regionally averaged GPCC precipitation or HadISDH RH, q and T and primary physical drivers (SST, wind direction and speed and SLP) as representative variables of the dynamical drivers are shown in Figs. 4.3 to 4.27 and S10 to S19. Significant correlations are highlighted in frames. They might be located directly in the regions under consideration, in the immediate vicinity, or further away from the region (teleconnections). Multiple variables at different locations can be teleconnected with respect to the region under study. The large-scale correlation patterns that extend beyond the area of the region can be indicative of climate variability (e.g.

SST-RH and SST-precipitation correlation patterns over eastern Brazil in December-January-February [DJF] in Fig. 4.3). To include all correlations relevant to this thesis in the analysis and to allow further analyses that go beyond this thesis but are based on the correlation maps shown, global maps are always shown.

Large-scale dynamical patterns act on different temporal levels from several weeks up to many years and decades and spatially connect processes between different locations, i.e. teleconnections. Corresponding patterns are expressed as indices, typically calculated from the above physical variables and are called modes of variability. Several modes of variability can affect a region (e.g., Ding et al., 2017, in the conjunction of the Pacific Decadal Oscillation [PDO], the Pacific North Atlantic Oscillation, the El Niño Southern Oscillation [ENSO] and the Arctic Oscillation [AO]). To this end, several modes can interfere and appear amplified or weakened, although, this superposition principle is not explored in detail in this project.

This analysis aims to explore whether any mode(s) can influence both the variability in regional RH and its long-term change (Sections 4.2 and 4.3). Regression analysis examines whether the modes can be used to retrospectively predict regional RH, i.e. to what extent a mode can capture the observed regional RH trend.

4.1 Exploring the impact of primary physical variables on regional RH

The primary physical variables, on the one hand, help to establish a basic understanding of how RH is influenced by respective changes both on-site and at a distance to the region and, on the other hand, help to interpret RH's relationships with the dynamical drivers, i.e. modes of variability. The primary physical variables, precipitation, SST, vector winds and wind speed and sea level pressure, are potential candidates to impact regional RH, both locally and at a distance, depending on atmospheric circulation.

In Sections 1.3.2 and 3.3, global and regional overviews are given of each primary physical parameter's climatological annual and seasonal pattern (Fig. S4). This Chapter explores the relationships between the primary physical variables and respective regional mean RH, q and T for those regions with significant RH trends.

While SST anomalies (cold/warm) and wind speed (weaker/stronger) are relatively straightforward to access, the task becomes more complex when several components are necessary for a complete description of the variable, such as for the vector winds, where the direction (angle) and the speed (vector) are combined, or if the interpretation depends on spatial comparisons, as in the case of the SLP, where the definition of a high or low-pressure area depends somewhat on the adjacent barometric pressure area. In the following subsections, trends of the primary physical variables are shown alongside correlations with RH from the region of interest. To aid with exploring the vector wind changes, which are complex to interpret, vectorised trends are also shown (Fig. 4.1). Here, if the trend arrow points in the same direction as the arrow of the climatology (right column in Fig. S4), the mean wind is anomalously strong in the same direction; if the trend arrow points in the opposite direction as the arrow of the climatology, the mean wind is weaker in the climatology direction or in the case of a large arrow, has changed direction.

In the northern hemisphere (NH), by definition, a negative trend in SLP leads to a cyclonic, i.e. counterclockwise, trend in winds, while a positive trend in SLP leads to an anticyclonic, i.e. clockwise, trend in winds. In the southern hemisphere (SH), this is the other way around, i.e. negative (positive) SLP trends with clockwise (anticlockwise) trends in winds.

On an annual level, and in DJF and March-April-May (MAM), negative (positive) pressure trends in the (early, i.e. 1979–1999) late period, i.e. 2000–2017 in the high (mid) latitudes of the SH lead to increased pressure gradients between those latitudes (Fig. 4.1). This gradient results in an increased prevailing westerly flow. With negative SLP trends over the southwestern Indian Ocean, there is increased southwesterly and decreased northeasterly flow around the southeast of southern Africa. Positive SLP trends occur over the Arabian Peninsula and northwestern India, leading to a trend of northeasterly offshore winds, indicating a weakening of monsoonal winds, which is also present in June-July-August (JJA), which form the main rainy season, and decreased northwesterly flow into the Red Sea region. The decrease in RH over the Red Sea region could potentially be explained by the reduction in humid Mediterranean airflow, which is also present in MAM, and partly in JJA. Tables 4.1 to 4.4 summarises significant ($p < 0.05$), thus, coloured SLP trends and corresponding wind trends in the late period and their impacts. Both the Tables and Fig. 4.1 will be used to interpret the regions in the context of winds and SLP.

The relationship between changes in SLP and wind and RH over the late period are described below for regions with a strong RH trend if a direct spatial relationship between changes in SLP and winds and regional RH could be established at the seasonal level from correlation maps in the individual sections on the regions, i.e. for southwestern Greenland, eastern Brazil, Tibet, southern Africa and Scandinavia. Changes in wind and SLP that show no direct link could support explanations further down in this Chapter via spatial and temporal shift.

Introduced by a negative SLP trend in DJF, cyclonic (counterclockwise) trends in the Norwegian Sea include stronger northeasterly winds into southwestern Greenland, which could potentially decrease RH through very cold, very dry Arctic air (Fig. 4.1; Table 4.1; Barry and Carleton, 2013). The trend was inverse in the early period, i.e. increased south-westerlies. The cyclonic trend also leads to a trend of southerly winds over Scandinavia, increasing the regional T. Warmer air masses could be associated with a shorter winter season and earlier melting, thus moisture available for evaporation, thus,

Table 4.1: Trends in SLP and winds of multiple adjacent grid boxes found at Fig. 4.1 for DJF in the late period (2000–2017) and their impact on regions over land. Regions with a strong RH trend in the late period are bold if relevant to the SLP and wind trends. Results from this Table will be discussed in the relevant region sections.

Season	Significance of SLP trend and/or wind direction trend	Location of change	Regional impact on land
DJF	Positive (to the southeast of the region; small region of negative to the northwest), i.e. anticyclonic/counter-clockwise; decreased u10, increased v10	Coast of Southeastern Brazil	Increased southeasterly onshore winds in the south of **eastern Brazil** region and decreased northeasterly flow in the north (Chapter 4.1.2)
	Positive (p>0.05), i.e. anticyclonic/clockwise	Mongolia	Increased flow out of **Mongolia** and decreased flow into the region (Chapter 4.1.6)
	Positive (p>0.05), i.e. anticyclonic/counter-clockwise; increased v10 over Patagonia	Southwest of Patagonia	Increased southerly flow from the high latitudes to the mid-latitudes of southern America/**Patagonia**, decreased northeasterlies. Note: Patagonia does not show a significantly negative RH trend in DJF.
	Negative, i.e. cyclonic/clockwise; increased v10 over Patagonia	Southern mid-latitudes of the Atlantic Ocean	
	Negative, i.e. cyclonic/clockwise	Southern Indian Ocean	-
	Negative; increased v10 along America's west coast	Central America and South American Westcoast	Increased southerly flow up the South American Westcoast
	Negative (p>0.05), i.e. cyclonic/counter-clockwise; decreased u10 and v10 over northeastern Greenland	Norwegian Sea	Stronger northeasterly, offshore winds over **southwestern Greenland** towards the coast of **eastern Canada**; northwesterly onshore winds to Europe; increased southerly (warm) offshore winds over **Scandinavia**. Note: southern Africa does not show a significantly negative RH trend in MAM.

increasing RH. In the early period, the trend was slightly different (southwestern winds). However, Scandinavia's RH did not significantly change in DJF. The RH increase could be lagged a warmer winter and more liquid water available during the year.

The anti-cyclonic (counterclockwise) trend east of Rio de Janeiro in DJF due to a positive SLP trend is more pronounced in the late period than in the early period (Fig. 4.1; Table 4.1). It leads to increased southeasterly onshore winds and, thus, a reduction in the tropical northeasterly trade winds. These tropical northeasterlies are maritime equatorial and thus warm and very moist (Fig. 1.8). The shift of winds implies a reduction of humid air into the region. Also, JJA, MAM and September-October-November

Table 4.2: As for Table 4.1, for MAM.

Season	**Significance of SLP trend and/or wind direction trend**	**Location of change**	**Regional impact on land**
MAM	Positive, i.e. anticyclonic/clockwise	Central Canada	Increased northwesterly flow into **eastern Canada** and **southwestern Greenland**. Note: the latter do not show significant RH changes in MAM.
	Positive, i.e. cyclonic/clockwise; decreased u10/v10 over the Gulf of Aden	Arabian Sea, Bay of Bengal	Weaker onshore winds towards India; (dry) winds from the Arabian Peninsula block Mediterranean winds towards the **Red Sea**
	Positive, i.e. cyclonic/clockwise	Philippine Sea, East China Sea	Decreased northerly flow southwestwards over the **East China Sea**
	Positive, i.e. anticyclonic/counter-clockwise	Southeastern Brazil	Increased southeasterly onshore winds to southeastern Brazil. Note: the southern part of the region does not show a significantly negative RH trend in MAM (Chapter 4.1.2); enhanced northeasterly flow in the northern part
	Positive, i.e. anticyclonic/counter-clockwise	Southwestern Pacific, southern mid-latitudes	Weaker southeastern onshore winds over northeastern Australia
	Positive, i.e. anticyclonic/counter-clockwise	Northeast of Southern Africa	Increased offshore winds over Namibia and southern South Africa. Note: southern Africa does not show a significantly negative RH trend in MAM.
	Negative (p>0.05), i.e. cyclonic/clockwise	Southwestern Indian Ocean	Southwesterly trend along the east coast of southern Africa, i.e. decreased easterly onshore winds. Note: southern Africa does not show a significantly negative RH trend in MAM.
	Negative, i.e. cyclonic/clockwise	Southeastern Pacific Ocean	Decreased southwesterly flow along the west coast of Patagonia. Note: Patagonia does not show a significantly negative RH trend in MAM.
	Negative, i.e. cyclonic/clockwise	SH high latitudes, southwestern Pacific and southeastern Indian Ocean	Increase in pressure gradient between SH mid- and high-latitudes and increased westerlies

(SON), u10 (v10) show a negative (positive) trend of southeasterly winds over north-eastern Brazil, reducing humid tropical airflow into the region, thus, RH over land (Fig.

Table 4.3: As for Table 4.1, for JJA.

Season	**Significance of SLP trend and/or wind direction trend**	**Location of change**	**Regional impact on land**
JJA	Positive (*p*>0.05)	Arabian Sea, Bay of Bengal	Weaker onshore winds towards northwestern India; decreased/blocking of moist Mediterranean northwesterly winds towards the **Red Sea**
	Positive (*p*<0.05), i.e. anticyclonic/counter-clockwise	Southern Indian Ocean	-
	Negative (*p*>0.05), i.e. cyclonic/counter-clockwise	Northwestern Atlantic Ocean	Decreased westerly flow towards **Eastern Canada**; Increased westerly flow over the northern part of the region **eastern USA**
	Negative, i.e. cyclonic/clockwise, decreased v10	Patagonia	Stronger westerly flow towards **Patagonia**
	Negative (*p*>0.05), i.e. cyclonic/clockwise	Southeast of Madagascar	Increased southwesterly/decreased northerly offshore flow at the southeastern tip of **southern Africa** (Chapter 4.1.7)
	No significant SLP trend; decreased u10, increased v10	SH equatorial Atlantic Ocean	Increased southeasterly flow to **Northeastern Brazil** (Chapter 4.1.2), and decreased northeasterly flow in NH equatorial Atlantic Ocean

4.1; Tables 4.2–4.5). These findings will benefit Section 4.1.2 on dynamical drivers over eastern Brazil. There are only weak trends in the early period, albeit in other directions.

Increased southwesterly flow out of northwestern Tibet due to a negative trend in SLP between eastern Mongolia and eastern Tibet could lead to a sub-regional RH decrease due to enhanced dry desert winds in SON. These findings will benefit from Section 4.1.4 on dynamical drivers over Tibet.

Although the negative SLP trend southeast of Madagascar in JJA is insignificant ($p < 0.05$), it is associated with a trend of southwesterly winds towards southern Africa (Fig. 4.1; Table 4.3). These would cause increased moisture advection in east South Africa. Indeed, this subregion shows an insignificant but positive RH trend in the late period (Fig. 3.3), while on regional average, RH is decreased in the late period (Fig. 3.15).
The negative SLP trend in the southern Indian Ocean in SON and the associated clockwise winds lead to decreased maritime tropical northeasterly flow to the eastern coast of southern Africa (Fig. 4.1; Table 4.4; Blamey et al., 2018). In the early period, the

Table 4.4: As for Table 4.1, for SON.

Season	**Significance of SLP trend and/or wind direction trend**	**Location of change**	**Regional impact on land**
SON	Positive, i.e. anticyclonic/counter-clockwise	SH mid-latitudes Atlantic Ocean	Increased southeasterly flow to **northeastern Brazil** (Chapter 4.1.2)
	Positive, i.e. anticyclonic/clockwise	NH mid latitude Atlantic Ocean	Decreased offshore winds from **eastern USA**
	Positive, i.e. anticyclonic/counter-clockwise	West coast of northern Chile	Stronger westerly flow towards **Patagonia**'s west coast; increased southerly flow along South America's west coast
	Negative, i.e. cyclonic/counter-clockwise	Northwestern USA	Decreased northerly flow along the western US coast (California). Note: California does not show a significant negative RH trend in SON.
	Negative; southwesterly	Between eastern Mongolia and eastern Tibet	Reduced westerly flow over northeastern Mongolia (Chapter 4.1.6), increased southwesterly flow out of northwestern **Tibet** (eastern Tibetan Plateau) (Chapter 4.1.3). Note: Northeastern Mongolia does not show a significant negative RH trend in SON.
	Negative, i.e. cyclonic/clockwise	Southern Indian Ocean	Decreased northeasterly onshore flow over the northeast of **Southern Africa** (Chapter 4.1.7)
	Negative, i.e. cyclonic/clockwise	South Atlantic, SH high latitudes	Increase in pressure gradient between SH mid- and high-latitudes and increased westerlies

trend in coastal winds was southwesterly, so the opposite. Less moisture advection from the tropics could decrease RH in the late period (Fig. 1.8). These findings will benefit Section 4.1.7 on dynamical drivers over southern Africa.

Indications that changes in SLP and winds could potentially be related to RH trends could be found in the regions of southwestern Greenland (DJF), Scandinavia (DJF), eastern Brazil (DJF, JJA, SON), Tibet (SON) and southern Africa (JJA, in particular, SON). Due to wind changes, more/less warmer/cooler, drier/humid air masses may have reached the regions. Since eastern Brazil, Tibet, and southern Africa show stronger regional RH trends than the other regions, for them, correlations between SLP, wind and RH are reviewed later (Sections 4.1.2–4.1.7).

Changes in the primary physical variables around the regions with significant RH trends, and their relationship with RH over the region, might be linked with modes of variability in addition to driving changes in RH independent from the influence of modes of variability. Linkages will be made, where possible, in Sections 4.2 and 4.3. To explore the degree to which the primary physical variables differently influence T and q, the variables directly related to RH, regional RH correlations with q and T from Section 3.3 are recalled. As a reminder, there is the thermodynamic driver of sea surface warming relative to land air warming, which directly drives changes in T and q. The dynamical drivers indirectly drive regional T and q by moving parcels of air/heat around the globe differently, leading to changes in RH. Lastly, the terrestrial drivers lead to changes in q from evaporation over land – or lack of it – and may moderate T by changing how much energy goes into latent heating versus sensible heating (land cover).

In the following sections, after exploring the relationship between precipitation and regional RH, the regions with the strongest annual drying trend in the late period (eastern Brazil, Tibet, the Caspian Sea region, California, Mongolia and southern Africa) are analysed in descending order of the magnitude their significant RH trend. Because atmospheric circulations are often seasonal and transitional, significant seasonal RH trends are addressed; otherwise, only the annual trends are analysed (California, the eastern USA, northwestern India), which are driven by seasonal, however, insignificant trends in most of the regions. Where correlations are not significant, they are not mentioned. Correlation and trend maps of the primary physical drivers and RH for southwestern Greenland, eastern USA, the Red Sea, Scandinavia, northwestern India and eastern Canada can be found in the supplement (Figs. S11–S19).

4.1.1 Precipitation

Local precipitation over land changes the amount of water on the near-surface and in soil and groundwater due to large amounts of rainfall or lack of it. These amounts of water are then available for evaporation and contribute to atmospheric humidity. Since precipitation falls from higher air layers, precipitation, which is cold compared to the ground, leads on shorter time scales to a decrease in temperature, especially in summer and outside the high latitudes. At the hourly or daily level, precipitation will enhance the RH when it falls. Over time that might contribute on a monthly level. But the more substantial effect will be the addition/subtraction of the water source to the land. For the liquid phase of precipitation (rainfall), a positive correlation with RH at unchanged or reduced temperature is generally assumed. A weaker correlation is expected for cold climates and snow sublimation for the solid form, such as snow and ice, which remains on the surface and does not seep away – more on the different types of evaporation in Chapter 5. The precipitation-RH correlations and precipitation trends in this analysis refer exclusively to land.

Globally, precipitation and RH correlate positively (Fig. 4.2). The correlation is strongest over the mid-latitudes and strongest in the summer hemisphere and weakest in the winter hemisphere. The correlation is weaker around the equator in the tropics. The precipitation-T correlate negatively, except in the NH upper mid-latitudes and the high latitudes in DJF where low T are accompanied by snow (not shown), leading to weaker precipitation-RH correlation.

Very significant ($p < 0.05$) regionally-averaged precipitation trends in the late period were found for eastern Brazil in DJF (-11.2 mm decade^{-1}; $r = 0.79$, $p = 0.0$ in the late period; particularly pronounced in the region's south), southern Africa in SON (-6.45 mm decade^{-1}; $r = 0.85$, $p = 0.0$; particularly pronounced in the region's east coast and southeast) and northwestern India (annual level: 7.55 mm decade^{-1}; $r = 0.65$, $p = 0.0$; particularly pronounced over eastern Afghanistan and central Pakistan), and a significant ($p < 0.1$) precipitation trend for Scandinavia in JJA (5.09 mm decade^{-1}; $r = 0.77$, $p = 0.0$; grid boxes with blue 'x' and red 'o' in Fig. 4.2). Together with a very significant ($p < 0.05$) and moderate to strong precipitation-RH correlation in the early and the late period in these regions, the decrease (increase) in precipitation may well have contributed to decreased (increased) RH in the late period. In the early period, precipitation trends for these regions are not significant.

For eastern Brazil (DJF) and southern Africa (SON), the regions with significant, negative RH and precipitation trends and significantly strong precipitation-RH correlations, the following interpretations result from the correlation analysis between regional precipitation and the primary physical variables SST, u10, v10 and si10.

Colder surface water over the southern tropical Atlantic and stronger easterlies over the land, in particular, the northern part, and lower SLP in the eastern Pacific (tropical and SH mid-latitudes, link to El Niño) and southwestern Atlantic lead to a reduction in precipitation in eastern Brazil (Fig. 4.3, left). The SST variations cause a latitudinal shift in the Intertropical Convergence Zone (ITCZ) northwards, thus, the tropical rain belt is shifted as well northwards, which occurs particularly during El Niños (Dai, 2021; Nobre & Srukla, 1996; Schneider et al., 2014a; Utida et al., 2019). The ITCZ gets drawn to where positive SST anomalies are. For example, in MAM, where SST-RH correlations are insignificant but fit with the pattern (Fig. 4.6 in Section 4.1.2), a negative Atlantic SST-RH correlation to the region's north, i.e. increased SST, and a positive SST-RH correlation to south, i.e. decreased SST, pull the ITCZ towards the north and away from Brazil resulting in reduced rainfall in Brazil. For inverted correlations, the ITCZ would remain for longer and increase precipitation over the region. Similar for SON regarding the colder south tropical Atlantic sea surface, but stronger easterlies over the ocean rather than over land (Fig. S9). Kayano and Andreoli (2006) emphasise the importance of considering South Atlantic SST variability among the ENSO and tropical Pacific climate variability, which can be time-lagged by several months when predicting rainfall over northeastern Brazil. Even though precipitation in MAM and JJA are less strongly correlated with RH with no significant ($p < 0.05$) precipitation trend, in MAM, increased tropical Pacific Ocean SST (El Niño), stronger southeasterlies over land for MAM and stronger easterlies for JJA also over both land and the ocean lead to a reduction in precipitation (not shown). In SON, JJA and MAM, the negative SLP-precipitation correlation over the region's southeast Atlantic is crucial, i.e. less rain with higher SLP over southwest tropical Atlantic (Fig. S7). In Section 4.1.2, the link between precipitation and seasonal RH is further explored.

There are strong positive correlations between the regional precipitation mean and RH in SON over southern Africa strongest in the region's centre. The negative u10-precipitation correlations to the southeast of the region (Fig. 4.3, right) indicate increased precipitation occurs with weaker westerly/stronger easterly flow. Fig. 4.1 and Table 4.4 show that in the late period there has been decreased easterlies over the southeast of the region and increased southwesterly winds, which could account for some of the decline in precipitation in the east and southeast of southern Africa in SON, and hence contribute to the regional RH decrease. This change in winds is aligned with a cyclonic wind trend in the southeast of southern Africa due to abnormally low SLP leading to a decrease in austral spring rainfall in the late period (Fig. 4.1; Fig. 8 in Mahlalela et al., 2020). Mahlalela et al. (2020) describe the SLP and wind anomalies as part of an SH mid-latitude "wavenumber 3 or 4 patterns" (quote by Mahlalela et al., 2020). They found no apparent links between the austral spring precipitation and the ENSO, the South Indian Ocean subtropical dipole, the Benguela Niño, or the Southern Annular Mode (SAM). Blamey et al. (2018) describe the weakening of the South Indian high pressure and the Angola Low, as well as the strengthening of the mid-level Botswana High as particularly strong in October-March 2015–2016, which partly fits the SLP trends in the late period in Fig. 4.1 and low regional RH values and high T during those months due to water absence (Fig. 3.15). Mahlalela et al. (2020) pointed out that the named oscillations take place in other seasons than those where the RH trend happened.

Significant precipitation trends on a sub-seasonal scale can be associated with RH despite the weak precipitation-RH correlation, for example, through groundwater storage and delayed evaporation to the atmosphere. This could be the case in Tibet, where in Myanmar and northern Laos (MAM), both RH and precipitation show a very significant ($p < 0.05$) negative trend in the late period (Fig. 4.2, grid boxes with a red 'o'). In JJA in the southern Tibetan Plateau and northern China (Mongolia), the precipitation decreased very significantly. JJA is the regional rainy season. Especially negative precipitation trends in the rainy season can substantially impact the hydrological cycle and RH, as this rain is often needed to replenish the water reserves in the groundwater. If the water reserves are not replenished, drought will result. In this case, the Lake Baikal basin has experienced severe land cover change during 2007–2017 with a decreased water body, NDVI and ice and snow (Dorjsuren et al., 2018). In north Pakistan and south Afghanistan (MAM) and Rajasthan (JJA), a significant positive precipitation trend was measured, which could lead to the annual RH trend in northwestern India (Figs. 4.2 and S9, grid boxes with a blue 'x'). Krakauer et al. (2019) found a positive GPCC precipitation trend over the Indus river since 2000. In addition, Zhu et al. (2021) confirmed a decrease in GRACE terrestrial water storage (TWS) linked to ineffective water management. Under the hypothesis that these trends can affect evaporation and thus RH with a time lag, these findings might further help to understand the impact of dynamical drivers on RH. Spatial lags, such as the drying up of rivers due to lack of rain, which leads to a region where the RH has changed, are not considered.

In regions where the correlations between the primary physical variable and RH are similar to the precipitation correlations (Sections 4.1.1 and 4.1.2 to 4.1.7, respectively), the RH change in eastern Brazil (DJF), southern Africa (SON), northwestern India (annual; negative u10/si10-RH/q correlations over the region; Fig. S9) and Scandinavia (JJA; Fig. S10) cases could be partly explained by the change in rain. Despite insignificant seasonal precipitation trends in the late period, the seasonal precipitation-RH correlations in the late period have been strong in eastern Brazil (SON) and the Caspian Sea region (JJA) and could be associated with the primary physical drivers; for these regions/seasons, the correlation maps for the primary physical variables and precipitation can be found in the Figs. S9 and S10, respectively. In Sections 4.1.2 to 4.1.7, the relationships between RH and the primary physical variables for the regions with the strongest negative annual RH trend in the late period are explored.

4.1.2 Eastern Brazil

Eastern Brazil shows very significant ($p < 0.05$) negative RH trends in all four standard seasons in the late period, strongest in SON (-3.43 %rh decade^{-1}), then DJF (-3.02 %rh decade^{-1}), JJA (-2.62 %rh decade^{-1}) and weakest in MAM (-1.4 %rh decade^{-1}) (Section 3.3.1.1). The trends are very pronounced along the coast, and in MAM and JJA, the trend is mainly concentrated in the north of the region. This makes eastern Brazil a key region of interest in terms of changes in RH.

The latitudinal range of the eastern Brazil region is 5° N to 25° S, hence in terms of the primary physical variables, the influence of the seasonal movement of the ITCZ and the trade winds can be seen (Fig. 4.1): the southeast trade winds are present over the whole of most of the country in JJA and SON (Fig. S4), as the ITCZ reaches its northernmost position, hence the subtropical high extends over the south of the region. In DJF and MAM, the northeast trade winds influence the very north of the region as the ITCZ is located at the northernmost limit of the region, with the southeast trades still dominant of the rest of the region, with the subtropical high in the southernmost part of the region. Most of the annual precipitation is recorded in DJF and in MAM in the north (Fig. S3).

Surrounding SSTs are generally very warm, with warmer waters in the south of eastern Brazil's coast during DJF and to the north in JJA (Fig. S4). The South Equatorial Ocean Current flows from the Atlantic to the eastern Brazil coast and flows southwards as the warm Brazil Current (Bonhoure et al., 2004).

Significant negative precipitation trends were found over southeastern Brazil in DJF and the region's north in JJA, respectively, and positive precipitation trends in MAM in the southeast (Section 4.1.1). In DJF and MAM, the ITCZ is located right in the region's north, with southeast trades over most of the region and northeast trades over the north (Figs. S3 and S4). Due to decreased SST and SLP in the southern tropical Atlantic in the late period, the ITCZ, the tropical rain belt, is shifted northwards (Fig. 4.3). There are increased southeasterlies with a positive SLP trend southeast of the region (Fig. 4.1) during the late period, particularly in DJF. DJF is the rainy season for most of the region (Fig. S3); thus, the reduction in precipitation might cause a lack of moisture availability. This idea confirms the similarity between physical primary drivers correlation with the precipitation and RH in DJF (Figs. 4.3 and 4.4) with less pronounced similarity in MAM and SON, and in JJA none (not shown), so that precipitation as a driver of RH in MAM and SON plays a lesser or hardly a role in JJA. However, in JJA, a trend of increased southeasterlies/decreased northeasterlies (Fig. 4.1); thus, less moist flow into the region is linked to the reduction of rainfall in the northern part of the region (Fig. 4.2). In DJF, precipitation-RH correlate significantly mainly in the region's west; an impact of precipitation on regional RH without time lags is not expected for large parts of the region.

During SON, the season with the largest negative trends in RH during the late period, the correlation between q-RH is strongly positive ($r = 0.8$, $p = 0.0$), particularly in northwestern Brazil, and not significant for T-RH (Section 3.3.1.1). Simultaneous negative trends in q are significant, while trends in T are not significant. Together, this suggests that in SON, changes in q play a stronger role than changes in T in terms of driving RH decreases. Precipitation and RH correlate significantly and strongly positively ($r = 0.79$, $p = 0.0$). The negative precipitation trend in the late period is not significant (not shown). However, the correlation pattern between the primary physical variables and precipitation (Fig. S9) are similar to the correlations between the former and q, which again are similar to those with RH, indicating that dynamical drivers are linked to a decrease in q due to reduced precipitation which results in the negative RH decrease in the late period.

SST-RH/q correlations are significant and positive around the coastline and eastwards across the Atlantic, whereas SST-T correlations are positive around the southern coastline but negative and lacking widespread significance around the northern coastline (Figs. 4.4 and 4.5). The SST-RH correlations differ substantially in the early period in that they are generally weakly negative but lacking significance. This suggests that decreased SSTs (negative SST trend in the late period) adjacent to the coast and extending eastwards are linked to a q-driven decrease in RH with increased southeast trade winds(negative u10 and v10 trend and positive si10 trend; Fig. 4.1) the late period. The increase in southeasterlies indicates stronger southeast trades indicating that the rain bringing ITCZ is north of the region (for longer), reducing q and RH over northeastern Brazil. Over the southern (western) subregion, southward (southwestward) wind trends indicate decreased moisture inflow from the Atlantic ocean (the distribution of drier air inland) (Figs. 4.1 and 4.4). In the early period, wind trends over the region's south were inverted, i.e. increased southwesterly inflow to the south due to a high-pressure trend over the southwest Atlantic (Fig. 4.1).

Correlations between the vector wind components (u10, v10) and RH (Fig. 4.10) are related to the above trends in SON: there are weak-to-moderate positive correlations over the region with weak-to-moderate negative correlations to the west and northeast. Much of the region outside of where the significant correlations occur has experienced significant negative trends in u10, i.e. an easterly trend. Although the pattern is broadly similar for the early period, the positive correlations are not significant and there are no significant trends. The north-south pattern is similar for u10-q and u10-T correlations. This suggests that particularly over the late period weakened westerly/stronger easterly winds are associated with lower q, T and RH over much of the region. For v10-RH, there is a west-east pattern with significant positive correlations inland compared to significant negative correlations at the coast and to the east. This suggests that stronger southerly/weaker northerly winds are associated with higher RH inland but lower RH at the coast, and vice versa. For v10-q and v10-T, the correlations are mostly significantly negative over the entire area. The similarity to the early period in the direction of correlation and the absence of late-period trends in v10 suggests that this is less important than the u10 component for changes in RH. For the wind speed (si10), the si10-q and si10-T correlations are stronger than for si10-RH, where they are generally negative yet positive in the northwest of the region. For si10-RH, the correlations are moderately negative and significant, weakening and losing significance over the ocean to the east and becoming positive to the north. This, together with the widespread significant positive trends in si10, suggests that increasing wind speed of south easterlies over the region's northern half and a northerly trend in the region's south are associated with decreasing RH across the region in the late period.

It is difficult to conclude exactly how changes in wind direction and speed have driven changes in q and, thus, RH because of the differences in correlation across the region and its surrounding area and the complexity of vector winds. However, it is clear that there are differences in winds on their impact on RH between the early and late periods and that these do relate to changes in moisture (q) and T.
SLP during SON mostly correlates negatively with RH in the southeast of the region towards the Atlantic. Decreased RH is related to increased pressure offshore of the eastern coast. The local pattern is similar to that of the early period but lacks significant correlations. The wider Pacific ocean shows quite a different early/late period pattern with almost Pacific-wide negative correlations with increased SLP over the central tropical Pacific in the early period but not in the late. Hence, in the late period, SLP over the Pacific Ocean is less relevant compared to the regional mid-latitudinal Atlantic SLP without significant trends.

During DJF, the rainy season in particular over the region's west (Fig. S3) and the season with the second-largest negative trends in RH during the late period, correlations between q-RH and T-RH are similar to those in SON: the correlation between q-RH is

moderately positive and significant ($r = 0.61$, $p = 0.01$) and not significant for T-RH in the late period (Chapter 3.10). Simultaneous negative trends in q are very significant, while trends in T are not significant. Together, this suggests that in DJF, as in SON, changes in q play a stronger role than changes in T in terms of driving RH decreases.
In the austral summer, precipitation and RH correlate significantly and strongly positively ($r = 0.75$, $p = 0.0$; Section 4.1.1). Precipitation shows a significant negative trend in the late period (-11.2 mm decade^{-1}, $p = 0.0$), i.e. a reduction in precipitation is coincident with reduced q and RH (Fig. 4.2).

For the vector wind components (u10, v10) in DJF, there are significant and positive u10-RH correlations over the eastern coast and the west of the region (Fig. 4.4). The regional pattern is similar for u10-q correlations, while u10-T correlate significant and positive in the southeast of the region over the Atlantic ocean and significantly and negatively in the northwest of the region (Fig. 4.5). The u10-RH patterns are similar to those in the early period but more strongly positive in the late period. The difference between both periods is more widespread significant late-period negative u10 trends across the region and to the east. This suggests that winds with a stronger easterly component are associated with lower RH over much of the region in the late period.
The v10-RH correlations are significantly negative, in particular, over the ocean around the northeastern coast and the west of the region (Fig. 4.4). In the southwest of the region, v10-RH correlations are significantly positive with significantly negative trends in v10. This suggests that stronger southerly/weaker northerly winds in the centre of the region and weaker southerly/stronger northerly winds southwest of the region are associated with lower RH over much of the region. Thus suggesting as in SON (Fig. 4.10) that weaker northeast/stronger southeast trade winds result in lower RH in the region, indicating that the ITCZ is to the north of the region. The SST-RH correlations also support this idea, with a region of positive SST-RH correlations in the SH tropical Atlantic along the coast of northeastern Brazil and extending eastwards (i.e. decreased RH with decreased SSTs) fitting with previous work (e.g. Uvo et al., 1998) of increased rainfall with warmer SSTs in this region. There has been a negative SST trend during the late period in the grid boxes closest to the coast.
For v10-q, the correlations are mostly negative and significant, i.e. q decreases with winds with a stronger southerly component, fitting with the RH results above. The v10-T correlations are almost not significant. This pattern is similar though weaker in the early period. As mentioned above, there are positive late-period trends in v10 over the centre of the region. For the wind speed, the correlations appear to be similar to the v10 pattern with significant negative correlations over the eastern coast for si10-RH and si10-q and towards the ocean to the east. This suggests that increasing wind speed is associated with decreasing q and RH across the region. There are widespread significant positive trends in si10 across the region and surrounding ocean and land in the late period but not the early period, as for SON.

Among the above mentioned correlations, a negative u10 trend and positive v10 and si10 trends suggest strengthened southeasterlies with decreasing q and, thus, RH over the late period, apart from in the south. As for SON, the question arises as to how changes in wind direction and speed between the early and the late period have driven changes in RH via changes in moisture and temperature in DJF. One hypothesis for the RH decrease in both DJF and SON could be that the colder sea surface leads to less evaporation over the ocean and less moisture supply for land. The drier air is then spread inland by stronger winds. Nobre and Srukla (1996) note that precipitation variability due to dynamical drivers is temporally lagged in the region's south.

SLP during DJF correlates significantly and strongly positively with regional RH over the southwestern Atlantic, touching the SH high-latitudes. This means that generally, decreased RH occurs alongside reduced SLP in this region. The local pattern is similar to that of the early period. Still, there are significant negative late-period trends in SLP only in the late period. Further north, there are positive SLP trends in the region's southeast but no SLP-RH correlation. These positive SLP trends across the climatologically higher pressure region increase the extra-tropics to tropics pressure gradient, which is likely to strengthen the southeast trades and is consistent with trends shown in u10, v10 and si10. The results, the strengthening of the southeasterly winds is similar to the result in SON, just the mechanisms of a change in SLP (positive over the southeast of the region and negative over the southwest Atlantic in DJF, negative over the north of South America and Patagonia in SON) are different between the two seasons. In DJF in the late period, RH over the northwestern subregion of easter Brazil was found to be significantly, strongly negatively correlated with the MEI (ENSO) and IPO (Section 4.3).

During JJA, the dry season, correlations between q-RH and T-RH are similar to those in DJF and SON: strongly positive q-RH correlations ($r = 0.76$, $p = 0.0$) and a not significant correlation for T-RH in the late period with negative and very significant trends in q and not significant trends in T. As for DJF and SON, together, this suggests that in JJA changes in q are playing a stronger role than changes in T in terms of driving RH decreases.

In contrast to the DJF and SON seasons, in JJA, SST-RH correlate negatively in a northward shifted Atlantic Multi-decadal Oscillation (AMO)-like pattern over the south-equatorial Atlantic and the North Atlantic (negative AMO), and, differently to the other seasons, SST-RH correlations are positive (negative) over the central-eastern (western) Pacific (and off the northeast coast of the region), which resembles the ENSO, i.e. decreased RH during La Niña. Note that El Niño, not La Nina, is typically associated with lower rainfall in NE Brazil. There are widespread positive SST trends in the central-eastern Pacific, perhaps indicative of more frequent El Niño conditions, as has been noted in recent decades (Bayr et al., 2014) (Section 4.2.1). This could indicate that the modes could influence annual variability rather than drive the RH trends. These SST correlations are stronger in the late period. The MEI correlates positively with RH over the late period, although the correlation is significant only in a minority of the grid boxes (Section 4.3). Due to the similarity in SST-RH correlation patterns with two modes, in JJA, it could potentially be that the stronger influence of the oceans could be having an effect.

In the region's northwest and to the west over the north of South America, u10-RH correlate significantly and moderately negatively in the late period. In that area, as well as towards the east, across the SH tropical Atlantic, there are negative u10 trends. The negative u10 trend only occurs in the late period, while the u10-RH correlation directions are similar but weaker in the early compared to the late period. The v10-RH correlations correlate significantly and moderately negatively over the region in both periods and especially on the east coast with isolated positive v10 trends over the region. Taken together with the negative u10 trends this could indicate a strengthening of the southeast trades, although not as widespread as in other seasons. There are no significant si10-RH correlations in the region. In connection with the negative u10 and positive si10 trends, increased southeasterlies in the northern part of the region would decrease RH (compare Fig. 4.1). For the most part, the wind direction trends and their correlations with RH do not go in the same directions, suggesting the difference in short-term (correlation based on detrended time series) and long-term impacts (trends) of winds on RH in eastern Brazil in JJA. This difference makes the explanation of RH by wind changes complex.

There are negative SLP-RH correlations over large parts of the Pacific, Chile and Argentine with significantly negative SLP trends over the continent and negative v10 trends southeast of Argentina in JJA in the late period (Fig. 4.8). However, these trends might be too far away from the region to impact regional RH. The correlations with the five physical primary variables revealed that the negative RH (and q and precipitation) trend focussing the northern half of eastern Brazil in JJA might be caused by increased southeasterlies over that subregion. Due to El Niño-shaped SST trends in the eastern tropical Pacific, El Niño could have contributed to the RH decrease. Stronger correlation patterns could be obtained by considering the northern, central and southern subregions separately.

During MAM, the rainy season for the northeast of the region (Fig. S3), the correlation between RH and its constituent variables is significant and moderately negative for T-RH ($r = -0.6$, $p = 0.0$) and not significant for q-RH in the late period, which stands in contrast to the other seasons (Section 3.3.1.1). MAM is the only season in which T-q correlate positively in the late period indicating that q changes with T. Neither trends in q nor in T are significant. This differentiates MAM from the other seasons. The q-RH correlation in DJF, JJA and SON but not MAM might imply that q drive RH more in those seasons, whereas changes in T drive RH more in MAM.

SST-RH correlation patterns behave similarly in the early and late periods (Fig. 4.6). There are positive but insignificant SST-RH correlations around eastern Brazil in both the early and the late periods during MAM, with insignificant negative correlations to the north and the south (compare Fig. 4b from Nobre and Srukla, 1996). There are positive SST trends along the coast of the region in the early period and none in the late period.

In MAM, the negative u10/v10 and positive si10 trends in the northwest of the region in the late period suggest low RH with an increase in the northeasterly wind speed over the region's north where u10-RH and si10-RH correlate significantly positively (Fig. 4.6). Over the tropical NH Atlantic, v10-RH correlate significantly negatively. The positive v10 trends 10° north of the Atlantic equator in the north of the region suggest a reduction in the northeast trades to the region's north (Figs. 4.1 and 4.6). Less orographic and, instead, shallower onshore winds that spend less time over the ocean before reaching the land might be less saturated and might result in drier conditions over the region. However, due to a low data resolution, no evidence for this can be given. There are also regions of negative v10 trends 10° south of the Atlantic equator that indicate that southeasterly winds are weaker, contributing to drier conditions over the northern part of the region. Where northeasterlies over the ocean weaken, v10-T correlate strongly positively, i.e. increased T over land with decreased meridional winds over the tropical Atlantic. In the southeast of the region, v10-T (v10-RH) correlate negatively, indicating increased (decreased) regional T (RH) with reduced southerlies/increased northerlies. However, these detrended correlations could explain short-term changes in T and RH, but there are no significant T trends in the late period. Easterly winds over land are increased in the north; they might spread the less saturated air from the coast over a wider area. However, due to a low data resolution, no evidence for this can be given.

Moderately negative SLP-RH correlations in the southern tropical Atlantic, positive correlations over central Europe and the Azores, extending to the southwestern North Atlantic, and negative correlations over Iceland resemble an AO-like SLP pattern (Fig. 4.6) and suggest low (high) regional RH (T) with a weaker Icelandic Low, weaker Azores High and higher pressure than normal in the southern tropical Atlantic during a negative AO, with a more northerly ITCZ (Liu et al., 2020). The latter indicates a weakening in the pressure gradient between the SH tropics and extratropics and would weaken easterlies, matching the wind correlations and trends in the late period. In the early period, the SLP-RH correlation patterns behave similarly but are less pronounced. The SLP-T correlations are opposite to the SLP-RH correlations in all cases in the late period, i.e. positive SLP-T correlations over the southern Atlantic and Iceland and negative correlations over central Europe.

For MAM, the correlation and trend analysis of primary physical variables show that the eastern Brazil region, particularly the north, is exposed to prevailing easterlies with less extensive southeasterly and, particularly, northeasterly fetches over the SH tropical and extratropical Atlantic.

Summarising the previous correlation and trend analyses, depending on the seasons, different primary dynamical variables influence RH: in DJF, JJA and SON, q dominates the change in RH, in MAM, it is T. The type of influence is not always clear, as correlation and trend contradict each other in many cases. As significant correlations between wind speed and direction indicate, northeasterlies (in the north during DJF and MAM) and southeasterlies impact RH through their links to the ITCZ position. Since both northeast and southeast trade winds influence the region, it could benefit the analysis to divide the region into subregions and differentiate between the coastal sections and the interior land instead of working with regional eastern Brazil mean for RH, q and T.

With a few exceptions (SLP in DJF, SST in SON), regional and remote correlation patterns between the primary physical drivers and RH are similar in their direction in the early and the late period. The difference relates primarily to the correlations' strength and the trend in the primary physical variables. Trends in the late period which differ from the early period are, in particular, increased SST over the southern tropical Atlantic (increased in the early period) and faster winds with a more pronounced easterly (southeasterly) component winds towards the north region's coast in SON (DJF), decreased SLP over the southwestern Atlantic in DJF and winds with an increased easterly component over the northern part over land (and the SH tropical ocean) in MAM (JJA).

In DJF (Figs. 4.4 and 4.5) and JJA (Figs. 4.8 and 4.9), less so in SON (Figs. 4.10 and 4.11), RH-correlations with the primary physical variables resemble q-correlations. This matches the seasonal q-RH correlations. Therefore, it seems that in DJF, JJA and SON, q (short-term via correlations and long term via the negative trend in q) would drive RH via dynamical drivers. In MAM, mainly, u10/si10-RH correlations are similar, indicating that T drives RH in MAM via the speed of winds with easterly components, which is the case in the northwestern part of the region (increased easterlies; Figs. 4.6 and 4.7). This significant trend in easterlies cannot be linked to a regional T trend as the latter is insignificant in MAM in the late period.

Correlations between RH and primary physical drivers are similar to precipitation correlations in all seasons, indicating a strong link between precipitation and RH during the rainy seasons with the most substantial rainfall in DJF (Figs. 4.3 and 4.4).

For the 2012 and 2015 droughts, as RH troughs particularly in DJF, MAM and SON (Fig. 3.10), Marengo et al. (2017) found increased evaporation from reservoirs and lakes as a result of an ITCZ position shift (Chapter 5). Nobre et al. (2016) say that the reservoirs in the region's south had reached a low of only 5% of their storage by January 2015. Costa et al. (2018) confirm the impact of Atlantic and Pacific SST and rainfall on basins in eastern Northeast Brazil. Nobre et al. (2016) explain the droughts during 2014–2015 through a long-lasting mid-troposphere blocking high over southeastern Brazil during DJF, i.e. high pressure blocks weather systems coming in, which is generally linked to subsidence which inhibits cloud formation and precipitation which act towards drought. The correlation analysis in this study works with seasons, so their temporal resolution is not high enough to discover sub-seasonal periods of time. Gateau-Rey et al. (2018) confirm the influence of El Niño on the drought in 2015–2016. During El Niño events, north (south) tropical Atlantic SSTs tend to be higher (lower) than average and, thus, negatively (positively) impact precipitation over eastern Brazil (Uvo et al., 1998).

For February, Uvo et al. (1998), and for MAM, Nobre and Srukla (1996) found positive correlations between the south equatorial Atlantic SST and precipitation over the region due to the migration of the ITCZ towards higher (lower) SST in the north (south), fitting with the SST-RH correlations in Fig. 4.4 during the late period. Utida et al. (2019) also found increased precipitation rates with higher SST over the SH tropical Atlantic and weaker southeast trades matching the positive u10-RH correlation, in DJF and SON over northeastern Brazil. This fits the positive SST-RH correlations and the negative SST trend in the south equatorial Atlantic in DJF in the late period. Kouadio et al. (2012) confirm the positive south equatorial Atlantic SST-precipitation correlation for heavy rainfall episodes in eastern Northeast Brazil through accelerated easterly trade winds and excess moisture transported due to increased convection over the Atlantic. Their findings for April-May (last two-thirds of MAM) match the moderate but insignificant SST-RH correlation pattern found in Fig. 4.6: negative SST-precipitation correlation in the north tropical Atlantic, positive SST-precipitation correlation in the south tropical Atlantic, in agreement with Nobre and Srukla (1996). Amorim et al. (2014) extend the correlations from April to June. However, there are no SST trends in MAM in the late period that could explain the RH increase. Uvo et al. (1998) and Coelho et al. (2002) further describe the relationship between regional precipitation and SST in the tropical Pacific and found (in March, Uvo et al., 1998) a negative SST-precipitation correlation matching findings in this study of negative SST-precipitation in the central equatorial Pacific and a positive SST trend in the eastern tropical Pacific (El Niño) in the late period (not shown for this season). Uvo et al. (1998) explain that the tropical Pacific and south tropical Atlantic SST in April and May only influence precipitation over a small region, northeastern Brazil if they do not occur in phase.

In MAM in the late period, there is a positive trend in tropical east Pacific SSTs but SSTs in this region show only weak correlations with RH. SST-RH correlation patterns reminiscent of ENSO were found in all seasons with stronger correlations in the late period, particularly in JJA with significantly positive SST trends over the eastern Pacific in all seasons. Costa et al. (2018) give the northern tropical Atlantic conditions a more decisive long-term influence on precipitation in eastern Northeast Brazil and emphasise that only extreme ENSO events influence rainy seasons. With a warmer tropical North Atlantic Ocean, the ITCZ moves northward, and the original ITCZ further north receives less precipitation (Marengo et al., 2017; Pereira et al., 2018). They also bring the PDO, and Pereira et al. (2018), the North Atlantic Oscillation (NAO)/AO come into play, which has more complex influences. Liu et al. (2018) explain that higher pressure in the Azores/southern North Atlantic (positive NAO/AO) pushes the ITCZ further south. This fits with the correlations, as this would mean ITCZ more over the region and increased RH. AO-like SST-RH correlation patterns are visible in MAM. Independent of the season, the AO, the AMO and the ENSO were found to have the strongest impact on RH in eastern Brazil (see Section 4.2.2) during the late period.

The north/south equatorial Atlantic SST-dipole influence on interannual variability and decadal RH variability in eastern Brazil was found, linked to some extent to ENSO-SST variability in the eastern tropical Pacific, particularly in DJF and SON. The negative

Atlantic SST trends adjacent to the northeastern coast in DJF and SON seem to be a late-period feature in dynamical drivers linked to shifts in the ITCZ position. The decreased RH in eastern Brazil might not be due to a trend in modes of variability (ENSO, and the AMO and AO to a lesser extent) but to several strong events. Suppose the rainy season in DJF and MAM have less rain. In that case, this lack of water could have implications for the dry season in JJA (Nobre & Srukla, 1996) and might even cause land cover changes introducing land-surface feedback decreasing RH further. When the groundwater supplies cannot be replenished, there is a lack of water during dry periods. In consequence, drying seasons could become abnormally dry. However, it is beyond the scope of this thesis to explore this hypothesis.

While Marengo et al. (2017) found the ENSO explaining only part of the Northeast's rainfall variability, Costa et al. (2016) emphasise for the whole region of eastern Brazil that mainly tropical SST in the Atlantic are linked to regional drought with the ENSO amplifying or inhibiting droughts. According to Pereira et al. (2018), extreme, dry events over the region have increased in frequency since the 1990s. Decreased RH over eastern Brazil might not be a trend as such or a trend in primary physical variables but a result of several events. The lack of HadISDH data over northeastern Brazil makes working with regionally averaged RH, q and T less reliable and ignores possible heterogeneity of the variables within the region. ERA-Interim could be a remedy for this spatial lack of data.

4.1.3 Tibet

The Tibet region shows very significant ($p < 0.05$) negative RH trends in JJA (-1.73 %rh decade^{-1}) and SON (-2.04 %rh decade^{-1}; Section 3.3.1.2). In JJA, the drying trend is most strongly pronounced in the north and northwest of the region. In SON, the drying trend is strongest in the northwest at altitudes higher than 4000 m on the Tibetan Plateau (Figs. 1.2 and 3.3). The region's northern half lies on the Tibetan Plateau; to the south, it extends to the Bay of Bengal and the Andaman Sea, covering countries Bangladesh, Bhutan, Nepal and Myanmar (Fig. 1.2; Section 3.3.1.2).

The regional topography strongly shapes the dynamics in the Tibet region: the Himalayan mountain range crosses in the two central-western grid boxes of the region. It blocks southerly air currents like the summer monsoon (Fig. S4). The South Asian summer monsoon is a strong influence on regional humidity in JJA. The contribution of the East Asia summer monsoon on Tibet was to be found weaker (Yang et al., 2014). Westerlies are found north of the region while these split in northern, southern and Tibetan Plateau westerlies in the winter (Yang et al., 2014). Northwards, the Tibetan Plateau adjoins the mountain range. The Tibetan plateau influences the monsoon cycle through its effect on the jet stream (see Section 11.2.2 in O'Hare et al., 2014). The elevated plain makes up the northern half of the region so that the region includes most but not all of the Plateau (Fig. 1.2). In this northern half, in particular, there are many lakes, such as Qinghai Lake, visible on the SST map (Fig. S4). Depending on the wind, these lakes can be decisive for atmospheric moisture via evaporation, particularly in SON (Li et al., 2016).

Most of the moisture supply in the region comes from the southwest monsoon (Galvin, 2008) in the seasons under consideration, with the westerlies being a stronger influence in the north of the region in winter. In JJA, strong southwest monsoon winds from the Arabian Sea and the Bay of Bengal influence the southern part of the region, linked to low pressure over India, which the Plateau strengthens to the north by providing a high altitude heat source (Fig. S4 ; O'Hare et al., 2014; Shenoi, 2002). In SON, onshore winds are much weakened as the summer monsoon weakens (Huber & Goldner, 2012; Zhang et al., 2015). Southwest winds over the northwest part of the region are increased in SON, with lower pressure over China (Fig. S4). As the RH trend is strongest in the northern part of the region in JJA, the Tibetan Plateau, and in SON in the west, westerlies are expected to have an impact on the interannual RH variability. In SON in the late period, a negative SLP trend in the region between eastern Mongolia and eastern Tibet resulted in a trend of southwesterly flow out of northwestern Tibet (Fig. 4.1) among negative v10-RH correlations (Fig. 4.14) and could have led to a sub-regional RH decrease due to enhanced dry desert winds in SON (Table 4.4, beginning of Section 4.1).

Considering now the moisture-temperature correlations: only in SON in the late period but not in JJA, the q-RH correlation is significant and moderately positive (r = 0.54, p = 0.02; T-RH correlations are insignificant in both seasons (Section 3.3.1.2). This suggests that moisture changes are driving SON RH changes rather than temperature. However, T very significant increases in both seasons in the late period, whereas there is no corresponding significant change in q, which means that T might be driving RH over the long term (Figs. S1 and S2). Negative, but mainly insignificant ($p > 0.1$) precipitation trends were found in the west and centre of the region over the southeastern Tibetan Plateau in JJA (Fig. 4.2) and focussing on the west in SON (not shown). A relationship between precipitation and RH is not expected without time lags as the precipitation-RH correlations are insignificant for the grid boxes where precipitation decreased (Fig. 4.2).

Considering now the primary variable correlations: in JJA in the late period, SST-RH (SST-T) correlate negatively (positively) over the southern Bay of Bengal towards the South China Sea and over the northeastern and central tropical Pacific (Fig. 4.12), i.e. increased SST in those regions is associated with lower regional mean RH (for the southeast of the region, Yang et al., 2012). Anomalously high SST in the boreal summer would weaken the temperature gradient between the land and the ocean, thus, decrease the pressure gradient, weakening the summer monsoon which could result in less moisture supply to the region. Kumar et al. (2020) found a declining trend in the Indian monsoon rainfall over most of India over the past three decades (but an enhancement over parts of Northwest India through a pronunciation in the meridional wind component of low-level jet). They associated the reduction in summer rainfall with a decrease in the southerly component of meridional winds over the Bay of Bengal and also with a reduction in

RH over the Bay. These reductions of both RH and winds might account for some of the decrease in RH over land. However, there are neither significant SST-q correlations nor significant SST trends over the Bay of Bengal over the late period (2000–2017; Fig. 4.13), which would have been expected if SST changes would impact the monsoonal rainfall on the region. Kulkarni (2012) suggests a weakening of Indian summer monsoon rainfall with the warming over the Indian country, which is the case in the late period (see Fig. S6). SLP over northwestern India and Tibetan RH/q correlate negatively in JJA, i.e. decreasing RH/q with increased SLP (Figs. 4.12 and 4.13). The positive SLP trend in the late period indicates a weakening of the low-pressure, thus, a weakening in onshore Indian monsoon winds from the Arabian Sea with reduced moisture supply towards the western Tibetan region (Fig. 4.12).

Considering Myanmar (in the southeast of the region), Sein et al. (2021) found a decrease in monsoon season (May–October; part of the JJA and SON season) precipitation since 2000, i.e. a weakening of the summer monsoon, and a positive precipitation trend before 2000 (Myanmar Average Precipitation. Trading Economics. Retrieved January 17, 2022, from https://tradingeconomics.com/myanmar/precipitation). The negative precipitation trend over Myanmar in MAM (Fig. 4.12) matches findings in this study of sub-regional precipitation decrease in the late period in MAM over Myanmar and northern Laos, and over the southern Tibetan Plateau in JJA. In particular, in JJA, during the rainy season, this negative trend is expected to have a strong impact on regional water resources, possibly leading to changes in moisture also after the rainy season, as precipitation and RH do not correlate without time lags in the region (Section 4.1.1). Sein et al. (2021) found the decrease in precipitation based on a negative correlation with the PDO and a positive association with the AMO. In both the early and the late period, aspects of the AMO and the PDO can be seen in the SST-RH correlation patterns (Fig. 4.12), with more significant positive SST correlations in the North Atlantic and a larger region of significant negative correlations in the centre in the Pacific (fitting with the direction of the relationship of Sein et al., 2021) in the late period, potentially indicating a greater role of the PDO in the late period. However, in the late period, the PDO is mainly found in a cold phase and the AMO in a warm phase (see Section 4.2.1) which would lead to increased precipitation (Sein et al., 2021), and according to the SST-RH correlations would lead to reduced RH. However, as described in the first section of this Chapter, in Tibet, the RH decrease is found in particular outside of Myanmar in the north of the region, suggesting that the precipitation-PDO-AMO linkages over Myanmar are less important for the change in RH.

There are only a few grid boxes in the abovementioned regions with significant JJA SST trends in the late period (Fig. 4.12). However, instead of a significant trend already one or more single year events of positive SST anomalies in the abovementioned regions might be enough to lead to significant SST-RH correlations and indicate a weaker monsoon in the region then that could plausibly lead to a drying trend in RH. These negative SST-RH correlations over the eastern Indian Ocean, which are closest to the region, are present only in the late period, whereas Pacific correlations are present but weakened in the early period. The correlation pattern partially resembles the positive SST-ENSO and SST-IOD pattern in both seasons (although for the latter there are no significant positive SST correlations in the western Indian Ocean). Positive ENSO (El Niño) and positive IOD, i.e. higher eastern Indian Ocean SST, go with decreased precipitation and increased dryness over Tibet, according to Bothe et al. (2009) and Wang et al. (2008a). Also, Sen Roy and Sen Roy (2011) found a negative precipitation-ENSO relationship over Myanmar, i.e. less rain during El Niño events. Niu et al. (2020) link the regional RH decrease in the late period (2003–2015) to a weakening of the eastern Asian monsoon due to a strongly pronounced high-pressure pattern over Eurasia centred on eastern Europe, which may fit with the negative SLP-RH correlation over Europe (Fig. 4.12) and blocking of winds from the Pacific Ocean by increased northeasterlies. A small region of negative si10 trends in the southwestern tropical Pacific Ocean might be not big enough to be linked to the strength of the East Asian monsoon during the late period (Fig. 4.12); Douville et al. (2021) state there has been a weakening of the East Asian Monsoon, but since the 1970s. However, this study neither found SLP-RH correlations nor SLP trends over the Eurasian continent (Figs. 4.12–4.15).

Significant JJA negative (positive) u10-RH and v10-RH correlations over the NH high (mid) latitudes, in particular over northern Europe (central Europe) in both the early and the late period and positive (negative) u10-T and v10-T correlations over the NH Atlantic high (mid) latitudes indicate an impact of Atlantic westerlies on regional RH that did not change much over the decades (Fig. 4.12). The stronger, negative SLP-RH correlation over northern, central and eastern Europe follows the findings of Bothe et al. (2009) suggesting that drought over Tibet is associated with high pressure over northern Europe. The North Atlantic storm track has a more south-west to northeast orientation under these circumstances (which some authors find may be associated with a positive ENSO; Bothe et al., 2009). This results in a Rossby wave train which modulates the subtropical westerly jet stream (SWJ) and the tropical easterly upper jet stream (TEJ). With the SWJ playing a more crucial role, a weakening (strengthening) and southward (northward) shift of the TEJ (SWJ) due to increased west-tropical Pacific SST was found to raise T over the Tibetan Plateau (Wang et al., 2012). The correlation is stronger and more widespread in the late period with a positive SST trend in the tropical Pacific (Fig. 4.12).

Negative u10-RH correlations in the tropical Pacific are stronger pronounced in the late period while positive u10-RH correlations in the Indian Ocean are stronger pronounced in the early period (Fig. 4.12). Also, v10-RH correlations in the Indian Ocean are not significant in the late period, whereas they are significantly positive in the early period, i.e. decreased RH with decreased southerly flow. Bothe et al. (2009)'s findings match the positive v10-RH correlation in the Bay of Bengal about this region being a moisture source for the Plateau. Gao and Yang (2009)) relate a weakening of the Bay of Bengal moisture transport to eastern China to the high tropospheric temperatures over the Tibetan Plateau in winter 2008–2009. They justify the warming with a reduction of snow over the plateau. The positive v10 trend in the late period over Myanmar would indicate enhanced southerlies which would not match reduced moisture flow into the region. However, the late-period positive v10-RH correlations do not reach up into the region, compared to the early period, indicating that the correlation is temporally stable but the spatial extent has decreased in the late period. Comparing the early period, Yang et al. (2014)) found for since the 1980s wind stilling due to warming differences in the high- and low-latitudes in Asia, decreased sunshine duration, increased precipitation, surface soil water content, less surface sensible heating and, thus, a lower Bowen-ratio and more evaporation when RH showed no (JJA) or a slightly increasing trend (SON). In the northwestern grid box of the region and the north towards the Mongolian Gobi desert, si10-RH and si10-q correlate negatively, i.e. increased wind speed with decreasing RH (Figs. 4.12 and 4.13). While with sufficient water availability, increased winds may lead to enhanced evaporation and moisture supply, the negative correlation suggests winds bringing dry air from the Gobi desert into the region (Ma et al., 2009). However, there is no significant correlation between the RH and the u10 or v10 indicating directional transport. While the wind speed might drive RH interannual variability, the positive v10 trends indicate stronger southerlies out of the region matching the insignificant southwesterly trend in Fig. 4.1.

In summary, in JJA, different atmospheric circulations may have been influencing the Tibet region. In particular, in the late period, links to the ENSO and the IOD could be found: during El Niño, such as in 2009–2010, SST in the central Pacific SSTs were increased, leading to weaker monsoons, i.e. increased SST over the Bay of Bengal (positive IOD) creating low-pressure and increased SLP over northwestern India resulted in a reduced land-ocean SLP gradient and a weakening in the Indian monsoon, thus, might have decreased precipitation, q and RH.

While RH correlations with winds and SLP over the northeastern Atlantic and Europe are quite stable between the early and late period, the ENSO-like SST correlation pattern were found to be more significant in the late period. The analysis of correlations between modes of variability and regional mean RH (Sections 4.2 and 4.3) confirmed significant links between the IPO and the MEI in the late period in SON but not in the full period (1979–2017). The PDO-RH correlation in both seasons were weak in the late period. The lack of widespread, significant trends in the primary physical variable in the late period does not permit further interpretations at this stage.

Considering relationships in SON, the boreal autumn, which follows the monsoon season (JJA), there are no significant links to westerlies over the Atlantic and Europe (Fig. 4.14). In SON in the late period, SST-RH correlates negatively south the Arabian Sea and the southern part of the Bay of Bengal with positive SST trends in some of these grid boxes. There are also areas of significant positive SST-RH correlations in the western tropical and mid-latitudinal Pacific, and negative correlations across the central and eastern tropical Pacific Ocean, suggesting a linkage to the ENSO/PDO/IPO, i.e. decreased RH with El Niño (Fig. 4.14). Widespread significant SST-RH correlations in these regions are only found in the late period, but not during the early period. The

SST-RH correlations are similar to the SST-q pattern in the late period (Fig. 4.15), which indicates that a change in SST impacts RH via a change in q.

SLP-RH and SLP-q correlation patterns behave similarly to the SST-RH/q correlation patterns. SLP-RH/q correlates positively with over large parts of the tropical Pacific Ocean, extending into SH mid-latitudes in the late period (Figs. 4.14 and 4.15). Negative SLP-RH/q patterns are found over the tropical Atlantic Ocean. These strong correlation patterns are not found in the early period. Figs. 4.14 and 4.15 indicate that the relationship between SLP and RH is through q, as the late period SLP-q correlation maps strongly resemble the SLP-RH maps. After these correlation patterns, decreased SLP over the tropical and east SH Pacific and the southwestern Atlantic and increased SLP over the tropical Atlantic would result in anomalously low q and RH over Tibet. The correlation pattern in the Pacific resembles the ENSO-SLP pattern and indicates a reduction of regional q and RH during El Niño events. This matches the Pacific SST-RH correlations and the above-mentioned findings by Bothe et al. (2009) and Wang et al. (2008b).

Negative u10-RH correlations within the region in the early and late period and negative v10-RH correlations in the northwestern corner of the region only in the late period, where southwesterly winds are strongest (Fig. 4.1), indicate decreasing RH with increased westerly winds (u10) over the region and increased southwesterlies (u10 and v10) in the northern region in SON. Both u10 and v10 show positive trends in the late period, whereas there is a negative u10 trend in the early period, i.e. decreased westerlies. These correlations and trends match the findings at the beginning of Section 4.1 of increased southerly flow out of northwestern Tibet with an inversed, negative u10 trend in the early period (Fig. 4.1). With the increased v10 trend in the north, a regional positive T trend (Fig. 3.11) concurs in the late period. In the northwest of the region, where the negative RH trend is in particular strong, the wind speed (si10) correlates negatively (positively) with RH (T) explaining the RH decrease in this subregion by faster SW winds and, thus, increasing T. The positive v10-RH correlations in the early, late and whole periods and the positive v10-q correlation in the late period over the Arabian Sea indicate increased RH with stronger southerly flow northeastwards. The v10 trend is positive in the early and full period in the Arabian Sea but not significant in the late period, indicating that there is less moisture advection in the late period. The lack of increased westerly flow over the Arabian sea could add to the decrease in regional q and, thus, RH.

A key finding is that the ENSO relationship is not present in the early period but becomes prominent in the late period. Therefore, it is not a trend but a change in modes that influence the region (enhanced ENSO influence). In JJA, teleconnections over Europe related to a shift in the westerlies, which according to the literature (Bothe et al., 2009) would then influence Rossby waves, modulating flow around the Tibetan Plateau. Regarding the drought in 2009–2010, Yang et al. (2012) refer in particular to the combination of negative AO and El Niño Modoki events (shift of the main pole from the eastern to the central Pacific) during autumn and winter: cyclonic anomalies over the Arabian Sea and anticyclonic anomalies over Tibet decrease the moisture transport into the region and bring in cold, dry air instead. The correlation of these patterns is present in both periods but more pronounced in the late period. El Niño Modoki events have increased over the last couple of decades (Gulev et al., 2021). In particular, in JJA, the ENSO link with SST and SLP as a large-scale driver is linked to regional interannual RH variability. In particular, in SON, the strengthening of the southwesterlies in the north of the region, which may bring warmer, dry air into the region, are evidence of regional-scale processes affecting RH. Sub-regional scale relationships are complex to explain but add evidence to local-scale changes in RH that could combine to lead to regional-scale RH changes via local decreases in q and more widespread T enhancements in the late period. In the late period, increased temperatures in all seasons are suggested to act as the main driver for RH over Tibet. The RH decrease via the T increase may be supported by dynamical drivers, many of which operate through teleconnections and maybe with time lags to the regional precipitation, which has decreased over parts of the regions in MAM and JJA, and less in SON, and RH and are therefore more complex to understand. The RH decrease in JJA might strongly impact the RH decrease in SON, supposing the ground and vegetation prolong the 'memory' of dryness in the soil moisture and reduced water, which would account further for the following years after an intense drying event.

4.1.4 The Caspian Sea region

The region of the Caspian Sea shows a very significant ($p < 0.05$) negative RH trend in JJA (-4.57 %rh decade^{-1}; Section 3.3.1.3) over the late period. The trend is particularly pronounced over the southern three-quarters of the region.

In this study, the Caspian Sea region is defined as covering (start latitude: 40° N, start longitude: 45° E, end latitude: 60° N, end latitude 60° E; Section 3.3.1.3), which includes the northern part of the Caspian Sea and a region further north covering the Caspian Sea catchment area (compare with Fig. 1 in Chen et al., 2017). The Caspian Sea region is mainly continental but obviously influenced by moisture flow from the Caspian Sea to the south and the Black Sea and the Sea of Azov to the west (Fig. 1.2). The surface temperatures of the Caspian Sea and surrounding areas have a large temperature difference between the seasons and are, as would be expected, higher in JJA (20-25 °C, Figs. S2 and S4). It should be noted that lake surface temperatures in ERA-Interim are prescribed from external data sources (Minallah & Steiner, 2021). The Caspian Sea lies on the western edge of the Eurasian high in DJF and to the north of low pressure over the Saudi Arabian Peninsula and India in JJA (Fig. S4). Hence in the region's east and southeast, the main wind direction is northerly towards this low pressure (the monsoon trough).

In terms of the relationship of q and T with RH, both q and T correlate moderately to strongly with RH in JJA. The negative T-RH correlation in the late period ($r = -0.7$,

$p = 0.0$) is a little stronger than the positive q-RH correlation in this period ($r = 0.6$, $p = 0.01$; Section 3.12). However, q decreases significantly, and T increases significantly in JJA in the late period. This suggests that both temperature and moisture changes are important for driving changes in RH both on shorter and longer time scales. There are no significant T-q correlations in the late period (Fig. 3.5).

In JJA, RH is strongly negatively correlated to surface temperatures within and also to the west and the south of the region, i.e. reduced RH with increased temperatures (Figs. 3.12 and S6). This initially seems counterintuitive for the region directly over and surrounding the Caspian Sea, as warmer SST implies more evaporation and moisture into the region, however, over the wider region would fit with the Clausius Clapeyron relationship. There are strong (and significant) warming trends in the southern half of the region (including over the Caspian Sea) and to the west and south of the region.

In this region, a reduction in the Caspian Sea lake level has been observed since the mid-1990s (Chen et al., 2017). These authors used a model to explore the precipitation-evaporation-runoff balance over the Caspian Sea. They noted positive sea level trends in the early period (1979–1995) and negative trends in the late period (1996–2015). They and Nandini-Weiss et al. (2020) found that the recent negative sea level trend was due to increased evaporation, which they link to temperature increases. Increased evaporation because of increased SST should increase RH unless air T increases more than SST. Both land and lake surface temperatures strongly positively correlate with RH (Fig. 4.16), and T over land and SST over the Caspian Sea have increased over this period as mentioned above. Neither air temperatures over land nor lake surface temperatures over the region are correlated with regional mean q, so that increased evaporation due to a rise in temperature does not apparently lead to increasing q (Fig. 4.17). However, the correlation maps are based on the regional averaged q and comprises the entire region, so both q over and close to the Caspian Sea and over land north of the Caspian Sea. In this context, Arpe et al. (2020) suggest increasing winds causing enhanced evaporation and, therefore, a Caspian Sea level decrease in the late period (after 1995). These authors also suggest that precipitation resulting from the change in winds would take place out of the region towards the east. There is a negative but insignificant precipitation trend in the late period (Section 4.1.1 and Fig. S10). Fig. 4.16 does show positive correlations between u10-RH and u10-q over the southern part of the region, indicating decreased RH and q with decreased westerly flow, while the negative u10-T correlations (Fig 4.17) indicate increasing T with decreased westerlies in the northwest of the Caspian Sea, and increased southwestward winds over Sea in the southwest of the region (positive v10-T correlations in two grid boxes), agreeing with Arpe et al. (2020)'s suggestion. Arpe et al. (2020) further point out the hot and dry airflow from the Iranian highlands towards the Caspian Sea coast, which matched the positive v10 trend in the southwest of the region. Due to the low resolution, the positive trend in wind speed over the open water body found by Arpe et al. (2020) in ERA-interim is not clearly visible in Fig. 4.16. Wind v10-RH correlate negatively in the south of the region, over the Caspian water body, i.e. decreasing RH with stronger southerly winds which fit with Arpe et al. (2020) (Figs. 4.1

and 4.16). To the north of the region, on the coastline with the Barents Sea, the u10-T (u10-RH and u10-q) correlations are positive (negative) and favour warmer temperatures (lower humidity) with stronger westerly winds. The surface temperature-RH and u and v wind-RH correlations are also visible over the early and the full period and have slightly increased in intensity in the late period. These results indicate that SSTs and wind trends may be related to the RH trend. In the northern part of the Caspian Sea region, SLP-RH and SLP-q correlations are negative and extend eastwards into Asia, i.e. decreasing RH with increased SLP. Positive SLP-RH and SLP-q correlation clusters are found over the Black Sea and the Russian Arctic coast, i.e. decreasing RH with decreasing SLP. The correlations match the positive correlation between the winds and RH. T shows inverted correlations. However, no SLP trends are evident in JJA in the regions of significant correlations. Whereas regional RH correlations with regional-scale SST and winds are similar in the early and late periods, there have been global, quite significant changes in SLP-RH correlations over the past between the early and the late periods (Fig. 4.16).

The RH was particularly low during the Russian heatwave in 2010 (Fig. 3.12). Arpe et al. (2012) and Arpe and Leroy (2007) describe a drop in precipitation over the Volga river basin and large discharge in the basin, which they suggest results in less water supply into the Caspian Sea and increased evaporation over the Caspian Sea. Indeed, there is a negative precipitation trend in the late period with troughs in both 2010 and 1975 (not shown) with extremely negative RH and q anomalies in the early period (Fig. 3.12), when RH dropped strongest over the past 45 years to 2006 (Section 4.1.1; Sidorenkov and Shveikina, 2021). Arpe et al. (2012) mention ENSO, particularly La Niña, associated with this heatwave. Previous studies have found some links between the ENSO, winds, temperature and precipitation and the Caspian Sea level and with the NAO, although the mechanisms for these links are unclear, e.g. Arpe et al. (2020), Lahijani et al. (2010) and Molavi-Arabshahi et al. (2016). As a result of correlations with interannual variability and not about an individual event and its potential influence on the trend, neither ENSO- nor strong NAO-like patterns are found in Figs. 4.16 and 4.16, not indicating a strong influence of these modes of variability. Neither accompanied by strong ENSO years and, thus, indicating that other oscillations than ENSO impact RH around the Caspian Sea, were the negative RH anomalies around 1975–1977 and the positive anomalies in 1994 that resulted in a positive RH trend in the early period (Fig 3.12).

The RH- and q-correlations with the primary physical variables (Figs. 4.16 and 4.17) behave very similarly to the precipitation correlations (Fig. S10), and precipitation-RH are strongly positively correlated (Section 4.1.1). This indicates that decreasing precipitation in JJA over the Caspian Sea in the late period may be – as for RH and q – related to the positive trend in SSTs of the Caspian and the Black Sea. A second possible driver could be the weakening in westerlies over eastern Europe, reducing precipitation. However, the negative precipitation trend in the late period is not significant.

The most apparent reason for decreasing RH was found to be the strong land warming in the boreal summer (JJA). Enhanced SST and land T enhance evaporation resulting in a decrease in the Caspian Sea level, with moisture being advected away, thus reducing RH over the Caspian Sea area in the late period. The warming happened already in the early period and expanded during the late period with a stronger negative temperature-RH correlation. There may be some contribution from decreased inflow from the Volga river linked to the 2010 drought (Arpe et al., 2012). Also, the relationship between zonal winds-RH seems relatively stable: the u10-RH correlation patterns were present in both the early and the late period with stronger patterns in the south of the region and a local negative u10 trend in the late period. The increase in RH(q) and RH(T) regression coefficients (Section 3.3.1.4 and Table 3.5) represents the increased sensitivity of RH to q and T changes in the late period.

Single strong events such as 1975–1977 (low RH), 1994 (high RH) and 2010 (low RH linked to the ENSO; Fig. 3.12) also may have an influence on trends over the longer period. In addition to single-event dynamical drivers, the dominant driving force is the thermodynamic drivers: the land (mainly the northern part of the region) is warmer, and moisture supply from influxes and the Caspian Sea itself (southern part of the region) is insufficient to keep RH constant via evaporation. As the Caspian Sea level decreases, the land area increases and the water area decreases (a negative trend in GRACE terrestrial water storage in Section 5.2.2; Rodell et al., 2018). This land cover change might increase the effect of the thermodynamic drivers, i.e. faster warming over more land than over the shrinking water body, thus, deviations from the Clausius-Clapeyron theory and decreased RH.

4.1.5 California

California shows no significant seasonal RH Trends but a very significant ($p < 0.05$) negative annual RH trend in the late period (-1.87 %rh decade^{-1}, $p = 0.0$; Section 3.3.1.4). The trends are especially pronounced along the coast, increasing towards the south, around the state of California (McKinnon et al., 2021).

The region is located on the eastern edge of the Pacific subtropical high. The mid-latitude westerlies influence the northern part of the region. The SST off of the coast of California shows a positive gradient from north to south, with a region of cooler temperatures off of the coast, linked to upwelling associated with northerly winds around the eastern flank of the high, and flow in the southward flowing cold California current (Fig. S4). The North Pacific current meets the northern coast of the region and results in the warm Alaska current towards the north and the California current towards the south.

The boreal winter (DJF) is the season with the strongest precipitation, in particular in the north of the region. In this season, the correlations of primary physical variables and RH (not shown) closely resemble the annual correlations, so a link between the impact of dynamical drivers on precipitation and RH might be possible. However, there is no significant precipitation-RH correlation in DJF and no significant precipitation trend in the late period (Fig. 4.2). During the boreal summer, the southwest of the region and of the entire USA is a lot drier than the eastern part (Fig. S3).

Given the coastal nature of this region, exposed to prevailing westerlies with extensive fetch over the Pacific Ocean, changes in RH might be expected to be largely driven by the thermodynamic factors of faster warming over land compared to the ocean. However, it is also plausible that other factors linked to dynamical and terrestrial drivers are contributing, hence the inclusion of the Californian region into this Chapter.
The correlations between the primary physical drivers with q and T (Fig. 4.19) look alike, matching the positive T-q correlations (Section 3.3.1.4). They do less resemble the RH-correlations (Fig.4.18). Therefore, dynamical drivers might impact q and T equally to some extent, and the dynamical impact on RH cannot be specified regarding dynamical changes in q and T.

Regarding correlations, q-RH correlates moderately positively in the late period ($r = 0.63$, $p = 0.0$) while T-RH do not correlate significantly ($r = -0.0$, $p = 0.98$; Chapter 3.3.1.4). This suggests that changes in RH are largely moisture driven; although the correlation is not classified as strong, it is significant. The annual regional T trend is significant and positive, the trend in q is not significant in this period (Figs. S5 and S6).

There has been a positive trend in annual SST along the region's coast in the late period, which is part of a larger region of positive SST trends extending to the south and west (Fig. 4.18). SST in a large region off of the west coast of the US correlates strongly positively with both q and T (Fig. 4.19). Correlations of SST with RH are weakly negative but lacking significance. This suggests that changes in SST alone in this region are not sufficient to drive the trends in RH.

In the late period, the strongly positive SST-RH correlation over the north-equatorial Atlantic is striking. Winds in this region (both u10 and v10) also have strong significant positive correlations with RH. However, neither SST nor winds show significant, unambiguous trends that could explain the regional RH decrease over California.

In the south of the region, u10-RH correlations are positive, i.e. decreased RH with decreased westerly onshore winds (Fig. 4.18), whereas correlations are negative in the northernmost part of the region. Both of these regions of correlations are part of larger meridional bands of correlations spreading eastwards across the US. The v10-RH correlations are weakly positive over the region, associating increased northerly/decreased southerly flow with lower RH. In the case of winds, correlations with q are largely similar, especially the negative u10-q correlations in the north of the region, and to a lesser extent with T. None of these are associated with any notable late period trends, however. So, while wind direction impacts RH, it is not clear how this could have driven a 20-year trend over the late period.

Moderate to strong negative correlations with the SLP are widespread across the region, and further south and east, covering a large area of the American continents and continuing over the tropical and mid-North Atlantic. This combines with significant negative trends over northern South America extending west into the eastern Pacific around Central America. The SLP-RH correlation becomes moderately positive over Iceland with no further SLP trends. The SLP might inversely match the inverse AO (Fig. 4.18), i.e. decreased RH with increased (decreased) SLP over California and the Atlantic NH mid-latitudes (Atlantic NH high latitudes), thus an increased pressure gradient and stronger westerlies over the Atlantic during a positive AO phase. The AO-RH correlation in the late period explored in Sections 4.2 and 4.3 is weak, and there is no significant trend in the AO. The tropical SST-RH correlation pattern in the late period resembles the Atlantic Multidecadal Oscillation (AMO), i.e. decreased RH with decreased tropical Atlantic SST during a negative AMO phase (Fig. 4.18). However, SSTs in the northern Atlantic correlate less strongly with RH, and the AMO is found rather in a positive phase in the late period so that the latter hypothesis might be denied. These two correlation patterns, SLP-RH and SST-RH over the Atlantic Ocean, do not show any SLP or SST trends in the late period. In the early period, the patterns are much weaker (Fig. 4.18). Sutton and Hodson (2005) found that positive Atlantic Ocean SST anomalies during the warm phase AMO were associated with decreased precipitation and western US droughts during the boreal summer (JJA), i.e. a negative AMO-precipitation correlation, which is the other way around to the AMO-like SST-RH pattern in Fig. 4.18. However, their results match the trend towards a positive AMO phase in the late period (Section 4.2.1). Kushnir et al. (2010) explored the influence of SSTs in the tropical Atlantic on North American precipitation and found that reduced precipitation over North America is related to reduced high pressure over the North Atlantic, due to positive SST anomalies in the tropical Atlantic and a weakening of the North Atlantic subtropical anticyclone. As for the results of Sutton and Hodson (2005) these results are somewhat surprisingly the other way round to the correlations in Fig. 4.18 for both SST and SLP, which show positive SST-RH correlations and negative SLP-RH correlations in the northern tropical Atlantic. Kushnir et al. (2010) emphasise a weaker AMO-coupling during the summer and stronger coupling between droughts and the ENSO. The cold phase of ENSO, La Niña, impacts drought via subsidence over western North America by weakening the Aleutian Low, after Kushnir et al. (2010) and Mo et al. (2009). However, neither correlations between SLP over the Aleutian low and RH at the US west coast nor ENSO/PDO-like SST footprint were found in Fig. 4.18 for the late period. In the early period, an ENSO/PDO-like SST footprint was found for the RH, and in the late period for q and T. Mo et al. (2009) further highlight the connection between the AMO and ENSO: only if both modes are opposite in phase, i.e. positive AMO with cold ENSO, are droughts over the southwestern USA enhanced. The AMO would serve to modulate the ENSO but alone standing the AMO would not influence regional droughts along the Pacific coasts. Liu et al. (2018) argue for a combination of AMO-like situations and ENSO to predict precipitation over western US coasts. Ruprich-Robert et al. (2018) underline the Atlantic warming's impact on the boreal summer Walker circulation, leading to increased trade winds over the Pacific, which again favours cold ENSO conditions in the boreal winter. They confirm the Atlantic multidecadal variability findings with a reduction in precipitation over northern Mexico and the southern United States, which includes part of the region, and warming through models, resulting in a decrease in RH.

McCabe et al. (2004) found enhanced droughts on the western US coast, particularly in the southwest of the US for positive AMO and negative PDO regimes. The AMO is found in more positive/warm phases in the past couple of decades, and the La Niña/cold PDO conditions around 2007–2009 would match the RH troughs over those years in California (Figs. 3.13 and 4.28). The 2013–2015 RH troughs cannot be associated with cold ENSO/PDO conditions. A significant, strongly positive AMO-RH correlation could be found in Section 4.3 in the late period, whereas the AMO-RH correlation in the early period and the AMO correlations with q and T are weak and insignificant. Benson et al. (2003) focused only on the positive correlation between the PDO maxima and drought over the Sierra Nevada, California and Nevada. Furthermore, McKinnon et al. (2021) suggest the North American monsoon impacting droughts over California. They concluded that the decrease in q was enhanced when T was high and coupled with anomalously low evaporation due to low summer soil moisture because of low summer precipitation. Regional evaporation rates and soil moisture will be explored in Chapter 5.

The analysis of Figs. 4.18 and 4.19 revealed some really interesting correlations: in the north and the south of the region, meridional and, directly over the region, zonal winds correlate strongly with RH. Other large regions of wind-RH, SST-RH and SLP-RH correlations are at a great distance from the region of interest located over the North Atlantic, and somewhat surprisingly do not match those found in the literature (Kushnir et al., 2010; Sutton & Hodson, 2005). Further analysis would be needed to determine whether this may be because the analysis in this thesis is undertaken with annual data, whereas the analysis of Sutton and Hodson (2005) is for boreal summer, and Kushnir et al. (2010) do their analysis for October-March and April-September. Much previous research points to teleconnections between the Atlantic SST and drought events at the western US coast and shows the interconnectedness of the climate system. However, no trends were found either over the eastern Pacific or over the Atlantic to suggest that dynamical drivers such as SST, wind or sea level pressure might be driving the observed RH long-term trend. It does not seem that dynamical drivers are causing any observed RH trends.

The detrended correlations used do not exclude that dynamical drivers impact regional RH over short periods. These impacts can drive the RH trend without a trend being seen in the primary physical variables or the modes.

It is noticeable that the low RH anomalies between 2007–2009 are driven by low q anomalies (Fig. 3.13, Christian-Smith et al., 2011). In 2014, the low RH anomalies were determined by high T. In contrast, RH was abnormally high in 2011 and q and T were balanced. This is an excellent example of how different mechanisms change RH at other points in time. The RH trough in 2014, for example, might be associated with warming in the tropical western Pacific and weak cooling in the east (Seager et al., 2015). These

ENSO temperature patterns keep the high-pressure system over the west coast stable, which leads to the suppression of precipitation. However, the correlation analysis does not deal with these very short periods.

As the California region is located right on the edge of the continent and next to the Pacific Ocean, westerlies are a source of moisture from the sea into the region, particularly over the northern part of the region. Thus, these prevailing winds would expect the region to be exposed to a lot of moisture. Changes in the flow could lead to droughts or wetting. However, significant trends in the westerlies were not found but the south has a well-known link with ENSO and tropical Atlantic variability, as discussed above. Diffenbaugh et al. (2015) found a positive influence of global warming on California drought in models. Mao et al. (2015) and Griffin and Anchukaitis (2014) found influences of variability in precipitation to be more involved in the dry years 2013–2014 than the positive temperature trend. Seager et al. (2015) see global warming as the reason for decreased winter precipitation over the region and a negative long-term trend in soil moisture, affecting RH.

In conclusion, winds impact RH over the eastern US coast strongly and could be driving RH variability over short periods. However, it is not obvious that they are driving a long term trend. Teleconnections between SST, winds, SLP over the Atlantic and RH over California suggest different explanations which are mainly shaped to short periods and extreme phases in modes (ENSO, AMO, PDO) in specific constellations (e.g. regional droughts during a warm AMO and cold ENSO/PDO). However, as those primary physical variables do not show a significant trend, they cannot be considered to change RH over the long term. Due to the significant positive trend in SST and its positive correlation with regional T in the late period and an absence of a trend in q, the thermodynamic driver seems most plausible for the negative RH trend. The faster land than ocean warming effect on RH might be enhanced by dynamical drivers over shorter periods, leading to increased T and reduced precipitation.

4.1.6 Mongolia

Mongolia shows very significant ($p < 0.05$) negative RH trends in DJF and MAM (-2.6 %rh decade^{-1}, -2.22 %rh decade^{-1}, respectively; Section 3.3.1.5). The trend in DJF is especially pronounced in the southeastern half of the region and in MAM in the east.

The Mongolia region is located south of Lake Baikal. Seasonal mean temperatures are below freezing in both DJF (whole region) and MAM (the northernmost part of the region) (Fig. S2). In DJF, climatological winds are easterly and stronger in the region's southeast; in the northwest, winds are southerly (Fig. S4). In MAM, the climatological wind direction is northwesterly and is more homogeneously distributed over the region than in other seasons. In DJF, Mongolia is located within the high-pressure system of China and southern Russia – the Siberian high. In MAM, the high-pressure system is located northwest of the region. Since Mongolia is far from the sea, SSTs might not directly contribute to a change in q and T, thus RH, but indicate correlations with any modes of variability with oceanic signature (ENSO, AMO, PDO).

Considering correlations with T and q: only in MAM does q-RH correlate positively in the late period ($r = 0.66$, $p = 0.0$; Section 3.3.1.5) with strongest correlations in the south and west (Fig. 3.6). T-RH correlations are significantly negative in the west of the region. In DJF, T-RH correlate strongly positively in the north of the region and negatively in the southern subregion (Section 3.3.1.5; Figs. 3.7 and 3.14) during the late period. Therefore, in MAM, dynamical drivers might be expected to cause the mean regional RH change rather through q than through T. In particular, in DJF, dynamical drivers might impact RH in the northern part of the region differently than RH in the south. In both seasons, late-period T-q correlations in the northern third of the region are strongly positive (Fig. 3.5).
In DJF, the q and T correlations with the primary physical drivers u10, v10, si10 and the SLP are very similar to each other, matching with the strong regional mean T-q correlation in this season (Figs. 3.5 and 4.21). The similarity of these q and T correlations indicate that atmospheric circulation is driving changes in moisture and temperature equally to some degree. Their correlations differ greatly from the much less significant and widespread but patchy RH correlations with the primary physical drivers (Fig. 4.20) indicating that the impact on dynamical drivers on q and T would not result in interannual RH changes due to the Clausius-Clapeyron equation. It is known from Chapter 3 that the slightest deviations from this equation can lead to a significant change in RH. As the correlation maps in this study are based on regional means for q, T and RH, subregional differences in the correlations' strength and direction (e.g. strongest positive q-RH correlations with positive T-RH correlations in the north and weaker q-RH correlations with negative T-RH correlations in the south in DJF; Figs. 3.6 and 3.7) were not taken into account in this analysis. Therefore, it is expected that the correlation analysis, which is based on detrended time series in this study, can only determine whether there is a relationship between winds or SLP and regional RH in DJF but not whether the dynamical change occurs via the change in q or T.

In the northern part of the region, precipitation (and q) shows a negative trend in JJA (Figs. 4.2 and 3.6). JJA is the season with the largest amount of precipitation, in the late period (Fig. S3). However, precipitation-RH in JJA are not correlated without time lags (which were not looked at). Therefore, whether this JJA precipitation decrease has influenced RH in DJF and MAM cannot be said at this stage.
In DJF, a positive but insignificant ($p > 0.05$, thus not indicated in colour in Fig. 4.1) anticyclonic/clockwise trend leads to increased (decreased) flow out of (into) Mongolia in the late period, particularly in the southeast where the negative RH trend is strongest (Table 4.1). Only the positive v10-RH correlation but not the negative u10/si10-RH correlations within the region in the late period can be associated with these wind trends (Fig. 4.20). In the early period, with a positive RH trend, the trend in winds have been significantly inverse in the southeastern part of the region, i.e. increased flow into the region; however, wind-RH correlations are weaker or insignificant in the early period.

Note that ERA-Interim at least did not appear to show decreasing wind speed trends over land that the in situ observations did. At the time, this was thought to be because ERA does not really include a realistic roughness length (affected by the height of buildings and trees), and it was this increase in roughness length that was thought to drive a decrease in wind speed. However, findings in this study might be linked to circulation or modes of variability (Zeng et al., 2019).

For the 20th century, Ye (2001), and for 2008–2009, Gao and Yang (2009), the winter with the lowest RH values (Fig. 1.1), precipitation and T in DJF were associated during droughts associated with ENSO. ENSO-like SST correlation patterns over the eastern Pacific are only partly significant in DJF and MAM in the late period. In winter 2008–2009, Gao and Yang (2009) find that La Niña increased the SST/T and SLP contrasts between the Indo-Pacific Ocean (matching with the positive SST-RH correlations over the northern Indian Ocean in the late period, i.e. decreased RH with decreased SST in this region; also found by Singh et al. (2013) and the Asian continent leading to a strengthening of the East Asian monsoon and northeasterly winds. With positive SLP-RH correlations over the tropical and SH western Pacific (Fig. 4.20), this may reflect a southward shift of the subtropical high pressure in the western Pacific, thus the more southerly ITCZ kept northern China free from warm and moist onshore winds and precipitation. The decrease in precipitation around the region of the city of Wuhan at the southwestern Chinese coast in the late period (Fig. 4.2) could be associated with Gao and Yang (2009)'s findings; to make this statement, however, links to more than one La Niña event would be needed. Niu et al. (2020) explain that less northeasterly moisture flow reached Mongolia with a strengthened Siberian high; consequently, they found regional RH decreasing in the late period compared to the decades before 2000. SLP-RH correlations are weakly negative over Siberia but insignificant (Fig. 4.20). Yatagai and Yasunari (1994) found the influence of decadal variability of the location of the Siberian high on winter T, which could be associated with the negative SLP-T/q correlations over wider Russia in the late period (Fig. 4.21). While SST and SLP correlations over the Pacific Ocean and the Asian continent, respectively, in the late period partly match the explanations of winter drought over Mongolia during La Niña, no SST or SLP trends were found, which indicates the uniqueness of the event. Its extreme impact on RH created the deepest RH trough driving the negative trend in the late period (Fig. 3.14). There are weak (but significant) positive correlations between late-period RH in DJF and the MEI (Table 4.9), fitting with the results of Gao and Yang (2009) discussed above. The MEI-RH and IPO-RH correlations in MAM are also significant and positive but they are not found in the same grid boxes as the RH trends (Section 4.3). Spatial and seasonal monsoon patterns were not analysed in this thesis.

Considering wind-RH correlations outside the region, their patterns are very different between the early (insignificant positive RH trend) and the late period (significant negative RH trend; Fig. 4.20). In DJF in the early period, positive (negative) u10-RH correlations focused on Europe (the northwestern African continent) instead of negative u10-RH correlations on the Indonesian region in the late period. However, explanations for the link of these winds in distance to the region and regional RH could not be found. In MAM, u10/si10/SLP-RH (v10-RH) are negatively (positively) correlated with regional RH in the region's northern two-thirds in the late period (Fig. 4.22). In contrast to DJF, In MAM, the u10/si10-RH correlations are very similar to the u10/si10-q, i.e. decreased q and RH with increased westerly flow (Figs. 4.22 and 4.23). These correlations do not match with the insignificant ($p > 0.05$) southeasterly wind trend in the region's southern half in Fig. 4.1, which would indicate a reduction in westerly winds or easterly winds. In the early period when RH significantly increased, regional, zonal westerly winds significantly decreased (negative u10/si10 and positive SLP trends), but they are more weakly correlated with the RH than in the late period. The combination of a lack of regional significant u10/si10/SLP trends and stronger correlations with RH in the late period might be linked to an impact of westerly flow to changed decreased RH in MAM.

In MAM, like in DJF, the wind-RH patterns outside the region differ between the early and the late period (Fig. 4.22). Over the Arabian Sea, the Bay of Bengal and the Gulf of Thailand u10-RH/q correlate significantly negatively, while SST-RH (SST-T) correlate positively (negatively) over these areas in MAM (Fig. 4.23). These correlations indicate that RH decreased with increased T over Tibet linked to increased SST and westerlies over the Arabian Sea, the Bay of Bengal and the Gulf of Thailand. While u10-RH and SST-RH correlations were stable between the early and the late period, the si10-RH correlations were insignificant over the early period. Despite the lack of trends, the difference in wind circulation patterns in relation to regional RH between the early and the late period might describe changes in RH over Mongolia.

Local wind-RH correlations are larger and stronger in the late period compared to the early period and in MAM compared to DJF (Figs. 4.20 and 4.22). While the RH-correlations with wind direction and speed and SLP further away from the region in DJF are larger and stronger in the early period, they are larger and stronger in MAM in the late period. This shows that even though the climatological means for local winds are similar in both seasons, the influence of local and remote dynamical drivers on Mongolian RH has changed between the early and the late period and that this change depends on the season.

With correlation patterns between the primary physical drivers and RH being differently strongly pronounced between the early and the late period, the rare significant correlations close to the region, the lack of trends in the late period and, particularly, the heterogeneity of regional RH trends and correlations with q and T make it challenging to explain the decreasing RH in Mongolia in context of the dynamical drivers. It might be local changes in early-period versus late-period winds impacting regional change in RH. In DJF, a potential contributing factor to the negative RH trend could be local but insignificant ($p > 0.05$) wind trends and enhanced outflow/decreased airflow into the region. MAM followed by the rain and growing season (JJA; Nandintsetseg et al., 2021) with decreased precipitation in the late period adding to a prolonging of dry conditions in the region. ENSO-like SST-RH correlation patterns were found in both seasons (Figs. 4.20 and 4.22), which could contribute to the explanation of the impact of dynamical drivers on RH, mainly, in DJF, for instance, via the strengthening of the East Asian moon and a southward shift of the ITCZ, thus, a reduction in precipitation.

Due to the heterogeneity of the region, it may be that the RH time series is heavily dependent on the grid boxes, so that, for example, the northern (including the Lake Baikal) and the southern subregion should be considered individually, as the subregional T-RH correlations suggest for DJF (Fig. 3.7). The low RH anomalies and drought events ('dzuds'; Rao et al., 2015) in the second half of the late period, 2009 and 2015, coincided with high T (and in DJF also with high q) anomalies (Fig. 3.14). The negative precipitation trend in JJA enhances the drought conditions. Due to the short duration of these droughts, the influence of drivers on these droughts may not be captured with the correlation analysis. The drought years should be examined in isolation, possibly for the impact of the Asian monsoon. In summary, except for the link with a southward shift in monsoonal winds due to La Niña, no apparent impact of dynamical drivers on RH could be defined. Non-dynamical drivers may play a more decisive role on humidity in Mongolia.

4.1.7 Southern Africa

RH in the late period shows significant negative annual trends over Southern Africa and in JJA in particular over the region's centre and towards the northeast of the region (-2.15 %rh decade^{-1}; note the low number of significant grid boxes) and in SON also over the southwestern part (-2.83 %rh decade^{-1}) (Section 3.3.1.6). The regional RH trend in JJA has only a small number of significant grid boxes.

The SSTs on the west of Southern Africa are lower than around the south and east coast given the cold Benguela ocean current from the southeastern of the Atlantic Ocean and the warm Agulhas and Mozambique currents from the southwestern Indian ocean (Fig. S4). The southern tip of the region is influenced by the northern edge of the SH westerlies, which are the furthest north in JJA. In this season, austral winter, the depressions embedded in the westerlies bring precipitation to the southwest of the region (the winter rainfall zone; Fig. S3; Hannaford et al., 2015). Easterlies from the Indian Ocean blow over the north-east of the region, continuing over land and partly becoming northerly over land, blowing from north to south, then meeting the Westerlies south of the region (Blamey et al., 2018). The offshore winds southeastwards at the southern tip of the region are more strongly pronounced in JJA. Southern Africa is located at the boundary between the subtropical high-pressure cell and the SH westerlies, which are the furthest north in JJA.

In JJA and SON in the late period, q and RH are strongly positively correlated ($r = 0.76$ and $r = 0.92$, both with $p = 0.0$, respectively; Section 3.3.1.6). Correlations between T-RH are negative and less strong in SON ($r = -0.52$, $p = 0.03$) while not significant in JJA. In the southwest, RH correlates more strongly with q, whereas in the northeast, the T-RH correlation is stronger than in other parts of the region (Figs. 3.6 and 3.7). This suggests that changes in q are driving RH changes more strongly than changes in T in JJA and SON on a regional average, and in the northeast, where the strongest RH is found, T might be dominant for changes. While q very significantly decreased in the late period in SON, T significantly increased matching the grid boxes with an RH and q trend.

In particular in SON on the southeast and east coast of southern Africa, and over Zimbabwe and southern Mozambique in JJA, precipitation shows a negative trend in the late period (Fig. 4.2). As precipitation-RH do not correlate in these subregions and seasons, a direct impact of precipitation on RH without time lags is not expected. However, on a regional mean, the correlations between precipitation and RH is strongly positive. In Section 4.1.1, it was identified that decreased easterlies and northeasterlies reduce precipitation on the eastern coast and RH inland. The weakening of these winds was linked to a weakening of the South Indian high pressure (negative SLP trend in Figs. 4.1 and 4.24) and the increased SLP west of southern Africa which resembles the anomalies in SLP patterns found by Mahlalela et al. (2020), focussing on spring (SON; Figs. 4.1 and 4.26), and Blamey et al. (2018). The late-period trend of SLP and winds and their impact on regional rainfall were found to be weaker in JJA (Figs. 4.1 and 4.2). These SLP patterns spatially do not significantly correlate with RH in either season (Figs. 4.24 and 4.26), so this study cannot manifest a direct link between precipitation via SLP and RH. This may be due to the fact that this study investigates a larger region and its mean than those in the eastern cape in the literature. The literature started from specific events, Blamey et al. (2018) in particular from 2015–2016, while this study analyses over several decades. The RH trend may be driven by recent events. In the south alone, SLP-RH correlate positively, more strongly in the late period than in the early period.

In JJA, SST-RH correlate positively with RH on the southern tip of Southern Africa and the South Atlantic band, i.e. reduced RH with reduced SST (Fig. 4.24). However, SST shows no significant trend in the late period, nor correlations with either q or T (Fig. 4.25). The SSTs on the east coast show a positive trend in the late period, spatially matching the negative RH trend but no correlation with regional RH, as well for SON. The u10 wind and si10 and RH correlate strongly negatively over the southern tip of the region, i.e. reduced RH with increased westerlies (Fig. 4.24). There have also been positive u10 wind trends in the east side of Southern Africa in part of this region of significant negative correlations, indicating there could be a link between reduced RH and enhanced westerly/reduced easterly flow. There are also significant negative correlations between regional q and both u-wind and si10 in a similar region. South of the region over the ocean, SLP-RH-q correlate positively, i.e. reduced regional RH due to reduced q and reduced SLP; SLP shows no significant trend (Figs. 4.24 and 4.25). In summary, only increased westerlies are directly associated with reduced RH in JJA. The different dynamical influences on T (southwest, northeast) makes determining the influence of dynamical drivers on RH challenging.

While the SST trends (negative on the west coast, positive on the northeast coast) in SON are similar to those of the JJA-SST trends, SST-RH do not correlate on coastal southern Africa in either season (Figs. 4.24 and 4.26). In SON, there are similar links as in JJA between the westerlies south of the region and regional RH and q: the u10-RH and u10-q also correlate negatively in the southern and southeastern half of the region, i.e. decreasing onshore flow from the (north)east and a reduction in moisture advection from the Indian Ocean leading to a regional decrease in RH (Fig. 4.26 and 4.27). Positive u10 trends over southeast Africa extending east could result in RH reductions through less moisture advection and thus, less precipitation. In the northeast of the region, there are positive u10-RH correlations but they are insignificant in most of the grid boxes. The significant u10-RH correlations and u10 trends are only found in the late period, not during the early period, indicating that the drying trend in the early period results from different mechanisms than the one in the late period. Also, only in the late period, there are negative v10-RH and v10-q correlations in the region's centre, the positive v10 trends over land to the southeast suggest decreased northerlies/increased southerlies over the region's south are linked to drying within the region. Together with positive si10 trends, this suggests a change in wind directions from northeasterlies to southwesterlies which might support a northward distribution of drier air masses than normal through the decrease in easterlies (Figs.4.1, 4.26 and 4.27). At the southwestern tip of the region, positive v10-RH and v10-q correlations indicate weaker southerlies at the west coast with low RH; thus, also in the western part of the region, an RH decrease through lower q. The u10 and v10 trends appear to be linked to the negative SLP trend in the southwestern Indian Ocean (Fig. 4.1). The positive SAM-like SLP-RH correlation over the southern tip of southern Africa in JJA and SON indicates higher RH with higher pressure, so anticlockwise flow and enhanced flow from the east, i.e. enhanced precipitation/moisture with enhanced pressure and vice versa (Mahlalela et al., 2020). This SLP-RH correlation matches the u10 wind pattern but is not accompanied by a significant SLP trend. The positive SAM trend in the late period is limited to the months DJF and MAM (Fig. 4.6). Interesting is the positive (negative) SLP south of Patagonia in JJA (SON) with a negative trend in the late period in SON strengthening westerlies (Fig 4.1). In both seasons in southern Africa, in the north and northeast (southeast) of the region, u10/v10-T correlate significantly negatively (positively), indicating stronger northeasterlies (southwesterlies) over land (from the ocean), bringing warm (moist) air into the region. However, there are no trends in u10 or v10.

The positive band of u10-RH and u10-q correlations in the SH's high latitudes in both seasons could indicate a connection of atmospheric moisture content and RH change over southern Africa with the Southern Annular Mode (SAM; Figs. 4.24–4.27). The SLP-RH correlations in the late period do show a SAM-like pattern, with positive correlations in mid-latitudes and negative correlations at high latitudes. However, the regions of significant grid boxes are mainly to the south of Southern Africa and in the Antarctic Peninsula/Weddell sea region, rather than across all longitudes. The region of positive RH-SLP correlations to the south of Southern Africa agrees with the findings of Mahlalela et al. (2020), who also find that below-average precipitation in the Eastern Cape region of South Africa is associated with cyclonic anomalies southeast of South Africa. This region's negative pressure anomalies would lead to enhanced westerly/reduced easterly flow, so it fits with the u10 correlations discussed above. They find this to be related to shifts in zonal wavenumber 3. At low RH values in 2012 and 2015, SAM is in a strongly positive phase (Figs. 3.15 and 4.28). A positive phase means that pressure is lower at high latitudes, and higher and mid-latitudes, resulting in a contraction of the mid-latitude westerlies towards the pole.

The SSTs in the southern Indian Ocean show a positive trend in both JJA and SON (Figs. 4.24 and 4.26; Li et al., 2017). Blamey et al. (2018) identified abnormally high SSTs in this region during the positive ENSO (El Niño) event in 2015–2016, which led to drier conditions over southeastern Africa. In that year, anomalously positive temperatures were documented for southern Africa (Fig. 3.15). However, in contrast to the early period, no ENSO-like SST pattern is discernible in the SST-RH correlation maps in SON in the late period. The RH troughs in 2005 and 2007 are characterised neither by strong El Niños nor strong SAM, indicating different reasons behind low RH values in the late period. Reason (2017) found that ENSO generally has a stronger impact than SAM on the region.
Strong phases of the SAM and ENSO are particularly found during the austral summer (DJF), the rainy season in southern Africa. Due to the time lag between the peak in modes of variability and seasons with a low RH trend, it is therefore challenging to track their impact on decreased RH in austral winter and spring (Mahlalela et al., 2020).

The correlation patterns between the primary physical variables and RH in the late period are different from those in the early period in SON (Fig. 4.26) but they are similar in JJA (Fig. 4.24). The lack of significant correlations over the full period in both seasons confirms that correlation patterns impacting RH in southern Africa differ between the early and the late period, particularly in SON. The RH trend through dynamical drivers in the late period, at least in part, can be explained by changes in the patterns.

In summary, two different circulation patterns impact RH in southern Africa, a region located at the boundary between tropical and subtropical mid-latitude, which makes the analysis complex: while easterlies influence RH in most of the region, southerlies dominate the moisture supply on the west coast. In both seasons, RH and q are strongly linked to the westerlies in the south of the region. A weakening of high pressure over the southern Indian Ocean and trends and correlations with wind directions and speed indicate a weakening of onshore easterly flow from Madagascar or even reversal of this to offshore winds (JJA with increased wind speed in the southeast). i.e. fewer onshore easterlies in and more offshore out lead to reduced precipitation. Precipitation is decreased in SON and correlated positively with RH. In JJA, decreased precipitation in MAM might be crucial (Section 4.1.1 and Fig. 4.2). Wind speed in SON has increased over the southern half of the land area during the late period. There is a northwestward trend on the west coast, so the onshore winds also decrease along the region's west coast.

The regional SST-RH correlations show a more ENSO-like pattern in the early period in SON, while the SLP-RH correlation maps show a more SAM-like structure in SON in the late period than in the early period. While the modes of variability are linked to the findings but do not fully explain the RH trend, the links with dynamical drivers, such as winds and SLP, do show links that could have contributed to the negative RH trend via the decrease of q. For SON where regional T is slightly increased, the subregional easterly onshore flow in the northwestern region determines T but shows no significant trend, neither SSTs close to the region show a link with RH. Findings regarding links to the ENSO match with findings by Blamey et al. (2018) and Mahlalela et al. (2020) who considered a smaller region, the Eastern Cape, on a smaller time scale (El Niño during 2015–2016). Correlation patterns differ between the early and the late period, e.g. the stronger influence of westerlies on q and RH in the late period, indicating a change in driving mechanisms over decades rather than a continuous link on RH and its drying trend, i.e. in addition to the aforementioned spatial heterogeneity, there is also temporal heterogeneity. Less moisture and rain being brought into the region in the late period matches the findings in Section 3.3.1.6 of RH's increased dependence on q in SON in the late period.

4.2 Which modes of variability have the strongest relationship with RH?

Various common patterns of primary physical variables occur whereby indices can usefully describe their combination. These indices show how climate properties change in different regions and, on different time scales (seasons, years and decades), and are so-called modes of variability. The following modes of variability are analysed: Arctic Oscillation (AO), Atlantic Multidecadal Oscillation (AMO), El Niño Southern Oscillation (via the Multivariate ENSO Index [MEI]), Interdecadal Pacific Oscillation (IPO), Pacific Decadal Oscillation (PDO), Pacific North Atlantic Oscillation (PNA), Southern Annular Mode (SAM) and Indian Ocean Dipole (IOD). Each mode of variability is described below, accompanied by an annual global correlation map between RH and the mode's index (Section 4.2.1).

Modes of variability are internal energy variations and influence the way that heat and moisture are moved around the atmosphere and ocean. Wind/atmospheric circulation changes can directly affect the movement of heat/moisture by advection of unusually warm/cool/moist/dry air, which affects the surface atmosphere, and can also influence moisture/precipitation for example through changes to storm tracks. The winds can also inhibit or enhance ocean circulation, downwelling and upwelling and lead to changes in sea surface temperature. Warmer or cooler waters being brought to the surface affect the temperature and moisture levels of the atmosphere above. So, modes of variability and atmospheric circulation changes can influence the surface atmospheric RH.

Table 4.5: Characterisation of modes of variability that are examined for correlations with RH (Dong & Dai, 2015; Fogt et al., 2011; Fogt et al., 2012; Garcia-Soto & Pingree, 2012; Gillett et al., 2006; Gulev et al., 2021; L'Hereux, 2021; Mann et al., 2021; Mantua & Hare, 2002; Saji et al., 1999; Salinger et al., 2001; Stammerjohn et al., 2008; Thompson & Wallace, 2000; Thompson et al., 2000; Wolter & Timlin, 2011).

Mode representing index	Key features for positive phase (with the negative phase mainly inverted)	Time scale (if applicable: strongest season, periodicity, phase response [see Fig. 4.28])	Trend over full period [unit decade^{-1}] (p-value); miscellaneous of interest
AO	Strong difference between the Icelandic Low and the Azores High (for the NAO) including the Aleutian low and the North Pacific High(for the AO/NAM; Thompson et al., 2000), jet stream stronger and further north, strong Polar vortex/westerlies preventing cold air to escape southwards, strong Gulf stream advection	Strongest season: DJF (Thompson et al., 2000); after a positive phase in the early 1990s, weakening of variability or even negative years (like 2010; Gulev et al., 2021)	0.05 (p=0.13)
AMO	Northward shift of the ITCZ, warmer (colder) SST in the northern (southern) North Atlantic providing energy for developing storm systems	No strongest seasons; 50-70y (Garcia-Soto and Pingree, 2012); positive since 1997-present (Gulev et al., 2021)	0.13 (p=0.0) The AMO might be not a natural variability and overlaid by the long-term SST global warming trend (Mann et al., 2021, Gulev et al., 2021).
ENSO - MEI	SST above (below) average in NH high and low (mid) latitudes and the eastern Pacific (western North Pacific towards Japan), low (high) SLP over the tropical eastern (western) Pacific, weaken Walker Circulation and easterly surface winds over Pacific; i.e. El Niño	Strongest season: DJF (although impacts occur in other seasons too); 2-5y (Wolter and Timlin, 2011); strong El Niños: 1973, 1987, 1992, 1997, 2014-15, strong La Niñas: 1975, 1999, 2008, 2011 (Gulev et al., 2021)	0.02 (p=0.51); shift of the main pole from the eastern to the central Pacific over the last couple of decades (known as El Niño Modoki; Gulev et al., 2021); no change in teleconnection patterns (in particular the Asian, Indian and East Asian monsoon) since the 17th century (Gulev et al., 2021)
IPO	Similar to the ENSO but taking place in a wider, rather tropical Pacific area, associated with stronger (weaker) El Niño (La Niña); IPO and PDO indices are significantly correlated (Gulev et al., 2021) with stronger SST anomalies in the extra tropical North Pacific for the PDO	Strongest seasons: SON, DJF; 40-60y (Salinger et al., 2001; Dong and Dai, 2015); peaks and troughs see the MEI; since 1999-2014 in a rather colder phase (Dong and Dai, 2015)	-0.02 (p=0.51)
PDO		No strongest season; 50-70y (Mantua et Hare, 2002); similar peaks and troughs as the MEI/IPO, mainly positive: 1979-98, 2014-17, mainly negative: 1999-2001, 2007-13, i.e. a regime shift around the year 2000 (Gulev et al., 2021)	-0.03 (p=0.33)
PNA	Lower (higher) SLP than average over the northern (southern) NH Pacific Ocean	Strongest season: DJF (L'Hereux, 2021)	0.05 (p=0.15)
SAM	Strong SLP difference between 40S and 65S, poleward shift of storm tracks, strong Polar vortex/westerlies preventing warm air to flow southwards; associated with La Niña (Fogt et al., 2011; Stammerjohn et al., 2008)	Important all year round. Season of strongest (positive) trends: DJF, caused by ozone depletion (Gillet et al., 2006; Fogt et al., 2012); positive since 2007-present	0.23 (p=0.0; Gilet et al., 2006)
IOD - DMI	Low (high) SST in the southeastern (western) tropical Indian Ocean, enhanced equatorial easterly wind, thus, enhanced convection and rainfall in the west	Strongest season: SON (Saji et al., 1999); positive since 1997-present	0.07 (p=0.0; Gulev et al., 2021)

The differences between the modes of variability in terms of their primary physical driver variables, regional extent (including teleconnections), time scale and frequency make such analysis highly complex. A ranking process has been undertaken to establish the strongest couplings for further investigation (Section 4.2.2). Firstly, the ranking establishes which modes are most important for RH in regions with significant trends in seasonal RH in the late period. Where there has been a trend or a change in the mode, these modes could explain some of the regional decreases in RH and have contributed to the global RH trend. Secondly, the ranking identifies which regions are most impacted by dynamical drivers.

The ranking is based on late-period annual and seasonal (with a strong late period RH trend) correlations of grid box RH with the relevant index for each mode. The correlations are ranked following the methodology described in Section 2.2. The highest-ranked correlations between regional RH and the modes of variability, i.e. the strongest and most significant interannual relationships, are analysed according to modes in Section 4.3.

4.2.1 Profiles of modes and annual correlations with RH

Potential impacts of modes on RH can be seen when a mode is significantly correlated to regional q or T, and the mode has a trend in the direction that could potentially contribute to regional T or q changes, the latter mainly through precipitation and changes to water storage. If q and T changes are equally big, RH would not have to change, according to Clausius-Clapeyron. From Chapter 3, it is known that small deviations in the changes can very well lead to changes in RH, e.g. southern Greenland (DJF) and eastern Canada (DJF) with very strong T-q correlations.

Table 4.6: Annual trends, i.e. change in index per decade, for the AMO index, the SAM index and the IOD index for the early (1973–1999), the late (2000–2017) and the full period (1973–2017).

Trends	AMO	SAM	IOD
Early period (1973-1999)	0.14 (p=0.0)	0.32 (p=0.01)	0.07 (p=0.01)
Late period (2000-2017)	0.07 (p=0.0)	0.43 (p=0.05)	0.09 (p=0.01)
Full period (1973-2017)	0.13 (p=0.0)	0.23 (p=0.0)	0.07 (p=0.0)

After defining the modes' indices in Section 2.1.5, the eight modes of variability are briefly characterised regarding their temporal scale and physical effects in Table 4.5 and

Fig. 4.28; the ENSO was described in Section 1.3.2.3. The regional patterns of significant annual mode-RH correlations are described for regions with an RH trend in the late period based on Fig. 4.29. to get an overview of the area of impact of the mode on interannual variability in RH. Since many modes have a seasonal characteristic, more robust correlations are only discussed in Chapter 4.3, if possible at the seasonal level.

The trend analysis (last column of Table 4.5) describes long-term temporal changes in the mode and can compare the mean phases in which the mode was found at different time periods. If the phase either remains with the same sign and has intensified or if a phase change has taken place, the effect of the mode on, among other things, regional precipitation and T can change, and thus change RH.

Over the full period, only the AMO, the SAM and the IOD show a significant annual trend (Table 4.6 and Fig. 4.28). Also, the seasonal trends of these modes are significantly ($p < 0.1$) positive, except for SAM in JJA and SON (not shown). It is assumed that in regions where the AMO, the SAM or the IOD and RH are significantly linked, changes in the mode could lead to RH trends in the late period.

The positive phase for the AMO, the SAM and the IOD was more pronounced in the late period than in the early period. For the low-frequency AMO, a clear phase change is visible. (Fig. 4.28) However, it is discussed in its nature as an oscillation (Mann et al., 2021). The MEI, IPO and PDO have a significantly positive trend in the late period (0.02, $p = 0.01$; 0.02, $p = 0.01$; 0.04, $p = 0.0$, respectively), indicating increased more positive (El Niño) years towards the end of the late period, due to an eastward shift of the Walker Circulation (Bayr et al., 2014).

This kind of phase change and extreme years might also impact regional RH trends in the late period. The other modes show no annual or seasonal trends over the full period. Their temporal behaviour is taken up in Section 4.3 in direct relation to the region in which the RH correlates.
Trends are determined by the difference between the beginning of a period and the end. At the beginning of the late period in 2000, the ENSO/IPO/PDO were negative (La Niña, cooler eastern tropical Pacific), the AMO and the SAM came just out of a positive phase peaking in 1998–1999 and 1997–1998 (Fig. 4.28). At the end of the late period towards 2017, all modes were in a positive phase with the MEI/IPO/PDO/PNA from 2014–2016. In particular, the phase change of the modes in the Pacific Ocean (ENSO, IPO, PDO) thus recorded a shift from negative (cold, between 2007–2013) to positive (warm, since 2013). The strongly pronounced phase change in combination with the other modes, e.g. AMO (cold in the early period, warm in the late period), may strongly impact regional RH.

The annual RH correlation pattern of the ENSO (MEI), the IPO, and the PDO are similar in their sign although they do differ regionally in their strength, e.g. over the Caspian Sea (Fig. 4.29). As the AO and the AMO feedback on each other, the sign of their correlation patterns appears to be inverse (Li et al., 2013; Seip et al., 2019). In contrast, the possible explanation of RH trend by modes is expected to depend on the different time scales of the modes, e.g. the PDO and AMO show longer time scales.

As expected, modes correlate with RH close to their place of origin, e.g. the positive AO-RH correlations in Scandinavia indicate that a positive AO increases RH over this region due to stronger westerlies resulting in above-average precipitation, and decreases RH over Central and eastern Europe due to below-average precipitation, while T increases in both regions (Wang & Schimel, 2003). Also, in eastern Canada (positive correlation with the AMO, negative correlation with the AO), southwestern Greenland (positive correlation with the AMO) modes are linked with interannual variability of RH not far from their place of origin. But teleconnections are also found, e.g. California (positive correlation with the AMO), the eastern USA (negative correlation with the PNA; Chen and Van den Dool, 2003; L'Hereux, 2021) and southern Africa (negative correlation with the MEI and the IPO in the northwest and with the AO in the east). In some regions, the RH is linked with several modes, e.g., in the Caspian Sea region, where the AO acts positively as well as the ENSO (MEI) and the IPO (for the latter in the southern sub-region). A mode can have different effects in a region, e.g. RH in eastern Brazil correlates positively (negatively) with the MEI and IPO in the south (north).

Less significant correlations in regions with a strong RH trend were found for the SAM and the IOP and the PDO, among others. This could be because q and T correlate similarly with the modes (e.g. more rainfall and high T anomalies) and, thus, offset correlations. If there are regional correlations only in the early or late period or in different seasons, it is possible that these correlations have different signs, these could also be offset.

The AMO is the only mode of variability that is both correlated with interannual variability of regional RH and has an annual trend. Its positive trend could explain the positive (negative) RH trend over eastern Canada (southwestern Greenland and California). However, NH Atlantic SST anomalies did not significantly correlate with Californian RH in the late period (Sections 4.1.5 and 4.3). The seasonal correlation of eastern Canada is discussed in Section 4.3.

4.2.2 Ranking of regional correlation strengths between detrended modes and RH

The ranking expands the annual global correlation maps between RH and modes over the full period (Section 4.2.1) by addressing seasonal correlations in the late period. The highly ranked correlations speak for strong, regionally wide-spread correlations and a strong link between mode and RH. They are analysed in Section 4.3.

The regions where RH correlates most strongly with modes of variability are Tibet, southwestern Greenland, and eastern Canada (Table 4.7). The interannual RH variab-

Table 4.7: Ranked regions in descending order, with strong annual and seasonal trends in RH in the late period (Table 3.3) for which RH correlates with modes based on the calculation methods for the ranking. Table 4.9 indicates the season in which the correlations are significant. For each region, the top three modes are mentioned. Bold modes indicate that the associated regional correlation is ranked in their top 3 in Table 4.8.

Rank	**Region (RH Trend)**	**Strongest 3 correlation with modes**
1	Tibet (-ve)	**IPO, MEI, PDO**
2	Southwestern Greenland (-ve)	**AO**, AMO, **SAM**
3	Eastern Canada (+ve)	**AO, AMO, IOD**
4	Scandinavia (+ve)	AO, **PDO, PNA**
5	Eastern Brazil (-ve)	AO, AMO, **MEI**
6	Mongolia (-ve)	**MEI, IPO, AMO**
7	Red Sea (-ve)	MEI, **IPO**, AO
8	Southern Africa (-ve)	SAM, MEI, PNA
9	Eastern USA (-ve)	**SAM**, IPO, MEI
10	California (-ve)	**AO, AMO, PNA**
11	Caspian Sea (-ve)	AO, **SAM**, AMO
12	Northern India (+ve)	**PNA**, SAM, MEI

ility is linked the strongest to the associated modes in these regions.

Based on the means of correlation and significance analysis, the most impactful modes on RH in regions where RH has changed in the late period are the AO, the ENSO (MEI), and the IPO (Table 4.8). Tables 4.7 and 4.8 complement each other. As expected, the MEI and the IPO correlate with RH in similar regions. As for the MEI and IPO, the PDO also addresses Tibet and Mongolia.

The ranking is based on correlations in the late period (Tables 4.7 and 4.8) and was calculated as well for the full period (not shown). The full period would almost equally prioritise the order of the regions (Table 4.7) and fully equally prioritise the order of the modes (Table 4.8). The similarity between the rankings over the late and full periods could indicate that the coupling of RH in most regions with the majority of the modes is stable. It is also possible that the modes affect the shorter time scale peaks and troughs of RH but not necessarily the trend. Modes are only clearly driving a trend in RH if

Table 4.8: Ranked modes of variability in descending order that most strongly correlate with regional RH in regions over the late period. The sign of the correlation (+ve, -ve) is given for significant ($p < 0.1$) correlations only. For each mode, the top three regions are mentioned. Bold regions indicate that the associated regional correlation is ranked in their top 3 in Table 4.7, i.e. a double/cross check.

Rank	Mode	Strongest 3 correlating regions (mode-RH)
1	AO	**Eastern Canada (DJF: -ve), Southern Greenland (DJF: -ve), California (annual: -ve)**
2	MEI	**Tibet (SON: -ve), Mongolia (DJF, MAM: +ve), Eastern Brazil (MAM: -ve, JJA: +ve),**
3	IPO	**Tibet (SON: -ve), Red Sea (SON: +ve), Mongolia (MAM: +ve)**
4	AMO	**Eastern Canada (DJF: +ve), California (annual: +ve), Mongolia (DJF, MAM: +ve)**
5	SAM	**Southern Greenland (DJF: -ve), Caspian Sea (JJA: -ve), Eastern USA (annual: -ve)**
6	PNA	**Northwestern India (annual: -ve), Scandinavia (SON: -ve), California (annual: +ve)**
7	PDO	**Scandinavia (SON: -ve)**, **Tibet (JJA, SON: -ve)**, Mongolia (MAM: +ve)
8	IOD	**Eastern Canada (not significant**), Eastern Brazil (DJF: +ve), Red Sea (not significant)

there is a trend in the mode or a cluster of the same phase (positive or negative) events in the late period.

Possibly for these reasons, annual correlation maps between the modes and RH over the full period (Fig. 4.29) give some information about the highest-ranked correlations (Tables 4.7 and 4.8). Many seasonal correlations in the late period are not significant on the annual scale over the full period, e.g. the MEI-RH correlation in Tibet and Mongolia. Annual correlations in the late period are only found in northwestern India (MEI) and California (AO, AMO, PNA). Therefore, it is essential to consider seasonal correlations (e.g. Fogt et al., 2012, on the SAM) whenever possible and distinguish between the early and late periods.

Caution is advised: the strength of the correlation and the number of grid boxes or the percentage of the area showing significant correlations do not necessarily have to correspond to one another. A low percentage and a strong correlation can take a similar place in the ranking as a high percentage and a relatively low correlation. For example, the ranking calculated strong relationships between the IOD and RH in eastern Canada and the Red Sea, which are not regionally significant (Table 4.8).

The ranking helps to guide the analysis on exploring the potential links between regional RH changes and dynamical drivers. Still, it may not manifest RH's dependence anymore or directly explain regional interannual RH variability or observed trends. The evaluation of the usefulness of the ranking will be discussed at the end of the Chapter.

4.3 Concluding to what extent the modes reflect the interannual RH variability or its trend

The ranking compared correlation coefficients, their significance and their significant area and provides an overview of the strongest relationships between the modes and regional RH in the late period. The correlations are broken down concerning their spatial and temporal behaviour for further analysis. The following eligibility criteria (EC) are used to determine whether the correlation between mode of variability and regional RH is sufficiently significant and strong and, thus, will be analysed in detail:

1. At least one-third of the number of total grid boxes in the region must be significantly ($p < 0.1$) correlated.
2. The correlation coefficient over regional averages must be moderate to strong ($r > 0.5$). If weak ($0.3 < r < 0.5$), then the global maps (Figs. 4.30–4.37) will be consulted to decide whether to include the correlation or subregional parts of it. Significant grid boxes, firstly, must be connected with each other and, secondly, most of them must show a significant RH trend.
3. The correlation coefficient between regional RH and the mode of variability must be significant ($p < 0.1$ / * or **) over the full period (1973–2017).

The first two ECs relate to the late period in which the regional and global RH trends seek explanations. The EC3 refers to the full period. By including the full period in the ECs, an enlarged length of the data and the correlation statement's accuracy are increased. This is an attempt to avoid coincidental correlations from short periods of data. Only the significance (p-value), not the magnitude of the correlation (r), is decisive in the full period. In addition to these spatially averaged correlations, correlation maps for annual and seasonal data (Figs. 4.30–4.37) are consulted to point to sub-regions, i.e. to consider agglomerations of individual grid-boxes with strong correlations which are offset in the regional correlation coefficients. As a reminder, the correlations listed in Table 4.9 show a very significant RH trend over the late period ($p < 0.05$ / **; selected from Table 3.3), and their correlation coefficient between regional RH and the mode of variability is significant ($p < 0.1$ / *) over the late period as a condition for the ranking.

Eight correlations, i.e. between the AO and RH in eastern Canada (DJF) and southwestern Greenland (DJF), between the MEI and RH in Mongolia (MAM), between the

Table 4.9: Performance of the highest-ranked, significant ($p < 0.1$) correlations between the modes of variability and regional and seasonal RH in the late period (bold mode-regions correlations in Tables 4.7 and 4.8) on three eligibility criteria (EC) indicating an impact of the mode of variability on RH. Correlations that fulfil all EC are bold.

Index of mode of variability	Region	Season	Corr coeff	Ratio	EC1 (0.33 grid boxes)	EC2 (r>0.5)	EC3 (full period)
AO	**E Canada**	**DJF**	**-0.53****	**6/10**	**yes**	**yes**	**yes**
	S Greenland	**DJF**	**-0.51****	**2/6**	**yes**	**yes**	**yes**
	California	annual	-0.29**	6/8	yes	no	yes
MEI	Tibet	SON	-0.55**	7/12	yes	yes	no
	Mongolia	DJF	0.42*	2/15	no	no	yes
	Mongolia	**MAM**	**0.56****	**6/15**	**yes**	**yes**	**yes**
	E Brazil	MAM	-0.43*	2/12	no	no	yes
	E Brazil	JJA	0.52**	3/12	no	yes	no
IPO	**Tibet**	**SON**	**-0.63****	**9/12**	**yes**	**yes**	**yes**
	Red Sea	**SON**	**0.6****	**4/8**	**yes**	**yes**	**yes**
	Mongolia	**MAM**	**0.55****	**6/15**	**yes**	**yes**	**yes**
AMO	**E Canada**	**DJF**	**0.66****	**6/10**	**yes**	**yes**	**yes**
	California	**annual**	**0.69****	**7/8**	**yes**	**yes**	**yes**
	Mongolia	DJF	0.53**	4/15	no	yes	no
	Mongolia	MAM	0.41*	3/15	no	no	yes
SAM	SGreenland	DJF	-0.52*	2/6	yes	yes	no
	Caspian	JJA	-0.47**	3/12	no	no	no
	E USA	annual	-0.13*	5/12	yes	no	yes
PNA	NW India	annual	-0.15**	5/8	yes	no	yes
	Scandinavia	SON	-0.52**	9/19	yes	yes	no
	California	annual	0.15**	4/8	yes	no	yes
PDO	Scandinavia	SON	-0.6**	10/19	yes	yes	no
	Tibet	JJA	-0.4*	4/12	yes	no	no
	Tibet	SON	-0.47*	4/12	yes	no	no
	Mongolia	MAM	0.42*	5/15	yes	no	no
IOD	E Brazil	DJF	0.49**	4/12	yes	no	yes

IPO and RH in Tibet (SON), around the Red Sea (SON) and Mongolia (MAM), and between the AMO and RH in eastern Canada (DJF) and California (annual), fulfil all of the EC and are very significant ($p < 0.05$; Table 4.9). Based on this filter, the latter are classified as sufficiently significant and strong to be analysed in detail.

Correlations between the MEI and RH in Tibet (SON) and between the PNA and PDO and RH in Scandinavia (SON) only correlate very significantly ($p < 0.05$) in the late period, but not in the full period (EC1 and EC2 fulfilled, EC3 failed), i.e. possible offset through insignificant correlation in the early period.

Figs. 4.30–4.37 were consulted to find strong sub-regional correlations. Significant correlations corresponding to all ECs were found for correlations between the MEI/IPO and northwest of eastern Brazil (DJF) with a negative sign. The correlations may explain the RH trend through modes at the sub-regional level.

The ranked selection of modes of variability with regional and seasonal RH relationships is examined below, grouped according to the modes, in order of their ranking. An overview of the mean index values in the early and late periods is given for each mode. Information about the mode's phase (positive/warm, negative/cold) helps interpretation. The phase change is of interest when exploring the interdecadal relationship. This assessment attempts to explain the seasonal impact of the modes of variability on regional RH using correlations on detrended data, such as between the modes and q and T and the primary physical variables (not shown). If there are similarities between the RH and mode correlations, the interannual RH variability or even the regional RH trend can be explained over the full and late periods. The degree of representation is determined using regression coefficients, which are used to calculate estimated RH time series and trends.

Starting from a significantly strong correlation and a significant regional RH trend, an attempt is now made to reconstruct RH using the regression relationship. The resulting estimated RH has the potential to reflect both the interannual RH variability (correlations) and its trend (regressions). Both predictions are evaluated by correlating the time series of the RH observations with that of the RH prediction and comparing the gradient, i.e. the trend, of both.

If neither the RH internal variability nor the trend can be reflected via the mode of variability, this does not mean that there is no connection between the two. The connection may be non-linear, for example, or temporal and spatial shifts must be considered for further analysis.

The second most impacting mode, according to the ranking (Table 4.8), the ENSO (in this work represented through the MEI), is expected to have a global footprint. Its temporally lagged impact on regional RH is examined. This way, further teleconnections can be made visible.

The AO and RH over southwestern Greenland and eastern Canada

The AO correlates significantly negatively with RH in two regions located in the NH high and upper mid-latitudes: eastern Canada ($r = -0.53$; $p = 0.02$) and southwestern Greenland ($r = -0.51$; $p = 0.03$). Negative AO indices are associated with high RH anomalies.

In DJF, the mean AO index post-2000 (-0.15), especially influenced by a trough in 2010, is more negative than the mean pre-2000 (-0.05), as there is a period of a positive index from 1988–1994. However, there is no significant trend in the AO over the full period so there is no indication of a change in regimes between the early and late period (Section 4.2.1). During a strongly negative AO phase, the polar vortex is weaker, as are the westerlies over the southern tip of Greenland and eastern Canada, with increased precipitation over the latter (Barry & Carleton, 2013; Office, 2018; Thompson & Wallace, 2000; Thompson et al., 2000). The negative AO in 2010 is associated with increased T over eastern Canada and Greenland, typical of this phase of the AO (Maidens et al., 2013; Osborn, 2011).

Table 4.10: Correlation coefficients (p-values and ratios between significant and insignificant grid boxes) between regional RH, q and T over eastern Canada and southwestern Greenland and the AO in DJF for the early and late period. Bold values are significant ($p < 0.1$).

Region, season	**Period**	RH trend in season	AO-RH corr (p; ratio)	AO-q corr (p; ratio)	AO-T corr (p; ratio)
E Canada, DJF	Early period	DJF	**-0.46 (0.02**; 5/10)**	-0.16 (0.45; 5/10)	-0.28 (0.2; 4/10)
	Late period	DJF**	**-0.53 (0.02**; 6/10)**	**-0.41 (0.09*; 4/10)**	**-0.42 (0.08*; 5/10)**
SW Greenland, DJF	Early period	DJF	**-0.45 (0.02**; 3/6)**	**-0.72 (0.0**; 6/6)**	**-0.7 (0.0**; 6/6)**
	Late period	DJF**	**-0.51 (0.03**; 2/6)**	**-0.69 (0.0**; 6/6)**	**-0.67 (0.0**; 6/6)**

In both regions, the q-RH, T-RH and T-q correlations are significant and moderate to strong correlate (Sections 3.3.1.7 and 3.3.2.4). Neither regional q nor T has significantly changed in the late period. The q and T have moderate to strong correlations with the AO in the late period only in southwestern Greenland. These negative correlations are apparent in 2010 (high RH, q, T during a negative AO; Osborn, 2011; Wollings et al., 2016), and inversely for 2015 (low RH, q, T during a positive AO; Fig. 4.28). Greenland's negative RH anomaly in 2015 is more pronounced than the positive anomalies in 2010, as in 2010 (2015), standardised T increases (decreases) more (less) than standardised q. These relationships are inversely for eastern Canada with weak AO-q and AO-T correlations (Table 4.10). The different degrees of impact of positive and negative AO on regional RH via q and T in 2010 and 2015 as example years can be an indication of the different regional signs of the RH trend, i.e. the positive RH trend in eastern

Canada could be strongly guided by the negative AO phase and the negative RH trend in southwestern Greenland by the positive AO phase.

The estimated RH using the regression relationships indicates that the AO explains some parts of the interannual variability of RH, i.e. peaks and troughs, in eastern Canada and southwestern Greenland (dark blue bold dashed line style, Fig. 4.38). However, the correlations between the observed and the estimated RH time series are insignificant over the full and late periods (for both periods, $r < 0.35$ and $p > 0.17$). The low correlation means that the AO is not linked to a high proportion of the interannual variability. However, the AO does not show a significant trend over the full period or a change in phase between the early and the late period (Table 4.5; Fig. 4.28). Therefore, the AO can explain only 5.23% of the observed regional RH trend in southwestern Greenland in the late period (dark blue thin dashed line style, Fig. 4.38). The estimated and observed linear RH trends in eastern Canada are of opposite signs. The AO alone can neither explain the interannual variability in RH nor its trend in eastern Canada and southwestern Greenland, although it appears to maybe influence RH in extreme years.

RH in both regions, southwestern Greenland and eastern Canada in DJF, respond negatively to the AO. While AO might drive their variability (RH peaks, troughs) similarly, the RH trends in those regions have opposite signs.

The ENSO and RH over eastern Brazil and eastern Canada

As a “dominant and most consequential” mode of variability (p. 201 in Cai et al., 2018; Schneider and Gies, 2004), both direct temporal influences on regional RH and temporally lagged influences are examined for the ENSO.

Table 4.11: As for Table 4.10, for the MEI seasonal correlations in DJF over the northwest of eastern Brazil.

Region, season	**Period**	RH trend in season	MEI-RH corr (*p*; ratio)	MEI-*q* corr (*p*; ratio)	MEI-*T* corr (*p*; ratio)
NW E Brazil, DJF	Early period	DJF	**-0.78 (0.0**; 3/3)**	**0.52 (0.01**; 3/3)**	**0.83 (0.0**; 3/3)**
	Late period	DJF**	**-0.7 (0.0**; 3/3)**	0.11 (0.66; 1/3)	**0.86 (0.0**; 3/3)**

ENSO’s impact without temporal lags

The correlation between the MEI and RH over Mongolia (MAM; $r = 0.56$, $p = 0.01$) fits all eligibility criteria. However, significant correlations are pronounced in the southwest, whereas significant RH trends are strongest in the northeast of the region (Figs. 3.3 and 4.32). In Section 4.1.6, La Niña could be associated with regional droughts through the literature but not in this study’s correlation analysis. Also, the correlation between the MEI and RH in Tibet (SON), which is only significant in the late period, do not coincide spatially. Therefore, only the strong MEI-RH correlation in the northwestern of eastern Brazil (DJF; $r = -0.71$, $p = 0.0$, 3/3 significant grid boxes; Fig. 4.32) is considered later. Low RH values in the northwestern part of eastern Brazil are associated with an increased MEI.

In DJF, the mean MEI index in the early period is more positive (0.26; driven by strong El Niños in 1983, 1992 and 1998; Fig. 4.28) than the mean in the late period (-0.01). The negative MEI-precipitation correlations and in particular, positive MEI-T correlation over the sub-region indicate that El Niño years lead to anomalous hot and dry austral summers, thus, low RH values (Table 4.11; Garreaud, 2009; Wang and Schimel, 2003; Watts et al., 2017). Especially during the intense El Niño period in 2014–2015, which contributes to the significantly positive ENSO trend in the late period, heating led to anomalous low RH (Fig. 4.39).

The dynamical drivers related to RH in this region were found in Section 4.1.2: the decrease in RH over the northwestern part of eastern Brazil in the late period could be significantly linked to a northward shift of the ITCZ rain belt and a decreased tropical moisture transport (positive [negative] correlation between RH [the MEI] and u10, a negative [positive] correlation between RH [the MEI] and si10; Fig. 4.4 and correlations for the MEI not shown; O'Hare et al., 2014; Utida et al., 2019). These winds show a negative u10 and a positive si10 trend in the late period. The regional SST-RH correlations are significantly positive off the coast of the region, and there is a negative trend in SSTs in this area in the late period. The MEI-SST correlations in the Atlantic Ocean around the northwest of eastern Brazil correlations are not significant (not shown).

Neither the q nor T in the northwestern part of eastern Brazil significantly increased in the late period (Figs. S5 and S6), nor the MEI shows a significant trend over the full period (Table 4.5). Above all, the latter would suggest that the negative RH trend over the full period cannot be explained by the ENSO (dark blue thin dashed line in Fig. 4.39). Also, in the late period, there is no significant trend in the MEI (0.36, $p = 0.44$). However, the increasing strength of El Niño events in the late period (Bayr et al., 2014) with low RH values during El Niño in 2015–2016 suggests that the ENSO can explain both the interannual variability of the regional RH and its trend party (compare Fig. 1.11: dryer and warmer conditions over northern Brazil during El Niño). The subregion and its temporal RH course closely represent the entire region of eastern Brazil (Fig. 4.39).

In the northwestern subregion of eastern Brazil, the observation RH (light blue) correlate with the estimated RH over the full period (dark blue; $r = 0.44$, $p = 0.02$), i.e. the MEI can represent interannual variability in the subregion. This correlation is reinforced over the late period ($r = 0.55$, $p = 0.03$). However, MEI's representation of the RH interannual variability is not transferable to the full region of eastern Brazil ($r = 0.18$, $p = 0.51$; late period: $r = 0.24$, $p = 0.49$; Fig. 4.39). In eastern Brazil and its subregion, the estimated RH does not decrease as observed and represents only 20.57%

of the observed trend. The MEI does not represent the RH trend either over the full or the late period. Additional drivers such as primary physical drivers and other modes or terrestrial changes should be found to represent and explain regional RH in eastern Brazil.

A potential influence is the variability of tropical south Atlantic SST adjacent to the coast of the northern part of the region stretching eastwards across the central Atlantic (Table 4.5), which have been found to drive dryness over northeastern Brazil drive (Kayano & Andreoli, 2006). For the entire eastern Brazil region (DJF), positive SST-RH correlations and a negative SST trend around the region's Atlantic coast in the late period could be found (Fig. 4.4). In the early period, these SSTs increased. It seems that ENSO explains interannual RH variability but not the trend, and these SST trends may potentially explain some of this trend.

This subregion shows an example that the change in RH results from insignificantly small changes of q and T due to changes in winds and SST in different locations. The change in winds is likely associated with the ENSO and through MEI correlations considering a link between tropical Pacific and Atlantic SST. The combination of additional drivers on different scales is visible in this subregion, consisting of only three grid boxes. It is an excellent example of the need for some analysis at the grid box level. However, the analysis at grid box level or already at a sub-regional level is beyond the scope of this work.

ENSO's impact with temporal lags

It is known that the ENSO has worldwide teleconnections (Alexander et al., 2002; Gershunov & Barnett, 1998). These teleconnections can occur with a time delay to the ENSO event. With a time lag of up to -6 months, the strongest ($r > 0.5$) correlations between MEI and following regional RHs were determined. For RH in eastern Brazil (JJA; $r = 0.56$, $p = 0.02$, 4/12 grid boxes significant) and Tibet (SON; $r = -0.62$, $p = 0.01$, 9/12 grid boxes significant), correlations with the MEI with a lag of -4 month (February-March-April and May-June-July, respectively) are significant, and for RH in DJF in southwestern Greenland ($r = -0.55$, $p = 0.02$; 3/6 grid boxes significant) and eastern Canada ($r = -0.59$, $p = 0.01$, 5/10 grid boxes significant) with a lag of -6 months (i.e. MEI in JJA).

RH over eastern Brazil (JJA) correlates in the JJA with MEI from February-March-April and fulfils all ECs (Table 4.12). However, only half of the grid boxes with a significant correlation occur in grid boxes with a significant RH trend in the late period (Figs. 3.3 and 4.33). Due to the spatial mismatch in eastern Brazil and the low area of agreement, the correlation is not investigated further. RH over Tibet (SON) correlate only in the late period and not over the full period with the MEI in May-June-July. Song et al. (2018a) found a weak negative maximum lag correlation between the ENSO and precipitation, which could be linked to decreased RH. Eastern Canada (DJF) is the

Table 4.12: As for Table 4.9, for the MEI with monthly lags.

Region	Season, lag of the ENSO in months	Corr coeff	Ratio	EC1 (0.33 grid boxes)	EC2 (r>0.5)	EC3 (full period)
E Brazil	**JJA, -4**	**0.56****	**4/12**	**yes**	**yes**	**yes**
Tibet	SON, -4	-0.62**	9/12	yes	yes	no
Mongolia	DJF, -6	-0.45*	8/15	yes	no	no
Greenland	DJF, -6	-0.55**	3/6	yes	yes	no
ECanada	**DJF, -6**	**-0.59****	**5/10**	**yes**	**yes**	**yes**

only region in which RH correlates with a lagged ENSO (MEI in JJA) and fulfils all ECs (Table 4.12). In the early period, MEI-RH correlations in eastern Canada are not significant (Table 4.13).

Table 4.13: As for Table 4.10, for the MEI with a lag of -6 months, i.e. in JJA the previous year, and seasonal correlations in DJF over eastern Canada.

ECanada, DJF; lag -6	RH trend in season	MEI-RH corr (p; ratio)	MEI-q corr (p; ratio)	MEI-T corr (p; ratio)
Early period	DJF	-0.21 (0.3; 1/10)	-0.1 (0.63; 0/10)	-0.18 (0.38; 1/10)
Late period	DJF**	**-0.59 (0.01**; 5/10)**	**-0.55 (0.02**; 8/10)**	**-0.61 (0.01**; 7/10)**

In JJA, the mean MEI hardly changes between the late and the early period (0.36, 0.37, respectively) and is mostly positive (Table 4.5). During the positive ENSO phase (El Niño), there are anomalously low q and T, thus, RH is expected and vice versa, due to negative correlations with the MEI (Table 4.13). In particular, the negative correlation is expressed in 2010 during the La Niña and high RH. As for the AO, negative MEI values seem to have a more decisive influence on RH than positive values (Fig. 4.40).

In eastern Canada, the correlation between the observed (light blue) and the estimated RH (dark blue) is insignificant over the full period ($r = 0.2$, $p = 0.29$) and late period ($r = 0.32$, $p = 0.23$), i.e. the MEI alone is able to represent neither the regional RH interannual variability nor the RH trend as the latter has different signs for the observations and the estimates (Fig. 4.40).

Without lags, the AO in DJF is associated with the eastern Canadian interannual RH variability, but not with the RH trend (Section 4.3). The AO and the ENSO behaviour show similar phases in 2010–2016 at different seasons and correlation with regional RH (compare Figs. 4.38 and 4.40). It is likely that both modes act on RH. This study

does not provide an analysis of the decoupling of the impact of AO and ENSO or the interaction of modes.
In this context, it should be noted that there is also an AO-RH correlation for southwestern Greenland in DJF (Section 4.3) but no MEI-RH correlation at the same time but with a lag of -6 months. There is a number of potential reasons for differences in trends, and one of the differences between RH-drivers in eastern Canada versus southwestern Greenland could be the ENSO. It is challenging to pursue the coupling with RH in a time delay since it is unclear which lags the individual physical primary variables enter.

The IPO and RH over eastern Brazil

Correlations between the IPO and RH in three regions fulfil all ECs (Table 4.9). The grid boxes with significant correlations do not widespread match the significant RH trend in the late period in either Tibet or the Red Sea region or Mongolia (all DJF) (compare Figs. 3.3 and 4.33). Like for the MEI, significant strongly negative correlations in the northwest of eastern Brazil (DJF) were found ($r = -0.7$, $p = 0.0$, 3/3 significant grid boxes; Fig. 4.33). Positive IPO events indicate low RH. In DJF, the mean IPO index in the early period is less negative (0.11) than the mean in the late period (-0.23).

Table 4.14: As for Table 4.10, for the IPO seasonal correlations in DJF over the northwest of eastern Brazil.

NW E Brazil, DJF	RH trend in season	IPO-RH corr (*p*; ratio)	IPO-*q* corr (*p*; ratio)	IPO-*T* corr (*p*; ratio)
Early period	DJF	**-0.78 (0.0**; 3/3)**	**0.45 (0.02**; 2/3)**	**0.77 (0.0**; 3/3)**
Late period	DJF**	**-0.69 (0.0**; 3/3)**	0.07 (0.79; 1/3)	**0.81 (0.0**; 3/3)**

The RH, q and T (Fig. 4.41; Table 4.14) and u10/si10 (not shown) correlations and the time series of the IPO and the MEI in DJF (Fig. 4.39) are very similar, e.g. positive in 2016. Both oscillations, on average, have changed their sign from positive to negative in the late period. The influence of IPO on regional RH is similar to that of ENSO. Also, the PDO correlates negatively with RH in the northwestern part of eastern Brazil in the late period (Fig. 4.34). The ENSO, the IPO and the PDO operate on different time scales (Section 4.2.1), which are of minor importance in the calculated correlations with detrended time series.

The IPO describes the RH interannual variability to a similar extent as by the MEI (over the full period: $r = 0.42$, $p = 0.03$; over the late period: $r = 0.55$, $p = 0.03$), and the negative RH trend in the late period is at 27% represented by the IPO.

The AMO and RH over California and eastern Canada

Eastern Canada (DJF; $r = 0.66$, $p = 0.0$, 6/10 significant grid boxes) and California (annual; $r = 0.66$, $p = 0.0$, 6/10 significant grid boxes) have the strongest large-scale correlations between the selected modes and regional RH. With a positive AMO, increased RH is expected in both regions.

The AMO shows a significant, positive trend over the full period, while in the late period, the annual and seasonal means in DJF are positive (0.17 and 0.09, respectively) and in the early period, negative (-0.13 and -0.17, respectively). In Section 4.1.5, weak links between a warm AMO (and cold ENSO/PDO) and droughts over California were found, where the AMO served as a modulator on Pacific modes (Liu et al., 2018; Mo et al., 2009; Ruprich-Robert et al., 2018). The late-period-Atlantic cooling in the upper mid-latitudes, southwest and southeast from Greenland, so-called "cold blob" for the years 2013–2015, is linked to ice sheet melting and is particularly strong in winter and spring in the late period (Frajka-Williams et al., 2017; Mooney, 2015). These regional SST anomalies are different from the actual warm AMO phase.

Table 4.15: As for Table 4.10, for the AMO seasonal (DJF) and annual correlations, respectively, over eastern Canada and California.

Region, season	**Period**	RH trend in season	AMO-RH corr (p; ratio)	AMO-q corr (p; ratio)	AMO-T corr (p; ratio)
E Canada, DJF	Early period	SON	0.29 (0.17; 2/10)	0.38 (0.06*; 3/10)	**0.51 (0.01**; 5/10)**
	Late period	SON**	**0.66 (0.00**; 6/10)**	**0.69 (0.00**; 9/10)**	**0.68 (0.00**; 10/10)**
California, annual	Early period	annual	0.24 (0.23; 0/8)	0.26 (0.19; 3/8)	0.24 (0.23; 4/8)
	Late period	annual**	**0.69 (0.00**; 7/8)**	0.4 (0.1*; 2/8)	-0.04 (0.87; 0/8)

During a positive AMO, the NH Atlantic heats up. East Canadian SSTs are above average in the late period and correlate positively with the regional RH and show a positive trend (e.g. Fig. 4.4). The strong regional q-RH and T-RH correlations (Section 3.3.2.4) reflect the strong correlations with the AMO (Table 4.15), i.e. T and q are above average in the late period during a positive AMO. There are also negative AMO-u10 and positive AMO-v10 correlations over the full and particularly in the late period indicating weaker northwesterlies towards eastern Canada matching the u10/v10 trends in Fig. 4.1. Consequently, during a positive AMO, RH increases primarily due to increased SST/T (Green et al., 2017) and q, presumably via evaporation, in the late period, supported by weaker northwesterlies which avoid inflow of cold air masses. The AMO correlations mentioned are more pronounced in the late period and less pronounced during the early period which coincides with a cooler AMO phase.

With below-average SLP in the northern part of California during a positive AMO and positive u10/v10/ si10-AMO correlations (not shown) over the full period but no significant trend in either of the primary physical variables in the late period, the correlations between the primary physical variables and RH (positive SST/u10-RH correlation over the NH tropical Atlantic, positive u10-RH correlations along the western Mexican coast towards the Pacific, negative u10-RH correlations in the Atlantic mid-latitudes, positive SLP-RH correlations over Iceland and negative SLP-RH correlations over the Atlantic mid-latitudes; Section 4.1.5) match the AMO correlations, except for the wind speed. This shows the link between the AMO and the RH, particularly in the late period, as also in Section 4.1.5 through correlations between the primary physical drivers and RH. The link concerns the interannual variability. However, it does not explain the RH trend.

Green et al. (2017) found the AMO's ocean warming and cooling linked to a shift of the ITCZ. Thus, a shift in precipitation could have contributed to a regional change in RH in lower latitudes but unlikely in the higher mid-latitudes.

In eastern Canada (DJF), the observed RH (light blue) weakly, but significantly at $p < 0.05$, correlates with the estimated RH (dark blue; $r = 0.43$, $p = 0.02$), i.e. to a certain extent, the AMO can represent interannual variability in the region over the full period (Fig. 4.42) but less over the late period ($r = 0.38$, $p = 0.19$). Due to the positive AMO trend over the full period, the eastern Canadian RH trend is represented to 88.46% of the observational trend. The late trend is represented at 22.41% only.

Despite the findings of AMO-like correlation pattern between the primary physical drivers and RH (Section 4.1.5) and RH troughs in 2007–2009 and 2014 occurring during AMO troughs (Fig. 4.42), the interannual variability of RH in California over a more extended period cannot be represented by the AMO (full period: $r = 0.11$, $p = 0.55$, late period: $r = 0.24$, $p = 0.35$). The trends of observation RH and estimated RH are of different signs, i.e. the AMO cannot explain the RH trend in California. However, the positive AMO trend over the full period (Table 4.6) and the findings by Liu et al. (2018), Mo et al. (2009) and Ruprich-Robert et al. (2018) match: a positive phase in the AMO leads to drought over the western USA. Furthermore, they found the AMO modulating the ENSO and interacting with the PDO, impacting regional precipitation and T (Mo et al., 2009). The co-impact of two modes is complex and challenging to be represented by decadal correlations, as explained in Section 4.1.5. Based on the RH troughs in 2008 (La Niña) and 2014 (El Niño), different mechanisms impacting RH change can be determined, e.g. the q decrease in 2008 and the T increase in 2014. These RH troughs might be differently strongly linked with AMO. Links with the AMO and RH could thus be established, but these require further analysis. A possible explanation of these links could benefit from analysing single-year or seasonal data to enhance the signal-to-noise ratio.

The AMO, thus, can partly explain the interannual RH variability and its trend in eastern Canada, but it is linked to only certain years in California. Note, that RH over eastern Canada in DJF correlates with the AO, and with a lag of -6 months with the MEI. However, it is under discussion whether the AMO actually exists or whether it is an artefact of anthropogenic forcing and volcanic eruptions (Mann et al., 2021; Mann et al., 2020). In addition, the positive AMO index conflicts with north Atlantic cooling (Frajka-Williams et al., 2017). Therefore, it is questionable to what extent the defined oscillation can represent regional RH.

The PNA and the PDO and RH over Scandinavia

The correlations between the PNA and PDO and RH over Scandinavia (SON) meet EC1 and EC2 but are not significant over the full period (Table 4.9). Neither regional q nor T correlates significantly with the modes (Table 4.16).

While in SON, the mean PNA in the late period is more positive (0.22) than in the early period (-0.03), the signs of the PDO are inverse (mean in the early period: 0.15, in late period: -0.31). These seasonal means do not correspond to the sign of the PDO annual mean. Both modes show no significant trend over the full period.

Table 4.16: As for Table 4.10, for PNA and PDO seasonal correlations in SON over Scandinavia.

Mode	**Period**	RH trend in season	mode-RH corr (*p*; ratio)	mode-*q* corr (*p*; ratio)	mode-*T* corr (*p*; ratio)
PNA	Early period	SON	0.07 (0.74; 0/19)	0.06 (0.76; 0/19)	-0.08 (0.69; 0/19)
	Late period	SON**	**-0.52 (0.03**; 9/19)**	-0.25 (0.32; 4/19)	-0.18 (0.48; 0/19)
PDO	Early period	SON	0.11 (0.59; 0/19)	-0.16 (0.42; 0/19)	-0.18 (0.36; 0/19)
	Late period	SON**	**-0.60 (0.01**; 10/19)**	**-0.55 (0.02**; 18/19)**	**-0.47 (0.05**; 14/19)**

The positive SST trend over the Barents Sea in the late period, which is positively linked with the regional RH, can be recognised by negative PDO-SST correlations (not shown). Positive v10-RH (Fig. S17) and negative v10-PDO correlation patterns (not shown) are also similar, while v10 shows no significant trend in the late period. There are negative (positive) SLP-RH (PDO-SLP) correlations over the Norwegian Sea with no SLP trends in the late period (Fig. S17; PDO-SLP correlations not shown). Wang and Schimel (2003) found increased precipitation during a cold/negative PDO over Scandinavia. The PNA correlations with the primary physical variables (not shown) show no agreement with those from RH .

Neither the RH interannual variability nor the RH trend over multiple decades over Scandinavia can be related to the PNA or PDO, and the correlation between the observed and the estimated RH is not significant ($r < 0.34$, $p > 0.27$). The RH peaks in 2011 alone correspond strongly with the negative PNA and PDO index (Fig. 4.43). The

RH trends can only be estimated by the PNA and PDO up to 3%.

The connection mechanisms cannot be clarified at this stage. There are known teleconnections between the tropical Pacific Ocean and higher latitudes, although this might be more established for the ENSO than the PDO.

4.4 Chapter summary and concluding remarks

Not being able to fully explain observed trends by the thermodynamic driver justifies looking at dynamical drivers acting on different spatial and temporal scales. The analysis of dynamical drivers was undertaken to explore which regions showing significant RH trends were impacted by dynamical drivers. Dynamical drivers included primary physical variables (SST, wind direction and speed, SLP) and modes of variability. Based on correlation and trend analysis this Chapter examined which sign their impact had on RH (positive, negative correlation), and how strong their impact was. Furthermore, this Chapter tried to answer whether the modes could be used to predict any of the recent RH trends by calculating the estimated RH time series using the regression coefficient. In Chapter 3, RH was found to be more strongly linked to moisture (q) than temperature (T); therefore, regional precipitation-RH correlations and precipitation trends were also identified. The strongly positive precipitation-RH correlations and SLP trends associated with wind changes on different spatial scales supported further analysis via primary physical variables, such as the SST, the wind directions u10 and v10, the wind speed and SLP for regions with the strongest RH trend.

Significant wind trends due to SLP trends in the late period were found in many regions (Section 4.1). These wind trends, especially with differences in the early and late period, served as important indicators for regional RH changes in the late period for both the six regions with the strongest annual RH trends (eastern Brazil, Tibet, the Caspian Sea, California, Mongolia and southern Africa), which have been examined in detail via correlation maps in Sections 4.1.2–4.1.7, and those with smaller RH trends. For example, in southwestern Greenland (DJF), late-period wind trends were opposite in the early period, such as a change in wind trends from increased south-westerlies in the early period to stronger northeasterly winds in the late period. Note, while the RH trend in the late period over southwestern Greenland was significantly negative, there was no significant trend in the early period. In eastern Brazil (DJF), a positive SLP trend in the southwestern Atlantic was associated with counterclockwise wind trends in the east of Rio de Janeiro, i.e. a positive southeasterly trend resulting in reduced tropical northeasterlies. Also in MAM, JJA, SON, a change in direction and strength of onshore winds to the Brazilian east coast was detected. In Tibet (SON), an increase in dry southwesterly winds in the northwest could be associated with a regional RH decrease. In southern Africa (SON), the negative late-period RH trend could be related to a negative SLP trend in the southern Indian Ocean, thus, decreased maritime northeasterly flow in the late period whereas, in the early period, a southwesterly trend towards the northeast of southern Africa was found. Further examples of wind changes in and around regions with a strong RH change were explained in Table 4.4 on the basis of Fig. 4.1. Wind trends that lead to a decrease in RH concern rather the wind direction than the wind speed. However, they do not show a discernible pattern given the regional heterogeneity in terms of prevailing winds and surrounding water bodies.

Precipitation, a result of the movement of air and moisture, and q and RH, was as would be expected, mostly positively correlated. This relationship was strongest over the mid-latitudes and in the summer hemisphere, and weakest in the winter hemisphere and around the equator in the tropics. Global precipitation-T correlations followed the T-RH correlation pattern (Sections 3.2 and 4.1.1), with mostly negative correlations and positive correlations in cold climates which might be linked to snow, leading to weaker precipitation-RH correlation. In eastern Brazil (DJF), southern Africa (SON), northwestern India (annual) and Scandinavia (JJA) there is a significant negative (and for northwestern India and Scandinavia positive) precipitation trend with positive precipitation-RH correlations in the late period, indicating that precipitation could be driving RH directly. For all four regions, correlations between the primary physical drivers and precipitation were analysed. Their patterns are similar to those between the primary physical drivers and RH, indicating that SST, wind speed and direction impact precipitation, q, and thus RH in those regions. In Tibet (MAM, JJA), Mongolia (JJA) and in Rajasthan (northwestern India, JJA) precipitation could be linked to RH with a temporal lag (significant precipitation trend but weak correlation with RH). Correlations between precipitation and RH with temporal lags were beyond the scope of this thesis. In eastern Brazil (SON) and the Caspian Sea (JJA), the interannual RH variability is driven by precipitation via dynamical drivers but there is no significant precipitation trend.

Among decadal precipitation trends, strong peaks/troughs in precipitation and seasons/years of flooding or drought are likely to determine RH in many regions. Further work could compare time series of regional and seasonal RH and precipitation to detect overlapping of strong peaks/troughs of both variables in each region.

Significant relationships were found between the primary physical variables and RH in the regions with the strongest negative RH trend in the late period. The q-driven RH in eastern Brazil in DJF and SON experienced a reduction of moist, tropical northeasterlies due to a northward shift of the ITCZ and precipitation to warmer NH tropical Atlantic SST (Section 4.1.2). The late period SH tropical Atlantic cooling at northeastern Brazil's coast could be associated with El Niño and negative MEI/IPO-RH correlations, particularly in the northern subregion in DJF (Section 4.3). The reduction of precipitation and RH centred in the northern part of this region in JJA and MAM, were associated with lower SLP in the northwest of the region towards the Amazon, and reduced northeasterlies over the ocean, thus, reduced moisture flow but increased over-land easterlies spreading drier air than normal westwards. In addition, in JJA, a reduction in southerly on-shore winds towards the southern part of the region and thus, reduced moisture flow onto land, could help explain the negative RH trend over the entire region of eastern Brazil. The wind trends are based on seasonal SLP trends: during all four seasons, there is a significant negative late period SLP trend northwest of the region. In DJF and MAM, there is a significant positive SLP trend over the region's southeast. Only in DJF, there is a significant negative SLP trend over the Atlantic in the southeast of the region strongly related to the seasonal RH decline.

In Tibet (JJA), the RH decrease could be linked to the ENSO and the IOD, in particular in the late period (Section 4.1.3). Increased SST in the central Pacific and SLP trends reducing the land-ocean SLP gradient led to weaker East Asia and Indian monsoons, thus, reduced moisture inflow, i.e. precipitation, with a more significant ENSO-like pattern in the late period. In SON, local northeastwards wind trends in the region's northwest match spatially the subregional RH trend; however, they are not significant. A negative SLP trend in the region's east and northeast is associated with regional increased T. In both seasons, the regional positive T trend could indicate that this region appears to be more driven by a change in T than a change in q.

In the north of Mongolia, the precipitation-poor rainy season JJA set favourable conditions for droughts. In DJF, there are strong correlations between the primary physical variables and q and T, but weaker for RH. La Niña-related, insignificant ($p > 0.05$) local wind trends indicated increased flow out/decreased flow into the region due to a southwards shift of the ITCZ and the East Asian monsoon towards warmer SST/T (Section 4.1.6). In MAM, insignificant decreased local northwesterlies/increased southeasterlies in the late period were in contrast to the early period, which could describe the interannual RH variability but not its trend. In Mongolia, increasing land cover/land use (LCLU) changes (coal mining, grazing, desertification) might have impacted RH (see Chapter 5). Both RH in Tibet and Mongolia could be linked to monsoon systems, which were not further analysed in this study.

Over the Caspian Sea region (JJA) experienced reduced precipitation associated with ENSO-linked increased winds (Section 4.1.4). These had the effect of delocating the precipitation, decreasing the chargement of the Caspian Sea by the Volga river and resulting in a shrinking lake surface. This shrinking is also associated with increased lake surface and surrounding land surface T and evaporation. The drying is associated with the inflow of hot, dry air from the Iranian highlands in the south. The difference in warming between the lake surface T and surrounding land surface is effectively a localised element of the global thermodynamical driver of RH decline relating to faster land warming versus slower ocean warming. Here, the process appears to be enhanced by aspects of dynamical drivers related to airflow and precipitation (Section 4.1.1). An interesting result is that land cover changes have been observed (Arpe et al., 2012; Rodell et al., 2018; Wang et al., 2018) in response to the reduced precipitation. As discussed in Chapter 5, a decrease in vegetation is a terrestrial driver component that can further contribute to RH decline.

With a reduction in precipitation in the southern Africa rainy season (DJF), RH in JJA was found to decrease due to an increased easterly wind component in the east leading to an offshore effect (Section 4.1.7). In SON, the low rainfall rates are associated with high Indian Ocean SST, El Niño, the SAM, decreased easterlies over the southeast of the region and increased easterly offshore winds due to abnormal low pressure.

A key line of investigation was the identification of any differences in trends and correlations between the early and late periods that could be contributing to the late period change in RH. Either a change in circulation pattern between the early and the late periods, or late period trend in primary physical variables correlating with RH, might be linked to regional RH trends. Some evidence of this was found but not for all regions with a strong RH trend. For example, in Mongolia (MAM) and southern Africa (SON), there are large differences in circulation patterns linked to regional RH (direction of correlations) between the early and the late period, indicating that different mechanisms drive RH (in the case of Mongolia, an increase RH in the early period and a decrease in the late period). This is not the case, for example, in eastern Brazil (DJF) and the Caspian Sea region (JJA), where only the correlation strength is higher in the late period compared to the early period, rather than of a different direction. Therefore, some regions, e.g. Mongolia, would benefit from analysing the early period, i.e. a strong but insignificant wetting RH trend, which is explained through dynamical drivers at a place different from the late period.

The seasonal correlation and trend analysis explained the impact of dynamical drivers on RH for almost all of the explored regions (eastern Brazil, Tibet (JJA), the Caspian Sea, southern Africa). For Mongolia (DJF, MAM) and California (annual), no evidence of dynamical drivers on RH could be found due to a lack of significant correlations and, particularly, trends in primary physical variables. For California (annual dominated by DJF, with DJF correlations as the strongest seasonal correlations; not shown), a stronger link of wind directions over the Atlantic and increased SST on the Pacific American west coast were found instead of a trend in onshore westerlies. The SSTs correlate strongly positively with q and T but not with RH, which might indicate the long-term impact of thermodynamic drivers; also, an AO-like SLP correlation pattern was visible in the late period. While in Mongolia (DJF), the correlations between the primary physical drivers and q and T were much stronger than for RH, a local increase in high-pressure systems over the region, thus, an anticyclonic wind trend could explain the RH decrease in the late period; however, the trend was not significant. For Mongolia (MAM), the analysis of links between primary physical variables and RH was not straightforward either due to a lack of trends and disagreement in direction with the correlations. The drought in these regions was due to precipitation deficits in other seasons. This lead to decreasing terrestrial water storage and vegetation changes (a change in LCLU) over the region that could further contribute to decreasing RH (see Chapter 5). In Tibet (SON), local wind trends were insignificant.

Links to the modes of variability could be found, mainly through SST and SLP correlation patterns with RH, because these two primary physical variables generally serve to calculate indices of modes. The strongest links were determined via a ranking.

Due to the large number of potential regions to study in more detail, a ranking method was developed to identify the regions with the strongest links between modes of variability and regional RH. This ranking identified that interannual RH variability in Tibet, southwestern Greenland, eastern Canada, Scandinavia and eastern Brazil would be most impacted by modes of variability. Modes of variability most impacting regions with a strong RH trend were the AO, modes covering the big oceans, i.e. in the Pacific, the ENSO and the IPO, and in the Atlantic, the AMO, and the SAM. RH-correlations with the latter turned out not to meet all the eligibility criteria (EC; Section 4.3) and, thus, the impact of the SAM on RH were not further analysed. The choice of the ECs was based on the significance and strength of correlations on the late and the full period. This choice ruled out further analysis of some correlations, for example, for regions in which a mode of variability impacted regional RH only over a certain period such as RH over Tibet and the MEI. This could be because one phase of the mode has been stronger or might be better captured than the other (e.g. El Niño with drier and warmer conditions over northern Brazil and no precipitation impact of La Niña [Fig. 1.11]), or might interfere differently with another mode in that period. The EC assured that only widespread significant correlations would be taken into account. However, a successful deviation from the EC was looking at clustered grid boxes of strong correlations on Figs. 4.30–4.37, so that RH in the northwestern subregion of eastern Brazil (DJF) could be successfully linked to the ENSO/IPO. In the example of eastern Brazil (DJF), correlations with q and T showed a strong ENSO-like SST pattern. As ENSO has been driving both q and T to a similar extent, the mode's impact on RH was less strong. Therefore, it is essential to look first at RH correlations and then try to explain the impact of variables and modes via the latter's impact on q and T. Modes of variability might explain why winds possibly do only occur in one period and not in the other.

Modes of variability were found to strongly drive q and T in some regions, e.g. in ENSO-like SST-q/T correlation patterns in eastern Brazil (DJF; Fig. 4.5), but according to the Clausius-Clapeyron equation, the ENSO would not necessarily impact regional RH if q and T changed to an equal extent under neither water nor energy-limited conditions. In other regions (e.g. the northwestern subregion of eastern Brazil in DJF with the ENSO), modes of variability were found to be linked with the interannual RH variability but not causing their trends. That might be because the mode did not show a significant trend. Only the AMO, the SAM and the IOD significantly increased in the full period. The MEI, IPO, PDO significantly increased in the late period indicating increased more positive years towards the end of the late period, with a strong La Niña-event at the beginning of the late period around 2000 finishing the late period with a strong El Niño event in 2015–2016. The study was not set up for non-linear relationships, and the trends and regressions, and also the detrending, are based on linear regressions, which might cause difficulties for modes due to their oscillating behaviour (e.g. the AMO; Fig. 4.28). Therefore, the average sign of mode in a period was calculated as the early/late period might have been a period where a mode has been more positive/negative/neutral than in the late/early period. This makes sense for modes of long periodicity, such as the PDO or the AMO. Looking at the decadal mean combined with an identified correlation between that mode and RH was then useful.

Only the AMO was found to be a strong predictor for RH trends: the AMO correlated positively with RH in California and eastern Canada (DJF) only in the late period (Section 4.3). For eastern Canada (DJF), the AMO was able to represent both the interannual RH variability and to 88% the positive RH trend in the late period associated with increased SST and increased onshore easterlies/decreased westerlies. Low-frequency modes as the AMO might stay in one phase for a longer time, thus, might have a perseverative impact on RH. Independently of the discussion as to whether the AMO is a real mode and not only an artefact of global warming (Mann et al., 2021; Mann et al., 2020), this study found the importance of Atlantic Ocean SST on RH (also see the ITCZ shift impacting Brazil's RH).

The AO (in winter similar to the NAO/NAM, Rogers and McHugh, 2002; negative RH correlation in eastern Canada [DJF] and southwestern Greenland [DJF]; Section 4.3) and the MEI/IPO without temporal lags (strongly negative RH correlation in the northwestern subregion of eastern Brazil [DJF]; Chapter 4.3) impacted regional RH to a similar extent in the early and the late period and might be a contributing factor. They could represent some parts of the regional RH variability but only the MEI could represent the regional RH trend to 21% through SST variability in the tropical Atlantic Ocean. Neither the lagged MEI (negative -6 months MEI-RH correlation in eastern Canada [DJF] only in the late period; Section 4.3) nor the PNA nor the PDO (negative RH correlation with Scandinavia [SON] only in the late period) were able to represent interannual RH variability or the RH trend in the late period. It is important to note that modes of variability have been defined for other reasons – often for characterising periods of unusual temperature or precipitation, and not specifically for looking at RH over a certain region. This could make the analysis of the role of the modes less conclusive and supports the exploration of the primary variables in the first instance.

The correlation analysis allowed a comparison of the contribution of various modes over the same or different periods of time. Suppose a mode-RH correlation coefficient is very (moderately) strong, such as the MEI/IPO on the northwestern subregion of eastern Brazil (DJF); in that case, other modes or drivers might be expected to contribute less (more). The stronger the correlations, the more sense it makes to calculate regression coefficients. The contribution from various modes in various phases could plausibly drive the RH peaks and troughs collectively, probably alongside other drivers, too. The trend direction could be driven by a few events only. Note, no two events are the same. Further work could explore these events via composite-analysis. As seen in the correlation analysis for the primary physical drivers, in some regions, more than one driver or mode of variability influences a given region. For example, RH over eastern Canada (DJF) with a strong RH peak in 2010 correlates negatively with the AO ($r = -0.51$;

negative phase in 2010), the ENSO ($r = -0.59$; La Niña in 2010) and strongest with the AMO ($r = 0.66$; warm/positive phase in 2010). SLP/SST-RH correlation maps helped quantify the impact of the links and how they combine, leading to a change in RH and disentangling if some modes are more responsible for a change in q while another would be more responsible for a change in T.
Although ENSO had a strong influence on the regional interannual RH variability and its trend, it was particularly phase-dependent in combination with other modes; climate impacts of ENSO differ between events and ENSO signals are not quite stable in teleconnected areas. Therefore, the impact of the ENSO on RH overall is quantitatively very little. Analytically, this study is unable to decouple the impact of modes on regional RH. The interplay between modes was important, for example, over eastern Brazil cold ENSO conditions combined with warm AMO conditions. Other studies have found global warming to enhance El Niño conditions (Bayr et al., 2014), have a negative feedback on Indian monsoons (Douville et al., 2021), as well as to enhance Modoki-Events (Yang et al., 2012). This study was not able to decouple the effects of modes on regional RH specifically. Another example is California: during El Niño events, the jet stream lies a bit further south. Simultaneous negative phases of the AO, when the warm pole in the tropical Pacific is in a slightly different place, lead to a jet stream shift that will be slightly different between ENSO events impacting the region differently. A separate analysis in the early and the late period or for specific RH peaks and troughs could be done as using the full range of 45 years might lead to loss of information whenever the mode is in a neutral state.

As with the example of the impact of AMO on RH in eastern Canada (positive correlation only in the late period), the temporal length of a significant correlation (only over two decades, i.e. the late period, instead of over the full period) does not provide any information about whether the oscillation drives the interannual RH variability or trend. The third ECs could have been dropped. Only the ENSO/IPO showed strong correlations with RH in the northwestern subregion of eastern Brazil over the early, the late and the full period.

Low HadISDH data coverage over eastern Brazil was particularly challenging, and regional heterogeneity in RH trends and RH-correlations with q and T (e.g. Mongolia [DJF, MAM], southern Africa [JJA]) did not help the correlation analysis as it was based on regional averages. Trends or correlations with different signs or of different strength within a region mean that the impact of primary physical drivers and modes on RH might be offset. For example, the SAM impacts only the very southern tip of southern Africa. As moisture and temperature inflow to southern Africa comes from two large different circulation patterns (easterlies towards the east coast and southerlies towards the south coast touching the west coast), trends in winds and their impact on subregional RH were challenging to detect. As for the spatial heterogeneity, it would also benefit the analysis to use increased temporal resolution. Firstly, for example, in California, the correlation analysis is based on annual values, which might offset seasonal drivers, particularly modes which act seasonally. The four standard seasons might not match the resolution of circulation patterns, modes or monsoon seasons. Secondly, the early and the late period include several decades in which the signal of single years or shorter periods of strong events (e.g. droughts) and modes (e.g. El Niño in 2015–2016) might be averaged out. In some cases, however, these events were very strong and impactful so that the analysis still represented them in trends or correlations. Clearly, interannual variability in the dynamical drivers is large and this is important for interannual variability in RH.

Wind speed in terms of evaporation and RH over the region was not taken into account, as in this case, wind speed can be considered a component of the terrestrial drivers. Positive si10 trends such as over eastern Brazil (DJF, JJA, SON), the northern part of eastern Brazil (MAM), southeastern Tibet (JJA), southern Tibet (SON), southeastern Africa (JJA), central southern Africa (SON), i.e. enhanced wind speed over land, could lead to increased evaporation if enough moisture is available or distributing dry air if not enough moisture is available. Negative si10 trends, i.e. decreased wind speed over land, was found in southeast Mongolia (MAM). This relationship could be explained in Chapter 5. Note that ERA-Interim wind speed trends differ from observation-based records: the latter have shown widespread decreases in wind speed over land until around 2010 and then a recovery (Azorin-Molina et al., 2021).

A summary of principal drivers in each region can be found in Section 6.2.1.

For regions with topographic heterogeneity, for example, Tibet, it may have been useful to use ERA-Interim 500 hPa for a clearer synoptic-scale flow.

In conclusion, the Chapter found strong evidence that some dynamical drivers contribute to RH changes in regions with strong RH trends. Modes (e.g. the AMO on winter RH in eastern Canada) and, particularly, their combination (e.g. cold ENSO and warm AMO on RH in the northwestern subregion of eastern Brazil), can explain large parts of the global RH trend as Pacific and Atlantic modes have global impacts, e.g. on the monsoon (e.g. southwards shift of monsoonal rain away from Mongolia during La Niña). Monsoon indices were not analysed. Seasons and temporal lags need to be taken into account. Dynamics that are explained by the modes are more extensive and possibly have a stronger/more distinguished pattern. More local dynamics do not have to be coupled with big modes, but can also have to do with regional or sub-regional things, e.g. terrestrial drivers, deforestation, shrinking lakes near weather stations etc. which would need to include land cover classification. The effects of climate change, in terms of increasing the frequency and intensity of modes of variability (e.g. simulated weaker spatial amplitudes and increased temporal frequency for the IPO and PDO; Xu and Hu, 2018), thus, their superposition with other modes, the impact on general atmospheric and oceanic circulations (e.g. weakening of the jet stream) and prolonged seasons (e.g. earlier greening) need to be considered. This study did not quantify dynamical drivers but detected their potential. Although dynamical drivers show a global impact on RH, not in all regions and seasons with strong RH trends, they were enough to explain regional RH changes. This study found evidence that the effects of dynamical drives could link to terrestrial drivers likely in regions like California or Mongolia. Only seasons with a drying trend were analysed but not other seasons, which might have an impact then on the following seasons, e.g. less rain in the rainy season could result in no change during the season but in less groundwater storage or less vegetation resulting in poorer water availability later on in the year, in the season with a drying trend. Thus, dynamical drivers might impact the land cover, i.e. terrestrial drivers which then again impact RH (e.g. Mongolia; see Chapter 5). The next step would be quantifying the impact of different modes acting on a region and changing RH and the impact compared to the other drivers.

Most notably, this study expected to find a more spatially and temporally widespread signal of a relationship between the modes of variability on RH, especially for the larger-scale modes such as ENSO. However, no such evidence could be detected. Instead, this study found that each region is unique in its exposure to the various modes and primary physical variables, and combination thereof. This study found that RH could be linked to various combinations of dynamical drivers on a regional and seasonal scale and that those combinations and relationships were also unique to each region. It is clear that dynamical drivers do play an important role in changing RH but that this is small in spatial and temporal scale, contributing to the large spatial and temporal variability of RH compared to other variables.

5 Terrestrial drivers

In many regions (e.g., eastern Brazil, the Caspian Sea region, California, and southern Africa), changes in relative humidity (RH) were found to be related to dynamical drivers, especially changes in sea surface temperature (SST), wind directions, and sea level pressure (SLP) (Chapter 4). A clear connection between modes of variability and RH resulted mainly from SST and SLP patterns. Only in the case of eastern Canada could a mode – namely, the Atlantic Multidecadal Oscillation (AMO) – explain the regional RH trend. The impact of the El Niño Southern Oscillation (ENSO) and the Interdecadal Pacific Oscillation (IPO) on tropical Atlantic SST and northeasterly tradewinds were found to be influencing RH over eastern Brazil. There was no evidence of dynamical drivers on RH trends over Tibet, California, and Mongolia. Particularly for the latter three regions but also as a contributing factor in other regions with a strong RH trend, the search continues for an explanation of the changes in RH based on changes in land evaporation in the latter three regions in particular, but as well in other regions as a contributing factor.

For the purpose of this thesis, terrestrial drivers are defined as two processes. First, there are the physiological effects of reduced stomatal conductance from increased CO_2, or reduced water availability, which could lead to decreases in RH via decreased evapotranspiration (E_t). Second, there are structural changes in the land cover or land use (LCLU) that lead to changes in evaporation (E) more generally and its related fractions. The terrestrial drivers are highly complex, with several interactions and feedback across the various processes. Additionally, the processes themselves can be affected by RH.

Evaporation is the vertical process that connects the land with atmospheric humidity and enriches it with water. Specific humidity (q) has a particularly prominent role in RH, as was shown in Chapter 3 (Fig. 3.8). A change in land evaporation causes a change in latent (q) and sensible heat (air temperature, T), which can influence near-surface RH. An E_t change over land is driven largely by changes in the amount, type, and stomatal behaviour of vegetation, in combination with soil moisture availability. There are also understandable leads and lags. According to Grossiord et al. (2020) and Gedney et al. (2006), if decreasing RH is driven by non-local processes (thermodynamic or dynamical drivers), the resulting increase in vapour pressure deficit (VPD) could drive a linear or non-linear increase in E_t, even if stomata are closing simultaneously due to heat, water, or stress from elevated CO_2 concentrations. Under limited water availability, soil water would be expected to be depleted and runoff to decrease. This scenario may be manifest as negative E_t-RH correlations. However, Xiao et al. (2020b) linked decreasing RH to small decreases in E_t because it induced further stomata closure in response to water stress. If local terrestrial drivers, such as deforestation, habitat modification (including invasive species), or CO_2 fertilisation, are contributing to a declining RH, specific types of LCLU are expected to change E_t, drive it or strengthen a decrease in it. In this case, soil water and runoff would be expected to increase: see, for example, the detection by Gedney et al. (2006) of a direct CO_2 effect in continental river runoff records. This scenario is generally associated with positive E_t-RH correlations. Clearly, the correlation of E_t with RH can be complex and dependent on the type and location of the terrestrial driver.

This Chapter uses correlation maps with integrated changes in the evaporation rates to help identify regions in which there are clear relationships with RH over the late period (2000–2017). For the analysis of correlations and trends, a larger significance ($p < 0.1$) was chosen, as data for variables considered terrestrial drivers are of larger variability. E was separated into its various fractions, and the evidence for potential terrestrial drivers is explored to identify whether they may be contributing to the change in RH or responding to it (Section 5.1). Correlation patterns are examined on the global and regional level, the relationship with q and T clarified, and strong trend features that support or contradict the theory are identified. An overview of the regional distribution of evaporation and its fractions supports the estimation. Following this, the causes of the evaporation change are explored (Section 5.2). Evaporation rates change with gradients of temperature and moisture, wind patterns, and surface material. As the impact of thermodynamic and dynamical drivers has already been explored, changes in water availability (surface soil moisture and root-zone soil moisture [Section 5.2.1] and total terrestrial water storage [TWS; Section 5.2.2]) and land cover (NDVI [Section 5.3]) remain for analysis. NDVI changes might indicate, for example, greening or deforestation, or simply a change in LCLU.

Furthermore, the impact of CO_2 on vegetation and, thus, its role in evaporation and RH is analysed. In the investigation of this coupling, the HadGEM2-ES model is used to help assess the effects of a rise in CO_2 – via radiative forcing, on one hand, and on the other as a physiological influence on the vegetation, via the stomatal conductance and a CO_2-fertilisation of growth (Section 5.4).

Section 5.5 concludes with a discussion of how the totality of terrestrial drivers can explain the regional and global RH change.

5.1 The interannual relationship between evaporation and RH

Assuming that terrestrial evaporation contributes heavily to RH over land, this section clarifies the strength and sign of the E-RH correlation depending on location and season. To identify how evaporation affects RH, global correlation maps of detrended E – including its various E fractions and RH, q and T, over the full period (1980–2017) – were created (Figs. 5.1 to 5.6). In a physical, or well-coupled system, open water evaporation (E_w) would be expected to correlate negatively with RH, if T increase relatively stronger than the evaporation rate (q). Taking E_w as the simplest fraction of evaporation, this investigation asks how land evaporation differently affects RH when there is a biological layer on top of the system. A global overview of the correlations for the four standard seasons is given. Afterwards, the significant ($p < 0.1$) and moderate to strong ($r \geq 0.5$) correlations are analysed, with regard to evaporation trends at the regional and subregional levels. If there is a strong E-RH correlation and a trend in E, E is considered a reason for the change in RH. The various E fractions are separately quantified for each region to determine whether there is a dominant fraction affecting regional RH.

At the annual level, E-RH correlate strongly positively, especially in the mid-latitudes, i.e. decreased E with decreased RH, while higher latitudes, eastern USA and eastern and southeastern Asia are weakly or negatively correlated (Fig. 5.1). Both positive and weak/negative E-RH correlations are particularly strong in June-July-August (JJA). The main message from these plots is the opposition to T: for the most part, where T correlates strongly positively, RH correlates weakly or strongly negatively, and vice versa. E-q correlations are mostly positive everywhere. In December-January-February (DJF), E correlates negatively with RH, q and T in the NH high latitudes.

The E-RH correlations largely mirror the E_t-RH correlations, as E_t is expected to be the largest E component over land. Negative E_t-RH correlations are weaker in DJF and more pronounced in JJA, due to the high vegetation density. The E_t-q correlations are stronger than E-q correlations (Fig. 5.2).

For interception loss (E_i), which this study expects to play a smaller role than E_t in RH, the E_i-RH correlation is positive and most strongly pronounced in JJA. As with E_t, this characteristic can be assigned to the strong plant growth in the boreal summer on the NH. E_i-q and E_i-T correlate similarly to their respective E and E_t correlations, but much less strongly (Fig. 5.3).

By definition, bare-soil evaporation (E_b) is only relevant where there is exposed unvegetated ground, so it is more regionally patchy than the other E fractions. Relationships typically have less pronounced latitudinal patterns (Fig. 5.4). E_b-RH and E_b-q correlate positively for the most part, especially in the mid-latitudes. As for the other E fractions, the E_b-T correlations tend to be more negative than for q and RH, but also more spatially variable.

For E_w, with a few exceptions, E_w-RH correlate strongly negatively, especially in JJA, in the NH, and in DJF, in the SH, i.e. increased E_w with decreased RH (Fig. 5.5). The correlation contrasts with the positive E_w-T correlation, i.e. increased E_w with increased RH, while weaker and mostly positive E_w-q correlations play a subordinate role.

For snow sublimation evaporation (E_s), there are obvious spatial limitations related to seasonal and latitudinal snow cover. Correlations between E_s-RH are only strongly negative in DJF in the high latitudes (Fig. 5.6), where widespread snow cover is globally at its highest. The correlation is supported by the even stronger, negative E_s-q and E_s-T correlations.

Table 5.1: Overview of global correlation pattern between the detrended GLEAM E, E_t, E_i, E_b, E_w and E_s and HadISDH RH, q and T anomalies.

Correlation	E, Et	Ei	Eb	Ew	Es (DJF, high-lats)
RH	+ve; high latitudes -ve (in particular in JJA)	+ve	+ve	-ve	-ve
q	+ve	+ve	+ve	NH: +ve, SH:-ve	-ve
T	Mid-to-low latitudes -ve, high latitudes +ve except for DJF. Generally, opposite to E-RH and Et-RH correlations but similar in DJF in the NH	-ve	-ve	+ve	-ve

Evaporation and different evaporation fractions correlate differently with RH, as a result of the combination of evaporation correlations with q and T (Table 5.1). While E, E_t, E_i, and E_b mainly positively correlate with RH, E_w and E_s mainly correlate negatively. E and E_t have similar patterns to one another in their RH, q and T correlations.

The relationship between E and RH appears to be weaker in the high latitudes, where E-T and E_t-T correlations are positive and usually strong, especially in JJA. RH correlations are stronger in the mid-to-low latitudes where E-T and E_t-T correlations are weak and/or negative. For E_i and E_b, the latitudinal differences are less clear.

Plausibly, a regional or sub-regional strong evaporation-RH correlation plus an evaporation trend in the late period could drive, or at least contribute to changes in RH. This is the case in the regions of eastern Brazil (DJF), southern Africa (September-October-November [SON]), Scandinavia (JJA) and northwestern India (annual) (Fig. 5.7). The first three regions and seasons experienced negative RH and evaporation trends in the late period, whereas the latter two experienced positive late-period trends. Since the strength of the correlations in a region is often not homogeneously distributed, the analysis is partly focused on the subregional level.

Of the regions and seasons in which significant negative late-period trends in RH have been found (Table 3.3), eastern Brazil (SON), Tibet (JJA) and Mongolia (DJF, March-April-May [MAM]) exhibit notable evaporation correlations that are either not strong enough ($r < 0.5$), do not correspond to the direction of the subregional RH trend, or do not combine with a significant evaporation trend. These are not discussed any further.

In the southwestern part of eastern Brazil, in DJF, E-RH, E_t-RH, and E_w-RH correlate significantly strongly negatively over both the early (1980–1999) and late periods and during the full period (Figs. 5.7, 5.8 and 5.11). In the full period, the E-q, E_t-q, and E_w-q correlations are significant and weakly negative; the E-T, E_t-T, and E_w-T correlations are significant and weakly positive (Figs. 5.1, 5.1 and 5.5). In the late period, E, E_t and E_w all show a positive trend while E_b significantly decreases. In addition to the decreasing RH trend during the late period, T does not show a significant trend and q decreases significantly. While the E-RH correlation and the E trend are only significant in one grid box, both the E_t-RH and E_w-RH correlations and their trends are widespread over the southern region.

Following Grossiord et al. (2020) and Gedney et al. (2006), negative correlations with RH and positive trends in E, E_t and E_w may indicate the presence of non-local processes driving changes in RH that lead to changes in evaporation. This would suggest that terrestrial drivers are not significantly influencing this region and season. The negative E_b trend could indicate a transformation from bare soil to open bodies of water or increased greening in the subregion, which may be detected through a change in the NDVI (Section 5.3). The land cover in the grid box is a mosaic of cropland and natural vegetation in the late period (Pan et al., 2018). Using data products BU MODIS C6 and SPOT/PROBA-V, Cortés et al. (2021) found no LAI trend since 2000, thus this does not appear to be the cause of decreasing E_b. Due to the small size of the sub-region, no further references to any theses can be made at this point, and the individual evaporation fraction as a proportion of total E is not calculated.

In the region of the Caspian Sea in JJA, E_w-RH correlate significantly strongly negatively over the early, late and full periods (Fig. 5.11). The E_w-T correlations are opposite and strongly positive, while the E_w-q correlations are weak. Over the late period, the E_w trend is positive. The negative E_w-RH correlation and positive E_w trend extend widely to the west across Europe. E-RH, E_t-RH and E_b-RH are significantly strongly positively correlated, but E, E_t, and E_b do not significantly ($p > 0.1$) change in the late period (Figs. 5.7, 5.8 and 5.10). In the early period, the E_w-RH correlation is somewhat weaker, and E_w shows no significant trend.

Alongside decreasing RH, q significantly decreased while T significantly increased. As in eastern Brazil, the negative E_w-RH correlations and positive E_w trends suggest non-local and non-terrestrial drivers affecting q, T and RH – and, in turn, influencing E_w. Increasing T could lead to increasing E_w, but this may not be sufficient to maintain RH, which would then consequently decrease. In the early period, T did not change significantly (Figs. 3.7 and 3.12). The significantly strongly negative precipitation trend in the late period (Section 4.1.1) also suggests that the observed decrease in the Caspian Sea endorheic basin since 2005 is due to increased E_w, resulting in surface and soil water loss (Wang et al., 2018). The water body cannot be replenished by rain. E_w was calculated to make up 12% of the total E in the entire region and is, therefore, an essential evaporation fraction after E_t.

In the region of southern Africa in JJA, the negative RH trend is concentrated in the northeast. There (in two grid boxes), E_w-RH correlates significantly strongly negatively over both the late and full period (Fig. 5.11). E_w-T correlations are significant but weakly positive, while E_w-q correlations are not significant (Fig. 5.5). Over the late period, the E_w trend is significantly ($p < 0.1$) positive (Fig. 5.11). Neither a significant E_w-RH correlation nor a significant E_w trend was found in the early period.
The E-RH and E_b-RH correlations are also regionally widespread positive correlations, but neither E nor E_b changes significantly (Figs. 5.7 and 5.10). The E_t-RH and E_i-RH correlations are significantly positive in the southeast but do not overlap with strong significant RH trends (Figs. 5.8 and 5.9). This highlights the complexity of the RH trends and drivers and shows how different processes may be important for different locations, even over small distances. As for the Caspian Sea region, it follows that E_w may have increased due to rising T, but insufficiently to maintain RH; thus, RH decreased. This again is indicative of non-local and non-terrestrial drivers. The main rainy season is the austral summer, when there is very little rain in JJA (Fig. S3). However, the precipitation trend in the JJA is significantly strongly negative in those two grid boxes (Chapter 4.2), which could have amplified the dry conditions. In the other seasons, the negative trend is not significant. Due to the small size of the sub-region, the individual evaporation fraction as a proportion of total E is not calculated.

In southern Africa in SON, significant, strong and positive E-RH and E_t-RH correlations are widespread over all periods, while E_i-RH and E_b-RH correlate significantly moderately positively (Figs. 5.7–5.10). Evaporation correlations with q are significantly moderately positive and weakly negative with T (Figs. 5.1–5.4). E, E_t, E_i, and E_b significantly ($p < 0.1$) decreased over the centre region in the late period with the strongest change in E_b, which is located in the grid box with the significant negative E trend. Late period T increased significantly while q decreased significantly (Fig. 3.15). E may decrease mainly due to E_t or E_b, which causes the decrease in RH rather through q showing stronger E-correlations than T in the late period. The E_t-RH and the E_i-RH correlations are weaker in the early period, and the evaporation trends are less significant across the board (Figs. 5.8 and 5.9). The E_b-RH correlation is similarly pronounced in the early and late periods (Fig. 5.10). The E_b decreasing trend in the early period is less significant across the whole area.

There is potential evidence of terrestrial drivers influencing RH in this region. Following Gedney et al. (2006) and Grossiord et al. (2020), positive correlations with RH and negative trends in E and E_t indicate local factors such as deforestation or increasing CO_2. However, the negative trends in E_i and E_b may be more indicative of non-terrestrial drivers. The decline is supported by a significant reduction in seasonal precipitation (Section 4.1.1; McCurley and Jawitz, 2019). This could lead to the conclusion that soil moisture is also reduced. The reduction in water availability would reduce vegetation (low NDVI), which, together with the decrease in precipitation, would decrease E_i. At the regional level in SON, the E_t represents the largest share of total evaporation with 67%; E_b is 15%, E_i only 2%.

Table 5.2: Overview of regional correlations between evaporation and HadISDH RH with significant evaporation [mm day^{-1} decade^{-1}], soil moisture [m^3 m^{-3} decade^{-1}] and precipitation trends in the late period (2000–2017). The correlation data for q and T refer to the full period (1980–2017).

	E	E_t	E_i	E_b	E_w	Soil moisture	Precipitation
Eastern Brazil, southwest (DJF)	Strong -ve corr. (1 grid box); weak -ve E-q, weak +ve E-T; +ve E trend	-ve corr. (widespread); weak -ve Et-q, weak +ve Et-T; +ve Et trend	/	/	-ve corr.; weak -ve Ew-q, weak +ve Ew-T; +ve Ew trend (widespread)	-ve surface SM trend	-ve trend
Caspian Sea (JJA)	Strong +ve corr. (widespread); moderate +ve E-q, weak -ve E-T; no E trend	/	/	/	-ve corr.; strong +ve Ew-T; +ve Ew trend (widespread)	-ve surface SM trend	-ve trend (not sig)
Southern Africa, northeast (JJA)	+ve corr. (widespread); weak +ve E-q, no E-T; no E trend	/	/	+ve corr.; no Eb trend (widespread)	-ve corr.; +ve Ew trend	+ve surface SM trend	-ve trend (not sig)
Southern Africa, northeast (SON)	Strong +ve corr. (widespread); moderate +ve E-q, weak -ve E-T; -ve E trend	+ve corr. (widespread); moderate +ve E-q; -ve Et trend	+ve corr.; -ve Ei trend	+ve corr.; -ve Eb trend	/	-ve surface SM trend	-ve trend
Scandinavia (JJA)	Weak -ve corr. (widespread); strong +ve E-q, strong +ve E-T; no E trend	-ve corr.; weak +ve Et-q, strong +ve Et-T corr; -ve Et trend (widespread)	+ve corr.; weak Ei-q/Ei-T corr.; +ve Et trend (widespread)	/	-ve corr.; strong +ve Ew-T corr; -ve Ew trend (widespread)	+ve root SM trend	+ve trend
NW India (annually)	Strong +ve corr.; strong +ve E-q/-ve E-T; +ve E trend	+ve corr.; weak +ve Et-q/-ve Et-T; +ve Et trend	+ve corr.; strong +ve Ei-q/-ve Ei-T; no Ei trend	+ve corr.; strong +ve Eb-q/-ve Eb-T; +ve Eb trend	/	+ve surface/root SM trend	+ve trend

In the region of Scandinavia in JJA, where RH increased significantly over the late period, E_t-RH and E_w-RH correlate significantly strongly negatively over the early, late and full periods (Figs. 5.8 and 5.8). Strong E_t-T and E_w-T correlations are generally opposed to the RH correlations in terms of direction (Figs. 5.2 and 5.5), and q correlates weakly. Over the late period, E_t and E_w trends are significantly ($p < 0.1$) negative and spatially match the E_t-RH and E_w-RH correlations. There are E_t-RH and E_w-RH correlations in the early period, but the negative E_t and E_w trends are significantly stronger in the late period. E_i-RH correlates significantly and strongly positively in all periods over a widespread area with a positive E_i trend only in the late period, not in the early period (Fig. 5.9). The positive E_i trend could be attributed to the significant positive precipitation trend in the late period (Section 4.1.1). The E_i-q correlations and E_i-T correlations are weak. There is no significant E trend in Scandinavia in JJA, indicating that the negative E_t and E_w trends might be offset from E_i trends, and total evaporation as a terrestrial driver might play a minor role in the RH change. In JJA, E_t makes up the largest proportion of total evaporation (77%), followed by E_i (16%) and E_w (4%).

In the region of northwestern India on an annual level, where RH is increasing, E-RH and all other evaporation types – except E_w and E_s – correlate significantly strongly positively over both the early and late periods and the full period (Figs. 5.7–5.10). Correlations are widespread and similar for q and reversed for T: namely, increased E, E_t, E_i and E_b with high q and low T and thus increased RH (Figs. 5.1–5.4). In particular, in the northwestern part of the region, E, E_t and E_b show a strong significant positive trend in the late period. In the early period, the E, E_i and E_t trends are less significant across the board (Figs. 5.7–5.9). In addition, E_b shows a negative trend in the early period (Fig. 5.10). The region's clear wetting and E_t trend could be related to an excess of water due to the significant increase in precipitation, potentially with links to the ENSO (Section 4.1.1; McCurley and Jawitz, 2019; Pascolini-Campbell et al., 2021; Vivek and Manoj Kumar, 2020), although Chapter 2 in Gulev et al. (2021) note an increase in NH monsoon precipitation from the 1980s to the present. Extended greening or irrigation have also been suggested as possible reasons for increased E (Gulev et al., 2021; Jia et al., 2019; Pant & Hingane, 1988; Rodell et al., 2018). This and the positive RH correlations suggest that terrestrial drivers could be somewhat important for northwestern India. While E_t accounts for 62% of the total evaporation in the region, E_b accounts for 26% and E_i <1%.

It is clear from the above analysis that significant relationships between E and RH that might lead to long-term changes are most apparent over small spatial scales. This suggests that terrestrial drivers are far more localised in their impact than dynamical or thermodynamical drivers. The only regions showing large-area, late-period, significant relationships with a negative RH trend are the south of the Caspian Sea (JJA), where RH correlates negatively with E_w, which is regionally increasing, and in southern Africa (SON), where RH correlates positively with E, E_t, E_i and E_b which are regionally decreasing (Table 5.2). Regions that have experienced a positive RH trend alongside extensive E relationships are Scandinavia (JJA), where RH correlates negatively with E_t, E_w which are regionally decreasing and positively with E_i, which is regionally increasing, and northwestern India (annually), where RH correlates positively with E, E_t and E_b which are regionally increasing.

Generally, E and E_t behave very similarly, and correlations with RH tend to be the reverse of those with T (Figs. 5.1 and 5.2). The correlations between RH and E_i and E_b are positive in all cases (Figs. 5.3 and 5.4), whereas correlations with E_w are negative (Fig. 5.5). An impact of E_s on regional RH change of interest in this study could not be detected (Fig. 5.12).

As on the global level, E_t makes up the largest portion of E in all four regions. In southern Africa and northwestern India, E_t shows the strongest changes, whereas E_i changes relatively the most in Scandinavia and E_w in the Caspian Sea region.

On a regional average level, none of the evaporation and soil moisture trends (see Section 5.2) are significant ($p < 0.1$). This is because both the evaporation fraction in the region and, thus, also the evaporation trends are heterogeneously distributed. The impact of evaporation and soil moisture should not be explored in terms of regional average but rather analysed at a higher resolution. The resolution of the HadISDH data might be too low to capture very local terrestrial drives, which have an impact on woodland or irrigated-farm level.

In summary, evaporation processes are strongly related to RH. However, this relationship with RH change in the selected regions is often only short-term (detrended correlations) and not long-term (with evaporation trends). Most of the long-term relationships detected are small in spatial scale and certainly sub-regional. It is also clear that the relationship between E and RH is complex. There is some small, localised evidence of terrestrial drivers in that E (or elements thereof) do appear to be affecting RH, but more generally, there is evidence of RH affecting E. In reality, it is quite possible that both mechanisms are in action, thus making detection of a clear signal difficult. The reasons for the change in E will be explored in the following two sections.

5.2 Exploring causes of the change in the evaporation processes through water availability

This section addresses local water availability as one of the reasons why a change in evaporation could occur. Water availability is dealt with at different depths: the surface soil moisture, which evaporates most directly the root-zone soil moisture, which contributes particularly to E_t and groundwater as storage and a source for irrigation. TWS as a variable has an advantage over various drought indices in that it can recognise drought early, when the water has been anthropogenically withdrawn (Dai, 2011).

Regarding terrestrial drivers, the question remains as to the role of land cover, particularly vegetation in the evaporation process. Soil moisture would be expected to decrease if terrestrial drivers controlled the decrease in RH by reducing E_t (negative soil moisture-RH correlation; Gedney et al., 2006; Grossiord et al., 2020). The hypothesis may need to distinguish between the physiological effects of reduced evaporation due to increased CO_2 and changes in evaporation due to land use (deforestation, afforestation, irrigation, lack of irrigation, and urbanisation). When RH is decreased by alternative drivers, the VPD increases and soil moisture and run-off are expected to decrease (positive soil moisture-RH correlation) as plants take up more water to compensate for greater water loss through E_t. An example of this could be a change in atmospheric circulation such that less moisture is advected over the region from elsewhere. As mentioned above though this can be complicated by the fact that plants may respond to lower RH (and higher VPD) by partially closing their stomata to reduce water loss (Xiao et al., 2020b). There may not be a noticeable decrease in soil moisture in this case. Clearly, it will be difficult to draw conclusions given the complexity of relationships.

Correlation maps between water availability (surface and root-zone soil moisture, TWS) and RH and water availability trends are examined. The spatial distance that water has to move from the ground to the atmosphere takes time to cover. While soil moisture changes move on a time scale of months and years, atmospheric changes last only a few weeks (Zhou et al., 2019). It is tested for links between TWS (including groundwater) and the maximal strength of RH by including temporal lags between changes in TWS and RH.

5.2.1 The relationship between surface soil moisture and root-zone soil moisture content and RH

As with evaporation, soil moisture can both affect RH and be affected by it, with evaporation and vegetation being the mechanisms. As a driver of reduced RH, low soil moisture could lead to vegetation mortality and negatively affect E_t, E_i, thus increasing T (Zhou et al., 2019). Conversely, high soil moisture could mean more water availability, for example, from irrigation or presumably an increase in precipitation, and lead to an increase in both evaporation and RH increase. This would result in a positive soil moisture-RH correlation.

Driven by low RH, soil moisture could increase if plants react to protect themselves against drought stress and contain their stomatal conductance through stomatal closure (Zhou et al., 2019), potentially further exacerbating the low RH. This negative soil moisture-RH correlation could also result from an increase in CO_2, which causes stomata to partially close, in turn reducing E_t. It is hypothesised that this lowered E_t also reduces RH. Consequently, soil moisture storage and runoff would increase if this were the dominant effect. In other words, if this mechanism is important, one would expect an inverse correlation between TWS and RH would be expected, i.e. the CO_2 effect would cause water to stay on the land, instead of evaporating into the atmosphere. An added layer of complexity is that there may be feedback whereby increased moisture availability in addition to elevated CO_2 causes a CO_2-mediated greening. i.e. increased LAI compensates for the CO_2-related reduction in water uptake from the soils. Stomatal closure would also occur alongside limited water availability to the roots, suggesting that soil moisture is already low. It is challenging to test this hypothesis as it would require decoupling the feedback.

A wide variety of scenarios are possible, depending on the different influences. To begin, it is necessary to identify the global pattern of soil moisture-RH.

Soil moisture and RH are positively correlated over most land (Figs. 5.13 and 5.14). The relationship is weaker during hemispheric winter, which makes sense given the more limited vegetation growth and potential for snow and ice-covered ground at that point. Surface soil moisture-RH correlations are stronger than root-zone soil moisture-RH, which is also confirmed by Zhou et al. (2019). Where there is only a weak correlation, Zhou et al. (2019)) suggest that RH could be determined by other factors, such as oceanic moisture circulation. There number of grid boxes with a significant ($p < 0.1$) soil moisture trend is low, suggesting that soil moisture is not a significant driver of RH trends. As discussed, soil moisture and its variability are highly complex, and its inputs and outputs strongly interlinked.

The Caspian Sea region (JJA), southern Africa (SON) and Scandinavia (JJA) show strong soil moisture-RH correlations but hardly any significant soil moisture trends (Figs. 5.13 and 5.14). The interannual RH variability over these regions might be affected by a change in soil moisture, but the long-term RH trend cannot be explained by any soil moisture trend. Northwestern India, where RH has increased, has experienced both strong positive correlations and a significant increase in both surface and root-zone soil moisture on the annual level in the late period. This fits with the positive precipitation trend and the increase in evaporation rates in the late period over this region. In the early period, soil moisture-RH correlations are less pronounced over northwestern India, and soil moisture shows a slightly negative but significant trend. According to the hypothesis, the positive correlation between soil moisture and RH would suggest thermodynamic/dynamical drivers RH control. However, irrigation may be important for this region but it is unlikely to be associated with such widespread relationships and trends. Here, there is high water availability for evaporation which keeps RH high. With such plentiful water, enhanced CO_2 levels could result in greater vegetation growth which would compensate for the reduced E_t from partial stomatal closure and could even result in increases in E_t. Neither irrigation nor CO_2 related greening is explicitly assessed here. Irrigation could occur in places where TWS has decreased and soil moisture or NDVI have simultaneously increased. CO_2 related greening in the HadGEM2-ES model experiments is explored in Section 5.4.

Other significant soil moisture trends stand out for their intensity and breadth in regions with RH change. These are southeastern Mongolia, where soil moisture is increasing, as reported by Yu et al. (2019), and northeastern Brazil, where soil moisture decreases (particularly surface soil moisture) over all seasons in the late period. The trends in northeastern Brazil are less pronounced in the early period. In Mongolia, the soil moisture trend is negative in the early period. Mongolia is sparsely vegetated with low soil moisture capacity and exposed to overgrazing and also shows a high evaporation rate (Gao et al., 2015; Yu et al., 2019). Neither northeastern Brazil nor Mongolia – areas with significant soil moisture trends – match with areas of significant soil moisture-RH correlations. For this reason, these two regions will not be discussed further at this point. Dai (2011) found significant correlations between soil moisture and drought indices in Mongolia.

Few negative soil moisture-RH correlations were found that would indicate physiological control over RH. Furthermore, there are no widespread significant trends in soil moisture over the late or full period. The presence of widespread strong positive correlations shows that soil moisture is essential for understanding changes in RH. However, it is not possible to use soil moisture to detect the presence of terrestrial drivers.

5.2.2 The ability of GRACE terrestrial water storage to represent RH

In the previous section, a GLEAM data set was used, based on observation data and model simulations. Since model simulations involve greater uncertainty than observations, it is desirable to use observation data, such as the GRACE data set. The aim is to find out whether and to what extent GRACE, as an observational data set, can explain the change in RH by providing information about where groundwater is located. The TWS, inclusive of groundwater, is not expected to contribute to RH without a lag, due to the time until stored water becomes available for evaporation. It takes a while for the water to become atmospherically 'coupled'. Due to the depth that the GRACE water column covers, water is available for evaporation for years after observations are made. Seasonal lags are expected such that a TWS change does not affect RH until months later. This could be the case, for example, if the rainfall season shows strong anomalies and the water is not used until the next growing season. For this purpose, global correlation maps between detrended TWS and RH include lags of three and six months. The change in correlation strength between TWS and RH for these temporal lags is considered.

The lags included are strongly region-dependent and can be changed by anthropological interventions such as irrigation (Siebert et al., 2006), thus correlations with lags (short-term) may be weak and generate no widespread regional patterns. Connecting RH trends with TWS trends (long-term) becomes complicated on a large spatial scale. In general, despite this, a positive correlation is expected.

A global decrease in groundwater has been observed (Fig. 5.15; Rodell et al., 2018). Irrigation is one of the reasons for this, especially in agricultural areas in drylands (e.g. around California and northwestern India in Gulev et al., 2021). Irrigation might be linked with an increase in RH due to greater water availability at the surface (positive soil moisture-RH correlation and positive soil moisture trend) and a decrease in TWS.

The TWS-RH correlations are largely weak to moderately positive but do not follow a latitudinal pattern. They are strongest in JJA in the NH; elsewhere, they rarely follow a seasonal pattern. This could be because groundwater storage does not change rapidly. An increase in the strength of the correlation following the inclusion of the temporal lag can be achieved in the seasonal case of SON, with TWS anomalies in SON connecting with RH change in DJF, especially in NH. A lag of -6 months is visible, i.e. TWS changes and six months later, RH changes, increasing the correlation only subregionally. TWS trends show little seasonal variability.

The positive TWS-RH correlations occur alongside globally extensive negative TWS-T correlations (most strongly negative in JJA and positive in NH high latitudes in DJF; not shown) and weaker, positive TWS-q correlations (not shown). For regions in which RH decreased, TWS also fell. This does not indicate the depth to which TWS is reduced.

In the regions in which the RH trend occurs alongside an evaporation trend (the Caspian Sea region in JJA, southern Africa in SON, Scandinavia in JJA, northwestern India on an annual level), a significant and strong positive correlation can be detected in the late period – though only in the boreal summer months in the Caspian Sea and Scandinavia (Fig. 5.1). The TWS-RH correlations are particularly strong without and with a lag of -3 months but weaken with a lag of -6 months, while TWS decreased (increased) around the Caspian Sea (in Scandinavia) independently of the lag, i.e. the season (Fig. 5.15). The TWS trend over Scandinavia is only significant in subregions. The RH decrease over the Caspian Sea region among positive E_w trends can be associated with decreasing TWS. That makes sense because E_w evaporates as a direct process, without a biological layer on the surface, due to T increase and continuously. Rodell et al. (2018) attribute the groundwater depletion in the Caspian Sea area and discharge from the Volga river to both human impact and meteorological variability.

Although TWS and RH do not correlate in the following regions, the regional RH trends might be linked to RH: the regional negative TWS trend together with the positive soil moisture trend matches the positive E and E_t trends in northwestern India, indicating irrigation, particularly among a positive NDVI trend (Section 5.2.1). The negative soil moisture trend in Section 5.2.1 in eastern Brazil and Mongolia (without correlation with RH) can be linked to a change in TWS (Fig. 5.15; supported by Yu et al., 2019). The negative TWS trend in Mongolia is explained by the decrease in lakes, grassland degradation and groundwater depletion for irrigation (Tao et al., 2015); a negative NDVI trend would be expected (see Section 5.3). In eastern Brazil, reduced precipitation might have caused a regional decrease in TWS. The reasons for a decreased TWS is expected to be different in each of the above regions. Therefore, TWS could be the reason for a decrease in RH, but equally, the atmospheric drying could have caused a negative TWS trend. The analyses in this study indicate that the direction of causality between the TWS and GRACE is not clear, for example, in eastern Brazil.

GRACE can be used regionally as an interstage product, connecting soil moisture with atmospheric humidity. It must be noted that groundwater does not have a huge direct impact on RH, but there is connectivity in the system, which may be heavily lagged. Links between modes of variability such as the ENSO (Ni et al., 2018; Wang et al., 2018) and the PDO (Guo et al., 2021) were not examined in this study as they are beyond the scope of the thesis.

If drought can be detected with GRACE, then some associated vegetation response should be seen. NDVI is broadly sensitive to leaf biomass/physiology changes, and thus (as a function of time) to inferred net/gross primary production (NPP/GPP) and water availability, i.e. TWS. Xie et al. (2019) and Andrew et al. (2016) found that NDVI, depending on the type of vegetation, lags up to one month after the TWS change, which is more rapid than precipitation, with an expected positive correlation. An inverse relationship between TWS and NDVI could also occur with a longer growing season, with deciduous leaf canopy in place for a longer time, i.e. positive NDVI trends outside the general growing season. In this scenario, warming and greening could draw down TWS to a greater extent, leading to increased RH during the greening season and decreased RH afterwards. TWS-NDVI correlations have not been calculated, as they are beyond the scope of the thesis.

5.3 Investigating to what extent the land cover influences RH

Land cover both determines and is affected by the type of evaporation and the soil moisture content. It also determines the albedo and helps shape the wind dynamics through the roughness length. Clearly, there are many mechanisms through which land cover change can have an impact on RH, and vice versa. Due to the complexity of the land cover changes as well as its feedback, it is challenging to deduce the effects on RH.

Land cover can be classified in different ways (Section 1.3.3.3). The vegetal layer determines E_t, which is the largest contributor to total land evaporation. During the growing season, plants make RH both a function of and a result of E_t. Hence, the vegetation cover of the land can be assumed to be the main terrestrial contributor to RH changes. That is why the vegetation index NDVI is used to infer the land cover and its changes (Eckert et al., 2015). The NDVI determines how photosynthetically active the land surface is. In general, a positive correlation between NDVI and RH would be expected. It might be useful to control for different biomes. If NDVI is decreased by reducing the vegetal portion, e.g. large deforestation, E_t would be reduced, and RH decrease. Tropical deforestation would remove a major terrestrial moisture source, causing local heating, which could further exacerbate a decrease in RH (Lawrence & Vandecar, 2014). With atmospheric drought (RH decrease), NDVI decreases. Some species are fairly drought-tolerant; therefore, this response varies according to the biome. The increased NDVI, through increased T or CO_2 fertilisation, is a response to greening or longer growing seasons and should lead to RH increases owing to more E_t. Irrigation would increase the seasonal water consumption and might lead to an exhaustion of water afterwards, resulting in a decrease in RH. In this case, it would be left lagged. In this study, the relationship between NDVI-RH is assumed to be without lags.

First, the short-term relationship between RH and changes in greenness (afforestation/deforestation, greening, a change in vegetation type) is assessed through detrended time-series correlation maps. This could explain regional the E_t-RH correlation and E_t trends (Section 5.1). In the second step, regardless of the correlation, it is checked whether strong NDVI trends (greening or deforestation) have coincided with RH trends in the late period, inferring a potential relationship and therefore the presence of terrestrial drivers.

On a global scale, the NDVI-RH pattern is relatively patchy in both strength and direction (Fig. 5.17). Positive NDVI-RH correlations are particularly pronounced in MAM in the SH mid-latitudes (e.g. southern Africa), and in JJA in the NH mid-latitudes. The strongest negative NDVI-RH correlations are found across the NH mid-latitudes in DJF and in the NH high-latitudes in JJA.

The NDVI-RH relationship is complex and likely depends on many factors in addition to the amount of greenness. The vegetation related change in evaporation and its fractions can drive changes in RH. This depends on: water availability, including soil moisture; stomatal conductance efficiency, which depends on CO_2 levels and also RH levels; and many other factors, including the dynamical drivers discussed in Chapter 4, and the thermodynamical driver discussed in Chapter 3. Exploring this interconnectedness further, the above variables of terrestrial drivers would correlate with NDVI, suggesting that strong links between NDVI and E_t could imply deforestation. For NDVI-E and NDVI-E_t, there are overall positive correlation coefficients outside of the desert regions where there is enough water; correlations are strongest in MAM and JJA in the NH (not shown). Their correlation patterns do not resemble those of the NDVI-RH. The NDVI-E_i correlations also show less complex patterns than NDVI-RH, namely mostly positive but weak (not shown). In contrast to the relatively simple links between NDVI, E and E_t, NDVI-surface soil moisture correlations (not shown) show a similar level of complexity in their patterns at the global level matching the NDVI-RH correlation patterns (Fig. 5.17). This implies that NDVI and RH are connected mainly via surface soil moisture.

It stands to reason that according to our physical understanding, NDVI and RH are connected mainly via the combination of surface and root-zone soil moisture, which supports the hypotheses based on Gedney et al. (2006) and Grossiord et al. (2020). Depending on the vegetation type, the plant draws water from different depths and processes with different WUE and greenness outcomes. The seasonal difference between soil moisture and NDVI correlations come about through energy availability: while radiation and temperature are unlimited in summer, they may be reduced in winter. Soil moisture can be present in abundance in winter, for example. Although RH is related to NDVI and soil moisture, local and seasonal differences arise and create complex correlation patterns between NDVI-RH.

The NDVI-RH pattern essentially results from NDVI-q and NDVI-T correlations (Fig. 5.16), which are generally stronger than the NDVI-RH correlations (Fig. 5.17). Positive NDVI-q correlations are weak over the year, except in MAM in the mid and high latitudes. Similarly, positive NDVI-T correlations are strong in NH mid-latitudes and high latitudes in MAM and the high latitudes in JJA. Strong negative correlations occur in the summer months for each hemisphere over much of the mid-latitudes. Elsewhere, they are weakly to moderately negative (Fig. 5.16; Fensholt et al., 2012). The springtime sees strong NDVI-q and NDVI-T correlations in the seasons of much growing and E_t, but as the summer warmth grows, perhaps this leads to plant die back/stress and more sensible heating. In SON, very few correlation patterns can be seen, as in q and T. Generally, NDVI-q and NDVI-T correlations do not move equally strongly in one direction depending on season and latitudinal, resulting in complex NDVI-RH correlations. The stronger NDVI-RH correlations tend to be over regions where NDVI-q and NDVI-T differ, such as southern Africa (MAM; Fensholt et al., 2012).

When breaking down the soil moisture and NDVI correlations with q and T, it is noticeable that NDVI-q (Fig. 5.16) and surface soil moisture-q (not shown) are similar in their annual averages. For seasonal means, q is much stronger and mostly positively correlated to surface soil moisture than NDVI (DJF, SON, JJA) and shows a much weaker correlation in MAM in the NH. The T is much stronger and mostly negatively correlated to surface soil moisture (SON, JJA) and shows an inverse pattern in MAM in the NH. Only in DJF, surface soil moisture and NDVI seem to correlate with T in similar patterns. The NDVI, RH, q and T correlations between surface and root-zone soil moisture are very similar and show small deviations, which can increase or decrease regionally in correlation with other variables.

The global NDVI-RH correlation patterns are stable over the early and late periods but show strong regional differences in significance, sign, and strength (Fig. 5.17). This regional correlation instability in time confirms the complexity of the NDVI impact on RH, and vice versa.

A positive NDVI trend was observed in recent decades and linked to increasing T, precipitation change and CO_2 fertilisation (Hong et al., 2019; Shukla et al., 2019; Winkler, 2020; Yuan et al., 2019). For the annual average, this positive trend is global in the early period, particularly strong in mid and lower high latitudes in the NH in JJA, and few negative trends are recorded. In the late period, the positive NDVI trend is weaker, which can be attributed to an increasing VPD (Yuan et al., 2019). It has mixed signs: in DJF, MAM and JJA, in the mid-latitudes, the NDVI trend is negative, while in the high latitudes in DJF and MAM, it is positive. In SON, the trend is also strongly negative in most of the high latitudes. This latitudinal, seasonal pattern might indicate early greening onset in the high latitudes in the late period, with greening well underway in boreal spring due to abnormally high temperatures (see significant T trends in Fig. S6). This was also found by Myers-Smith et al. (2020) and Piao et al. (2019). It is assumed that the well documented greening trend in temperate and boreal latitudes caused by warming has an influence on RH. This lengthens the growing season and presumably, increases the seasonal water consumption. Water could be expected to run out late in the season so that in boreal autumn, the NDVI might be decreased earlier than normal (negative NDVI trend in SON) because of insufficient soil moisture (Fig. 5.13). However, a negative soil moisture trend in the late period can be only partly confirmed (Figs. 5.13 and 5.14); and due to the time period covered by the dataset, GRACE TWS does not provide any comparative trends between the early and late periods. Correlation strength between NDVI-T did not change in the high latitudes between the early and late periods (Fig. 5.6).

A negative (positive) NDVI trend in the late period in the mid-latitudes could be associated with a negative (positive) RH trend in regions like the Caspian Sea in JJA (northwestern India, annual). Since there are no widespread strong NDVI-RH correlations, neither a direct connection nor connection via soil moisture and water availability (correlation maps not shown) for vegetation growth can be confirmed for the entire regions. In the north of the Mongolia region (DJF) in the late period, NDVI significantly declines, but there are no significant NDVI-RH, -q, or -T correlations (Figs. 5.16 and 5.17). Since 2000, land cover in the Lake Baikal basin has changed significantly: while forest and wetland have increased, water bodies, grassland and the NDVI, permanent snow and ice have decreased (Dorjsuren et al., 2018).

In the late period, no significant NDVI-RH correlations were found with a significant NDVI trend covering greater than one contiguous grid box for annual or seasonal levels in regions with an RH trend. The absence of large-scale significant NDVI-RH correlations and NDVI trends also applies to regions in which an E_t or E_i change can explain a regional RH change (southern Africa in SON; Scandinavia in JJA), or where a significant soil moisture trend was measured (northeastern Brazil, Mongolia). Therefore, the regional analysis of the impact of NDVI on RH and the declaration of NDVI as an indicator of LCLU change as an explanation for global RH decrease is discontinued at this point. Fensholt and Proud (2012) link the negative (positive) NDVI trends with negative (positive) precipitation trends around the Caspian Sea region and northwestern India with precipitation trends, which indicates dynamical drivers affecting both NDVI and RH. Compared to the regional connectivity of precipitation and RH (see Section 4.1.1), the link between NDVI and RH seems small, but based on the analysis in this thesis, it cannot be ruled out that the latter two are influencing one other.

Since 2000, there has been forest loss in California, the western USA, northeastern Brazil, the eastern coast of southern Africa, Mongolia, and southern Tibet, and forest cover gain in the southern part of eastern Brazil, albeit less extensively (Hansen et al., 2013a; Hansen et al., 2013b). These forest trends could not be detected via NDVI at this resolution in this project, therefore the impact of deforestation on RH could not be detected either.

Regional time series of NDVI were not calculated as correlation and trends were only found in single grid boxes. Due to the low resolution of the RH and NDVI dataset GIMMS, the spatial distance of the measured RH and NDVI values cannot be estimated, thus the averaged measurements may be far apart. Regional time series at a higher resolution could help to reveal the links between NDVI and RH.

The global and regional RH decrease due to changes in NDVI, ergo the impact of deforestation, or presumably afforestation, or CO_2 related enhanced greening or urbanisation which might appear as reduced NDVI, could not be detected with the datasets analysed. A positive NDVI trend was observed in the early period and this was strongly weakened in the late period. The cause of this complexity is that NDVI has different effects determined by different parameters at different spatial scales, including variables such as vegetation type, which are below the selected resolution limit. As a result, no large-scale correlations or trends could be found. In addition to the spatial scale, NDVI change can take place on different time scales, and deforestation is assumed to be a gradual effect. Lags between NDVI change and RH change were not considered in this study, as this would be beyond the scope of the thesis.

5.4 Model scenario: How does RH respond to the radiative versus the physiological response to CO_2?

Determining the impact of enhanced CO_2 on RH is challenging owing to the number of processes and interactions between them. The existing vegetation type, water availability and even RH itself all affect stomatal efficiency. Experimentally, data are available from Free-Air CO_2 Enrichment (FACE) experiments. However, these are highly specific to external atmospheric and land types, such as soil and plant characteristics, and are only available for a period of up to a few years. Therefore, to determine the influence of elevated CO_2 concentrations on spatially and temporally large-scale RH, the available model simulations/runs of HadGEM2-ES are therefore used instead. HadGEM2-ES is part of CMIP5 and was assessed for its correlations between RH and q and T in Section 3.4. The analysis revealed striking differences between the HadISDH observations and HadGEM2-ES historical runs in terms of T-RH correlations in the high latitudes. HadGEM2-ES correlations were negative in contrast to the positive correlations in the observations. This should be kept in mind when interpreting changes in RH in the model over the high latitudes.

The prediction would be that rising CO_2 causes stomata to partially close, which would reduce E_t. In line with Grossiord et al. (2020) and Gedney et al. (2006), this study hypothesises that this lowered E_t would reduce RH. Soil moisture storage and runoff would increase if this were the dominant effect. In other words, if this mechanism were important, an inverse correlation between TWS and RH would be expected. The CO_2 effect would then cause water to stay on the land, rather than evaporating into the atmosphere - unless there were feedback that meant increased moisture availability caused a CO_2-mediated greening. i.e. increased LAI, which compensates for the CO_2-related water saving per leaf (Norby & Zak, 2011). No evidence of the hypothesised negative TWS-RH could be found in Section 5.2.2, but this does not necessarily mean that the process is not happening, just that it is not detectable.

A positive correlation between CO_2 and RH is expected if there is a structural response from the vegetation, i.e. CO_2 fertilisation, if NDVI increased, and thus E_t and q lead to increased RH. Note that NDVI has a non-linear relationship with LAI, i.e. the biomass, and that it is noisy at low LAI levels (e.g. semi-arid) and saturates at high LAI levels (e.g. tropical forest). In the case of a radiative effect in which CO_2 leads to increased temperature, greening can occur, especially in high latitudes, thus increasing NDVI and RH. A negative CO_2-RH correlation occurs due to increased T and drought-stressed, partial stomatal closure and, therefore, increased WUE, decreased E_t, decreased RH and, potentially plant mortality. The stomata also close when there is excess CO_2. Both the radiative and physiological response of CO_2 on vegetation can decrease and increase RH via NDVI and E_t.

Clearly, a CO_2-RH relationship is not straightforward but this study hypothesises that in the absence of other changes, an increase in CO_2 should lead to a decrease in RH. To identify whether there is a change in RH linked to stomatal change due to increased CO_2 and whether the CO_2 driven stomatal changes would be enough to drive changes in RH without CO_2 driven warming, this study looks at the historical runs of HadGEM2-ES (Section 3.4) and the following two experiments $esmFdbk2$ and $esmFixClim2$. The historical runs should represent thermodynamic, dynamical (to some extent, albeit not necessarily temporally matched), LCLU and physiological drivers. The $esmFdbk2$ experiment includes all the above except LCLU changes but importantly, only the radiative effect of CO_2 is included as the carbon cycle is not exposed to increasing CO_2. The $esmFixClim2$ does not include thermodynamic or dynamical drivers as only the carbon cycle, and not the radiation, is exposed to increasing CO_2. This study infers from this experiment that any response of RH to increased CO_2 is linked to changes brought on by CO_2 enhanced stomatal conductance efficiency leading to decreases in E_t. The available output variables are RH ($hurs$), q ($huss$) and air T (tas), showing how RH responds to the radiative versus the physiological response to elevated atmospheric CO_2 concentrations. If there is a change in RH when there is a CO_2 forcing seen by the carbon cycle only (stomatal conductance response, $esmFixClim2$), then it can be inferred that there should be a stomatal driven component of the real world RH drying. The magnitude of any RH changes between the carbon cycle forcing only ($emsFixClim2$) versus radiative forcing only ($esmFdbk2$) can be compared to say something about the size of the driver of the stomatal conductance changes. The entire period (1860–2099) is examined because if there is a trend, it may be tiny, and a longer period will make it easier to find.

On a global average, $esmFdbk2$ hurs, and particularly, $huss$ and tas trends are stronger than $esmFixClim2$ trends, i.e. under a CO_2 increase, thermodynamic and dynamical changes have a stronger impact on RH (and q and T) than stomatal efficiency changes (Figs. 5.18 and 5.19). This is as expected. Generally, q and T trends are significantly positive for both experiments. The spatial patterns of q and T trends between the two experiments are also very similar, but the regions of small or negative trends in $esmFdbk2$ become regions of stronger negative trends in $esmFixClim2$. For RH, trends in both experiments are mostly negative over land, with more regions of strong significant negative trends than strong significant positive trends. Generally, the regions of strong negative RH trends align with regions of strong positive T trends for both experiments, although this is less clear for $esmFixClim2$. The presence of widespread, strong, significant negative RH trends in $esmFixClim2$ does suggest that CO_2 enhanced stomatal conductance efficiency could be playing a role in real-world RH change. The negative RH trends in $esmFixClim2$ appear to be more widespread, and of similar strength to those in *esmFdbk*2, suggesting that the physiological effect of increased CO_2 can actually be considerable.

Under the radiative response to elevated CO_2 concentrations (*esmFdbk*2), the q change shows a latitudinal pattern (Fig. 5.18), with the strongest increase in the tropics, which follows high NDVI, E_t, E and T climatologies. The strength of the T increase behaves inversely to the q changes, such that the largest RH decreases tend to be in regions where there is less vegetation and evaporation and a smaller or even negative trend in q (e.g. southern Africa [especially in JJA], Mexico and the north of eastern Brazil [especially in SON]; Fig. 5.18), but with a strong T increase.

With a physiological response only to elevated CO_2 concentrations (*esmFixClim*2), q shows a very similar pattern to the *esmFdbk*2, albeit much weaker (Fig. 5.19). The regions of negative or small positive trends seem to be the same as those in *esmFdbk*2, too. Regional T patterns are less obvious but there are very similar patterns in some of the regions of greater warming with strong negative RH trend regions. With the strongest T trends in DJF, which is the dormant season for NH vegetation, in the NH high latitudes, T trends in *esmFixClim*2 are much weaker than in *esmFdbk*2.

The *esmFdbk*2 trends indicate a positive q-RH and negative T-RH relationship in terms of long-term trends. The T-RH relationships appear stronger in a radiative response (*esmFdbk*2) to elevated CO_2 concentrations than in the physiological response (*esmFixClim*2). Based on this, the CO_2 component of the terrestrial drivers (*esmFixClim2*) is concluded to be small in comparison to the thermodynamic and dynamical ones (*esmFdbk*2).

Regional RH changes in *esmFdbk*2 are assumed to be evidence of thermodynamic and dynamical changes. Considering our regions of interest, similarities of regions with strong RH trends between the HadISDH observations and the model can be seen particularly in southern Africa (JJA, SON) and eastern Brazil (JJA, SON), but also in eastern Brazil (DJF), southwestern Greenland (DJF), the Caspian Sea (JJA), and eastern USA (annually) (Fig. 5.18). The differences between the observations and the model can be found in Mongolia (particularly in MAM) with a positive RH (*hurs*) trend in the model, and Mexico, northwestern India (particularly in DJF) and Australia with a negative *hurs* trend.
RH changes due to changes in stomatal efficiency under increasing CO_2 (*esmFixClim*2) matching the observations can be seen in eastern Brazil (all four seasons), southern Africa (JJA, SON), southwestern Greenland (DJF), Tibet (JJA, SON) and the eastern USA and California (annual level) (Fig. 5.19). Conversely, trends are not consistent in Mongolia, where RH shows a positive trend, particularly in MAM in the model. Although the time periods between the observations and the model are very different, there may still be evidence that these drivers are contributing to historical trends.

In most places and on the global average, RH responds more strongly to the radiative response to CO_2 than to the physiological response to CO_2. This might be due to T, which in most regions (with the exception of high-latitudes, DJF) correlates negatively with RH in observations. In the model experiments, there were quite strong similarities between RH and T, and plenty of regions where q trends were different in patterns. In the scenario of $esmFdbk2$, there are clear links between q, T and RH trends but they are not all the same in terms of trend patterns. In some regions, RH and T appear more closely related and in some regions, q and RH appear more closely related. One reason for T increasing when only the carbon cycle sees increases in CO_2 ($esmFixClim2$), and not radiation, could be that increased CO_2 concentrations leads to partial stomatal closure which in turn increases the WUE, thereby reducing the surface latent heat flux. This would result in an RH decrease with $esmFixClim2$.

In the early period (1973–1999) the CO_2 concentration increased annually by around 39 ($\pm$0.12) ppm (1.44 ppm year^{-1}, although the increase was not linear). The increase was increased in the late period (2000–2017) by an average of 37 ($\pm$0.11) ppm year^{-1} (2.06 ppm year^{-1}; annual mean data Mauna Loa, Hawaii; https://gml.noaa.gov/ccgg/trends/gr.html, data of access: 11 November 2021). The model runs for 239 years with an increase of 130 ppm CO_2 until 2021 (*historical*, $historicalEXT$; https://www.eea.europa.eu/data-and-maps/daviz/atmospheric-concentration-of-carbon-dioxide-5, data of access: 14 February 2022) and another increase of 234ppm from the present until 2100 (with RCP4.5 reaching an approximately 650 ppm CO_2-equivalent by 2100; Thomson et al., 2011a). The extra years of RCP4.5 were included to magnify any potential stomatal closure driven change in RH, given that the effect is thought to be small and difficult to detect, and to enhance the signal-to-noise ratio. This results in a total increase of 364 ppm CO_2, i.e. 1.52 ppm year^{-1}. The increase in CO_2 per year in the observations and in the models can thus be compared. Figs. 5.18 and 5.19 show weaker RH trends, q and T trends due to increased CO_2 than this study based on HadISDH RH considered. As described above, positive q and T trends are stronger in $esmFdbk2$ and weaker in $esmFixClim2$, indicating that the carbon cycle response has a weaker impact on q and T compared to the radiative response. Negative q trends are regionally stronger in $esmFixClim2$, indicating that stomatal closure due to increased CO_2 negatively impacts q, resulting in an effect of a slightly smaller magnitude on RH than the radiative response. The model might contain thresholds or reversal points that are only visible over long periods of time or a certain CO_2 concentration, or there may be effects underestimated that would be offset, for example, by certain plant species responding with increased stomatal conductance to increased CO_2 (Purcell et al., 2018).

As there is a change in RH when there is a CO_2 forcing seen by the carbon cycle (stomatal conductance response, $esmFixClim2$), there should be a stomatal driven component of the real world RH drying. CO_2 driven stomatal changes ($esmFixClim2$) are enough to drive changes in RH without a CO_2 driven warming. However, the magnitude of these changes is regionally weaker than the CO_2 driven thermodynamic and dynamical drivers, i.e. the driver of the stomatal conductance might be very small.

Note that, according to Collins et al. (2011), the HadGEM2-ES model does not do well in representing vegetation areas, i.e. too much tropical forest and grass, too little shrub, and, in Australia and western India, too much bare soil. Vegetation cover in high latitudes and regions with low temperatures is overestimated in an ensemble of Global Earth System models from the CMIP5 (Keenan & Riley, 2018). However, vegetation in cold climates will be less temperature limited under global warming; thus, the physiological effects on RH might be increased in the future. Recent climate models have underestimated the increased CO_2 fixation and GPP increase; thus, they might overestimate T increase (Winkler et al., 2019), and therefore any RH decrease. Furthermore, CMIP5 models sometimes underestimate soil moisture-RH (Zhou et al., 2019).

5.5 Chapter summary and concluding remarks

In this Chapter, an attempt was made to explain the observed RH change in the late period in terms of terrestrial drivers. Land evaporation was used as the cornerstone of this analysis. Total evaporation and E_t behave similarly: with RH and q, they correlated positively, except in the high latitudes, and with T negatively, except in DJF. The other evaporation types show different latitudinal and seasonal patterns.

In particular, in the regions of the Caspian Sea and northwestern India, a relationship between land evaporation types and RH and evaporation trends was successfully established (Section 5.1): around the Caspian Sea, increased T led to increased E_w but insufficiently, such that RH was maintained, alongside a TWS and NDVI decrease, which might be linked to reduced precipitation in the late period. In northwestern India, RH increased in the late period, alongside increased soil moisture and E, E_t, E_i and E_b which might be linked to increased precipitation or irrigation with decreased TWS. Even if total evaporation did not change because two or more evaporation types were offset, as in Scandinavia with a decrease in E_t and E_w and an increase in E_i, correlations of detrended RH and E time series could enable conclusions to be drawn about regional and subregional relationships between E and land-surface processes, e.g. E_s describing snow pattern, albedo and T. The decrease in land evaporation can be linked to precipitation in all cases except southern Africa in JJA, which means an impact on RH of dynamical drivers, rather than terrestrial drivers. The land evaporation differed depending on the region and season, but the changes in E_t, E_w and E_b had the most decisive impact on RH change, indicating that terrestrial drivers could be having an effect on RH.

Water availability and vegetation change were then explored as a reason for some of the changes in E, in essence, as a proxy for change in land cover and land use. The evaporation trends could only be explained in the region of northwestern India by a change in soil moisture availability (in this case, increased irrigation, rice plantation and unlimited soil water) (Section 5.2). It was confirmed that TWS and RH region-dependently correlated only under temporal lags of several months. The only-observation data set of TWS was GRACE, and this could not directly help explain changes in RH but be indirectly linked to RH via soil moisture and NDVI changes (e.g. decreased TWS and increased soil moisture in northwestern India, indicating increased E, thus, increased RH). The analysis of NDVI as an indicator of LCLU-change found a difference between the stronger greening trend in the early period and the weaker trend in the late period, which confirmed then Yuan et al. (2019) findings of increased VPD resulting in weaker GPP on the global average (Section 5.3). However, these could not be brought into a significant correlation with RH on a larger spatial scale.

Finally, the influences of increased CO_2 on RH via enhanced stomatal conductance efficiency was explored by isolating the radiative and physiological response of RH, q and T to increased CO_2 using the $esmFdbk2$ and $esmFixClim2$ experiments of the HadGEM2-ES model. It was found that the radiative impact had a more substantial effect on the three variables, particularly on T, than the physiological impact (Section 5.4), as expected, but an effect on RH was detected in the absence of a radiative response. This suggested that CO_2 enhanced stomatal conductance efficiency could be contributing to decreasing RH, but only to a small degree. The RH trends generally show the same sign in both simulations, indicating that the response of the carbon cycle to CO_2, and therefore, the physiological effect (closing stomata in response to declining RH) or the structural effect (lower LAI in response to declining RH) could amplify the thermodynamic and dynamical drivers leading to a decrease in RH.

The detection of the effect of vegetation on RH was less successful, but the effect of surface-water availability and terrestrial water bodies could, for example, be detected in northwestern India and the Caspian Sea region, respectively. This study found that open water bodies, their surface area decrease and E_w play a crucial role in the impact of land evaporation on RH (e.g., the Caspian Sea region; Koriche et al., 2021a; Koriche et al., 2021b). These impacts and the interaction between open land water and soil moisture might be missed by the model.

In addition to terrestrial water availability and LCLU, land evaporation can also be influenced by wind speed. Wind can have different effects, depending on the direction it comes from and its properties (q, T). If a dry wind hits a region or if there is an increased wind speed over it, more moisture is evaporated and transported away, and RH is reduced. This would likely lead to an increase in E_t. If it is moist wind, the moisture gradient between ground and atmosphere is decreased, so E_t decreases and RH then would possibly be increased by the moist wind. This is an example of the complexity of the system, showing how that which is classed here as a dynamical driver can influence vegetation responses that might then affect RH.

In the regions in which land evaporation change affects RH change, the impact of the wind speed si10 on E and thus RH is investigated using si10-E correlation maps and change in si10 for the sake of completeness. Changes in wind speed are discussed in detail in Section 4.1. In the Caspian Sea region (JJA), si10-E correlate significantly negatively and in Scandinavia (JJA) partly positively (Fig. 5.20). The correlations are only partially significant and of only moderate strength. As there are no significant trends in si10 in the late period, the change in RH through a change in land evaporation cannot be explained by a change in wind speed. The significant and strongly negative si10-E correlation with a negative si10 trend in northwestern India (annual) can explain the RH increase in the late period: linked to a decrease in wind speed, increased land evaporation enhanced the atmospheric moisture (q; see Fig. S5) and therefore the RH.

A summary of principal drivers in each region can be found in Section 6.2.1.

It is very clear that the processes driving RH are highly complex and affected by RH themselves in many cases. This thesis has drawn some connections between the other non-terrestrial drivers in RH. The connections between dynamical and terrestrial drivers are limited to circulation, i.e. wind and precipitation. Pascolini-Campbell et al. (2021) examined the impact of modes of variability on global E_t and found positive correlations between E_t and ENSO, for example. This study did not explore the impact of modes on terrestrial drivers or teleconnections, nor temporal lags were considered to explain RH variability and trends, as this would have been beyond the scope of the thesis.

The NDVI correlation and trend analyses (Section 5.3) clarify that the direction of causality cannot be inferred from the findings of this study. The negative NDVI trend in the late period is reduced due to increased VPD/decreased RH, and not the other way around (Yuan et al., 2019).

In the model runs, the strong T increase in the NH high latitudes in $esmFdbk2$ and even more distinct in $esmFixClim2$ is noticeable (not mentioned in the model section 5.3). For the high latitudes, a negative T-RH correlation in HadGEM2-ES was found in Section 3.4, in contrast to the observational data. With the strong T increase due to increased CO_2, the model shows an RH decrease in the high latitudes. The analysis has enriched the understanding of this amplification of increased CO_2 in the opposite direction from RH in the model run.

The dataset grid box resolution of 5° by 5°, used in this study and based on the data set HadISDH, does not seem to be sufficient to depict vegetal processes in particular. Heterogeneous vegetation increases with LCLU change and there is enormous uncertainty at a scale of 5 km, which influences E_t and wind differences (Woodward & Lomas, 2001). To avoid this uncertainty, a high-resolution LCLU map (including soil character) would have to be used and analysed for the spatial scale of the weather stations, based on suitable studies and, if possible, a long-term FACE; Duke and ORNL in the eastern USA have a variety of hydrological data (Donohue et al., 2017a; Leakey et al., 2012). The latter option is more precise but would still involve uncertainties around plant species and plant age (Medlyn et al., 2001). The phenology should also be looked at more closely, i.e. at NPP as the integral of start season, growing season and end of season, which are strongly impacted by rising temperatures in NH mid and high latitudes (Hou et al., 2013). Cloud detection should be considered when looking at NDVI to obtain more regular NDVI patterns (Chen et al., 2003). Due to increased precipitation and permafrost degradation, lakes on the Qinghai-Tibet-Plateau expanded during the late period (Liu et al., 2021). In addition, there was also shrinkage in single cases. If a weather station were present near the shrunken lake, local decreased E_w and RH could be measured.

Due to the complexity of the terrestrial drivers in the context of the ground-atmosphere interactions and the compilation of RH from q and T, it is challenging to explain the RH change through terrestrial drivers with a low resolution. Evidence of the impact of terrestrial drivers on RH was found for a couple of regions (the Caspian Sea and northwestern India), and the model runs showed that the carbon cycle response to increased CO_2 did lead to decreasing RH, inferring as evidence that CO_2 enhanced stomatal conductance led to reduced E_t and therefore RH.

Evaporation and land cover certainly have a strong impact on RH, but on a smaller scale. This study was not able to use the HadISDH dataset to examine at this small scale. Land evaporation terrestrial drivers are interesting for regional and local RH change but not for global RH change. However, this study did not find large-scale land cover change to affect RH change. The thermodynamic and dynamical drivers have a stronger impact on a larger scale.

6 Discussion and conclusion

In this thesis, the global RH trend over land was analysed, with a particular focus on the sharp decline since 2000. Underpinning this large-scale average signal are a very diverse set of regional relationships and trends. The analysis here therefore takes a bottom-to-top approach, so that on a spatial level, regions represent the global trend, and on a temporal level, seasons and single years helped to analyse the decadal trend. Correlation analysis provided information on short-term relationships, and regression analyses helped to identify drivers of the RH trend. While the thermodynamic driver (land warming faster than ocean) constitutes the largest component of RH change, this work finds that a spatially and temporally varying combination of dynamical and terrestrial drivers could help to explain the regional and seasonal details within the large-scale trend. There are lots of climate impacts related to the hydrological cycle. A correct calculation of RH in global climate models is essential to projecting these climate impacts to prepare for future climate change. Notably, the Coupled Model Intercomparison Project Phase 5 (CMIP5) models do not closely reconstruct the historical observations, and that therefore results in uncertainty over future climate projections related to the hydrological cycle.

Section 6.2.1 and Tables 6.1 to 6.3 include a summary of principal drivers in each region.

6.1 Understanding the large-scale trend through regional-scale relationships and trends

The drying signal shows a latitudinal pattern and extends close to the tropics, so it is essentially an extratropics and mid-latitudes feature. Regions were selected that show a significant annual RH trend in the late period (2000–2017). Eastern Brazil, Tibet, the Caspian Sea region, California, Mongolia, southern Africa, eastern USA and the Red Sea experienced a negative RH trend. Northwestern India and eastern Canada had a positive RH trend. Furthermore, the high latitude regions of southwestern Greenland and Scandinavia showed a negative and positive RH trend respectively. The nine regions with a drying trend strongly contributed to the global trend. The three regions with a wetting trend were examined to understand RH change more broadly.

It was expected that most regional RH changes would have common large-scale signals of drivers due to their latitudinal location, e.g. a single mode of variability or primary physical variable being clearly linked to RH change through the same relationship for several regions. During the first analyses after characterisation of RH by specific humidity (q) and air temperature (T), the uniqueness of the regional trends became apparent, which suggests that the contribution from dynamical and terrestrial drivers is very different for each region.

6.1.1 How are regional trend differences manifested?

Depending on the region and season, RH, q and T vary and correlate differently, so RH decrease is also expected to differ by region and season. While low T-q correlation coefficients indicate water-limitation, weaker or decreased $q(T)$ regression coefficients and increased positive RH(q) regression coefficients are indicators for decreasing RH, meaning that there is insufficient q to react to a change in T, and that RH reacts more strongly to a q change. Small changes could therefore have a substantial influence on RH and thus generate a trend. The reason for this could be a change in water or energy availability.

According to the Clausius-Clapeyron relationship, a weak T-q correlation represents water-limited areas, since with a T increase, not enough water evaporates to maintain atmospheric saturation. However, it is not only arid areas that show a negative RH trend. In the late period, the T-q relationship was significantly weakened in eastern Brazil (June-July-August [JJA], September-October-November [SON]), Tibet (JJA, SON), Mongolia (March-April-May [MAM]), southern Africa (SON) and the Red Sea (JJA). Whereas a significant negative T-q relationship is considered the strongest criterion for water-limitation and negative RH trend, increased RH(q) regression also indicates dryness in eastern Brazil (JJA, SON) and southern Africa (SON). In contrast, in the Caspian Sea region, in addition to an increased RH(q) regression, the RH(T) regression is also increased in the late period compared to the early period (1973–1999). In most regions, coherent significant q trends point to the RH trends. Conversely, T trends are strongly seen in the Caspian Sea region (JJA) and are primarily linked to decreasing RH.

Based on these T-q-RH relationships, the inequality of regions with a strong RH trend is manifested. So, all these are indicators for an RH trend and suggest that different drivers determine RH in these regions.

6.1.2 Why do we see apparent latitudinal patterns in the decrease of RH?

The thermodynamic driver as the fundamental driver, the land-ocean warming ratio, combined with regional circulation patterns and regional land surface properties, determines the regionally unique path of RH change in a specific region. The thermodynamic driver is reflected clearly in the extratropical and mid-latitude drying pattern. Land surface moisture is largely due to the general atmospheric circulation pattern advecting moist/dry air around the planet. If the land warms more than the ocean, it can become water-limited, and the Clausius-Clapeyron equation is deviated from. The air above the land therefore dries out in terms of saturation, or RH. This is because the ocean, which warms more slowly, does not evaporate sufficient moisture to keep pace with the evaporative demand of the faster warming land. This effect is near-global (Chadwick et al., 2016, Figs. 1f and 2f), excluding regions of strong convergence, particularly around warm tropical oceans such as over northern India. Thus, to some degree, the thermodynamically driven RH trend follows the "wet gets wetter, dry gets drier" premise. For the most part, this pattern is observed using the HadISDH and ERA-Interim datasets. However, there are other drivers relating to modes of variability and changes to atmospheric circulation (dynamical drivers) and to changes in land surface properties (terrestrial drivers) which play an important role. This study hypothesised that deviations from, or even part of, the general thermodynamically driven pattern could be coming from these other drivers.

The regions with positive RH trends tend to be around the tropics and high latitudes. In these areas there must be enough water to maintain RH, and processes at work resulting in its increase. The Intertropical Convergence Zone (ITCZ) generally provides atmospheric saturation in the tropics and convergence of the moist air. Note that a shift in the ITCZ, which is considered within the dynamical drivers through zonal (u10) and meridional winds (v10), might seasonally affect tropical regions at the edge of the ITCZ, such as northeastern Brazil or East Asian monsoon precipitation towards Mongolia. In the high latitudes, a rise in T is generally associated with reduced snow and ice cover, resulting in more open water or vegetated surfaces that then provide a moisture source for evaporation. Even though these regions do not contribute to the drying trend, but rather partially offset it, this study was able to draw on the RH behaviour, such as (i) the positive T-RH correlation in cold climates (high latitudes, December-January-February [DJF]), which is very different to the negative T-RH correlation in warmer climates, and (ii) strong q-T-RH correlations, such as in southwestern Greenland, Scandinavia and eastern Canada during the winter season. These regions of moistening highlight the deep complexity of drivers and their interaction with each other. The presence of a warm, saturated convergence zone would technically come under our classification of a thermodynamic driver, but changes to the location of that convergence zone are classed as a dynamical driver. The reduction of snow and ice cover might be thought of as a terrestrial driver in that it constitutes a change to the land surface property.

In JJA, the boreal summer, the global RH trend is strongest. The land-sea temperature contrast is greatest in the summer compared to winter. Therefore, the thermodynamic driver is expected to be strongest in the hemispheric summer. For most regions outside of the tropics, the summertime is the drier season and the period of greatest water-limitation, with lower RH in general, and is therefore close to a negative deviation from the Clausius-Clapeyron theory and exacerbates the relative drying.

6.1.3 Issues and further work: spatial heterogeneity and deviations from the four standard seasons

The analyses were approached from an average regional perspective. Due to spatial heterogeneity, it was necessary to work at the sub-regional level in some regions. For example, in southern Africa, there are two large circulation patterns (easterlies towards the east coast and southerlies towards the south coast touching the west coast), which might impact RH in different ways. In Mongolia, the T-RH correlation in the region's north (south) is positive (negative) in DJF, and there is a strong positive RH correlation in MAM only in the south. The q and T correlations with RH are related to the regional characteristics and can help to explain the influence of the driver. Heterogeneity at the sub-regional level and the sometimes sparse and uneven location of stations particularly affected analyses of terrestrial drivers and local wind changes. A higher, more equally distributed spatial resolution of the data sets would be advantageous. In particular, weather stations are sparse over eastern Canada, unequally distributed by only lying around the coastline in southwestern Greenland, and there is a lack of data inland in eastern Brazil. The resolution 5° by 5° was useful for focusing on larger effects, such as the thermodynamic and large-scale dynamical drivers. The temporal resolution was limited to monthly averages, and analyses used annual values and the four standard seasons. While these seasons usually describe the mid-latitudes well, they are less valid for regions with rainy seasons, like the south Asian monsoon in northwestern India and Tibet. Further work would benefit from analysis at the highest resolution level to account for spatial and temporal heterogeneity. Furthermore, there are uncertainties in each data set relating to the observations themselves and also the processing methods, and numerical model in the case of ERA-Interim. These were not easily incorporated into the analyses here, so the results should still be treated cautiously to some degree. Note the good agreement between ERA-Interim and HadISDH RH generally provides good confidence in the observed decreasing RH.

6.2 Interconnectivity between the thermodynamic, dynamical and terrestrial drivers

RH is controlled by heating/cooling and drying/moistening, and these processes are affected by the three drivers that this study distinguishes between. The thermodynamic driver comprises changes to temperatures and evaporation. The dynamical drivers incorporate changes to advection and modes of variability related to evaporation and temperature, and the terrestrial driver assimilates changes to evaporation and temperature. The drivers can describe the interannual RH variability (explored through correlations) or the RH trend (change in driver). It is apparent that more than one driver describes RH variability and change, and the drivers interact in most regions. Vice versa, RH can also impact the driver, which has not been addressed in this thesis, but the direction of the cause-effect relationship cannot always be clearly established.

6.2.1 Variables are part of both the dynamical and terrestrial stories

The most fundamental driver, the thermodynamic driver, is also observed on regional scales. For example, in the Caspian Sea region, the region with the strongest negative seasonal RH trend, the summer warming (notably, the Russian heatwave in 2010) generates an open water evaporation (E_w) trend, but this increased evaporation is insufficient to maintain RH. In addition, there are dynamical drivers: over the region, it rains less, as the rain is shifted eastwards, outside of the region. Thus, the inflow of air into the Caspian Sea is less saturated. Both a negative terrestrial water storage (TWS) trend and a negative normalised difference vegetation index (NDVI) trend express less water availability. This land drying indicates land cover change, as in the shrinking of the Caspian Sea. The size of the sea is essential as a surface for evaporation (Azevedo et al., 2018; Koriche et al., 2021a; Koriche et al., 2021b). The thermodynamic driver can thus be observed on a small scale, i.e. faster land-than-lake warming.

The water availability and thus the precipitation as input plays a major role for eastern Brazil (DJF), southern Africa (SON) and northwestern India (annually). In northwestern India, there is a positive precipitation trend, in particular over the Indus basin, but not enough to prevent the negative TWS trend. TWS can decline due to anthropogenic transfer of groundwater upwards (irrigation; Siebert et al., 2006). Soil moisture and NDVI increased, resulting in E_t, E_i and E_b rise, indicating enhanced q and RH. Wind stilling over northwestern India annually and in MAM and JJA appears to be linked to enhanced evaporation. This makes northwestern India the only region where RH can be associated with a change in wind speed. A link to the monsoon could not be established because this was beyond the scope of the thesis.

The rain reduction in northeastern Brazil (in particular DJF) is based on dynamical drivers, namely on the strongest rainfall driver in this region: the ITCZ. This experienced a northward shift potentially linked to negative sea surface temperature (SST) anomalies in the southern hemisphere tropical Atlantic. In SON and JJA, this effect is less intense, but the change in the mean circulation is also given: stronger southeasterlies and weaker northeasterlies mean that the ITCZ is further away from the region. The drier conditions of this reduction in rainfall and warming can be linked to larger-scale circulation such as El Niño and a warmer Interdecadal Pacific Oscillation (IPO), particularly in DJF.

The impact of wind changes is particularly strong when there are opposing trends between the early period and the late period, as in southern Africa, where the onshore Indian Ocean easterlies are reinforced in the early period and weakened in the late period, and thus lead to a reduction in rainfall. With reduced austral winter rain, dry conditions are given for the late-period spring with little rain: surface moisture and evaporation is decreased.
Over the Red Sea (MAM), dry winds from the Arabian Peninsula block moist winds from the Mediterranean in the late period causing regional drying. In contrast, north-

westerlies from the Mediterranean were increased in the early period. Southwestern Greenland (DJF) experienced increased dry northeasterlies in the late period in contrast to increased warm and moist southwesterlies in the early period. These regions would need further study.

As large scale movements of air, several modes of variability have been found to be related to the interannual RH variability (e.g. the Arctic Oscillation [AO], the El Niño Southern Oscillation [ENSO] and the Atlantic Multi-decadal Oscillation [AMO] on California) and impact the RH trend in the late period. The modes do not necessarily have to show a trend: only the AMO, the SAM, and the IOD significantly increased over the full period (1973–2017). The MEI and the IPO increased over the late period (Cai et al., 2018). The RH trend is linked to the interplay between modes in combination. For example, the RH trend in eastern Brazil is linked to a number of these large-scale drivers, such as the ENSO (particularly in DJF), but also with decreased SST in the SH tropical Atlantic, the AO (particularly in JJA; Liu et al., 2020), and regional wind direction trends out of the region, thus blocking onshore winds in SON. Each mode peak or trough is unique, like the negative AO which caused the Russian heatwave in 2010 (Wright et al., 2014) contributing to the negative RH trend over the Caspian Sea. In particular for teleconnected areas, this work found mode-like variability, but not exactly a footprint of the mode. For example, over Tibet (SON), a reminiscence of the Indian Ocean Dipole (IOD) in the SST-RH correlation patterns was detected in the tropical Indian Ocean, but not further south. Also for Tibet (SON), the pressure variability over Europe resembles the AO in JJA, but the storm tracks are differently affected.
In this mixture of signals, this research study found only one mode that strongly reflects the regional interannual RH variability and its trend. Warmer SST around eastern Canada in DJF led to increased RH relating to the AMO pattern in the late period. The AMO has been in a positive phase since 2000. This is thus the only phenomenon that has been in one phase with relatively little variability over the late period of study.

Given the short period of data (2000–2017), the RH trend is influenced by individual years. Even if there is no trend in the dynamical drivers, such as in the modes, extreme years of the drivers can contribute to the long-term trend by causing abnormally hot or dry years in certain regions, such as 2010 in the Caspian Sea region. The trend direction can be driven by a few events, with no two events being the same. On a global scale, the RH peaks in 2000, troughs in 2007–2009, 2012–2013 and 2015, the latter particularly in JJA, the season with the strongest negative RH trend. These years coincide with years in which some modes are in extreme phases, e.g. the strong La Niña (cold IPO/PDO) in 2000 and the El Niño (warm IPO/PDO) in 2014–2015. These extreme years are also well represented in regional RH time series, so there is high confidence that these extreme RH anomalies are strongly influenced by dynamical drivers.

On a much smaller scale than modes of variability, for example, in addition to wind trends concerning northeast Brazil and the SH tropical Atlantic, local wind changes occur in SON in the southeast of eastern Brazil, with increased onshore winds in the early and offshore winds in the late periods. Wind changes are often found on such a small spatial scale that their trends are not significant, e.g. in Mongolia (DJF): the insignificant anticyclonic trend pushes air from the interior out of the region in all directions, counteracting the inflow of humid air from the outside. In addition, this work found increased soil moisture and TWS decrease resulting from irrigation practices, indicating an anthropogenic impact on moisture availability. This connection may occur with a time delay due to the insignificance of correlations with RH. In Tibet, RH decreases with a strengthening of the southwesterlies in the northwest region, with southeasterlies predominating in the early period, which coincides with decreased soil moisture and decreased TWS, i.e. reduced water availability to maintain RH levels. Due to a lack of significant correlations and trends in primary physical variables, evidence of dynamical drivers on RH cannot be found for all seasonal trends in Mongolia and Tibet.

The direction of causality for small-spatial-scale drivers, such as NDVI and soil moisture, is not clear via correlation coefficients in particular: is RH reduced because of reduced NDVI and evapotranspiration (E_t), or vice versa, e.g. over the Caspian Sea region. Reduced soil moisture amplifies decreased RH and vice versa, as in northeastern Brazil.

6.2.2 Challenges in detecting non-thermodynamic drivers

Chadwick et al. (2016) (Figs. 1f and 2f) found the thermodynamic driver to be globally represented, most strongly in eastern Brazil, southern Africa and the eastern USA. In fact, for many other regions with strong RH trends in observations, other drivers were found in this study: dynamical drivers on regional scales, terrestrial drivers on smaller scales. The HadGEM2-ES showed that CO_2 driven stomatal changes might cause a negative q trend and thus a decline in RH, but this is much weaker than a decline caused by the thermodynamic or dynamical drivers. Due to high spatial heterogeneity, terrestrial drivers are often only detectable at the grid box level or perhaps only at the weather station level. These small scales can change RH over temporal or spatial lags (e.g. transport of precipitation water in rivers or underground to place of RH change) (e.g. Mongolia with a soil moisture, evaporation and TWS change, and northwestern India with spatial heterogeneity in rainfall in JJA). For this, lags would have to be investigated, and ideally at a high resolution. The Hansen dataset (Hansen et al., 2013a) offers a high resolution of afforestation/deforestation, which might be more informative than just NDVI. Since E_t as a response to CO_2 depends on plant functional types (PFT), regional FACE experiments could be more involved in case studies; they would provide quantitative data on the impact of CO_2 driven stomatal change on RH. Concerning aerodynamic resistance and roughness length, a differentiation of plants depending on height would also be interesting (e.g. trees versus crops versus grass). Furthermore, the root depth of vegetation could be an important parameter concerning evaporation. Since evaporation depends strongly on the land surface temperature, this variable would be good to bring together with T to determine evaporated water rate. Work could also be done on the Bowen ratio and surface conditions such as average wind speed, solar/net radiation. Radiation would have to include clouds and aerosols. land cover and land use (LCLU) change was measured directly only via the NDVI. Areas of deforestation could not be detected in this study, which might be due to the spatial resolution of data. Terrestrial drivers were not clearly identifiable for most regions. Model experiments that contain land use change differences could however be used to detect impacts of large-scale LCLU change as a potential impact on RH.

Quantification of the impact of the drivers could be done via the calculation of time expansion coefficients, by projecting the anomalies of a variable onto the regression map between RH and that variable to create a timeseries of that map, for example, between global SST and regionally averaged RH. Multiple regressions could also be undertaken. Here, too, it would be necessary to proceed on as small a scale as possible and not to use regional averages, e.g. Mongolia with T-RH correlations of opposite sign in the north and south in DJF and subregional T-RH and q-RH correlations also in MAM. Whereas TWS in Mongolia decreases spatially over large-scales in the late period, evaporation and their fractions, soil moisture, and NDVI show a very patchy pattern of trends with rare correlations. With a lack of significant trends in T in both seasons and a significant q trend in MAM but rare significant indicators of dynamical and terrestrial drivers in the same grid boxes, for Mongolia, it was challenging to detect an explanation for the negative RH trend in the late period. Droughts over the region have been linked with anthropogenic agriculture (overgrazing), mining and (ineffective) water management, which could be linked to strongly negative TWS trends. Over large regional areas, the variables of drivers do not correlate with RH. The same applies to Tibet (JJA, SON) and the south of the California region, with only the latter region with a significant T trend but no significant q trends in either of the regions: a negative TWS trend with time-lagged correlations to RH was also found, while neither terrestrial nor dynamical drivers showed a clear and spatially coherent trend.

6.3 Differences between the observations and the model HadGEM2-ES

The CMIP5 models, including the HadGEM2-ES model focused on here, can reproduce the dominant thermodynamic driver (Chadwick et al., 2016; Dunn et al., 2017) to some degree. They do not, however, capture the strong amplifying and mitigating effects of regionally and seasonally different dynamical drivers and terrestrial drivers. They cannot therefore represent the RH trend to the same pattern and magnitude as in the observations. The knowledge acquired in this thesis, on the one hand, based on the observations, and, on the other hand, their differences to the model, could be used to improve these coupled models or at least better understand the uncertainty surrounding them.

This study found supporting evidence as to why models might not be expected to do well in reconstructing observations. A key difference between models and observations applies to the correlations between detrended time series of q, T and RH. The models were found to imply overly negative T-q correlations. In the high latitudes in DJF, the HadGEM2-ES model presented negative q-RH and positive T-RH, which is the opposite of the observations. Possibly, this could be linked to boundary layer processes in the models (Pers. Comm. J. Edwards) but this has not yet been investigated. On the one hand, HadGEM2-ES uses the zero-layer snow scheme, i.e. it neglects the insulating effect of snow on the soil. With this missing insulating effect, heat and moisture flux from the surface into the atmosphere via evaporation would be overestimated if cold air masses move over the snow. Fluxes would be too large until the snow cools down. On the other hand, due to the surface layer being extended high up in the models, there is extensive mixing in the surface boundary layer. Extensive mixing could result in moisture from high altitudes coming down to the surface.

The fact that each region is unique in terms of its drivers on RH, and the relationships between the drivers themselves, and with RH, is a key reason why models cannot be expected to closely replicate the observations. This study does find evidence of dynamical drivers, and that in particular is something that the models may not necessarily be able to replicate in the same time frame as the observations if the changes in the drivers are not externally forced and are due to internal climate variability. Furthermore, the models cannot be expected to include a perfect representation of LCLU, such as different types of vegetation and anthropogenic processes relating to water management and irrigation (e.g. in northwestern India; Siebert et al., 2006), because these are highly complex. Therefore, evidence of terrestrial drivers linked to LCLU change also suggests reasons why the models would not do well.

Clearly the key areas of improvement for the models are as follows: getting latitudinal and seasonal correlations of q and T with RH correct, and introducing a more temporally similar approximation of the interplay of climate variability and deep complexity of terrestrial drivers. Climate models are incredibly powerful tools with which we can explore possible future exposure to important impacts. However, understanding the uncertainties relating to them is crucial.

6.4 Concluding remarks and outlook

By analysing the observed RH at different spatial and temporal levels, both interannual RH variability could be better understood, and its trend could be explained based on different drivers. The subregional interaction of dynamical drivers and terrestrial drivers both contribute to and counter the thermodynamic driver. Further studies should mainly address the heterogeneity of the land-surface process by increasing the spatial resolution at which analysis is undertaken.

The data in this thesis ended in 2017. The RH trend has continued since then (Willett et al., 2021a), with extreme events of dryness that contributed to the northern California fires in 2018 (Brewer & Clements, 2019) and 2021 and 2020 in Australia (Gulev et al., 2021). Since then, global T has remained high, with 2020 and 2019 as the second and the third hottest years after 2016 (NOAA National Centers for Environmental Information, 2022). Even though a regional prediction of RH is complex, under rising global T in the near future, which is expected, given anthropogenic climate change, an RH decrease over land is expected to continue due to the thermodynamic driver, since the land is still warming faster than the ocean. Given the findings in this thesis, the current state of research expects to see other small scale changes in RH due to anthropogenic practices of irrigation and groundwater use, changes to vegetation cover through afforestation/deforestation, and CO_2-driven enhanced stomatal conductance. Changes in the modes of variability and circulation in general can also impact RH on a regional to local level.

Coupled Model Intercomparison Project Phase 6 (CMIP6) models predict a likelihood of near-surface RH declining over land, particularly over subtropical latitudes, due to ocean-advection and evapotranspiration (Lee et al., 2021). In relation to this, the CMIP6 models estimate a decrease in precipitation over the subtropics, e.g. southern Africa and the Mediterranean, due to circulation changes and land-warming ocean contrasts. However, as found in this study, dynamical drivers on different spatial scales contribute to the RH change. Dynamical drivers and large circulation changes, often with a background of modes of variability, still cause major challenges for the current CMIP6 climate models. For example, the ENSO is predicted to remain the dominant mode, and enhanced rainfall variability could also be associated with it (Lee et al., 2021). However, there is no strong model consensus regarding the ENSO's impact on SST variability. Modelling the ENSO's impact on SST variability would be essential, among other things, to determine the RH change due to latitudinal ITCZ shift due to trends in the tropical Atlantic SST, which is linked to the tropical Pacific SST, thus, the ENSO. With an improved representation of climate variability and its teleconnections, regional processes and extreme years are more likely to be captured.

A realistic representation on small spatial scales in climate models is particularly important concerning the terrestrial drivers, such as the representation of vegetation processes, LCLU change, and evapotranspiration. The hope for high resolution could be so-called digital twins, i.e. climate models simulating reality to a high extent, such as the "Destination Earth" of the European Commission, the European Space Agency (ESA), the European Centre for Medium-Range Weather Forecasts (ECMWF) and the European Organisation for the Exploitation of Meteorological Satellites (EUMETSAT) system with 1 km spatial resolution by the end of 2030. Since small-scale processes are involved, an even higher resolution would be necessary to represent clouds. There is still a very high degree of uncertainty in models in the cloud parameterization, thus in radiation and the warming/cooling effect, long-distance transportation of water and release, linked to the hydrological cycle, including the terrestrial hydrological cycle and related surface processes (runoff, infiltration, groundwater flow, evaporation) which might be potential candidate processes affecting near-surface RH. With the increasing CO_2 concentrations, the political and economic interest in improving climate models and predicting climate sensitivity is growing in addition to the scientific one. This trend allows model development to happen quickly in terms of resolution and speed, and we can look forward to improvements in the future.

The new knowledge gained in this thesis will improve understanding of model uncertainty, and even the models themselves and their representation of the hydrological cycle, as well as climate events and their scientific, social and economic impact in the context of climate change. This thesis demonstrates the importance of dynamical and terrestrial drivers for subregional seasonal changes in RH, and the complexity of the climate system.

Table 6.1: Conclusion of important mechanisms and drivers in regions with a strong negative RH trend over the late period (eastern Brazil, Tibet and the Caspian Sea region), based on Table 3.4, and related sections.

	Main findings	Sections
Regions with a strong negative RH trend over the late period		
Eastern Brazil	• Particularly in northeastern Brazil in DJF, a cooler southern tropical Atlantic led to a northward shift of the ITCZ, thus, reduced rainfall and soil moisture and increased E_w, in the south, and reduced TWS along the east coast. • No clear ENSO-footprint, but a striking El Niño in 2016 in DJF. • In SON, the RH(q) regression coefficient has increased since 2000. The regional-scale wind changes reduce moisture transport from the ocean to the land. While rain shows no significant trends but strong correlations with RH, E and, particularly E_t (not E_w though) and soil moisture are reduced. • In conclusion, evidence for dynamical drivers linked to regional ocean warming was found for DJF and to a weaker extent in SON. Evidence for dynamical drivers on a smaller spatial scale was found for SON. - Mind spatial data is lacking in this region! • Negative RH trend in HadGEM2-ES *esmFixClim2*, i.e. stomatal efficiency change under increasing CO_2 in all four seasons	3.3.1.1; 4.1.1; 4.1.2; 4.3; 5.1; 5.2.2; 5.4
Tibet	• In SON, a reminiscence of the Indian Ocean Dipole (IOD) in the SST-RH correlation patterns was detected in the tropical Indian Ocean, but not further south. Also for SON, the pressure variability over Europe resembles the Arctic Oscillation (AO) in JJA, but the storm tracks are differently affected. RH decreases with a strengthening of the southwesterlies in the northwest region, with southeasterlies predominating in the early period, which coincides with decreased soil moisture and decreased TWS, i.e. reduced water availability to maintain RH levels. • Due to a lack of significant correlations and trends in primary physical variables, evidence of dynamical drivers on RH could not be found. • Negative RH trend in HadGEM2-ES *esmFixClim2*, i.e. stomatal efficiency change under increasing CO_2 in JJA and SON	3.3.1.2; 4.1.3; 5.4
Caspian Sea region	• Particularly in JJA, the RH(q) and RH(T) regression coefficients have increased since 2000. In the region, increased T and SST led to increased but insufficient evaporation (E_w), accompanied by low precipitation and decreasing TWS. • Observed decrease in the Caspian Sea endorheic basin in the late period • Northwesterlies play an interannual, non-trend-related role on q/T/RH/precipitation. • No clear AO-footprint (SLP) but a striking negative AO in 2010 • In conclusion, the thermodynamic driver (faster land-than-lake warming) causes a land-cover change (terrestrial drivers), thus, the RH decreases. A trend in dynamical drivers is not found but could have been important in 2010; further research would be needed regarding winds during the Russian heat wave.	3.3.1.3; 4.1.4; 5.1; 5.2.2

Table 6.2: As for Table 6.1, for regions with a strong negative RH trend over the late period (California, Mongolia and southern Africa).

	Main findings	Sections
Regions with a strong negative RH trend over the late period		
California	• Prevailing winds from the Pacific towards the region and large wind, SST and SLP patterns over the NH Atlantic ocean determine the interannual variability but do not show a trend, thus, could not be considered to change RH over the long-term. • Due to significant positive trends in SST and its positive correlation with regional *T* and *q* but not with RH in the late period and an absence of a trend in *q*, the thermodynamic driver seems most plausible for the negative RH trend. The faster land than ocean warming might be enhanced by dynamical drivers over shorter periods. For details, further research would be needed. • An AO-like SLP correlation pattern visible in the late period • Negative RH trend in HadGEM2-ES *esmFixClim2*, i.e. stomatal efficiency change under increasing CO_2	3.3.1.4; 4.1.5; 4.3; 5.4
Mongolia	• In DJF, the insignificant anticyclonic trend pushes air from the interior out of the region in all directions, counteracting the inflow of humid air from the outside. • Increased soil moisture and decreased TWS may result from irrigation practices, indicating an anthropogenic impact on moisture availability. This connection may occur with a time delay due to the insignificance of correlations with RH. • Due to a lack of significant correlations and trends in primary physical variables, evidence of dynamical drivers on RH could not be found.	3.3.1.5; 4.1.6; 5.2.2
Southern Africa	• In the north of southern Africa in JJA, RH could have decreased due to little changes in *q* and *T* or negative *q* trends. Decreased onshore easterlies due to increased SST around the Straits of Mozambique (Archer et al., 2017; IOD) and decreased SLP east of Madagascar led to a reduction in precipitation, thus, TWS over the northeastern part, and extreme *T* (no significant trend but peaks in 2005, 2008 and 2012). • In the north of southern Africa in SON, *T* increased (2005, 2015) due to increased SST in the Indian Ocean and maybe due to northerly wind trends. Precipitation decreased significantly, *q* insignificantly. • In the south of southern Africa in SON, *q* decreased (2002, 2011, 2013) with a *T* peak in 2015. RH is linked to winds over the southern tip of the region, resulting in decreased root-soil moisture. There is a clear Southern Annular Mode (SAM)-footprint and a negative SAM in 2015. • Evidence for dynamical drivers on a smaller spatial scale was found. • Negative RH trend in HadGEM2-ES *esmFixClim2*, i.e. stomatal efficiency change under increasing CO_2 in JJA and SON	3.3.1.6; 4.1.7; 5.1; 5.4

Table 6.3: As for Table 6.1, for regions with a strong negative (southwestern Greenland, eastern USA, the Red Sea and Patagonia) or a strong positive RH trend over the late period (Scandinavia, northwestern India and eastern Canada).

	Main findings	**Sections**
Regions with a strong negative RH trend over the late period		
Southwestern Greenland	• In DJF, dry northeasterlies increased in the late period in contrast to increased warm and moist southwesterlies in the early period. For details, further research would be needed. • Negative RH trend in HadGEM2-ES *esmFixClim2*, i.e. stomatal efficiency change under increasing CO_2 in DJF	3.3.1.7; 4.1; 4.3; 5.4
Eastern USA	• No evidence in the explored dynamical drivers was found. • Negative RH trend in HadGEM2-ES *esmFixClim2*, i.e. stomatal efficiency change under increasing CO_2 in all four seasons	3.3.1.8; 5.4
Red Sea	In MAM, dry winds from the Arabian Peninsula block moist winds from the Mediterranean in the late period causing regional drying. In contrast, northwesterlies from the Mediterranean were increased in the early period. For details, further research would be needed.	3.3.1.9; 4.1
Patagonia	No evidence in the explored drivers was found; further research would be needed.	3.3.1.10
Regions with a strong positive RH trend over the late period		
Scandinavia	• In JJA, a strong correlation between precipitation and RH and a positive trend in the latter was found. Significant negative (positive) E_t and E_w (E_i) trends result in no significant E trend possibly through offetting; for details, further research would be needed. • In both JJA and SON, the Barents Sea has been warming in the late period; for details, further research would be needed.	3.3.2.1; 4.3; 5.1
Northwestern India	• In northwestern India, annual RH increased already in the early period with a RH trough in 2000. RH and q have increased due to more rainfall, increased soil moisture and increased evaporation (E, E_t, E_i, E_b), indicating extended greening (NDVI) and irrigation. • In JJA, the monsoon season, precipitation trend but no RH trend • Water availability above ground has been increasing, while below ground it has been decreasing, particularly around the Indus river region. • Evidence for terrestrial drivers were found. • Decreased wind speed is linked to increased land E, and enhanced q, thus RH.	3.3.2.3; 5.1; 5.2.1; 5.5
Eastern Canada	Warmer SST around the region in DJF led to increased RH relating to the AMO pattern in the late period. The AMO has been in a positive phase since 2000. This is thus the only phenomenon that has been in one phase with relatively little variability over the late period of study. For details, further research would be needed.	3.3.2.4; 4.3

Bibliography

AghaKouchak, A., Feldman, D., Hoerling, M., Huxman, T. & Lund, J. (2015). Water and climate: Recognize anthropogenic drought. *Nature*, *524*(7566), 409–411.

Ainsworth, E. A. & Long, S. P. (2005). What have we learned from 15 years of free-air CO2 enrichment (FACE)? a meta-analytic review of the responses of photosynthesis, canopy properties and plant production to rising CO2. *New Phytol.*, *165*(2), 351–371.

Alexander, M. A., Bladé, I., Newman, M., Lanzante, J. R., Lau, N.-C. & Scott, J. D. (2002). The atmospheric bridge: The influence of ENSO teleconnections on Air–Sea interaction over the global oceans. *J. Clim.*, *15*(16), 2205–2231.

Al-Hamdan, M. Z., Oduor, P., Flores, A. I., Kotikot, S. M., Mugo, R., Ababu, J. & Farah, H. (2017). Evaluating land cover changes in eastern and southern africa from 2000 to 2010 using validated landsat and MODIS data. *Int. J. Appl. Earth Obs. Geoinf.*, *62*, 8–26.

Alkama, R. & Cescatti, A. (2016). Biophysical climate impacts of recent changes in global forest cover. *Science*, *351*(6273), 600–604.

Allan, R. P., Barlow, M., Byrne, M. P., Cherchi, A., Douville, H., Fowler, H. J., Gan, T. Y., Pendergrass, A. G., Rosenfeld, D., Swann, A. L. S., Wilcox, L. J. & Zolina, O. (2020). Advances in understanding large-scale responses of the water cycle to climate change. *Ann. N. Y. Acad. Sci.*

Amorim, A. C. B., Chaves, R. R. & Silva, C. M. S. (2014). Influence of the tropical atlantic ocean's sea surface temperature in the eastern northeast brazil precipitation.

Andrew, R. L., Guan, H. & Batelaan, O. (2016). Large-scale vegetation responses to terrestrial moisture storage changes. *Hydrol. Earth Syst. Sci. Discuss.*, 1–13.

Archer, E. R. (2019). Learning from south africa's recent summer rainfall droughts: How might we think differently about response? *Area*, *51*(3), 603–608.

Archer, E. R. M., Landman, W. A., Tadross, M. A., Malherbe, J., Weepener, H., Maluleke, P. & Marumbwa, F. M. (2017). Understanding the evolution of the 2014–2016 summer rainfall seasons in southern africa: Key lessons.

Arpe, K., Leroy, S. A. G., Lahijani, H. & Khan, V. (2012). Impact of the european russia drought in 2010 on the caspian sea level.

Arpe, K. & Leroy, S. A. G. (2007). The caspian sea level forced by the atmospheric circulation, as observed and modelled. *Quat. Int.*, *173-174*, 144–152.

Arpe, K., Molavi-Arabshahi, M. & Leroy, S. A. G. (2020). Wind variability over the caspian sea, its impact on caspian seawater level and link with ENSO. *Int. J. Climatol.*, *40*(14), 6039–6054.

Ashok, K., Behera, S. K., Rao, S. A., Weng, H. & Yamagata, T. (2007). El niño modoki and its possible teleconnection. *J. Geophys. Res.*, *112*(C11).

Ashok, K. & Yamagata, T. (2009). The el niño with a difference. *Nature*, *461*(7263), 481–484.

Asner, G. P., Brodrick, P. G., Anderson, C. B. et al. (2016). Progressive forest canopy water loss during the 2012–2015 california drought. *Proceedings of the.*

Azevedo, S. C. d., Cardim, G. P., Puga, F., Singh, R. P. & Silva, E. A. d. (2018). Analysis of the 2012-2016 drought in the northeast brazil and its impacts on the sobradinho water reservoir. *Remote Sens. Lett.*, *9*(5), 438–446.

Azorin-Molina, C., Dunn, R. J. H., Ricciardulli, L., Mears, C. A., McVicar, T. & icolas, J. (2021). Global climate] land and ocean surface winds - in state of the climate in 2020. *Bull. Am. Meteorol. Soc.*, *102*(8), Si–S475.

Azorin-Molina, C., Rehman, S., Guijarro, J. A., McVicar, T. R., Minola, L., Chen, D. & Vicente-Serrano, S. M. (2018). Recent trends in wind speed across saudi arabia, 1978-2013: A break in the stilling. *Int. J. Climatol.*, *38*, e966–e984.

Barnston, A. G. & Livezey, R. E. (1987). Classification, seasonality and persistence of Low-Frequency atmospheric circulation patterns. *Mon. Weather Rev.*, *115*(6), 1083–1126.

Barry, R. G. & Carleton, A. M. (2013). *Synoptic and dynamic climatology.* Routledge.

Barry, R. G. & Chorley, R. J. (2009). *Atmosphere, weather and climate.* Routledge.

Bayr, T., Dommenget, D., Martin, T. & Power, S. B. (2014). The eastward shift of the walker circulation in response to global warming and its relationship to ENSO variability. *Clim. Dyn.*, *43*(9-10), 2747–2763.

Beck, H. E., Zimmermann, N. E., McVicar, T. R., Vergopolan, N., Berg, A. & Wood, E. F. (2018). Present and future Köppen-Geiger climate classification maps at 1-km resolution. *Sci Data*, *5*, 180214.

Becker, A., Finger, P., Meyer-Christoffer, A., Rudolf, B., Schamm, K., Schneider, U. & Ziese, M. (2013). A description of the global land-surface precipitation data products of the global precipitation climatology centre with sample applications including centennial (trend) analysis from 1901–present.

Bellouin, N., Collins, W. J., Culverwell, I. D., Halloran, P. R., Hardiman, S. C., Hinton, T. J., Jones, C. D., McDonald, R. E., McLaren, A. J., O'Connor, F. M. et al.

(2011). The HadGEM2 family of met office unified model climate configurations. *Geoscientific Model Development*, *4*(3), 723–757.

Benson, L., Linsley, B., Smoot, J., Mensing, S., Lund, S., Stine, S. & Sarna-Wojcicki, A. (2003). Influence of the pacific decadal oscillation on the climate of the sierra nevada, california and nevada. *Quat. Res.*, *59*(2), 151–159.

Berdahl, M., Rennermalm, A., Hammann, A., Mioduszweski, J., Hameed, S., Tedesco, M., Stroeve, J., Mote, T., Koyama, T. & McConnell, J. R. (2018). Southeast greenland winter precipitation strongly linked to the icelandic low position. *J. Clim.*, *31*(11), 4483–4500.

Berg, A., Findell, K., Lintner, B., Giannini, A., Seneviratne, S. I., van den Hurk, B., Lorenz, R., Pitman, A., Hagemann, S., Meier, A., Cheruy, F., Ducharne, A., Malyshev, S. & Milly, P. C. D. (2016). Land–atmosphere feedbacks amplify aridity increase over land under global warming. *Nat. Clim. Chang.*, *6*, 869.

Berrisford, P., Dee, D., Poli, P., Brugge, R., Fielding, K., Fuentes, M., Kållberg, P., Kobayashi, S., Uppala, S. & Simmons, A. (2011). The era-interim archive version 2.0, shinfield park. *Reading*, *1*, 23.

Best, M. J., Pryor, M., Clark, D. B., Rooney, G. G., Essery, R., Ménard, C. B., Edwards, J. M., Hendry, M. A., Porson, A., Gedney, N. et al. (2011). The joint UK land environment simulator (JULES), model description–part 1: Energy and water fluxes. *Geoscientific Model Development*, *4*(3), 677–699.

Bettadpur, S. (2007). Level-2 gravity field product user handbook. *The GRACE Project (Jet Propulsion Laboratory, Pasadena, CA, 2003).*

Betts, R. A., Golding, N., Gonzalez, P., Gornall, J., Kahana, R., Kay, G., Mitchell, L. & Wiltshire, A. (2015). Climate and land use change impacts on global terrestrial ecosystems and river flows in the hadgem2-es earth system model using the representative concentration pathways. *Biogeosciences*, *12*(5), 1317–1338.

Betts, R. A., Boucher, O., Collins, M., Cox, P. M., Falloon, P. D., Gedney, N., Hemming, D. L., Huntingford, C., Jones, C. D., Sexton, D. M. H. & Webb, M. J. (2007). Projected increase in continental runoff due to plant responses to increasing carbon dioxide. *Nature*, *448*(7157), 1037–1041.

Betts, R. A., Cox, P. M., Lee, S. E. & Woodward, F. I. (1997). Contrasting physiological and structural vegetation feedbacks in climate change simulations. *Nature*, *387*, 796.

Blamey, R. C., Kolusu, S. R., Mahlalela, P., Todd, M. C. & Reason, C. J. C. (2018). The role of regional circulation features in regulating el niño climate impacts over southern africa: A comparison of the 2015/2016 drought with previous events. *Int. J. Climatol.*

Blunden, J. & Boyer, T. (2021). State of the climate in 2020. *Bull. Am. Meteorol. Soc.*, *102*(8), S1–S475.

Bonan, G. B. (1999). FROST FOLLOWED THE PLOW: IMPACTS OF DEFORESTATION ON THE CLIMATE OF THE UNITED STATES. *Ecol. Appl.*, *9*(4), 1305–1315.

Bonhoure, D., Rowe, E., Mariano, A. J. & Ryan, E. H. (2004). The south equatorial sys current. *Ocean surface currents [online]. Available from http://oceancurrents. rsmas. miami. edu/atlantic/south-equatorial. html [accessed 8 November 2012].*

Bonne, J.-L., Steen-Larsen, H. C., Risi, C., Werner, M., Sodemann, H., Lacour, J.-L., Fettweis, X., Cesana, G., Delmotte, M., Cattani, O., Vallelonga, P., Kjaer, H. A., Clerbaux, C., Sveinbjörnsdóttir, Á. E. & Masson-Delmotte, V. (2015). The summer 2012 greenland heat wave: In situ and remote sensing observations of water vapor isotopic composition during an atmospheric river event. *J. Geophys. Res.*, *120*(7), 2970–2989.

Bormann, K. J., Brown, R. D., Derksen, C. & Painter, T. H. (2018). Estimating snow-cover trends from space. *Nat. Clim. Chang.*, *8*(11), 924–928.

Bothe, O., Fraedrich, K. & Zhu, X. (2009). The large-scale circulations and summer drought and wetness on the tibetan plateau.

Boucher, O., Jones, A. & Betts, R. A. (2009). Climate response to the physiological impact of carbon dioxide on plants in the met office unified model HadCM3. *Clim. Dyn.*, *32*(2), 237–249.

Boyer, J. S., Byrne, P., Cassman, K. G., Cooper, M., Delmer, D., Greene, T., Gruis, F., Habben, J., Hausmann, N., Kenny, N., Lafitte, R., Paszkiewicz, S., Porter, D., Schlegel, A., Schussler, J., Setter, T., Shanahan, J., Sharp, R. E., Vyn, T. J., … Gaffney, J. (2013). The U.S. drought of 2012 in perspective: A call to action. *Glob. Food Sec.*, *2*(3), 139–143.

Brewer, M. J. & Clements, C. B. (2019). The 2018 camp fire: Meteorological analysis using in situ observations and numerical simulations. *Atmosphere*, *11*(1), 47.

Bunce, J. A. (2004). Carbon dioxide effects on stomatal responses to the environment and water use by crops under field conditions. *Oecologia*, *140*(1), 1–10.

Byrne, M. P. & O'Gorman, P. A. (2013a). Link between land-ocean warming contrast and surface relative humidities in simulations with coupled climate models. *Geophys. Res. Lett.*

Byrne, M. P. & O'Gorman, P. A. (2013b). Land–Ocean warming contrast over a wide range of climates: Convective Quasi-Equilibrium theory and idealized simulations. *J. Clim.*, *26*(12), 4000–4016.

Byrne, M. P. & O'Gorman, P. A. (2016). Understanding decreases in land relative humidity with global warming: Conceptual model and GCM simulations. *J. Clim.*, *29*(24), 9045–9061.

Byrne, M. P. & O'Gorman, P. A. (2018). Trends in continental temperature and humidity directly linked to ocean warming. *Proc. Natl. Acad. Sci. U. S. A.*, *115*(19), 4863–4868.

Cai, W., Borlace, S., Lengaigne, M., van Rensch, P., Collins, M., Vecchi, G., Timmermann, A., Santoso, A., McPhaden, M. J., Wu, L., England, M. H., Wang, G., Guilyardi, E. & Jin, F.-F. (2014). Increasing frequency of extreme el niño events due to greenhouse warming. *Nat. Clim. Chang.*, *4*(2), 111–116.

Cai, W., Ng, B., Geng, T., Wu, L., Santoso, A. & McPhaden, M. J. (2021). Addendum: Butterfly effect and a self-modulating el niño response to global warming. *Nature*, *591*(7849), E14–E15.

Cai, W., Santoso, A., Wang, G., Yeh, S.-W., An, S.-I., Cobb, K. M., Collins, M., Guilyardi, E., Jin, F.-F., Kug, J.-S., Lengaigne, M., McPhaden, M. J., Takahashi, K., Timmermann, A., Vecchi, G., Watanabe, M. & Wu, L. (2015). ENSO and greenhouse warming. *Nat. Clim. Chang.*, *5*(9), 849–859.

Cai, W., Wang, G., Dewitte, B., Wu, L., Santoso, A., Takahashi, K., Yang, Y., Carréric, A. & McPhaden, M. J. (2018). Increased variability of eastern pacific el niño under greenhouse warming.

Callaghan, T. V., Johansson, M., Brown, R. D., Groisman, P. Y., Labba, N., Radionov, V., Barry, R. G., Bulygina, O. N., Essery, R. L. H., Frolov, D. M., Golubev, V. N., Grenfell, T. C., Petrushina, M. N., Razuvaev, V. N., Robinson, D. A., Romanov, P., Shindell, D., Shmakin, A. B., Sokratov, S. A., … Yang, D. (2011). The changing face of arctic snow cover: A synthesis of observed and projected changes. *Ambio*, *40*(1), 17–31.

Cao, L., Bala, G., Caldeira, K., Nemani, R. & Ban-Weiss, G. (2010). Importance of carbon dioxide physiological forcing to future climate change. *Proc. Natl. Acad. Sci. U. S. A.*, *107*(21), 9513–9518.

Cazenave, A. (2006). How fast are the ice sheets melting? *Science*.

Cazenave, A., Bonnefond, P., Dominh, K. et al. (1997). Caspian sea level from Topex-Poseidon altimetry: Level now falling. *Geophysical*.

Chadwick, R., Good, P. & Willett, K. (2016). A simple moisture advection model of specific humidity change over land in response to SST warming. *J. Clim.*, *29*(21), 7613–7632.

Chaidez, V., Dreano, D., Agusti, S., Duarte, C. M. & Hoteit, I. (2017). Decadal trends in red sea maximum surface temperature. *Sci. Rep.*, *7*(1), 8144.

Chan, K. H., Peiris, J. S. M., Lam, S. Y., Poon, L. L. M., Yuen, K. Y. & Seto, W. H. (2011). The effects of temperature and relative humidity on the viability of the SARS coronavirus. *Adv. Virol.*, *2011*, 734690.

Changnon, S. A. (2000). *El niño 1997-1998: The climate event of the century*. Oxford University Press.

Chen, C., Li, D., Li, Y., Piao, S., Wang, X., Huang, M., Gentine, P., Nemani, R. R. & Myneni, R. B. (2020). Biophysical impacts of earth greening largely controlled by aerodynamic resistance. *Sci. Adv.*, *6*(47), eabb1981.

Chen, J. L., Pekker, T., Wilson, C. R. et al. (2017). Long-term caspian sea level change. *Geophysical*.

Chen, P.-Y., Srinivasan, R., Fedosejevs, G. & Kiniry, J. R. (2003). Evaluating different NDVI composite techniques using NOAA-14 AVHRR data.

Chen, S.-C., Liao, C.-M., Chio, C.-P., Chou, H.-H., You, S.-H. & Cheng, Y.-H. (2010). Lagged temperature effect with mosquito transmission potential explains dengue variability in southern taiwan: Insights from a statistical analysis. *Sci. Total Environ.*, *408*(19), 4069–4075.

Chen, W. Y. & Van den Dool, H. (2003). Sensitivity of teleconnection patterns to the sign of their primary action center. *Mon. Weather Rev.*, *131*(11), 2885–2899.

Christensen, J. H., Kanikicharla, K. K., Aldrian, E., An, S. I., Cavalcanti, I. F. A., de Castro, M., Dong, W., Goswami, P., Hall, A., Kanyanga, J. K. et al. (2013). Climate phenomena and their relevance for future regional climate change. *Climate change 2013 the physical science basis: Working group i contribution to the fifth assessment report of the intergovernmental panel on climate change* (pp. 1217–1308). Cambridge University Press.

Christian-Smith, J., Levy, M., Gleick, P. H., Ross, N. & Luu, P. (2011). *Impacts of the california drought from 2007 to 2009*. Pacific Institute Oakland, CA.

Chu, V. W. (2014). Greenland ice sheet hydrology: A review. *Progress in Physical Geography: Earth and Environment*, *38*(1), 19–54.

Clark, D. B., Mercado, L. M., Sitch, S., Jones, C. D., Gedney, N., Best, M. J., Pryor, M., Rooney, G. G., Essery, R., Blyth, E. et al. (2011). The joint UK land environment simulator (JULES), model description–part 2: Carbon fluxes and vegetation dynamics. *Geoscientific Model Development*, *4*(3), 701–722.

Coelho, C. A. S., Uvo, C. B. & Ambrizzi, T. (2002). Exploring the impacts of the tropical pacific SST on the precipitation patterns over south america during ENSO periods. *Theor. Appl. Climatol.*, *71*(3), 185–197.

Collins, M., Knutti, R., Arblaster, J., Dufresne, J.-L., Fichefet, T., Friedlingstein, P., Gao, X., Gutowski, W. J., Johns, T., Krinner, G. et al. (2013). Long-term climate change: Projections, commitments and irreversibility. *Climate change 2013-the* *physical science basis: Contribution of working group I to the fifth assessment report of the intergovernmental panel on climate change* (pp. 1029–1136). Cambridge University Press.

Collins, W. J., Bellouin, N., Doutriaux-Boucher, M., Gedney, N., Halloran, P., Hinton, T., Hughes, J., Jones, C. D., Joshi, M., Liddicoat, S., Martin, G., O'Connor, F., Rae, J., Senior, C., Sitch, S., Totterdell, I., Wiltshire, A. & Woodward, S. (2011). Development and evaluation of an Earth-System model – HadGEM2.

Collins, W. J., Bellouin, N., Doutriaux-Boucher, M., Gedney, N., Hinton, T., Jones, C. D., Liddicoat, S., Martin, G., O'Connor, F., Rae, J. et al. (2008). *Evaluation of the HadGEM2 model*. Met Office Exeter, UK.

Cook, B. I., Smerdon, J. E., Seager, R. & Coats, S. (2014). Global warming and 21st century drying. *Clim. Dyn.*, *43*(9-10), 2607–2627.

Cortés, J., Mahecha, M. D., Reichstein, M., Myneni, R. B., Chen, C. & Brenning, A. (2021). Where are global vegetation greening and browning trends significant? *Geophys. Res. Lett.*, *48*(6).

Costa, D. D., da Silva Pereira, T. A., Fragoso, C. R., Madani, K. & Uvo, C. B. (2016). Understanding drought dynamics during dry season in eastern northeast brazil.

Costa, D. D., Uvo, C. B., Rolim Da Paz, A., De Oliveira Carvalho, F. & Fragoso, C. R., Jr. (2018). Long-term relationships between climate oscillation and basin-scale hydrological variability during rainy season in eastern northeast brazil. *Hydrol. Sci. J.*, *63*(11), 1636–1652.

Cox, P. (2001). Description of the "TRIFFID" dynamic global vegetation model. *undefined*.

Dai, A. (2011). Characteristics and trends in various forms of the palmer drought severity index during 1900–2008. *J. Geophys. Res.*, *116*(D12).

Dai, A. (2021). Hydroclimatic trends during 1950–2018 over global land. *Clim. Dyn.*, *56*(11), 4027–4049.

Davarzani, H., Smits, K., Tolene, R. M. & Illangasekare, T. (2014). Study of the effect of wind speed on evaporation from soil through integrated modeling of the atmospheric boundary layer and shallow subsurface.

Dee, D. P., Uppala, S. M., Simmons, A. J., Berrisford, P., Poli, P., Kobayashi, S., Andrae, U., Balmaseda, M., Balsamo, G., Bauer, d. P. et al. (2011). The era-interim reanalysis: Configuration and performance of the data assimilation system. *Quarterly Journal of the royal meteorological society*, *137*(656), 553–597.

de Jong, R., de Bruin, S., de Wit, A., Schaepman, M. E. & Dent, D. L. (2011). Analysis of monotonic greening and browning trends from global NDVI time-series. *Remote Sens. Environ.*, *115*(2), 692–702.

Descloux, E., Mangeas, M., Menkes, C. E., Lengaigne, M., Leroy, A., Tehei, T., Guillaumot, L., Teurlai, M., Gourinat, A.-C., Benzler, J., Pfannstiel, A., Grangeon, J.-P., Degallier, N. & De Lamballerie, X. (2012). Climate-based models for understanding and forecasting dengue epidemics. *PLoS Negl. Trop. Dis.*, *6*(2), e1470.

Deser, C., Guo, R. & Lehner, F. (2017). The relative contributions of tropical pacific sea surface temperatures and atmospheric internal variability to the recent global warming hiatus.

Dessler, A. E. & Sherwood, S. C. (2009). A matter of humidity. *Science*, *323*(5917), 1020–1021.

Di Liberto, T. (2021). High temperatures smash all-time records in alaska in early july 2019 [Accessed: 2022-1-20].

Dickey, J. O., Bentley, C. R., Bilham, R., Carton, J. A., Eanes, R. J., Herring, T. A., Kaula, W. M., Lagerloef, G. S. E., Rojstaczer, S., Smith, W. H. F., van den Dool, H. M., Wahr, J. M. & Zuber, M. T. (1998). Satellite gravity and the geosphere: Contributions to the study of the solid earth and its fluid earth.

Diffenbaugh, N. S., Swain, D. L. & Touma, D. (2015). Anthropogenic warming has increased drought risk in california. *Proc. Natl. Acad. Sci. U. S. A.*, *112*(13), 3931–3936.

Dimri, A. P. (2013). Relationship between ENSO phases with northwest india winter precipitation. *Int. J. Climatol.*, *33*(8), 1917–1923.

Ding, S., Chen, W., Feng, J. & Graf, H.-F. (2017). Combined impacts of PDO and two types of la niña on climate anomalies in europe. *J. Clim.*, *30*(9), 3253–3278.

Donat, M. G., Angélil, O. & Ukkola, A. M. (2019). Intensification of precipitation extremes in the world's humid and water-limited regions. *Environmental Research Letters*, *14*(6), 065003.

Dong, B. & Dai, A. (2015). The influence of the interdecadal pacific oscillation on temperature and precipitation over the globe.

Dong, B., Gregory, J. M. & Sutton, R. T. (2009). Understanding Land–Sea warming contrast in response to increasing greenhouse gases. part i: Transient adjustment. *J. Clim.*, *22*(11), 3079–3097.

Donohue, R. J., Roderick, M. L., McVicar, T. R. & Yang, Y. (2017a). A simple hypothesis of how leaf and canopy-level transpiration and assimilation respond to elevated CO2 reveals distinct response patterns between disturbed and undisturbed vegetation. *Journal of Geophysical Research: Biogeosciences*, *122*(1), 168–184.

Donohue, R. J., Roderick, M. L., McVicar, T. R. & Yang, Y. (2017b). A simple hypothesis of how leaf and canopy-level transpiration and assimilation respond to elevated co2 reveals distinct response patterns between disturbed and undisturbed vegetation.

Dorigo, W., de Jeu, R., Chung, D., Parinussa, R., Liu, Y., Wagner, W. & Fernández-Prieto, D. (2012). Evaluating global trends (1988-2010) in harmonized multi-satellite surface soil moisture. *Geophys. Res. Lett.*, *39*(18).

Dorigo, W., Dietrich, S., Aires, F., Brocca, L., Carter, S., Cretaux, J.-F., Dunkerley, D., Enomoto, H., Forsberg, R., Güntner, A., Hegglin, M. I., Hollmann, R., Hurst, D. F., Johannessen, J. A., Kummerow, C., Lee, T., Luojus, K., Looser, U., Miralles, D. G., ... Aich, V. (2021). Closing the water cycle from observations across scales: Where do we stand? *Bull. Am. Meteorol. Soc.*, *-1*(aop), 1–95.

Dorjsuren, B., Yan, D., Wang, H., Chonokhuu, S., Enkhbold, A., Davaasuren, D., Girma, A., Abiyu, A., Jing, L. & Gedefaw, M. (2018). Observed trends of climate and land cover changes in lake baikal basin. *Environ. Earth Sci.*, *77*(20), 725.

Douville, H., Raghavan, K., Renwick, J., Allan, R. P., Arias, P. A., Barlow, M., Cerezo-Mota, R., Cherchi, A., Gan, T. Y., Gergis, J., Jiang, D., Khan, W., A. andPokam-Mba, Rosenfeld, D., Tierney, J. & Zolina, O. (2021). Water cycle changes. In V. Masson-Delmotte, P. Zhai, A. Pirani, S. L. Connors, C. Péan, S. Berger, N. Caud, Y. Chen, L. Goldfarb, M. I. Gomis, M. Huang, K. Leitzell, E. Lonnoy, J.B.R. Matthews, T. K. Maycock, T. Waterfield, O. Yelekçi, R. Yu and B. Zhou (eds.) (Ed.), *Climate change 2021: The physical science basis. contribution of working group i to 45 the sixth assessment report of the intergovernmental panel on climate change*. Cambridge University Press. In Press.

Douville, H., Decharme, B., Delire, C., Colin, J., Joetzjer, E., Roehrig, R., Saint-Martin, D., Oudar, T., Stchepounoff, R. & Voldoire, A. (2020). Drivers of the enhanced decline of land near-surface relative humidity to abrupt 4xCO 2 in CNRM-CM6-1. *Clim. Dyn.*, *55*(5), 1613–1629.

Druckenmiller, M., Moon, T. & Thoman, R. (2021). State of the climate in 2020 - the arctic. *Bulletin of The American Meteorological Society*, *102*(8).

Dunlap, W. P., Jones, M. B. & Bittner, A. C. (1983). Average correlations vs. correlated averages. *Bull. Psychon. Soc.*, *21*(3), 213–216.

Dunn, R. J. H. (2019). *HadISD version 3: Monthly updates, hadley centre technical note* (tech. rep.).

Dunn, R. J. H., Aldred, F., Gobron, N., Miller, J. & Willett, K. M. (2021). Global climate [in state of the climate in 2020]. *Bull. Am. Meteorol. Soc.*, *102*(8), S11–S141.

Dunn, R. J. H., Willett, K. M., Morice, C. P. & Parker, D. E. (2014). Pairwise homogeneity assessment of HadISD. *Clim. Past*, *10*(4), 1501–1522.

Dunn, R. J. H., Willett, K. M., Thorne, P. W., Woolley, E. V., Durre, I., Dai, A., Parker, D. E. & Vose, R. S. (2012). HadISD: A quality-controlled global synoptic report database for selected variables at long-term stations from 1973–2011.

Dunn, R. J. H., Willett, K. M., Ciavarella, A. & Stott, P. A. (2017). Comparison of land surface humidity between observations and CMIP5 models. *Earth System Dynamics; Gottingen*, *8*(3), 719–747.

Dunn, R. J. H., Willett, K. M., Parker, D. E. & Mitchell, L. (2016). Expanding HadISD: Quality-controlled, sub-daily station data from 1931. *Geoscientific Instrumentation, Methods and Data Systems*, *5*(2), 473–491.

Dutra, E., Stepanenko, V. M., Balsamo, G., Viterbo, P., Miranda, P., Mironov, D. & Schär, C. (2010). An offline study of the impact of lakes on the performance of the ecmwf surface scheme.

Duveiller, G., Filipponi, F., Ceglar, A., Bojanowski, J., Alkama, R. & Cescatti, A. (2021). Revealing the widespread potential of forests to increase low level cloud cover. *Nat. Commun.*, *12*(1), 4337.

Easterling, D., Kunkel, K., Arnold, J., Knutson, T., LeGrande, A., Leung, L., Vose, R., Waliser, D. & Wehner, M. (2017). Precipitation change in the united states. in climate science special report: Fourth national climate assessment, volume I.[Wuebbles d, fahey d, hibbard k, dokken d, stewart b, maycock T (eds.)]. US global change research program, washington, DC, 207–230.

Eckert, S., Hüsler, F., Liniger, H. & Hodel, E. (2015). Trend analysis of MODIS NDVI time series for detecting land degradation and regeneration in mongolia. *J. Arid Environ.*, *113*, 16–28.

Ellsworth, D. S., Anderson, I. C., Crous, K. Y., Cooke, J., Drake, J. E., Gherlenda, A. N., Gimeno, T. E., Macdonald, C. A., Medlyn, B. E., Powell, J. R., Tjoelker, M. G. & Reich, P. B. (2017). Elevated CO2 does not increase eucalypt forest productivity on a low-phosphorus soil. *Nat. Clim. Chang.*, *7*(4), 279–282.

El-Sharkawy, M. A., Cock, J. H. & Del Pilar Hernandez, A. (1985). Stomatal response to air humidity and its relation to stomatal density in a wide range of warm climate species. *Photosynth. Res.*, *7*(2), 137–149.

Emori, S., Taylor, K., Hewitson, B., Zermoglio, F., Juckes, M., Lautenschlager, M. & Stockhause, M. (2016). CMIP5 data provided at the IPCC data distribution centre. *IPCC Task Group on Data and Scenario Support for Impact and Climate Analysis (TGICA)*, 8.

Enfield, D. B., Mestas-Nuñez, A. M. & Trimble, P. J. (2001). The atlantic multidecadal oscillation and its relation to rainfall and river flows in the continental US. *Geophys. Res. Lett.*, *28*(10), 2077–2080.

England, M. H., McGregor, S., Spence, P., Meehl, G. A., Timmermann, A., Cai, W., Gupta, A. S., McPhaden, M. J., Purich, A. & Santoso, A. (2014). Recent intensification of wind-driven circulation in the pacific and the ongoing warming hiatus. *Nat. Clim. Chang.*, *4*(3), 222–227.

Essery, R. L. H., Best, M. J., Betts, R. A., Cox, P. M. & Taylor, C. M. (2003). Explicit representation of subgrid heterogeneity in a GCM land surface scheme. *J. Hydrometeorol.*, *4*(3), 530–543.

FAO. (2022). State of the world's forest.

Farahmand, A., AghaKouchak, A. & Teixeira, J. (2015). A vantage from space can detect earlier drought onset: An approach using relative humidity. *Sci. Rep.*, *5*, 8553.

Fasullo, J. T. (2010). Robust Land–Ocean contrasts in energy and water cycle feedbacks. *J. Clim.*, *23*(17), 4677–4693.

Feng, S. & Fu, Q. (2013). Expansion of global drylands under a warming climate. *Atmos. Chem. Phys.*, *13*(19), 10081–10094.

Feng, W., Zhong, M., Lemoine, J.-M., Biancale, R., Hsu, H.-T. & Xia, J. (2013). Evaluation of groundwater depletion in north china using the gravity recovery and climate experiment (GRACE) data and ground-based measurements.

Fensholt, R., Horion, S., Tagesson, T., Ehammer, A., Grogan, K., Tian, F., Huber, S., Verbesselt, J., Prince, S. D., Tucker, C. J. & Rasmussen, K. (2015). Assessment of vegetation trends in drylands from time series of earth observation data. In C. Kuenzer, S. Dech & W. Wagner (Eds.), *Remote sensing time series: Revealing land surface dynamics* (pp. 159–182). Springer International Publishing.

Fensholt, R., Langanke, T., Rasmussen, K., Reenberg, A., Prince, S. D., Tucker, C., Scholes, R. J., Le, Q. B., Bondeau, A., Eastman, R., Epstein, H., Gaughan, A. E., Hellden, U., Mbow, C., Olsson, L., Paruelo, J., Schweitzer, C., Seaquist, J. & Wessels, K. (2012). Greenness in semi-arid areas across the globe 1981–2007 — an earth observing satellite based analysis of trends and drivers. *Remote Sens. Environ.*, *121*, 144–158.

Fensholt, R. & Proud, S. R. (2012). Evaluation of earth observation based global long term vegetation trends — comparing GIMMS and MODIS global NDVI time series.

Fensholt, R., Sandholt, I. & Rasmussen, M. S. (2004). Evaluation of MODIS LAI, fAPAR and the relation between fAPAR and NDVI in a semi-arid environment using in situ measurements. *Remote Sens. Environ.*, *91*(3), 490–507.

Fernandez-Gimenez, M. E., Baival, B., Fassnacht, S. R. & Wilson, D. (2015). Building resilience of mongolian rangelands: A trans-disciplinary research conference.

Field, C. B., Jackson, R. B. & Mooney, H. A. (1995). Stomatal responses to increased CO2: Implications from the plant to the global scale. *Plant Cell Environ.*, *18*(10), 1214–1225.

Fogt, R. L., Bromwich, D. H. & Hines, K. M. (2011). Understanding the SAM influence on the south pacific ENSO teleconnection. *Clim. Dyn.*, *36*(7-8), 1555–1576.

Fogt, R. L., Jones, J. M. & Renwick, J. (2012). Seasonal zonal asymmetries in the southern annular mode and their impact on regional temperature anomalies. *J. Clim.*, *25*(18), 6253–6270.

Fogt, R. L. & Marshall, G. J. (2020). The southern annular mode: Variability, trends, and climate impacts across the southern hemisphere. *Wiley Interdiscip. Rev. Clim. Change*, *11*(4).

Frajka-Williams, E., Beaulieu, C. & Duchez, A. (2017). Emerging negative atlantic multidecadal oscillation index in spite of warm subtropics. *Sci. Rep.*, *7*(1), 1–8.

Friedl, M. A., McIver, D. K., Hodges, J. C. F., Zhang, X. Y., Muchoney, D., Strahler, A. H., Woodcock, C. E., Gopal, S., Schneider, A., Cooper, A., Baccini, A., Gao, F. & Schaaf, C. (2002). Global land cover mapping from MODIS: Algorithms and early results. *Remote Sens. Environ.*, *83*(1), 287–302.

Fu, Q. & Feng, S. (2014). Responses of terrestrial aridity to global warming. *J. Geophys. Res.*, *119*(13), 7863–7875.

Galvin, J. F. P. (2008). The weather and climate of the tropics: Part 6–monsoons. *Weather*, *63*(5), 129–137.

Gandhi, G. M., Parthiban, b., Thummalu, N. & Christy, A. (2015). Ndvi: Vegetation change detection using remote sensing and gis–a case study of vellore district. *Procedia computer science*, *57*, 1199–1210.

Gao, H. & Yang, S. (2009). A severe drought event in northern china in winter 2008–2009 and the possible influences of la niña and tibetan plateau. *J. Geophys. Res.*, *114*(D24).

Gao, W., Angerer, J. P., Fernandez-Gimenez, M. E. & Reid, R. S. (2015). Is overgrazing a pervasive problem across mongolia? an examination of livestock forage demand and forage availability from 2000 to 2014. *Proceedings of building resilience of Mongolian rangelands. A trans-disciplinary research conference. Nutag Action and Research Institute, Ulaanbaatar*, 35–41.

Garcia-Soto, C. & Pingree, R. D. (2012). Atlantic multidecadal oscillation (AMO) and sea surface temperature in the bay of biscay and adjacent regions. *J. Mar. Biol. Assoc. U. K.*, *92*(2), 213–234.

Garreaud, R. D. (2009). The andes climate and weather. *Adv. Geosci.*, *22*, 3–11.

Garreaud, R. D. (2018). Record-breaking climate anomalies lead to severe drought and environmental disruption in western patagonia in 2016. *Clim. Res.*, *74*(3), 217–229.

Gateau-Rey, L., Tanner, E. V. J., Rapidel, B., Marelli, J.-P. & Royaert, S. (2018). Climate change could threaten cocoa production: Effects of 2015-16 el niño-related drought on cocoa agroforests in bahia, brazil. *PLoS One*, *13*(7), e0200454.

Gedney, N., Cox, P. M., Betts, R. A., Boucher, O., Huntingford, C. & Stott, P. A. (2006). Detection of a direct carbon dioxide effect in continental river runoff records. *Nature*, *439*(7078), 835–838.

Geneva, S. (2012). Standardized precipitation index user Guide.[Google scholar].

Gershunov, A. & Barnett, T. P. (1998). Interdecadal modulation of ENSO teleconnections. *Bull. Am. Meteorol. Soc.*, *79*(12), 2715–2726.

Gillett, N. P., Kell, T. D. & Jones, P. D. (2006). Regional climate impacts of the southern annular mode. *Geophys. Res. Lett.*, *33*(23), D12106.

Gimeno, T. E., McVicar, T. R., O'Grady, A. P., Tissue, D. T. & Ellsworth, D. S. (2018). Elevated CO2 did not affect the hydrological balance of a mature native eucalyptus woodland. *Glob. Chang. Biol.*, *24*(7), 3010–3024.

Glenn, E. P., Huete, A. R., Nagler, P. L. & Nelson, S. G. (2008). Relationship between remotely-sensed vegetation indices, canopy attributes and plant physiological processes: What vegetation indices can and cannot tell us about the landscape. *Sensors*, *8*(4), 2136–2160.

Gordon, L. J., Steffen, W., Jönsson, B. F., Folke, C., Falkenmark, M. & Johannessen, A. (2005). Human modification of global water vapor flows from the land surface. *Proc. Natl. Acad. Sci. U. S. A.*, *102*(21), 7612–7617.

Gore, M., Abiodun, B. J. & Kucharski, F. (2020). Understanding the influence of enso patterns on drought over southern africa using speedy. *Climate Dynamics*, *54*(1), 307–327.

Gray, S. B., Dermody, O., Klein, S. P., Locke, A. M., McGrath, J. M., Paul, R. E., Rosenthal, D. M., Ruiz-Vera, U. M., Siebers, M. H., Strellner, R., Ainsworth, E. A., Bernacchi, C. J., Long, S. P., Ort, D. R. & Leakey, A. D. B. (2016). Intensifying drought eliminates the expected benefits of elevated carbon dioxide for soybean. *Nat Plants*, *2*(9), 16132.

Green, B., Marshall, J. & Donohoe, A. (2017). Twentieth century correlations between extratropical SST variability and ITCZ shifts. *Geophys. Res. Lett.*, *44*(17), 9039–9047.

Greve, P., Roderick, M. L., Ukkola, A. M. & Wada, Y. (2019). The aridity index under global warming. *Environ. Res. Lett.*, *14*(12), 124006.

Greve, P., Orlowsky, B., Mueller, B., Sheffield, J., Reichstein, M. & Seneviratne, S. I. (2014). Global assessment of trends in wetting and drying over land.

Griffin, D. & Anchukaitis, K. J. (2014). How unusual is the 2012-2014 california drought? *Geophys. Res. Lett.*, *41*(24), 9017–9023.

Grise, K. M. & Davis, S. M. (2020). Hadley cell expansion in CMIP6 models. *Atmos. Chem. Phys.*, *20*(9), 5249–5268.

Grossiord, C., Buckley, T. N., Cernusak, L. A., Novick, K. A., Poulter, B., Siegwolf, R. T. W., Sperry, J. S. & McDowell, N. G. (2020). Plant responses to rising vapor pressure deficit. *New Phytol.*

Gruère, G., Shigemitsu, M. & Crawford, S. (2020). Agriculture and water policy changes: Stocktaking and alignment with OECD and G20 recommendations.

Gulev, S., Thorne, P., Ahn, J., Dentener, F., Domingues, C., Gerland, S., Gong, D., Kaufman, D., Nnamchi, H., Quaas, J., Rivera, J., Sathyendranath, S., Smith, S., Trewin, B., Schumann, K. & Rose, R. (2021). Changing state of the climate system – climate change 2021: The physical science basis. contribution of working group I to the sixth assessment report of the intergovernmental panel on climate change. In MassonDelmotte, V., P. Zhai, A. Pirani, S.L. Connors, C. Péan, S. Berger, N. Caud, Y. Chen, L. Goldfarb, M.I. Gomis, M. Huang, K. Leitzell, E. Lonnoy, J.B.R. Matthews, T.K. Maycock, T. Waterfield, O. Yelekçi, R. Yu, and B. Zhou (eds.) (Ed.). Cambridge University Press. In Press.

Guo, L., Li, T., Chen, D., Liu, J., He, B. & Zhang, Y. (2021). Links between global terrestrial water storage and large-scale modes of climatic variability. *J. Hydrol.*, *598*, 126419.

Hanna, E. & Cappelen, J. (2003). Recent cooling in coastal southern greenland and relation with the north atlantic oscillation. *Geophys. Res. Lett.*, *30*(3).

Hanna, E., Fettweis, X., Mernild, S. H., Cappelen, J., Ribergaard, M. H., Shuman, C. A., Steffen, K., Wood, L. & Mote, T. L. (2014). Atmospheric and oceanic climate forcing of the exceptional greenland ice sheet surface melt in summer 2012. *Int. J. Climatol.*, *34*(4), 1022–1037.

Hannaford, M. J., Jones, J. M. & Bigg, G. R. (2015). Early-nineteenth-century southern african precipitation reconstructions from ships' logbooks.

Hansen, M. C., Potapov, P. V., Moore, R., Hancher, M., Turubanova, S. A., Tyukavina, A., Thau, D., Stehman, S. V., Goetz, S. J., Loveland, T. R., Kommareddy, A., Egorov, A., Chini, L., Justice, C. O. & Townshend, J. R. G. (2013a). High-resolution global maps of 21st-century forest cover change. *Science*, *342*(6160), 850–853.

Hansen, Potapov, Moore & Hancher. (2013b). Global forest change [Accessed: 2022-2-NA].

Hartmann Dennis, L. (1994). Global physical climatology.

Haverd, V., Smith, B., Canadell, J. G., Cuntz, M., Mikaloff-Fletcher, S., Farquhar, G., Woodgate, W., Briggs, P. R. & Trudinger, C. M. (2020). Higher than expected co2 fertilization inferred from leaf to global observations. *Glob. Chang. Biol.*

Helbig, M., Waddington, J. M., Alekseychik, P., Amiro, B. D., Aurela, M., Barr, A. G., Black, T. A., Blanken, P. D., Carey, S. K., Chen, J., Chi, J., Desai, A. R., Dunn, A., Euskirchen, E. S., Flanagan, L. B., Forbrich, I., Friborg, T., Grelle, A., Harder, S., ... Zyrianov, V. (2020). Increasing contribution of peatlands to boreal evapotranspiration in a warming climate. *Nat. Clim. Chang.*

Henley, B. J., Gergis, J., Karoly, D. J., Power, S., Kennedy, J. & Folland, C. K. (2015). A tripole index for the interdecadal pacific oscillation. *Clim. Dyn.*, *45*(11), 3077–3090.

Hersbach, H., Bell, B., Berrisford, P., Hirahara, S., Horányi, A., Muñoz-Sabater, J., Nicolas, J., Peubey, C., Radu, R., Schepers, D., Simmons, A., Soci, C., Abdalla, S., Abellan, X., Balsamo, G., Bechtold, P., Biavati, G., Bidlot, J., Bonavita, M., ... Jean-Noël Thépaut. (2020). The ERA5 global reanalysis. *Quart. J. Roy. Meteor. Soc.*, *146*(730), 1999–2049.

Hessl, A. E., Anchukaitis, K. J., Jelsema, C., Cook, B., Byambasuren, O., Leland, C., Nachin, B., Pederson, N., Tian, H. & Hayles, L. A. (2018). Past and future drought in mongolia. *Sci Adv*, *4*(3), e1701832.

Higgins, R. W., Leetmaa, A., Xue, Y. & Barnston, A. (2000). Dominant factors influencing the seasonal predictability of U.S. precipitation and surface air temperature. *J. Clim.*, *13*(22), 3994–4017.

Hobbins, M. (2004). *Colorado state university* (Doctoral dissertation).

Hoekstra, A. Y. & Mekonnen, M. M. (2012). The water footprint of humanity. *Proc. Natl. Acad. Sci. U. S. A.*, *109*(9), 3232–3237.

Hoerling, M., Eischeid, J., Perlwitz, J., Quan, X., Zhang, T. & Pegion, P. (2012). On the increased frequency of mediterranean drought. *J. Clim.*, *25*(6), 2146–2161.

Hong, T., Dong, W., Ji, D., Dai, T., Yang, S. & Wei, T. (2019). The response of vegetation to rising co2 concentrations plays an important role in future changes in the hydrological cycle. *Theoretical and Applied Climatology*, *136*(1), 135–144.

Hou, S., Lei, L. & Zeng, Z. (2013). The response of global net primary productivity (NPP) to CO2. *Int. J. Food Agric. Environ.*, *11*(1), 937–944.

Huber, M. & Goldner, A. (2012). Eocene monsoons. *J. Asian Earth Sci.*, *44*, 3–23.

Hugalde, I. P. & Vila, H. F. (2014). Isohydric or anisohydric behaviour in grapevine..., a never-ending controversy. *RIA (Revista de Investigaciones Agrpecuarias)*, *40*(1), 75–82.

Hurrell, J. W. (2003). CLIMATE VARIABILITY — north atlantic and arctic oscillation.

Hurrell, J. W., Kushnir, Y., Ottersen, G. & Visbeck, M. (2003). An overview of the north atlantic oscillation. *The north atlantic oscillation: Climatic significance and environmental impact* (pp. 1–35). American Geophysical Union.

Jia, G., Shevliakova, E., Artaxo, P., De-Docoudré, N., Houghton, R., House, J., Kitajima, K., Lennard, C., Popp, A., Sirin, A. et al. (2019). Land–climate interactions. *Spe-*

cial report on climate change and land: An ipcc special report on climate change, desertification, land degradation, sustainable land management, food security, and greenhouse gas fluxes in terrestrial ecosystems (pp. 133–206). IPCC.

Jones, C. D., Hughes, J. K., Bellouin, N., Hardiman, S. C., Jones, G. S., Knight, J., Liddicoat, S., O'Connor, F. M., Andres, R. J., Bell, C., Boo, K.-O., Bozzo, A., Butchart, N., Cadule, P., Corbin, K. D., Doutriaux-Boucher, M., Friedlingstein, P., Gornall, J., Gray, L., … Zerroukat, M. (2011). The HadGEM2-ES implementation of CMIP5 centennial simulations. *Geosci. Model Dev. Discuss.*, *4*(1), 689–763.

Joshi, M. M., Gregory, J. M., Webb, M. J., Sexton, D. M. H. & Johns, T. C. (2008). Mechanisms for the land/sea warming contrast exhibited by simulations of climate change. *Clim. Dyn.*, *30*(5), 455–465.

Julien, Y. & Sobrino, J. A. (2009). Global land surface phenology trends from GIMMS database. *Int. J. Remote Sens.*, *30*(13), 3495–3513.

Jung, M., Reichstein, M., Ciais, P., Seneviratne, S. I., Sheffield, J., Goulden, M. L., Bonan, G., Cescatti, A., Chen, J., de Jeu, R., Dolman, A. J., Eugster, W., Gerten, D., Gianelle, D., Gobron, N., Heinke, J., Kimball, J., Law, B. E., Montagnani, L., … Zhang, K. (2010). Recent decline in the global land evapotranspiration trend due to limited moisture supply. *Nature*, *467*(7318), 951–954.

Jury, M. R. & Levey, K. (1993). The climatology and characteristics of drought in the eastern cape of south africa. *Int. J. Climatol.*, *13*(6), 629–641.

Kaplan, A. (2011). Patterns and indices of climate variability [in" state of the climate in 2010"]. *Bull. Am. Meteorol. Soc.*, *92*(6), S20–S25.

Kapos, V. (1989). Effects of isolation on the water status of forest patches in the brazilian amazon. *J. Trop. Ecol.*, *5*(2), 173–185.

Kauwe, M. G. D., De Kauwe, M. G., Medlyn, B. E., Zaehle, S., Walker, A. P., Dietze, M. C., Hickler, T., Jain, A. K., Luo, Y., Parton, W. J., Colin Prentice, I., Smith, B., Thornton, P. E., Wang, S., Wang, Y.-P., Wårlind, D., Weng, E., Crous, K. Y., Ellsworth, D. S., … Norby, R. J. (2013). Forest water use and water use efficiency at elevated CO2: A model-data intercomparison at two contrasting temperate forest FACE sites.

Kayano, M. T. & Andreoli, R. V. (2006). Relationships between rainfall anomalies over northeastern brazil and the el niño–southern oscillation. *J. Geophys. Res.*, *111*(D13).

Keenan, R. J., Reams, G. A., Achard, F., de Freitas, J. V., Grainger, A. & Lindquist, E. (2015). Dynamics of global forest area: Results from the FAO global forest resources assessment 2015. *For. Ecol. Manage.*, *352*, 9–20.

Keenan, T. F. & Riley, W. J. (2018). Greening of the land surface in the world's cold regions consistent with recent warming. *Nat. Clim. Chang.*, *8*, 825–828.

Keenan, T. F., Hollinger, D. Y., Bohrer, G., Dragoni, D., Munger, J. W., Schmid, H. P. & Richardson, A. D. (2013). Increase in forest water-use efficiency as atmospheric carbon dioxide concentrations rise. *Nature*, *499*(7458), 324–327.

Kohnemann, S. H. E., Heinemann, G., Bromwich, D. H. & Gutjahr, O. (2017). Extreme warming in the kara sea and barents sea during the winter period 2000–16. *J. Clim.*, *30*(22), 8913–8927.

Kooperman, G. J., Chen, Y., Hoffman, F. M., Koven, C. D., Lindsay, K., Pritchard, M. S., Swann, A. L. S. & Randerson, J. T. (2018). Forest response to rising CO2 drives zonally asymmetric rainfall change over tropical land.

Koriche, S. A., Nandini-Weiss, S. D., Prange, M., Singarayer, J. S., Arpe, K., Cloke, H. L., Schulz, M., Bakker, P., Leroy, S. A. G. & Coe, M. (2021a). Impacts of variations in caspian sea surface area on catchment-scale and large-scale climate. *J. Geophys. Res.*, *126*(18).

Koriche, S. A., Singarayer, J. S. & Cloke, H. L. (2021b). The fate of the caspian sea under projected climate change and water extraction during the 21st century. *Environ. Res. Lett.*, *16*(9), 094024.

Kosaka, Y. & Xie, S.-P. (2013). Recent global-warming hiatus tied to equatorial pacific surface cooling. *Nature*, *501*(7467), 403–407.

Kouadio, Y. K., Servain, J., Machado, L. A. T. & Lentini, C. A. D. (2012). Heavy rainfall episodes in the eastern northeast brazil linked to Large-Scale Ocean-Atmosphere conditions in the tropical atlantic.

Koutsoyiannis, D. (2012). Clausius–Clapeyron equation and saturation vapour pressure: Simple theory reconciled with practice.

Krakauer, N. Y., Lakhankar, T. & Dars, G. H. (2019). Precipitation trends over the indus basin. *Climate*, *7*(10), 116.

Kulkarni, A. (2012). Weakening of indian summer monsoon rainfall in warming environment. *Theor. Appl. Climatol.*, *109*(3), 447–459.

Kumar, A., Zhang, L. & Wang, W. (2012). Sea surface Temperature–Precipitation relationship in different reanalyses. *American Meteorological Society Journals, Mon. Weather Rev.*, *141*(3), 1118–1123.

Kumar, P. V., Naidu, C. V. & Prasanna, K. (2020). Recent unprecedented weakening of indian summer monsoon in warming environment. *Theor. Appl. Climatol.*, *140*(1), 467–486.

Kushnir, Y., Seager, R., Ting, M., Naik, N. & Nakamura, J. (2010). Mechanisms of tropical atlantic SST influence on north american precipitation variability*.

Lahijani, H., Leroy, S., Beni, M. N. & Arpe, K. (2010). Blaze in volga: Is it a critical point for the fall in caspian sea level. *Episodes*, *33*(3), 208–208.

Lambin, E. F., Turner, B. L., Geist, H. J., Agbola, S. B., Angelsen, A., Bruce, J. W., Coomes, O. T., Dirzo, R., Fischer, G., Folke, C., George, P. S., Homewood, K., Imbernon, J., Leemans, R., Li, X., Moran, E. F., Mortimore, M., Ramakrishnan, P. S., Richards, J. F., . . . Xu, J. (2001). The causes of land-use and land-cover change: Moving beyond the myths. *Glob. Environ. Change*, *11*(4), 261–269.

Landerer, F. W. & Swenson, S. C. (2012). Accuracy of scaled GRACE terrestrial water storage estimates. *Water Resour. Res.*, *48*(4).

Lapola, D. M., Oyama, M. D. & Nobre, C. A. (2009). Exploring the range of climate biome projections for tropical south america: The role of CO2fertilization and seasonality. *Global Biogeochem. Cycles*, *23*(3).

Lawrence, D. & Vandecar, K. (2014). Effects of tropical deforestation on climate and agriculture. *Nat. Clim. Chang.*, *5*, 27.

Lawrence, M. G. (2005). The relationship between relative humidity and the dewpoint temperature in moist air: A simple conversion and applications. *Bull. Am. Meteorol. Soc.*, *86*(2), 225–234.

Leakey, A. D. B. (2009). Rising atmospheric carbon dioxide concentration and the future of C4 crops for food and fuel. *Proc. Biol. Sci.*, *276*(1666), 2333–2343.

Leakey, A. D. B., Bishop, K. A. & Ainsworth, E. A. (2012). A multi-biome gap in understanding of crop and ecosystem responses to elevated CO2. *Curr. Opin. Plant Biol.*, *15*(3), 228–236.

Lee, J. Y., Marotzke, J., Bala, G., Cao, L., Corti, S., Dunne, J. P., Engelbrecht, F., Fischer, E., Fyfe, J. C., Jones, C., Maycock, A., Mutemi, J., Ndiaye, O., Panickal, S. & Zhou, T. (2021). Future global climate: Scenario based projections and Near-Term information. in: Climate change 2021: The physical science basis. contribution of working group I to the sixth assessment report of the intergovernmental panel on climate change. In V. Masson-Delmotte, P. Zhai, A. Pirani, S. L. Connors, C. Péan, S. Berger, N. Caud, Y. Chen, L. Goldfarb, M. I. Gomis, M. Huang, K. Leitzell, E. Lonnoy, J. B. R. Matthews, T. K. Maycock, T. Waterfield, O. Yelekçi, R. Yu & B. Zhou (Eds.). Cambridge University Press. In Press.

Lefsky, M. A. (2010). A global forest canopy height map from the moderate resolution imaging spectroradiometer and the geoscience laser altimeter system. *Geophys. Res. Lett.*, *37*(15).

Lejeune, Q., Davin, E. L., Gudmundsson, L., Winckler, J. & Seneviratne, S. I. (2018). Historical deforestation locally increased the intensity of hot days in northern mid-latitudes.

Levine, A. F. Z., McPhaden, M. J. & Frierson, D. M. W. (2017). The impact of the AMO on multidecadal ENSO variability. *Geophys. Res. Lett.*, *44*(8), 3877–3886.

Lewis, G., Osterberg, E., Hawley, R., Marshall, H. P., Meehan, T., Graeter, K., McCarthy, F., Overly, T., Thundercloud, Z. & Ferris, D. (2019). Recent precipitation decrease across the western greenland ice sheet percolation zone. *The Cryosphere*, *13*(11), 2797–2815.

L'Hereux, M. (2021). The Pacific-North american pattern: The stomach sleeper of the atmosphere [Accessed: 2021-12-29].

Li, J., Sun, C. & Jin, F.-F. (2013). NAO implicated as a predictor of northern hemisphere mean temperature multidecadal variability. *Geophys. Res. Lett.*, *40*(20), 5497–5502.

Li, Q., Ma, M., Wu, X. & Yang, H. (2018). Snow cover and Vegetation-Induced decrease in global albedo from 2002 to 2016.

Li, X.-Y., Ma, Y.-J., Huang, Y.-M., Hu, X., Wu, X.-C., Wang, P., Li, G.-Y., Zhang, S.-Y., Wu, H.-W., Jiang, Z.-Y., Cui, B.-L. & Liu, L. (2016). Evaporation and surface energy budget over the largest high-altitude saline lake on the Qinghai-Tibet plateau.

Li, Y., Han, W. & Zhang, L. (2017). Enhanced decadal warming of the southeast indian ocean during the recent global surface warming slowdown. *Geophys. Res. Lett.*, *44*(19), 9876–9884.

Lind, S., Ingvaldsen, R. B. & Furevik, T. (2018). Arctic warming hotspot in the northern barents sea linked to declining sea-ice import. *Nat. Clim. Chang.*, *8*(7), 634–639.

Liu, C., Liao, X., Qiu, J., Yang, Y., Feng, X., Allan, R. P., Cao, N., Long, J. & Xu, J. (2020). Observed variability of intertropical convergence zone over 1998—2018. *Environ. Res. Lett.*, *15*(10), 104011.

Liu, L., Yang, G., Zhao, X., Feng, L., Han, G., Wu, Y. & Yu, W. (2017). Why was the indian ocean dipole weak in the context of the extreme el niño in 2015? *J. Clim.*, *30*(12), 4755–4761.

Liu, W., Xie, C., Zhao, L., Li, R., Liu, G., Wang, W., Liu, H., Wu, T., Yang, G., Zhang, Y. & Zhao, S. (2021). Rapid expansion of lakes in the endorheic basin on the Qinghai-Tibet plateau since 2000 and its potential drivers. *Catena*, *197*, 104942.

Liu, Y.-C., Di, P., Chen, S.-H. & DaMassa, J. (2018). Relationships of rainy season precipitation and temperature to climate indices in california: Long-Term variability and extreme events. *J. Clim.*, *31*(5), 1921–1942.

Long, D., Longuevergne, L. & Scanlon, B. R. (2014). Uncertainty in evapotranspiration from land surface modeling, remote sensing, and GRACE satellites. *Water Resour. Res.*, *50*(2), 1131–1151.

Loveland, T. R., Reed, B. C., Brown, J. F., Ohlen, D. O., Zhu, Z., Yang, L. & Merchant, J. W. (2000). Development of a global land cover characteristics database and IGBP DISCover from 1 km AVHRR data. *Int. J. Remote Sens.*, *21*(6-7), 1303–1330.

Lowen, A. C., Mubareka, S., Steel, J. & Palese, P. (2007). Influenza virus transmission is dependent on relative humidity and temperature. *PLoS Pathog.*, *3*(10), 1470–1476.

Luo, L. & Wood, E. F. (2007). Monitoring and predicting the 2007 U.S. drought. *Geophys. Res. Lett.*, *34*(22).

Ma, J., Ding, Z., Edmunds, W. M., Gates, J. B. & Huang, T. (2009). Limits to recharge of groundwater from tibetan plateau to the gobi desert, implications for water management in the mountain front. *J. Hydrol.*, *364*(1), 128–141.

Ma, Y., Zhao, Y., Liu, J., He, X., Wang, B., Fu, S., Yan, J., Niu, J., Zhou, J. & Luo, B. (2020). Effects of temperature variation and humidity on the death of COVID-19 in wuhan, china. *Sci. Total Environ.*, *724*, 138226.

Mahlalela, P. T., Blamey, R. C., Hart, N. C. G. & Reason, C. J. C. (2020). Drought in the eastern cape region of south africa and trends in rainfall characteristics. *Clim. Dyn.*, 1–17.

Maidens, A., Arribas, A., Scaife, A. A., MacLachlan, C., Peterson, D. & Knight, J. (2013). The influence of surface forcings on prediction of the north atlantic oscillation regime of winter 2010/11. *Mon. Weather Rev.*, *141*(11), 3801–3813.

Mallya, G., Zhao, L., Song, X. C., Niyogi, D. & Govindaraju, R. S. (2013). 2012 midwest drought in the united states. *J. Hydrol. Eng.*, *18*(7), 737–745.

Manabe, S. & Wetherald, R. T. (1967). Thermal equilibrium of the atmosphere with a given distribution of relative humidity. *J. Atmos. Sci.*, *24*(3), 241–259.

Manabe, S. & Wetherald, R. T. (1975). The effects of doubling the CO2Concentration on the climate of a general circulation model. *J. Atmos. Sci.*, *32*(1), 3–15.

Mann, M. E., Steinman, B. A., Brouillette, D. J. & Miller, S. K. (2021). Multidecadal climate oscillations during the past millennium driven by volcanic forcing. *Science*, *371*(6533), 1014–1019.

Mann, M. E., Steinman, B. A. & Miller, S. K. (2020). Absence of internal multidecadal and interdecadal oscillations in climate model simulations. *Nat. Commun.*, *11*(1), 49.

Mantua, N. J. & Hare, S. R. (2002). The pacific decadal oscillation. *J. Oceanogr.*, *58*(1), 35–44.

Mantua, N. J., Hare, S. R., Zhang, Y., Wallace, J. M. & Francis, R. C. (1997). A pacific interdecadal climate oscillation with impacts on salmon production. *Bull. Am. Meteorol. Soc.*, *78*(6), 1069–1079.

Mao, Y., Nijssen, B. & Lettenmaier, D. P. (2015). Is climate change implicated in the 2013-2014 california drought? a hydrologic perspective. *Geophys. Res. Lett.*, *42*(8), 2805–2813.

Marengo, J. A. & Bernasconi, M. (2015). Regional differences in aridity/drought conditions over northeast brazil: Present state and future projections.

Marengo, J. A., Torres, R. R. & Alves, L. M. (2017). Drought in northeast brazil—past, present, and future. *Theor. Appl. Climatol.*, *129*(3), 1189–1200.

Marshall, G. J. (2003). Trends in the southern annular mode from observations and reanalyses. *J. Clim.*, *16*(24), 4134–4143.

Martens, B., Miralles, D., Lievens, H., Fernández-Prieto, D. & Verhoest, N. E. C. (2016). Improving terrestrial evaporation estimates over continental australia through assimilation of SMOS soil moisture. *Int. J. Appl. Earth Obs. Geoinf.*, *48*, 146–162.

Martens, B., Miralles, D. G., Lievens, H., van der Schalie, R., de Jeu, R. A. M., Férnandez-Prieto, D., Beck, H. E., Dorigo, W. A. & Verhoest, N. E. C. (2017). GLEAM v3: Satellite-based land evaporation and root-zone soil moisture. *Geoscientific Model Development*, *10*, 1903–1925.

Martens, B., Waegeman, W., Dorigo, W. A., Verhoest, N. E. C. & Miralles, D. G. (2018). Terrestrial evaporation response to modes of climate variability. *npj Climate and Atmospheric Science*, *1*(1), 1–7.

Masson-Delmotte, V., Zhai, P., Pirani, A., Connors, S., Péan, C., Berger, S., Caud, N., Chen, Y., Goldfarb, L., Gomis, M., Huang, M., Leitzell, K., Lonnoy, E., Matthews, J., Maycok, T., Waterfield, T., Yelekçi, O., Yu, R. & Zhou, B. (2021). IPCC - climate change 2021: The physical science basis. contribution of working group I to the sixth assessment report of the intergovernmental panel on climate change. In MassonDelmotte, V., P. Zhai, A. Pirani, S.L. Connors, C. Péan, S. Berger, N. Caud, Y. Chen, L. Goldfarb, M.I. Gomis, M. Huang, K. Leitzell, E. Lonnoy, J.B.R. Matthews, T.K. Maycock, T. Waterfield, O. Yelekçi, R. Yu, and B. Zhou (eds.) (Ed.). Cambridge University Press. In Press.

McCabe, G. J., Palecki, M. A. & Betancourt, J. L. (2004). Pacific and atlantic ocean influences on multidecadal drought frequency in the united states. *Proc. Natl. Acad. Sci. U. S. A.*, *101*(12), 4136–4141.

McCarthy, M. P. & Toumi, R. (2004). Observed interannual variability of tropical troposphere relative humidity. *J. Clim.*, *17*(16), 3181–3191.

McCurley, K. & Jawitz, J. W. (2019). Drivers of evapotranspiration in global climate zones. *2019*, H22B–06.

McCurley Pisarello, K. L. & Jawitz, J. W. (2021). Coherence of global hydroclimate classification systems. *Hydrol. Earth Syst. Sci.*, *25*(12), 6173–6183.

McDowell, N., Pockman, W. T., Allen, C. D., Breshears, D. D., Cobb, N., Kolb, T., Plaut, J., Sperry, J., West, A., Williams, D. G. & Yepez, E. A. (2008). Mechanisms of plant survival and mortality during drought: Why do some plants survive while others succumb to drought? *New Phytol.*, *178*(4), 719–739.

McKinnon, K. A., Poppick, A. & Simpson, I. R. (2021). Hot extremes have become drier in the united states southwest. *Nat. Clim. Chang.*, 1–7.

McPhaden, M. J. (1999). The child prodigy of 1997-98. *Nature*, *398*(6728), 559–561.

McVicar, T. R., Roderick, M. L., Donohue, R. J., Li, L. T., Van Niel, T. G., Thomas, A., Grieser, J., Jhajharia, D., Himri, Y., Mahowald, N. M., Mescherskaya, A. V., Kruger, A. C., Rehman, S. & Dinpashoh, Y. (2012). Global review and synthesis of trends in observed terrestrial near-surface wind speeds: Implications for evaporation. *J. Hydrol.*, *416-417*, 182–205.

McVicar, T. R., Van Niel, T. G., Li, L. T., Roderick, M. L., Rayner, D. P., Ricciardulli, L. & Donohue, R. J. (2008). Wind speed climatology and trends for australia, 1975–2006: Capturing the stilling phenomenon and comparison with near-surface reanalysis output. *Geophys. Res. Lett.*, *35*(20).

Medlyn, B. E., Badeck, F.-W., De Pury, D., Barton, C., Broadmeadow, M., Ceulemans, R., De Angelis, P., Forstreuter, M., Jach, M. E., Kellomäki, S. et al. (1999). Effects of elevated [CO2] on photosynthesis in european forest species: A meta-analysis of model parameters. *Plant Cell Environ.*, *22*(12), 1475–1495.

Medlyn, B. E., Barton, C. V. M., Broadmeadow, M. S. J., Ceulemans, R., De Angelis, P., Forstreuter, M., Freeman, M., Jackson, S. B., Kellomäki, S., Laitat, E., Rey, A., Roberntz, P., Sigurdsson, B. D., Strassemeyer, J., Wang, K., Curtis, P. S. & Jarvis, P. G. (2001). Stomatal conductance of forest species after long-term exposure to elevated co2 concentration: A synthesis. *New Phytol.*, *149*(2), 247–264.

Menne, M. J. & Williams, C. N. (2009). Homogenization of temperature series via pairwise comparisons. *J. Clim.*, *22*(7), 1700–1717.

Mernild, S. H., Hanna, E., McConnell, J. R., Sigl, M., Beckerman, A. P., Yde, J. C., Cappelen, J., Malmros, J. K. & Steffen, K. (2015). Greenland precipitation trends in a long-term instrumental climate context (1890-2012): Evaluation of coastal and ice core records. *Int. J. Climatol.*, *35*(2), 303–320.

Micklin, P. (2007). The aral sea disaster.

Micklin, P. (2010). The past, present, and future aral sea. *Lakes & Reservoirs: Science, Policy and Management for Sustainable Use*, *15*(3), 193–213.

Minallah, S. & Steiner, A. L. (2021). The effects of lake representation on the regional hydroclimate in the ECMWF reanalyses. *Mon. Weather Rev.*, *149*(6), 1747–1766.

Miralles, D. G., Brutsaert, W., Dolman, A. J. & Gash, J. H. (2020). On the use of the term “evapotranspiration”.

Miralles, D. G., De Jeu, R. A. M., Gash, J. H., Holmes, T. R. H. & Dolman, A. J. (2011). Magnitude and variability of land evaporation and its components at the global scale. *Hydrol. Earth Syst. Sci.*, *15*(3), 967–981.

Miralles, D. G., Holmes, T. R. H., De Jeu, R. A. M., Gash, J. H., Meesters, A. G. C. A. & Dolman, A. J. (2010a). Global land-surface evaporation estimated from satellite-based observations. *Hydrol. Earth Syst. Sci. Discuss.*, *7*(5), 8479–8519.

Miralles, D. G., Gash, J. H., Holmes, T. R. H., de Jeu, R. A. M. & Dolman, A. J. (2010b). Global canopy interception from satellite observations. *J. Geophys. Res.*, *115*(D16).

Miralles, D. G., Nieto, R., McDowell, N. G., Dorigo, W. A., Verhoest, N. E. C., Liu, Y. Y., Teuling, A. J., Dolman, A. J., Good, S. P. & Gimeno, L. (2016). Contribution of water-limited ecoregions to their own supply of rainfall. *Environ. Res. Lett.*, *11*(12), 124007.

Miralles, D. G., van den Berg, M. J., Gash, J. H., Parinussa, R. M., de Jeu, R. A. M., Beck, H. E., Holmes, T. R. H., Jiménez, C., Verhoest, N. E. C., Dorigo, W. A., Teuling, A. J. & Johannes Dolman, A. (2013). El niño–la niña cycle and recent trends in continental evaporation. *Nat. Clim. Chang.*, *4*(2), 122–126.

Mo, K. C., Schemm, J.-K. E. & Yoo, S.-H. (2009). Influence of ENSO and the atlantic multidecadal oscillation on drought over the united states. *J. Clim.*, *22*(22), 5962–5982.

Molavi-Arabshahi, M., Arpe, K. & Leroy, S. A. G. (2016). Precipitation and temperature of the southwest caspian sea region during the last 55 years: Their trends and teleconnections with large-scale atmospheric phenomena.

Monin, B. & Oppenheimer, D. M. (2005). Correlated averages vs. averaged correlations: Demonstrating the warm glow heuristic beyond aggregation. *Soc. Cogn.*, *23*(3), 257–278.

Moon, J.-H., Kim, T., Son, Y. B., Hong, J.-S., Lee, J.-H., Chang, P.-H. & Kim, S.-K. (2019). Contribution of low-salinity water to sea surface warming of the east china sea in the summer of 2016. *Prog. Oceanogr.*, *175*, 68–80.

Mooney, C. (2015). Why some scientists are worried about a cold ‘blob’in the north atlantic ocean. *Washington Post https://www. washingtonpost. com/news/energy-*

environment/wp/2015/09/24/why-some-scientists-are-worried-about-a-cold-blob-in-the-north-atlantic-ocean.

Mortensen, L. M. (1986). Effect of relative humidity on growth and flowering of some greenhouse plants. *Sci. Hortic.*, *29*(4), 301–307.

Mosley-Thompson, E., Readinger, C. R., Craigmile, P., Thompson, L. G. & Calder, C. A. (2005). Regional sensitivity of greenland precipitation to NAO variability. *Geophys. Res. Lett.*, *32*(24).

Myers-Smith, I. H., Kerby, J. T., Phoenix, G. K., Bjerke, J. W., Epstein, H. E., Assmann, J. J., John, C., Andreu-Hayles, L., Angers-Blondin, S., Beck, P. S. A., Berner, L. T., Bhatt, U. S., Bjorkman, A. D., Blok, D., Bryn, A., Christiansen, C. T., Cornelissen, J. H. C., Cunliffe, A. M., Elmendorf, S. C., ... Wipf, S. (2020). Complexity revealed in the greening of the arctic. *Nat. Clim. Chang.*, *10*(2), 106–117.

Nandini-Weiss, S. D., Prange, M., Arpe, K., Merkel, U. & Schulz, M. (2020). Past and future impact of the winter north atlantic oscillation in the caspian sea catchment area. *Int. J. Climatol.*, *40*(5), 2717–2731.

Nandintsetseg, B., Boldgiv, B., Chang, J., Ciais, P., Davaanyam, E., Batbold, A., Bat-Oyun, T. & Stenseth, N. C. (2021). Risk and vulnerability of mongolian grasslands under climate change.

Newman, M., Alexander, M. A., Ault, T. R., Cobb, K. M., Deser, C., Di Lorenzo, E., Mantua, N. J., Miller, A. J., Minobe, S., Nakamura, H., Schneider, N., Vimont, D. J., Phillips, A. S., Scott, J. D. & Smith, C. A. (2016). The pacific decadal oscillation, revisited. *J. Clim.*, *29*(12), 4399–4427.

Newman, M., Compo, G. P. & Alexander, M. A. (2003). ENSO-Forced variability of the pacific decadal oscillation. *J. Clim.*, *16*(23), 3853–3857.

Nghiem, S. V., Hall, D. K., Mote, T. L., Tedesco, M., Albert, M. R., Keegan, K., Shuman, C. A., DiGirolamo, N. E. & Neumann, G. (2012). The extreme melt across the greenland ice sheet in 2012. *Geophys. Res. Lett.*, *39*(20).

Ni, S., Chen, J., Wilson, C. R., Li, J., Hu, X. & Fu, R. (2018). Global terrestrial water storage changes and connections to ENSO events. *Surv. Geophys.*, *39*(1), 1–22.

Niu, Z., Wang, L., Fang, L., Li, J. & Yao, R. (2020). Spatiotemporal variations in monthly relative humidity in china based on observations and CMIP5 models. *Int. J. Climatol.*, *40*(15), 6382–6395.

NOAA National Centers for Environmental Information. (2016). *State of the climate: Global climate report for annual 2015* (tech. rep.).

NOAA National Centers for Environmental Information. (2022). *State of the climate: Global climate report for annual 2021* (tech. rep.).

Nobre, C. A., Marengo, J. A., Seluchi, M. E., Cuartas, L. A. & Alves, L. M. (2016). Some characteristics and impacts of the drought and water crisis in southeastern brazil during 2014 and 2015. *J. Water Resource Prot.*, *08*(02), 252–262.

Nobre, P. & Srukla, J. (1996). Variations of sea surface temperature, wind stress, and rainfall over the tropical atlantic and south america.

Norby, R. J. & Zak, D. R. (2011). Ecological lessons from Free-Air CO2 enrichment (FACE) experiments.

Notarnicola, C. (2020). Hotspots of snow cover changes in global mountain regions over 2000–2018. *Remote Sens. Environ.*, *243*, 111781.

Office, M. (2018). The north atlantic oscillation - met office [Accessed: 2018-6-5].

O'Gorman, P. A. & Muller, C. J. (2010). How closely do changes in surface and column water vapor follow Clausius–Clapeyron scaling in climate change simulations?

O'Hare, G., Sweeney, J. & Wilby, R. (2014). *Weather, climate and climate change: Human perspectives*. Routledge.

Oke, T. R. (2002). *Boundary layer climates*. Routledge.

Oki, T. & Kanae, S. (2006). Global hydrological cycles and world water resources. *Science*, *313*(5790), 1068–1072.

Osborn, T. J. (2011). Winter 2009/2010 temperatures and a record-breaking north atlantic oscillation index. *Weather*, *66*(1), 19–21.

Osborne, C. P. (2016). Crop yields: CO2 fertilization dries up. *Nat Plants*, *2*(9), 16138.

Padrón, R. S., Gudmundsson, L., Decharme, B., Ducharne, A., Lawrence, D. M., Mao, J., Peano, D., Krinner, G., Kim, H. & Seneviratne, S. I. (2020). Observed changes in dry-season water availability attributed to human-induced climate change. *Nat. Geosci.*, *13*(7), 477–481.

PaiMazumder, D. & Done, J. M. (2016). Potential predictability sources of the 2012 US drought in observations and a regional model ensemble. *J. Geophys. Res. D: Atmos.*, *121*(21), 12–581.

Palmer, M. D. & McNeall, D. J. (2014). Internal variability of earth's energy budget simulated by CMIP5 climate models. *Environ. Res. Lett.*, *9*(3), 034016.

Pan, N., Feng, X., Fu, B., Wang, S., Ji, F. & Pan, S. (2018). Increasing global vegetation browning hidden in overall vegetation greening: Insights from time-varying trends. *Remote Sens. Environ.*, *214*, 59–72.

Pan, Y., Birdsey, R. A., Phillips, O. L. & Jackson, R. B. (2013). The structure, distribution, and biomass of the world's forests. *Annu. Rev. Ecol. Evol. Syst.*, *44*(1), 593–622.

Pant, G. B. & Hingane, L. S. (1988). Climatic changes in and around the rajasthan desert during the 20th century. *J. Climatol.*, *8*(4), 391–401.

Pascolini-Campbell, M., Reager, J. T., Chandanpurkar, H. A. & Rodell, M. (2021). A 10 per cent increase in global land evapotranspiration from 2003 to 2019. *Nature*, *593*(7860), 543–547.

Peel, M. C., Finlayson, B. L. & McMahon, T. A. (2007). Updated world map of the Köppen-Geiger climate classification. *Hydrol. Earth Syst. Sci. Discuss.*, *4*(2), 439–473.

Peixoto, J. & Oort, A. H. (1996). The climatology of relative humidity in the atmosphere. *J. Clim.*, *9*(12), 3443–3463.

Peng, J., Loew, A., Merlin, O. & Verhoest, N. E. C. (2017). A review of spatial downscaling of satellite remotely sensed soil moisture. *Rev. Geophys.*, *55*(2), 341–366.

Pereira, T. d. S., da Silva Pereira, T., Costa, D. D., Fragoso, C., Jr, Montenegro, S. G. L. & Uvo, C. B. (2018). Key climate oscillation factors controlling precipitation variability during the dry season in eastern northeast brazil: Study case of mundaú and paraıba do meio river basins.

Peterson, T. C., Easterling, D. R., Karl, T. R., Groisman, P., Nicholls, N., Plummer, N., Torok, S., Auer, I., Boehm, R., Gullett, D., Vincent, L., Heino, R., Tuomenvirta, H., Mestre, O., Szentimrey, T., Salinger, J., Førland, E. J., Hanssen-Bauer, I., Alexandersson, H., ... Parker, D. (1998). Homogeneity adjustments ofin situ atmospheric climate data: A review.

Peterson, T. C., Willett, K. M. & Thorne, P. W. (2011). Observed changes in surface atmospheric energy over land. *Geophys. Res. Lett.*, *38*(16).

Philander, S. G. H. (1983). Meteorology: Anomalous el niño of 1982–83. *Nature*, *305*(5929), 16–16.

Piao, S., Friedlingstein, P., Ciais, P., de Noblet-Ducoudré, N., Labat, D. & Zaehle, S. (2007). Changes in climate and land use have a larger direct impact than rising CO2 on global river runoff trends. *Proc. Natl. Acad. Sci. U. S. A.*, *104*(39), 15242–15247.

Piao, S., Wang, X., Park, T., Chen, C., Lian, X., He, Y., Bjerke, J. W., Chen, A., Ciais, P., Tømmervik, H., Nemani, R. R. & Myneni, R. B. (2019). Characteristics, drivers and feedbacks of global greening. *Nature Reviews Earth & Environment*, *1*(1), 14–27.

Pinzon, J. E. & Tucker, C. J. (2016). A Non-Stationary 1981-2015 AVHRR NDVI3 g. v1 time series: An update. *preparation for submission to Remote Sensing.*

Pinzon, J. E. & Tucker, C. J. (2014). A Non-Stationary 1981–2012 AVHRR NDVI3g time series. *Remote Sensing*, *6*(8), 6929–6960.

Power, S., Casey, T., Folland, C., Colman, A. & Mehta, V. (1999). Inter-decadal modulation of the impact of enso on australia. *Clim. Dyn.*, *15*(5), 319–324.

Purcell, C., Batke, S. P., Yiotis, C., Caballero, R., Soh, W. K., Murray, M. & McElwain, J. C. (2018). Increasing stomatal conductance in response to rising atmospheric CO2. *Ann. Bot.*, *121*(7), 1427.

Querin, C. A. S., Beneditti, C. A., Machado, N. G., da Silva, M. J. G., da silva Querino, J. K. A., dos Santos Neto, L. A. & Biudes, M. S. (2016). Spatiotemporal NDVI, LAI, albedo, and surface temperature dynamics in the southwest of the brazilian amazon forest. *JARS*, *10*(2), 026007.

Rao, M. P., Davi, N. K., D'Arrigo, R. D., Skees, J., Nachin, B., Leland, C., Lyon, B., Wang, S.-Y. & Byambasuren, O. (2015). Dzuds, droughts, and livestock mortality in mongolia. *Environ. Res. Lett.*, *10*(7), 074012.

Rathore & S., M. (2004). *State level analysis of drought policies and impacts in rajasthan, india.* IWMI.

Ratnam, J. V., Behera, S. K., Masumoto, Y. & Yamagata, T. (2014). Remote effects of el niño and modoki events on the austral summer precipitation of southern africa. *J. Clim.*, *27*(10), 3802–3815.

Reason, C. J. C. (2017). Climate of southern africa. *Oxford research encyclopedia of climate science.*

Rippey, B. R. (2015). The u.s. drought of 2012. *Weather Clim. Extrem.*, *10*, 57–64.

Roberts, C. D., Palmer, M. D., McNeall, D. & Collins, M. (2015). Quantifying the likelihood of a continued hiatus in global warming. *Nat. Clim. Chang.*, *5*, 337.

Robinson, P. J. & Henderson-Sellers, A. (1999). *Contemporary climatology.* 2nd end. Longman, London.

Rodell, M., Famiglietti, J. S., Chen, J., Seneviratne, S. I., Viterbo, P., Holl, S. & Wilson, C. R. (2004). Basin scale estimates of evapotranspiration using GRACE and other observations. *Geophys. Res. Lett.*, *31*(20).

Rodell, M., Famiglietti, J. S., Wiese, D. N., Reager, J. T., Beaudoing, H. K., Landerer, F. W. & Lo, M.-H. (2018). Emerging trends in global freshwater availability. *Nature*, *557*(7707), 651–659.

Roderick, M. L., Rotstayn, L. D., Farquhar, G. D. & Hobbins, M. T. (2007). On the attribution of changing pan evaporation. *Geophys. Res. Lett.*, *34*(17).

Rodrigues, R. R. & McPhaden, M. J. (2014). Why did the 2011-2012 la niña cause a severe drought in the brazilian northeast? *Geophys. Res. Lett.*, *41*(3), 1012–1018.

Rogers, J. & McHugh, M. (2002). On the separability of the north atlantic oscillation and arctic oscillation. *Clim. Dyn.*, *19*(7), 599–608.

Rowell, D. P. & Jones, R. G. (2006). Causes and uncertainty of future summer drying over europe. *Clim. Dyn.*, *27*(2-3), 281–299.

Ruggiero, A., Punzo, P., Landi, S., Costa, A., Van Oosten, M. & Grillo, S. (2017). Improving plant water use efficiency through molecular genetics.

Ruprich-Robert, Y., Delworth, T., Msadek, R., Castruccio, F., Yeager, S. & Danabasoglu, G. (2018). Impacts of the atlantic multidecadal variability on north american summer climate and heat waves. *J. Clim.*, *31*(9), 3679–3700.

Ryan, J. C., Smith, L. C., van As, D., Cooley, S. W., Cooper, M. G., Pitcher, L. H. & Hubbard, A. (2019). Greenland ice sheet surface melt amplified by snowline migration and bare ice exposure.

Sajadi, M. M., Habibzadeh, P., Vintzileos, A., Shokouhi, S., Miralles-Wilhelm, F. & Amoroso, A. (2020). Temperature, humidity, and latitude analysis to estimate potential spread and seasonality of coronavirus disease 2019 (covid-19). *JAMA Netw Open*, *3*(6), e2011834.

Saji, N. H., Goswami, B. N., Vinayachandran, P. N. & Yamagata, T. (1999). A dipole mode in the tropical indian ocean. *Nature*, *401*(6751), 360–363.

Saji, N. H. & Yamagata, T. (2003). Possible impacts of indian ocean dipole mode events on global climate. *Clim. Res.*, *25*, 151–169.

Salinger, M. J., Renwick, J. A. & Mullan, A. B. (2001). Interdecadal pacific oscillation and south pacific climate. *Int. J. Climatol.*, *21*(14), 1705–1721.

Santer, B. D., Thorne, P. W., Haimberger, L., Taylor, K. E., Wigley, T. M. L., Lanzante, J. R., Solomon, S., Free, M., Gleckler, P. J., Jones, P. D., Karl, T. R., Klein, S. A., Mears, C., Nychka, D., Schmidt, G. A., Sherwood, S. C. & Wentz, F. J. (2008). Consistency of modelled and observed temperature trends in the tropical troposphere. *Int. J. Climatol.*, *28*(13), 1703–1722.

Santoso, A., Mcphaden, M. J. & Cai, W. (2017). The defining characteristics of ENSO extremes and the strong 2015/2016 el niño. *Rev. Geophys.*, *55*(4), 1079–1129.

Save, H. (2019). CSR GRACE RL06 mascon solutions. *UN91VR, Texas Data Repository Dataverse*.

Save, H., Bettadpur, S. & Tapley, B. D. (2016). High-resolution CSR GRACE RL05 mascons. *J. Geophys. Res. [Solid Earth]*, *121*(10), 7547–7569.

Scheff, J. & Frierson, D. M. W. (2015). Terrestrial aridity and its response to greenhouse warming across CMIP5 climate models. *J. Clim.*, *28*(14), 5583–5600.

Schmidt, D. F. & Grise, K. M. (2017). The response of local precipitation and sea level pressure to hadley cell expansion. *Geophysical Research Letters*, *44*(20), 10–573.

Schneider, C. & Gies, D. (2004). Effects of el niño–southern oscillation on southernmost south america precipitation at 53 degree s revealed from NCEP–NCAR reanalyses and weather station data. *Int. J. Climatol.*, *24*(9), 1057–1076.

Schneider, T., Bischoff, T. & Haug, G. H. (2014a). Migrations and dynamics of the intertropical convergence zone. *Nature*, *513*(7516), 45–53.

Schneider, U., Becker, A., Finger, P., Meyer-Christoffer, A., Ziese, M. & Rudolf, B. (2014b). GPCC's new land surface precipitation climatology based on quality-controlled in situ data and its role in quantifying the global water cycle. *Theor. Appl. Climatol.*, *115*(1-2), 15–40.

Schneider, U., Becker, A., Finger, P., Rustemeier, E. & Ziese, M. (2020). Gpcc full data monthly product version 2020 at 2.5 degree: Monthly Land-Surface precipitation from Rain-Gauges built on gts-based and historical data.

Schneider, U., Fuchs, T., Meyer-Christoffer, A. & Rudolf, B. (2008). Global precipitation analysis products of the GPCC. *Global Precipitation Climatology Centre (GPCC), DWD, Internet Publikation*, *112*.

Seager, R., Hoerling, M., Schubert, S., Wang, H., Lyon, B., Kumar, A., Nakamura, J. & Henderson, N. (2015). Causes of the 2011–14 california drought. *J. Clim.*, *28*(18), 6997–7024.

Sein, Z. M. M., Ullah, I., Saleem, F., Zhi, X., Syed, S. & Azam, K. (2021). Interdecadal variability in myanmar rainfall in the monsoon season (May–October) using eigen methods.

Seip, K. L., Grøn, Ø. & Wang, H. (2019). The north atlantic oscillations: Cycle times for the NAO, the AMO and the AMOC.

Sellers, P. J., Bounoua, L., Collatz, G. J., Randall, D. A. et al. (1996). Comparison of radiative and physiological effects of doubled atmospheric CO2 on climate.

Sen Roy, S. & Sen Roy, N. (2011). Influence of pacific decadal oscillation and el niño southern oscillation on the summer monsoon precipitation in myanmar. *Int. J. Climatol.*, *31*(1), 14–21.

Setimela, P., Gasura, E., Thierfelder, C. et al. (2018). When the going gets tough: Performance of stress tolerant maize during the 2015/16 (el niño) and 2016/17 (la niña) season in southern africa. *Agric. Ecosyst. Environ.*

Shenbin, C., Yunfeng, L. & Thomas, A. (2006). Climatic change on the tibetan plateau: Potential evapotranspiration trends from 1961–2000. *Clim. Change*, *76*(3-4), 291–319.

Shenoi, S. S. C. (2002). Differences in heat budgets of the near-surface arabian sea and bay of bengal: Implications for the summer monsoon. *J. Geophys. Res.*, *107*(C6).

Sherwood, S. & Fu, Q. (2014). A drier future? *Science*, *343*(6172), 737–739.

Sherwood, S. C., Ingram, W., Tsushima, Y., Satoh, M., Roberts, M., Vidale, P. L. & O'Gorman, P. A. (2010). Relative humidity changes in a warmer climate.

Shukla, J. & Mintz, Y. (1982). Influence of Land-Surface evapotranspiration on the earth's climate. *Science*, *215*(4539), 1498–1501.

Shukla, P. R., Skeg, J., Buendia, E. C., Masson-Delmotte, V., Pörtner, H.-O., Roberts, D., Zhai, P., Slade, R., Connors, S., van Diemen, S. et al. (2019). Climate change and land: An ipcc special report on climate change, desertification, land degradation, sustainable land management, food security, and greenhouse gas fluxes in terrestrial ecosystems.

Siderius, C., Gannon, K., Ndiyoi, M., Opere, A., Batisani, N., Olago, D., Pardoe, J. & Conway, D. (2018). Hydrological response and complex impact pathways of the 2015/2016 el niño in eastern and southern africa. *Earth's Future*, *6*(1), 2–22.

Sidorenkov, N. & Shveikina, V. (2021). Changes in the climatic regime on the caspian see regions over the past century [Accessed: 2021-7-31].

Siebert, S., Hoogeveen, J., Döll, P., Faurèsb, J.-M., Feick, S. & Frenken, K. (2006). The digital global map of irrigation areas–development and validation of map version 4. *lınea], En: Conference on International Agricultural Research for Development, Tropentag. University of Bonn, Bonn, Germany*, *11*.

Simmons, A. J., Willett, K. M., Jones, P. D., Thorne, P. W. & Dee, D. P. (2010). Low-frequency variations in surface atmospheric humidity, temperature, and precipitation: Inferences from reanalyses and monthly gridded observational data sets. *J. Geophys. Res.*, *115*(D1).

Simmons, A., Hersbach, H., Munoz-Sabater, J., Nicolas, J., Vamborg, F., Berrisford, P., de Rosnay, P., Willett, K. & Woollen, J. (2021). Low frequency variability and trends in surface air temperature and humidity from ERA5 and other datasets.

Singh, P., Chowdary, J. S. & Gnanaseelan, C. (2013). Impact of prolonged la niña events on the indian ocean with a special emphasis on southwest tropical indian ocean SST. *Glob. Planet. Change*, *100*, 28–37.

Skagseth, Ø., Eldevik, T., Årthun, M., Asbjørnsen, H., Lien, V. S. & Smedsrud, L. H. (2020). Reduced efficiency of the barents sea cooling machine. *Nat. Clim. Chang.*, *10*(7), 661–666.

Smith, A., Lott, N. & Vose, R. (2011). The integrated surface database: Recent developments and partnerships.

Song, H., Wang, J., Tian, J., Huang, J. & Zhang, Z. (2018a). Spatio-temporal climate data causality analytics-an analysis of ENSO's global impacts. *Proceedings of the 8th International Workshop on Climate Informatics (CI2018)*.

Song, X.-P., Hansen, M. C., Stehman, S. V., Potapov, P. V., Tyukavina, A., Vermote, E. F. & Townshend, J. R. (2018b). Global land change from 1982 to 2016. *Nature*, *560*(7720), 639–643.

Spinoni, J., Micale, F., Carrao, H., Naumann, G., Barbosa, P. & Vogt, J. (2013). Global and continental changes of arid areas using the FAO aridity index over the periods 1951-1980 and 1981-2010, EGU2013–9262.

Srivastava, K. & Pradhan, D. (2018). Real-time extremely heavy rainfall forecast and warning over rajasthan during the monsoon season (2016). *Pure Appl. Geophys.*, *175*(1), 421–448.

Stammerjohn, S. E., Martinson, D. G., Smith, R. C., Yuan, X. & Rind, D. (2008). Trends in antarctic annual sea ice retreat and advance and their relation to el niño–southern oscillation and southern annular mode variability. *J. Geophys. Res.*, *113*(C3).

Sutton, R. T. & Hodson, D. L. R. (2005). Atlantic ocean forcing of north american and european summer climate. *Science*, *309*(5731), 115–118.

Svoboda, M. D. & Fuchs, B. A. (2017). Handbook of drought indicators and indices. *Drought and water crises* (pp. 155–208). CRC Press.

Swemmer, A. M. (2020). Locally high, but regionally low: The impact of the 2014–2016 drought on the trees of semi-arid savannas, south africa. *Afr. J. Range Forage Sci.*, *37*(1), 31–42.

Syed, T. H., Famiglietti, J. S., Rodell, M., Chen, J. & Wilson, C. R. (2008). Analysis of terrestrial water storage changes from GRACE and GLDAS. *Water Resour. Res.*, *44*(2).

Tao, S., Fang, J., Zhao, X., Zhao, S., Shen, H., Hu, H., Tang, Z., Wang, Z. & Guo, Q. (2015). Rapid loss of lakes on the mongolian plateau. *Proc. Natl. Acad. Sci. U. S. A.*, *112*(7), 2281–2286.

Tapley, B. D., Watkins, M. M., Flechtner, F., Reigber, C., Bettadpur, S., Rodell, M., Sasgen, I., Famiglietti, J. S., Landerer, F. W., Chambers, D. P., Reager, J. T., Gardner, A. S., Save, H., Ivins, E. R., Swenson, S. C., Boening, C., Dahle, C., Wiese, D. N., Dobslaw, H., ... Velicogna, I. (2019). Contributions of GRACE to understanding climate change. *Nat. Clim. Chang.*, *5*(5), 358–369.

Taylor, K. E., Stouffer, R. J. & Meehl, G. A. (2012a). An overview of CMIP5 and the experiment design. *Bull. Am. Meteorol. Soc.*, *93*(4), 485–498.

Taylor, R. G., Scanlon, B., Döll, P., Rodell, M., van Beek, R., Wada, Y., Longuevergne, L., Leblanc, M., Famiglietti, J. S., Edmunds, M., Konikow, L., Green, T. R., Chen, J., Taniguchi, M., Bierkens, M. F. P., MacDonald, A., Fan, Y., Maxwell, R. M., Yechieli, Y., ... Treidel, H. (2012b). Ground water and climate change. *Nat. Clim. Chang.*, *3*(4), 322–329.

Thiis, T. K., Burud, I., Flø, A., Kraniotis, D., Charisi, S. & Stefansson, P. (2017). Monitoring and simulation of diurnal surface conditions of a wooden façade.

Thompson, D. W. J. & Wallace, J. M. (1998). The arctic oscillation signature in the wintertime geopotential height and temperature fields. *Geophys. Res. Lett.*, *25*(9), 1297–1300.

Thompson, D. W. J. & Wallace, J. M. (2000). Annular modes in the extratropical circulation. part i: Month-to-Month variability. *J. Clim.*, *13*(5), 1000–1016.

Thompson, D. W. J., Wallace, J. M. & Hegerl, G. C. (2000). Annular modes in the extratropical circulation. part II: Trends. *J. Clim.*, *13*(5), 1018–1036.

Thomson, A. M., Calvin, K. V., Smith, S. J., Kyle, G. P., Volke, A., Patel, P., Delgado-Arias, S., Bond-Lamberty, B., Wise, M. A., Clarke, L. E. et al. (2011a). Rcp4. 5: A pathway for stabilization of radiative forcing by 2100. *Climatic change*, *109*(1), 77–94.

Thomson, A. M., Calvin, K. V., Smith, S. J., Kyle, G. P., Volke, A., Patel, P., Delgado-Arias, S., Bond-Lamberty, B., Wise, M. A., Clarke, L. E. & Edmonds, J. A. (2011b). RCP4.5: A pathway for stabilization of radiative forcing by 2100. *Clim. Change*, *109*(1), 77.

Timmermann, A., An, S.-I., Kug, J.-S., Jin, F.-F., Cai, W., Capotondi, A., Cobb, K. M., Lengaigne, M., McPhaden, M. J., Stuecker, M. F., Stein, K., Wittenberg, A. T., Yun, K.-S., Bayr, T., Chen, H.-C., Chikamoto, Y., Dewitte, B., Dommenget, D., Grothe, P., ... Zhang, X. (2018). El niño–southern oscillation complexity. *Nature*, *559*(7715), 535–545.

Todd, A., Collins, M., Hugo Lambert, F. & Chadwick, R. (2018). Diagnosing ENSO and global warming tropical precipitation shifts using surface relative humidity and temperature. *J. Clim.*, *31*(4), 1413–1433.

Tokinaga, H., Xie, S.-P., Deser, C., Kosaka, Y. & Okumura, Y. M. (2012). Slowdown of the walker circulation driven by tropical Indo-Pacific warming. *Nature*, *491*(7424), 439–443.

Torralba, V., Doblas-Reyes, F. J. & Gonzalez-Reviriego, N. (2017). Uncertainty in recent near-surface wind speed trends: A global reanalysis intercomparison. *Environ. Res. Lett.*, *12*(11), 114019.

Trenberth, K. E. (2011). Changes in precipitation with climate change. *Clim. Res.*, *47*(1), 123–138.

Trenberth, K. E. & Fasullo, J. T. (2013). An apparent hiatus in global warming? *Earth's Future*, *1*(1), 19–32.

Trenberth, K. E., Fasullo, J. T. & Kiehl, J. (2009). Earth's global energy budget. *Bull. Am. Meteorol. Soc.*, *90*(3), 311–324.

Tucker, C. J., Pinzon, J. E., Brown, M. E., Slayback, D. A., Pak, E. W., Mahoney, R., Vermote, E. F. & El Saleous, N. (2005). An extended avhrr 8-km ndvi dataset compatible with MODIS and spot vegetation ndvi data.

Utari, P. A., Khakim, M. Y. N., Setiabudidaya, D. & Iskandar, I. (2020). Dynamics of 2015 positive indian ocean dipole. *JSHESS*, *69*(1), 75–83.

Utida, G., Cruz, F. W., Etourneau, J., Bouloubassi, I., Schefuß, E., Vuille, M., Novello, V. F., Prado, L. F., Sifeddine, A., Klein, V., Zular, A., Viana, J. C. C. & Turcq, B. (2019). Tropical south atlantic influence on northeastern brazil precipitation and ITCZ displacement during the past 2300 years.

Uvo, C. B., Repelli, C. A., Zebiak, S. E. & Kushnir, Y. (1998). The relationships between tropical pacific and atlantic SST and northeast brazil monthly precipitation. *J. Clim.*, *11*(4), 551–562.

Van Der Sleen, P., Groenendijk, P., Vlam, M., Anten, N. P. R., Boom, A., Bongers, F., Pons, T. L., Terburg, G. & Zuidema, P. A. (2015). No growth stimulation of tropical trees by 150 years of CO 2 fertilization but water-use efficiency increased. *Nat. Geosci.*, *8*(1), 24–28.

van der Sleen, P., Groenendijk, P., Vlam, M., Anten, N. P. R., Boom, A., Bongers, F., Pons, T. L., Terburg, G. & Zuidema, P. A. (2014). No growth stimulation of tropical trees by 150 years of CO_2 fertilization but water-use efficiency increased. *Nat. Geosci.*, *8*, 24.

Various. (1996). *Diercke weltatlas.* westermann.

Vautard, R., Cattiaux, J., Yiou, P., Jean-Noël Thépaut & Ciais, P. (2010). Northern hemisphere atmospheric stilling partly attributed to an increase in surface roughness.

Verdon, D. C. & Franks, S. W. (2006). Long-term behaviour of ENSO: Interactions with the PDO over the past 400 years inferred from paleoclimate records. *Geophys. Res. Lett.*, *33*(6).

Vicente-Serrano, S. M., Nieto, R., Gimeno, L., Azorin-Molina, C., Drumond, A., El Kenawy, A., Dominguez-Castro, F., Tomas-Burguera, M. & Peña-Gallardo, M. (2018). Recent changes of relative humidity: Regional connections with land and ocean processes. *Earth Syst. Dyn.*, *9*(2), 915–937.

Vivek, G. & Manoj Kumar, J. (2020). Impact of ENSO, global warming, and land surface elevation on extreme precipitation in india. *J. Hydrol. Eng.*, *25*(1), 05019032.

Wahr, J., Molenaar, M. & Bryan, F. (1998). Time variability of the earth's gravity field: Hydrological and oceanic effects and their possible detection using GRACE. *J. Geophys. Res.*, *103*(B12), 30205–30229.

Wahr, J., Swenson, S., Zlotnicki, V. & Velicogna, I. (2004). Time-variable gravity from grace: First results. *Geophys. Res. Lett.*, *31*(11).

Wallace, C. J. & Joshi, M. (2018). Comparison of land–ocean warming ratios in updated observed records and cmip5 climate models. *Environ. Res. Lett.*, *13*(11), 114011.

Wang, B., Bao, Q., Hoskins, B., Wu, G. & Liu, Y. (2008a). Tibetan plateau warming and precipitation changes in east asia. *Geophys. Res. Lett.*, *35*(14).

Wang, B., Wu, Z., Li, J., Liu, J., Chang, C.-P., Ding, Y. & Wu, G. (2008b). How to measure the strength of the east asian summer monsoon. *J. Clim.*, *21*(17), 4449–4463.

Wang, C., Yu, L. & Huang, B. (2012). The impact of warm pool SST and general circulation on increased temperature over the tibetan plateau. *Adv. Atmos. Sci.*, *29*(2), 274–284.

Wang, G. & Schimel, D. (2003). Climate change, climate modes, and climate impacts. *Annu. Rev. Environ. Resour.*, *28*(1), 1–28.

Wang, J., Song, C., Reager, J. T., Yao, F., Famiglietti, J. S., Sheng, Y., MacDonald, G. M., Brun, F., Schmied, H. M., Marston, R. A. & Wada, Y. (2018). Recent global decline in endorheic basin water storages. *Nat. Geosci.*, *11*, 926–932.

Wang, X., Jiang, D. & Lang, X. (2021). Future changes in aridity index at two and four degrees of global warming above preindustrial levels.

Watts, D., Durán, P. & Flores, Y. (2017). How does el niño southern oscillation impact the wind resource in chile? a techno-economical assessment of the influence of el niño and la niña on the wind power.

Wentz, F. J., Ricciardulli, L., Hilburn, K. & Mears, C. (2007). How much more rain will global warming bring? *Science*, *317*(5835), 233–235.

Wiederhold, P. R. (2012). *Water vapor measurement: Methods and instrumentation.* CRC Press.

Willett, K. M., Dunn, R. J. H., Thorne, P. W., Bell, S., de Podesta, M., Parker, D. E., Jones, P. D. & Jr, C. N. W. (2014). HadISDH land surface multi-variable humidity and temperature record for climate monitoring. *Climate of the Past; Katlenburg-Lindau*, *10*(6), 1983.

Willett, K. M., Vance, A., Simmons, A., Bosilovic, M., Berry, D. I. & Lanvers, D. (2021a). Global climate surface humidity in state of the climate in 2020. *Bull. Am. Meteorol. Soc.*, *102*, S51–S53.

Willett, K. M., Vance, A., Simmons, A., Bosilovich, M., Berry, D. I. & Lavers, D. (2021b). Global climate surface humidity in state of the climate in 2020. *Bull. Am. Meteorol. Soc.*, *102*(8), S51–S53.

Willett, K. M., Williams, C. N., Jr, Dunn, R. J. H., Thorne, P. W., Bell, S., de Podesta, M., Jones, P. D. & Parker, D. E. (2013). HadISDH: An updateable land surface specific humidity product for climate monitoring. *Clim. Past*, *9*(2), 657–677.

Willett, K. M., Dunn, R. J. H., Kennedy, J. J. & Berry, D. I. (2020). Development of the HadISDH.marine humidity climate monitoring dataset.

Winkler, A. (2020). The response of global terrestrial photosynthesis to rising CO2.

Winkler, A. J., Myneni, R. B., Alexandrov, G. A. & Brovkin, V. (2019). Earth system models underestimate carbon fixation by plants in the high latitudes.

Winkler, A. J., Myneni, R. B., Hannart, A., Sitch, S., Haverd, V., Lombardozzi, D., Arora, V. K., Pongratz, J., Nabel, J. E., Goll, D. S. et al. (2021). Slow-down of the greening trend in natural vegetation with further rise in atmospheric CO 2. *Biogeosci. Discuss.*, 1–36.

Wollings, T., Papritz, L., Mbengue, C. & Spengler, T. (2016). Diabatic heating and jet stream shifts: A case study of the 2010 negative north atlantic oscillation winter. *Geophysical Research Letters*, *43*(18), 9994–10, 002.

Wolter, K. & Timlin, M. S. (2011). El niño/southern oscillation behaviour since 1871 as diagnosed in an extended multivariate ENSO index (MEI.ext). *Int. J. Climatol.*, *31*(7), 1074–1087.

Wong, N. H. & Peck, T. T. (2005). The impact of vegetation on the environmental conditions of housing estates in singapore. *International Journal on Architectural Science*, *6*(1), 31–37.

Woodward, F. I. & Lomas, M. R. (2001). Integrating fluxes from heterogeneous vegetation. *Glob. Ecol. Biogeogr.*, *10*(6), 595–601.

Wright, C. K., de Beurs, K. M. & Henebry, G. M. (2014). Land surface anomalies preceding the 2010 russian heat wave and a link to the north atlantic oscillation. *Environ. Res. Lett.*, *9*(12), 124015.

Xiao, F., Wang, D. & Leung, M. Y. T. (2020a). Early and extreme warming in the south china sea during 2015/2016: Role of an unusual indian ocean dipole event. *Geophys. Res. Lett.*, *47*(17).

Xiao, M., Yu, Z., Kong, D., Gu, X., Mammarella, I., Montagnani, L., Altaf Arain, M., Merbold, L., Magliulo, V., Lohila, A., Buchmann, N., Wolf, S., Gharun, M., Hörtnagl, L., Beringer, J. & Gioli, B. (2020b). Stomatal response to decreased relative humidity constrains the acceleration of terrestrial evapotranspiration. *Environ. Res. Lett.*, *15*(9), 094066.

Xie, X., He, B., Guo, L., Miao, C. & Zhang, Y. (2019). Detecting hotspots of interactions between vegetation greenness and terrestrial water storage using satellite observations. *Remote Sens. Environ.*, *231*, 111259.

Xu, C.-Y., Gong, L., Jiang, T., Chen, D. & Singh, V. P. (2006). Analysis of spatial distribution and temporal trend of reference evapotranspiration and pan evaporation in changjiang (yangtze river) catchment. *J. Hydrol.*, *327*(1), 81–93.

Xu, Y. & Hu, A. (2018). How would the Twenty-First-Century warming influence pacific decadal variability and its connection to north american rainfall: Assessment based on a revised procedure for the IPO/PDO.

Yadav, R. R., Gupta, A. K., Kotlia, B. S., Singh, V., Misra, K. G., Yadava, A. K. & Singh, A. K. (2017). Recent wetting and glacier expansion in the northwest himalaya and karakoram.

Yang, J., Gong, D., Wang, W., Hu, M. & Mao, R. (2012). Extreme drought event of 2009/2010 over southwestern china. *Meteorol. Atmos. Phys.*, *115*(3-4), 173–184.

Yang, K., Wu, H., Qin, J., Lin, C., Tang, W. & Chen, Y. (2014). Recent climate changes over the tibetan plateau and their impacts on energy and water cycle: A review. *Glob. Planet. Change*, *112*, 79–91.

Yatagai, A. & Yasunari, T. (1994). Trends and decadal-scale fluctuations of surface air temperature and precipitation over china and mongolia during the recent 40 year period (1951-1990). *Journal of the Meteorological Society of Japan. ser. ii*, *72*(6), 937–957.

Ye, H. (2001). Characteristics of winter precipitation variation over northern central eurasia and their connections to sea surface temperatures over the atlantic and pacific oceans. *J. Clim.*, *14*(14), 3140–3155.

Yeh, S.-W., Kug, J.-S., Dewitte, B., Kwon, M.-H., Kirtman, B. P. & Jin, F.-F. (2009). El niño in a changing climate. *Nature*, *461*(7263), 511–514.

You, Q., Kang, S., Flügel, W. A., Pepin, N., Yan, Y. & Huang, J. (2010). Decreasing wind speed and weakening latitudinal surface pressure gradients in the tibetan plateau. *Clim. Res.*, *42*(1), 57–64.

Yu, W., Li, Y., Cao, Y. & Schillerberg, T. (2019). Drought assessment using GRACE terrestrial water storage deficit in mongolia from 2002 to 2017. *Water*, *11*(6), 1301.

Yu, W., Wu, T., Wang, W., Li, R., Wang, T., Qin, Y., Wang, W. & Zhu, X. (2016). Spatiotemporal changes of reference evapotranspiration in mongolia during 1980–2006. *Advances in Meteorology*, *2016*.

Yuan, W., Zheng, Y., Piao, S., Ciais, P., Lombardozzi, D., Wang, Y., Ryu, Y., Chen, G., Dong, W., Hu, Z., Jain, A. K., Jiang, C., Kato, E., Li, S., Lienert, S., Liu, S., Nabel, J. E. M. S., Qin, Z., Quine, T., . . . Yang, S. (2019). Increased atmospheric vapor pressure deficit reduces global vegetation growth. *Sci Adv*, *5*(8), eaax1396.

Zampieri, M., D'Andrea, F., Vautard, R., Ciais, P., de Noblet-Ducoudré, N. & Yiou, P. (2009). Hot european summers and the role of soil moisture in the propagation of mediterranean drought.

Zeng, Z., Ziegler, A. D., Searchinger, T., Yang, L., Chen, A., Ju, K., Piao, S., Li, L. Z. X., Ciais, P., Chen, D., Liu, J., Azorin-Molina, C., Chappell, A., Medvigy, D. &

Wood, E. F. (2019). A reversal in global terrestrial stilling and its implications for wind energy production. *Nat. Clim. Chang.*, *9*(12), 979–985.

Zhang, G., Zhang, Y., Dong, J. & Xiao, X. (2013). Green-up dates in the tibetan plateau have continuously advanced from 1982 to 2011. *Proc. Natl. Acad. Sci. U. S. A.*, *110*(11), 4309–4314.

Zhang, J., Ma, Q., Chen, H., Zhao, S. & Chen, Z. (2021). Increasing Warm-Season precipitation in asian drylands and response to reducing spring snow cover over the tibetan plateau. *J. Clim.*, *34*(8), 3129–3144.

Zhang, K., Kimball, J. S., Nemani, R. R. & Running, S. W. (2010). A continuous satellite-derived global record of land surface evapotranspiration from 1983 to 2006. *Water Resour. Res.*, *46*(9).

Zhang, K., Kimball, J. S. & Running, S. W. (2016a). A review of remote sensing based actual evapotranspiration estimation. *Wiley Interdisciplinary Reviews: Water*, *3*(6), 834–853.

Zhang, L., Du, Y. & Cai, W. (2018). Low-frequency variability and the unusual indian ocean dipole events in 2015 and 2016. *Geophys. Res. Lett.*, *45*(2), 1040–1048.

Zhang, R., Jiang, D., Zhang, Z. & Yu, E. (2015). The impact of regional uplift of the tibetan plateau on the asian monsoon climate. *Palaeogeogr. Palaeoclimatol. Palaeoecol.*, *417*, 137–150.

Zhang, Y., Liu, C., Tang, Y. & Yang, Y. (2007). Trends in pan evaporation and reference and actual evapotranspiration across the tibetan plateau. *J. Geophys. Res.*, *112*(D12).

Zhang, Y., Peña-Arancibia, J. L., McVicar, T. R., Chiew, F. H. S., Vaze, J., Liu, C., Lu, X., Zheng, H., Wang, Y., Liu, Y. Y., Miralles, D. G. & Pan, M. (2016b). Multi-decadal trends in global terrestrial evapotranspiration and its components.

Zhang, Y., Wallace, J. M. & Battisti, D. S. (1997). ENSO-like interdecadal variability: 1900–93. *J. Clim.*, *10*(5), 1004–1020.

Zhang, Z. & Wang, K. (2020). Stilling and recovery of the surface wind speed based on observation, reanalysis, and geostrophic wind theory over china from 1960 to 2017. *J. Clim.*, *33*(10), 3989–4008.

Zhao, C., Huang, Y., Li, Z. & Chen, M. (2018). Drought monitoring of southwestern china using insufficient GRACE data for the Long-Term mean reference frame under global change. *J. Clim.*, *31*(17), 6897–6911.

Zheng, C. W., Pan, J. & Li, C. Y. (2016). Global oceanic wind speed trends. *Ocean Coast. Manag.*, *129*, 15–24.

Zhongming, Z., Linong, L., Wangqiang, Z., Wei, L. et al. (2016). WMO statement on the status of the global climate in 2015.

Zhou, S., Williams, A. P., Berg, A. M. et al. (2019). Land–atmosphere feedbacks exacerbate concurrent soil drought and atmospheric aridity. *Proceedings of the.*

Zhou, S., Miller, A. J., Wang, J. & Angell, J. K. (2001). Trends of NAO and AO and their associations with stratospheric processes. *Geophys. Res. Lett.*, *28*(21), 4107–4110.

Zhu, Y., Liu, S., Yi, Y., Xie, F., Grünwald, R., Miao, W., Wu, K., Qi, M., Gao, Y. & Singh, D. (2021). Overview of terrestrial water storage changes over the indus river basin based on GRACE/GRACE-FO solutions. *Sci. Total Environ.*, *799*, 149366.

Zurbenko, I. & Luo, M. (2015). Surface humidity changes in different temporal scales. *Am. J. Clim. Change*, *04*(03), 226–238.

Why is the atmosphere over land becoming drier?

Exploring the roles of atmospheric and land-surface processes on relative humidity

Kirsten Maria Florentine Weber

Volume II

Submitted in partial fulfillment of the requirement for the degree of Doctor of Philosophy

The University of Sheffield
Department of Geography

March 2022

Figures and supplementary material

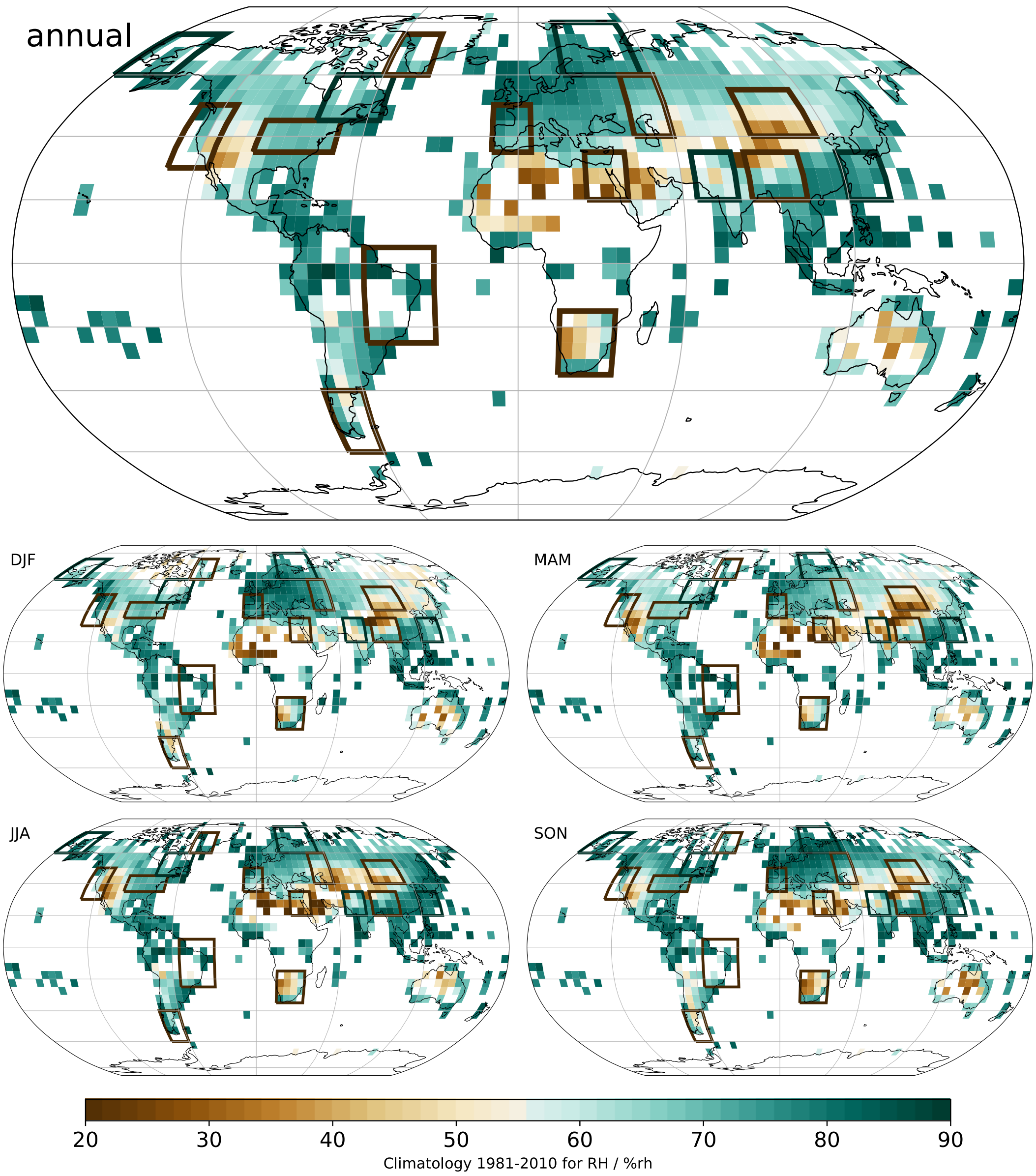

Figure 1.1: Global maps of average HadISDH RH for the four standard seasons and annual values for the climatology over the 1981–2010 period.

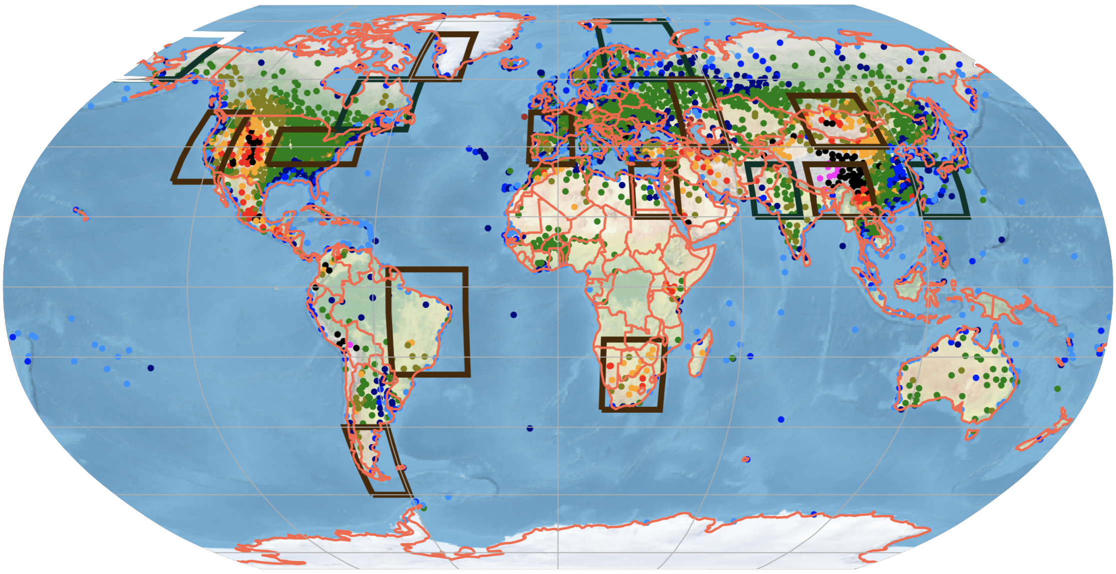

Figure 1.2: Location and elevation of weather stations included in the HadISDH.land-v4.0.0.2017f dataset. White dots indicate weather stations deeper than 340 m below sea level, and brown dots indicate weather stations below sea level but higher than 340 m below sea level. Sky-blue weather stations are at an elevation between 0 and 25 m above sea level, 25 m < blue < 50 m < navy < 100 m < green < 500 m < olive < 1000 m < orange < 1500 m < red < 2000 m < black < 4000 m, and fuchsia dots indicate weather stations at elevations higher than 4000 m. Regions with a strong average trend in RH in the late period (2000–2017), thus, regions of interest in this study (see Chapter 3), are framed in ochre (negative trends) and turquoise (positive trends).

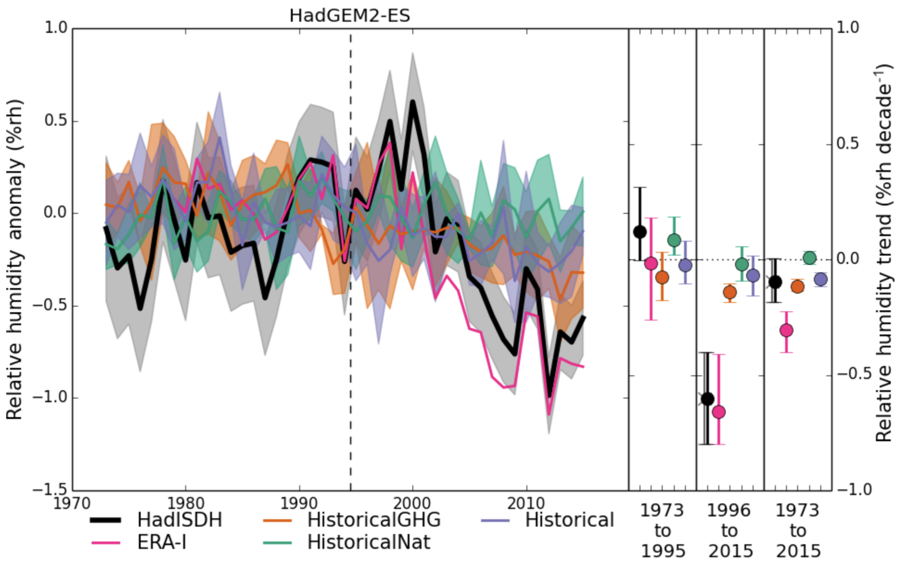

Figure 1.3: Global annual RH anomalies for HadISDH observation data set (black), ERA-Interim re-analysis (magenta) and historical runs of the CMIP5 Met Office's model HadGEM2-ES (Collins et al., 2011; Jones et al., 2011), relative to the 1976—2005 climatology. Fig. from Dunn et al. (2017).

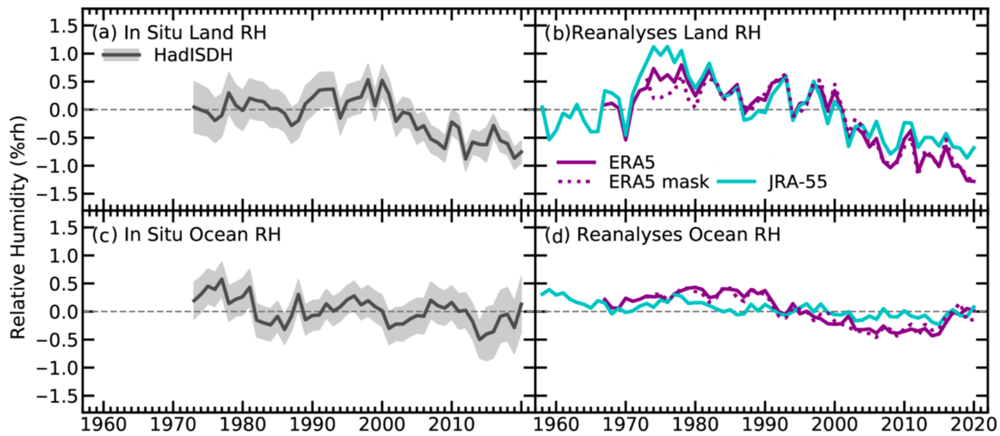

Figure 1.4: Global annual land (top) and ocean (bottom) RH anomalies for in situ data set HadISDH (grey, left) and reanalyses data sets ERA5 and ERA5 mask (ERA5-masked to the HadISDH coverage) (purple solid and dotted, respectively) relative to the 1981–2010 base period. Fig. adapted from Willett et al., 2021b, S52, Fig. 2.19.

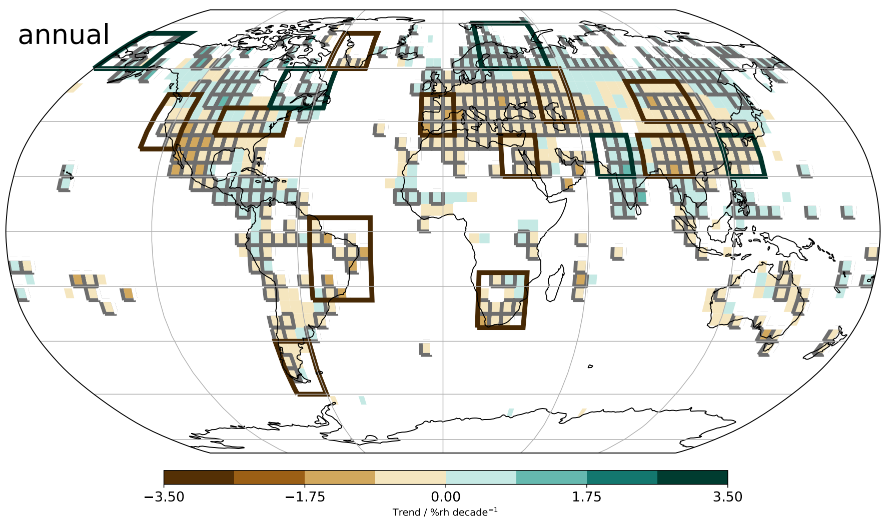

Figure 1.5: Annual HadISDH RH trends in anomalies over land for the full period (1973–2017) relative to a climatology over the 1981–2010 period, resolution 5° by 5°. Grid boxes of very significant trends ($p < 0.05$) are framed in grey. Regions with a strong average trend in RH in the late period are framed in ochre (negative trends) and turquoise (positive trends). White space represents either missing data or ocean.

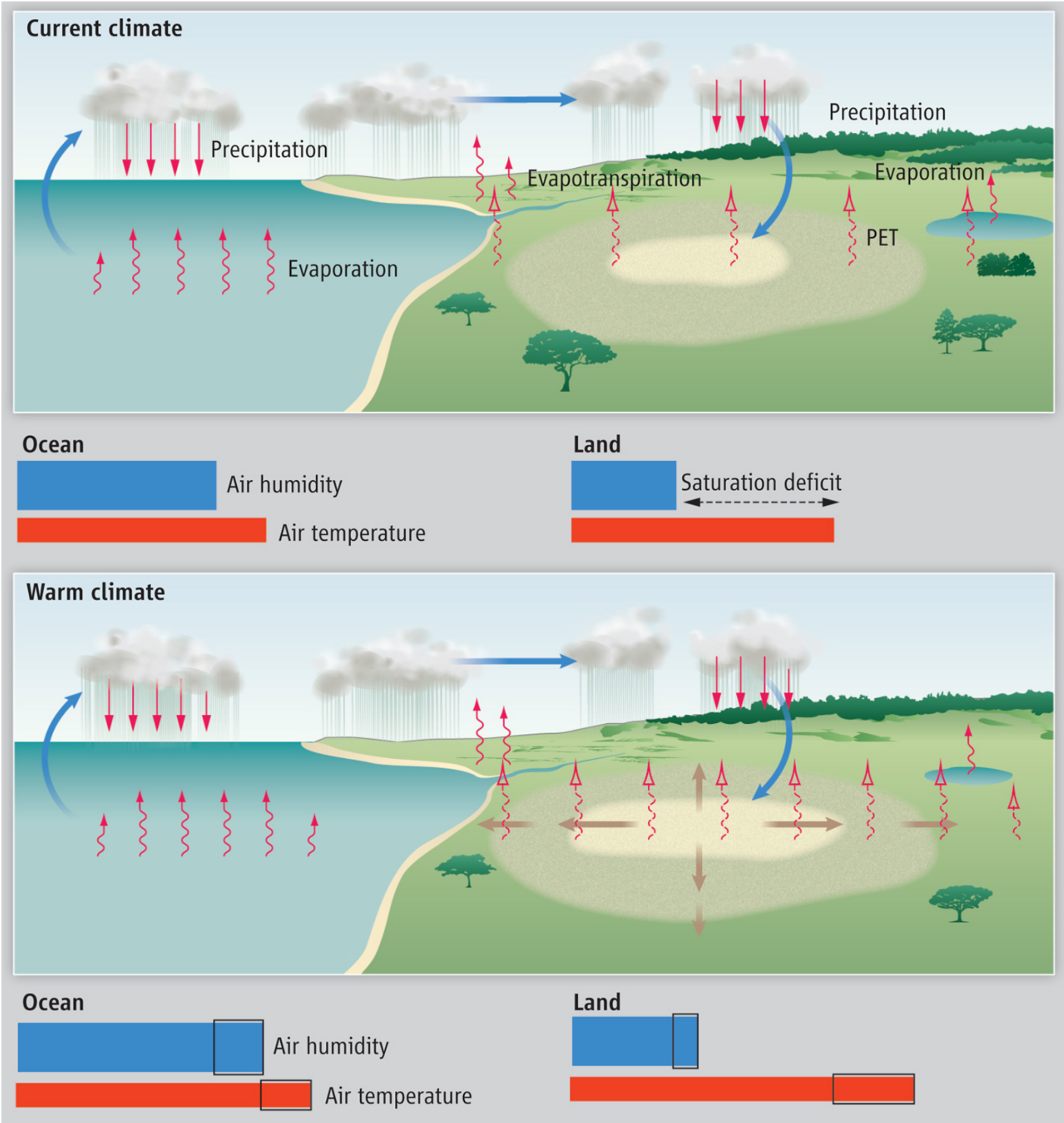

Figure 1.6: Impacts of rising air temperatures (lower figure) on the hydrological cycle over ocean (left) and over land (right). Aridity increases in warmer climates, leading to expansion of dry climate zones. Evaporation and precipitation increase modestly, but on land, evaporative demand (broken wavy arrows) increases faster than precipitation, because the strong increases in air temperature and consequently saturated water vapour concentration over land (red bars at lower right) exceed growth in actual water vapour concentration (blue bars). Increases in sensible and latent heat (associated, respectively, with temperature and water vapour, and represented by the area of each bar) have the same sum over land and ocean, with sensible heat increasing more over land than oceans and latent heat increasing more over oceans. RH (ratio of blue to red bar length) decreases over land. Fig. and caption taken from Sherwood and Fu (2014), p. 738, Fig. "Warmer, drier".

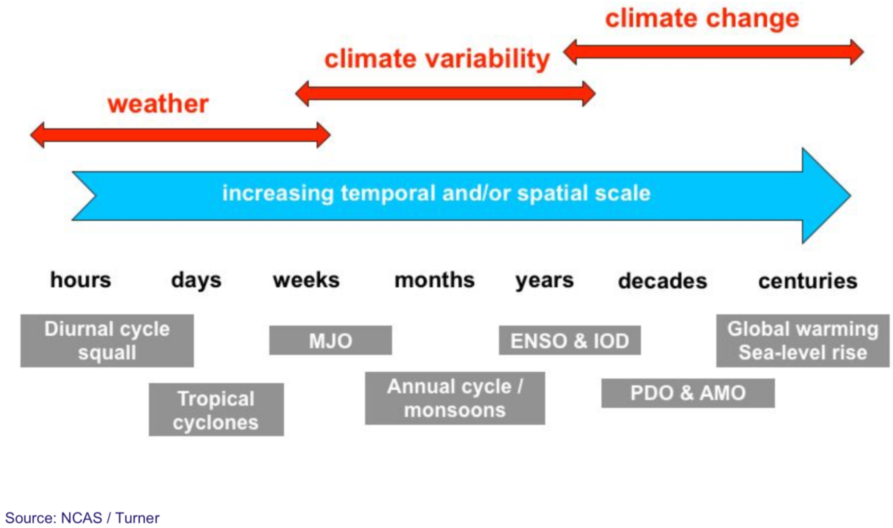

Figure 1.7: Differences between weather, climate variability and climate change concerning temporal and spatial scales and examples for changes on different temporal scales. MJO stands for the Madden-Julian Oscillation, ENSO for the El Niño Southern Oscillation, IOD for the Indian Ocean Dipole, PDO for the Pacific Decadal Oscillation and AMO for the Atlantic Multidecadal Oscillation. Fig. by A. Turner.

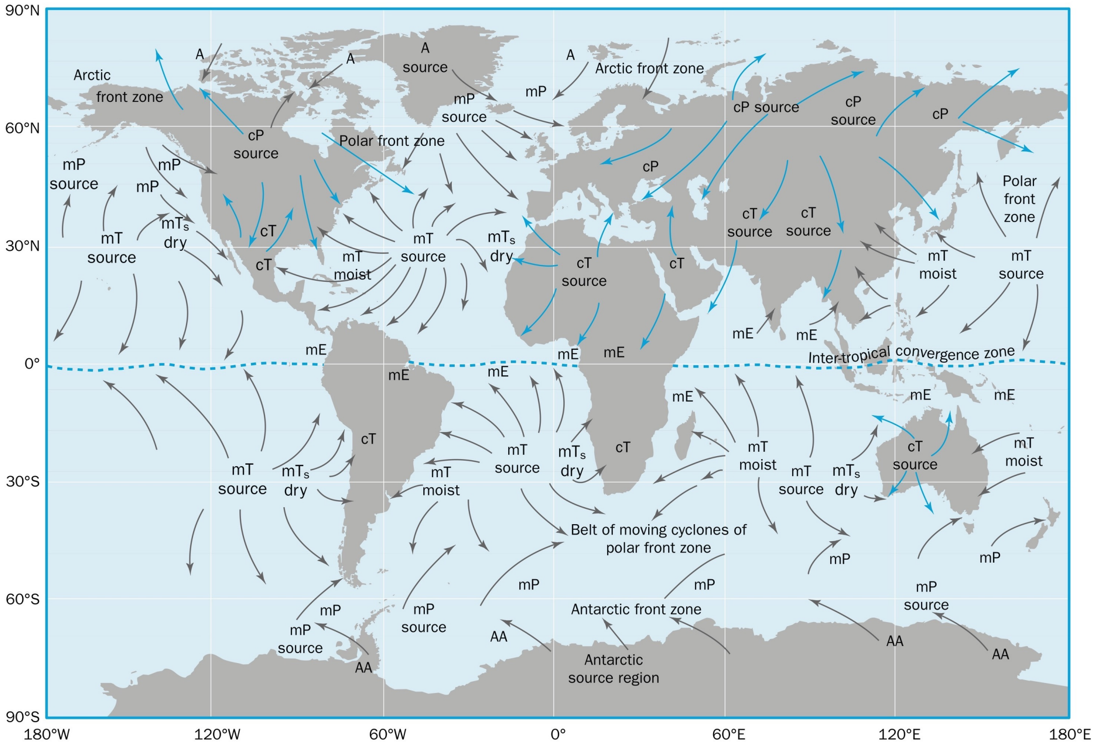

Figure 1.8: Global distribution of air mass source regions and main air mass trajectories. Key: mE maritime equatorial (warm, very moist), mT maritime tropical (mild, moist), mTs maritropical subsiding, cT continental tropical (warm, dry), cP continental polar (cold, dry), mP maritime polar (cool, moist), A arctic, AA antarctic and cA continental air (very cold, very dry; not shown). Fig. and caption taken from O'Hare et al. (2014) (p. 101, Fig. 4.12) based on Robinson and Henderson-Sellers (1999) (p. 161).

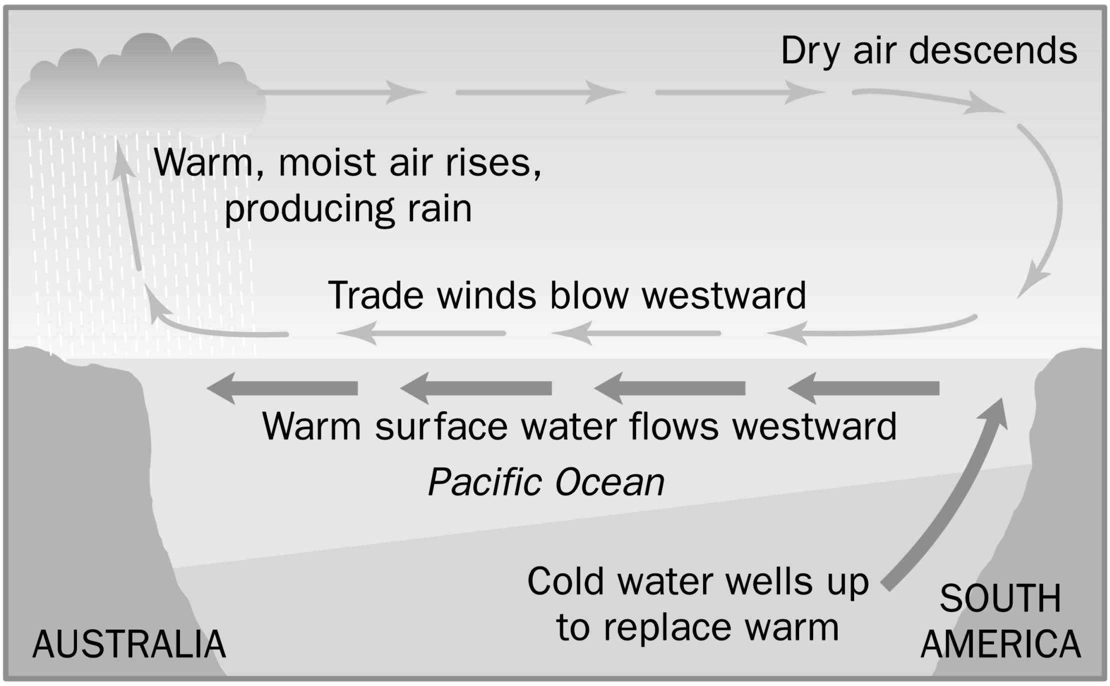

Figure 1.9: Schematic representation of the neutral phase of the ENSO in the Pacific Ocean. Fig. taken from O'Hare et al., 2014, p. 132, Fig. 5.5, a.

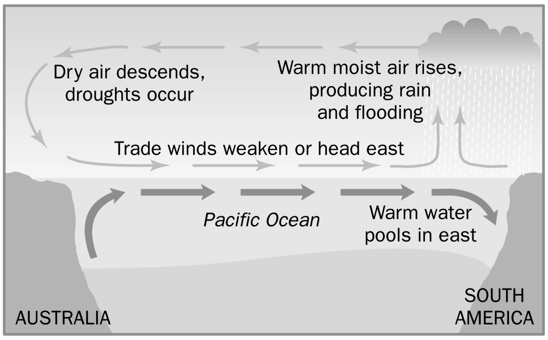

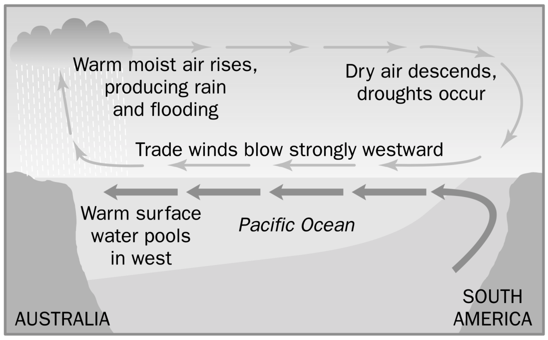

Figure 1.10: Schematic representation of El Niño (left) and La Niña (right) atmospheric and oceanic conditions in the Pacific Ocean. Fig. taken from O'Hare et al., 2014, p. 132, Fig. 5.5, b and c.

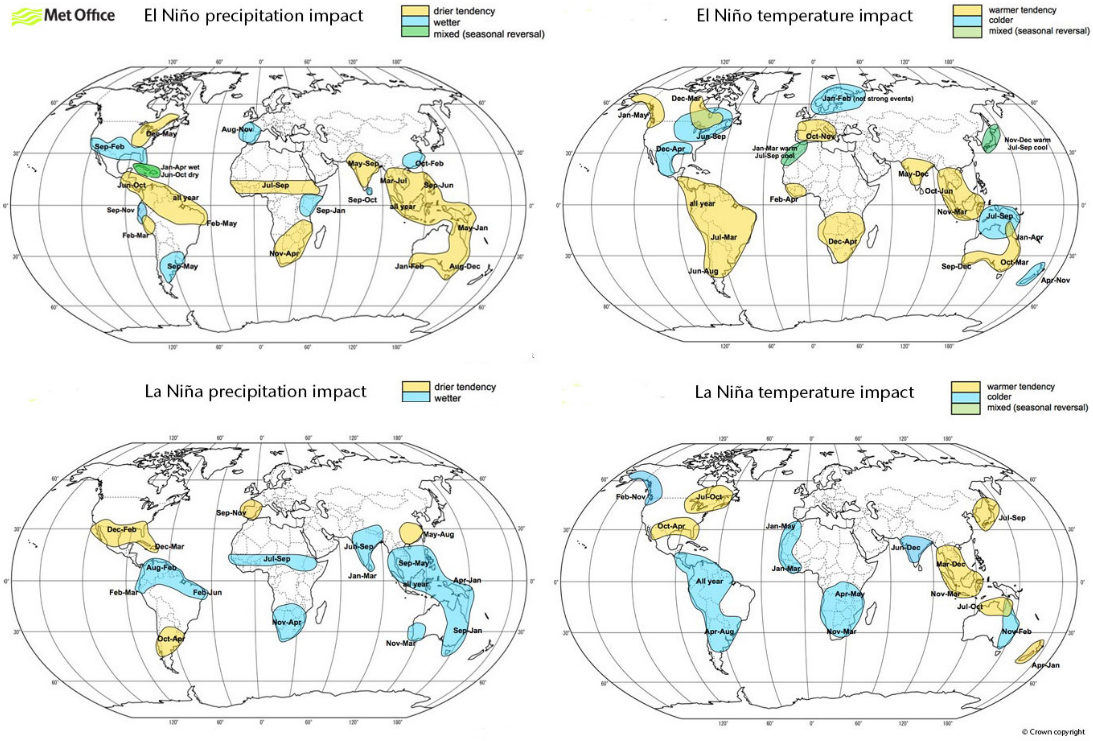

Figure 1.11: Global impact of El Niño (above) and La Niña (below) on regional precipitation (left) and temperature (right) (ENSO impacts. Met Office. Available at: https://www.metoffice.gov.uk/research/climate/seasonal-to-decadal/gpc-outlooks/el-nino-la-nina/enso-impacts [Accessed November 25, 2021]).

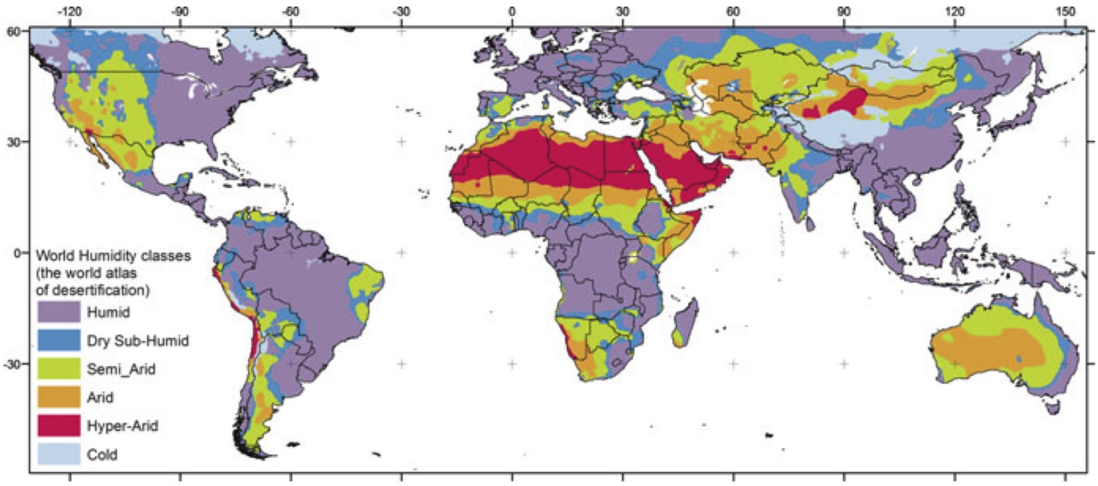

Figure 1.12: World humidity classes (World Atlas of Desertification, United Nations Environment Programme 1997). Drylands are classified into four ranges of the Aridity Index (AI, the ratio between the mean annual precipitation and the mean annual potential evaporation): hyperarid, AI<0.05 (7.5% of global land area); arid, 0.05<AI<0.20 (12.1% land); semi-Arid, 0.20<AI<0.50 (17.7% land); dry subhumid, 0.50<AI<0.65 (9.9% land). Fig. and caption taken from Fensholt et al., 2015, p. 160, Fig. 8.1.

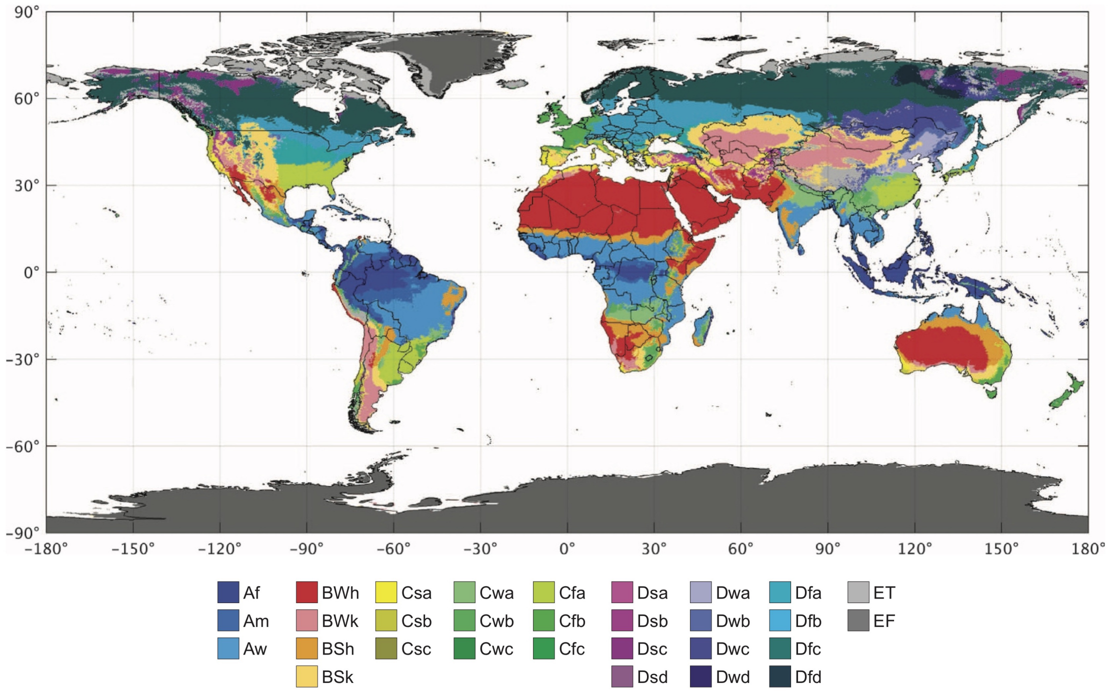

Figure 1.13: Present-day map (1980–2016) of Koeppen-Geiger classifications. Fig. and capture taken from Fig. 1 in Beck et al. (2018).

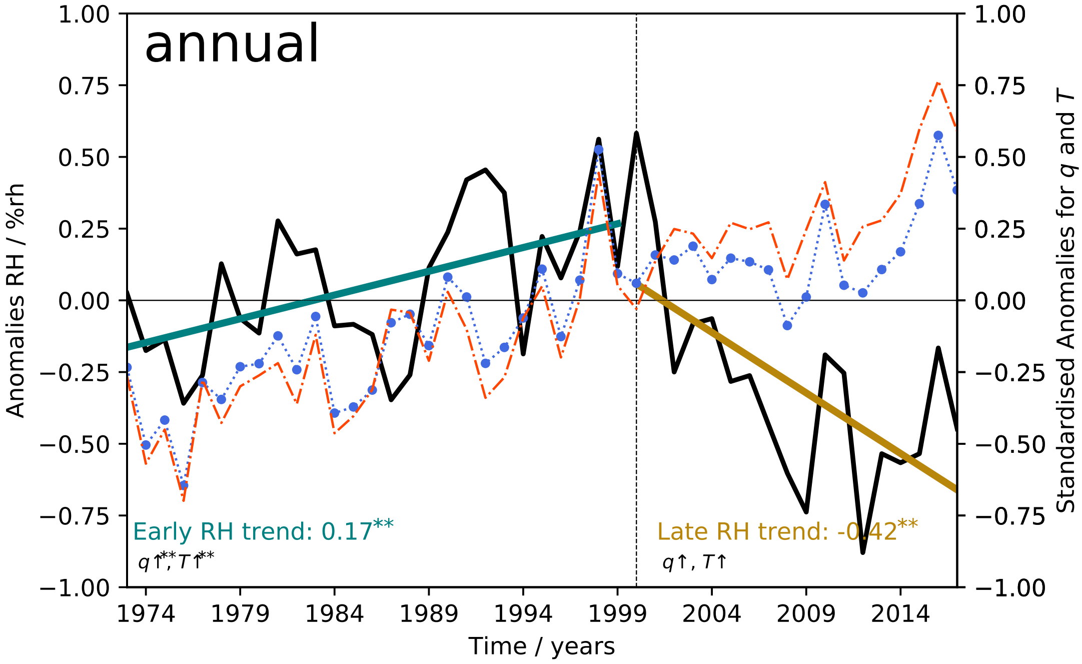

Figure 3.1: HadISDH global annual time series and trends over land for the early (1973–1999) and the late periods (2000–2017). Linear trends for RH are turquoise if positive or ochre if negative; for q and T trends are shown by an up arrow if positive or down arrow if negative. The RH trends are based on anomalies (black line), the q and T trends on standardised anomalies (respectively, blue and orange dots and line), relative to a climatology over the 1981–2010 period. Starred trends are significant ($p < 0.1$), double starred trends are very significant ($p < 0.05$).

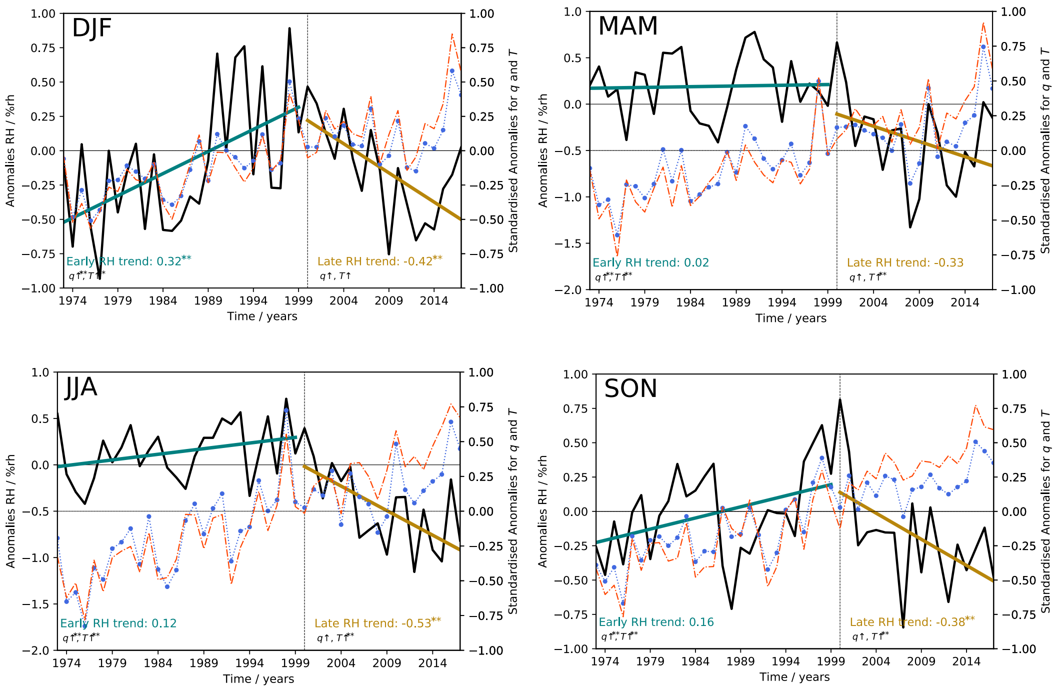

Figure 3.2: As for Fig. 3.1, for global seasonal HadISDH data.

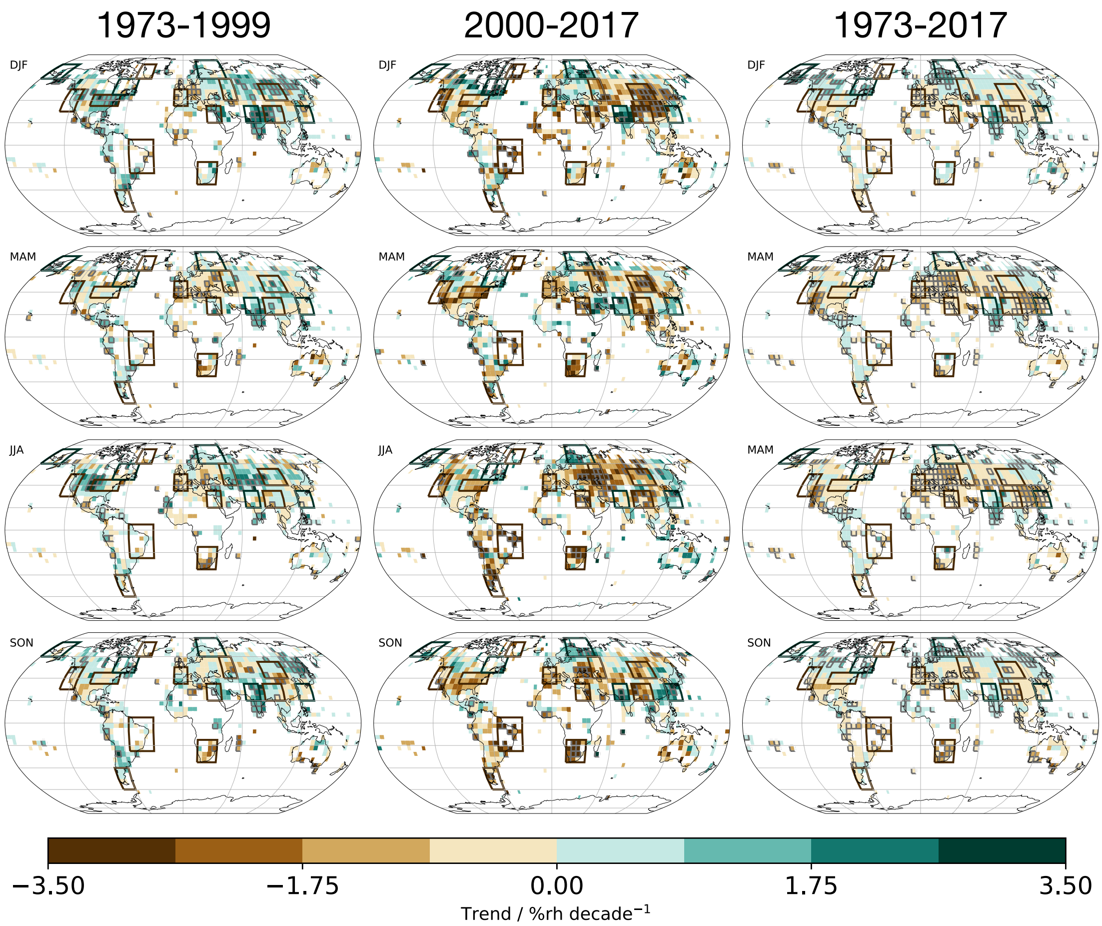

Figure 3.3: As for Fig. 1.5, for seasonal HadISDH RH trends for the early (1973–1999, left column), the late (2000–2017, centre column) and the full periods (right column).

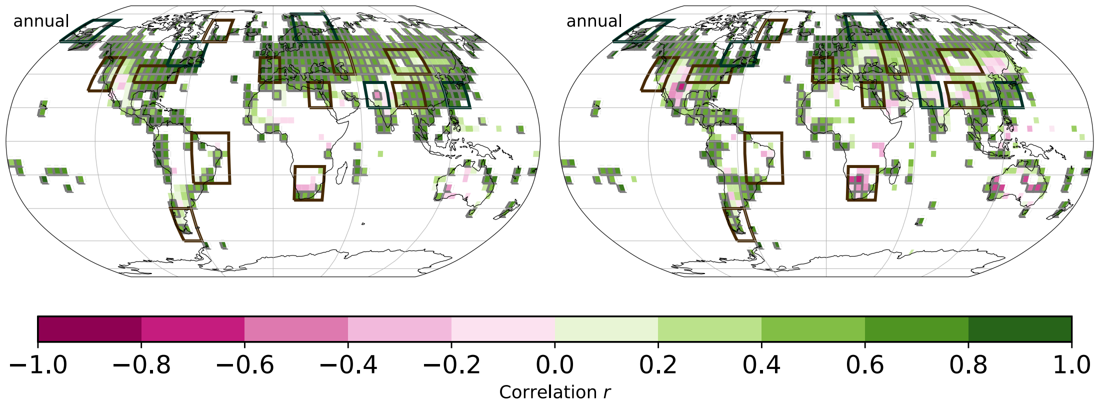

Figure 3.4: Annual correlations between the detrended HadISDH T and q anomalies over land, relative to a climatology over the 1981–2010 period, in the early (left) and the late period (right). Grid boxes of very significant correlations ($p < 0.05$) are framed in grey. Regions with a strong average trend in RH in the late period are framed in ochre (negative trends) and turquoise (positive trends). White space represents either missing data or ocean.

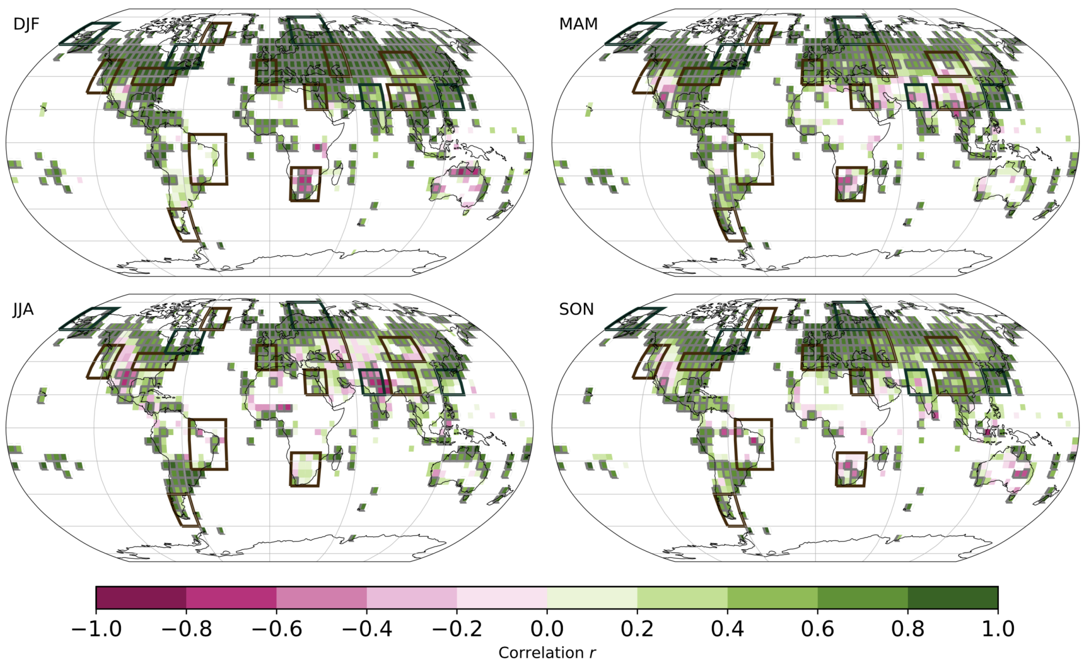

Figure 3.5: As for Fig. 3.4, for seasonal correlations between the HadISDH T and q in the late period.

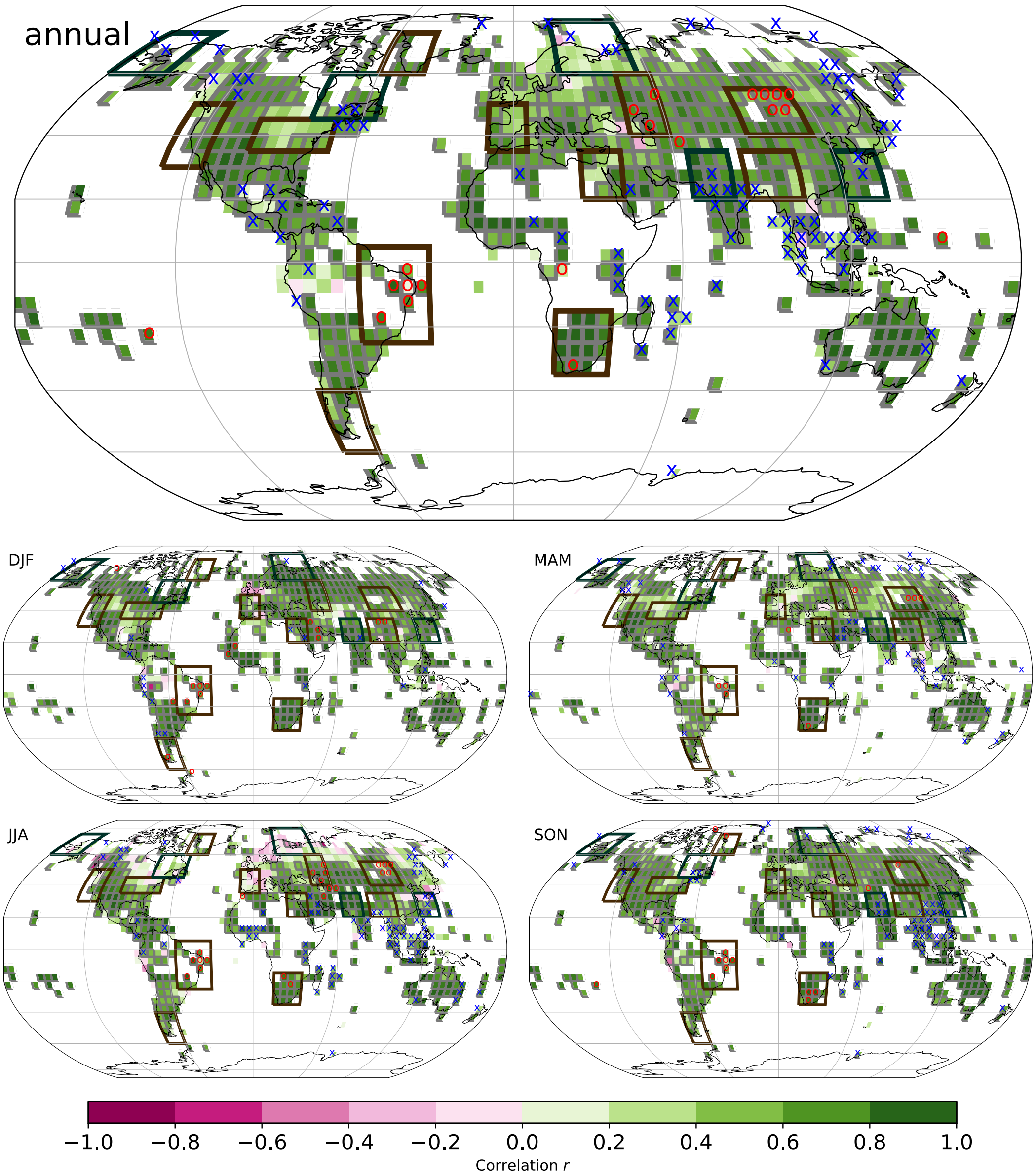

Figure 3.6: As for Fig. 3.4, for annual and seasonal HadISDH q and RH in the late period. Positive (negative) q trends relative to a climatology over the 1981–2010 period are marked with an 'x' (red 'o'), if very significant ($p < 0.05$).

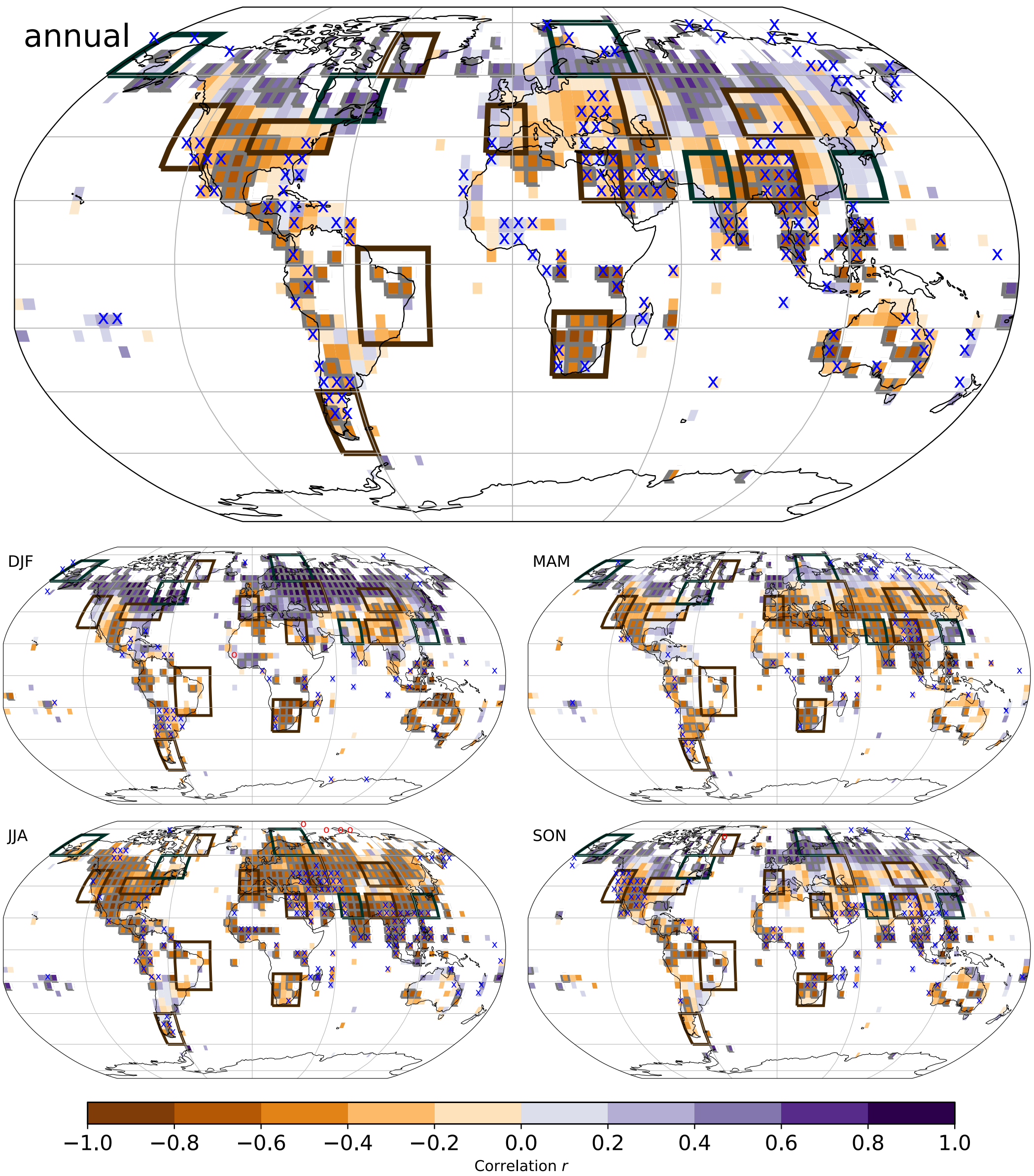

Figure 3.7: As for Fig. 3.6, for HadISDH T and RH.

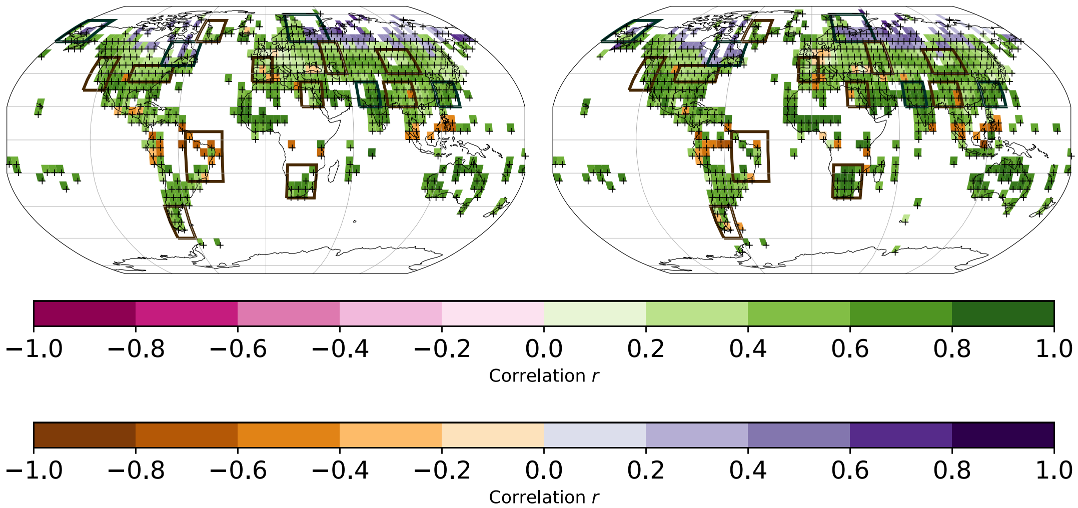

Figure 3.8: Annual correlations for the detrended HadISDH anomalies over land, relative to a climatology over the 1981–2010 period, between q-RH (positive: green, negative: pink) and T-RH (positive: purple, negative: orange) in the early (left) and the late periods (right). The correlation strength between q-RH and T-RH was compared, and the stronger one plotted for the grid box. Grid boxes of very significant correlations ($p < 0.05$) are crossed. White space represents either missing data or ocean.

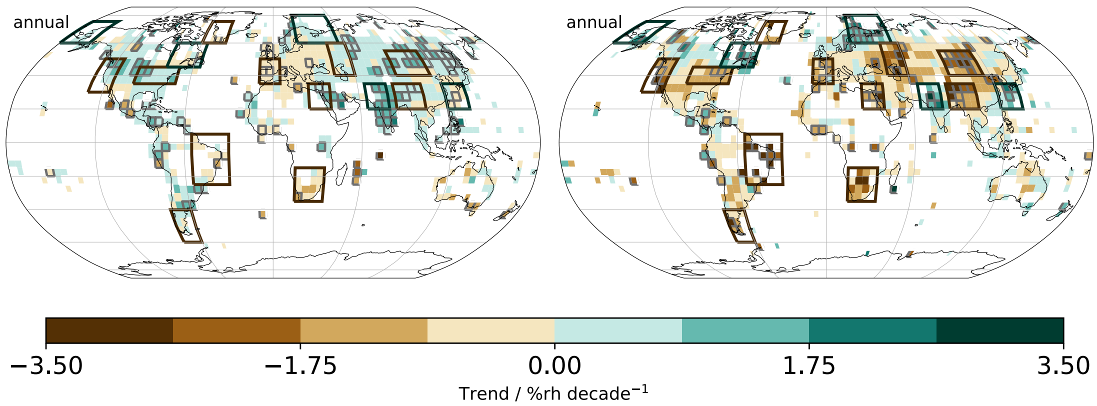

Figure 3.9: As for Fig. 1.5, for annual HadISDH RH trends for the early and the late periods.

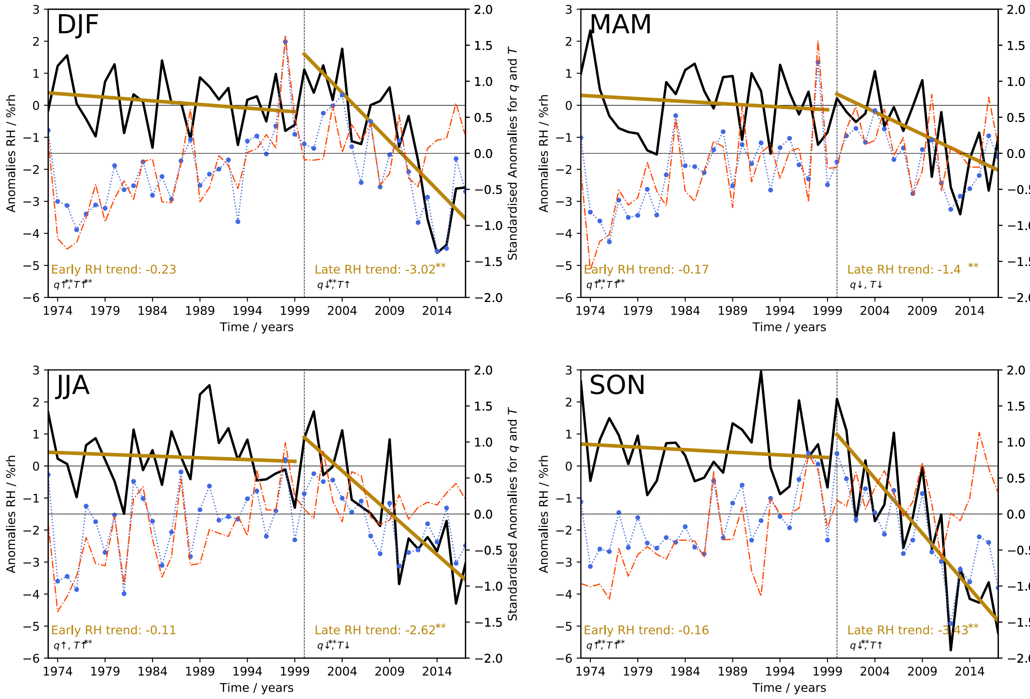

Figure 3.10: As for Fig. 3.2, for eastern Brazil.

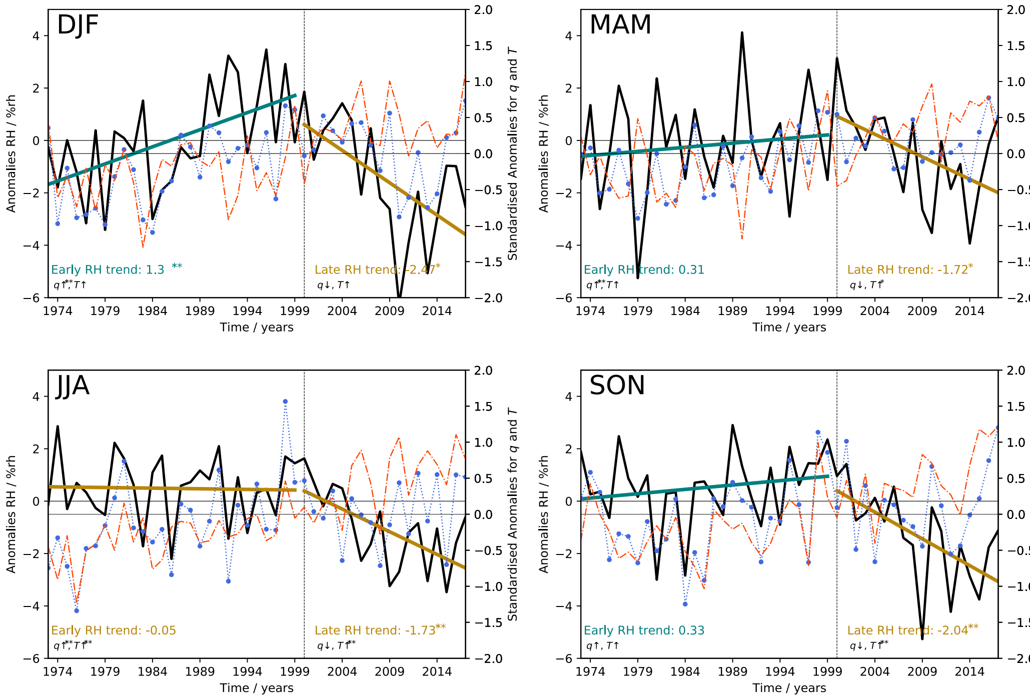

Figure 3.11: As for Fig. 3.2, for Tibet.

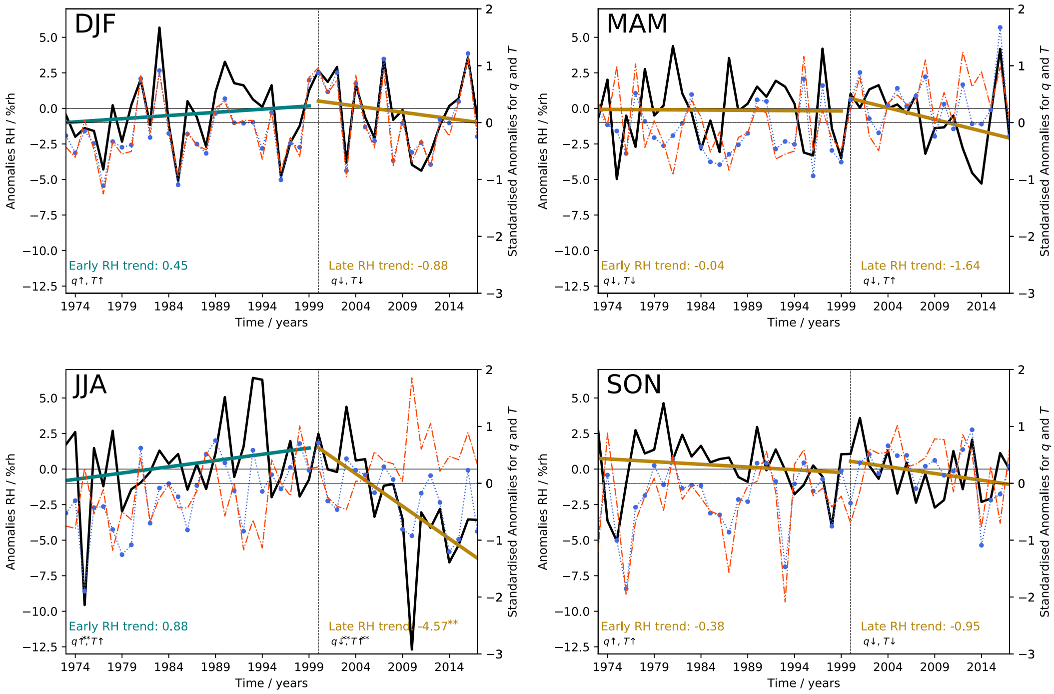

Figure 3.12: As for Fig. 3.2, for the Caspian Sea region.

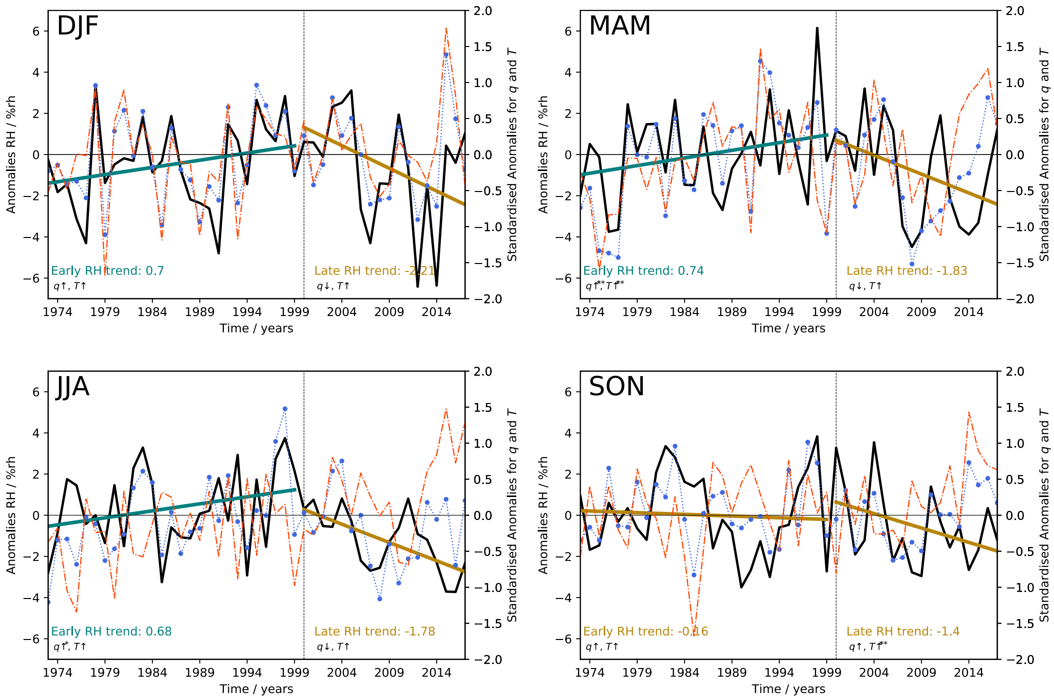

Figure 3.13: As for Fig. 3.2, for California.

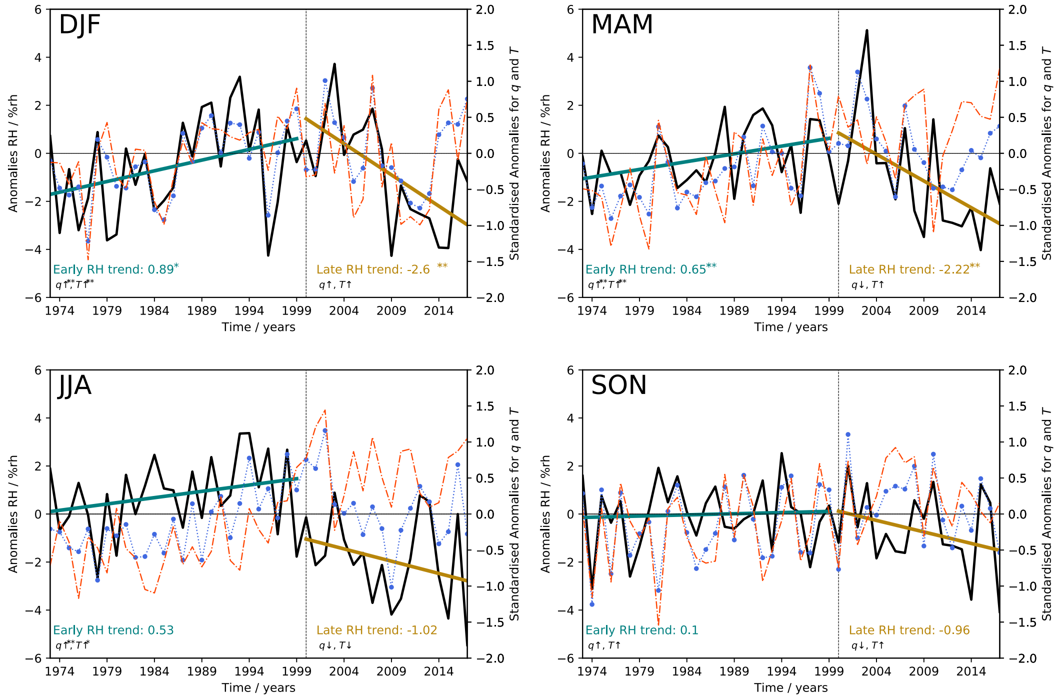

Figure 3.14: As for Fig. 3.2, for Mongolia.

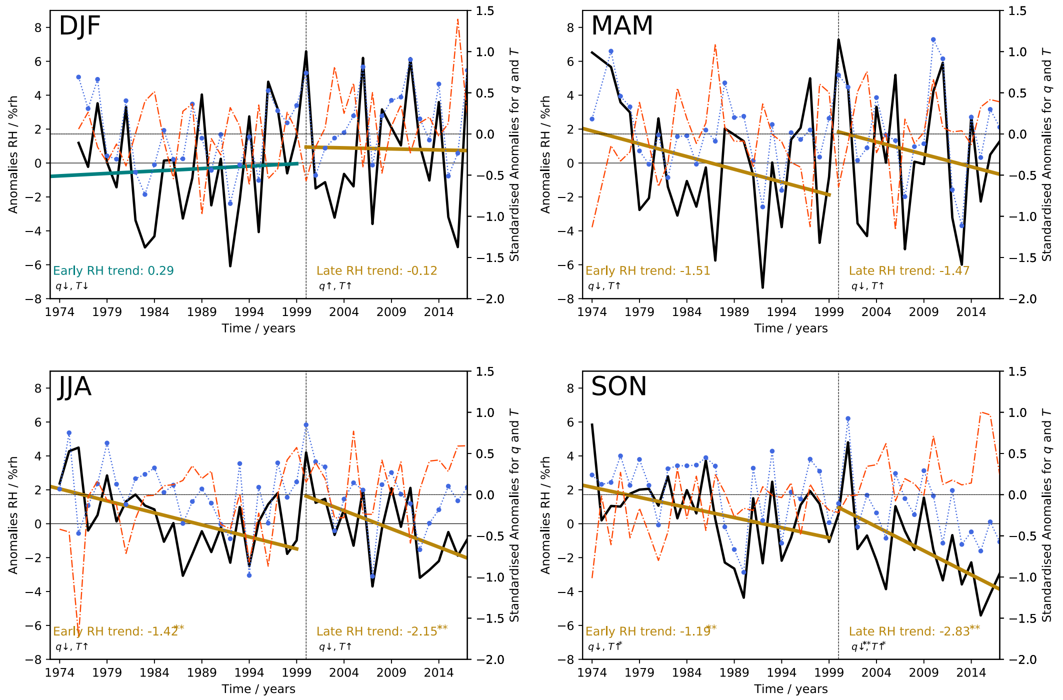

Figure 3.15: As for Fig. 3.2, for southern Africa.

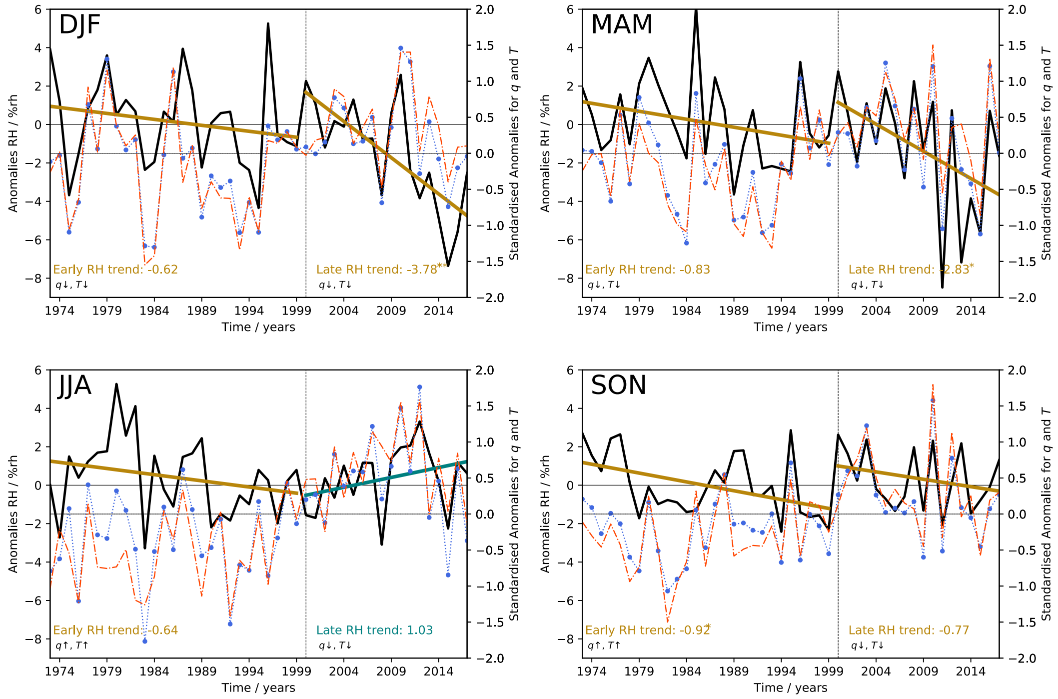

Figure 3.16: As for Fig. 3.2, for southwestern Greenland.

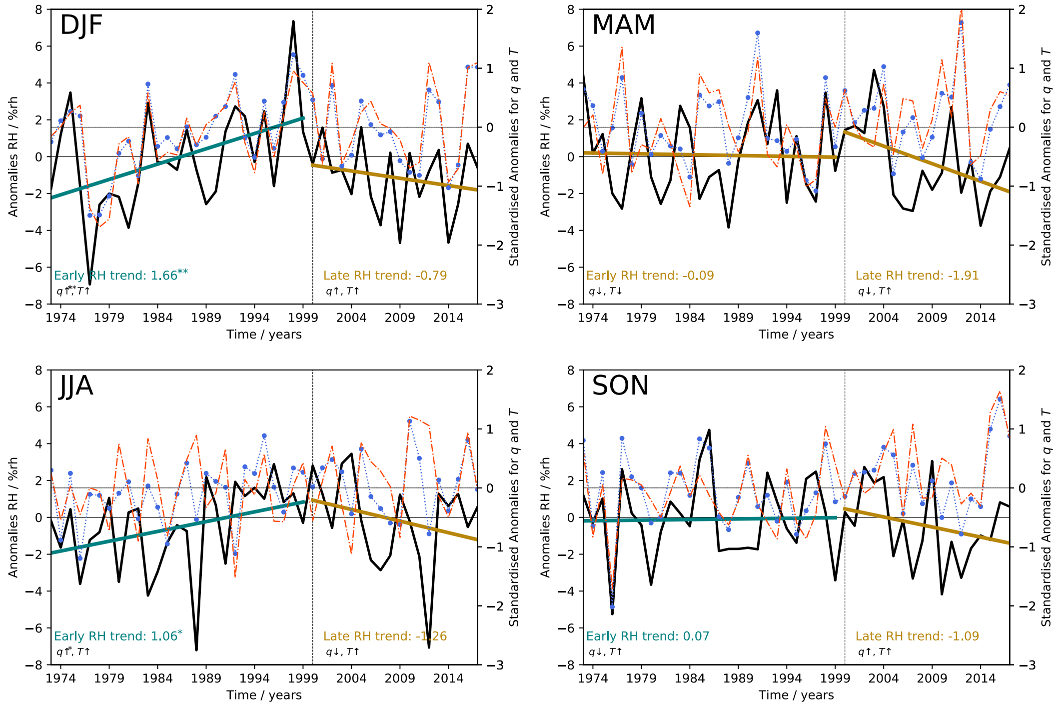

Figure 3.17: As for Fig. 3.2, for the eastern USA.

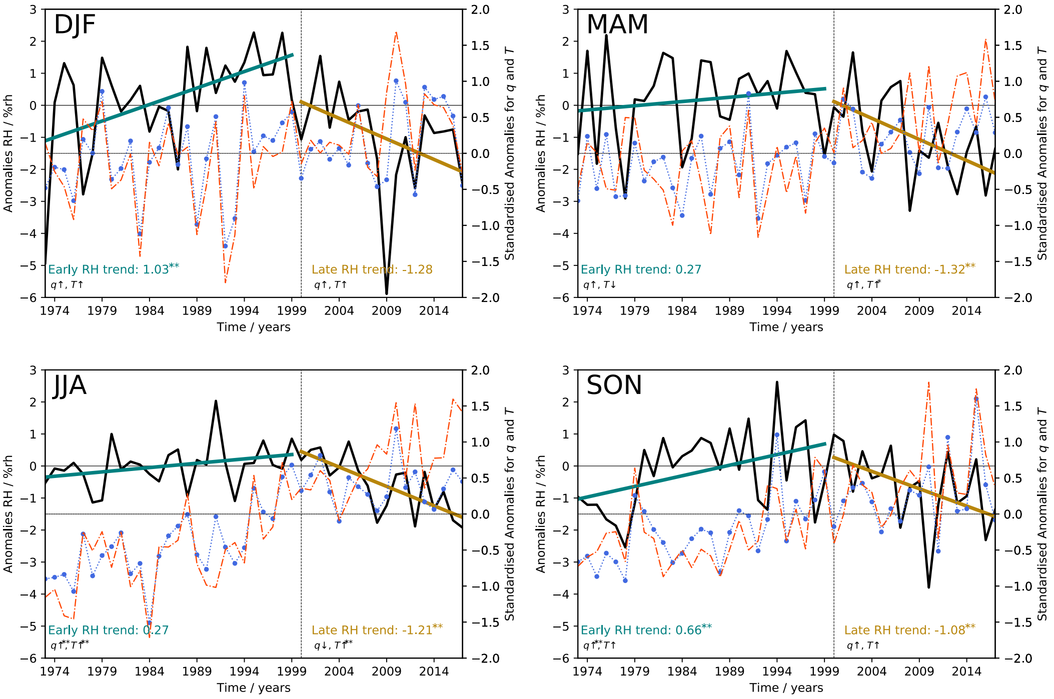

Figure 3.18: As for Fig. 3.2, for the Red Sea.

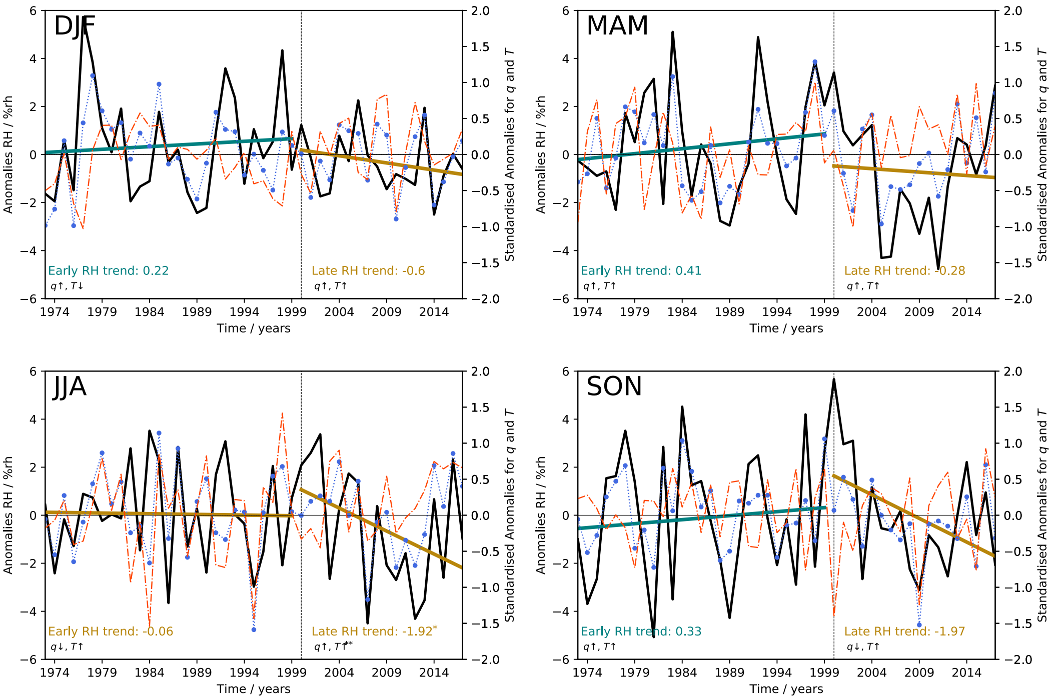

Figure 3.19: As for Fig. 3.2, for Patagonia.

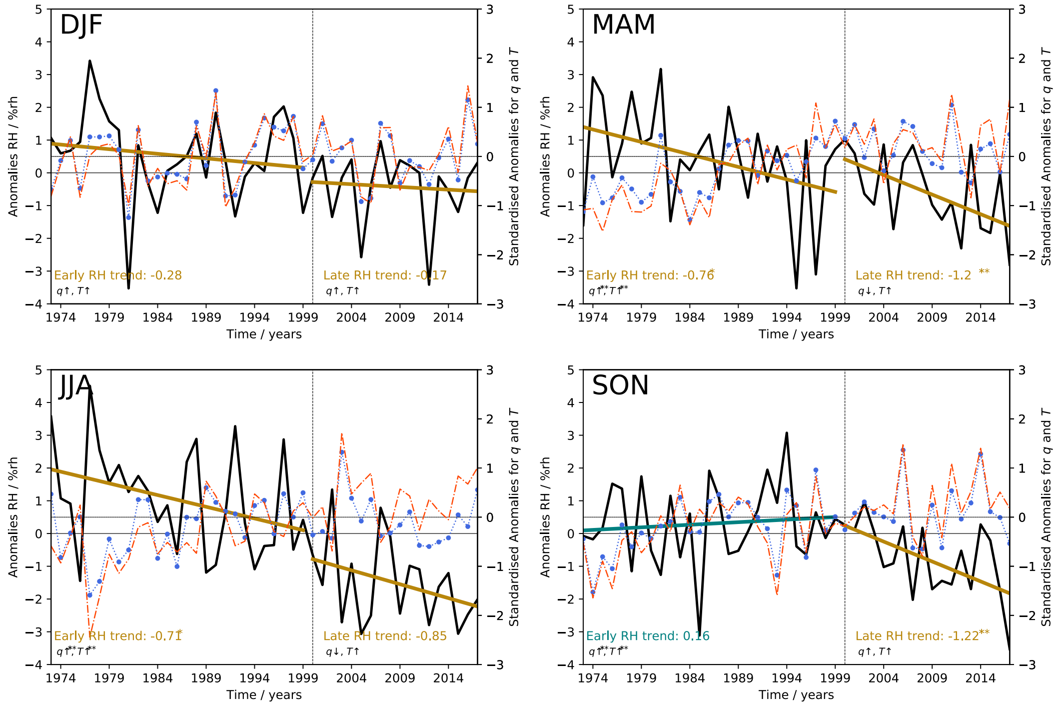

Figure 3.20: As for Fig. 3.2, for the western Mediterranean region.

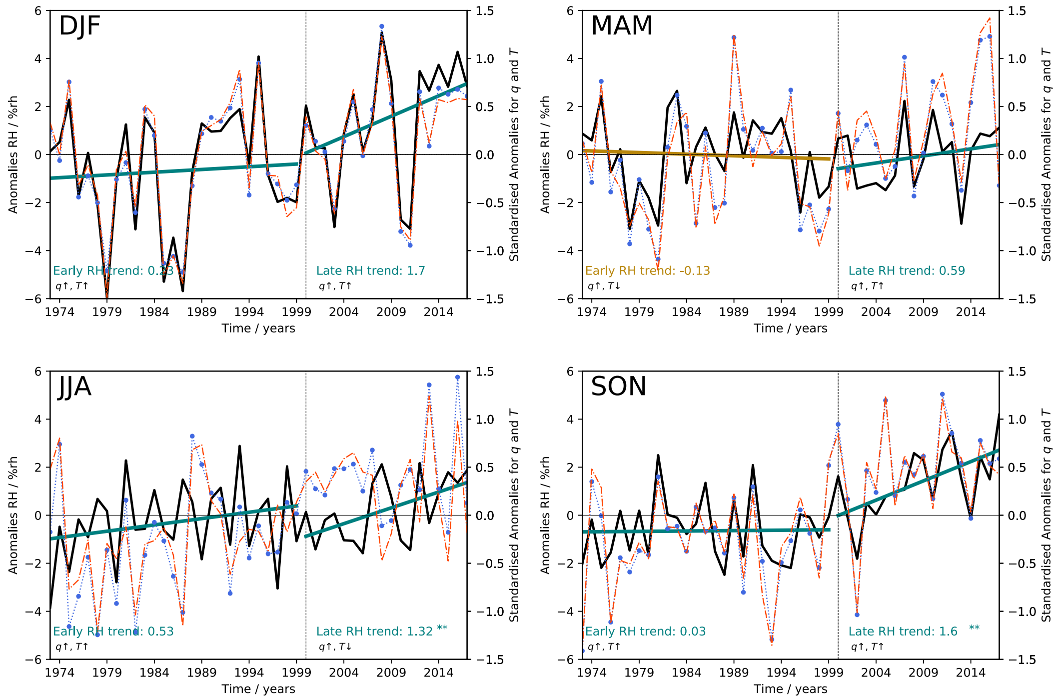

Figure 3.21: As for Fig. 3.2, for Scandinavia.

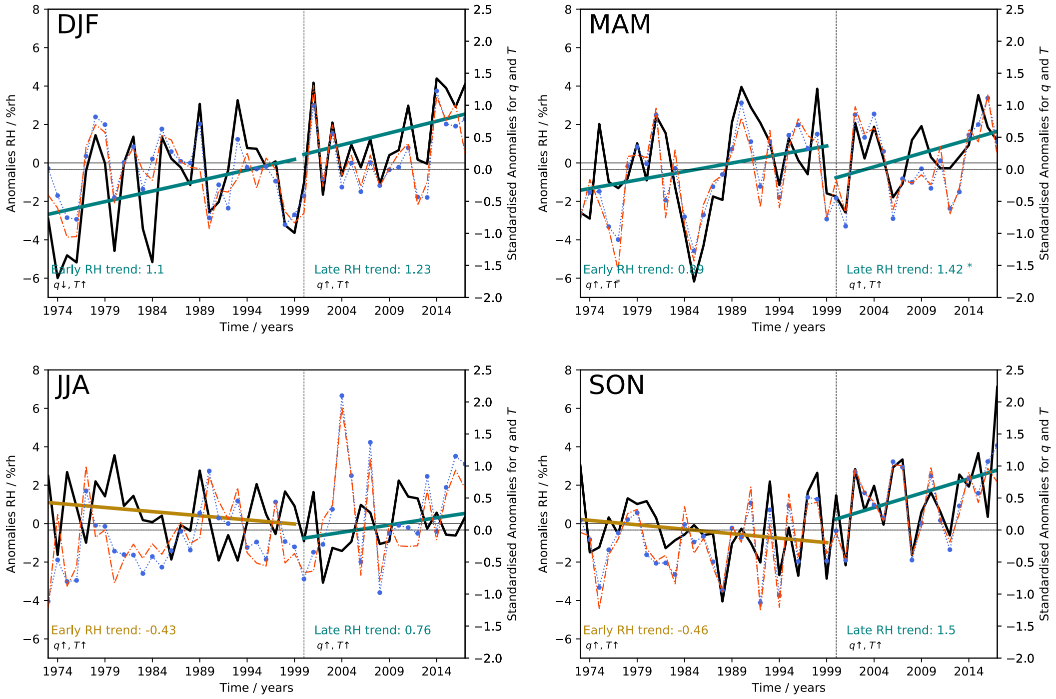

Figure 3.22: As for Fig. 3.2, for western Alaska.

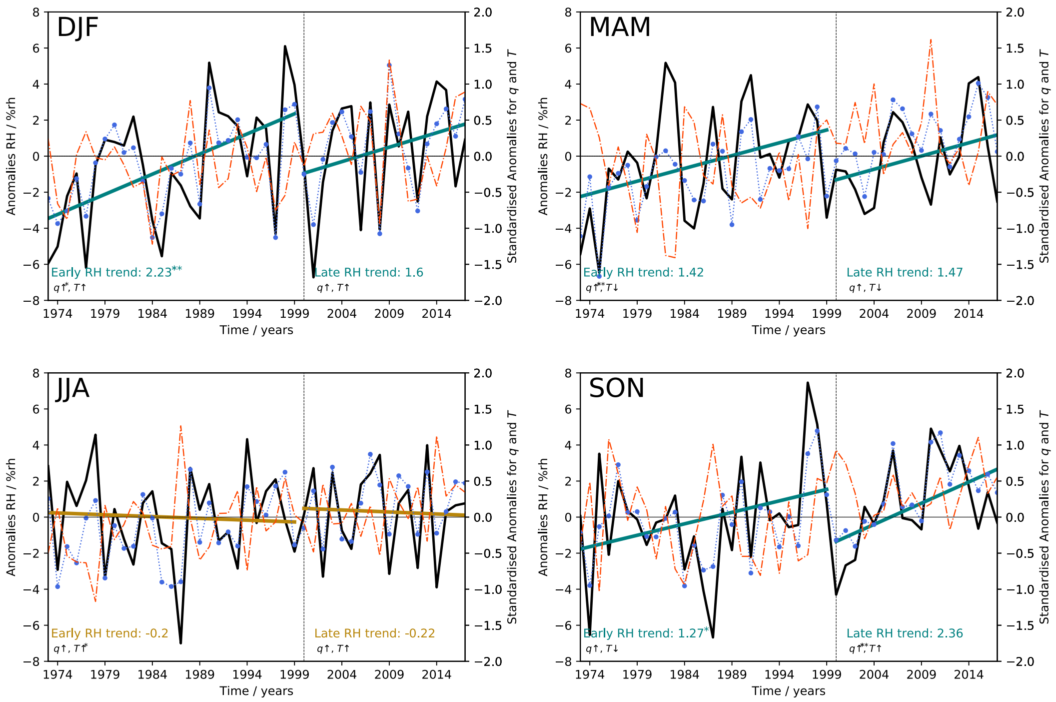

Figure 3.23: As for Fig. 3.2, for northwestern India.

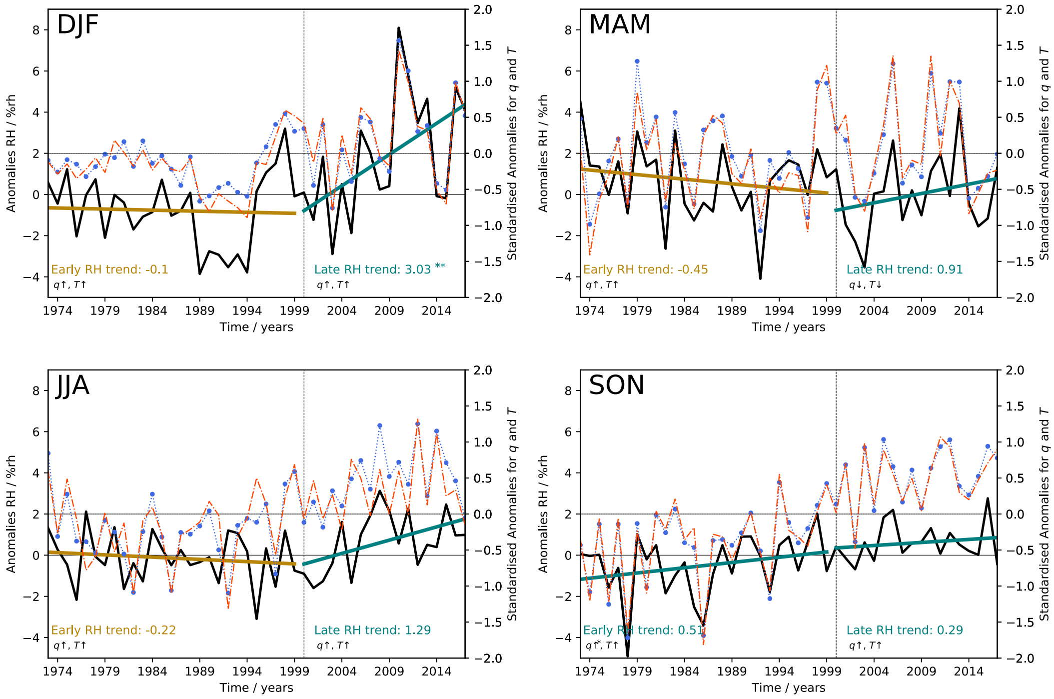

Figure 3.24: As for Fig. 3.2, for eastern Canada.

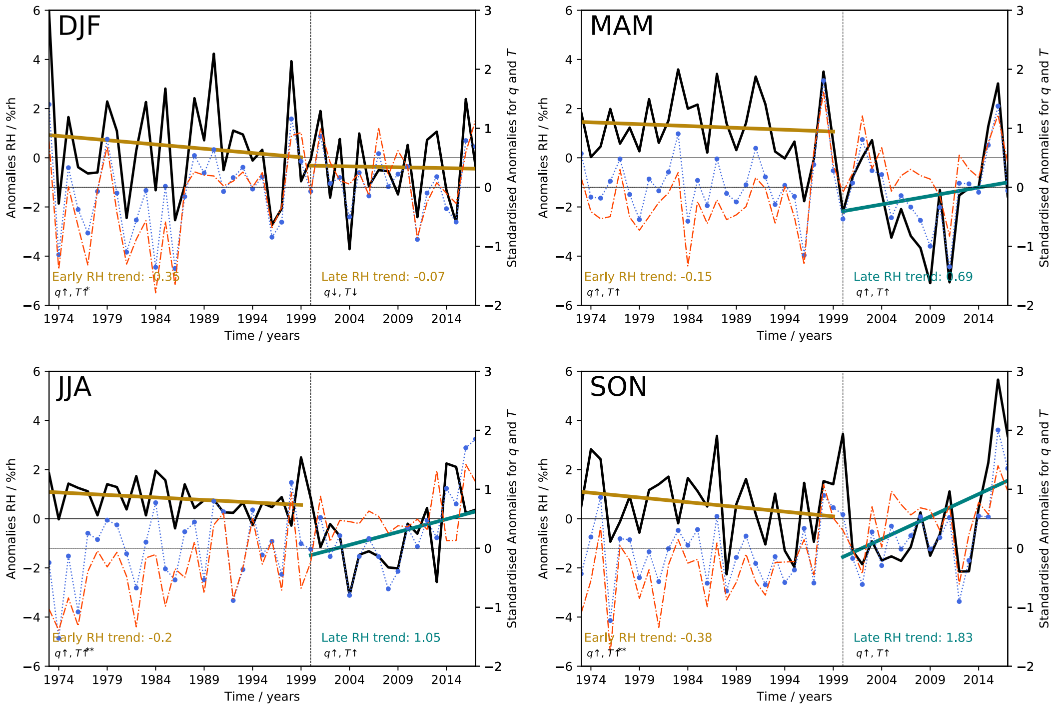

Figure 3.25: As for Fig. 3.2, for the East China Sea.

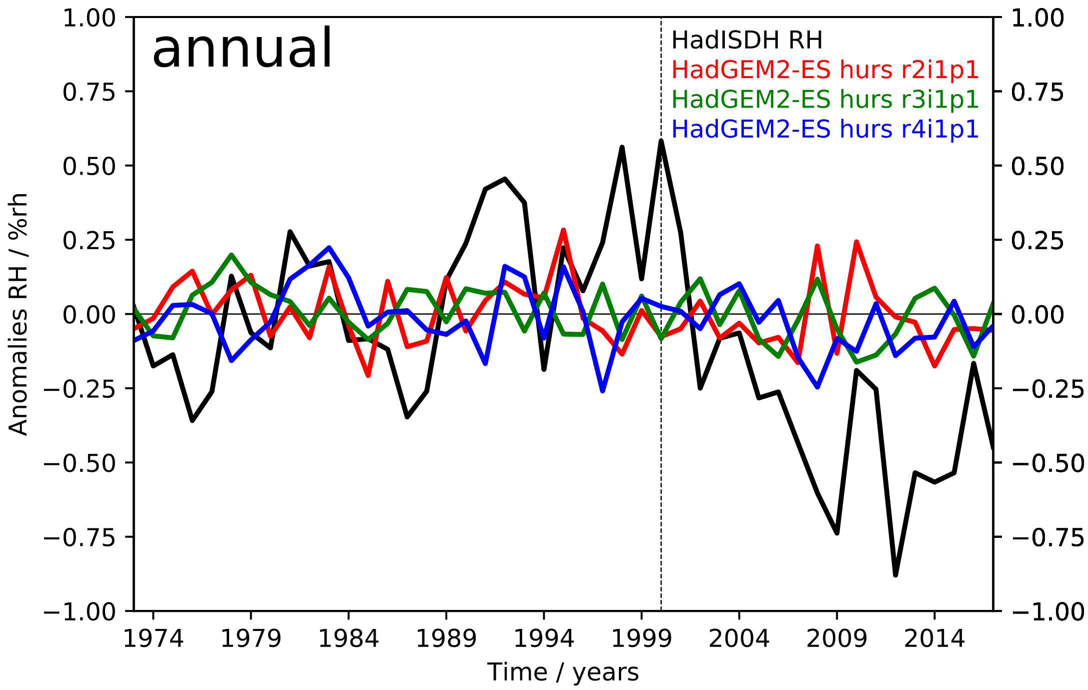

Figure 3.26: HadISDH and HadGEM2-ES *historical* + *historicalExt* RH global annual anomalies over land for the early and the late periods (for HadISDH: black; for HadGEM2-ES *r*2*i*1*p*1: red, *r*3*i*1*p*1: green, *r*4*i*1*p*1: blue), relative to a climatology over the 1981–2010 period.

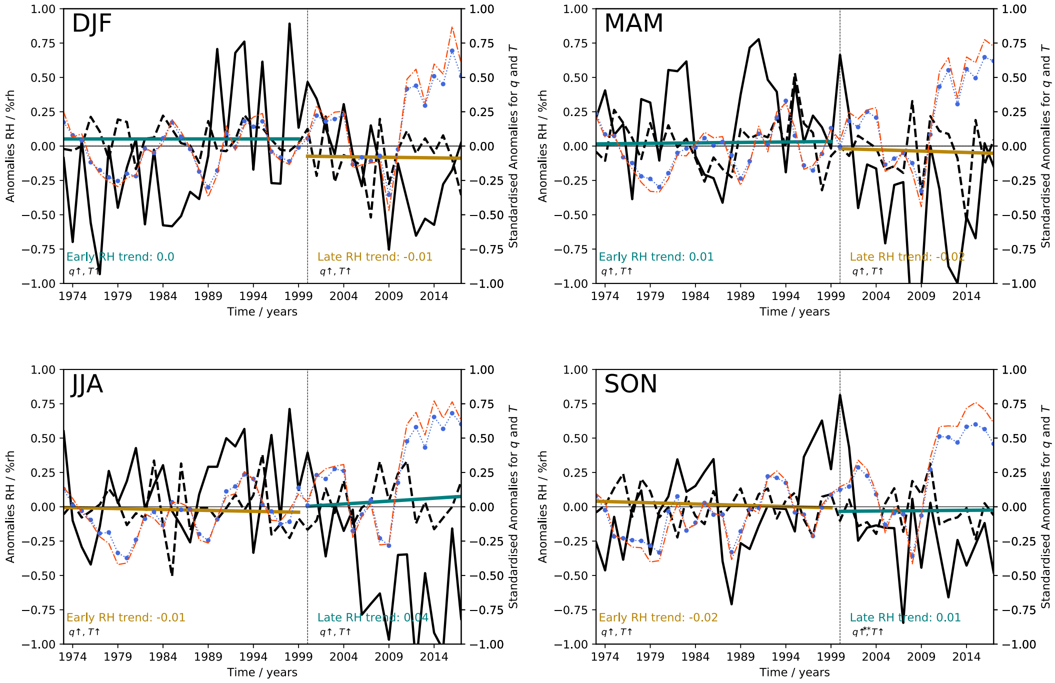

Figure 3.27: As for Fig. 3.2, for HadISDH RH anomalies (black, continuous line) and the HadGEM2-ES *historical* + *historicalExt* simulation run *r*2*i*1*p*1 RH anomalies (black, dashed line) and q and T.

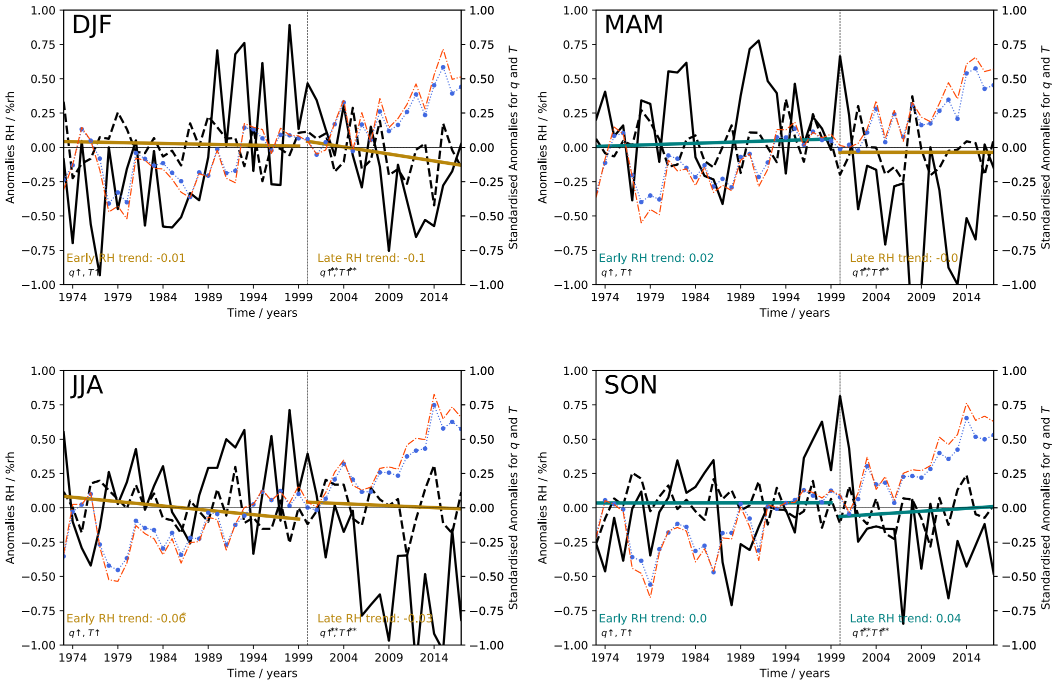

Figure 3.28: As for Fig. 3.27, for the HadGEM2-ES *historical* + *historicalExt* simulation run *r*3*i*1*p*1.

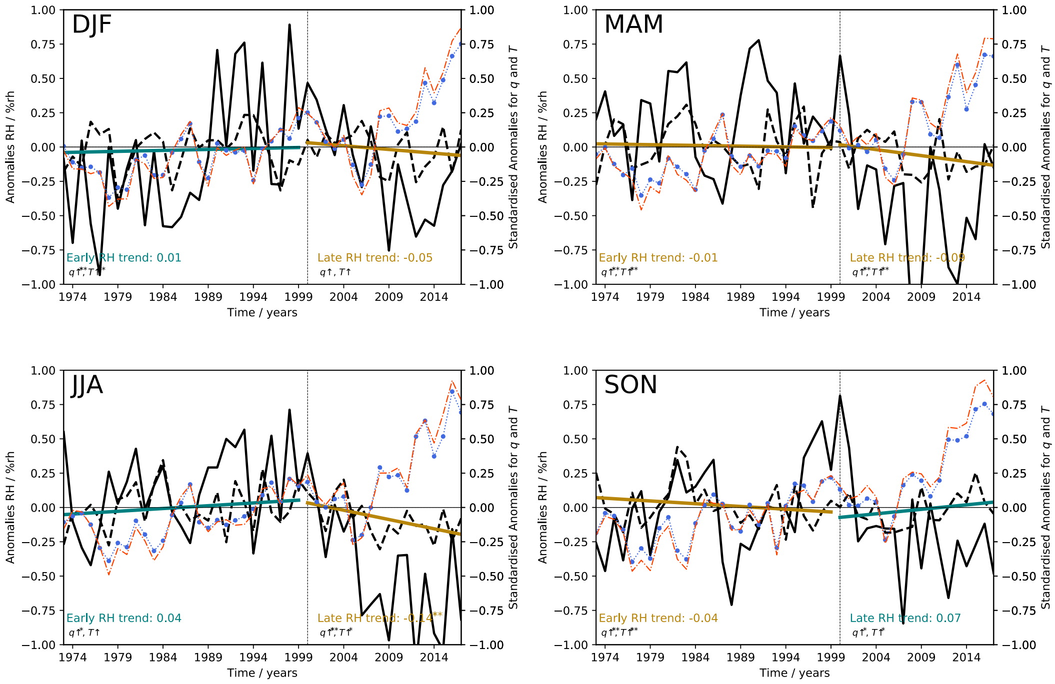

Figure 3.29: As for Fig. 3.27, for HadGEM2-ES *historical* + *historicalExt* simulation run *r4i1p1*.

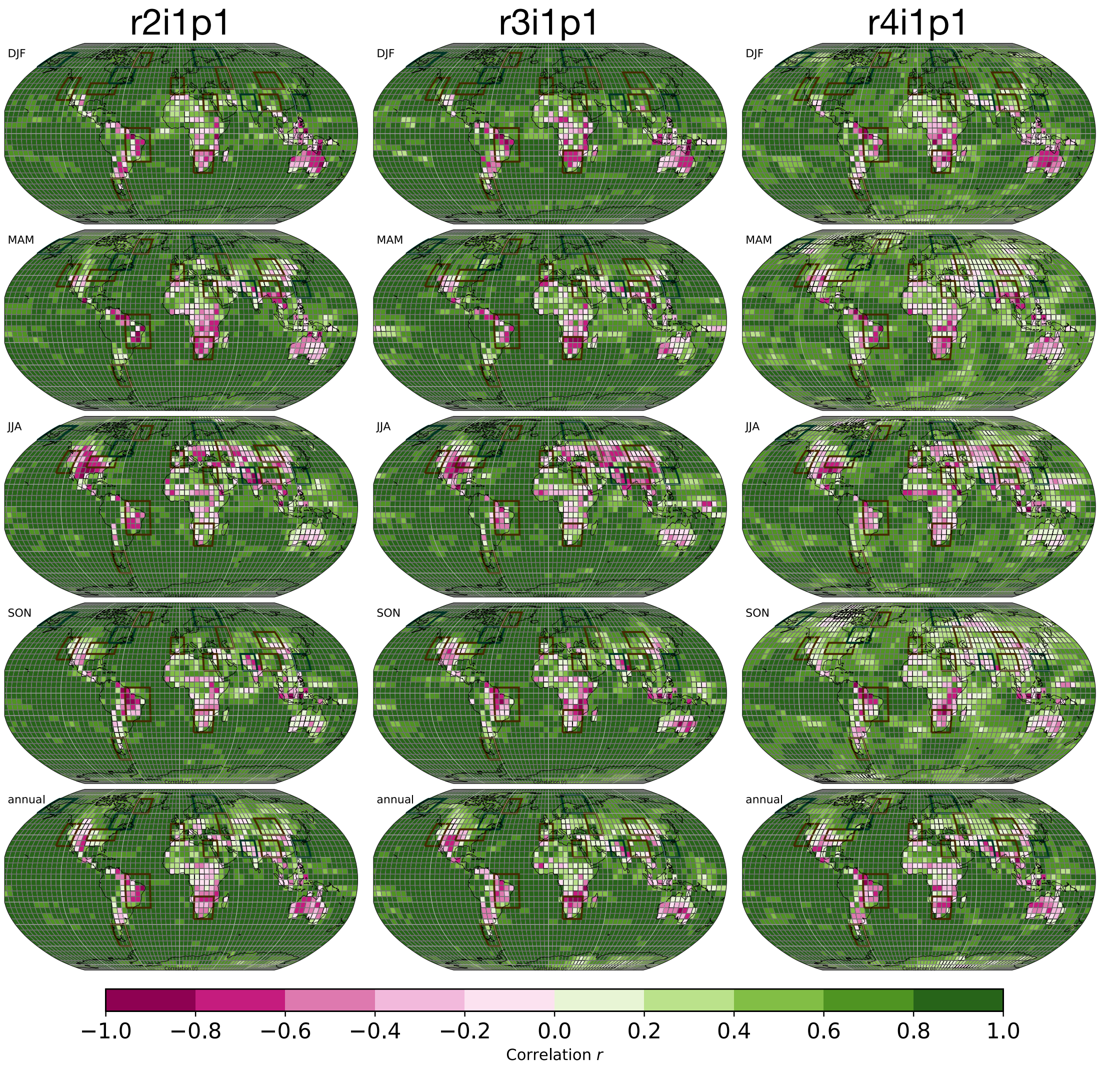

Figure 3.30: As for Fig. 3.4, for annual (bottom) and seasonal (upper four rows) HadGEM2-ES *historical* + *historicalExt* simulation runs $r2i1p1$ (left column), $r3i1p1$ (centre column) and $r4i1p1$ (right column) correlations between T and q in the full period.

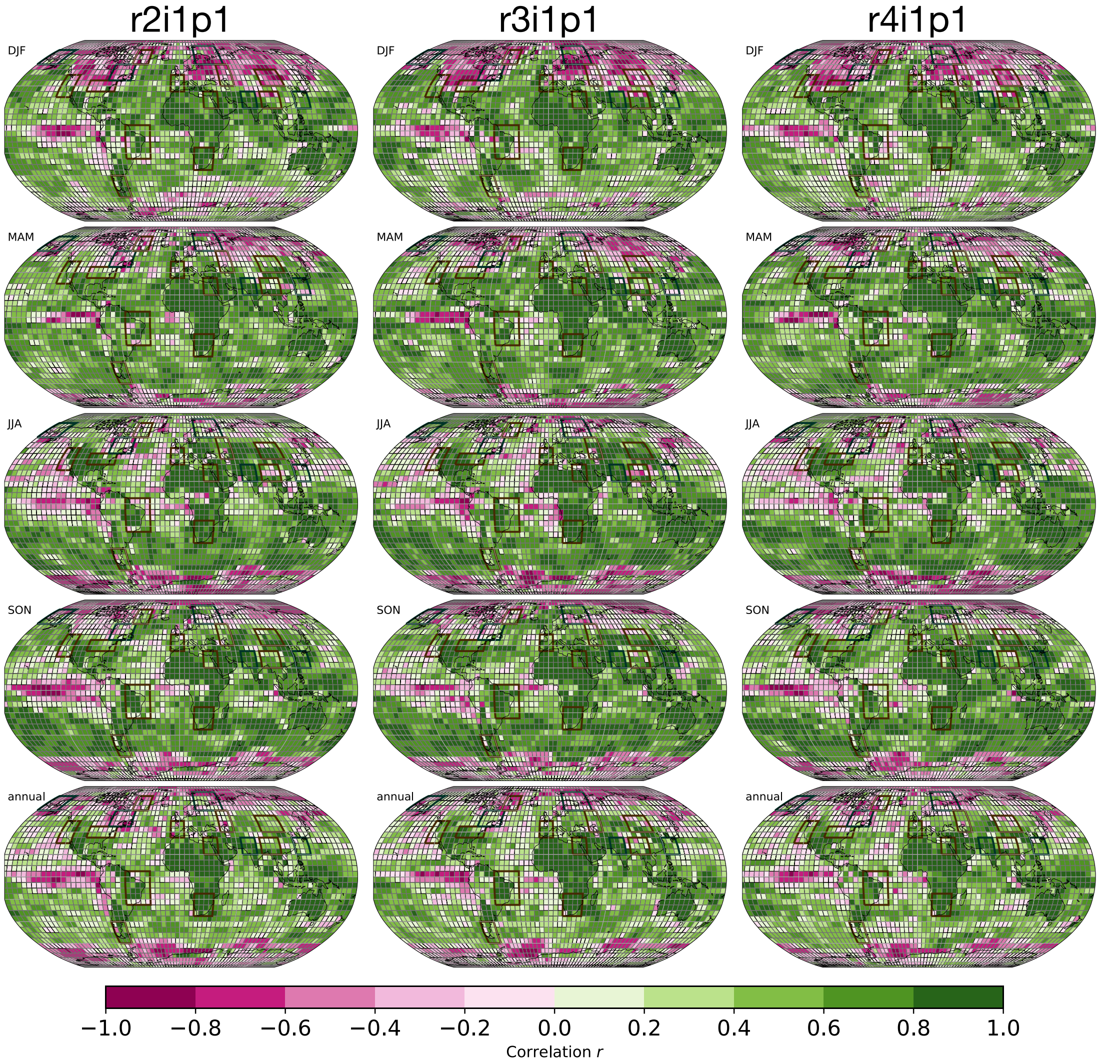

Figure 3.31: As for Fig. 3.30, for correlations between q and RH in the full period.

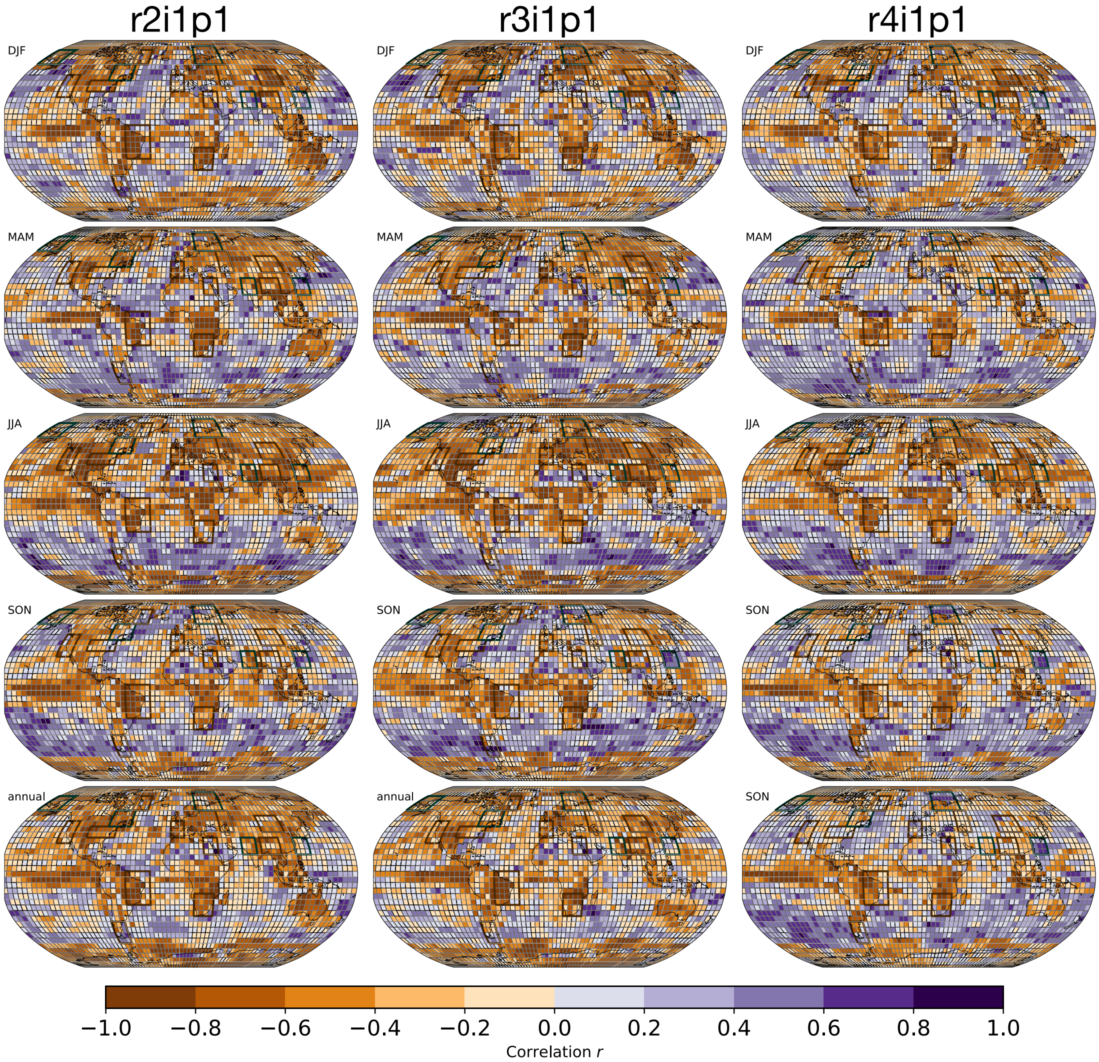

Figure 3.32: As for Fig. 3.30, for correlations between T and RH in the full period.

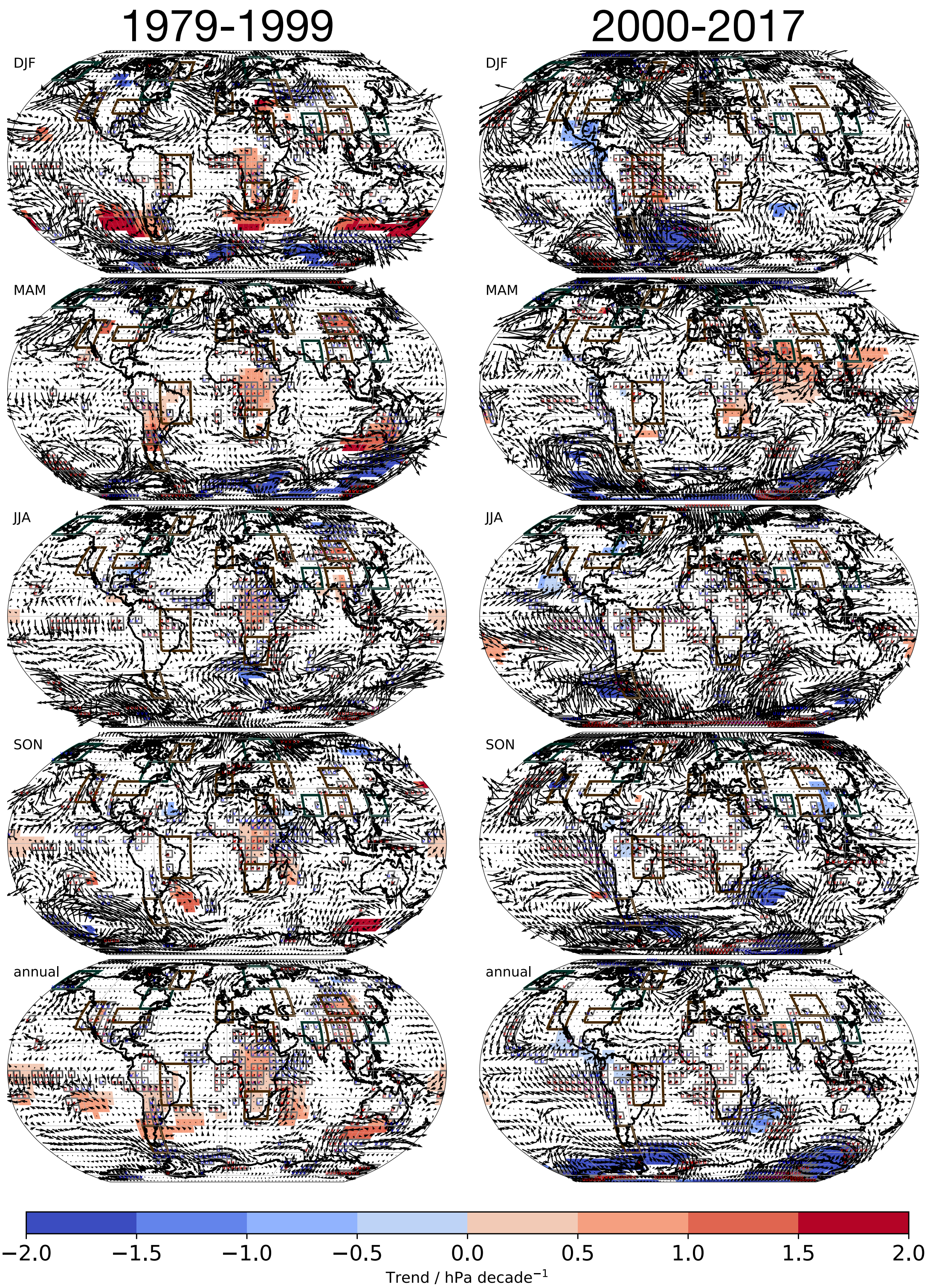

Figure 4.1: Annual (bottom) and seasonal (upper four rows) ERA-Interim quivered u10, v10 trends (arrows) and SLP trends (colour) for the early (1979–1999, left column) and the late periods (2000–2017, right column) relative to a climatology over the 1981-2010 period. Grid boxes of very significant ($p < 0.05$) positive (negative) u10 and v10 trends separately are stated in blue (red) letters 'u' and 'v', respectively. Only grid boxes of very significant ($p < 0.05$) SLP trends are coloured. Regions with a strong average trend in RH in the late period are framed in ochre (negative trends) and turquoise (positive trends). White space represents either missing data or ocean.

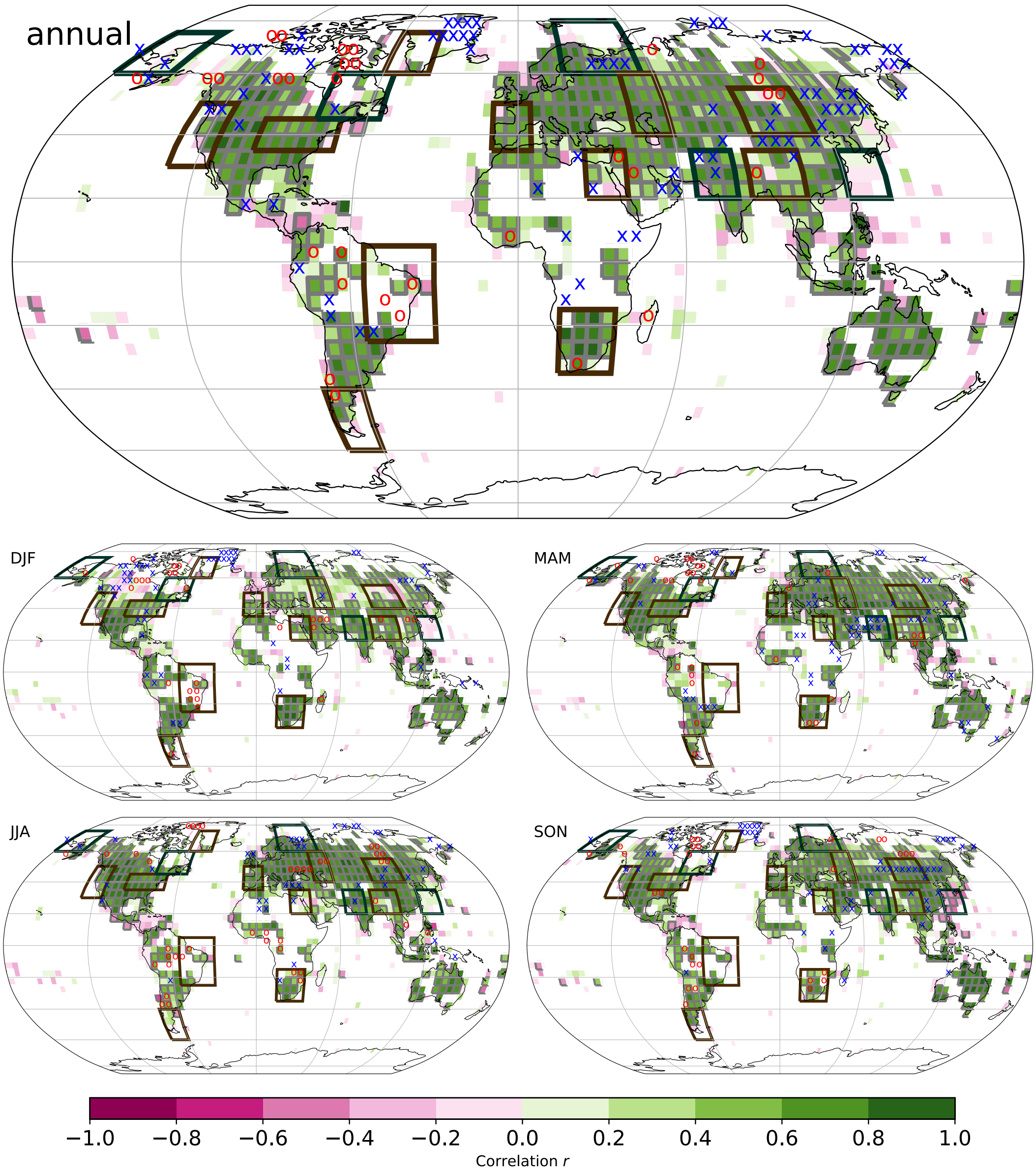

Figure 4.2: Annual and seasonal correlations between detrended GPCC precipitation and HadISDH RH anomalies over land in the late period, relative to a climatology over the 1981-2010 period. Grid boxes of very significant trends ($p < 0.05$) are framed in grey. Grid boxes of significant ($p < 0.1$) correlations are framed in grey; significantly positive (negative) trends in precipitation relative to the climatology over the 1981–2010 period show a blue ‘x’ (red ‘o’).

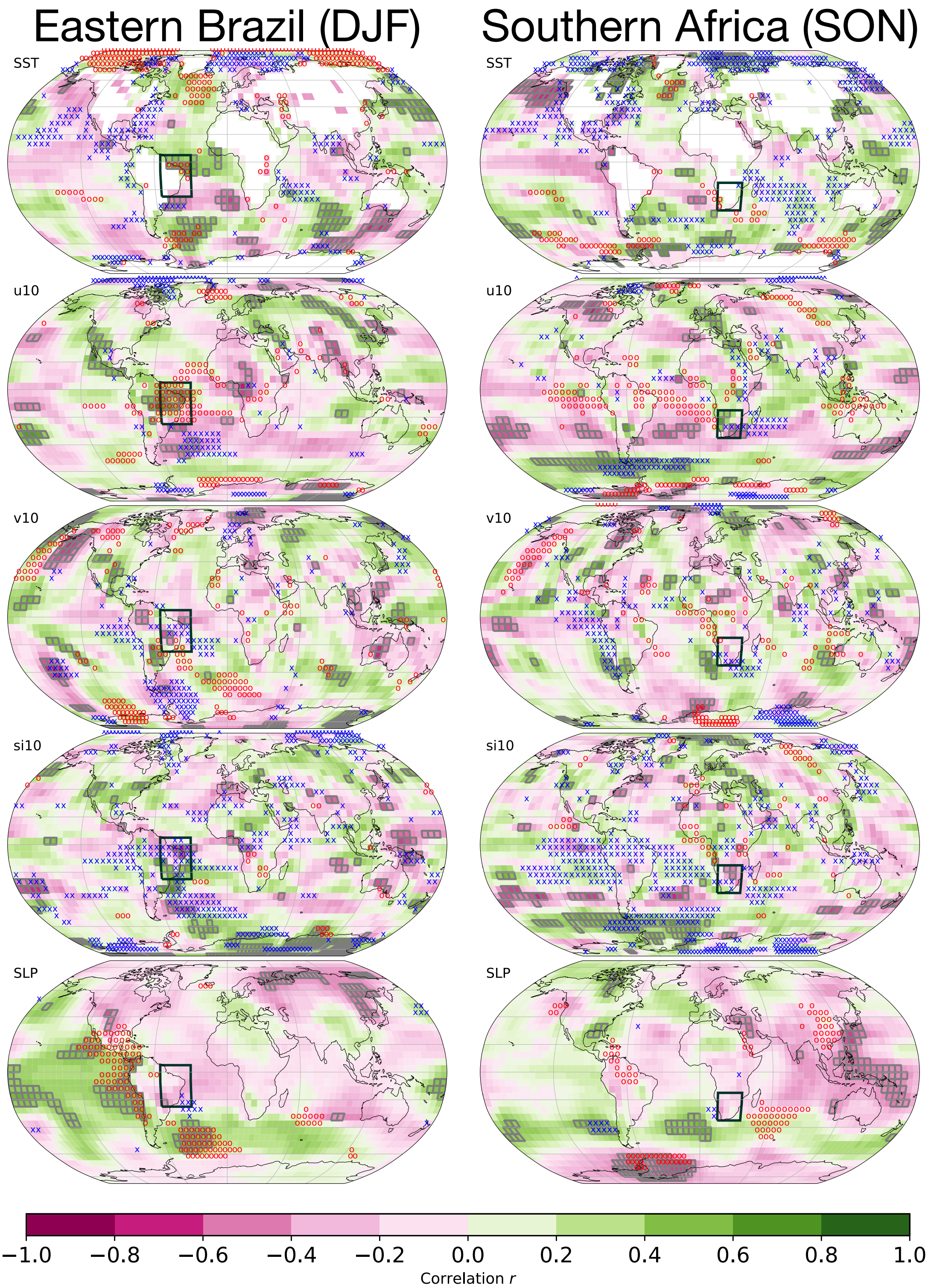

Figure 4.3: Correlations between anomalies of ERA-Interim SST, 10 m wind vectors in u and v direction, wind speed and SLP (top to bottom) and regional GPCC precipitation over eastern Brazil (DJF; left column) and southern Africa (SON; right column) for the late period (2000–2017). Grid boxes of very significant ($p < 0.05$) correlations are framed in grey; significantly positive (negative) trends in primary physical variables relative to the climatology over the 1981-2010 period show a blue 'x' (red 'o').

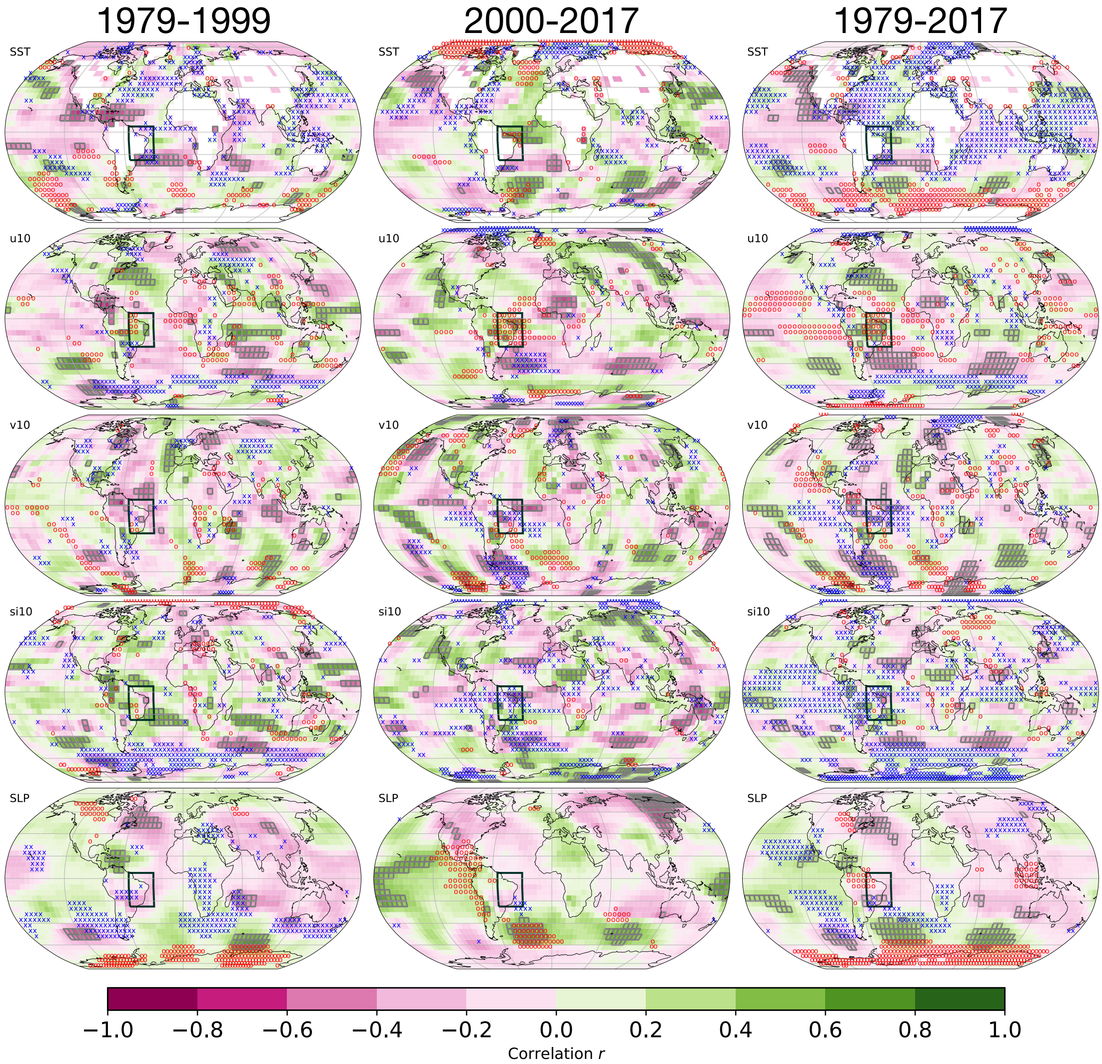

Figure 4.4: Correlations between ERA-Interim anomalies of SST, 10 m wind vectors in u and v direction, wind speed and SLP (top to bottom) and regional HadISDH RH over eastern Brazil (DJF) for the early period (1979–1999, left column), the late period (2000–2017, centre column) and the full period (right column). Grid boxes of very significant ($p < 0.05$) correlations are framed in grey; significantly ($p < 0.1$) positive (negative) trends in primary physical variables relative to the climatology over the 1981–2010 period show a blue 'x' (red 'o').

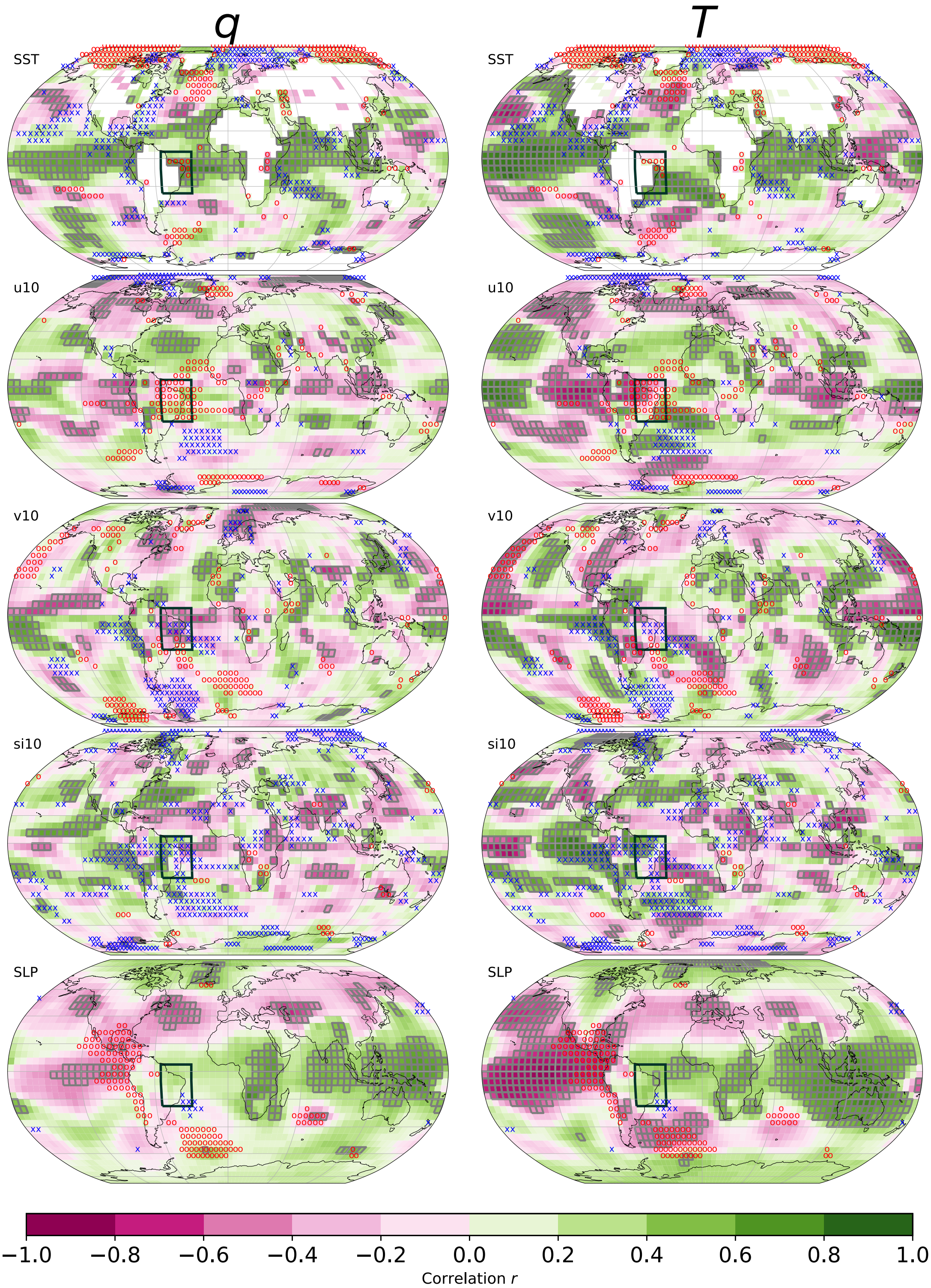

Figure 4.5: Correlations between ERA-Interim anomalies of SST, 10 m wind vectors in u and v direction, wind speed and SLP (top to bottom) and regional HadISDH q (left) and T (right) over eastern Brazil (DJF) for the late period (2000–2017). Grid boxes of very significant ($p < 0.05$) correlations are framed in grey, significantly positive (negative) trends in primary physical variables relative to the climatology over the 1981-2010 period show a blue ‘x’ (red ‘o’).

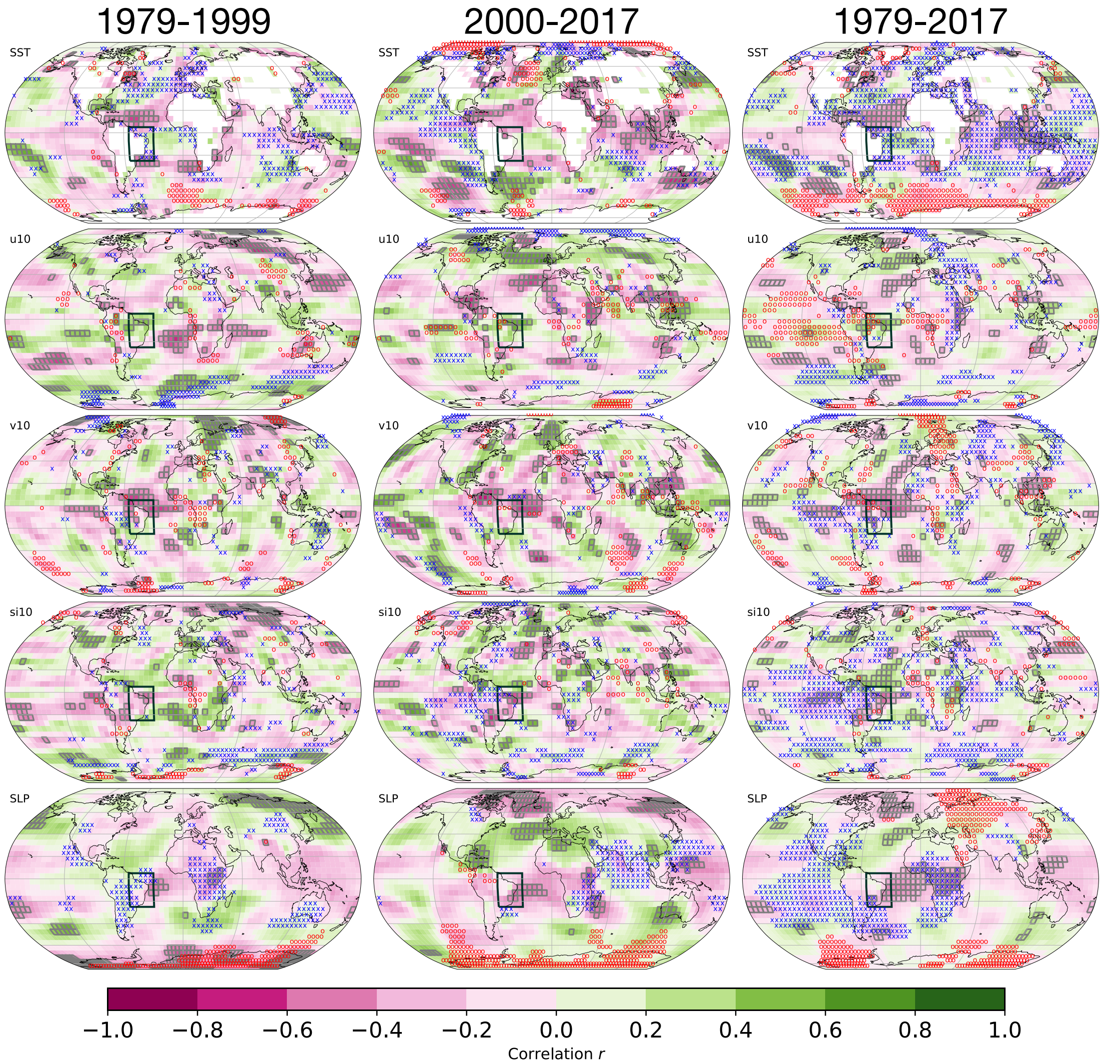

Figure 4.6: As for Fig. 4.4, for eastern Brazil (MAM).

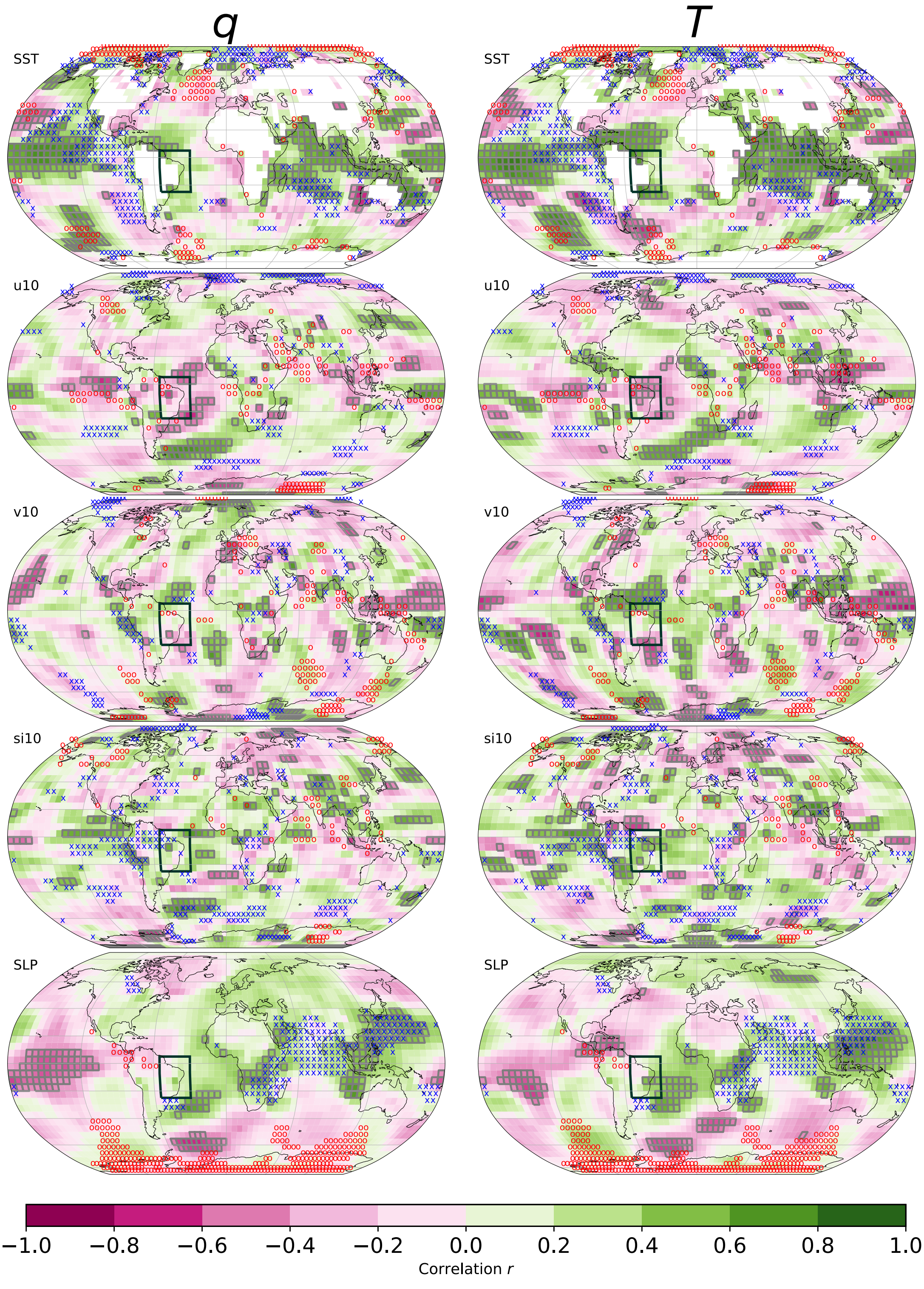

Figure 4.7: As for Fig. 4.5, for eastern Brazil (MAM).

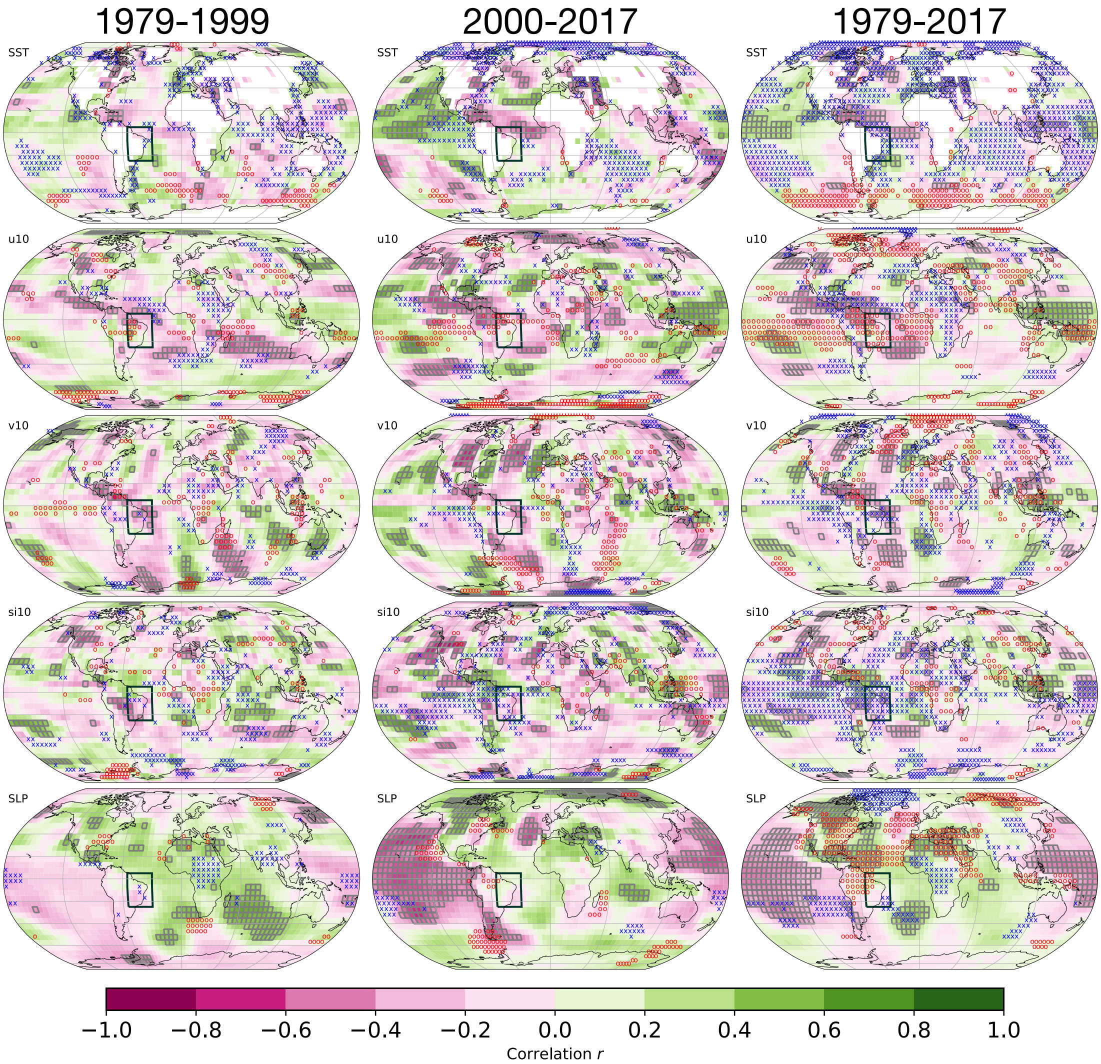

Figure 4.8: As for Fig. 4.4, for eastern Brazil (JJA).

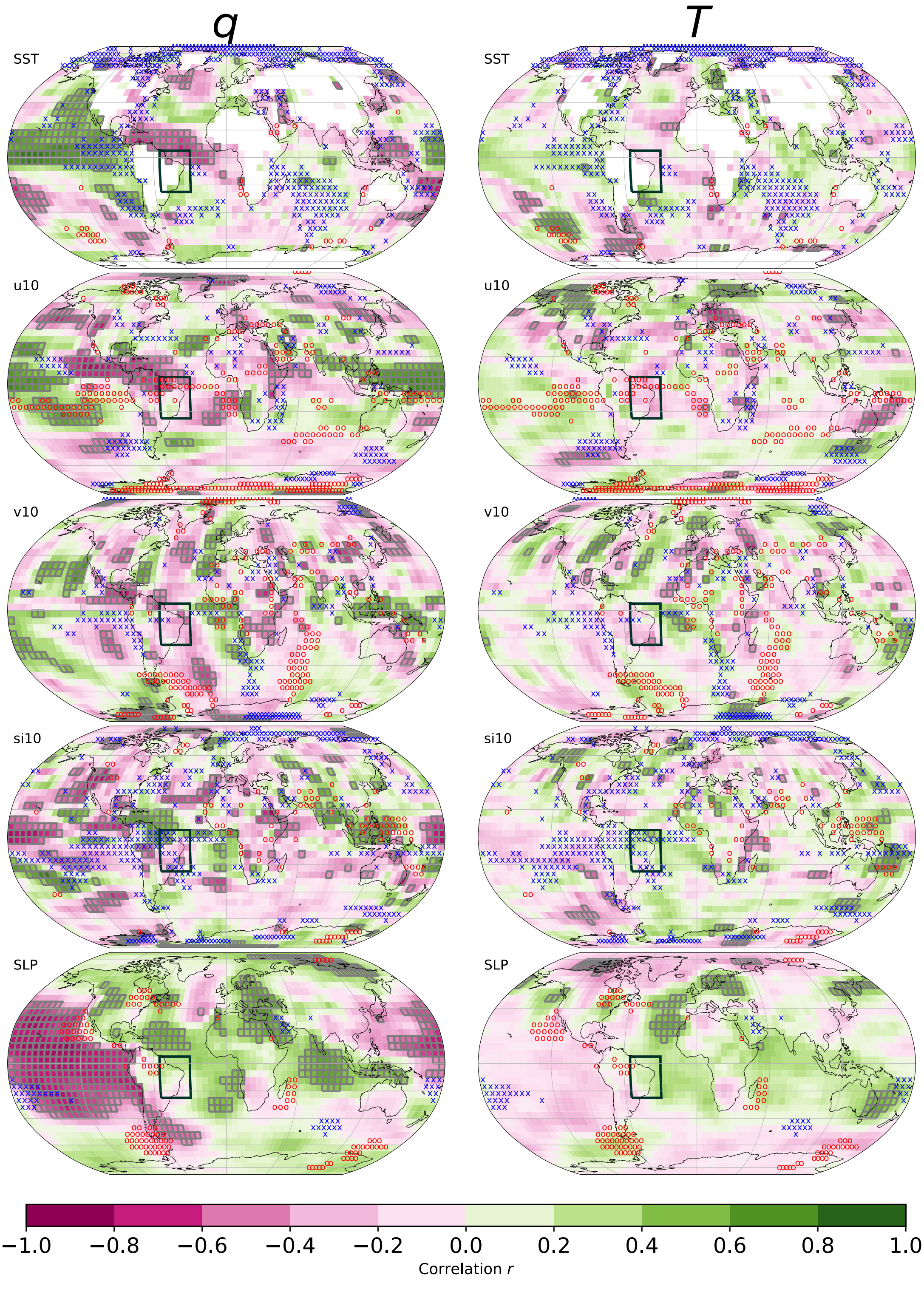

Figure 4.9: As for Fig. 4.5, for eastern Brazil (JJA).

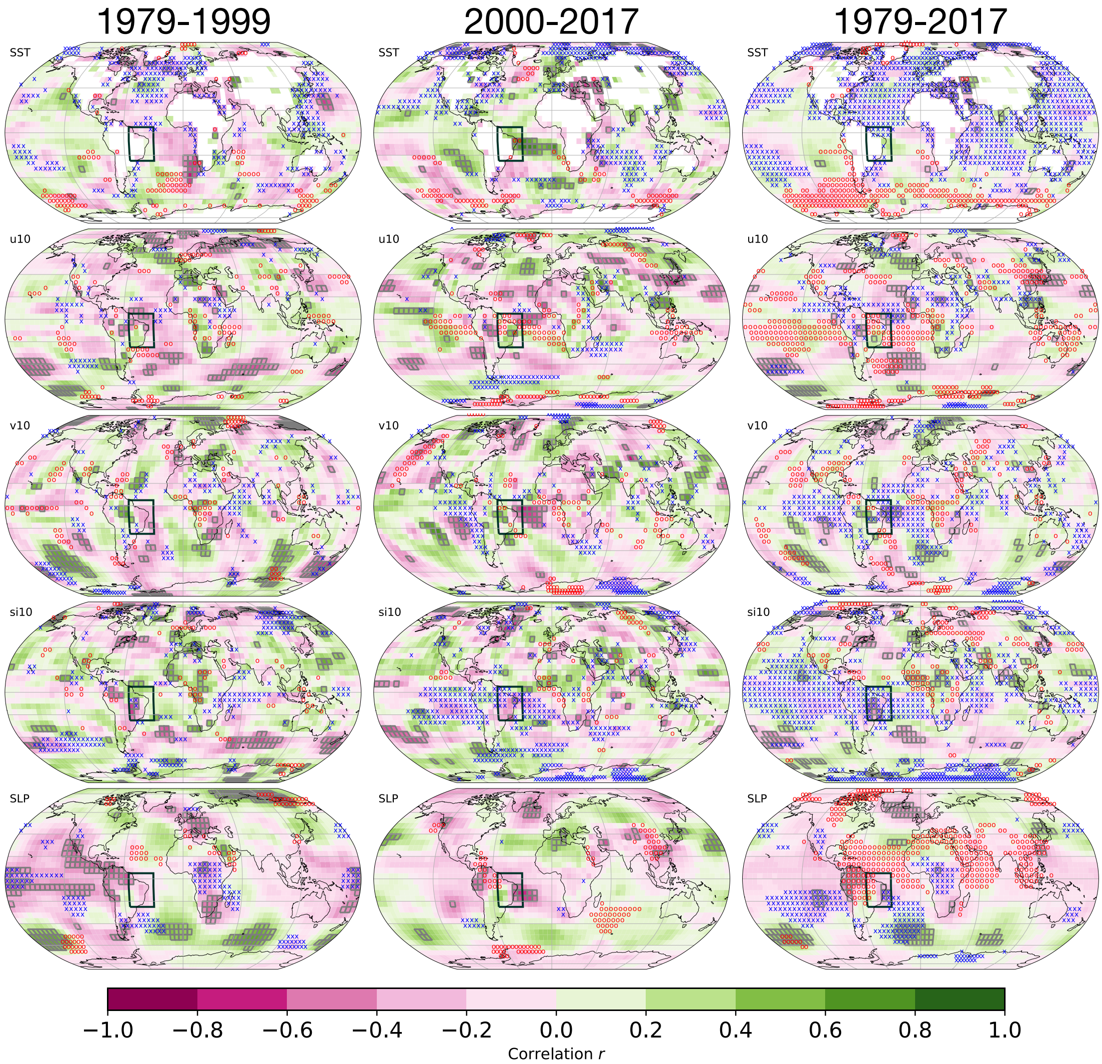

Figure 4.10: As for Fig. 4.4, for eastern Brazil (SON).

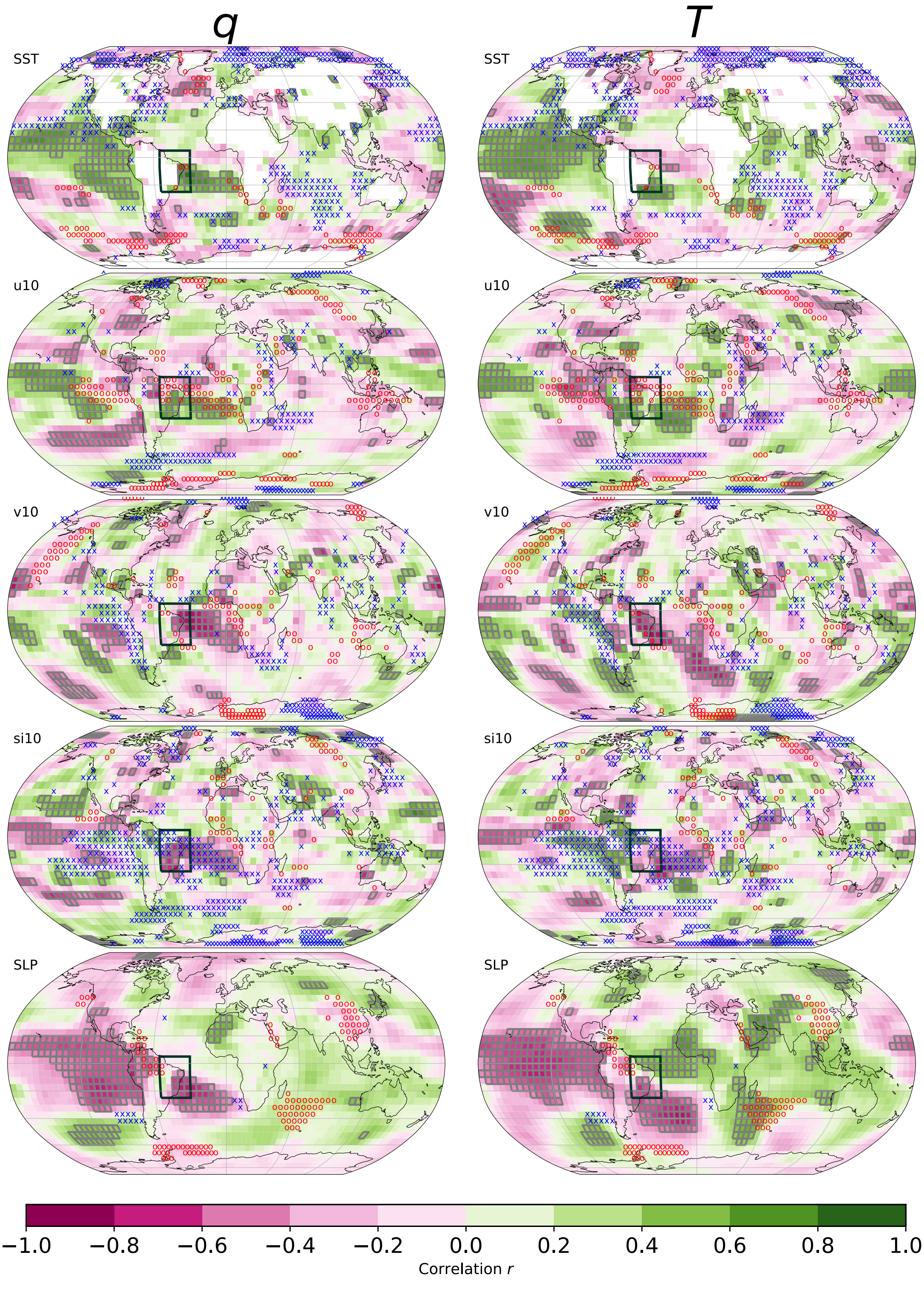

Figure 4.11: As for Fig. 4.5, for eastern Brazil (SON).

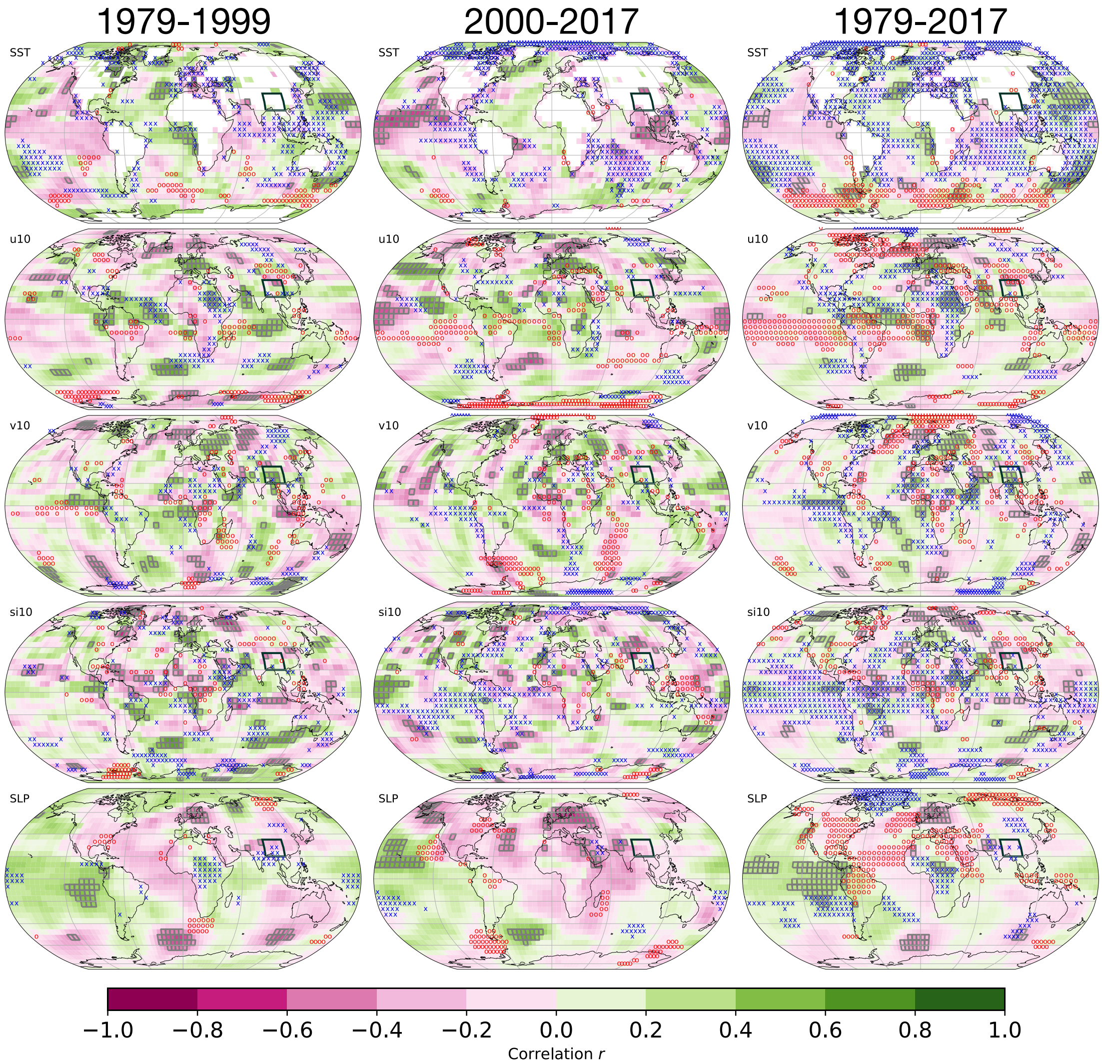

Figure 4.12: As for Fig. 4.4, for Tibet (JJA).

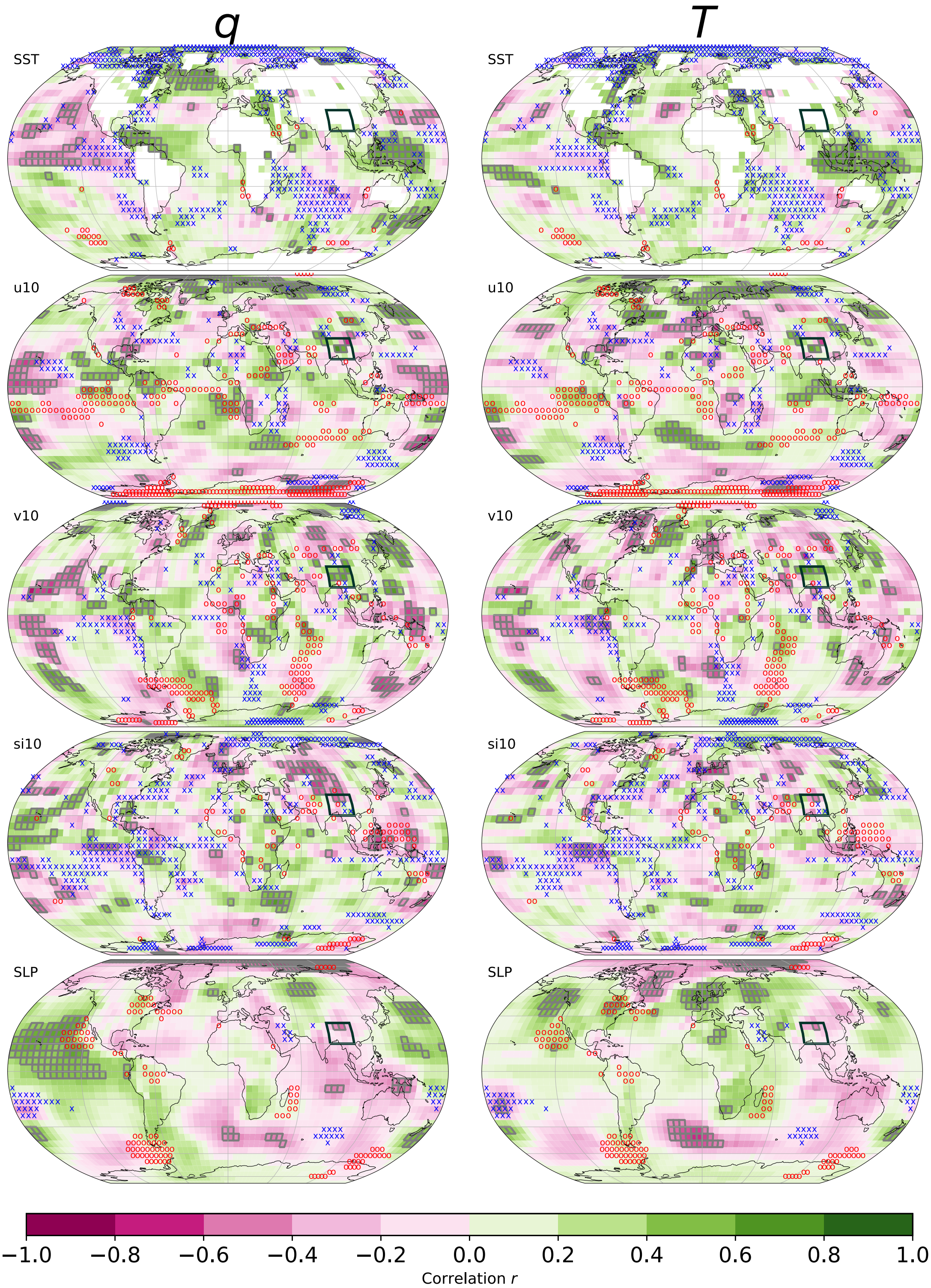

Figure 4.13: As for Fig. 4.5, for Tibet (JJA).

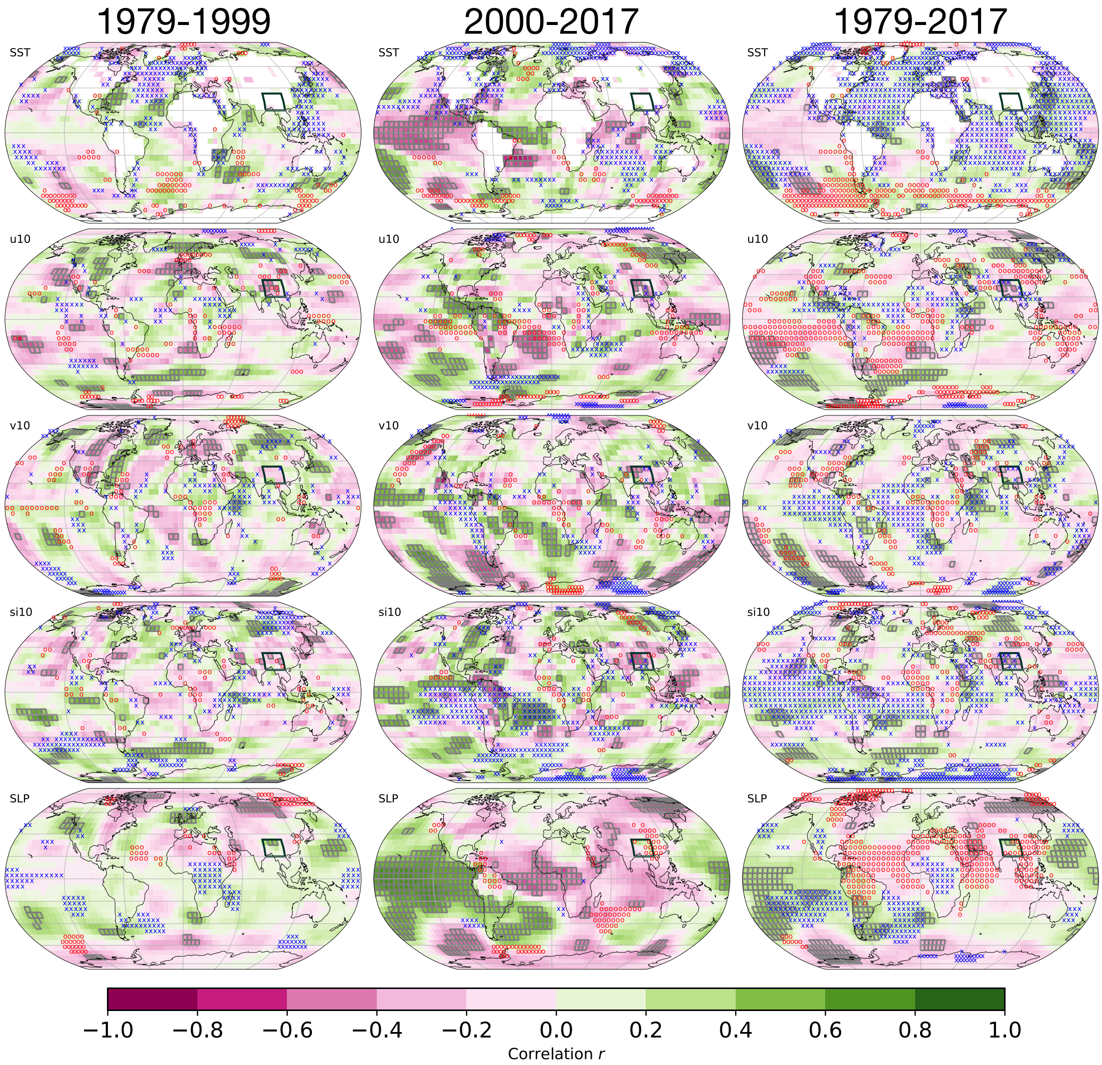

Figure 4.14: As for Fig. 4.4, for Tibet (SON).

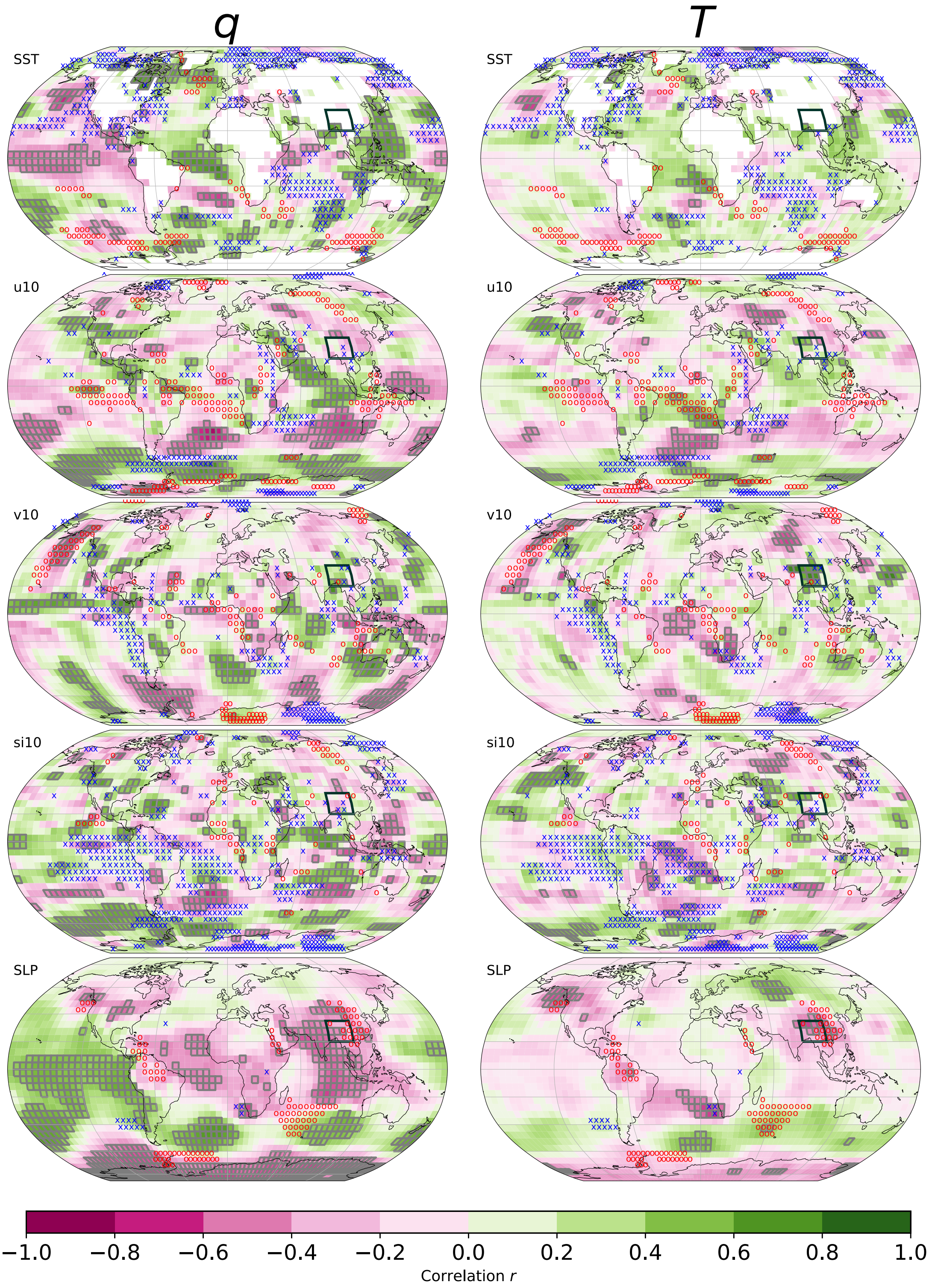

Figure 4.15: As for Fig. 4.5, for Tibet (SON).

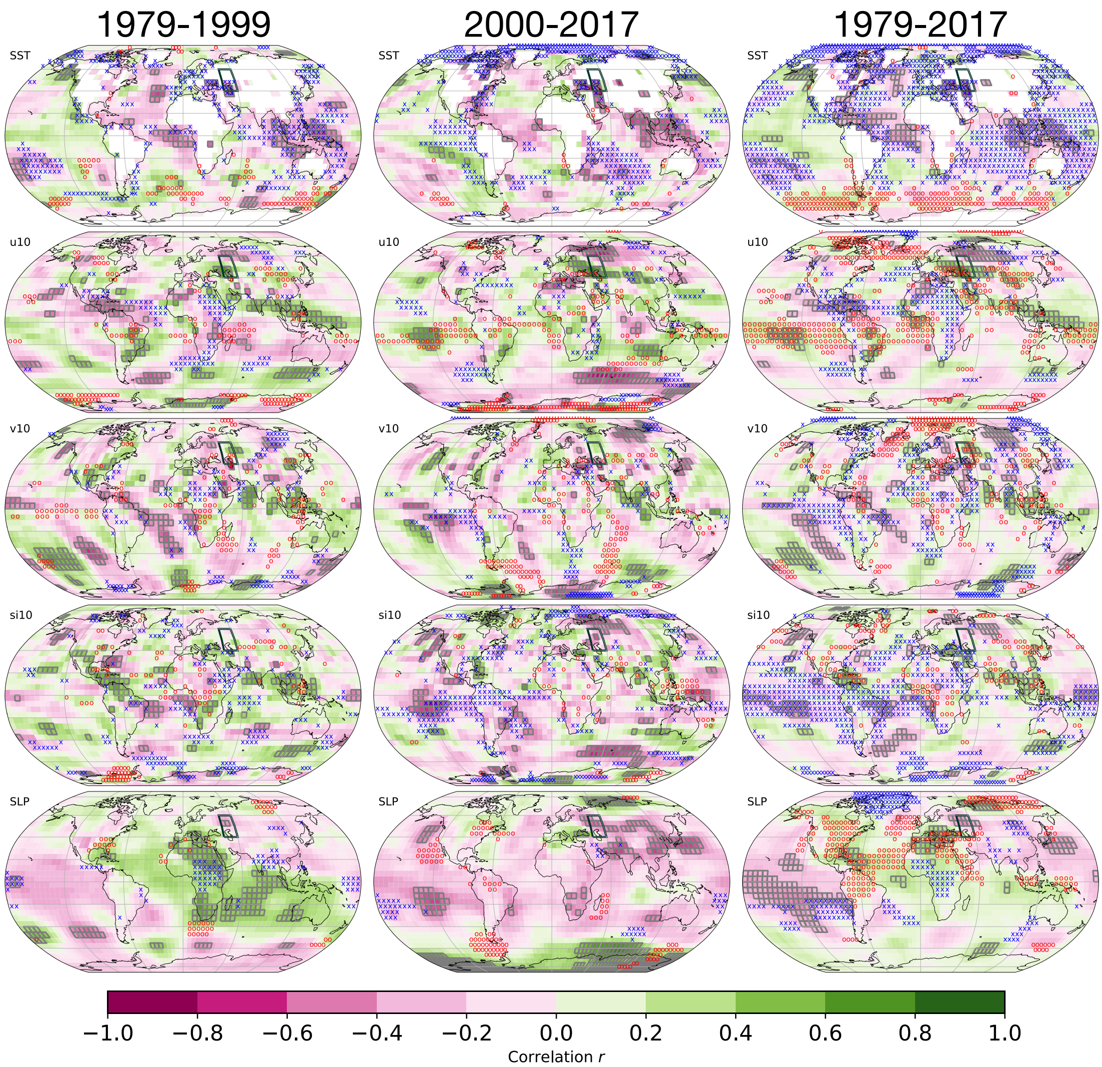

Figure 4.16: As for Fig. 4.4, for the Caspian Sea region (JJA).

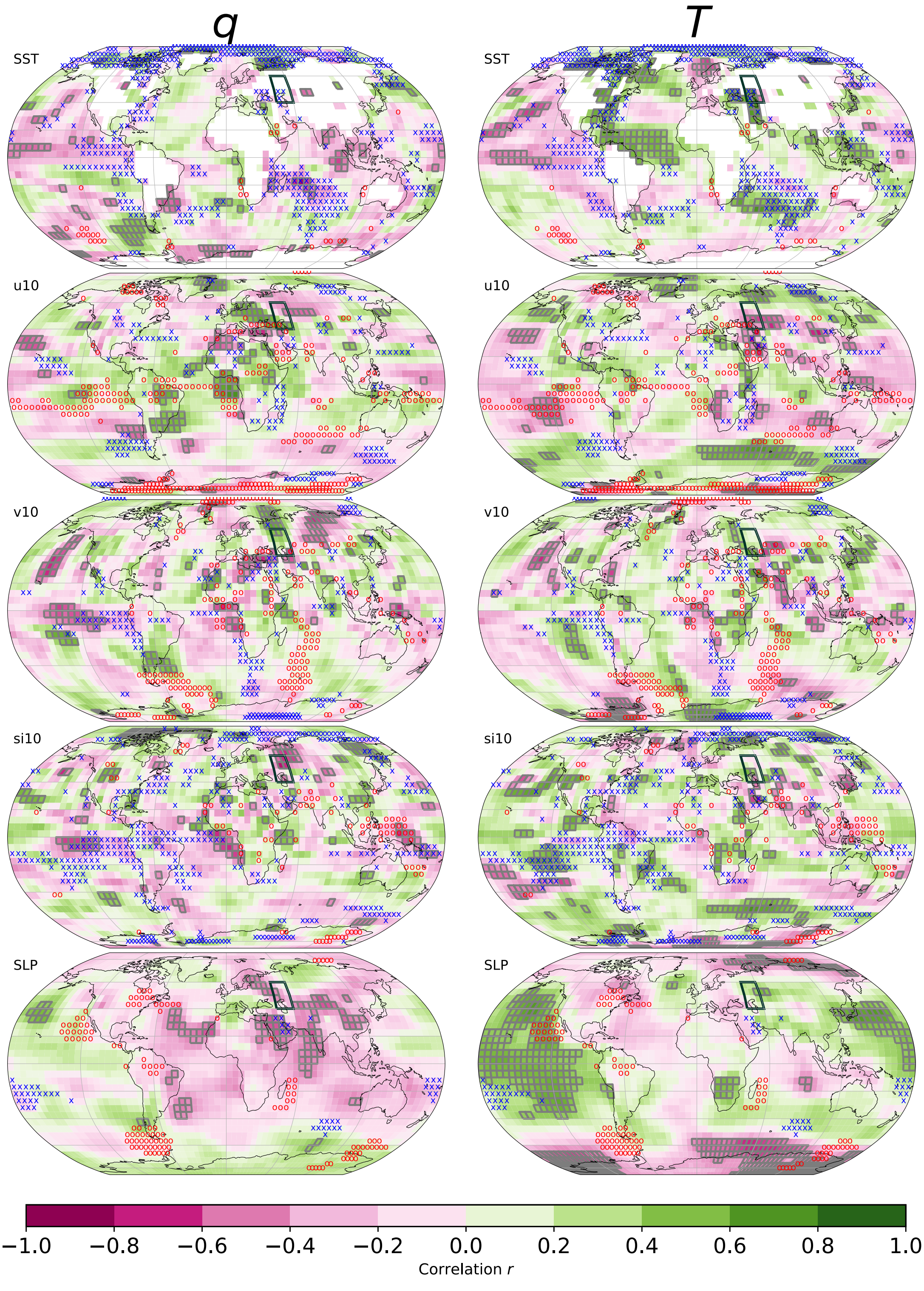

Figure 4.17: As for Fig. 4.5, for the Caspian Sea region (JJA).

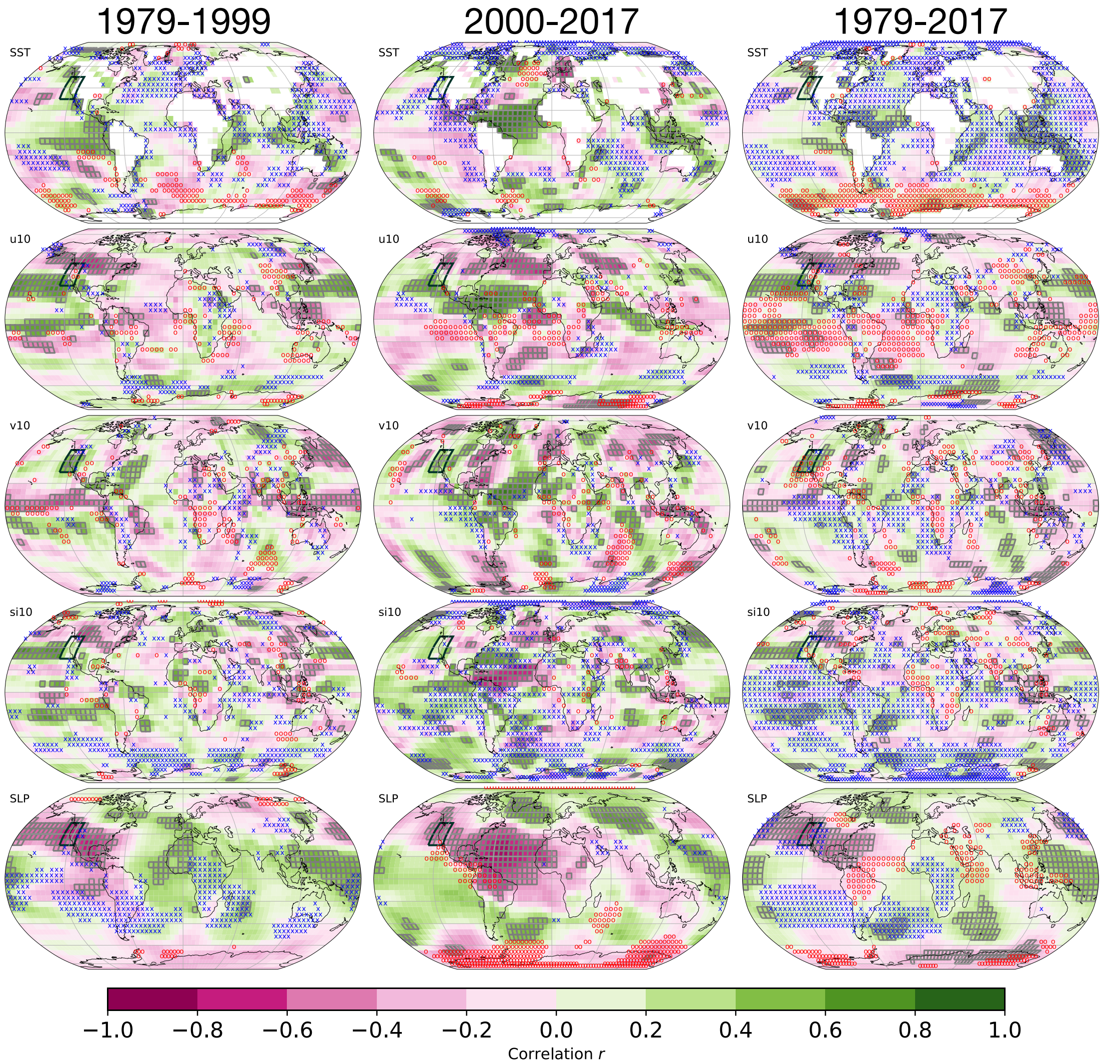

Figure 4.18: As for Fig. 4.4, for California (annual).

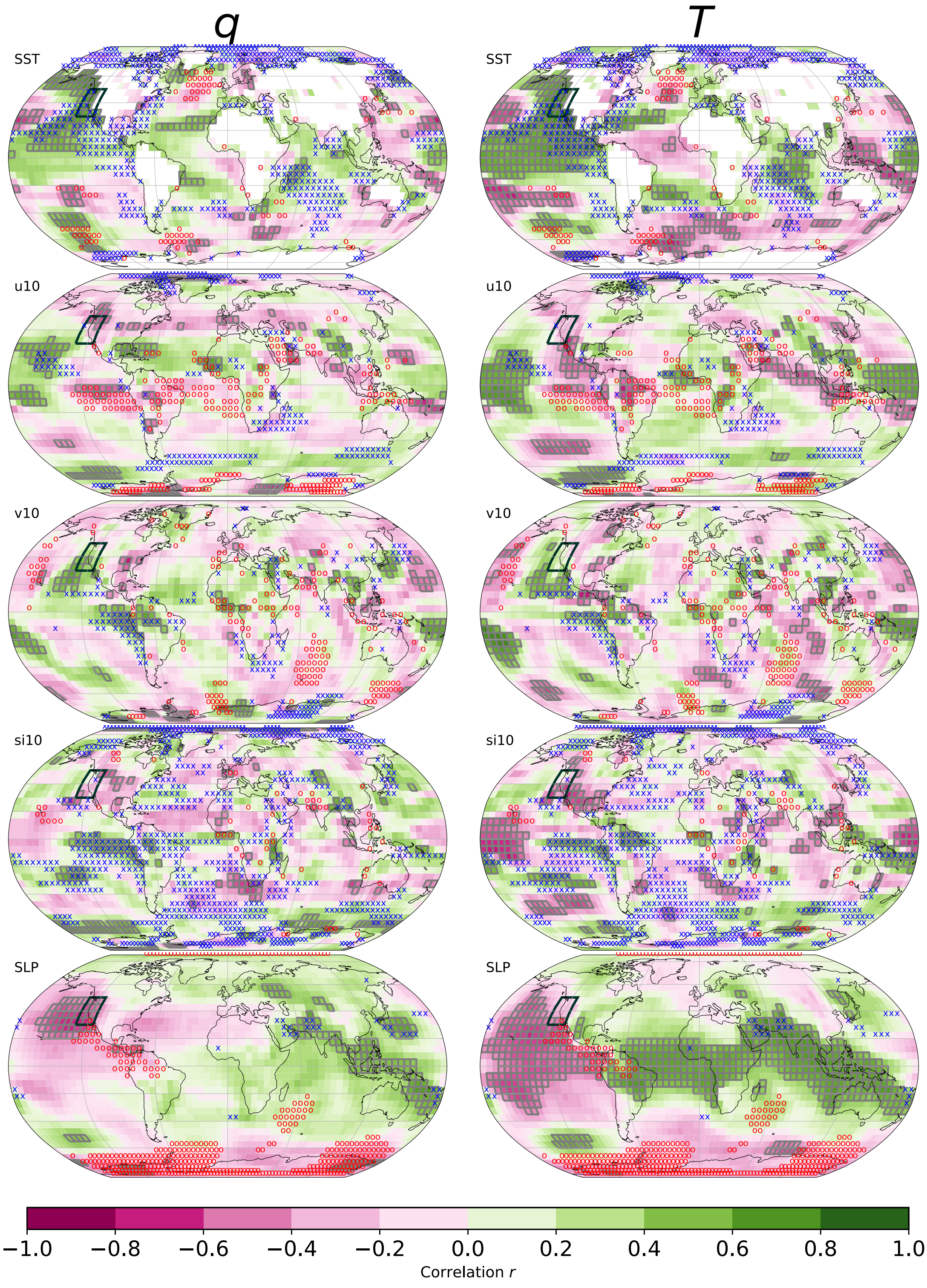

Figure 4.19: As for Fig. 4.5, for California (annual).

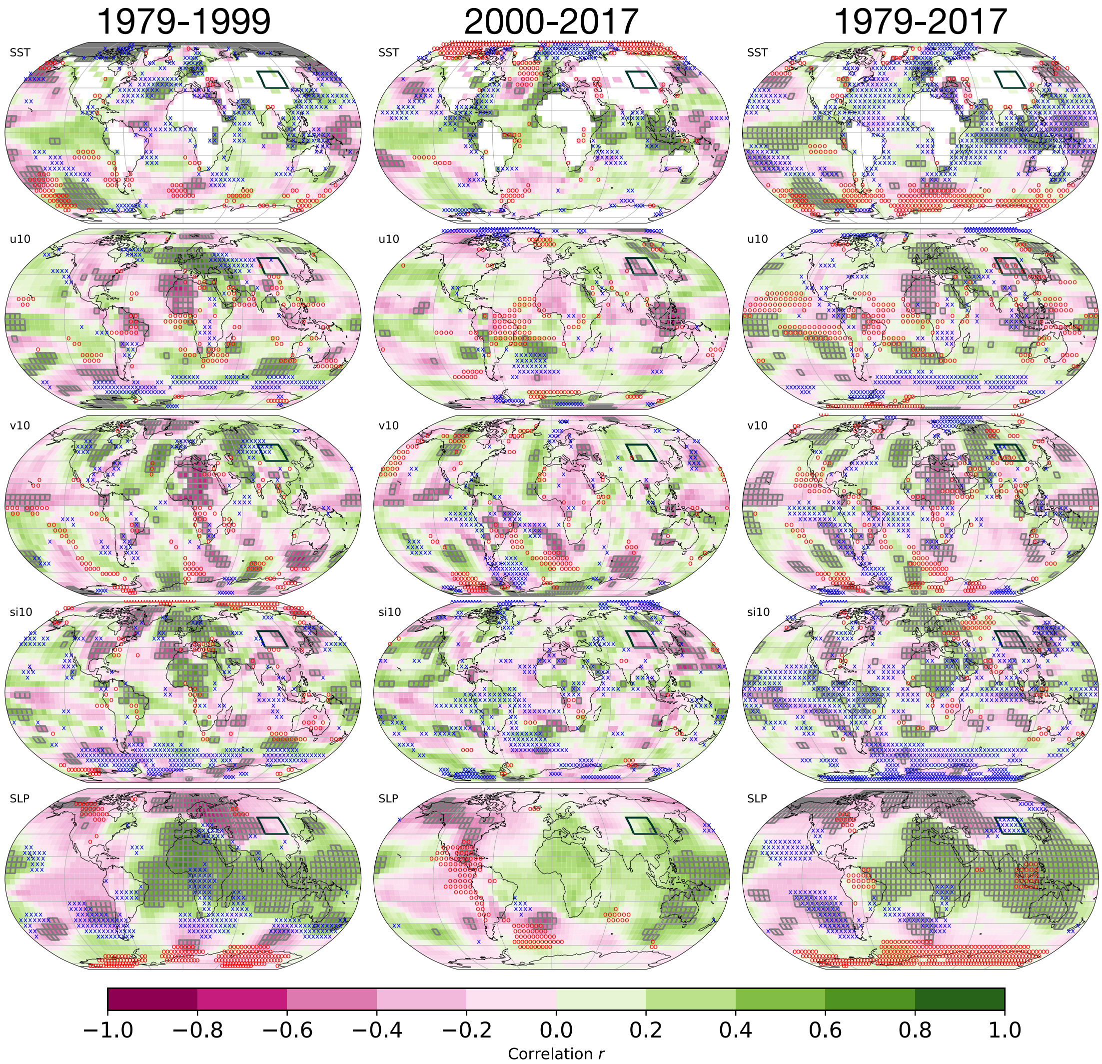

Figure 4.20: As for Fig. 4.4, for Mongolia (DJF).

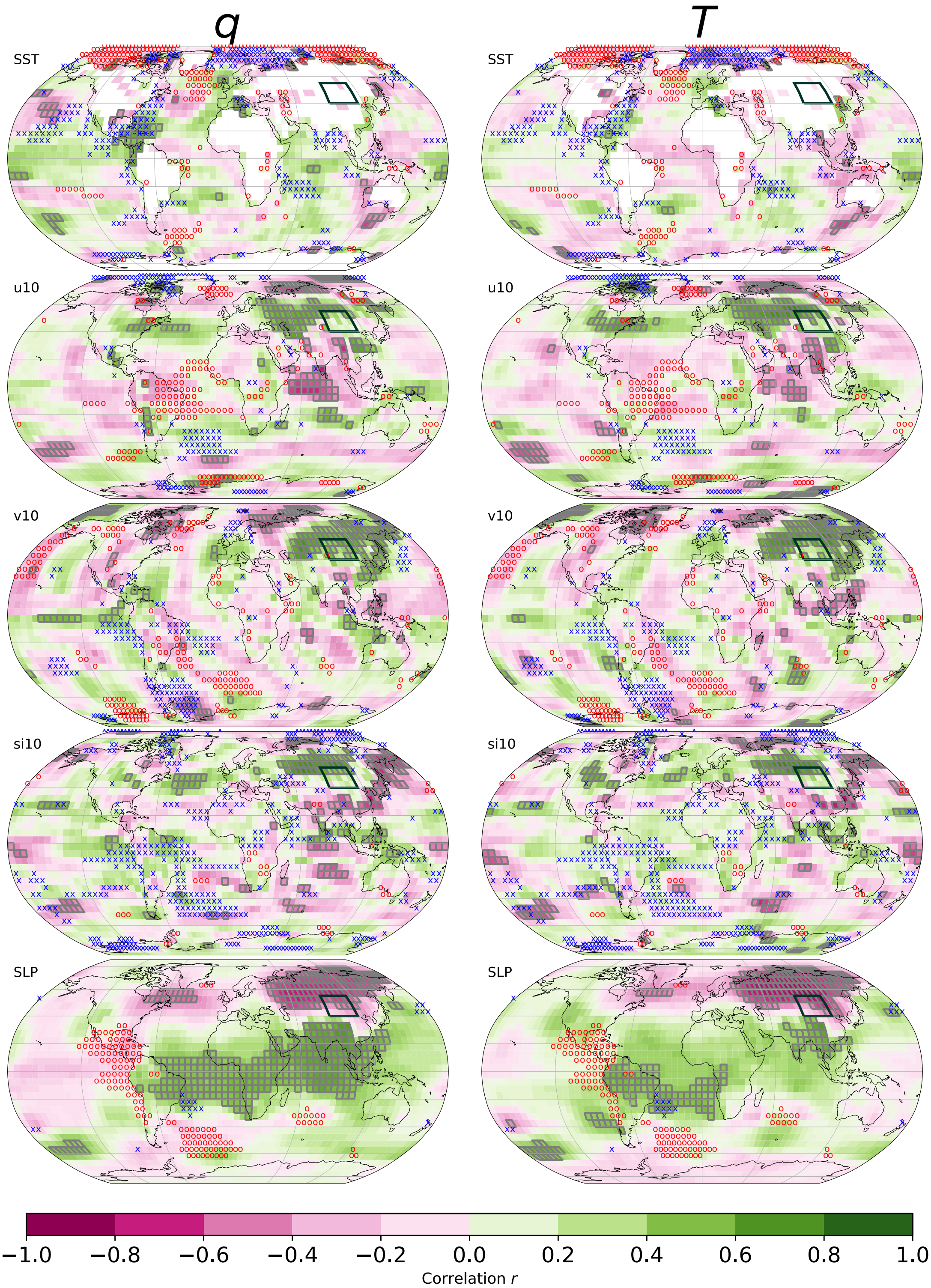

Figure 4.21: As for Fig. 4.5, for Mongolia (DJF).

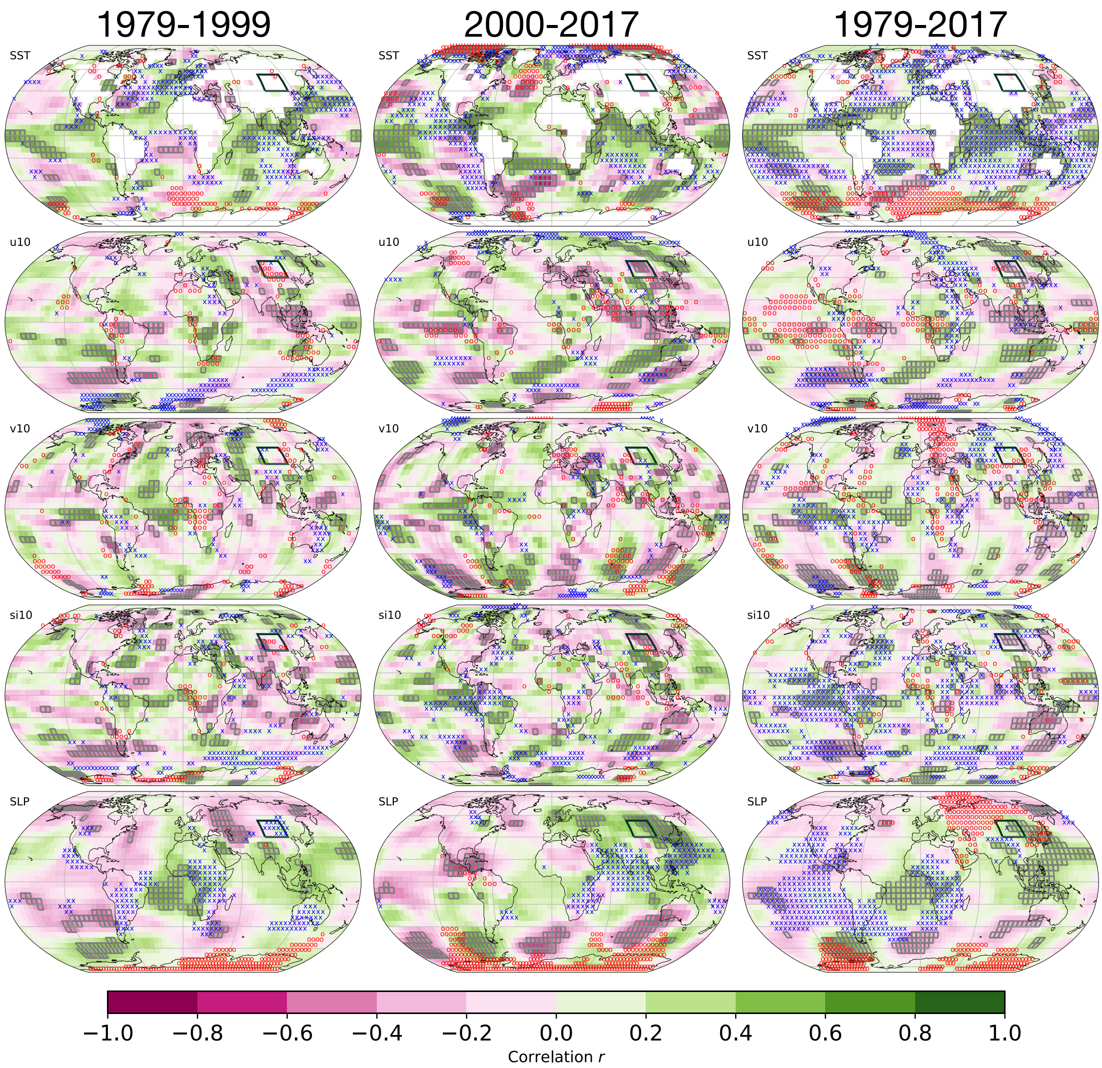

Figure 4.22: As for Fig. 4.4, for Mongolia (MAM).

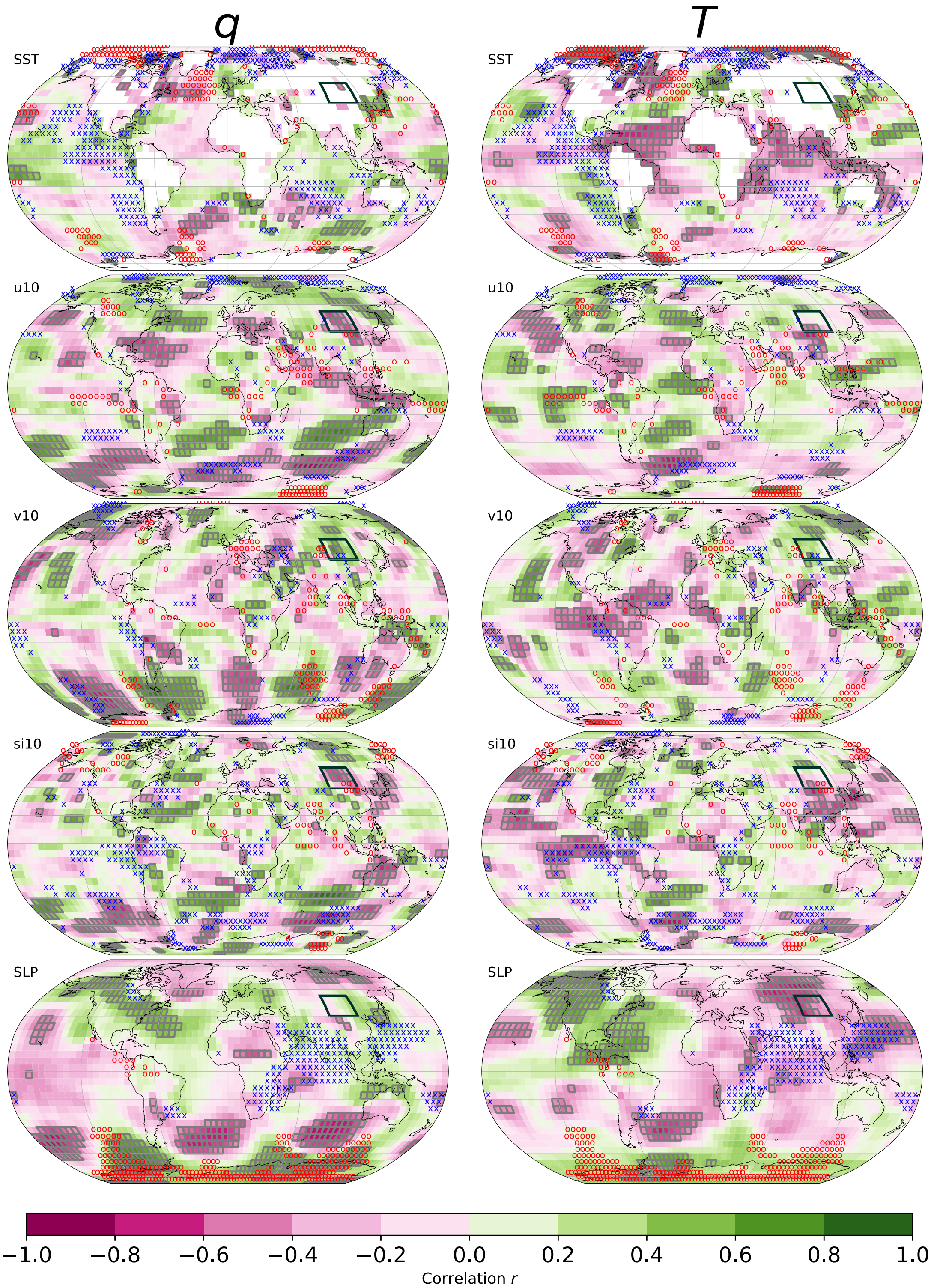

Figure 4.23: As for Fig. 4.5, for Mongolia (MAM).

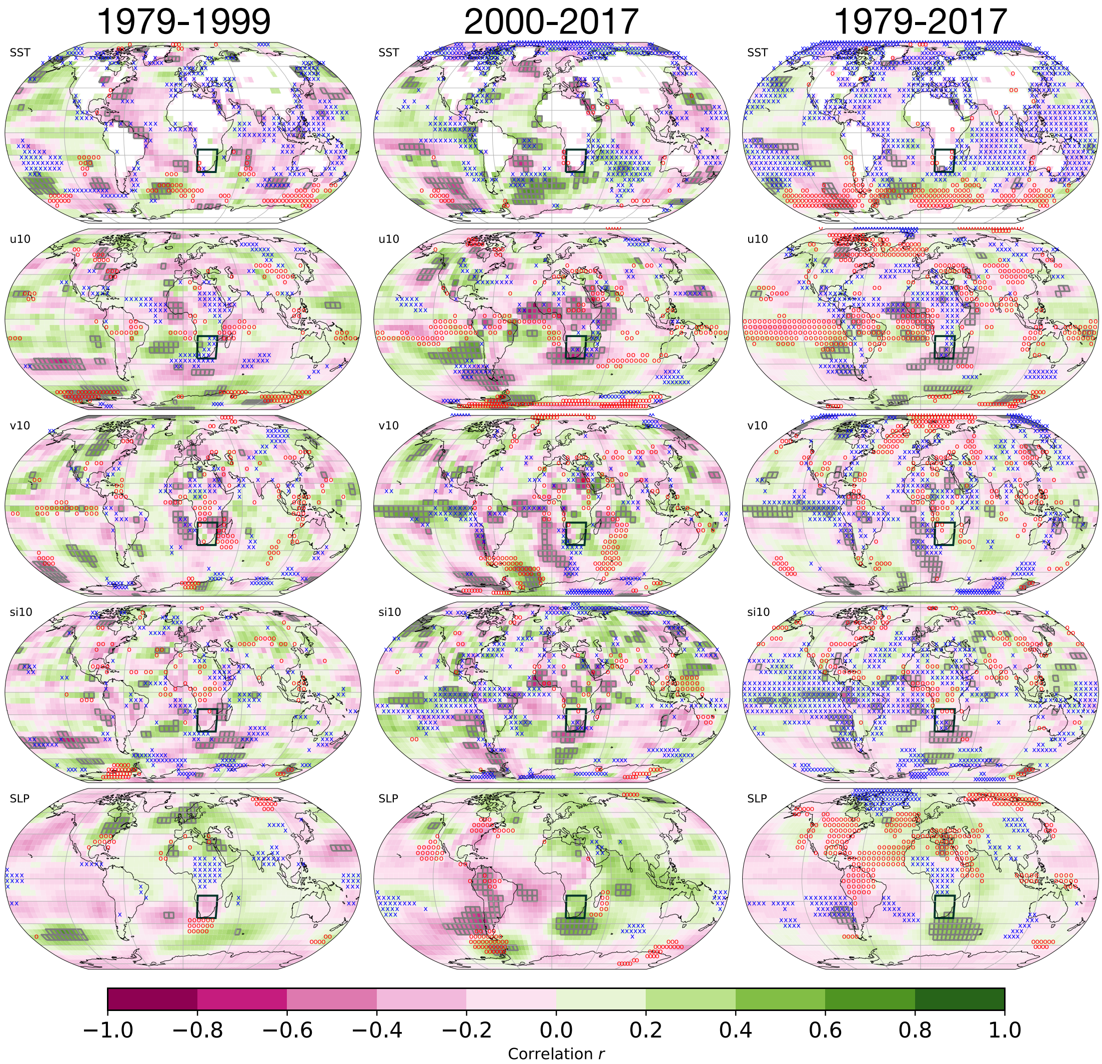

Figure 4.24: As for Fig. 4.4, for southern Africa (JJA).

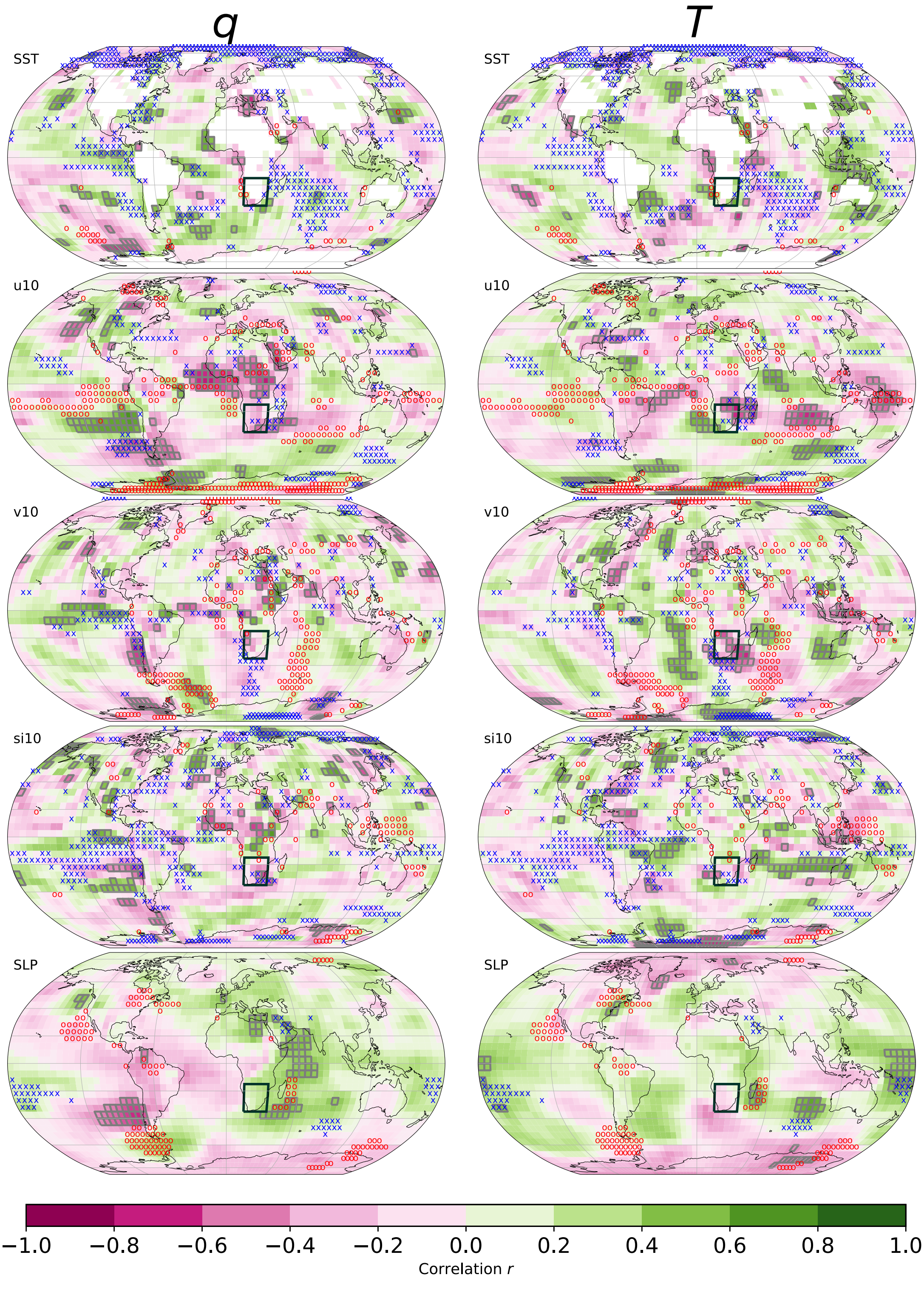

Figure 4.25: As for Fig. 4.5, for southern Africa (JJA).

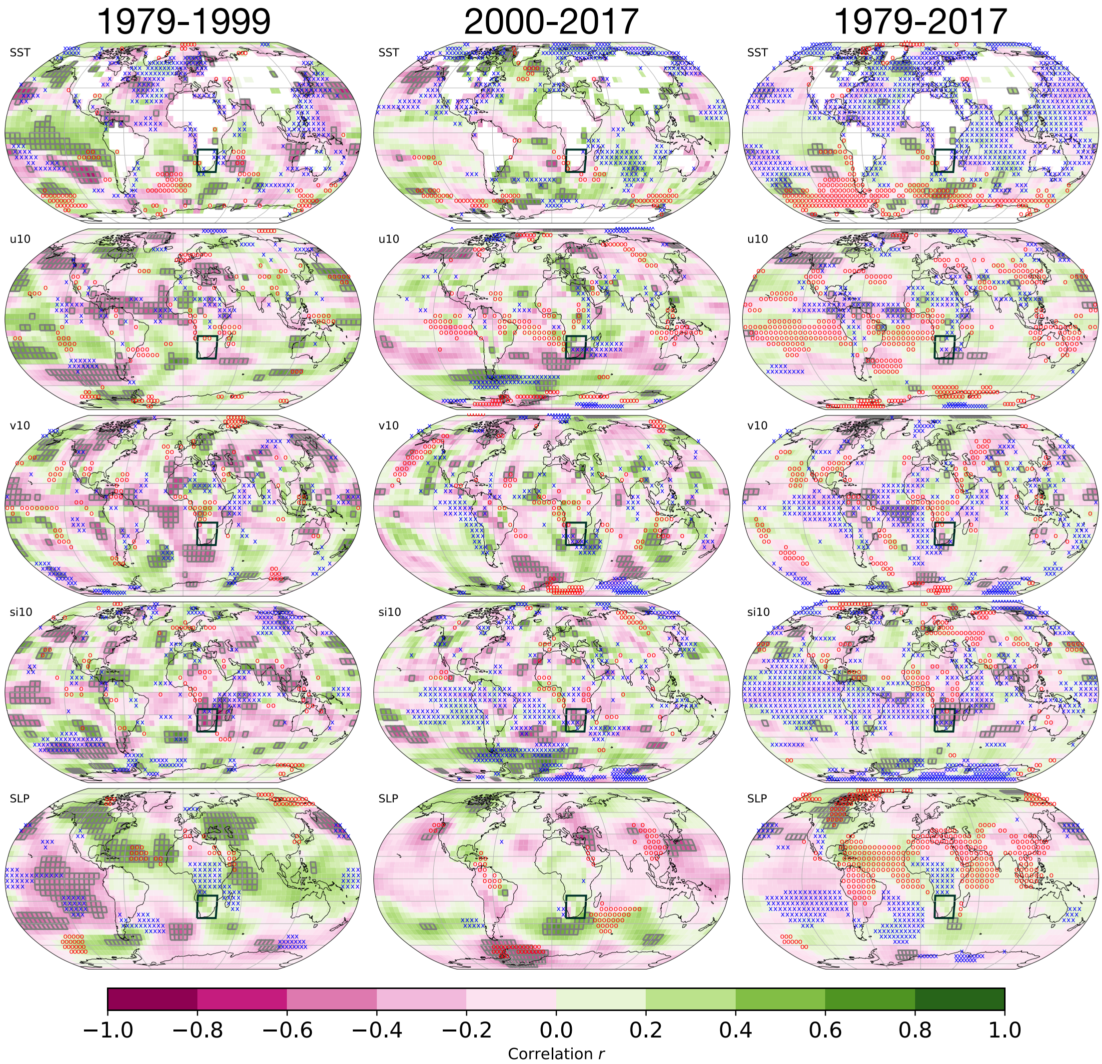

Figure 4.26: As for Fig. 4.4, for southern Africa (SON).

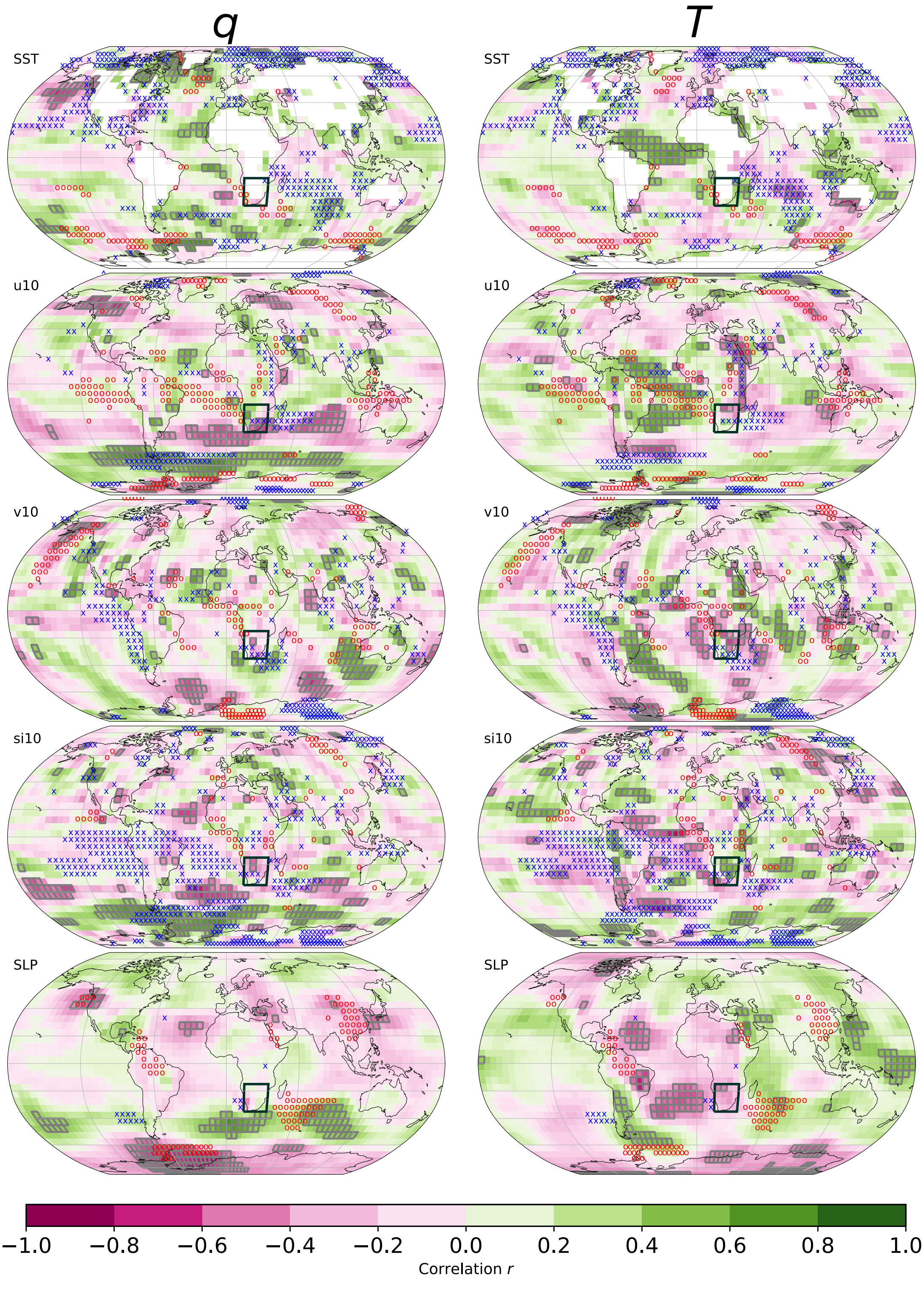

Figure 4.27: As for Fig. 4.5, for southern Africa (SON).

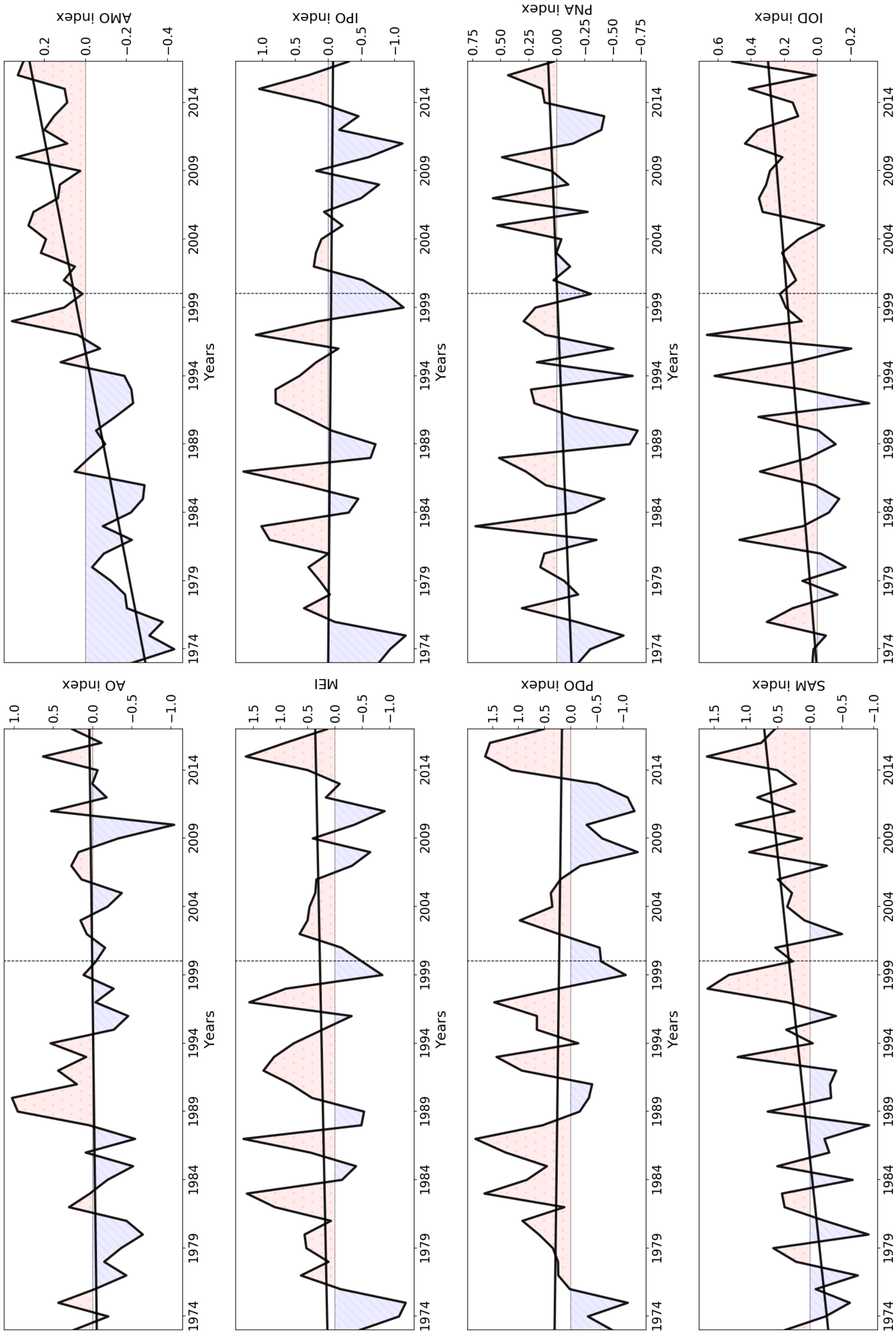

Figure 4.28: Time series for the indices of modes of variability over the full period (1973–2017): from top to bottom, in the left column, the AO, the MEI, the PDO, the SAM, and in the right column, the AMO, the IPO, the PNA and the IOD.

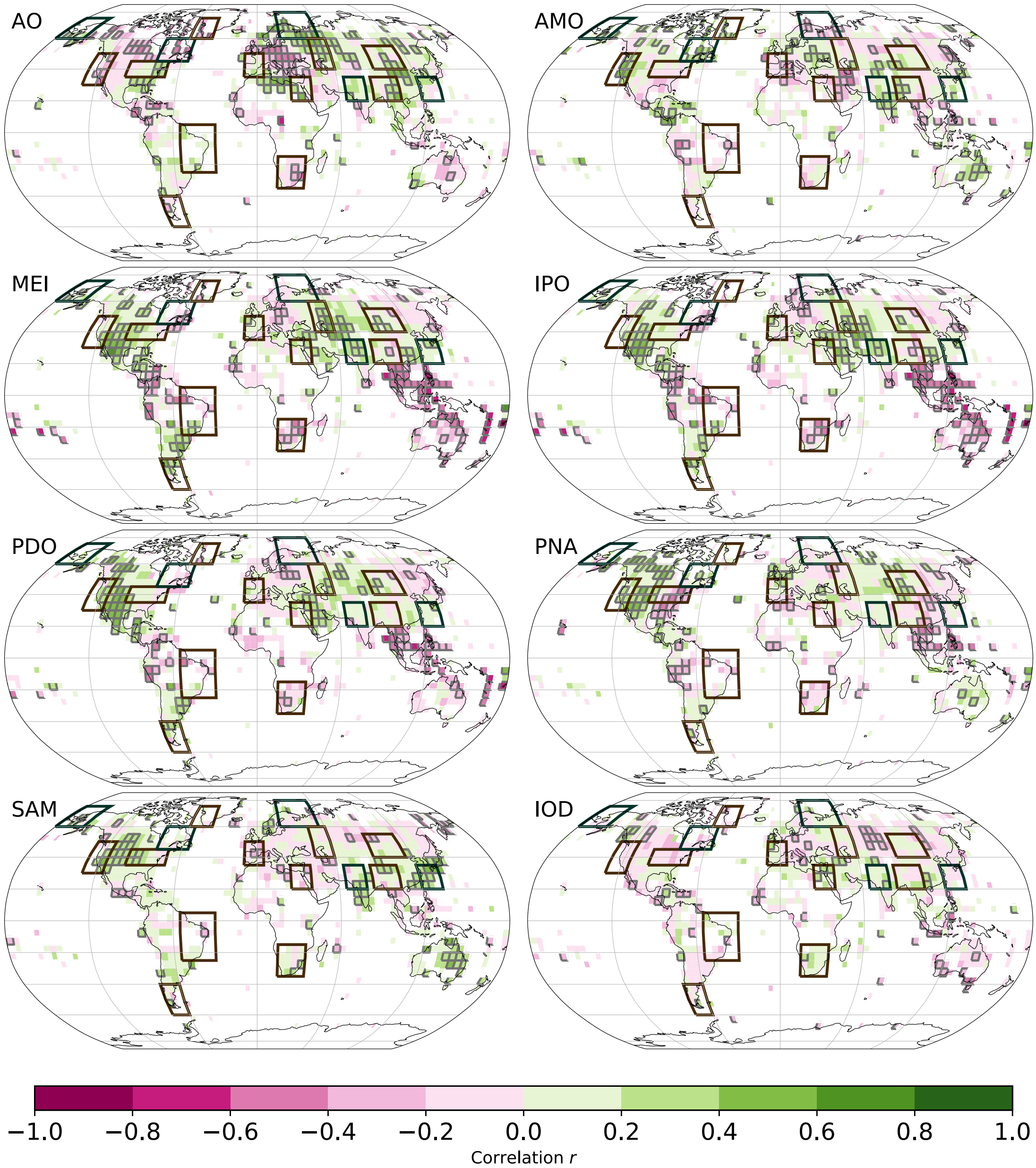

Figure 4.29: Annual correlation maps between modes of variability and RH over land for the full period (1973–2017). Grid boxes of significant correlations ($p < 0.1$) are framed in grey.

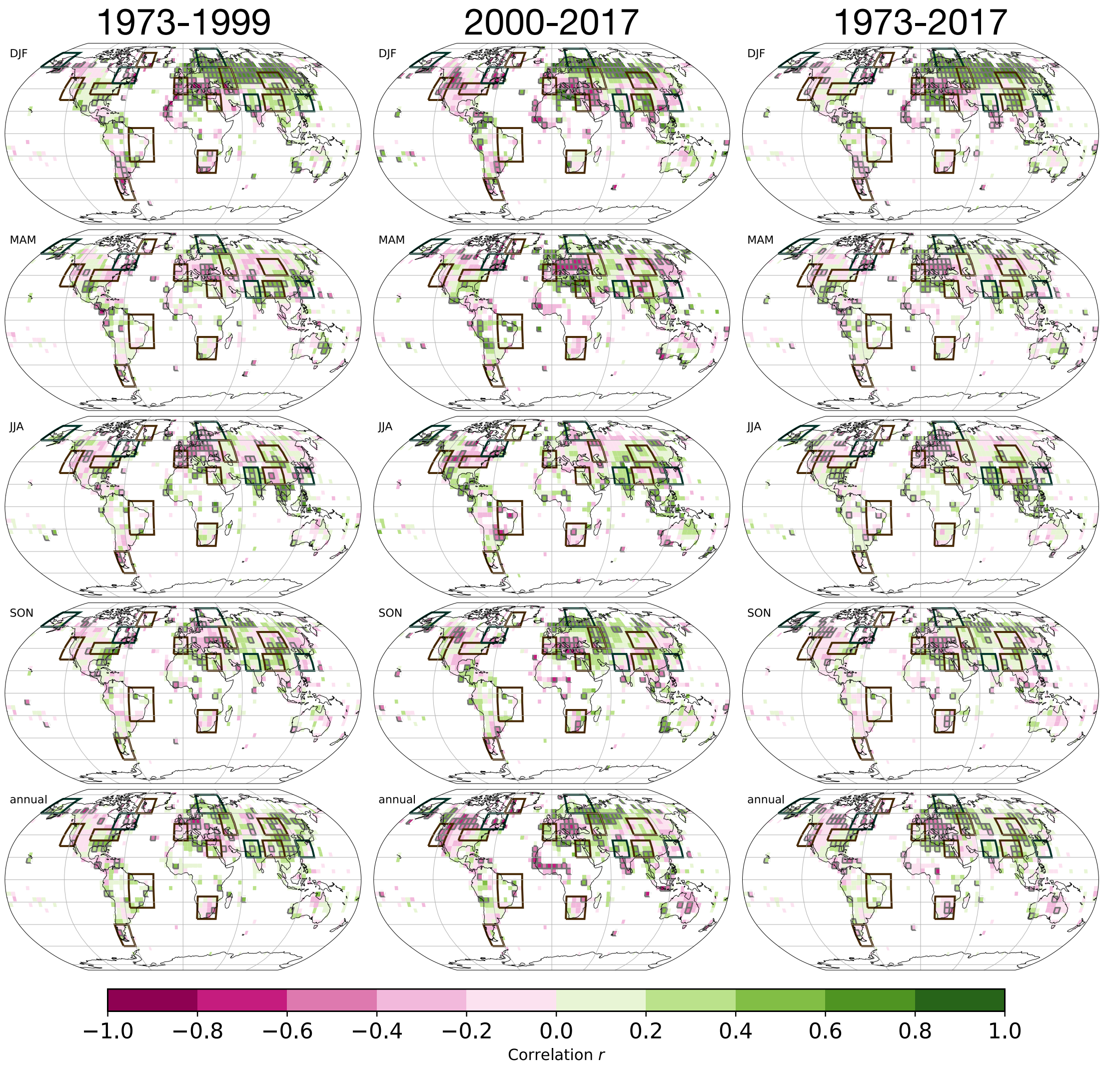

Figure 4.30: Annual (bottom line) and seasonal (upper four rows) correlation maps between the detrended AO and HadISDH RH over the early, the late and the full periods (left to right). Grid boxes of significant correlations ($p < 0.1$) are framed in grey.

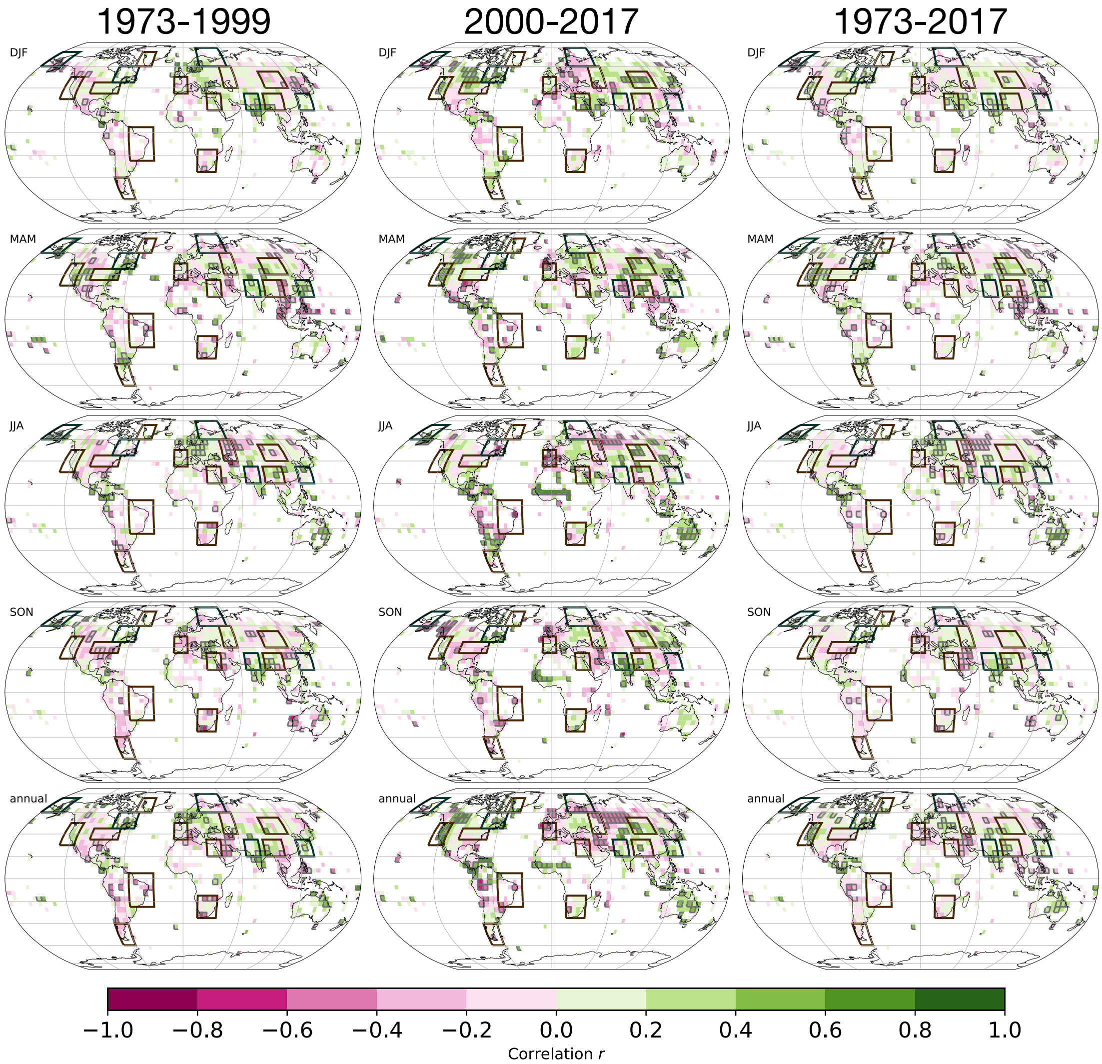

Figure 4.31: As for Fig. 4.30, for the AMO.

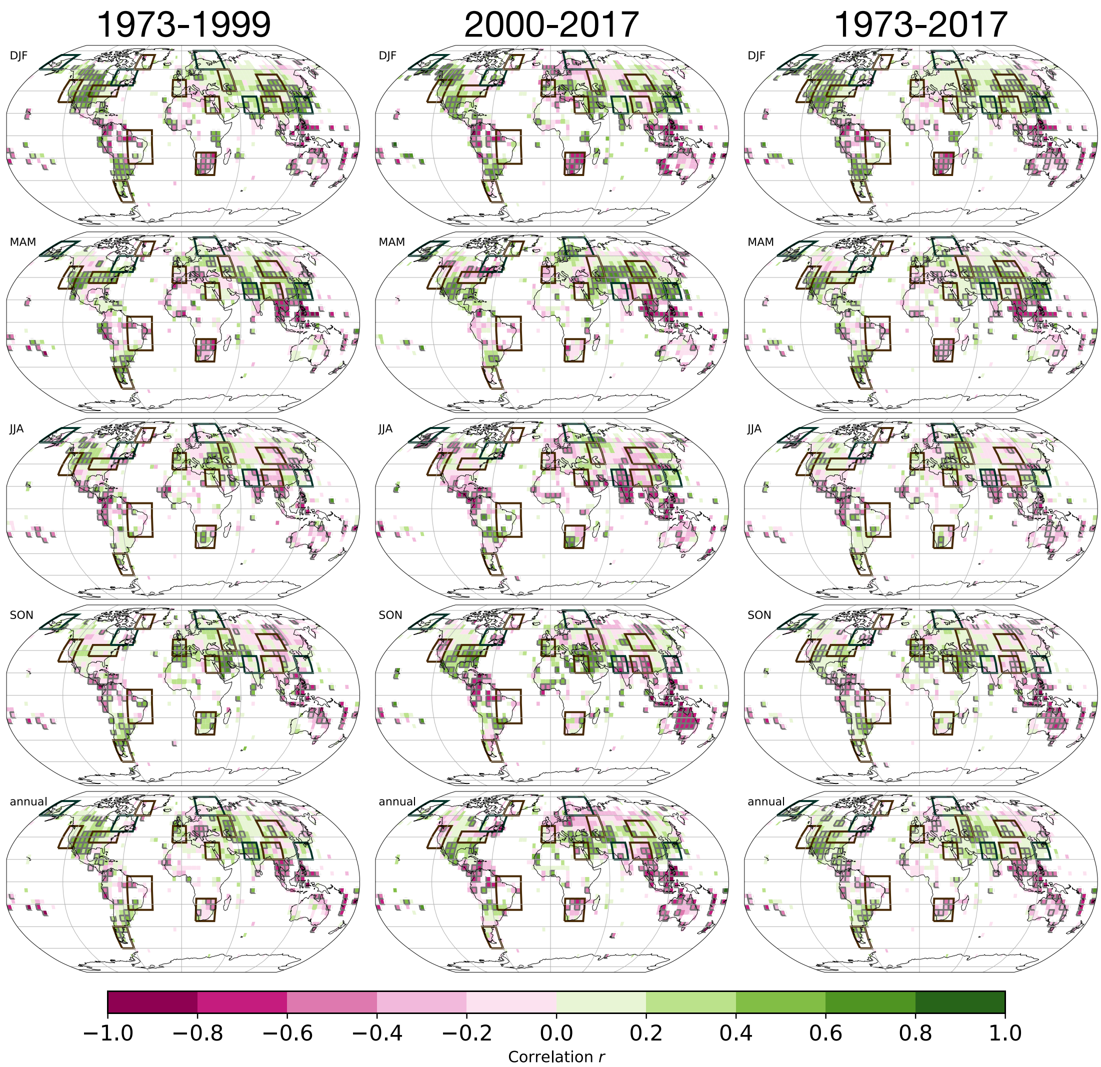

Figure 4.32: As for Fig. 4.30, for the ENSO (MEI).

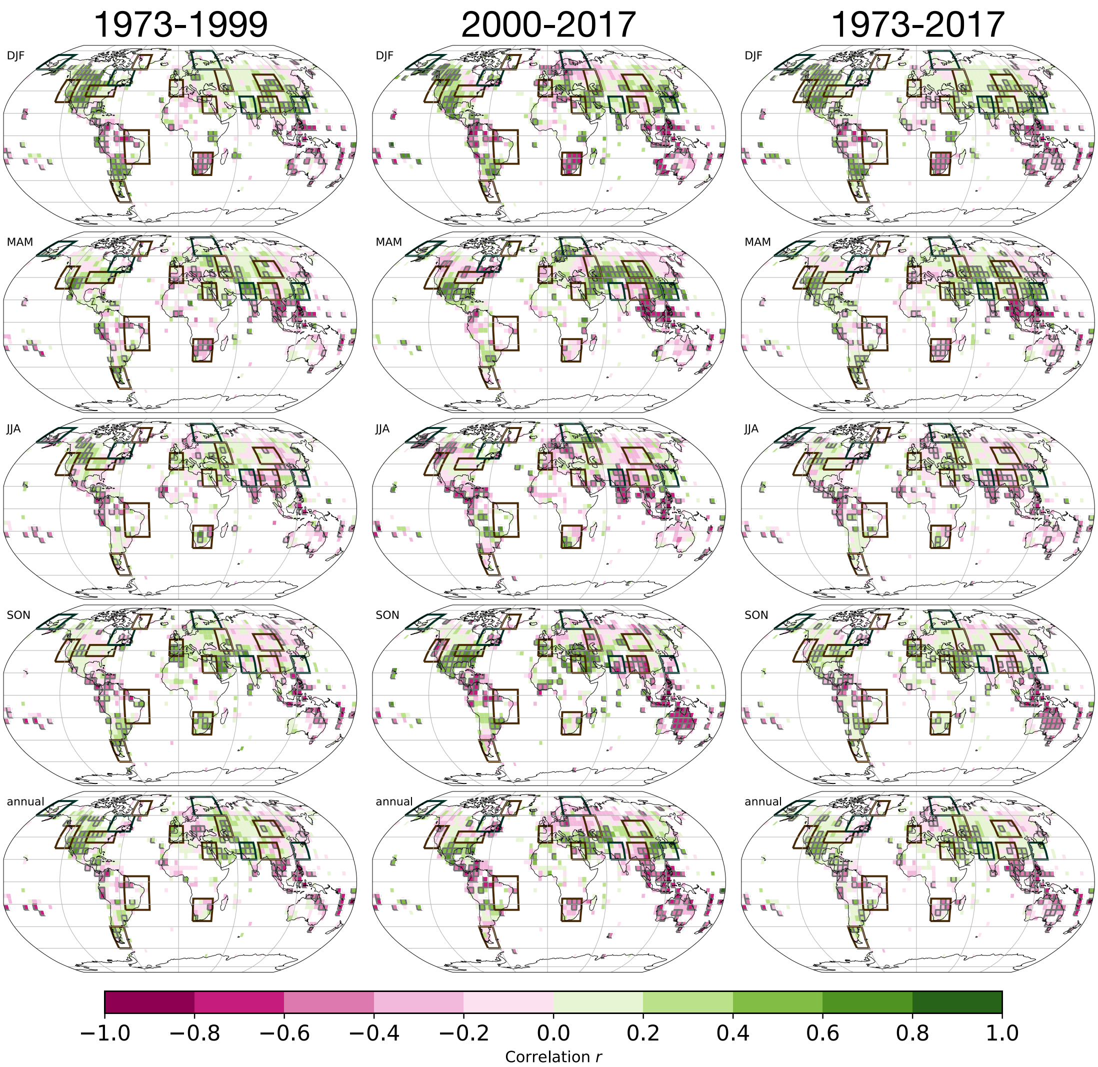

Figure 4.33: As for Fig. 4.30, for the IPO.

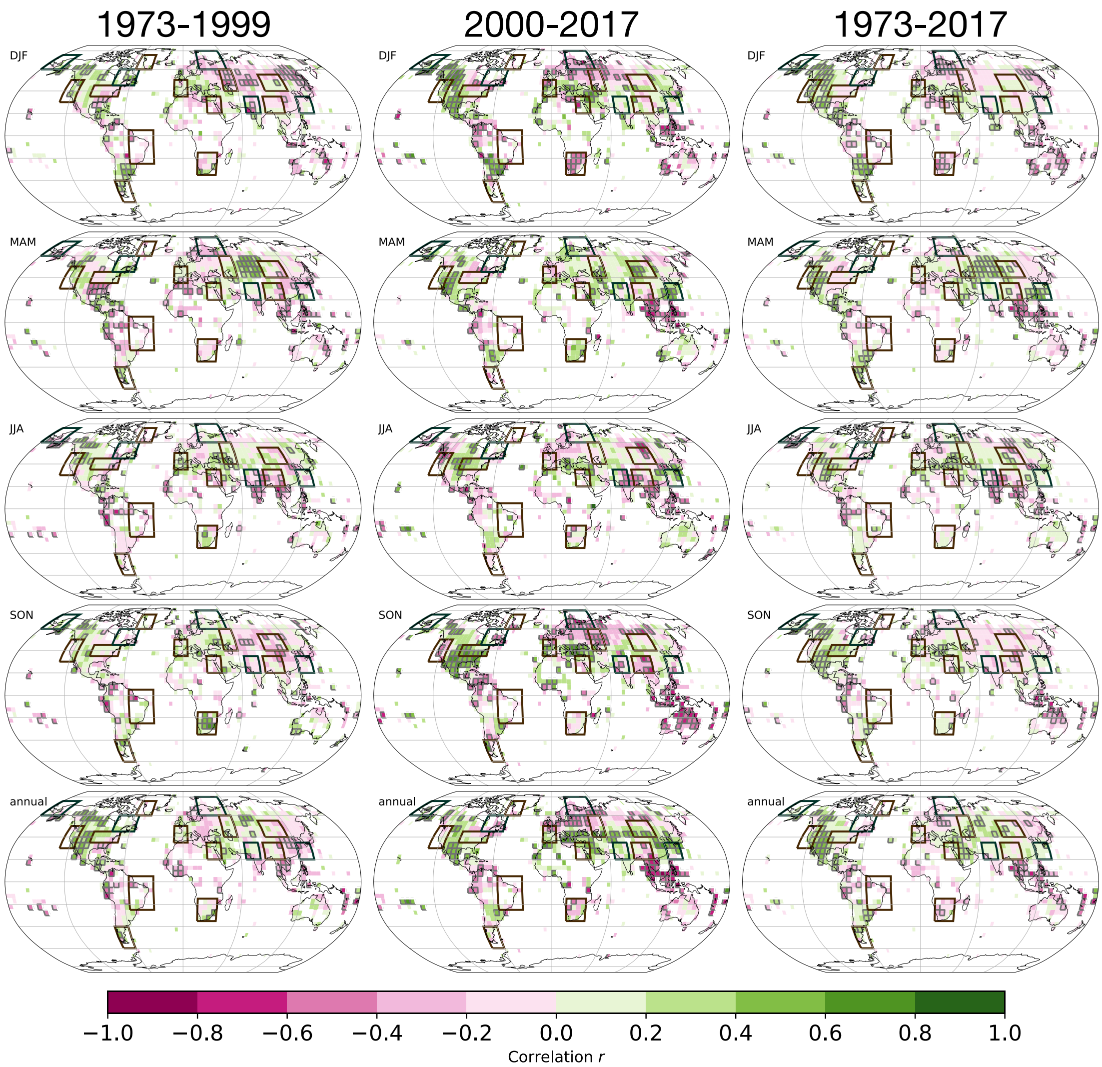

Figure 4.34: As for Fig. 4.30, for the PDO.

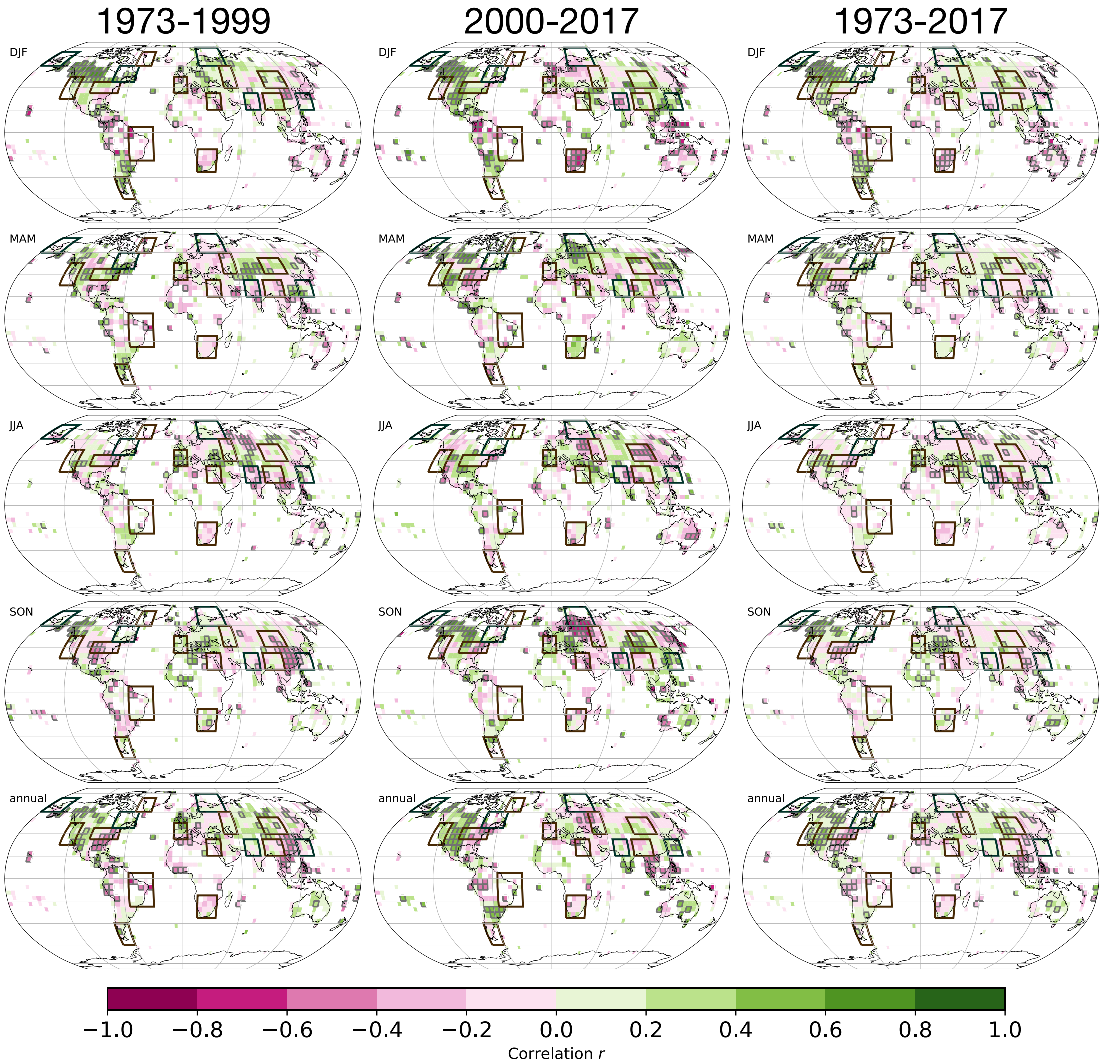

Figure 4.35: As for Fig. 4.30, for the PNA.

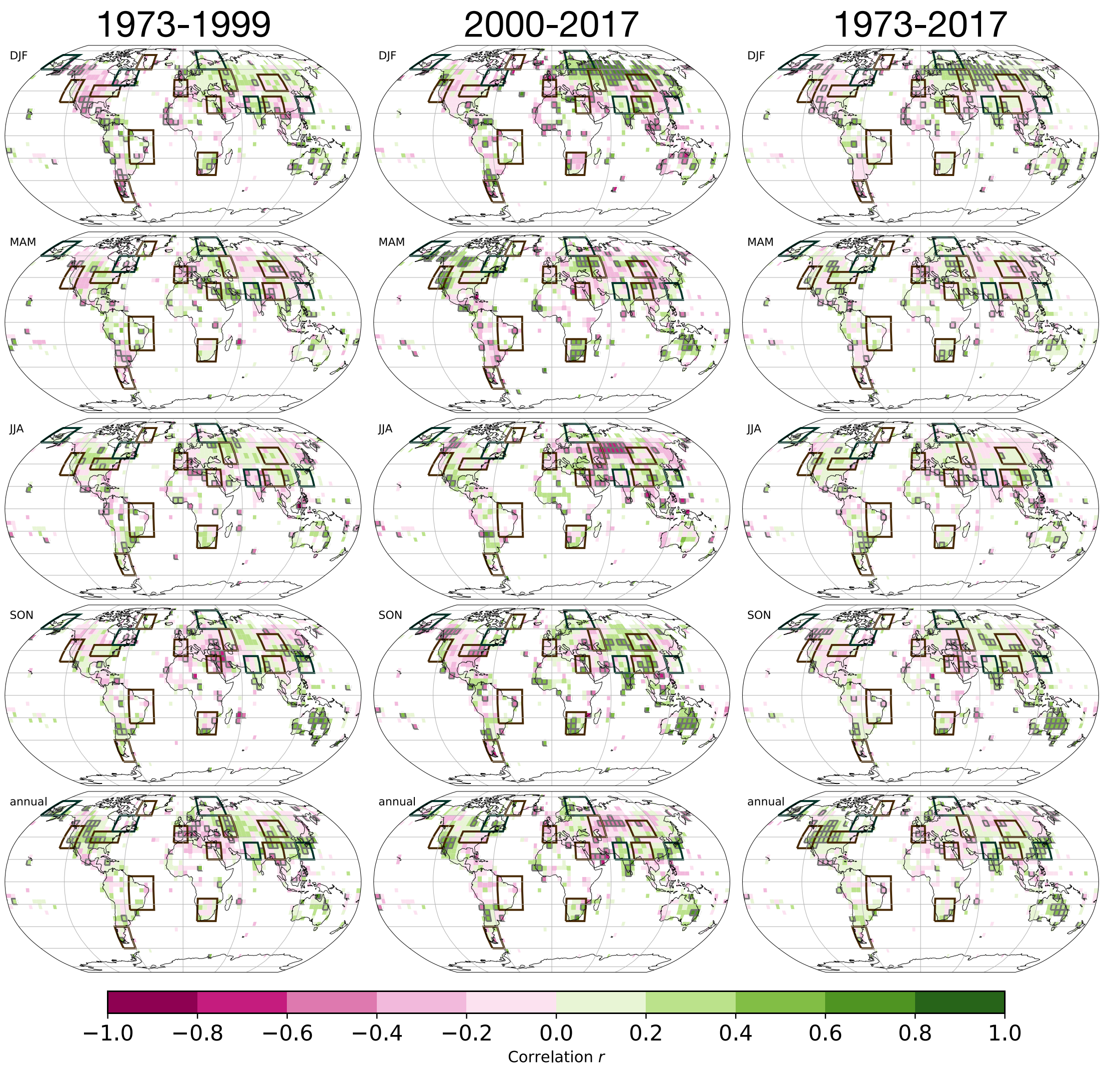

Figure 4.36: As for Fig. 4.30, for the SAM.

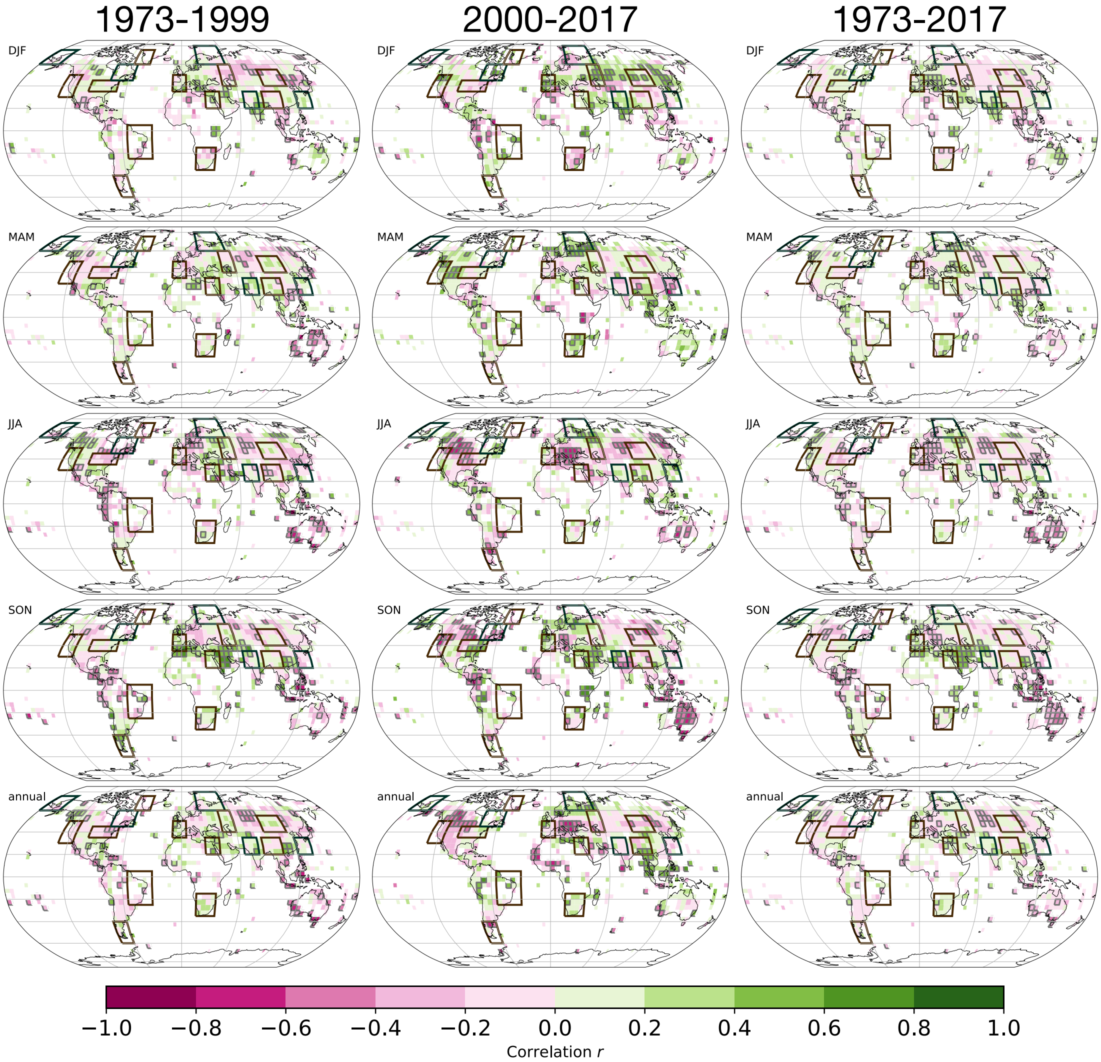

Figure 4.37: As for Fig. 4.30, for the IOD.

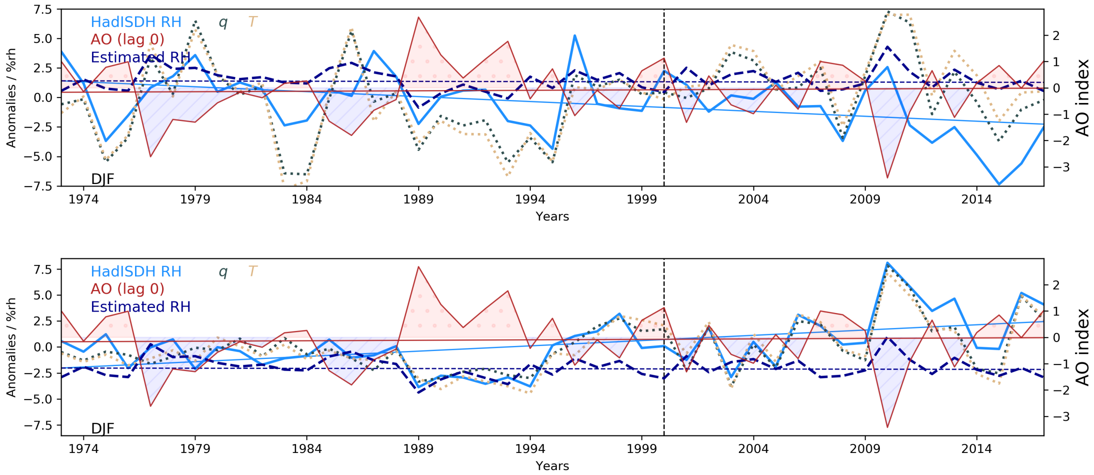

Figure 4.38: Time plots and linear fits of HadISDH RH anomalies (light blue) in southwestern Greenland (top) and Eastern Canada (bottom) in DJF and by the regression through the AO (red) estimated RH (dark blue dashed), furthermore q (dark green) and T standardised anomalies (yellow) over the full period (1973–2017). Positive AO phases are indicated by filled red dots and negative phases by blue stripes. The vertical line indicates the year 2000, the end of the early period and the start of the late period.

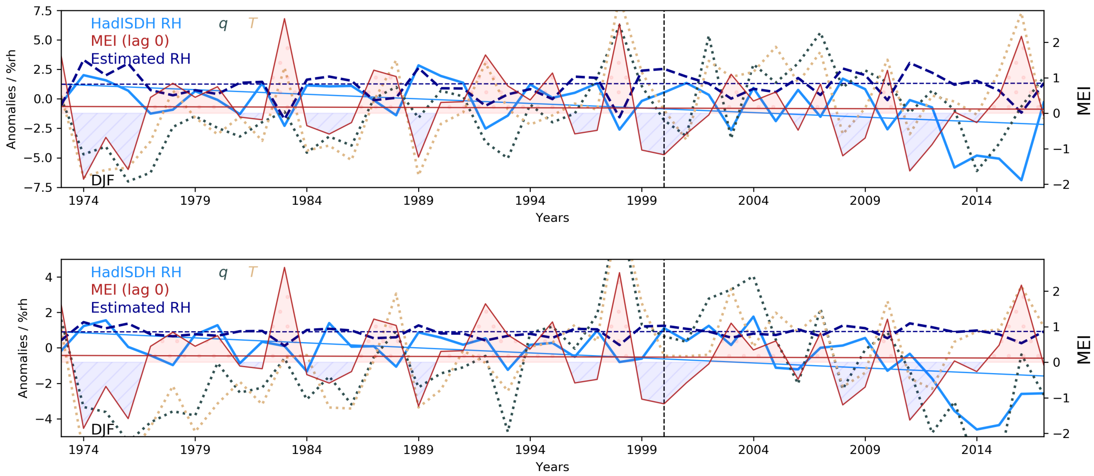

Figure 4.39: As for Fig. 4.38, for HadISDH anomalies in the northwest of eastern Brazil (top) and eastern Brazil (bottom) and the MEI in DJF.

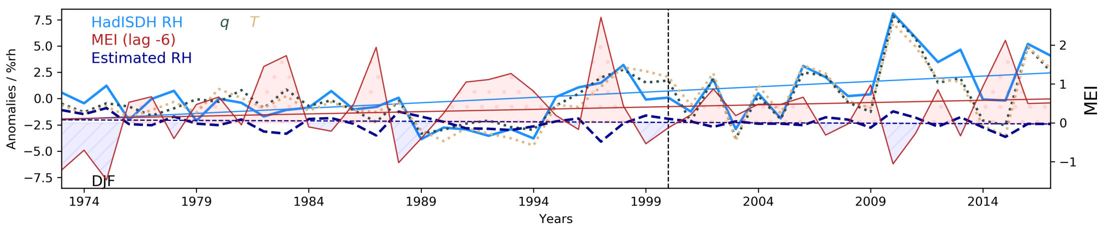

Figure 4.40: As for Fig. 4.38, for HadISDH anomalies in eastern Canada (DJF) and the MEI with a lag of -6 months, i.e. in JJA the previous year.

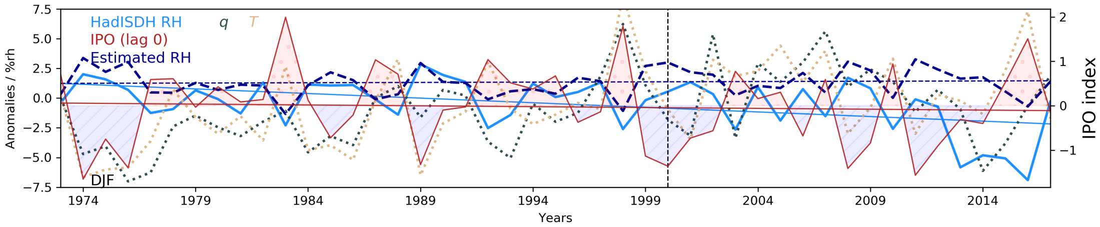

Figure 4.41: As for Fig. 4.38, for HadISDH anomalies in the northwest of eastern Brazil and the IPO in DJF.

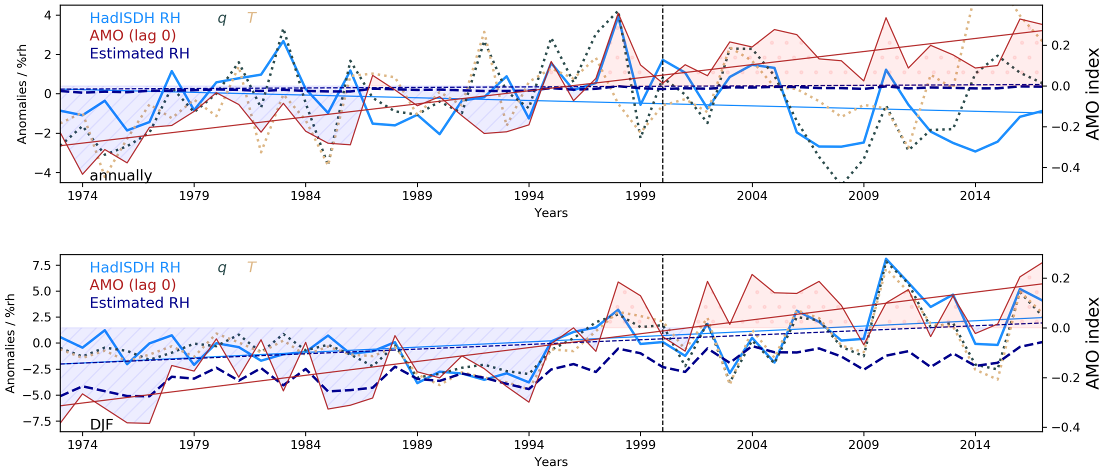

Figure 4.42: As for Fig. 4.38, for HadISDH anomalies in California (annual; top) and eastern Canada (DJF; bottom) and the AMO.

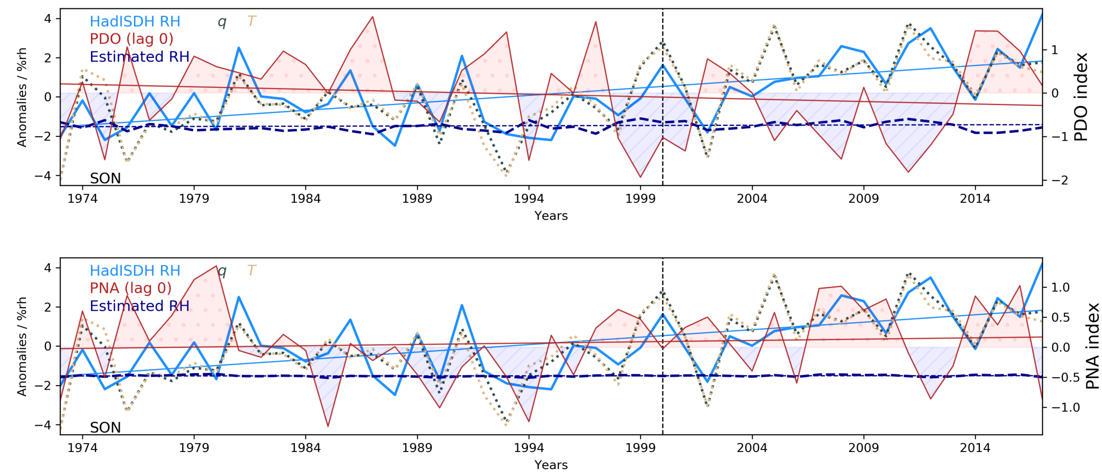

Figure 4.43: As for Fig. 4.38, for HadISDH anomalies in Scandinavia and the PDO (top) and the PNA (bottom) in SON.

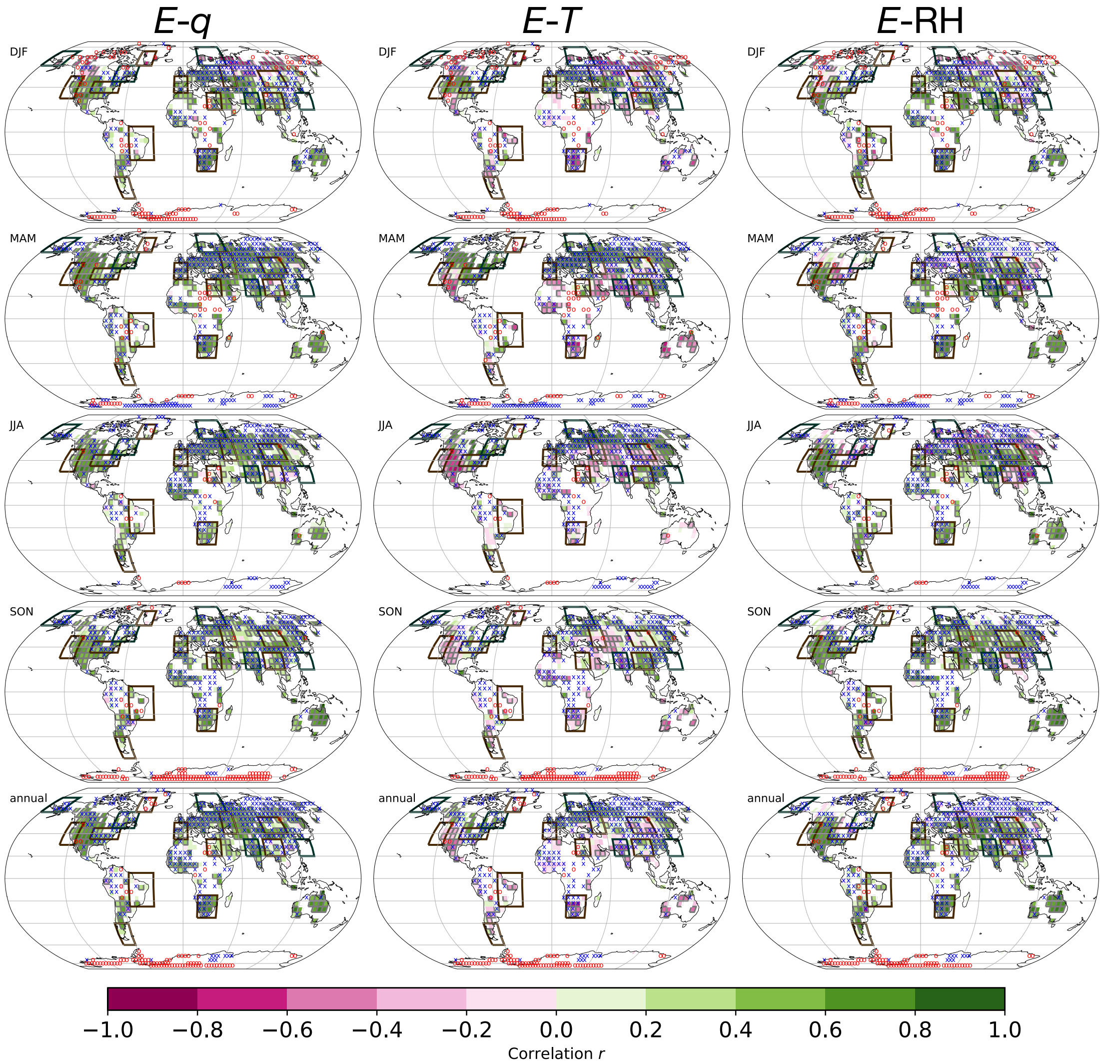

Figure 5.1: Correlations between the detrended GLEAM E and HadISDH RH, q and T anomalies over land for annual data (bottom) and the four standard seasons (upper four rows) over the full period (1980–2017). Grid boxes of significant ($p < 0.1$) correlations are framed in grey; significantly positive (negative) trends in GLEAM E relative to the climatology over the 1981–2010 period show a blue 'x' (red 'o'). Regions with a strong average trend in RH in the late period are framed in ochre (negative trends) and turquoise (positive trends). White space represents either missing data or ocean.

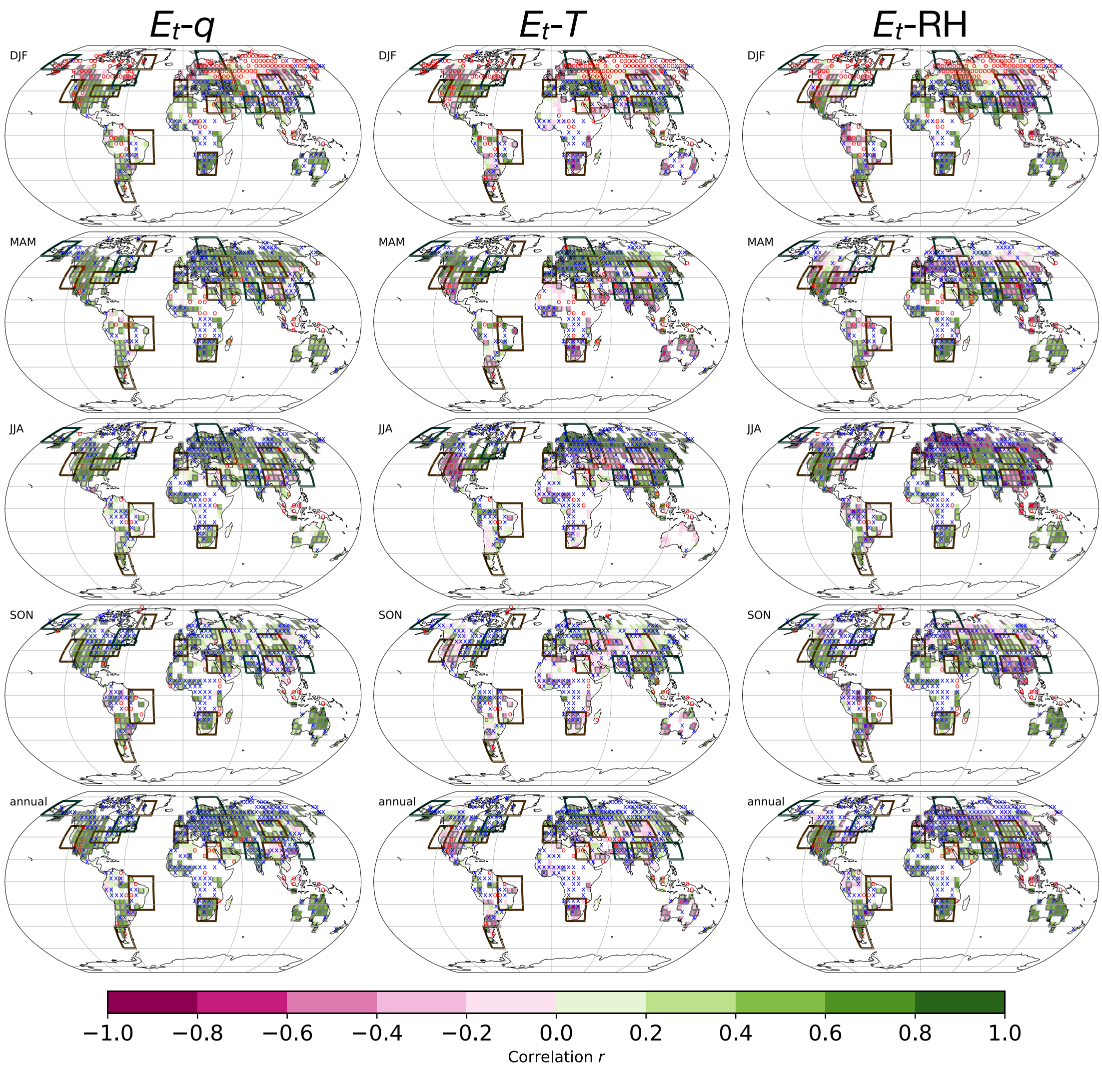

Figure 5.2: As for Fig. 5.1, for E_t.

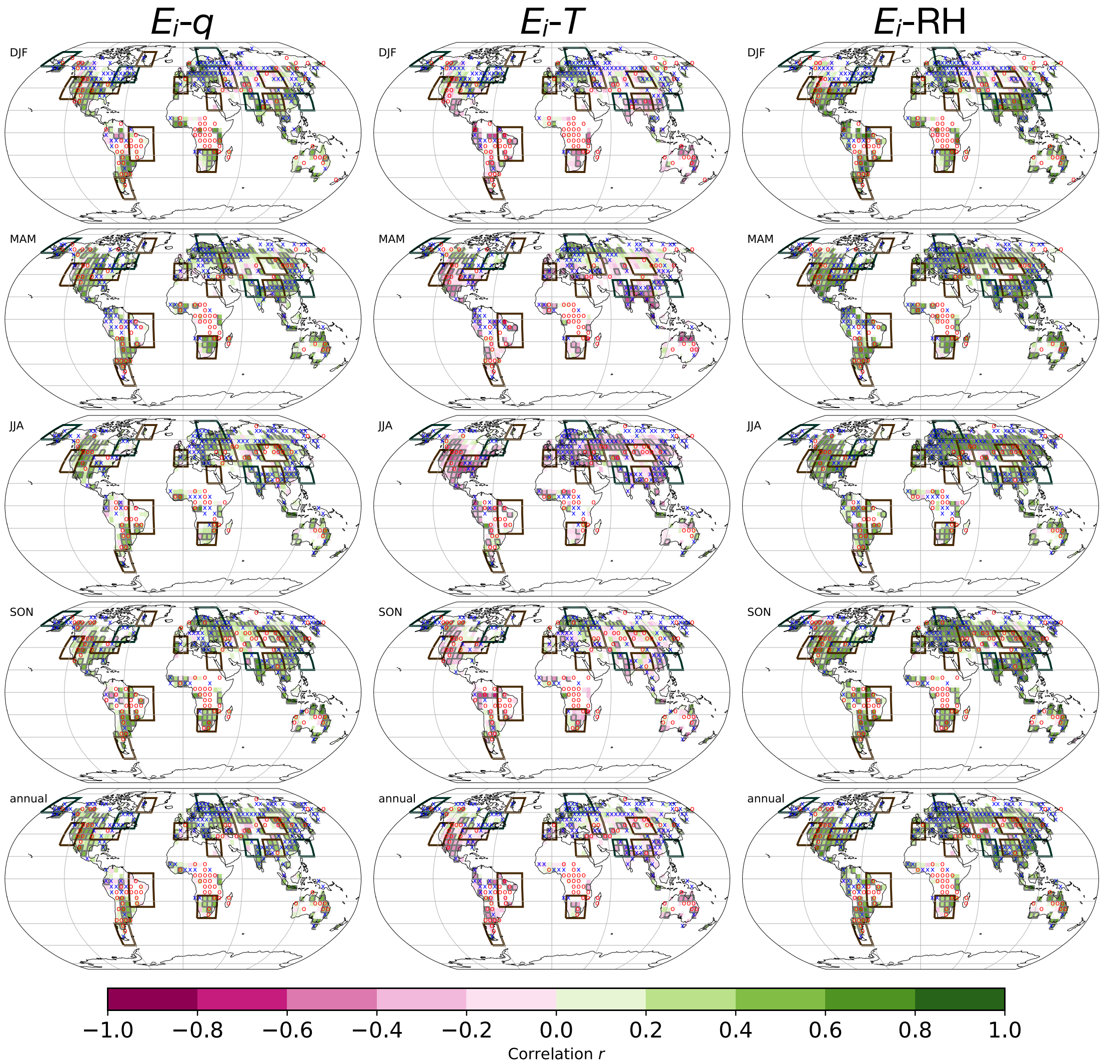

Figure 5.3: As for Fig. 5.1, for E_i.

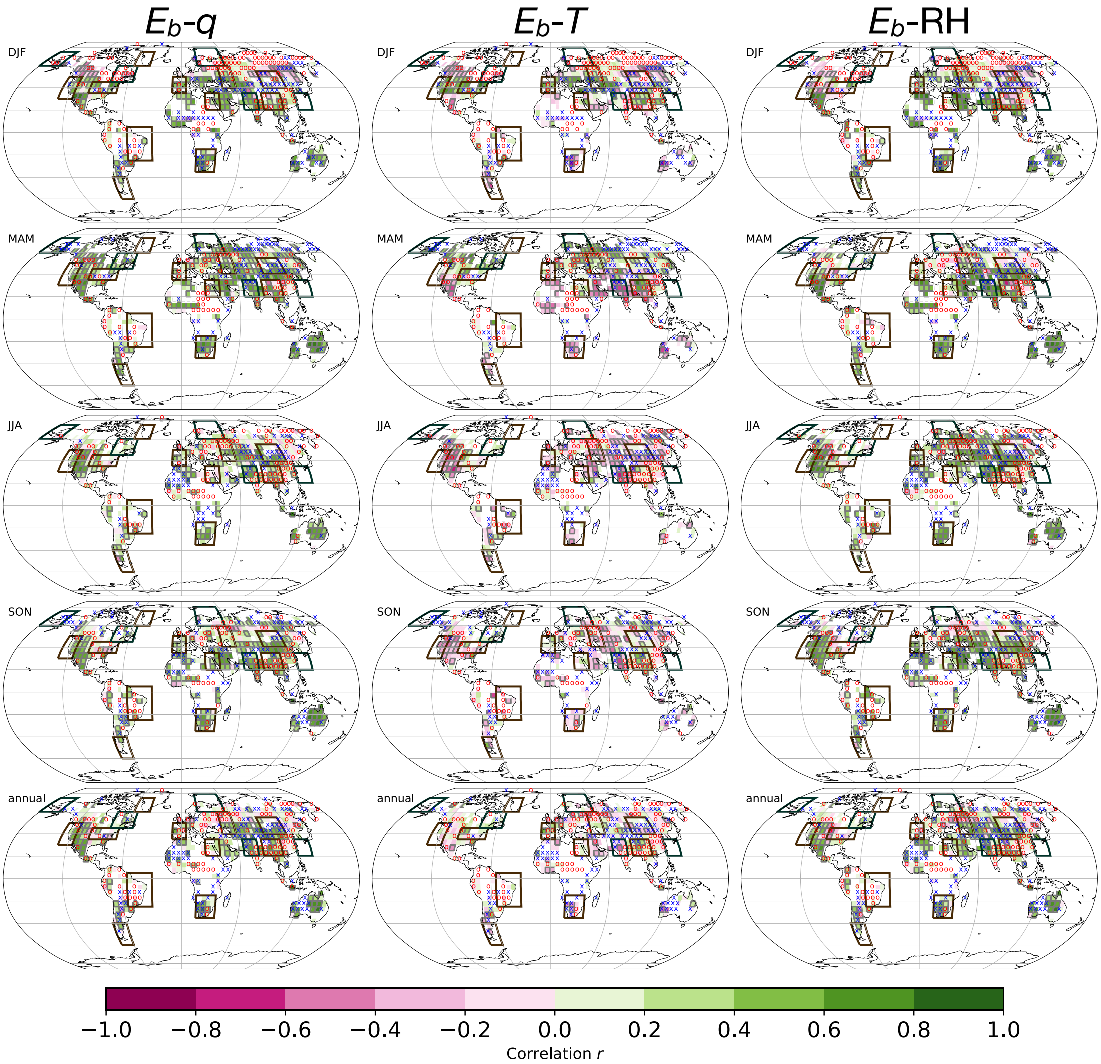

Figure 5.4: As for Fig. 5.1, for E_b.

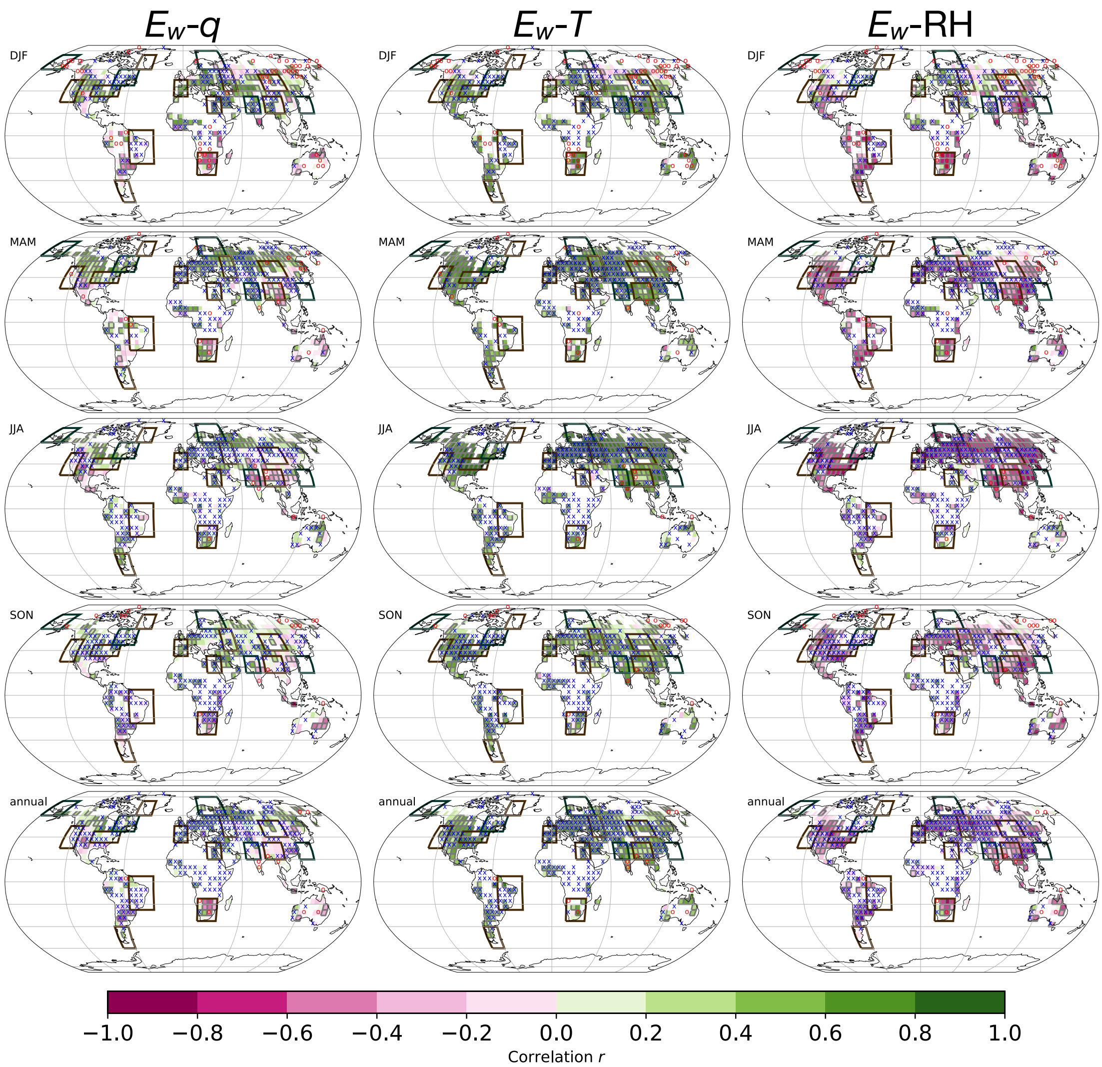

Figure 5.5: As for Fig. 5.1, for E_w.

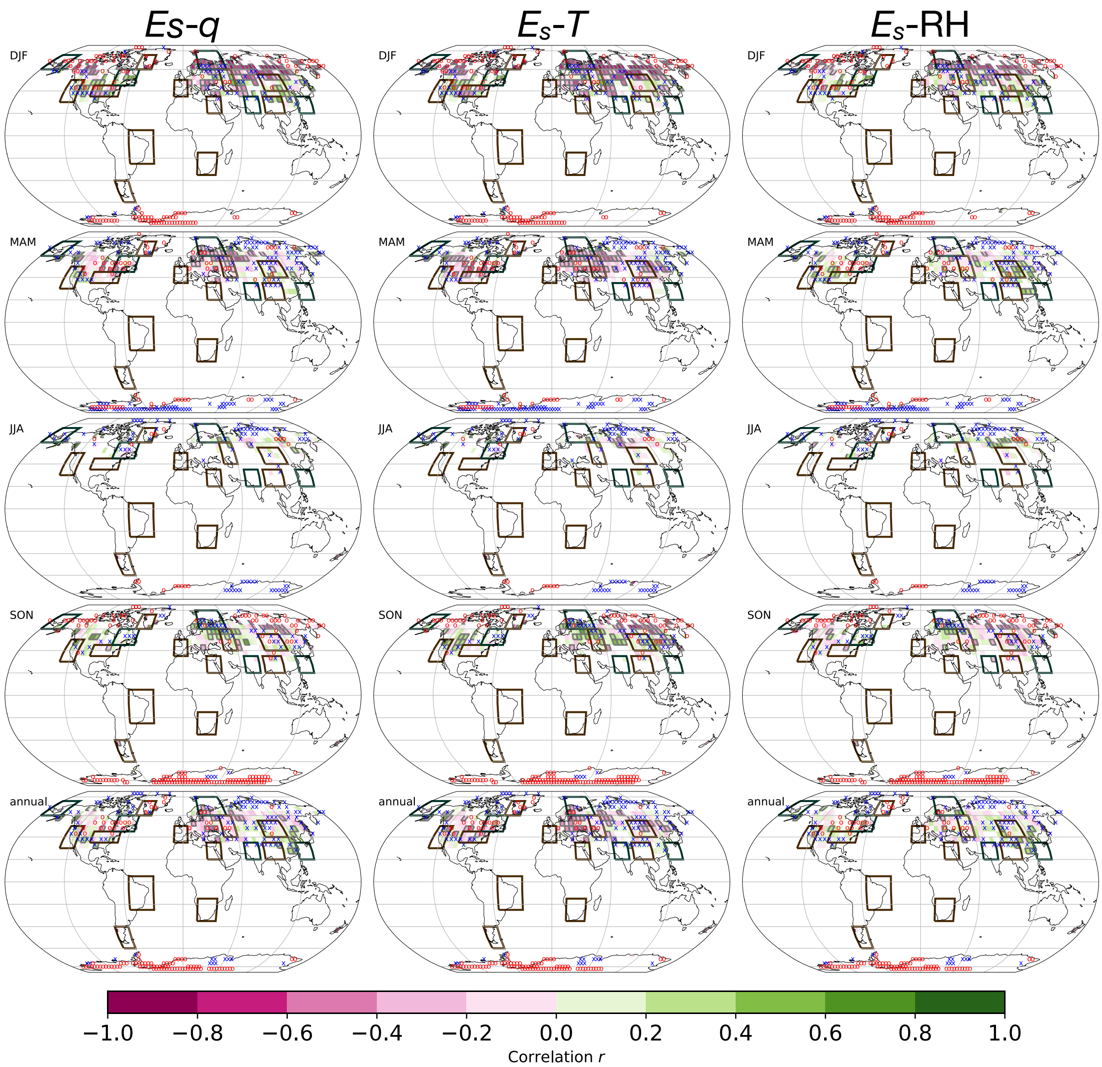

Figure 5.6: As for Fig. 5.1, for E_s.

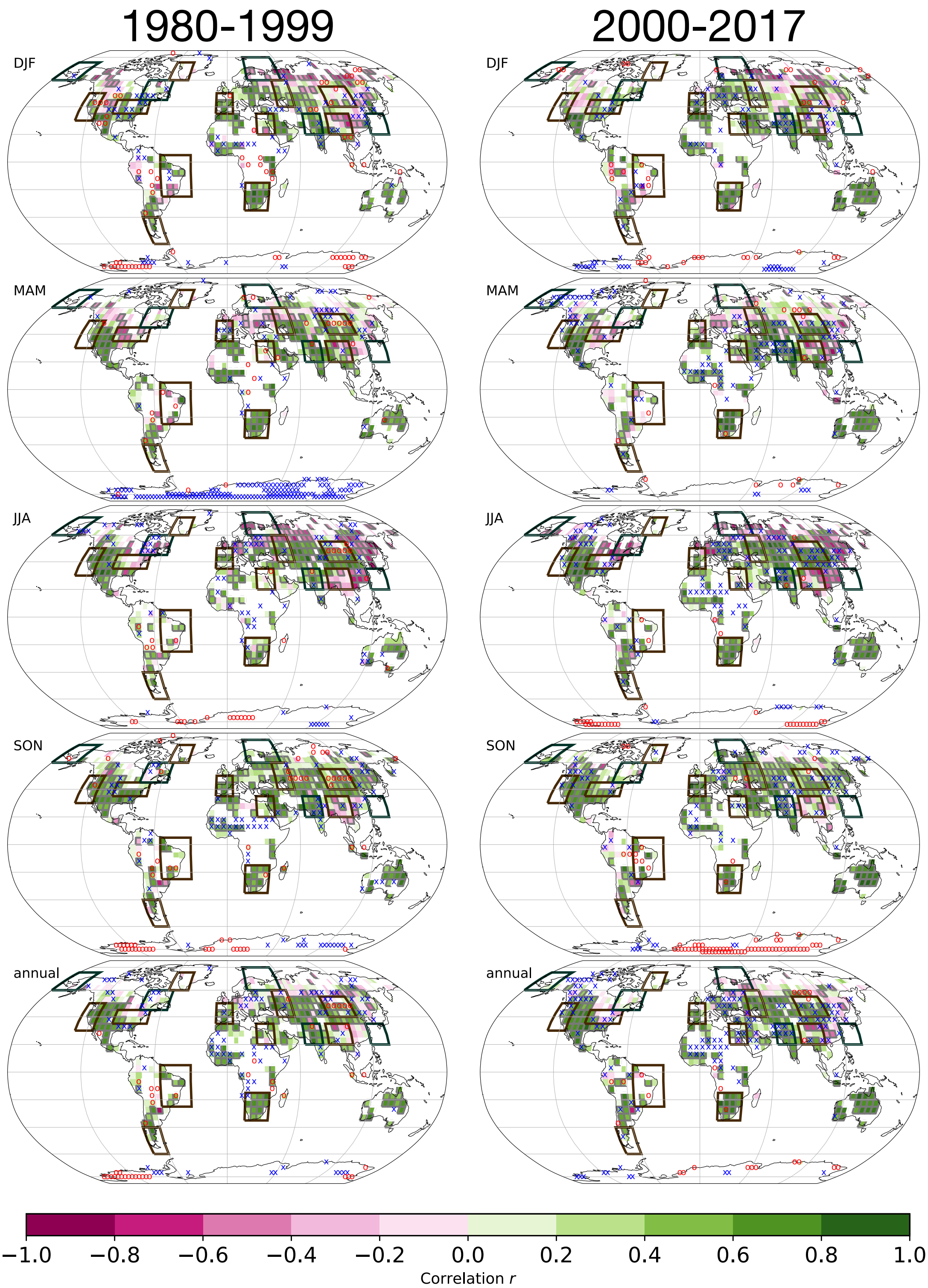

Figure 5.7: Correlations between the detrended GLEAM E and HadISDH RH anomalies over land for annual data (bottom) and the four standard seasons (upper four rows) over the early (1980–1999), the late (2000–2017) and the full period (1980–2017). Grid boxes of significant correlations ($p < 0.1$) are framed grey; significantly positive (negative) trends in GLEAM E relative to the climatology over the 1981–2010 period show a blue 'x' (red 'o').

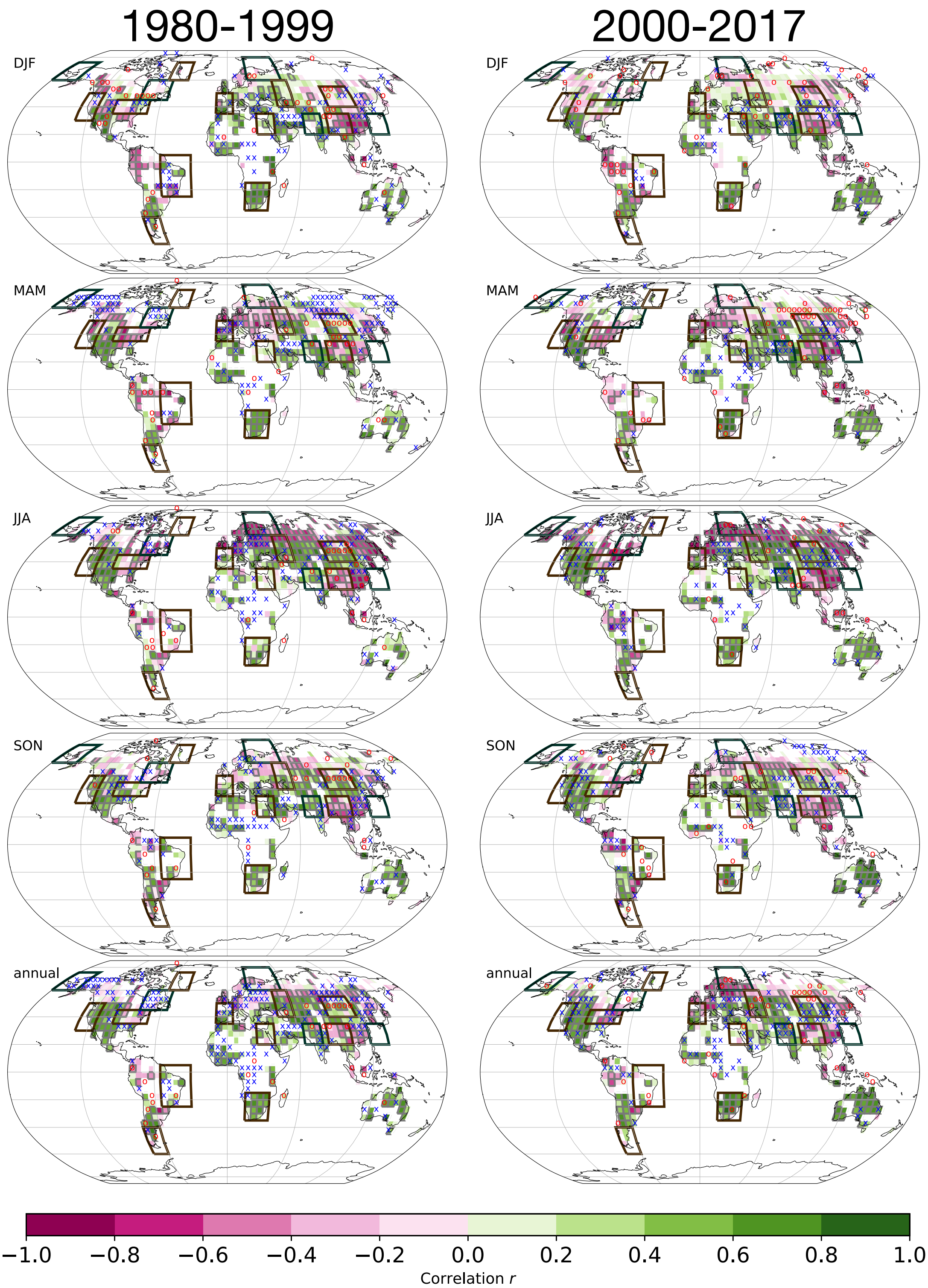

Figure 5.8: As for Fig. 5.7, for E_t.

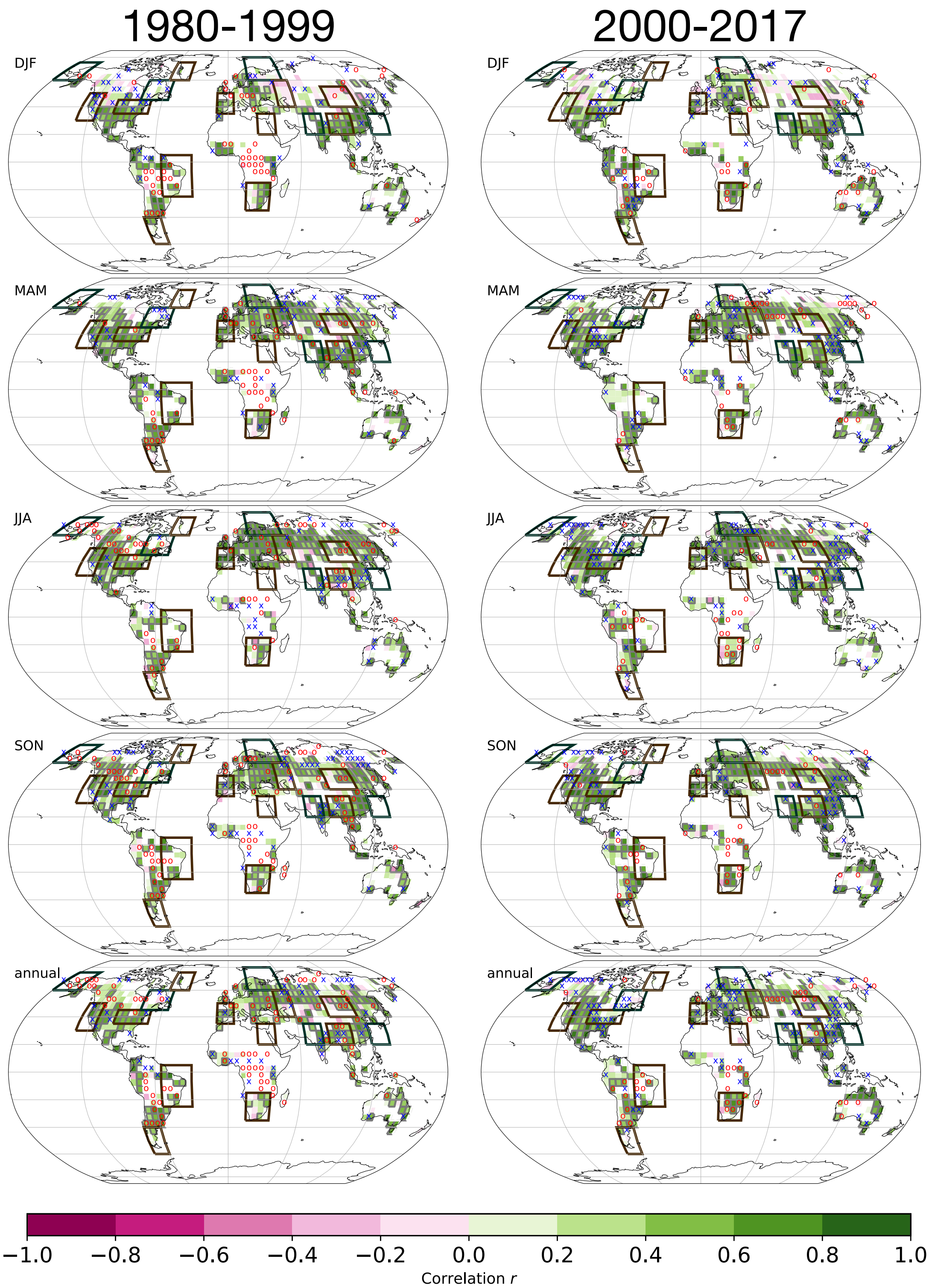

Figure 5.9: As for Fig. 5.7, for E_i.

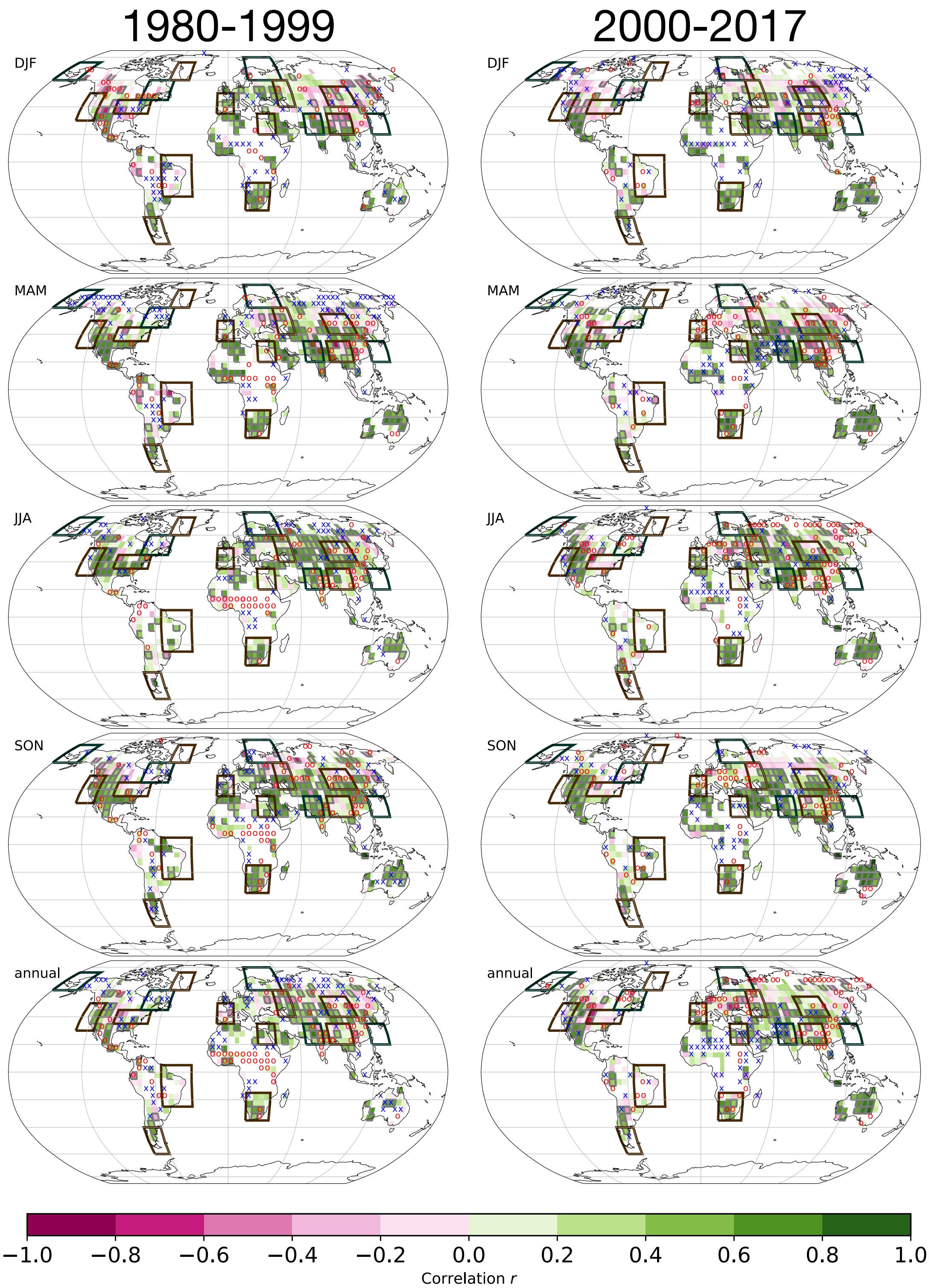

Figure 5.10: As for Fig. 5.7, for E_b.

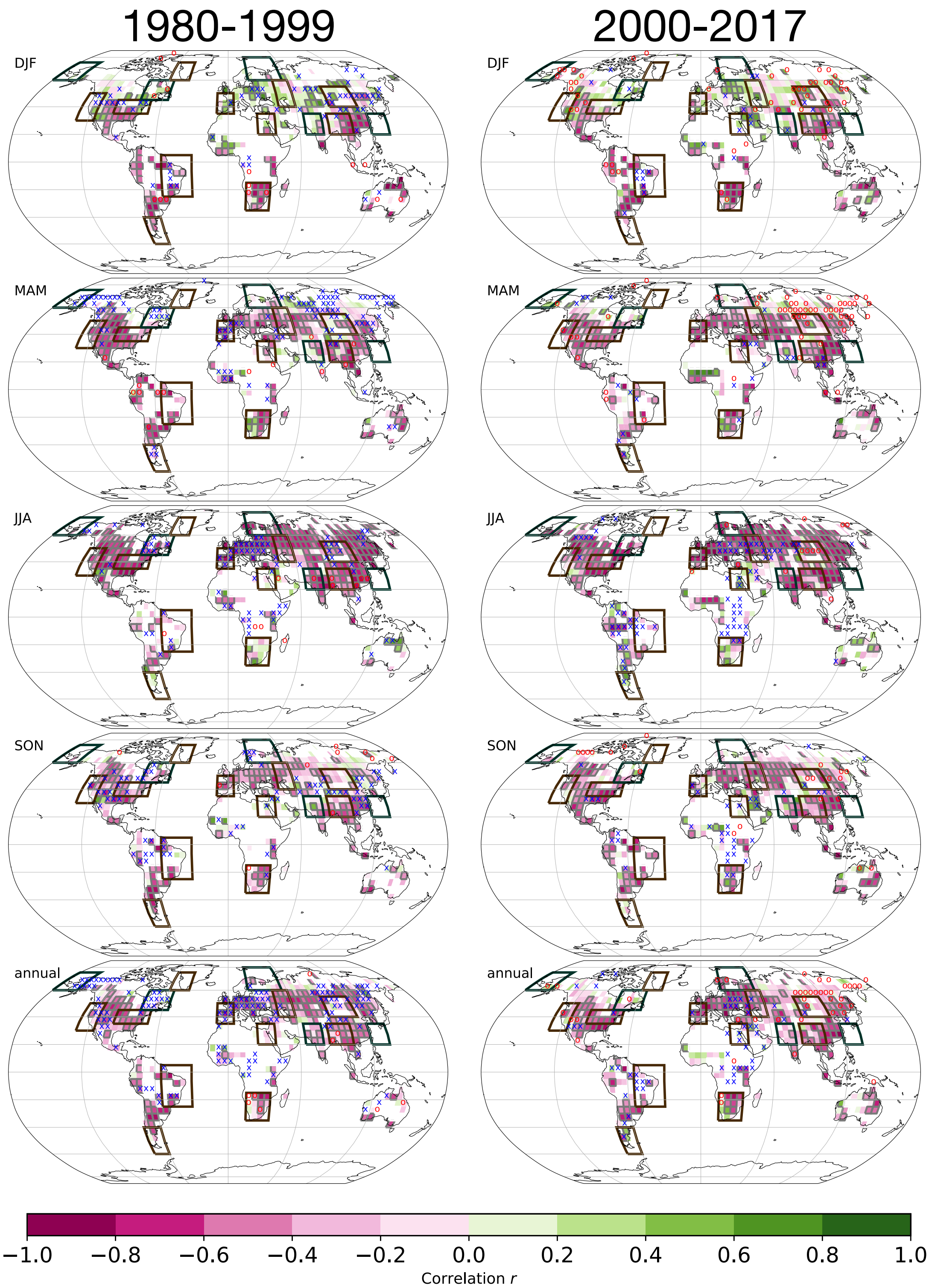

Figure 5.11: As for Fig. 5.7, for E_w.

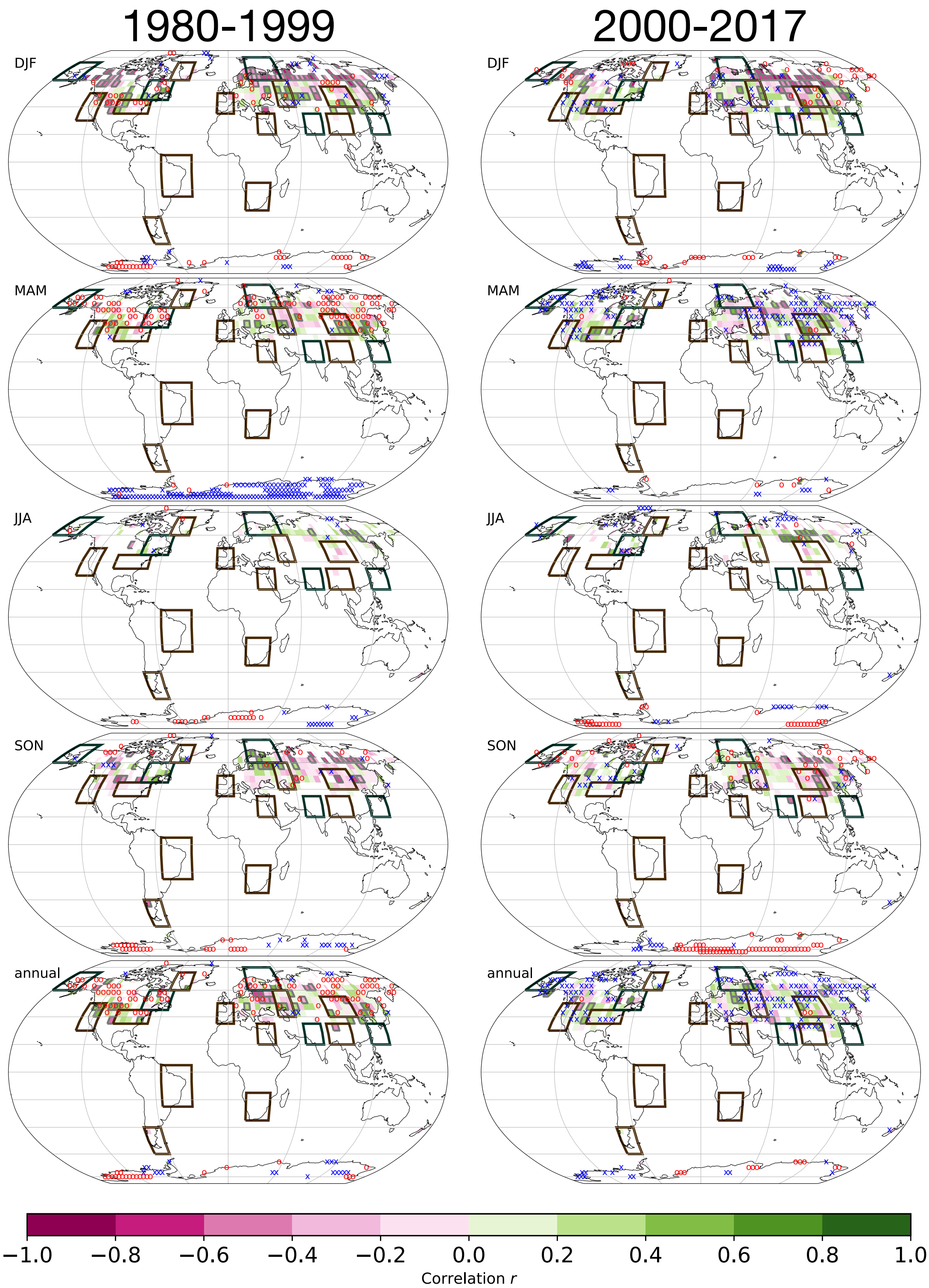

Figure 5.12: As for Fig. 5.7, for E_s.

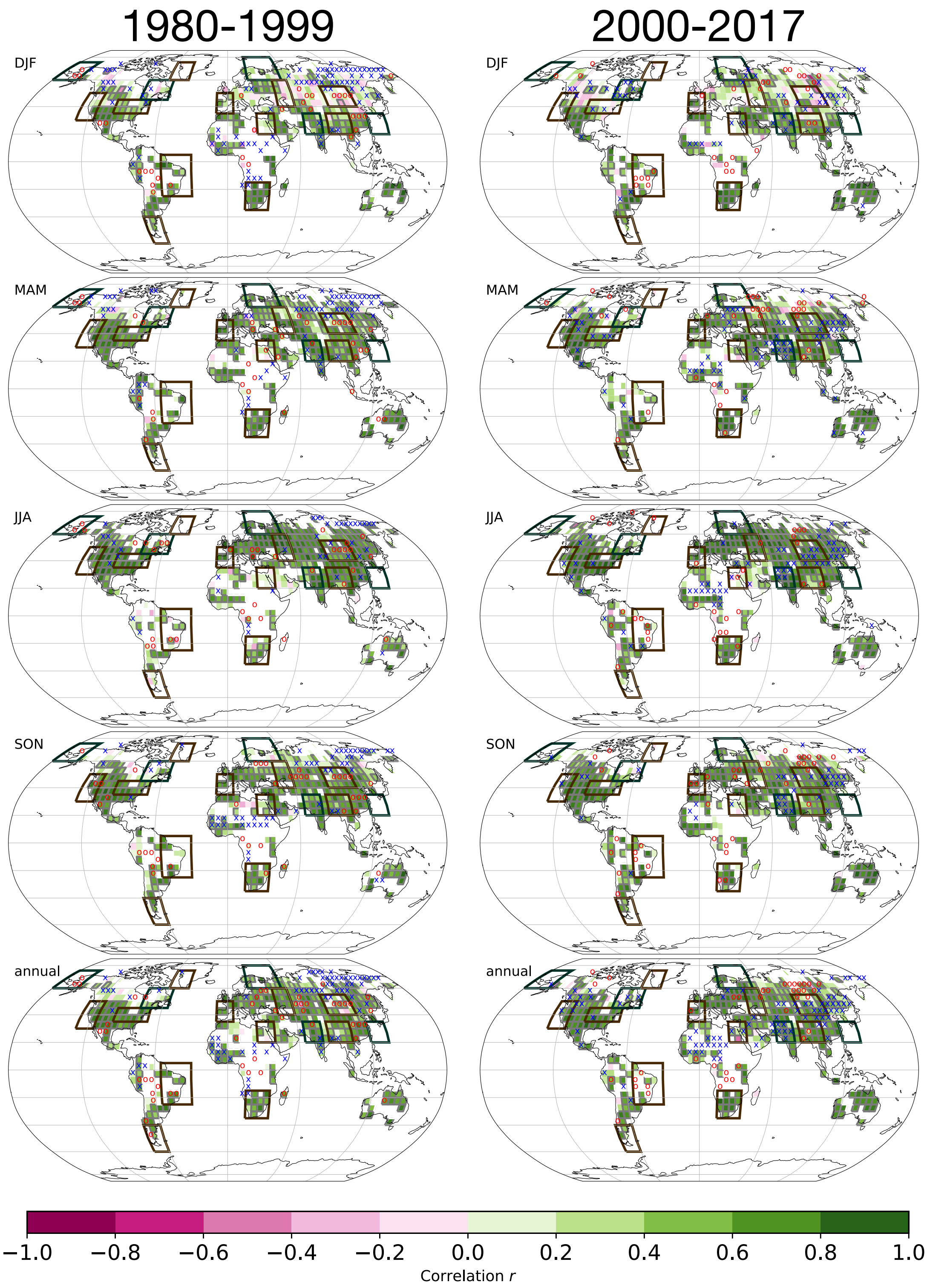

Figure 5.13: As for Fig. 5.7, for surface soil moisture.

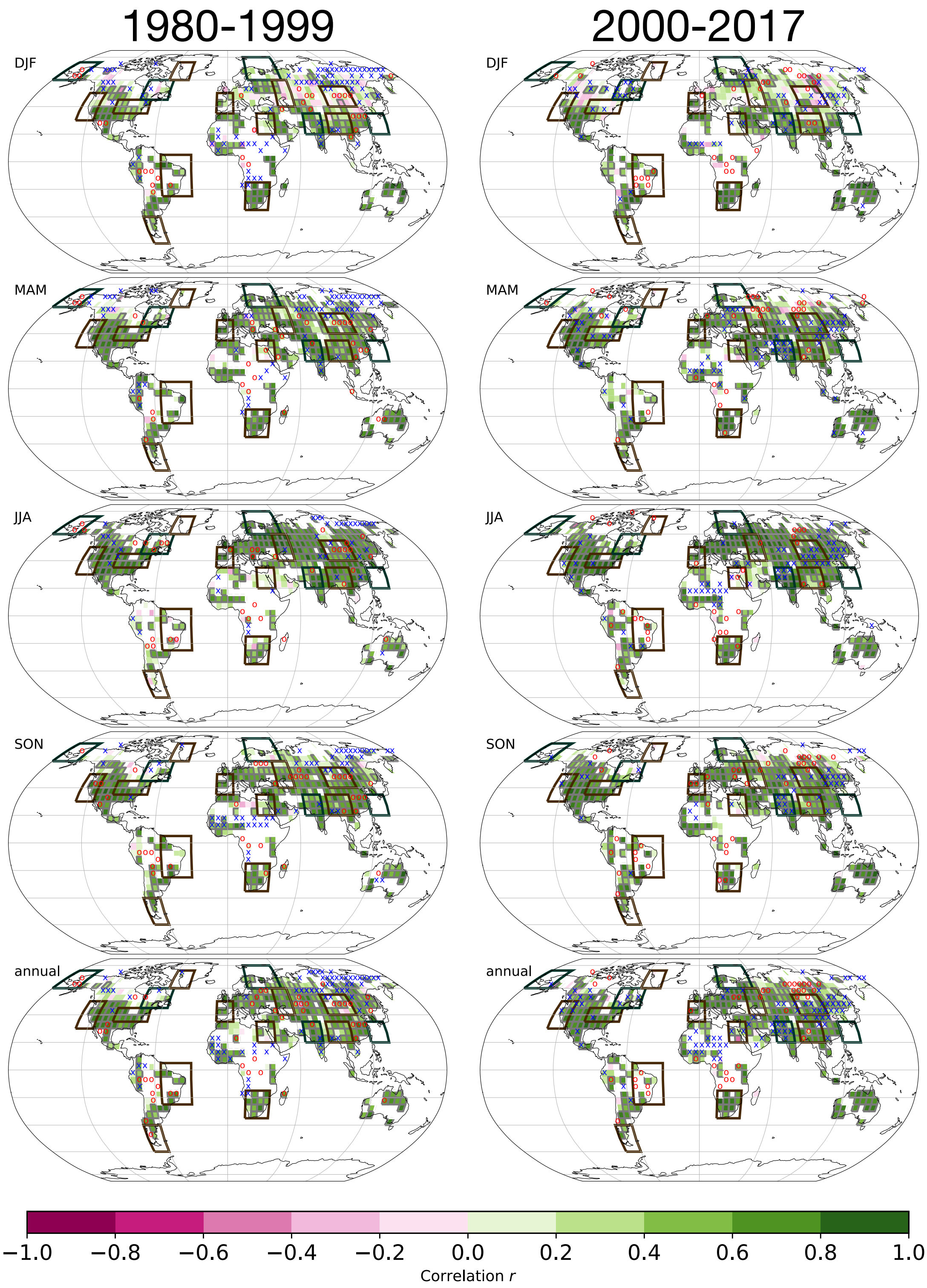

Figure 5.14: As for Fig. 5.7, for root-zone soil moisture.

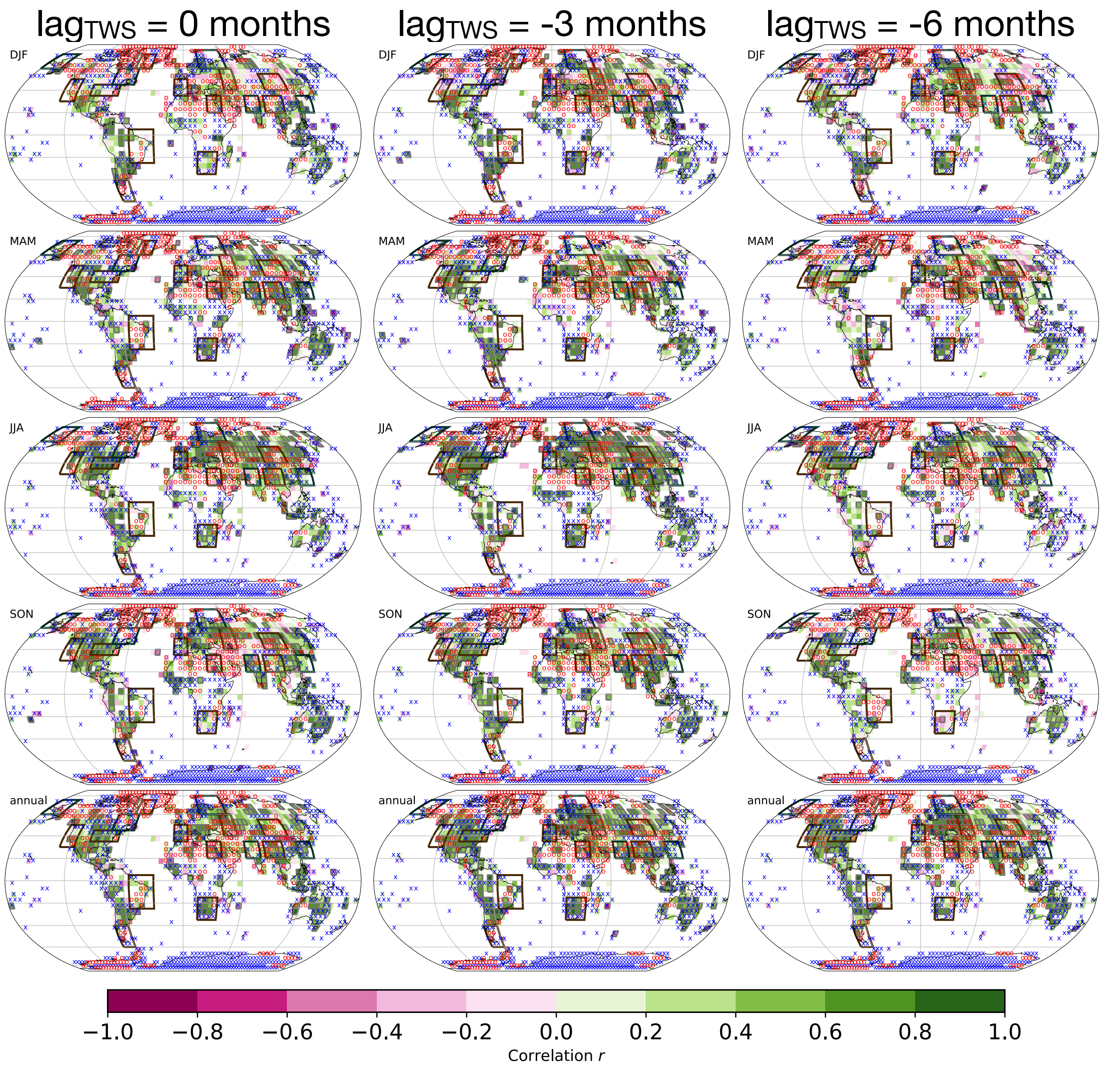

Figure 5.15: Correlations between the detrended GRACE TWS and HadISDH RH anomalies over land for annual data (bottom) and the four standard seasons (upper four rows) over the late period (2002–2017) with no temporal lag (left column), a temporal lag of -3 months (centre column) and a temporal lag of -6 months (right column) for TWS. Grid boxes of significant correlations ($p < 0.1$) are framed grey; significantly positive (negative) trends in TWS relative to the climatology over the 2005–2009 period show a blue ‘x’ (red ‘o’).

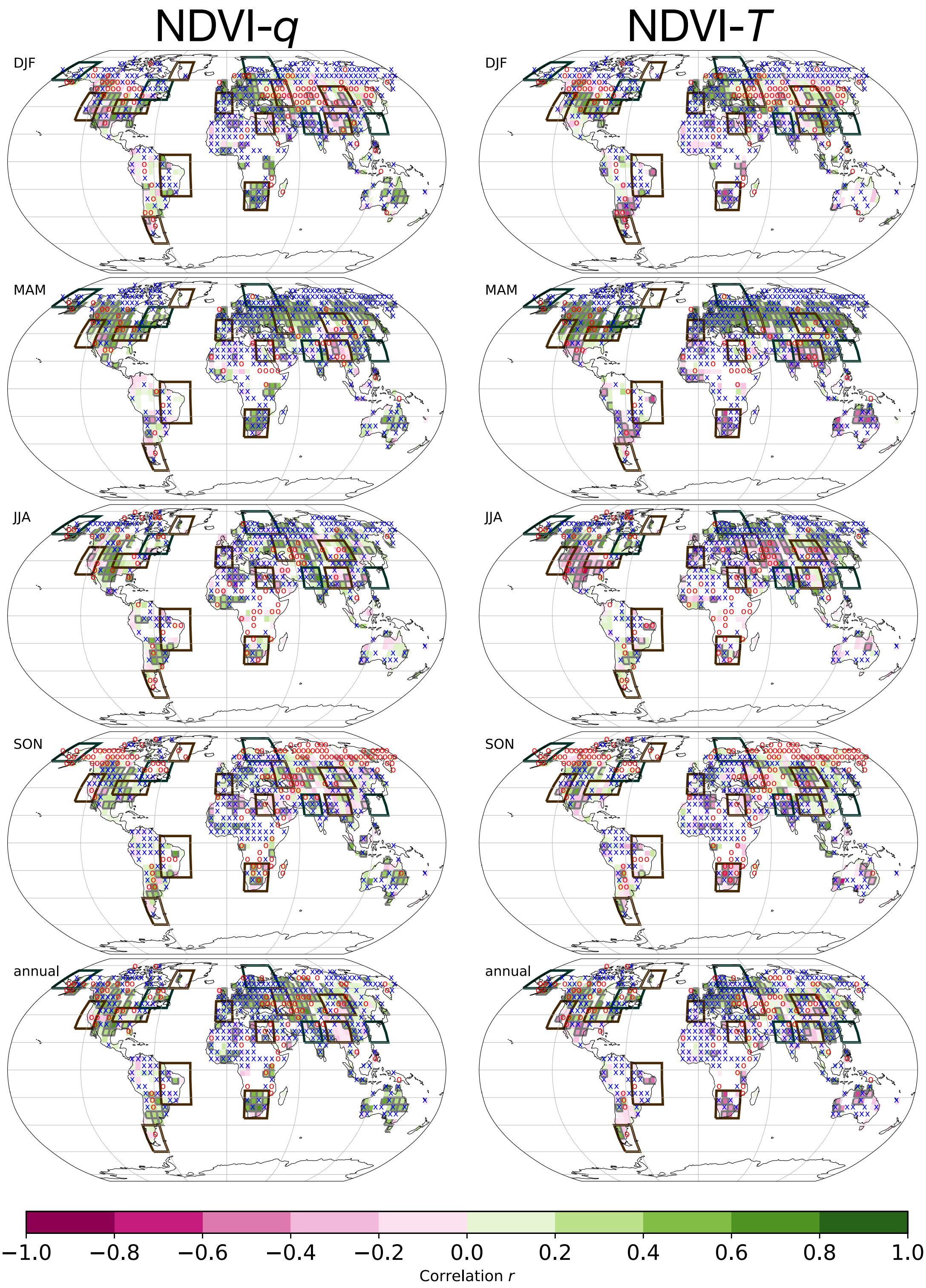

Figure 5.16: Correlations between the detrended GIMMS NDVI and HadISDH q and T anomalies over land for annual data (bottom) and the four standard seasons (upper four rows) over the full period (1982–2015). Grid boxes of significant ($p < 0.1$) correlations are framed in grey; significantly positive (negative) trends in the NDVI relative to the climatology over the 1982–2010 period show a blue 'x' (red 'o').

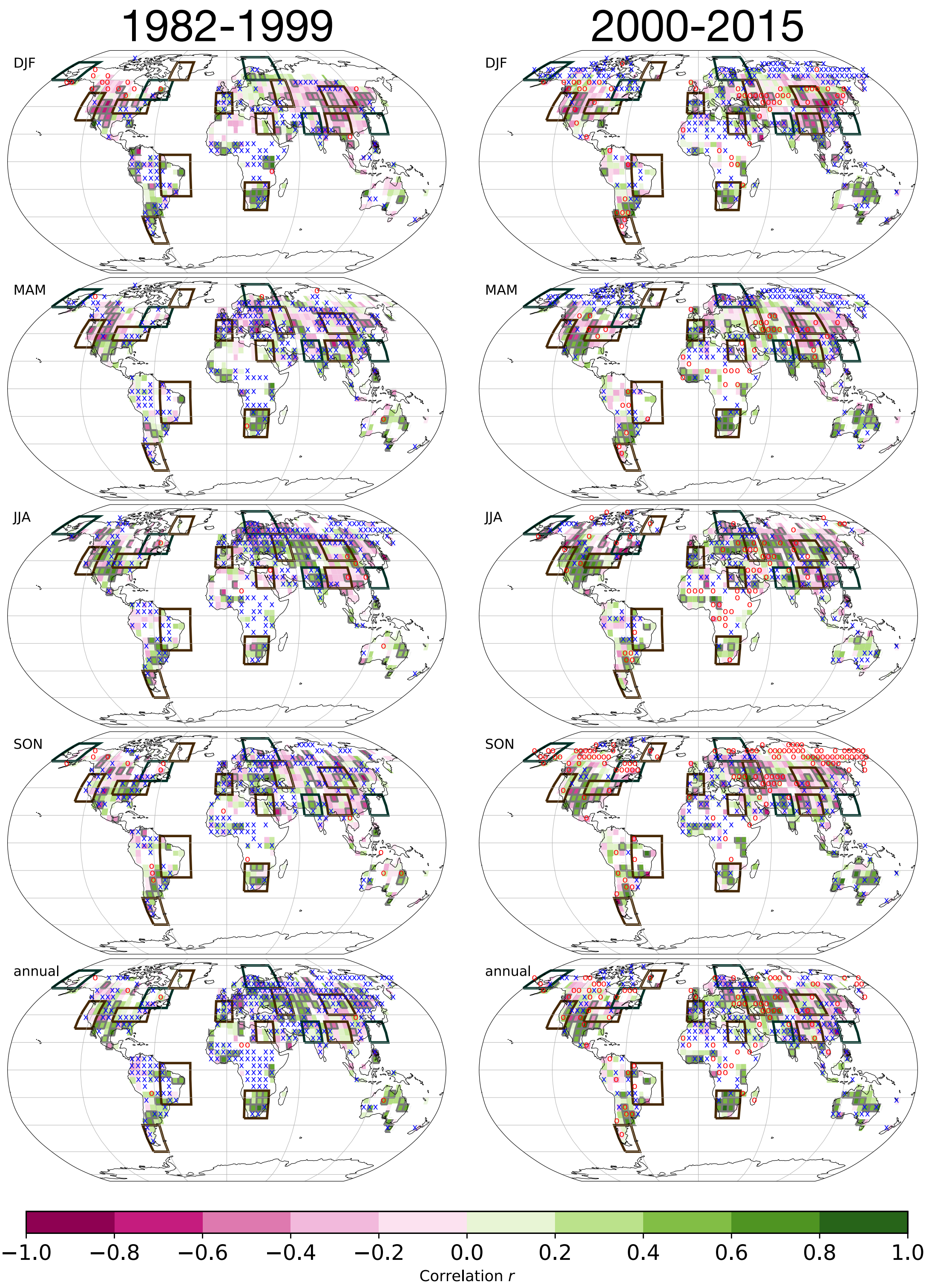

Figure 5.17: Correlations between the detrended GIMMS NDVI and HadISDH RH anomalies over land for annual data (bottom) and the four standard seasons (upper four rows) over the early (1982–1999), the late (2000–2015) and the full period (1982–2015). Grid boxes of significant correlations ($p < 0.1$) are framed grey; significantly positive (negative) trends in the NDVI relative to the climatology over the 1982-2010 period show a blue 'x' (red 'o').

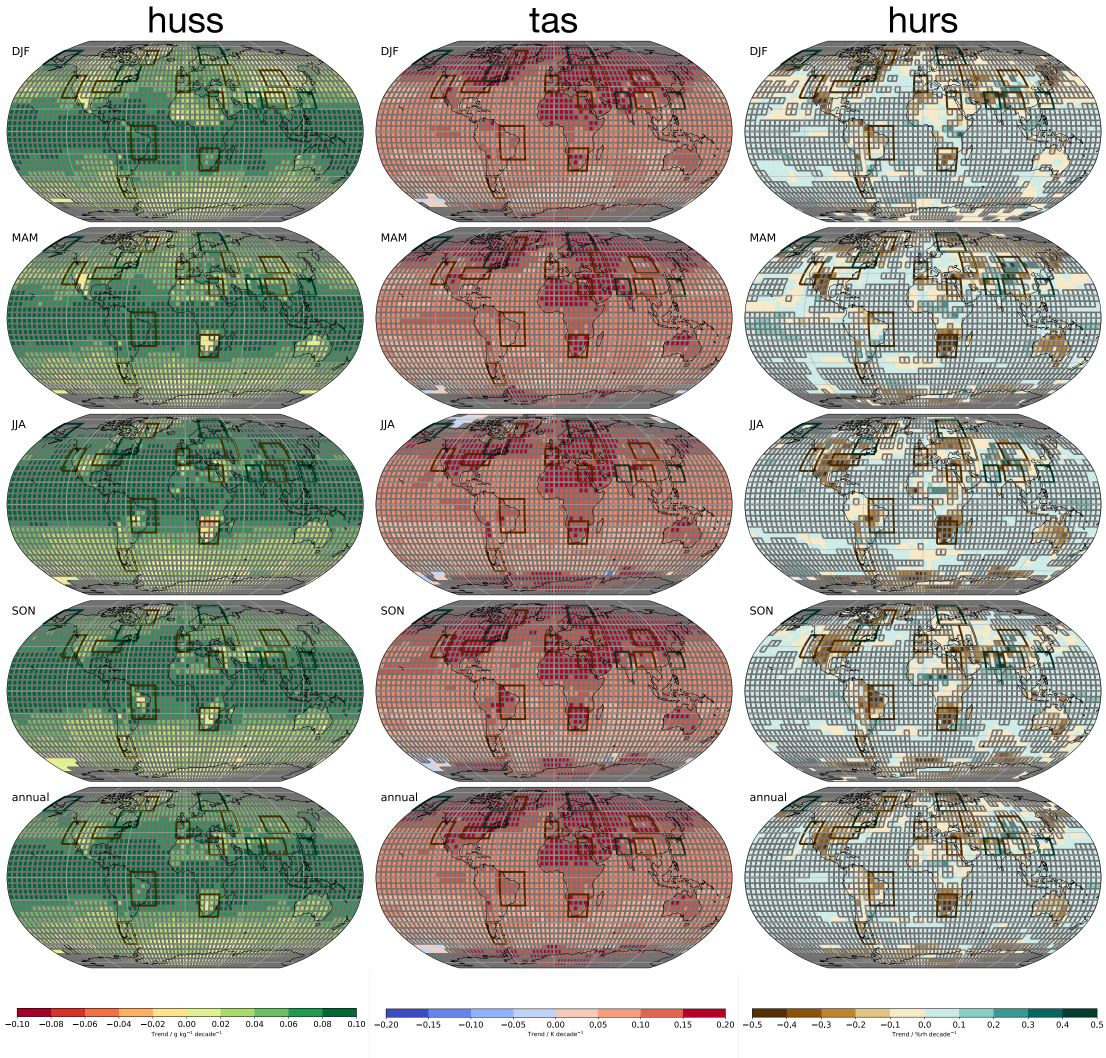

Figure 5.18: Seasonal HadGEM2-ES huss (q), tas (T) and hurs (RH) trends for the experiment $esmFdbk2$ for the full period (1860–2099) relative to a climatology over the 1981–2010 period. Grid boxes of very significant trends separately ($p < 0.05$) are framed in grey. Regions with a strong average trend in RH in the late period in the HadISDH observations are framed in ochre (negative trends) and turquoise (positive trends).

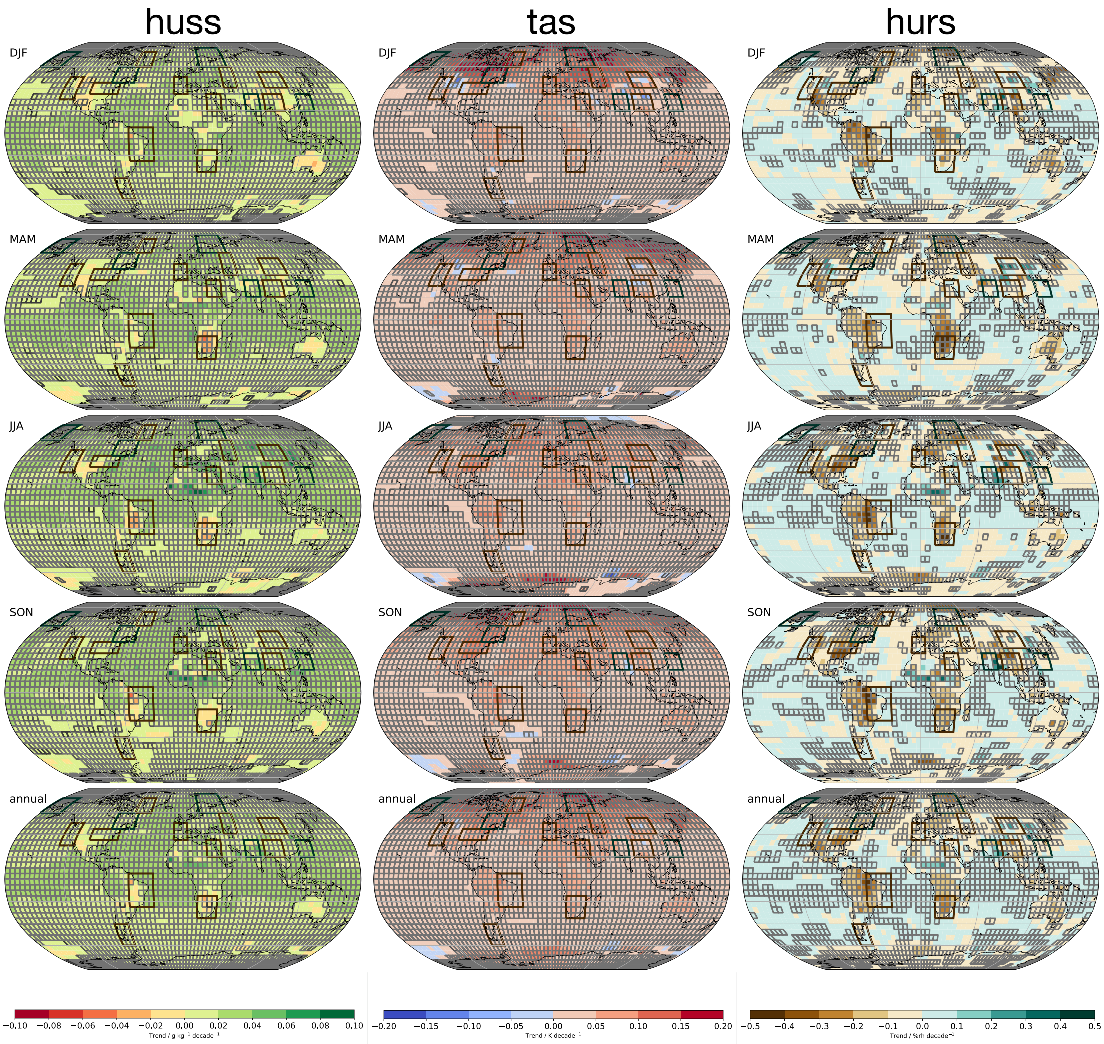

Figure 5.19: As for Fig. 5.18, for HadGEM2-ES $esmFixClim2$.

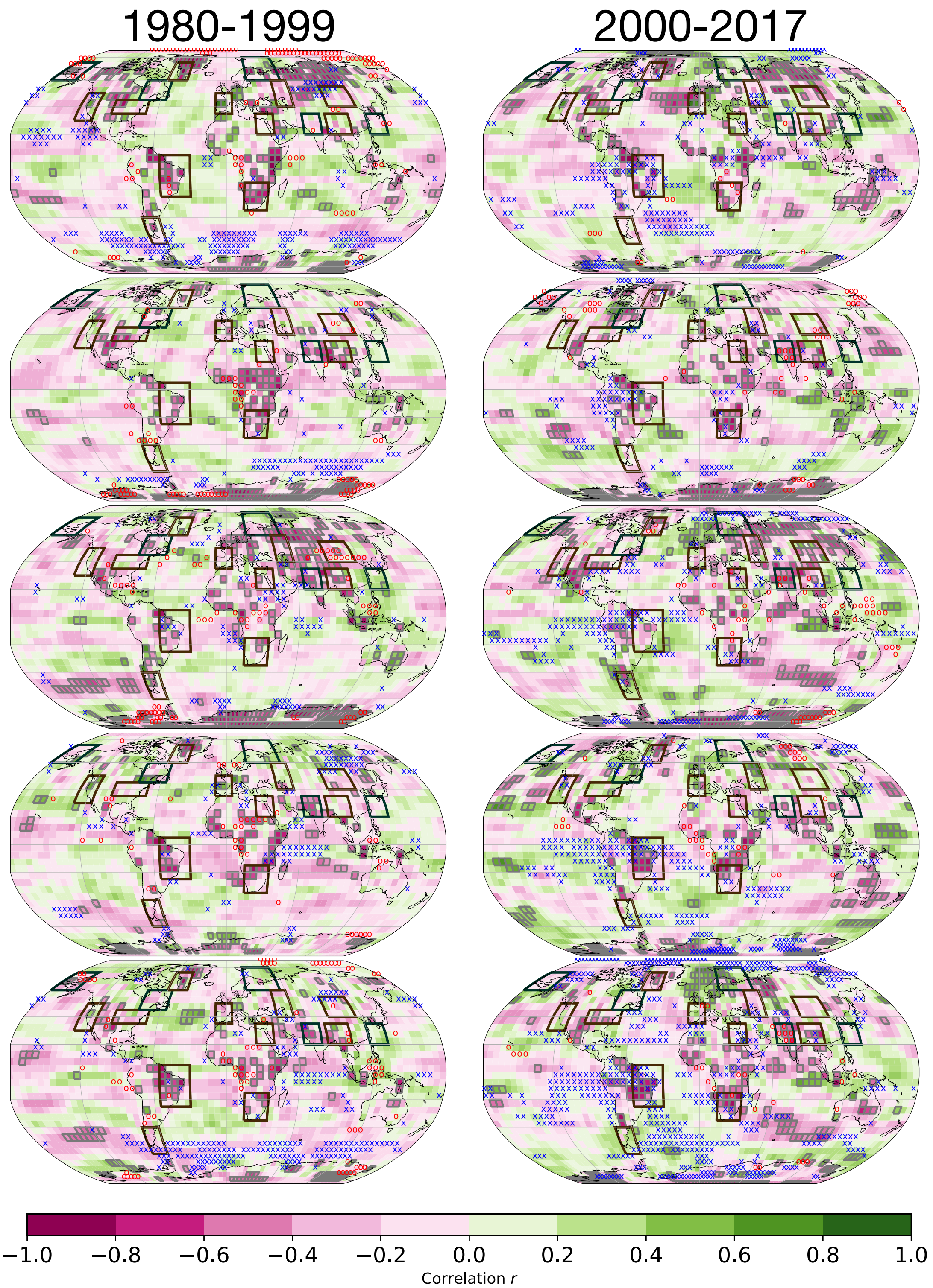

Figure 5.20: Correlations between the detrended ERA-Interim wind speed and GLEAM E over land for annual data (bottom) and the four standard seasons (upper four rows) over the early (1980–1999) and the late periods (2000–2017). Grid boxes of significant ($p < 0.1$) correlations are framed in grey; significantly positive (negative) trends in si10 relative to the climatology over the 1982–2010 period show a blue 'x' (red 'o').

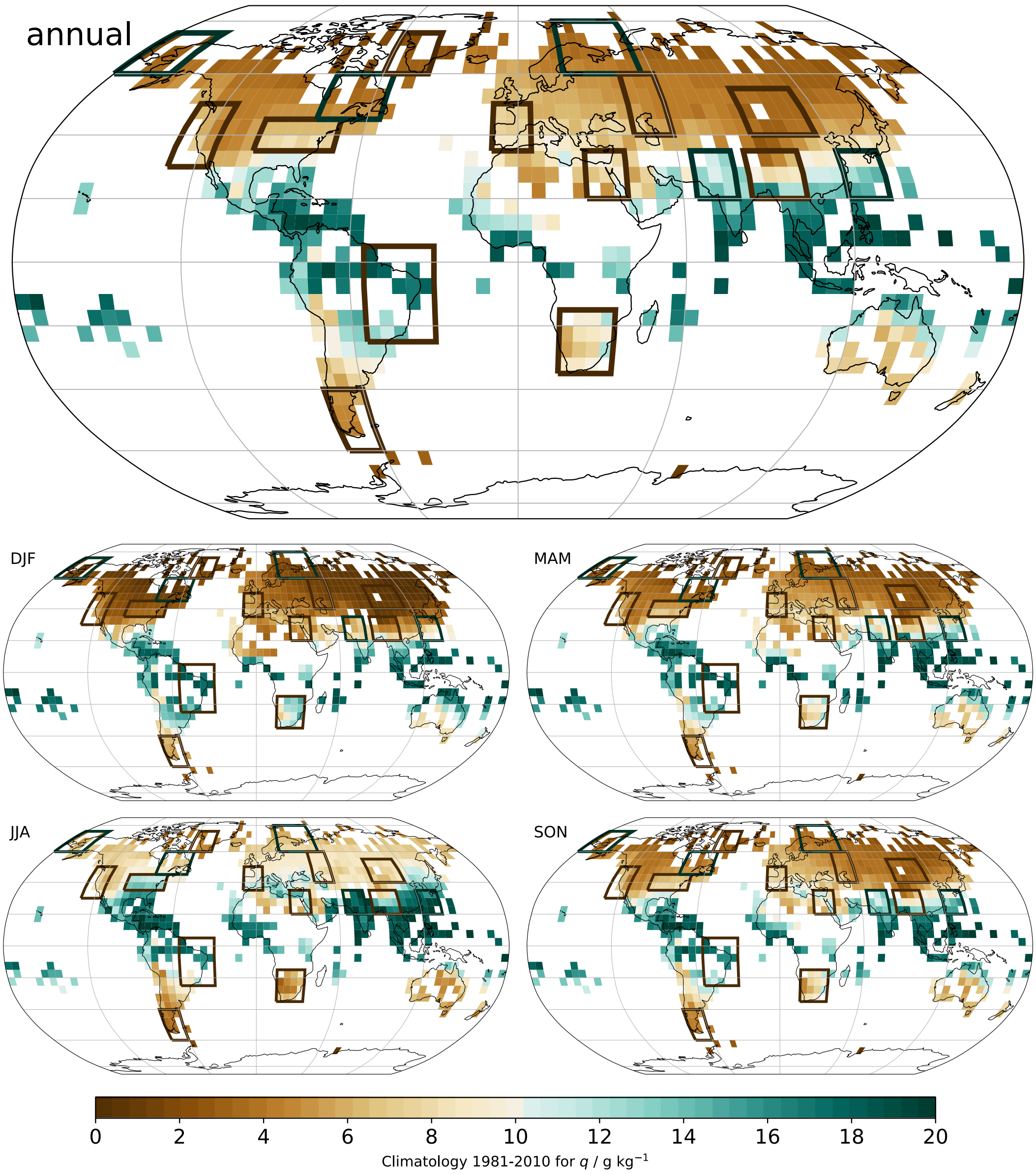

Figure S1: As for Fig. 1.1, for q.

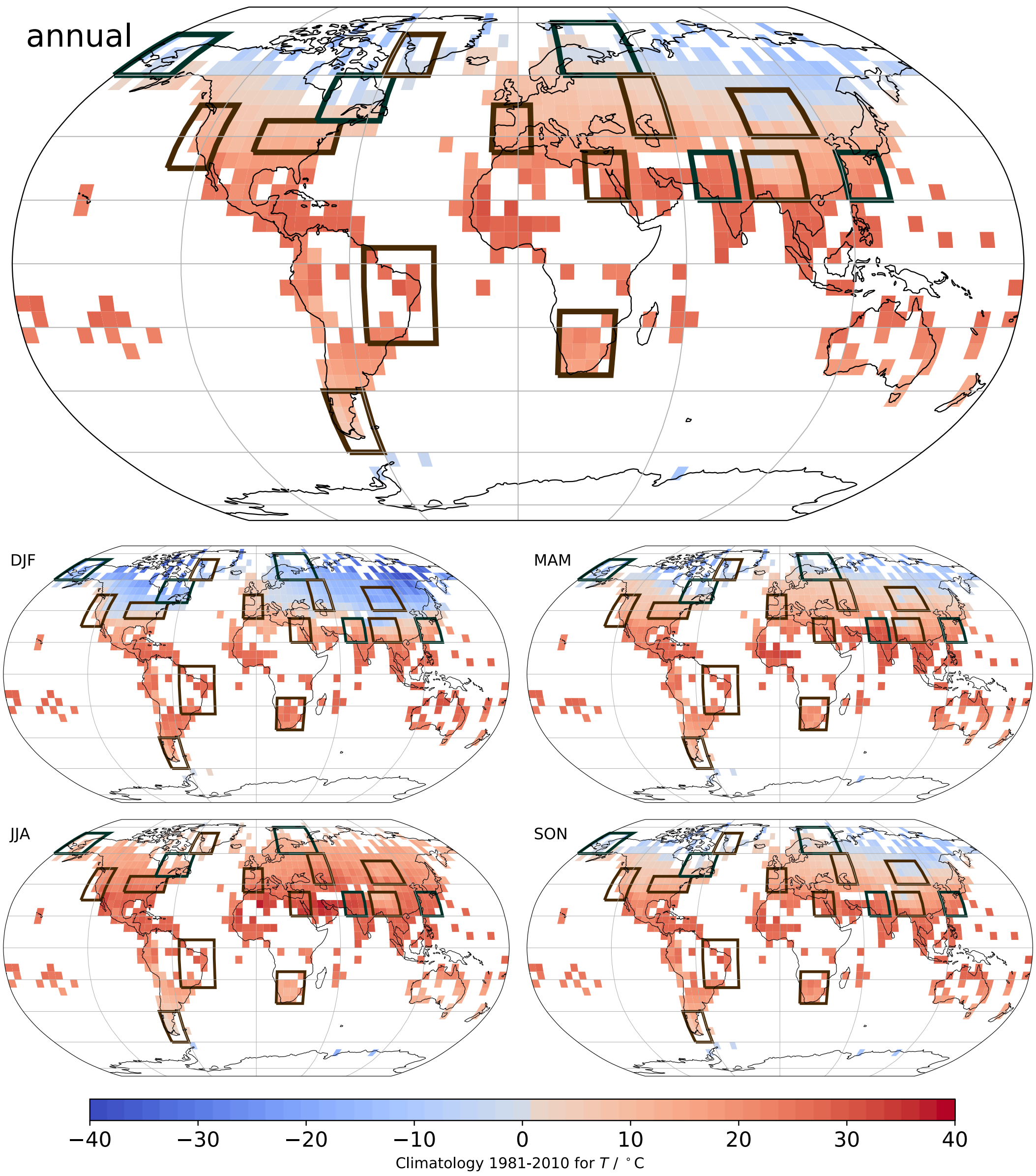

Figure S2: As for Fig. 1.1, for T.

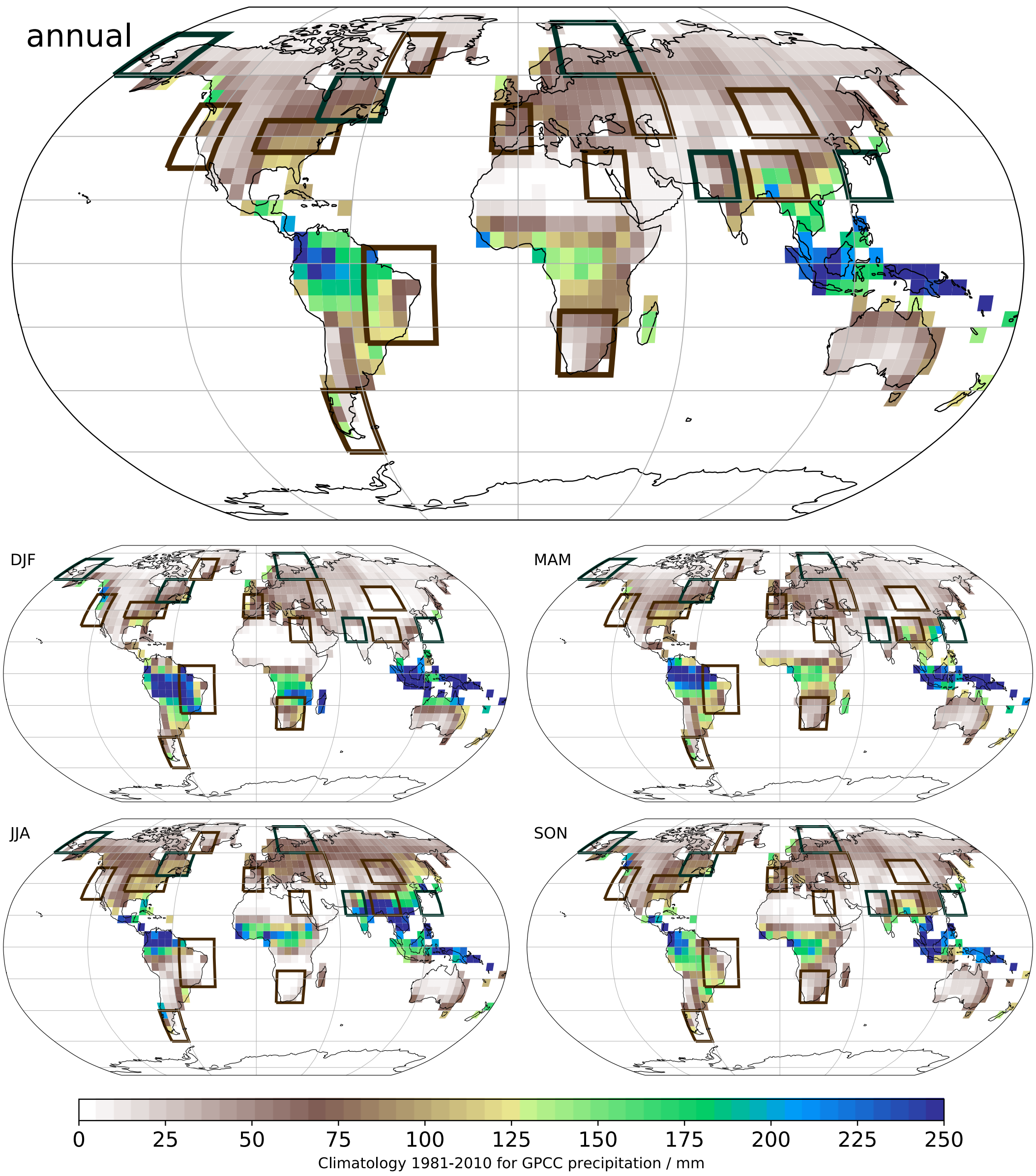

Figure S3: As for Fig. 1.1, for GPCC precipitation.

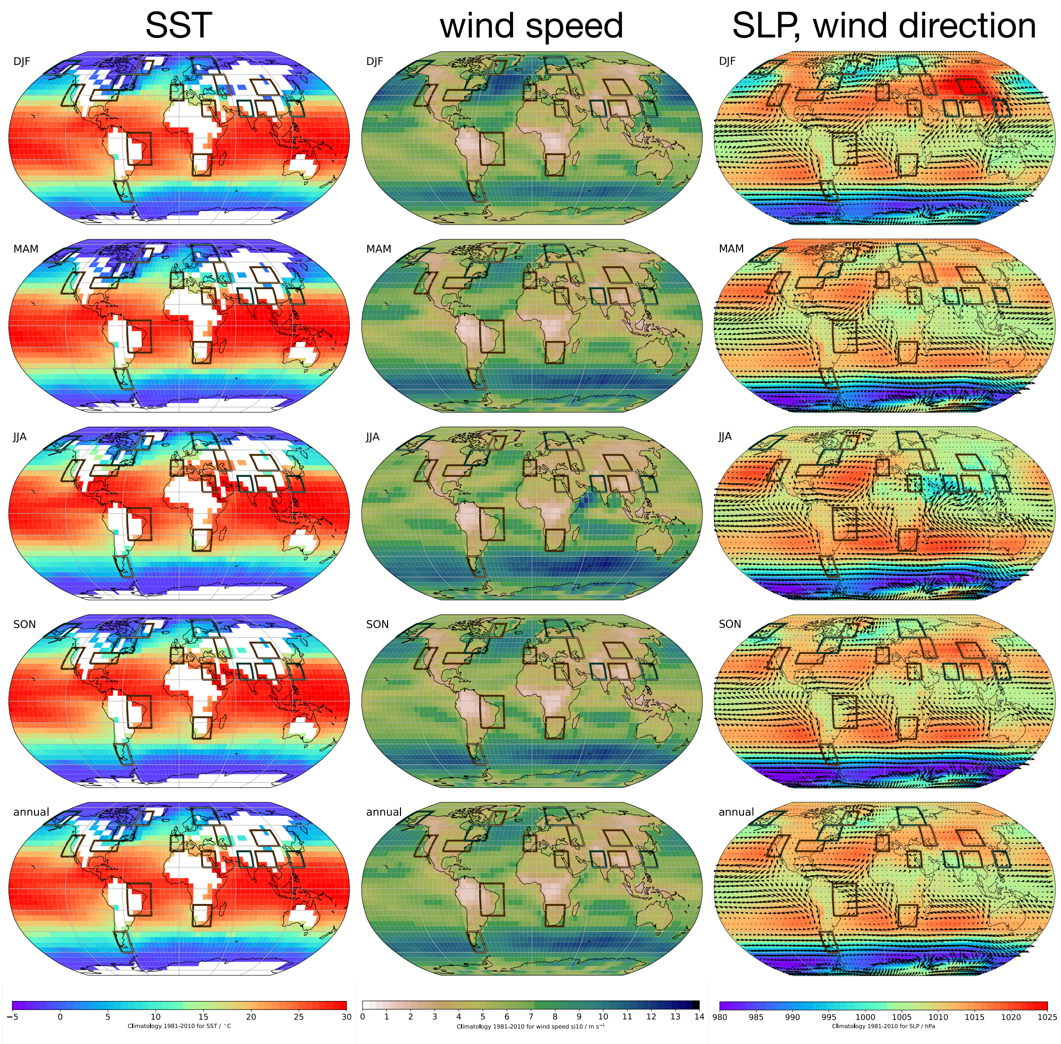

Figure S4: As for Fig. 1.1, for ERA-Interim SST, wind speed, SLP and 10 m wind vectors (left to right).

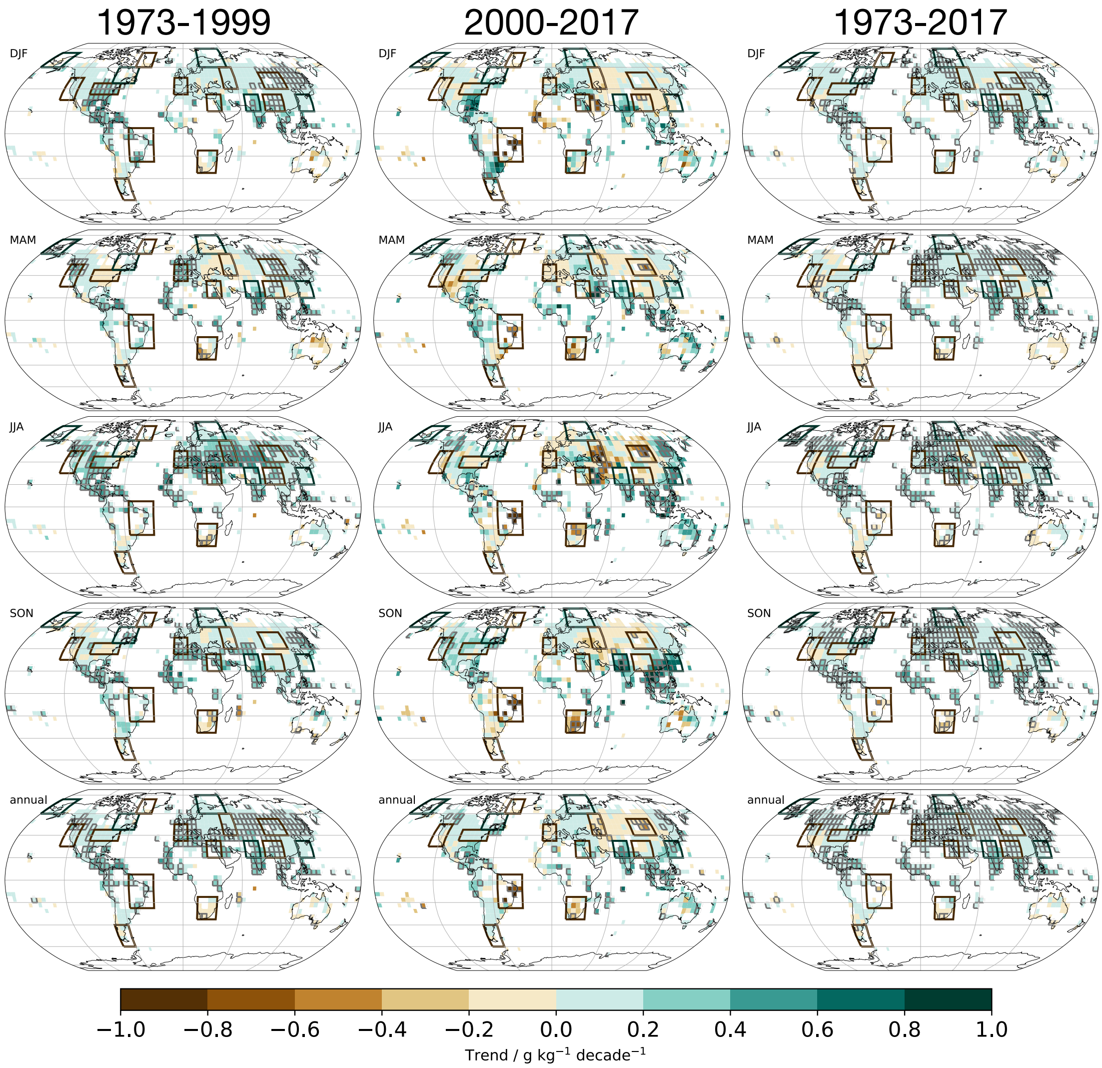

Figure S5: As for Fig. 1.5, for seasonal HadISDH q trends for the early period (1973-1999, left column), the late period (2000-2017, centre column) and the full period (right column).

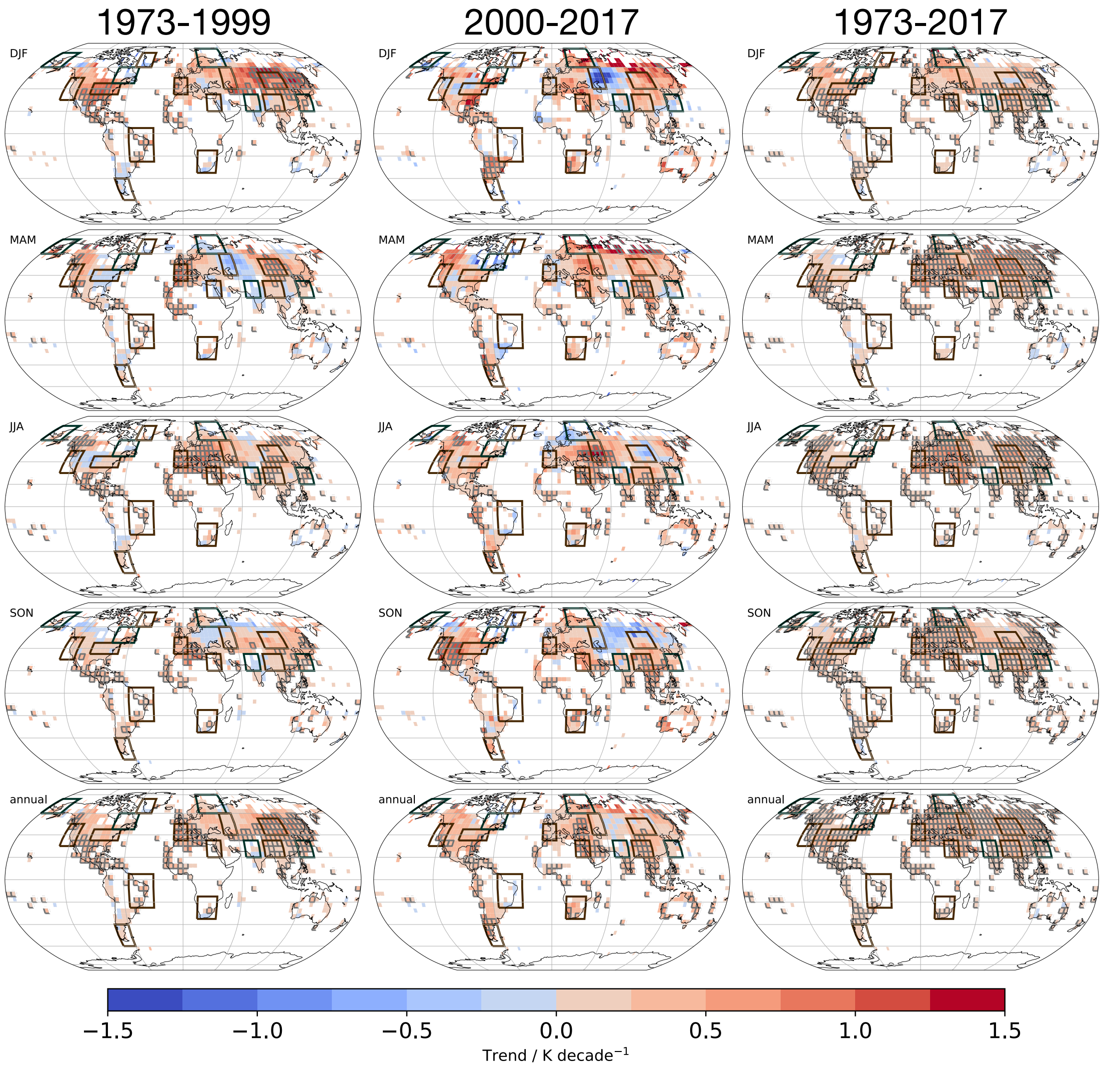

Figure S6: As for Fig. 1.5, for seasonal HadISDH T trends for the early period (1973-1999, left column), the late period (2000-2017, centre column) and the full period (right column).

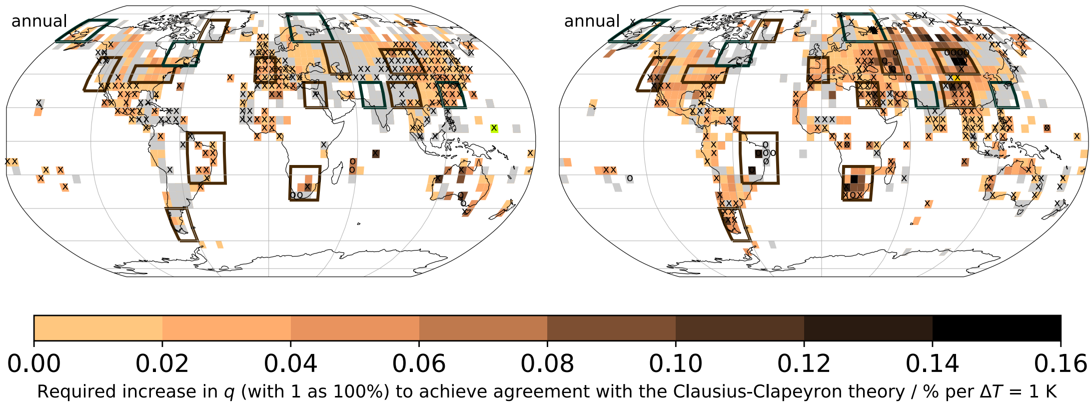

Figure S7: Annual deviations from the Clausius-Clapeyron equation (7% q increase for 1 K increase in T) as the required increase in q to achieve agreement with the theory over the early (left) and the late periods (right), for positive T trends and q increase $< 7\%/\text{K}$ only. Grid boxes with a significant ($p < 0.05$) decrease in q are marked with an 'o', with a significant increase in T are marked with an 'x'. Grey grid boxes indicate a T decrease or a q increase $> 7\%/\text{K}$.

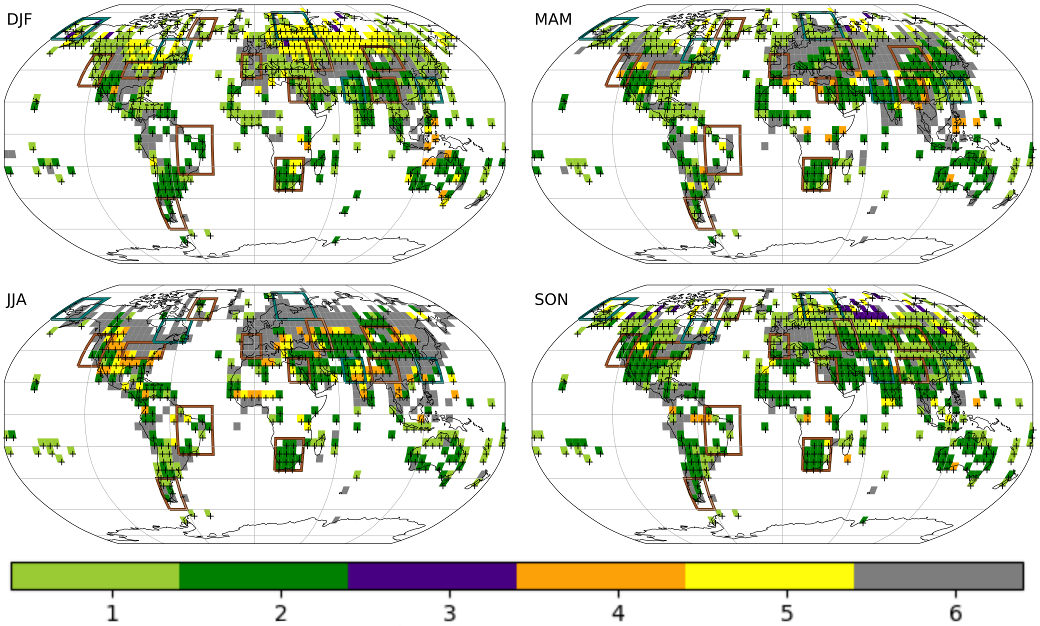

<table>
<tr><td colspan="5">If either of the absolute correlation r > 0.5, and the difference of their correlation strengths > 0.05:</td></tr>
<tr><td rowspan="2"></td><td colspan="2">Stronger <u>q-RH</u> correlation by comparison:</td><td colspan="2">Stronger <u>T-RH</u> correlation by comparison:</td></tr>
<tr><td>Positive T-RH correlation</td><td>Negative T-RH correlation</td><td>Positive T-RH correlation</td><td>Negative T-RH correlation</td></tr>
<tr><td>Positive q-RH correlation</td><td>Light green (1)</td><td>Dark green (2)</td><td>Purple (3)</td><td>Orange (4)</td></tr>
<tr><td>Negative q-RH correlation</td><td colspan="4">[not occuring]</td></tr>
<tr><td colspan="5">If either of the absolute correlation r > 0.5, and the difference of their correlation strengths < 0.05: Yellow (5)</td></tr>
<tr><td colspan="5">If none of the absolute correlation is r > 0.5: Grey (6)</td></tr>
</table>

Figure S8: Similar to Fig. 3.8, the coexistence of seasonal HadISDH q-RH and T-RH correlations ($r > 0.45$).

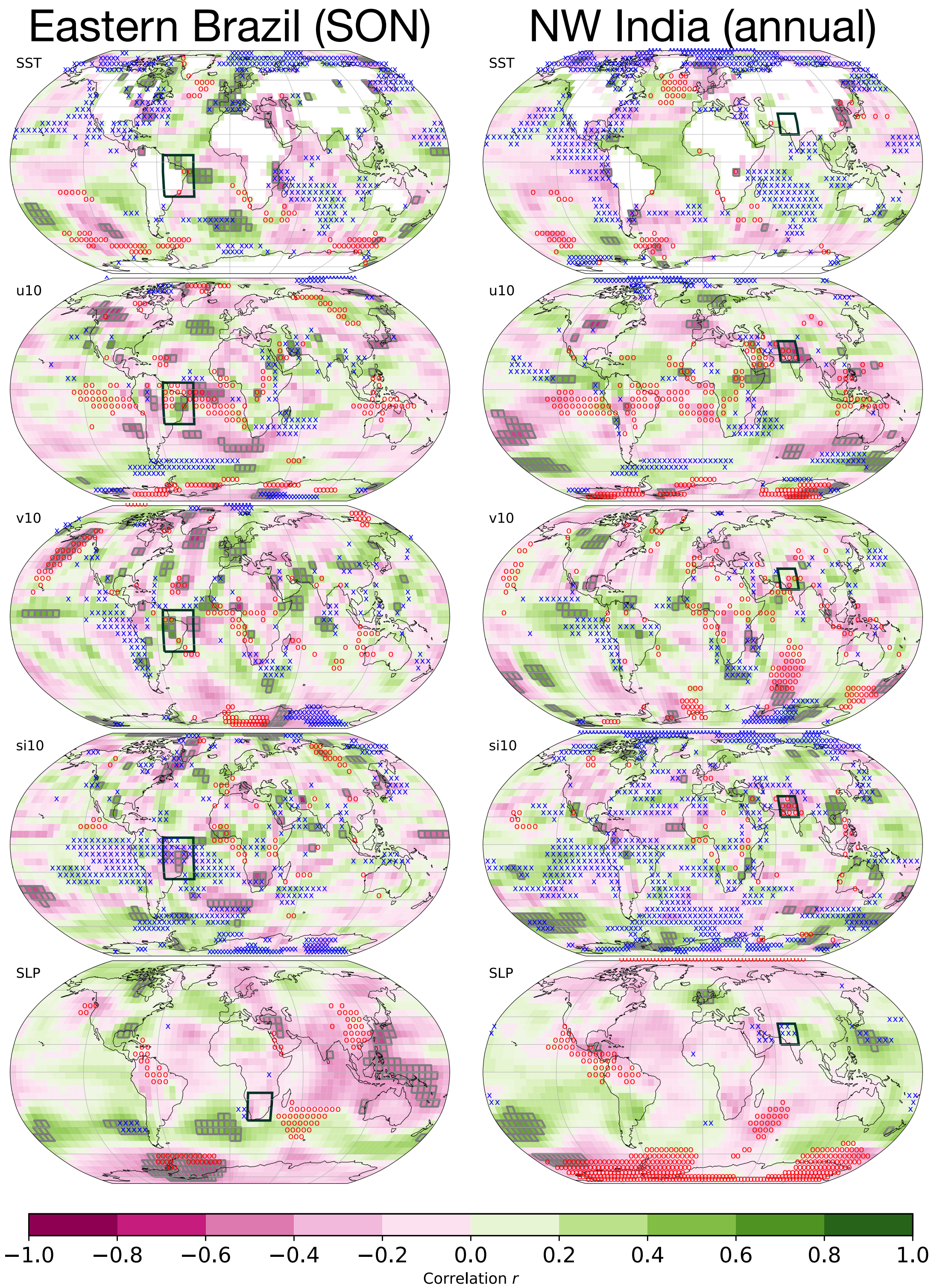

Figure S9: As for Fig. 4.3, for eastern Brazil (SON) and northwestern India (annual).

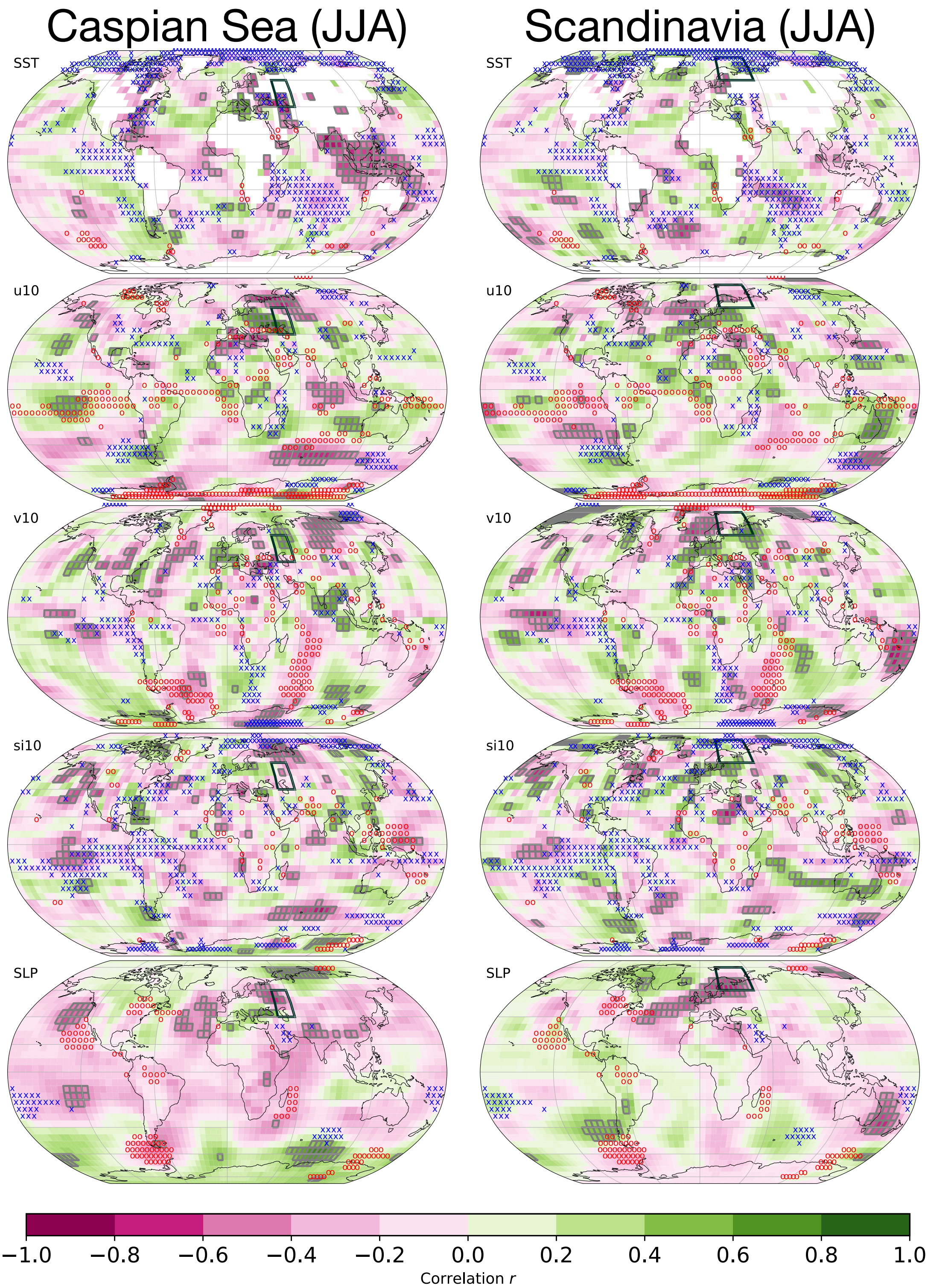

Figure S10: As for Fig. 4.3, for the Caspian Sea region (JJA) and Scandinavia (JJA).

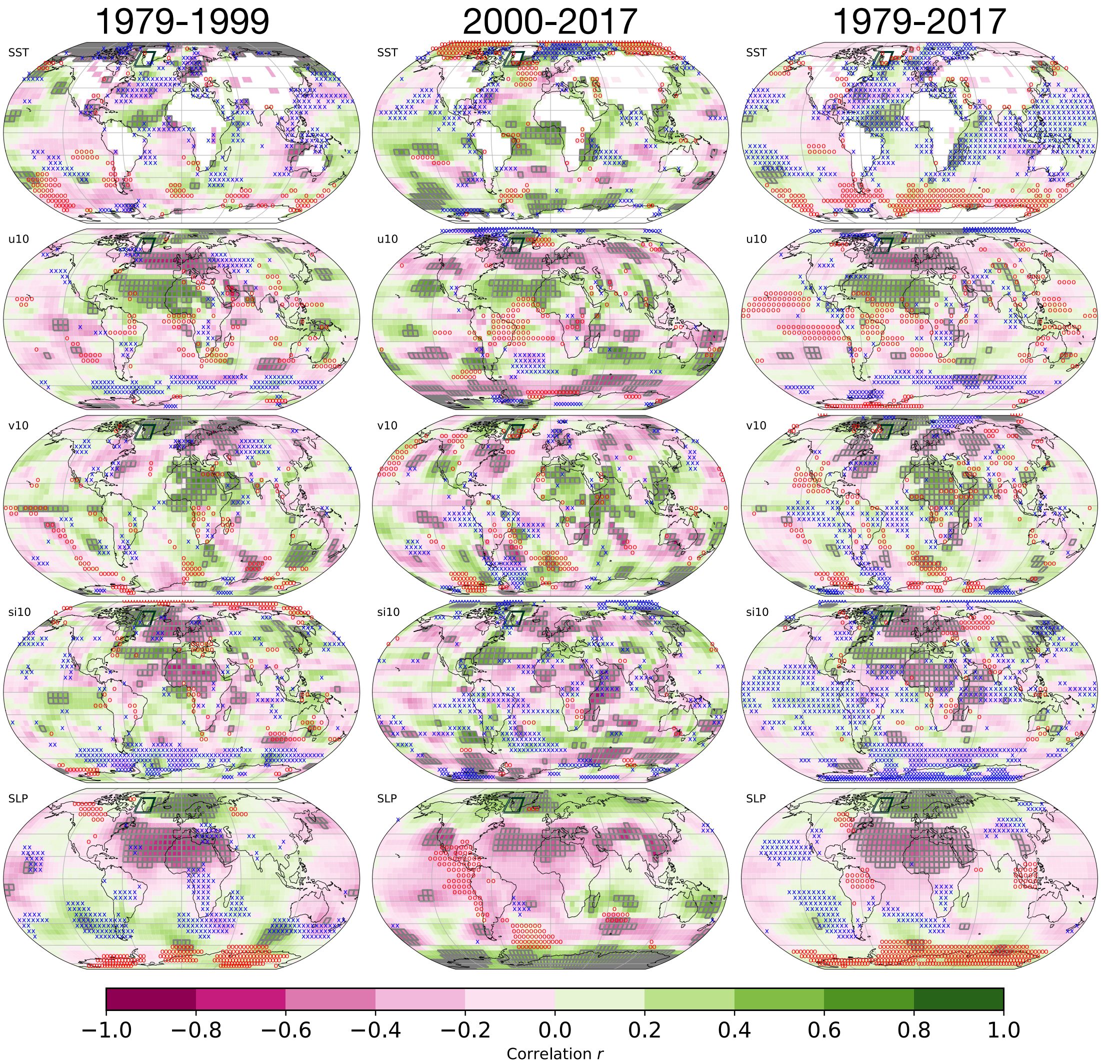

Figure S11: As for Fig. 4.4, for southwestern Greenland (DJF).

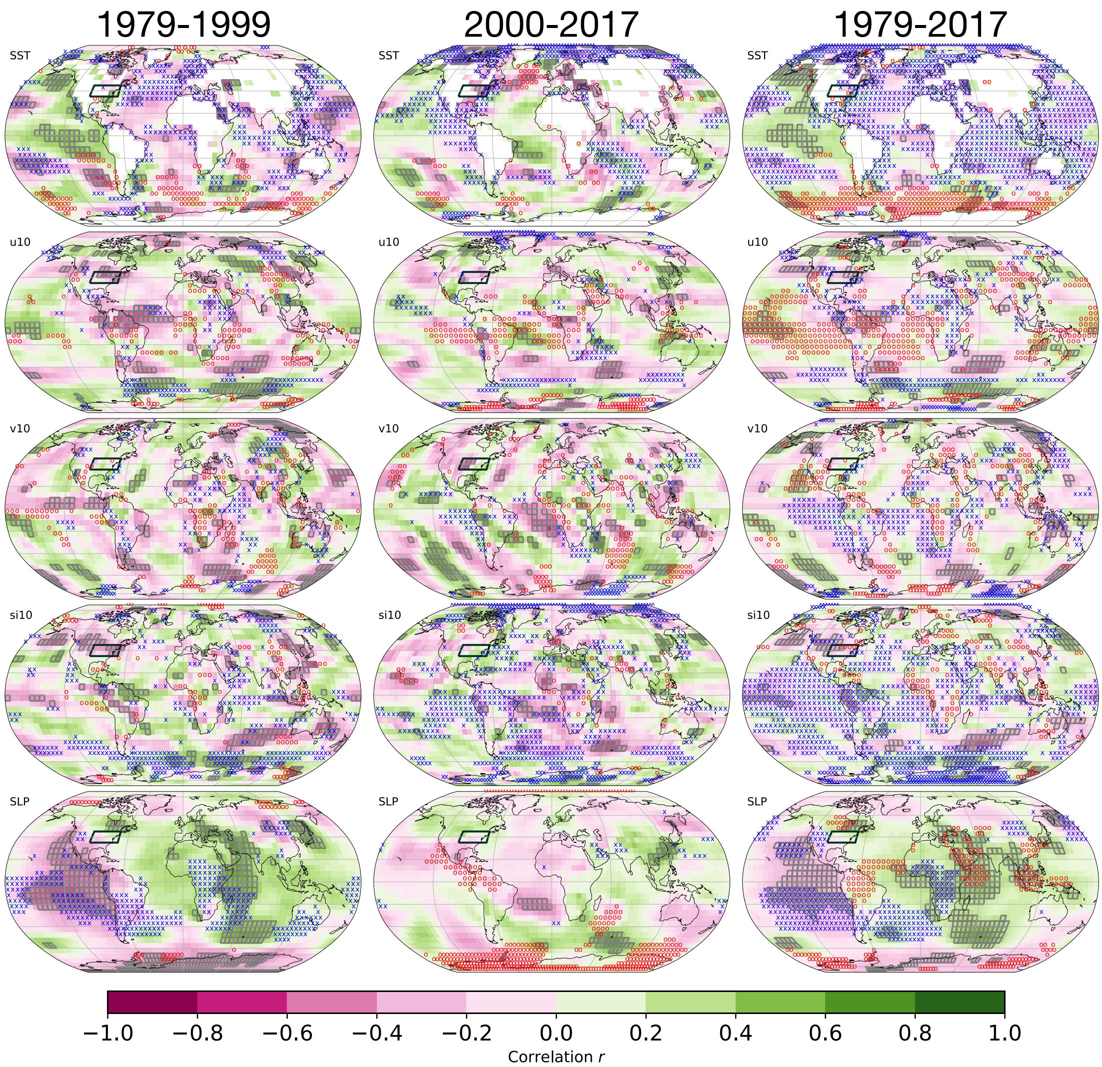

Figure S12: As for Fig. 4.4, for the eastern USA (annual).

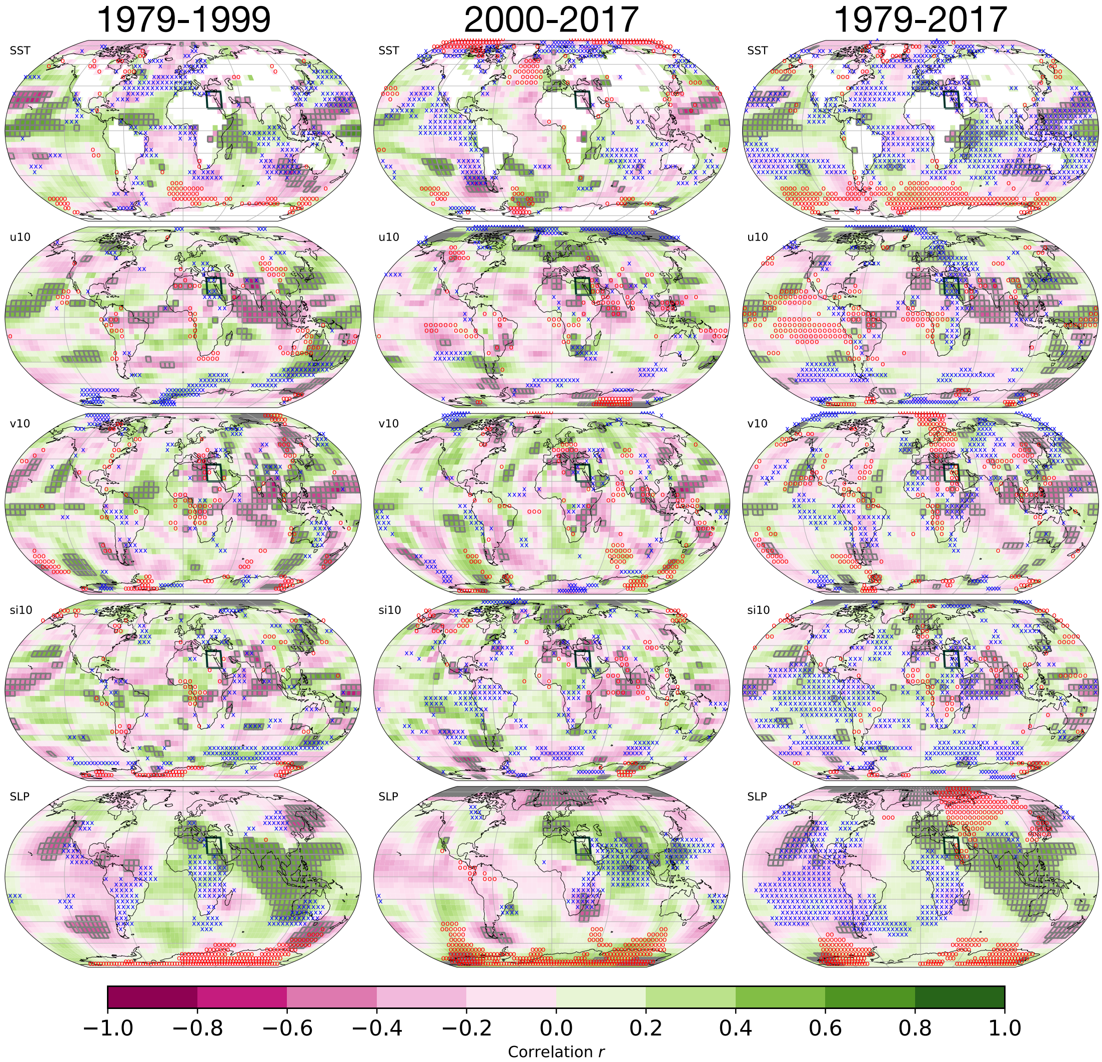

Figure S13: As for Fig. 4.4, for the Red Sea region (MAM).

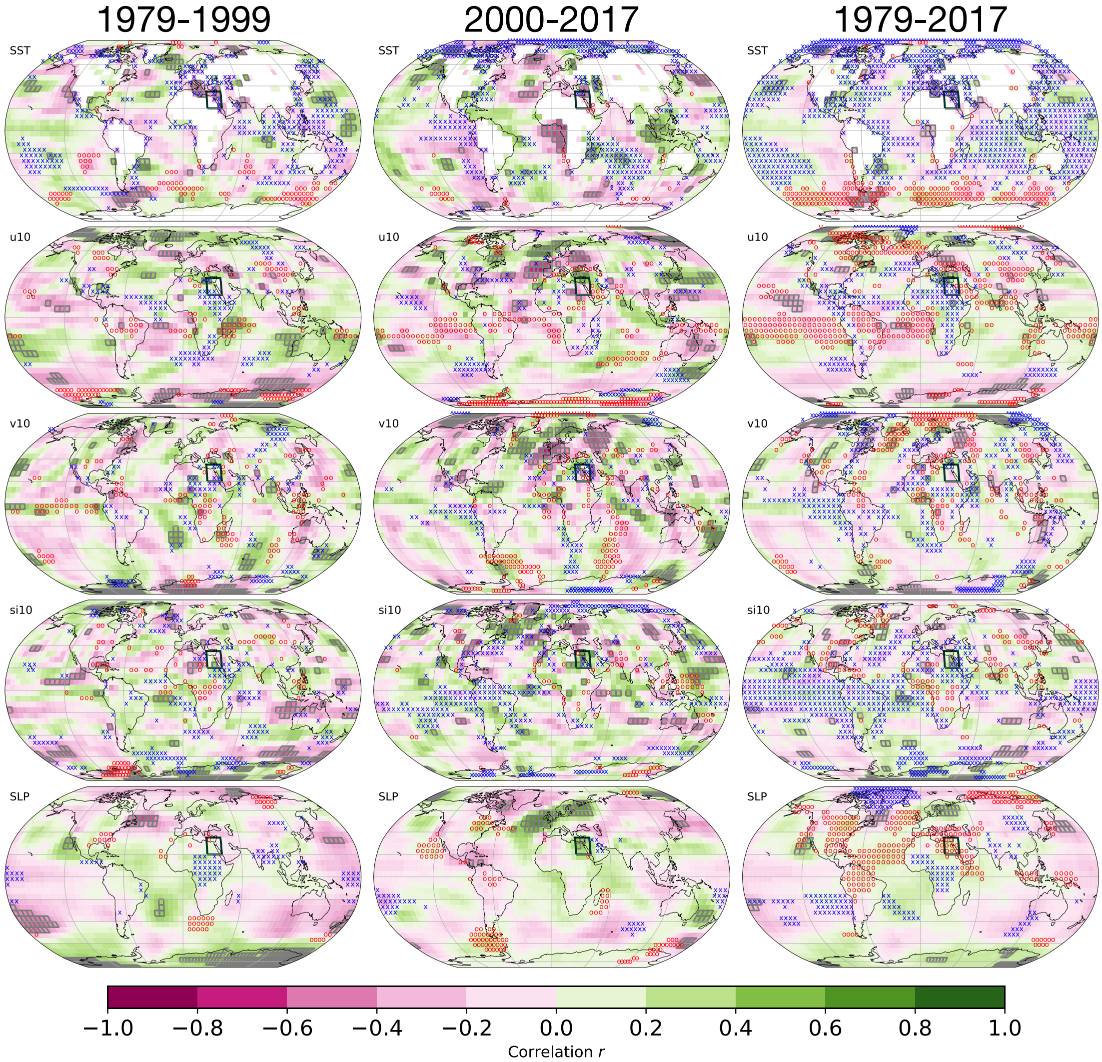

Figure S14: As for Fig. 4.4, for the Red Sea region (JJA).

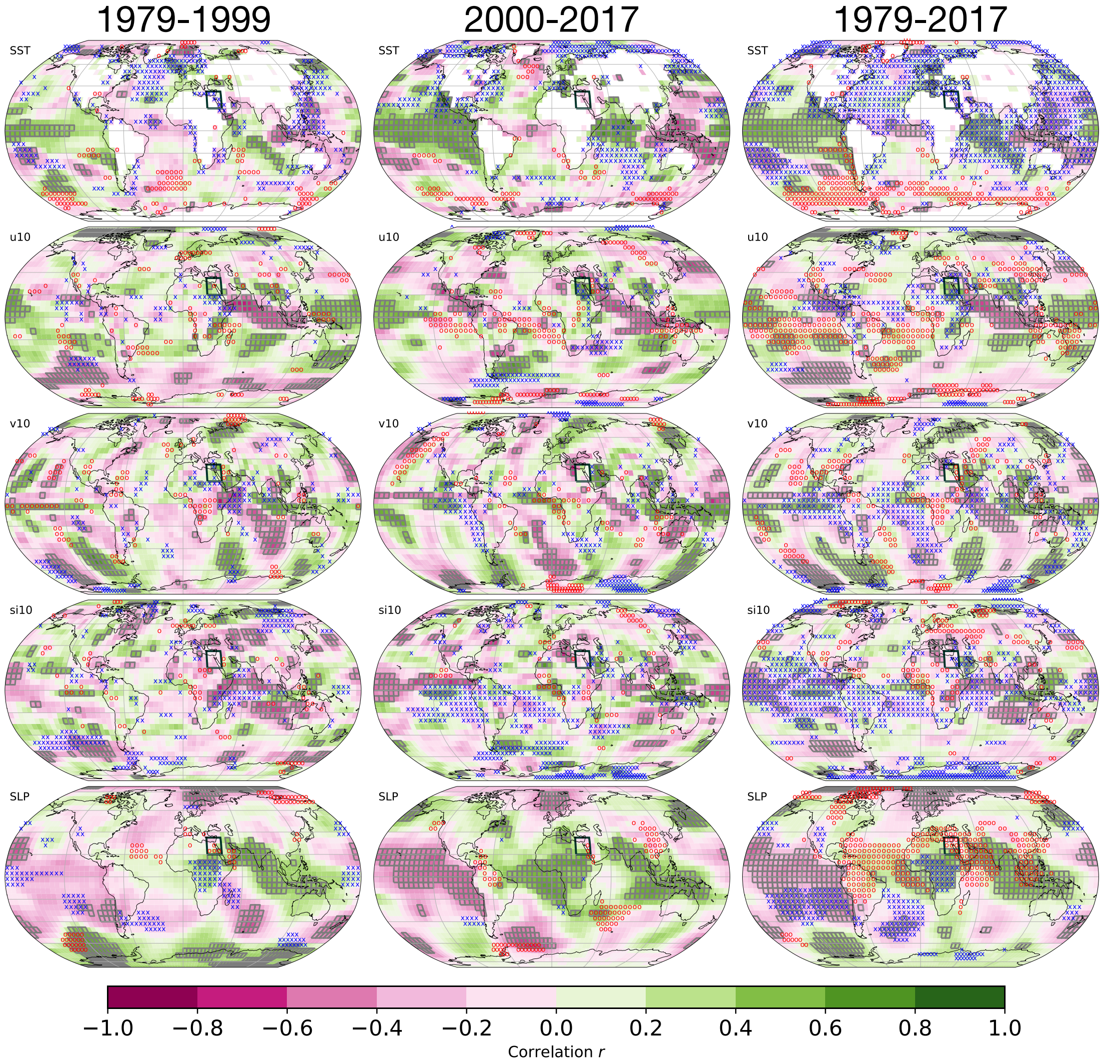

Figure S15: As for Fig. 4.4, for the Red Sea region (SON).

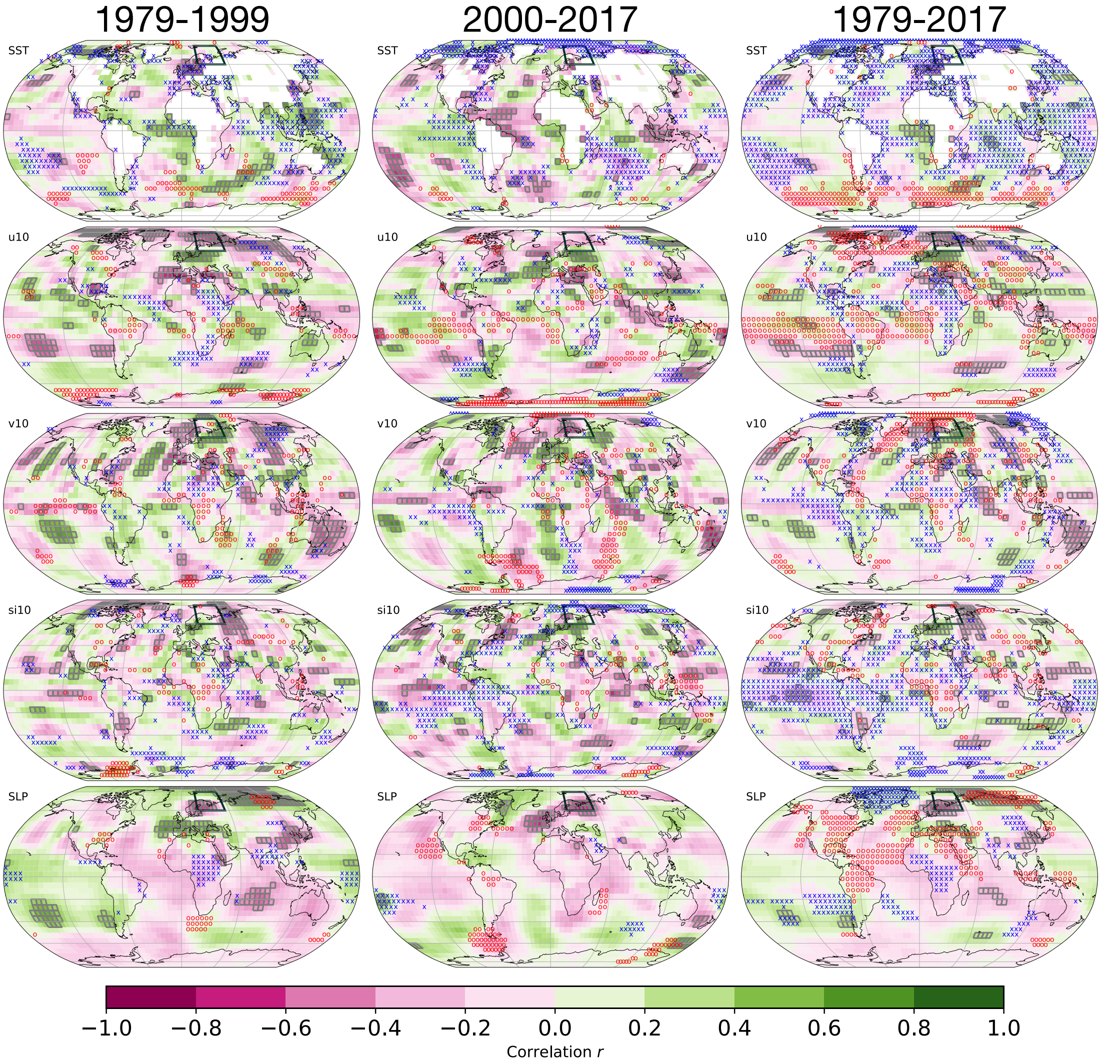

Figure S16: As for Fig. 4.4, for Scandinavia (JJA).

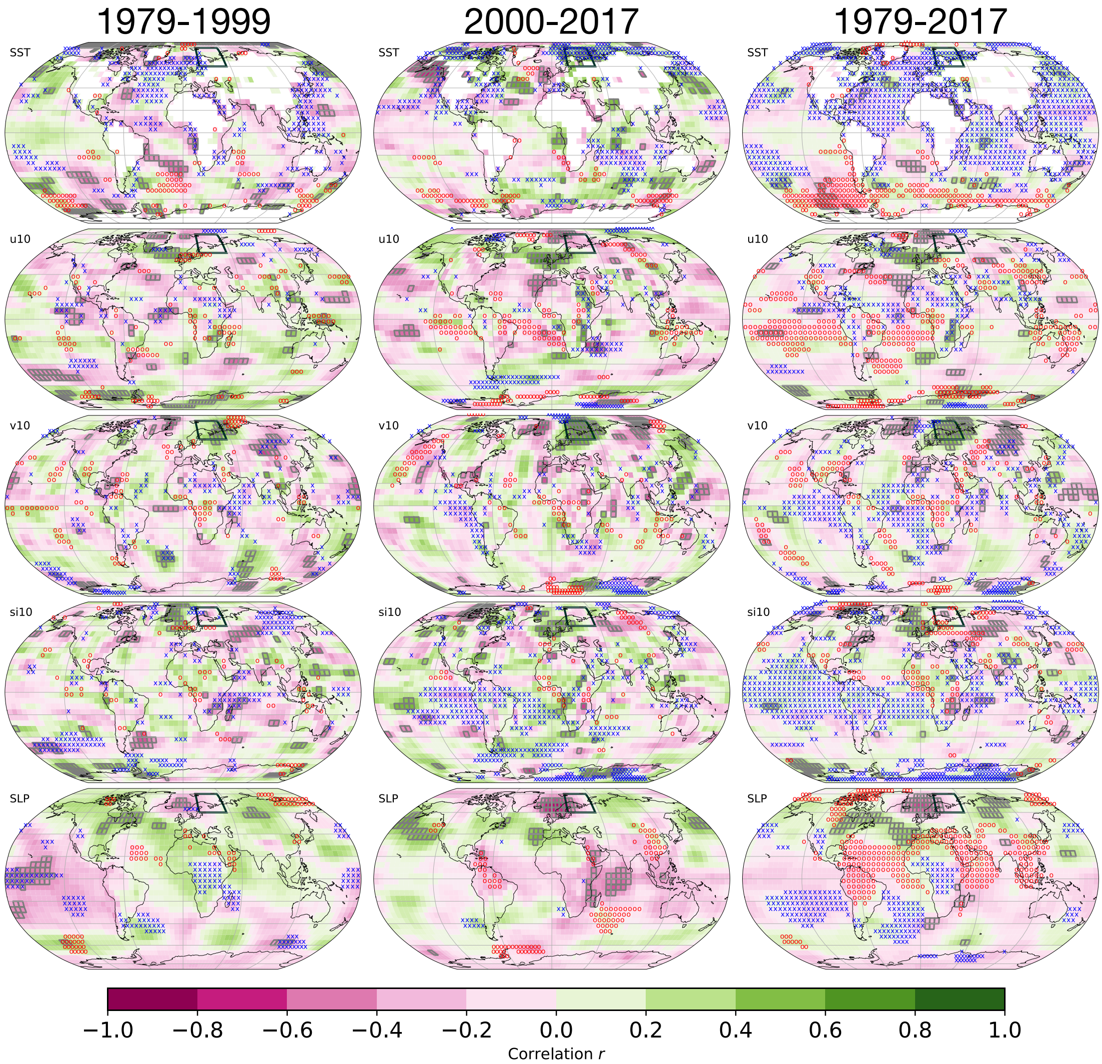

Figure S17: As for Fig. 4.4, for Scandinavia (SON).

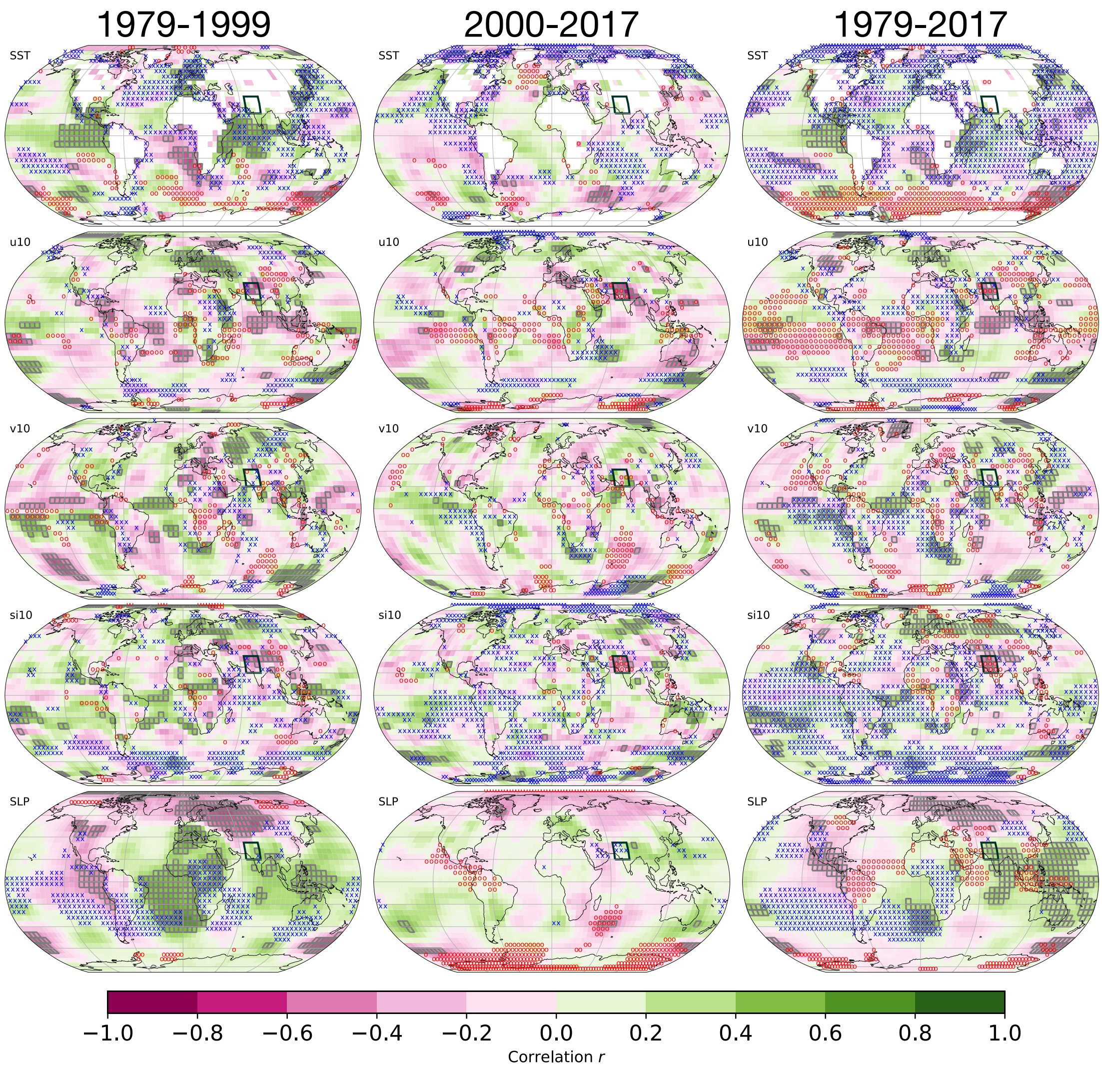

Figure S18: As for Fig. 4.4, for northwestern India (annual).

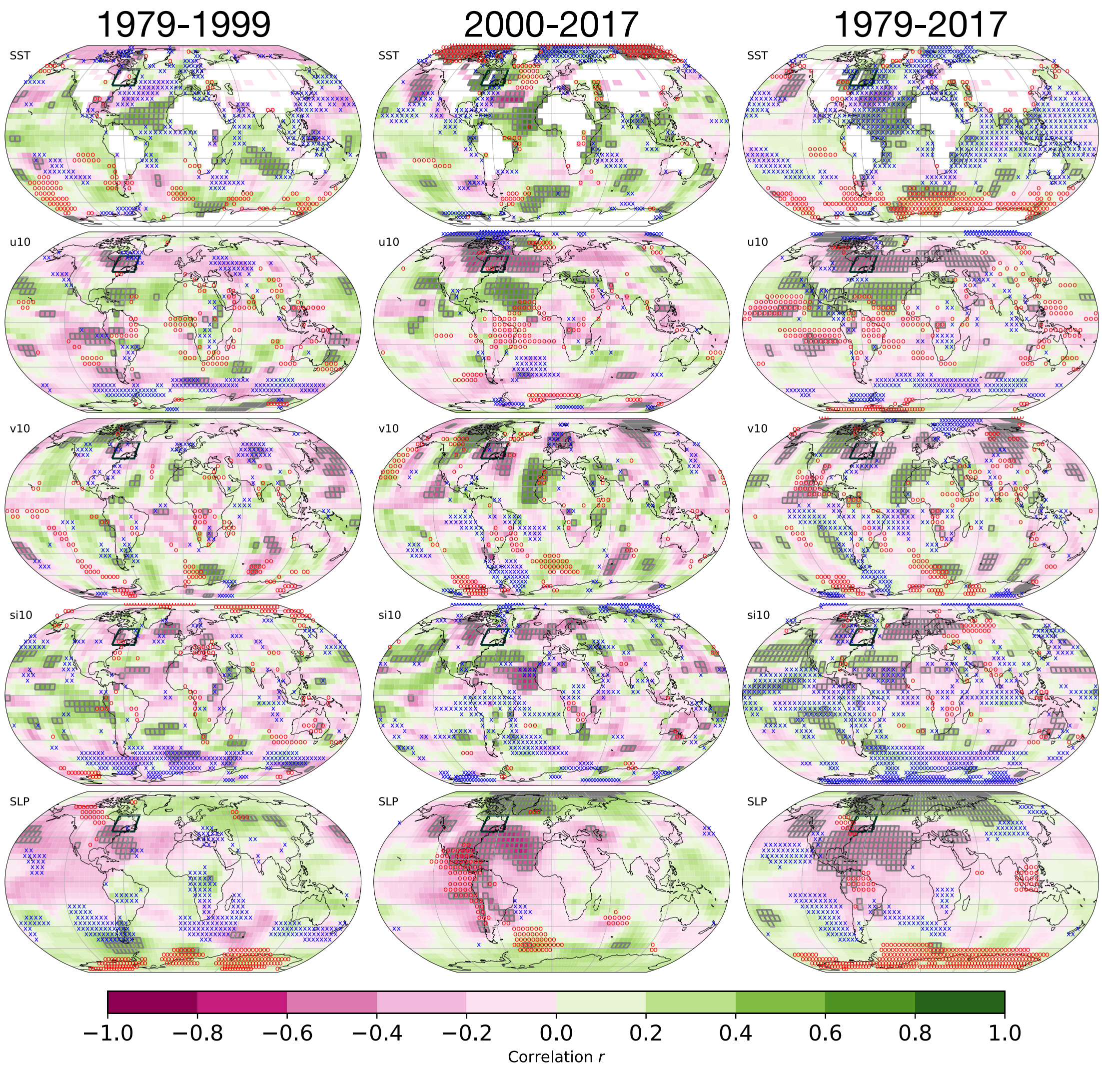

Figure S19: As for Fig. 4.4, for eastern Canada (DJF).